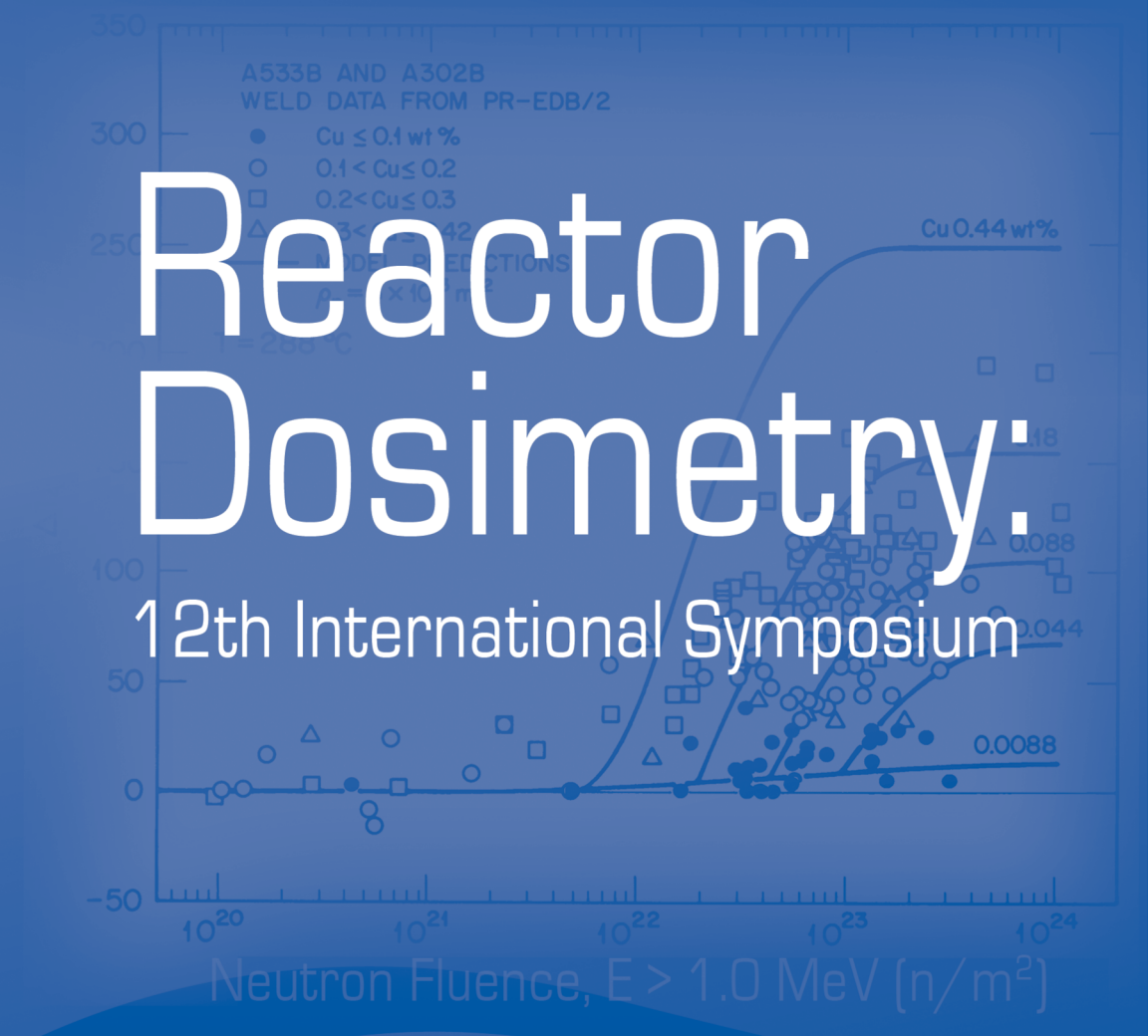

Reactor Dosimetry:

12th International Symposium

STP 1490

Editors:
David W. Vehar
David M. Gilliam
James M. Adams

ASTM INTERNATIONAL
Standards Worldwide

STP 1490

Reactor Dosimetry

12th International Symposium

David W. Vehar,
David G. Gilliam
and
James M. Adams, editors

ASTM Stock Number: STP1490

ASTM
100 Barr Harbor Drive
PO Box C700
West Conshohocken, PA 19428-2959

Printed in the U.S.A.

Library of Congress Cataloging-in-Publication Data

Reactor Dosimetry: 12th Volume / D. W. Vehar…(et al).
p. cm.
"ASTM Stock Number: STP 1490"
Includes Bibliographical references and index
ISBN: 978-0-8031-3412
Nuclear reactors-Materials-Effect of radiation on—Congresses. 2. Radiation Dosimetry-Congresses. I. Vehar, D. W. (David W.) II. International Symposium On Reactor Dosimetry (12th Volume: 2005: Gatlinburg, TN)

Peer Review Policy

Each paper published in this volume was evaluated by two peer reviewers and at least one editor. The authors addressed all of the reviewers' comments to the satisfaction of both the technical editor(s) and the ASTM International Committee on Publications.

The quality of the papers in this publication reflects not only the obvious efforts of the authors and the technical editor(s), but also the work of the peer reviewers. In keeping with long-standing publication practices, ASTM International maintains the anonymity of the peer reviewers. The ASTM International Committee on Publications acknowledges with appreciation their dedication and contribution of time and effort on behalf of ASTM International.

Printed in the USA
December, 2007

Foreword

The Twelfth International Symposium on Reactor Dosimetry was held in Gatlinburg, Tennessee, USA, May 8–13, 2005. This Symposium was jointly sponsored by ASTM International, the European Working Group on Reactor Dosimetry (EWGRD), and the Atomic Energy Society of Japan (AESJ). It was organized by ASTM Committee E10 on Nuclear Technology and Applications and the EWGRD. The Local Organizing Committee was chaired by Douglas L. Selby of Oak Ridge National Laboratory (ORNL). Co-sponsors were Sandia National Laboratory, UT-Battelle (ORNL), ThermoElectron/RMD, Canberra Industries, the National Institute of Standards and Technology, and the U.S. Department of Energy.

Contents

BENCHMARKS AND INTERCOMPARISONS

CROSS SECTIONS AND NUCLEAR DATA; DAMAGE CORRELATIONS

IN MEMORIAM

Masaharu Nakazawa, 1944–2006

We lost our friend and colleague Prof. Masaharu Nakazawa, who died of heart failure on March 10, 2006. From 1967 until his death, Masaharu worked at Faculty of Engineering, the University of Tokyo, where he progressed from research associate to become Director of Research Center for Nuclear Science and Technology. For nearly 40 years, he had contributed to the establishment of nuclear engineering in Japan as one of the leaders in radiation measurement and dosimetry. His special expertise and accomplishments were in the neutron dosimetry, in particular, unfolding neutron energy spectra from foil activation detector and 3He proportional counter measurements, in the application of lasers and optical fibers to radiation measurement and reactor vessel surveillance, and in the development of superconducting X-ray detectors. Recently, he was also very enthusiastic about the spread of advanced medical and diagnostic applications of radiation in Japan.

Masaharu was well known to participants of the International Reactor Dosimetry Symposia. He was actively involved in the organization of the 10th Symposium held in Osaka in 1999, and also was a member of the program committee of the 11th Symposium in Brussels in 2002. He was always loved and respected by his colleagues and students in Japan and elsewhere for his originality, foresight, good humor and constant dedication to research and education.

Francis Kam, 1929–2005

Francis Kam, known to many of us as Frank, died November 15, 2005 at age 76. He was a researcher at Oak Ridge National Laboratory for 33 years starting in 1961. During that time period, he was deeply involved in and made significant contributions to ASTM E10 and the field of nuclear dosimetry. Frank was involved in the development, documentation, and application of several computer codes used for neutron transport analysis, including the O5R Monte Carlo Code. His publication list in the area of dosimetry included 19 journal articles, 4 book chapters and an assortment of conference publications and reports. Although retired, he was able to attend the 12th International Symposium on Reactor Dosimetry in May of 2005 where he was recognized for his lifetime achievements. Frank is clearly one of those people where it can honestly be said that he made a difference and he will be missed by many.

Harry Farrar IV, 1935–2007

Harry Farrar IV will be long remembered for his contributions to ASTM and to many of the past symposia on reactor dosimetry. Born in England, he emigrated at an early age with his family to Canada. After receiving his PhD from McMaster University, he joined Rockwell International, where he developed a helium mass spectrometer system that formed the basis for a number of dosimetry applications. These include the Helium Accumulation Fluence Monitor, which received an IR-100 award in 1978. Harry participated in early efforts to resolve discrepancies in neutron fluence measurements, starting with the Inter-Laboratory Reaction Rate Program in the early 1970s.

Harry was a contributor to the First ASTM-Euratom Symposium on Reactor Dosimetry in 1975, and continued to serve this symposium series in various capacities, including several terms as

chairman. Harry also initiated and chaired several ASTM international workshops on radiation dosimetry. In 1984, Harry formed a task group "Radiation Dosimetry for Food Processing", which was later expanded to include dosimetry standards for all forms of radiation processing. In 1988 this group became ASTM E10.01, "Dosimetry for Radiation Processing." Under Harry's leadership, it became one of the most successful activities of Committee E10. He was also instrumental in a pioneering effort to have these ASTM standards accepted internationally as ISO standards. Harry has held several ASTM Committee E10 offices, including two terms as chairman. His contributions have been recognized with numerous E10 awards, as well as the ASTM Award-of-Merit in 1992.

Harry was a world traveler, an award-winning amateur photographer, and a man of many other accomplishments. He had an uncanny knack for making friends and creating a warm environment wherever he went. Harry led an amazing life and shared it with all of us.

Overview

The papers in this volume were presented at the Twelfth International Symposium on Reactor Dosimetry, and subsequently published in the Journal of ASTM International (JAI) following peer review. Eighty-seven participants from twenty countries attended the meeting.

Several trends are evident in the papers presented at this symposium. As operating nuclear power reactors have aged and continue to operate on extended operating licenses, new pressure vessel surveillance techniques have been required. In many cases, the original loadings of metallurgical surveillance specimens and their dosimeters have been completely used up. Innovative retrospective dosimetric techniques based on stable isotope transmutation or in-vessel gamma spectrometry are being developed and applied. Eastern European PWR's (especially those of the VVER-440 type) continue to have greater concerns about steel embrittlement, because of higher neutron radiation exposures than most Western European and US reactors. Accordingly, broader dosimetry studies are being made on the VVER reactors through retrospective dosimetry, ex-vessel dosimetry, and careful re-analysis of previously reported data. Vastly improved computer capabilities, international cooperation in nuclear data evaluations, maturation of analytic and adjustment software, and new data from "autopsies" of old decommissioned reactors have all contributed to greater reliability of reactor performance and materials calculations. Throughout the industry and regulatory bodies, there appears to be greater reliance on calculations in place of traditional methods of dosimetry and associated quality assurance.

The opening and keynote session included two papers, one on the very large new Olkiluoto 3 reactor under construction in Finland and one on the new Spallation Neutron Source under construction at Oak Ridge National Laboratory, the host laboratory.

There were seven plenary oral sessions of five or six papers each, and two poster sessions of about twenty-four papers each. In addition, there were two tutorials in parallel, and three workshop sessions with two parallel topics during each session.

The tutorials focused on materials science—one on radiation effects on materials, and one on materials science experiments based on neutron scattering.

Both the oral and poster sessions included the topics Power Reactor Surveillance; Test Reactors, Accelerators, and Advanced Systems; Benchmarks and Intercomparisons; Cross Sections, Nuclear Data, and Damage Correlations; Transport Calculations; Adjustment Methods and Reactor Dosimetry; and Experimental Techniques. In these proceedings, no distinction is made between the poster and oral papers, other than the notation of the awards for best poster papers.

The workshop sessions emphasized a discussion format rather than formal presentations. Workshop topics were LWR Surveillance and Retrospective Dosimetry; Dosimetry for Irradiation Facilities at Test and Research Reactors; Cross-Section Files and Uncertainties; Fusion and High Energy Neutrons; Adjustment Methods and Uncertainties; and Radiation Damage Correlations.

Best poster-paper awards were presented to Desislava Kirilova for "Validation of the Neutron Fluence on the VVER-440 RPV Support Structure," *K. Ilieva, S. Belousov, D. Kirilova, B. Petrov, E. Polk*, and to Mike Luker for " Application of a Silicon Calorimeter in Fast Burst Reactors," *S. M. Luker, K. R. DePriest, P. J. Griffin, D. B. King, G. E. Naranjo, A. J. Suo-Anttila*.

David W. Vehar
Sandia National Laboratories
Albuquerque, NM

David G. Gilliam
National Institute of Standards and Technology
Gaithersburg, MD

James M. Adams
National Institute of Standards and Technology
Gaithersburg, MD

ORGANIZING COMMITTEE

Symposium Organizing Committee Officers

David W. Vehar, Symposium Chair, SNL
David M. Gilliam, Program Committee Chair, NIST
James M. Adams, Symposium Secretary, NIST
Mary Helen Sparks, Workshop Sessions Chair, WSMR
Douglas L. Selby, Local Organizing Committee Chair, ORNL
Patrick J. Griffin, Chairman, ASTM Subcommittee E10.05, SNL
Roger E. Stoller, Chairman ASTM Committee E10, ORNL
Pierre D'hondt, EWGRD Symposium Chairman, SCK·CEN
Jan Wagemans, EWGRD Scientific Secretary, SCK·CEN
Willem Voorbraak, EWGRD Workshop Chairman, NRG

Local Organizing Committee

Tony Gabriel
Louis Mansur
Larry Miller
Randy Nanstad
Igor Remec

Program Committee and Session Chairs

ASTM
Allan Carlson
Arnold Fero
Mike Flanders
Larry Greenwood
Alireza Haghighat
Ayman Hawari
Craig Heimbach
E. Parvin Lippincott
Louis Mansur
Igor Remec
Frank H. Ruddy
Wes Sallee
James Stubbins
Jehudah Wagschal
John G. Williams

EWGRD
Hamid Aït Abderrahim
Alain Alberman
Antonio Ballesteros
Bertram Boehmer
Milan Brumovský
Ana Fernandes
Josef Hógel
Krassimira Ilieva
Milan Marek
Karl Noack
Henk Nolthenius
Bohumil Ošmera
Rainer Salomaa
Tom Serén
Dean Thornton
Willem Voorbraak
Sergei Zaritsky
Eva Zsolnay

SPONSORS

The organizers wish to acknowledge the support of their sponsors:
- Sandia National Laboratories
- Thermo Electron/RMP
- UT-Battelle (Oak Ridge National Laboratory)
- Canberra Industries
- National Institute of Standards and Technology
- U.S. Department of Energy

WORKSHOP SUMMARIES

Mary Helen Sparks (White Sands Missile Range), ASTM Workshops Chair
Wim Voorbraak (ECN, Petten), EWGRD Workshops Co-Chair

Six workshops were held during the Symposium with the intent of providing an informal exchange of information on a selected variety of topics. The topics were approved by EWGRD and ASTM committees in advance of the meeting. A concerted effort was made to schedule concurrent workshops to allow maximum participation.

The number of workshops was reduced to six with two concurrent meetings on three consecutive days. Two co-chairmen, one each from ASTM and EWGRD, organized each workshop, defined the scope of the meeting and kept the meetings to a workshop atmosphere rather than additional oral session.

The attendance and participation at the workshops was most rewarding. The summaries of each workshop follow.

I-A. LWR SURVEILLANCE AND RETROSPECTIVE DOSIMETRY
Chaired by: E. P. Lippincott and S. Zaritsky

The workshop on LWR Surveillance and Retrospective Dosimetry was attended by 30 participants representing 13 countries. The workshop encompassed discussions on three major topics: surveillance dosimetry, fluence determination, and retrospective dosimetry measurements.

The importance of surveillance dosimetry measurements was emphasized by many of the participants. Of special importance are the dosimetry measurement programs for the VVER reactors. The measurement needs were summarized by J. Hogel as follows:

VVER 440

More (as good as possible) information is needed about the radiation exposure of RPV materials for the lifetime extension of VVER 440 reactors. Reasons for this are:

- The neutron flux during irradiation is significantly higher than for western PWRs, as well as for the VVER 1000 vessels.
- The standard surveillance program (SP) was not good enough.

Experimental tools include:

- New extended SP with well designed neutron dosimetry enabling the neutron fluence in each specimen to be determined. The large lead factor in these plants allows enough time to obtain the necessary specimen exposure levels.
- Continuous ex-vessel monitoring will provide necessary results for the SP dosimetry evaluation.
- Measurement of Nb activation in scraping samples from the inner cladding of the RPV provides evaluation of the neutron fluence for the whole time of operation. Combined with the ex-vessel dosimetry, the attenuation factor through the vessel wall could be obtained.

VVER 1000

All new units are equipped with the new type of surveillance program (e.g. Temelin and Kola 3). The use of reconstituted surveillance specimens (which occupy 1/4 of the space of regular specimens) enables a large number to be irradiated. It is also possible to use "guest" reactors for the irradiation of materials from the older generations of power plants.

B. Osmera added comments on the role of benchmark experiments (such as mock-up experiments in the LR-0 reactor) for decreasing systematic uncertainties. The experiments on VVER 440 and VVER 1000 mock-ups can significantly improve the reliability of surveillance programs and pressure vessel dosimetry results.

Discussion was also held on the need for surveillance dosimetry in the fourth-generation reactors to be built in the future. It was concluded that surveillance programs will still be needed for these reactors to address future questions that may arise. In addition, new requirements may arise for measurements in other environments such as high intensity spallation sources. Additional data may be needed to establish accurate methods for assessment of fluence of higher energy neutrons. Future needs may also include more accurate fluence determinations at reactor locations not presently deemed important for damage considerations, especially to satisfy life extension requirements.

Fluence determination in high flux regions in reactors appears to be in good shape, with estimated uncertainties of 15% or better. Some improvement in fluence assessment may result when systematic discrepancies are investigated in detail. For example, new thickness measurements of reactor components using radiography or other measurement techniques may help resolve differences from plant to plant between measurement and calculation of reactor cavity flux levels. This could reduce the spread in C/M ratios that Stan Anderson indicated presently has a standard deviation of 7.5% for Westinghouse PWRs.

The discussion on retrospective dosimetry centered on its usefulness for determination of exposure in reactor geometries where no measurement data otherwise exist. The limitations of retrospective dosimetry are important. These include the small number of reactions available for measurement and the lack of accurate characterization of the materials to be analyzed. In some cases the uncertainty in the position of the samples adds a significant error contribution.

In the case of some VVER surveillance capsules, retrospective dosimetry using samples from specimens has made a significant reduction in the fluence uncertainty. S. Zaritsky mentioned the new proposal for using diamond detectors for neutron fluence retrodosimetry of VVER 1000 surveillance specimens. These detectors are located in each surveillance container as irradiation temperature monitors, and after corresponding calibration can also be used as fluence monitors by precise measurement of the extension of the diamond crystal lattice caused by the irradiation. Since the diamond integrates the fluence over the entire irradiation history, information about the global and local power history is not required. Thus, the diamond detectors have the potential to be a useful alternative fluence integration tool.

I-B. DOSIMETRY FOR IRRADIATION FACILITIES AT TEST AND RESEARCH REACTORS
Chaired by: A. Hawari and W. Voorbraak

The workshop was attended by 27 participants. After an introduction round, where everyone could express his/her interest, several topics were discussed in a good atmosphere. All participants were willing to exchange experience with each other, contacts were made for further discussions after the workshop. Discussion centered around the following topics:

Active (on-line) monitoring: SNL is experienced in various counting techniques for neutrons as well as gamma rays, e.g. self powered neutron detectors (SPNDs), fission chambers, ionization chambers, diamond photo conducting detectors (PCD) and silicon PIN diodes (see paper 2.01). CEN Saclay has a lot of experience with calorimeters based on graphite and with SPNDs based on Ag and Rh. Today there are few limitations on the availability of good electronic equipment. The challenge is the discrimination between the signal component in a mixed field in which one is interested and other components that may contribute as much as 70%. There is a need to distinguish between thermal and epithermal neutrons. There are also other irradiation-time-dependent effects, such as activation of the detector and noise generated in signal cables. There are very few suitable benchmark fields in which to test the detectors.

High temperature detectors: There are many activation detectors that can be used between 1000 and 1500 °C, needed for use in Generation IV (e.g., the VHTR) and space reactor applications. NRG has had good experience up to 1100 °C with encapsulation in quartz. The quartz tube fixed the volume of the detector during melting. Such detectors will be measured after irradiation inside the quartz tube. Quartz may be brittle in certain atmospheres. In case of doubt, use extra iron encapsulation or consult a specialist in the application of quartz. Helium Accumulated Fluence Monitors/detectors (HAFM) may be an alternative for temperatures close to 1000 °C.

Determination of gamma-ray spectra, e.g. from a reactor beam may be done by measuring a small part of the beam with a Ge detector using a pencil collimator or a part of the beam that is deflected. The opinion was expressed that this will not be easy, as modern electronics will have serious problems with count rates $>$60k/sec. An extra barrier directly after the beam exit could help. Dependence on gamma ray energy could be investigated using computer (e.g., MCNP) simulations.

There is a growing concern for the continued operation of small reactors. Possible uses include biological applications such as Boron Neutron Capture Therapy, and use of activation analysis as a forensic tool. For example, NIST exposes paintings for the Smithsonian Museum. After exposure, different photographic films successively cover the painting. These films absorb gamma rays from the radiated painting, starting with the reaction products with the shortest half-lives. This provides information on the images from deeper layers, and therefore about the way that the painting has been created. NRG Petten has also applied this technique for a few old Dutch paintings. In addition to the classic approach of neutron radiography based on Gd and photographic film, CCD devices and ZnS screen are being used to digitize the images.

Reactors in the US are beginning to offer on-line reactor laboratory courses. An extensive program has been started between North Carolina State University and the University of Tennessee in this area. Information can be distributed in real time via the internet during an exercise, including reactor parameters such as power, temperature, control rod positions, etc., and experimental results, such as neutron images.

Computer codes such as MCNP, DORT and TORT are used to perform calculations prior to new experiments and changes in reactor cores. Each code has its advantages and disadvantages related to precision and computer time. Fuel burn-up is taken into account as part of the core modeling. The consequences of conversion to low enriched uranium fueled reactors have also been discussed.

II-A. CROSS-SECTION FILES AND UNCERTAINTIES
Chaired by: P. J. Griffin and E. Zsolnay

A major topic of discussion was the release of the IRDF-2002 dosimetry library. This library was included in the symposium distribution to all participants along with the draft papers that were presented at this symposium. This new dosimetry cross section library was the result of a request by the community at the workshop during the 10th ISRD. The workshop participants welcomed this library release and expressed their thanks to the IAEA. Many participants had already used the library and reported on the experiences. The following observations were made:

- A problem was observed with the MN55G reaction covariance. The problem was traced to the LB=8 component of the covariance that resulted in a very large uncertainty in one energy bin. The IAEA was requested to resolve the issue by confirming the evaluator's intent to have this large of an uncertainty in the one energy group, correct the problem if it was the result of the reversal of two numbers, or provide guidance to the community on the recommended approach to treating this covariance in spectrum adjustments.
- There was a request to add cross sections to the library required to treat parasitic burnup reactions that might interfere with the interpretation of the Ag, Nb, and Co (n,γ) dosimetry reactions.
- There was a request to the general community and, in particular, to the national standards laboratories, to gather additional validation data for reactions in the ^{252}Cf spontaneous fission standard benchmark field. The experiment data is required to validate the dosimetry cross sections. Data was also requested for the ^{235}U reference benchmark field.
- A request was made to add carbon dpa to the damage cross sections in the IRDF-2002 library.
- A request was made to add proper covariance files for the ^{197}Au(n,γ) and ^{235}U(n,f) reference benchmark reactions. These data are expected to be available from the international cross section standards community within the year. The request was to issue a revision to the IRDF-2002 library as soon as the data became available.
- Several reactions in the library only have a diagonal covariance matrix. This suggests that the covariance was not properly evaluated. Requests were made to do a re-evaluation for these reactions.
- A request was made for some new evaluations. These requests will be transmitted to the WPEC. Specific requests were for a new evaluation of the MN55G reaction and the ^{nat}Cd absorption cross section in the resonance region.
- Several cases were cited where the IRDF-2002 library appears to have resonance integrals with large deviations from the recommended experimental values. An evaluation of the resonance parameters and a reconciliation of the recommendations was requested for these reactions.
- The community requested the IRDF-2002 library to add (γ,f) photofission and (γ,γ') photonuclear cross sections that might produce the same products as dosimetry reactions. Even if these reactions did not have covariance matrices, the use of standard recom-

mended cross sections would benefit the community in bounding the importance of the interference reactions.
- Additional gas production cross sections were also requested.
- The publication of the benchmark field validation testing of the library was requested. These data are desired for use in simultaneous field spectrum adjustments, e.g. in the LEPRICON methodology.
- Requests were made for the spectrum covariance in the reference and validation field testing. This request also highlighted the problem in including such data within the framework of the existing ENDF-6 file format. This issue will be pursued with the CSWEG community.

The discussion revealed that many users had problems in using the new data in their spectrum adjustment codes due to the lack of data processing tools and difficulty in format conversions. A request was made to also provide the library in a processed form that would be compatible with the commonly used spectrum adjustment codes. The requests included support for LSL, STAYS'L, SAND-II, and text format data. The text format should include full covariance matrices in order to facilitate ease of use with a variety of processing methods. The desire was expressed to have the nuclear data file as well as the cross sections and covariance matrices available in more human-readable format. Volunteers were found to provide conversions of the exiting library into these formats. The community will request that the IAEA post these format conversions on the IRDF-2002 web site so that the whole community could more easily benefit from the data.

II-B. FUSION AND HIGH ENERGY NEUTRONS
Chaired by: L. Greenwood and P. D'hondt

There was only one paper in this symposium directly related to the topic of fusion dosimetry, although irradiations of fusion materials are frequently performed in fission reactors. Techniques for dosimetry in simulated fusion reactor fields are very similar to those employed in fission reactors, with the main difference being the higher energy neutrons near 14 MeV. There was agreement that cross sections are generally not so well known in the 10-13 MeV energy range, as has been noted in cross section evaluations as well as experiments, such as the work with MUSE by M. Plaschy, et al. Some improvement is needed in this energy region to improve the accuracy of fusion dosimetry and radiation damage calculations.

For spallation neutron sources such as the ADS (Accelerator Driven Systems) in Europe or SNS (Spallation Neutron Source) in the US, more accelerator measurements are needed to improve dosimetry cross sections and radiation damage cross sections. In Europe, two programs have been performed for $E > 20$ MeV in the framework of the EC (European Commission), HINDAS and n-TOF programs. The results of these programs will be made available in the JEF files in the future. There were several papers at the conference from the US, all connected with LAMPF or SNS. A paper by F. Gallmeier, et al, discussed the extension of neutronics techniques up to GeV energies. A paper by P. Ferguson, et al, showed the development of radiation damage and gas production cross sections to GeV energies. Such efforts in the United States are somewhat limited at present, since the main application of spallation neutron sources is for cold neutrons for neutron scattering, and the SNS currently has no provision for irradiation of samples close to the target. Neutron experiments conducted close to spallation targets, but not directly in the beam, have neutron spectra that resemble fast reactors with the addition of a high energy tail up to the beam energy. Generally, neutrons above 20 MeV comprise only about 10% of such

spectra. However, considerably more work is needed to expand the database of high energy cross sections for dosimetry, radiation damage, and gas production and other transmutation.

There was some discussion of whether there is any information available on gamma production at higher neutron energies and whether such data are needed for spallation or space applications. Some work in this area has been reported at previous symposia; however, the status of this work is not currently known. Space programs are thought to have similar nuclear data needs as for spallation sources regarding higher energy neutrons that may be present from cosmic rays. Much of the charged particle data currently used by spallation neutron sources was originally developed for astrophysical applications.

Finally, there was a discussion of active detectors that can be used at higher energies and whether such detectors could be used in higher temperature applications. F. Ruddy mentioned that SiC detectors are being tested for applications at higher neutron energies.

The workshop was attended by 15 participants.

III-A. ADJUSTMENT METHODS AND UNCERTAINTIES
Chaired by: W. Sallee and T. Serén

The current state of the technology and methodologies were discussed in some detail. Old and new codes were discussed with their liabilities and strengths. There are some promising new methods becoming available (a couple of which were discussed in papers presented at this meeting).

The addition of the IRDF 2002 library is very much appreciated by this community as these data underpin all of the adjustment methodologies.

Several key issues remain for most (not all) users. One is how to address the use of covers. This issue was discussed extensively and two approaches were mentioned on how to handle the uncertainty and covariance data correctly. However, no movement was made toward programmatically treating this persistent problem. Most users still use only simple exponential attenuation. T. Serén mentioned a code he is developing for adding degrees of anisotropy to this simplistic approach. This is currently under test and is only available as a replacement for the LSL-M2 "COVER" auxiliary code. It addresses only the cross section data, not how to adjust the attendant covariance data. The strictly correct procedure would be to model (e.g. with MCNP) the situations with and without covers as different, but highly correlated, neutron fields. This would also address downscatter into resonance energies, which occasionally leads to *higher* reaction rates with covers than without. Some problems related to covers also occur when treating self-shielding effects.

Several suggestions for simplifying the input streams for the various codes were made but not well received. There could be particular benefit in the development of a standard input format. However, it was not as clear what that actually would mean or how that might actually be accomplished.

The other major topic of discussion for the workshop was the issue of uncertainty and covariance information in transport calculations. The right way to do it was discussed, as were several "approximations." M. Plaschy described his use of repeated perturbations to generate uncertainty

information. It was also pointed out that covariance matrices are being provided in the IRDF-2002 files for some standard and evaluated fields. These data were deemed better by most of the participants than the currently recommended method of fabricating a matrix when one is not available (e.g. using algorithms recommended in at least two ASTM standards). It would be highly desirable to have covariances available for a much larger collection of different neutron fields than those treated in the LEPRICON system. It was suggested that this topic or a subset that involves perturbation or sensitivity analysis be considered for a tutorial at a future meeting.

The final topic of discussion was correctly collapsing the IDRF 2002 cross sections to a smaller group structure. There appears to be differences between the FLXPRO and X333 processing codes when applied to the same data [specifically ^{58}Fe(n,γ), see paper A.14 by Serén & Wasastjerna]. The two codes have also been tested for ^{54}Fe(n,p) and ^{58}Ni(n,p), but in those cases the results agreed well. Obviously there can be pitfalls when using the processing codes as "black boxes" without further checking. The largest discrepancies between the two codes have been traced to incorrect use of keywords in FLXPRO (*I, *D and *P for integral, differential and point spectra, *I being the default). However, subtle differences still remain, possibly traceable to the use of single precision in the codes.

III-B. RADIATION DAMAGE CORRELATIONS
Chaired by: L. K. Mansur and D. A. Thornton

The workshop was attended by 23 participants who engaged in a lively and wide-ranging discussion on damage radiation effects and the correlation against exposure parameters. A brief introduction, given by Lou Mansur, proposed the objectives of the workshop and gave initial points to help focus the discussion. The participants introduced themselves and stated their interests, which included damage modeling and correlation, gamma radiation induced damage, electronic materials, determination of life-time exposure, computation transport calculations, reactor internals and prediction of life-limiting effects, and fission/fusion and spallation related applications.

The discussion began by considering the circumstances in which gamma radiation induced displacements might give rise to significant levels of damage. Lou Mansur reviewed the experience from HFIR in which a ratio of hard gamma radiation fluence to fast neutron fluence of order 10^4 was required for gamma induced damage to dominate the production of atomic displacements. Analyses describing the physical bases of this determination are described in reference [1]. As a corollary to this, analysts should begin to consider gamma radiation effects at hard gamma to fast neutron fluence ratios of order 10^2. Larry Greenwood cited work by Baumann on displacement cross-sections of gamma rays [2] and noted that the NRC had commissioned a study on the significance of gamma radiation induced damage in other reactors. It had concluded that displacements produced by gamma rays would not be significant in current LWR designs.

The discussion moved on to consider damage mechanisms within electrical and electronic materials. It was noted that the fluence ranges relevant to these effects are very much less than those considered in the assessment of structural materials. It is necessary to take account of ionization/excitation both by neutrons and gamma radiation in addition to displacement damage. Dean Thornton drew an analogy with graphite in which irradiation induces both corrosion, via ionization, and dimensional changes, via neutron damage. It was queried whether there is any prospect for the development of a coherent unified approach to correlation of these effects against ion-

ization and displacement damage. Although special circumstances exist where this may be achieved, any broad based approach would prove very challenging.

Alain Alberman raised the question of new materials for Generation IV reactors. Such materials may include ceramics and metallic alloys for high temperature performance. It was agreed that it would be necessary to address the effects of ionization damage in ceramic materials, in addition to displacement damage.

Larry Greenwood reminded the participants that transmutation reactions induced by thermal neutrons should not be overlooked. Lou Mansur drew a parallel with the formation of transmutation products caused by high energy protons in the spallation targets of high energy proton accelerators. In both cases transmutation production can be substantially higher than what is typical for fast reactor neutrons.

Roger Stoller confirmed that there is now significant evidence for the existence of dose rate effects in pressure vessel steel embrittlement, and that analysts should take them into account. However, the magnitude of the effects is sometimes small if the dose rate range is not very large and may be influenced by the accumulated damage. An example of such a property is swelling, which is important to reactor internals. This property shows a clear dose rate effect where the temperature range at which maximum swelling occurs (for a given exposure) tends to shift depending on dose rate.

Displacement, gas production, and other transmutation cross-sections have been developed to the range of GeV for protons and neutrons, partially from measured cross-sections at low energies and calculated cross-sections at high energies. However, for spallation sources, it was felt that this range is only of primary importance for the target and that beyond the target, damage cross-sections below 20 MeV are more relevant.

At previous symposia, workshop participants have discussed the results of French experiments to determine most appropriate parameters for neutron exposure [3]. These have shown that use of dpa did not improve upon the correlation against fluence $>$1MeV. Participants continued to express surprise at this outcome. The potential role of thermal and epi-thermal neutron induced displacements within these experiments was discussed.

References

[1] L. K. Mansur and K. Farrell. “Mechanisms of radiation-induced degradation of reactor vessel materials,” J. Nucl. Materials, 244 (1997) 212-218.
[2] N. P. Baumann, *Proceedings of the 7th ASTM-Euratom Symposium on Reactor Dosimetry*, Strasbourg, France, 1990, pp 689-697.
[3] A. Albermain, H. Carcreff, G. Ermont, P. Soulant, D. Beretz, C. Pichon, C. Brillaud, “Neutron Spectrum Effect and Damage Analysis of Pressure Vessel Steels Irradiations”, *Proceedings of the 9th International Symposium on Reactor Dosimetry*, World Scientific (1996), pp. 524-534.

Journal of ASTM International, Vol. 3, No. 7
Paper ID JAI100359
Available online at www.astm.org

Katsumi Hayashi,[1] *Ryuuichi Tayama,*[1] *Yoshio Watanabe,*[1] *Tomomi Nakamura,*[1] *Isamu Kubota,*[2] *Haruhisa Hayashi,*[3] *Tadashi Yamasaki,*[3] *and Hideki Yuya*[3]

Feasibility Study on a Simple Method of Retrospective Neutron Dosimetry for Reactor Internals and Reactor Vessel

ABSTRACT: Nondestructive and simple retrospective dosimetry method was developed. Mercuric iodide or cadmium zinc telluride detector was used as a detector to measure ^{54}Mn, ^{58}Co, and ^{60}Co that were created in reactor internals and vessels. Detector is surrounded by tungsten collimator which shield background gamma rays and detect gamma rays from desired measuring point. Photopeak count rate of this detector were calculated using the MCNP-4C code. This response was calculated for each reactor internal geometry that was irradiated by unit neutron flux which energy spectrum was calculated by the TORT code. Neutron fluence is calculated using precalculated response, measuring time, decay time and reactor power history. We can also get Displacement per Atom (DPA), hydrogen and helium production simultaneously using neutron spectrum precalculated in reactor vessel. Because the time and cost of this method are much less than the sampling method, we can measure at many positions and even get a contour map.

KEYWORDS: retrospective dosimetry, nondestructive, reactor internals, reactor vessel, HgI_2, MCNP

Introduction

Accurate estimation on the neutron flux distribution in a reactor vessel is necessary to predict the material lifetime, maintenance dose, and radioactivity at decommissioning phase. For these purposes, precise calculation using the three-dimensional (3D) Sn method and Monte Carlo method [1] are preferable. Simultaneously, measured data is indispensable to assure the calculated results for the necessary position.

It is also an important point that sometimes we meet difficulties to prepare precise data for calculation, for example, burn-up data for each position of fuel rod is not available, or geometry around the necessary position is too complicated. In this occasion, measurement is the only way to get neutron flux information.

For this purpose, retrospective dosimetry [2] is a good approach for a plant in operation. Because the sampling of the metal and the following procedure of gamma or beta counting is time consuming and costly in retrospective dosimetry, the number of sampling should be limited. In this paper we present a simple method of retrospective neutron dosimetry that can be used at less time and cost.

Method

In ordinary retrospective dosimetry, it is usual to take a small amount of irradiated metal from structural material. We performed a feasibility study of retrospective dosimetry by direct gamma-ray counting of structural material.

As for the nuclide, ^{54}Mn(half life:312 days), ^{58}Co(70 days), and ^{60}Co(5.27 years) are chosen as main nuclides to be measured. ^{59}Fe(44 days) and ^{51}Cr(27 days) are also supplemental nuclide for checking of short irradiation range. ^{54}Mn and ^{58}Co are produced by fast neutron and ^{60}Co, ^{59}Fe and ^{51}Cr are by thermal neutron.

These nuclides are produced by the following reactions:

Manuscript received June 20, 2005; accepted for publication May 24, 2006; published online June 2006. Presented at ASTM Symposium on Reactor Dosimetry, 12th International Symposium on 8–13 May 2005 in Gatlinburg, TN; D. W. Vehar, D. M. Gilliam, and J. M. Adams, Guest Editors.

[1] Hitachi Ltd., 3-1-1, Saiwai-cho, Hitachi, Ibaraki, 317-8511, Japan.
[2] Hitachi Engineering Company, 3-2-1, Saiwai-cho, Hitachi, Ibaraki, 317-0073, Japan.
[3] Chubu Electric Power Co., Inc., 20-1, Kitasekiyama, Ohdaka-cho, Midori-ku, Nagoya, Aichi, 459-8522, Japan.

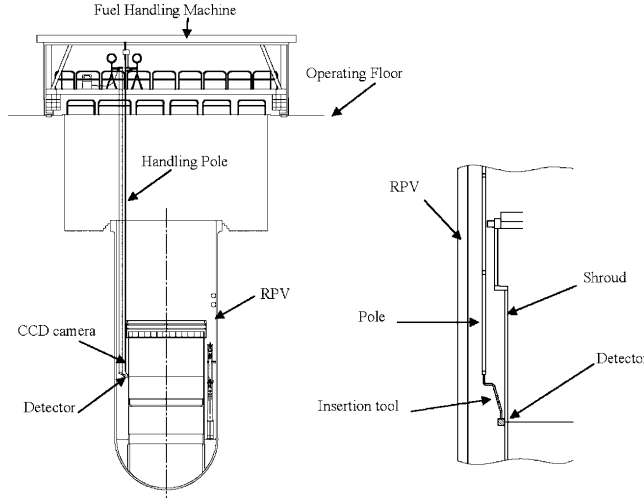

FIG. 1—*Concept of measuring method.*

$^{54}Fe(n,p)^{54}Mn$, $^{58}Ni(n,p)^{58}Co$, $^{59}Co(n,\gamma)^{60}Co$, $^{58}Fe(n,\gamma)^{59}Fe$, $^{50}Cr(n,\gamma)^{51}Cr$, $^{54}Fe(n,\gamma)^{51}Cr$

In this direct counting method, it is essential that initial composition is well known. Because iron and nickel are the main composition of steel and stainless steel, it is easy to find in mil-sheets. For a minor composition like cobalt, it is better to measure composition by energy-dispersive x-ray fluorescence spectrometer (EDXRF) analysis. If it is not available, it can be calibrated by a few simultaneous sampling measurements at the same point.

There are many items to be considered when adopting the direct gamma-ray counting method:

(1) Radionuclide distribution in thickness direction.
(2) Self-shielding of gamma ray produced inside the structural material.
(3) Background gamma ray from another structure around measurement point.
(4) Contribution of gamma ray from radioactive crud.

Although we should consider the items mentioned above, the direct counting method is preferable from the following point of view:

(1) Time and cost of measurement is reasonable.
(2) It is easy to measure many points, therefore, we can make a contour map.
(3) It is a nondestructive measurement; therefore, licensing procedure is not necessary.

Concept of Measurement Work

Simple direct gamma-ray counting of irradiated structural material was investigated. Figure 1 shows the concept of measurement work of the Boiling Water Reactor (BWR) shroud.

After removing all the fuel assembly from core to the spent fuel storage pool, we put the detector closer to the measuring point on the shroud or reactor pressure vessel using a handling pole. Although the possible area of measurement is limited because jet-pumps exist, an attached insertion tool at a tip of the handling pole helps to enlarge the measurement area. We can also put the detector closer to the inner surface of the shroud through the top guide. We can determine the detector position with the help of a television (TV) monitor camera.

Necessary Conditions for Measurement

It is necessary that measurement should start after the residual heat remove system (RHR) stops and reactor water is motionless because handling of the detector pole and TV camera in moving water is very

TABLE 1—*Assumed radioactivity for calculation.*

Nuclide	Radioactivity (Bq/g)
Cr-51	2.07×10^9
Mn-54	9.97×10^7
Co-60	1.01×10^9
Co-58	1.69×10^8
Fe-59	1.53×10^8

hard. Also, to reduce background gamma ray from fuel, it is necessary to remove fuel assembly from the core. Also, the water temperature should be less than 40°C from the limitation of an ordinary charge coupled device (CCD) camera. From the past record, reactor water temperature after removing all fuel (10 days from reactor shutdown) is under 40°C.

Selection of Detector

The detector was chosen to be mercuric iodide (HgI_2) or cadmium zinc telluride (CZT) from the following:

(1) Detector should be small enough to insert into limited space between internal structures.
(2) It should have high efficiency to measure in a short period.
(3) Its energy resolution is good enough to distinguish ^{54}Mn(0.835 MeV) to ^{58}Co(0.811 MeV).
(4) No cooling system for crystal is necessary.
(5) It can be used under the temperature of 40°C.

To determine the most suitable detector, we performed Monte Carlo simulation to get pulse height distributions of HgI_2 and CZT.

Table 1 shows the assumed radioactivity used for calculation. The crystal size of HgI_2 and CZT are chosen to be 3 mm in width, 5 mm in height, and 5 mm in length. The reason is that this is about the maximum crystal size available for HgI_2 and we need the biggest crystal to get good total-absorption-peak efficiency for ^{60}Co.

Calculations were performed using MCNP4C [3]. Figure 2 shows calculation geometry. Figure 3 shows the pulse height distribution for HgI_2 and CZT. This figure does not include the effect of detector resolution. From this figure, we can see all the total-absorption peak of five nuclides by HgI_2 crystal. On the other hand, by CZT, the 1.099 MeV peak from ^{59}Fe is not clear because it submerges under the Compton edge of ^{60}Co. Also, ^{54}Mn and ^{58}Co peak are smaller than HgI_2 crystal. Therefore we selected HgI_2 crystal for gamma-ray spectrum measurement.

The basic idea of using HgI_2 crystal perpendicular to the source (see Fig. 2) is that we can get maximum total-absorption-peak efficiency in a higher energy region. This method is also ideal to reduce background gamma ray from other directions.

Figure 4 shows the example of HgI_2 detector assembly. The size of HgI_2 crystal is 3 mm in width, 5 mm in height, and 5 mm in length. The HgI_2 crystal is set just inside the detector case end. The preamplifier circuit is also mounted in the detector case.

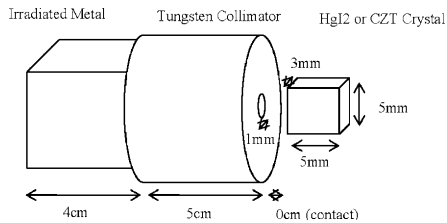

FIG. 2—*Calculation geometry for HgI_2 and CZT.*

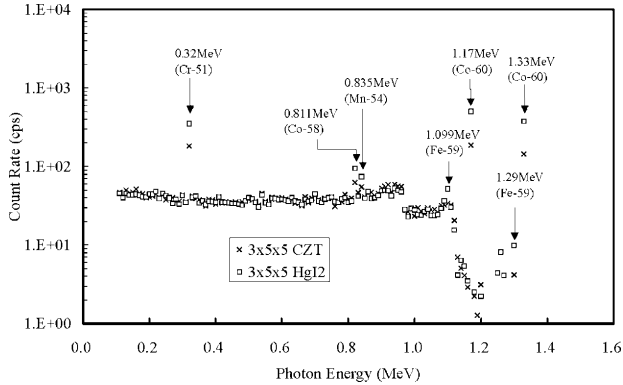

FIG. 3—*Calculated pulse height distribution for HgI_2 and CZT.*

Background Shield

To shield background gamma rays from behind and to limit the measuring area, tungsten shield 50 mm thick with a collimator hole 1 mm or 2 mm in diameter is used. Figure 5 shows an attenuation factor of 1.33 MeV gamma ray in tungsten calculated by MCNP4C. The thickness was determined to reduce background gamma ray below 0.1 %. The diameter of the collimator hole was determined to be 1 mm and 2 mm because the crystal width is only 3 mm.

Figure 6 shows a tungsten collimator shield and containment shell made by stainless steel. The containment shell has flange. We can change the front part of the tungsten collimator whose hole size is 1 mm or 2 mm by opening this flange. We can increase efficiency four times when using a 2 mm hole collimator versus 1 mm hole collimator.

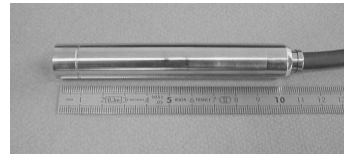

FIG. 4—*HgI_2 detector assembly.*

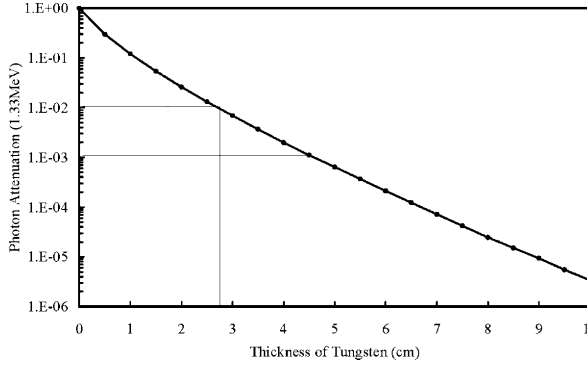

FIG. 5—*Attenuation of 1.33 MeV gamma ray in tungsten.*

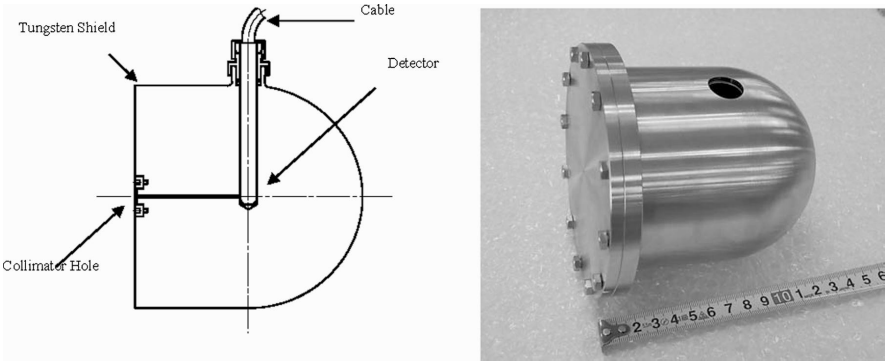

FIG. 6—*Collimator shield and containment shell.*

Statistical Error, Dead Time, and Counting Time

Because the output pulse shape of the semiconductor detector has a relatively long decay time (~ms), we should be careful for dead time. We estimated a count rate using the MCNP4C code. It was found that with a 1 mm hole collimator detector, we will get $\sim 10^3$ cps at shroud outer surface of core center height. This means that a 1 mm hole is reasonable to measure a higher activated region with tolerable dead time.

As for a peak count of 0.83 MeV(^{54}Mn), which is smallest of all the peaks, the necessary counting time to get a statistical error under 1 % is a few seconds for shroud outer surface of core center height and one minute for the Reactor Pressure Vessel (RPV) inner surface of core center height. This means that we can get sufficient statistics in reasonable counting time.

Relative Radioactivity Distribution in Reactor Internals and Reactor Vessel

There are many items to be considered when adopting the direct gamma-ray counting method as mentioned in the previous section.

(1) Nuclide distribution in thickness direction.
(2) Self-shielding of gamma ray produced inside the structural material.
(3) Background gamma ray around measurement point.

To solve these problems, we used calculated relative activity distribution in structural material by the TORT code [4]. Figure 7 shows the thermal flux distribution in the reactor pressure vessel of 800 MWe BWR plant [1].

Convert Procedure from Measured Photon Counts to Neutron Fluence, DPA, and Gas Production

Figure 8 shows a convert procedure from measured photon counts to neutron fluence, DPA, and gas production.

At first, we prepared effective macroscopic cross sections by using each relative spectrum calculated by the TORT code [1] and each reaction cross section. Effective macroscopic cross sections are prepared not only for activation reactions but also for DPA and gas production reaction.

We also prepared detector responses for each geometry, namely, shroud measurement from inside, shroud measurement from outside, and reactor vessel measurement from inside, etc., for each nuclide by using the MCNP4C Monte Carlo code. The correction factor for background gamma ray from the nearby region of the collimator hole was prepared using the MCNP4C code.

By using these responses with measured photon counts, decay constant, and power histories, we can get neutron fluence, DPA, and gas production quantity. This process is coded using VISUAL BASIC EDITOR, Microsoft. Just after counting, we can start the nuclide identification program and subsequent dosimetry program on a PC. Desired output are shown on the display and stored in a PC.

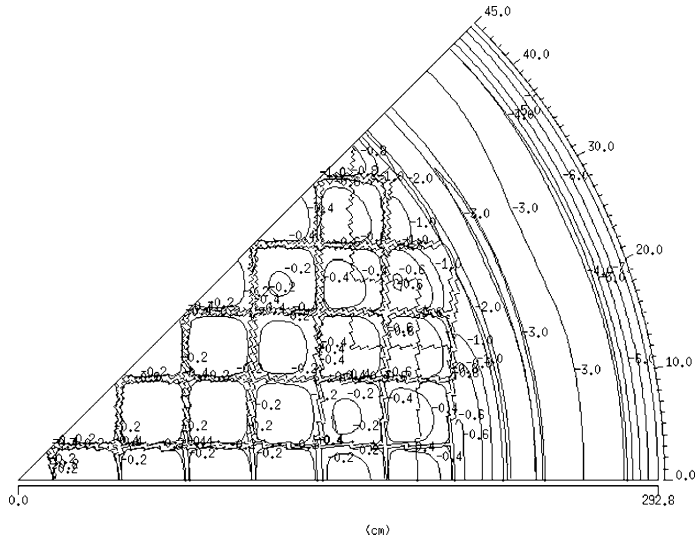

FIG. 7—*Thermal flux distributions in 800 MWe BWR (in logarithmic scale).*

Power Supply, Pulse Height Analysis, and Data Accumulation

Figure 9 shows the rough configuration of the measurement system. High voltage power for the detector and low voltage power for the preamplifier in the detector assembly are supplied by a power supply bin and its module, and the signal cable from the preamplifier is connected to the main-amplifier module in the power supply bin. The output signal from the main amplifier is connected to an analog-to-digital converter (ADC) and multichannel analyzer (MCA) board equipped in a PC. On the same PC, the nuclide identification and subsequent dosimetry programs are installed.

Consideration of Interference by Radioactive Crud

One of disturbances that cannot be removed by collimator shield and precalculated activity distribution is influence of radioactive crud on surfaces of shroud and RPV. Radioactivity of crud strongly depends on

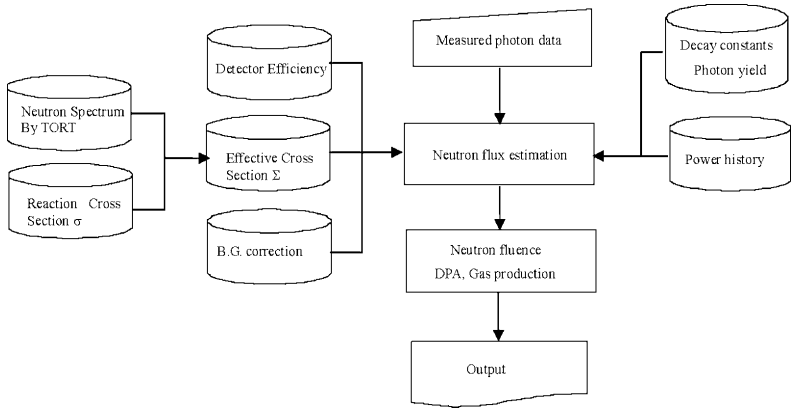

FIG. 8—*Convert procedures from measured photon counts to neutron fluence, etc.*

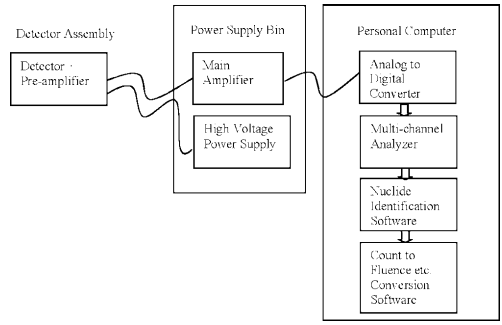

FIG. 9—*Power supply, pulse height analysis, and data accumulation.*

radiochemical management of plant operation. Therefore, we investigated its influence by assuming crud activity as 10^5 Bq/cm^2 and nuclide fractions of ^{60}Co:^{54}Mn:^{58}Co:^{59}Fe as 6:2:1:1.

The calculation of nonscattered gamma ray from the crud and the activated structural material are done using QAD-CGGP2 [5] code. It was found that disturbances of crud are less than 1 % in effective fuel length height of shroud and RPV. If we need measurement without disturbance of crud, we should prepare crud remover for the small area near the measurement point.

Uncertainty in this Method

Uncertainty of obtained data comes from measurement, conversion procedure, and initial composition.

Measurement

Background gamma rays which come from another direction were suppressed under 0.1 % by tungsten shield. Crud disturbance was under 1 % when crud activity is 10^5 Bq/cm^2. Statistical error of measurement is normally planned to be less than 1 % by alternating counting time. Therefore, the subtotal of uncertainty from measurement is 2 %.

Conversion Procedure

We estimated uncertainty of detector response to be 3 % from the experience of another counter. It should be confirmed by standard source measurement. Gamma rays from a neighbor region around the collimator hole were considered by MCNP4C calculation. Its uncertainty is also 3 %. Uncertainty of relative radioactivity distributions is less than 10 %, considering the absolute uncertainty obtained from Ref. [1]. Therefore, the subtotal of uncertainty from the conversion process is 16 %.

Initial Composition

Data spread of composition obtained by former material research was about 10 % for Cr, Fe, Ni, but 200 % for Co. We can eliminate this uncertainty by mil-sheet and EDXRF analysis. If it cannot be done, uncertainty of Co composition can be checked by thermal fluence obtained by another reaction (^{59}Fe and ^{51}Cr). Therefore, uncertainty from initial composition is 10 % which comes from data spread.

Total uncertainty from all is about 30 %. When initial composition analysis was done, uncertainty is about 20 %. These uncertainties are bigger than normal measurement, but this simple measurement system will be useful to give information to decide material replacement and welding of irradiated material.

Future Work

Currently, we are making a prototype system and planning to test its applicability.

(1) Confirmation of calculated detector response by measurement of standard source.

(2) Confirmation of calculated collimator effect by measurement of irradiated shroud sample.
(3) Test of detector handling by reactor simulation pool.

After these tests, we plan to do a final test in an actual reactor.

Conclusion

Concept design of simple retrospective dosimetry method was performed. By this method, we can measure neutron fluence, DPA and gas production data in reasonable counting time. Because time and cost of this method is much less than the sampling method used in ordinary retrospective dosimetry, we can do measurements at many positions and even get a measured fluence contour map.

References

[1] Tsukiyama, T. et al., "Benchmark Validation of TORT code using KKM Measurement and its application to 800 MWe BWR," *Reactor Dosimetry in the 21st Century*, World Scientific Publishing Co. Pte. Ltd., Singapore, Jan Wagemans et al., ed., 2003.

[2] Greenwood, L. R., and B. M. Oliver, "Retrospective Reactor Dosimetry for Neutron Fluence, Helium, and Boron Measurement," *Reactor Dosimetry in the 21st Century*, World Scientific Publishing Co. Pte. Ltd., Singapore, Jan Wagemans et al., ed., 2003.

[3] Briesmeister, J. F., ed., "MCNP—A General Monte Carlo N-Particle Transport Code Version 4C," Report No. LA-13709-M, Los Alamos National Laboratory, 2000.

[4] Rhoades, W. A., and Simpson, D. B., "The TORT Three-Dimensional Discrete Ordinates Neutron/Photon Transport Code (TORT version 3)," Report No. ORNL/TM-13221, Oak Ridge National Laboratory, 1997.

[5] Sakamoto, Y., and Tanaka, S., "QAD-CGGP2 and G33-GP2: Revised Versions of QAD-CGGP and G33-GP Codes with Conversion Factors from Exposure to Ambient and Maximum Dose Equivalents," Report No. JAERI-M 90-110, Japan Atomic Energy Research Institute, 1990.

Journal of ASTM International, Vol. 3, No. 4
Paper ID JAI13441
Available online at www.astm.org

G. Borodkin,[1] *N. Khrennikov,*[1] *A. Dmitriev,*[1] *M. Miroshnichenko,*[2] *and V. Grivizirsky*[2]

Reactor Dosimetry Issues During Justification of Extension of Service Life of Nonrestorable Equipment of Russian VVER

ABSTRACT: Reactor dosimetry issues have been analyzed in every aspect of extension of service life of non-restorable equipment of the Russian Vodo-Vodianoy Energetichesky Reactor (rus.) (VVER)-type reactors. A special attention has been focused on the role of neutron fluence and fluence rate uncertainties in prediction of the lifetime of the equipment. Results of analysis of service life justification of the first generation VVERs have been presented. A comparison of calculational and experimental dosimetry results are discussed in this paper. Usefulness of the Niobium-93 technique of fluence measurements as applied to template and trepan specimen dosimetry is especially emphasized in this paper.

KEYWORDS: reactor dosimetry, VVER, service life, pressure vessel, support structures, fluence, calculation

Introduction

The nonrestorable equipment of (VVER)-type reactors is a key component to be considered in the context of safe operation of a nuclear power plant (NPP) unit. Such equipment is the primary target of the analysis of the current status and residual lifetime prediction as regards the justification of a unit license renewal. Besides the aging of the equipment due to temperature effects and cyclic loads, the degradation of material properties is also caused by the reactor irradiation (neutrons and gammas).

With reference to VVER-type reactors the effect of the aging under irradiation, for example, radiation embrittlement of ferritic steel, is essential for long operation of such nonrestorable equipment as the reactor pressure vessel (RPV) and support structures (SS) of the reactor.

The process of operation extension has now begun for VVER-type reactors of design series V-179 (Novovoronezh NPP, units 3 and 4) and V-230 (Kola NPP, units 1 and 2). These reactors are termed as the first generation VVERs. The assigned design service life of these reactors was 30 years. By present, these reactors have been granted service life extensions. The next stage is to consider such service life extension for the second generation of VVERs (design series V-213) and VVER-1000.

The review of the Utility's documents submitted along with the application for the service life extension includes an expert analysis of safety criteria. Within the framework of the licensing procedure this expert analysis is based on the system of regulatory documents of Rostechnadzor [1]. Such analysis covers reactor dosimetry issues of nonrestorable equipment. This analysis is guided by the developed regulatory approach [2] to the estimation of equipment service life resulting from the accumulated fast neutron fluence. This approach is based on the principle of conservative margins for values of neutron fluence and other parameters used in the equipment lifetime evaluation. The values of conservative margins are estimated by the analysis of uncertainties of the parameters. In this connection a thorough investigation is aimed at the analysis of reliability of current evaluation and prediction of the radiation exposure at critical points of the equipment.

The expert analysis of predicted lifetime of the equipment of the first generation VVERs has shown

Manuscript received June 20, 2005; accepted for publication October 27, 2005; published online January 2006. Presented at ASTM Symposium on Reactor Dosimetry, 12th International Symposium on 8–13 May 2005 in Gatlinburg, TN; D. W. Vehar, D. M. Gilliam, and J. M. Adams, Guest Editors.

[1] Head of group (G. Borodkin), Head of Department (N. Khrennikov), and Deputy Director (A. Dmitriev), SEC NRS of Rostechnadzor, 2/8, bld. 5, Malaya Krasnoselskaya ul., 107140 Moscow, Russia.
[2] Head of Department (M. Miroshnichenko) and Deputy Head of Department (V. Grivizirsky), Rostechnadzor, 34 Taganskaya str., 109147 Moscow, Russia.

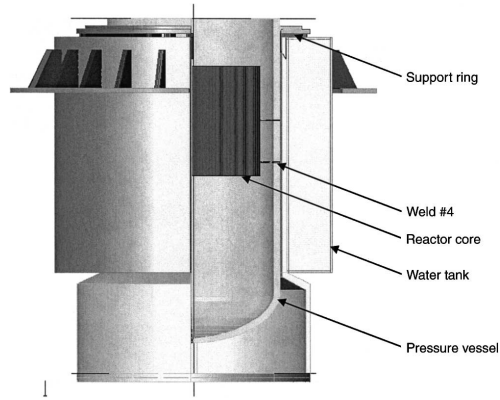

FIG. 1—*Nonrestorable equipment of the first generation VVER.*

that the uncertainty of radiation load parameters at critical points of the equipment may have influence on duration of the extended operation period. Investigations performed on units with VVER-1000 also show that uncertainty of neutron fluence at the reactor pressure vessel and variations of radiation load depending on neutron-physical characteristics of the reactor core may be also important as regards the justification of the service life extension.

The expert conclusions are based on the results of calculated-experimental research of radiation loads on the equipment. Neutron and gamma dosimetry evaluations are derived from calculations by code (DORT) [3]. The calculational methods used for fluence prediction on RPV and SS are validated by neutron-activation measurements at the cavity near the outer surface of RPV (ex-vessel measurements).

New results of calculation and experimental neutron dosimetry investigations performed within the expert analysis of safety of the Russian first generation VVERs are discussed in this paper.

Reactor Dosimetry and Prediction of Nonrestorable Equipment Lifetime

Nonrestorable Equipment under Reactor Irradiation

The reactor pressure vessel and support structures are the key components of the non-restorable equipment of VVERs. As regards the first generation VVERs, the lifetime of RPV and SS are determining factors of a NPP service life extension. Figure 1 shows the layout of RPV and SS of this type of VVER. From the point of view of radiation embrittlement the critical place (component) of the VVER pressure vessel is the circumferential weld No. 4, which is located within the reactor core height (30 cm above the bottom level of the core). During operation, ferritic steel of the water tank and support ring is exposed to neutron fluence ($E > 0.5$ MeV) of more than 10^{18} n/cm^2. Its properties should be analyzed from the point of view of brittle fracture strength. In this regard the attention was paid to the support structures of the first generation VVERs as considered by their life extension justification. A potential problem could be the likely effect of low temperature embrittlement at a low neutron fluence rate irradiation. The possibility of this effect is analyzed, for example, by McElroy et al. [4]. In this reference there is a necessity to have reliable evaluations of the parameters of radiation load on RPV and SS of VVERs.

Review Procedure of the Safety Justification of NPP Operation Extension

The safety justification review for the purpose of a NPP unit's service life extension is performed in the framework of the licensing procedure defined by the system of regulatory documents of Rostechnadzor [1]. This procedure is shown in Fig. 2.

The life extension application and set of documents to justify safe operation of the VVER during the extended period are prepared by the Russian Utility (Concern "Rosenergoatom"—the only nuclear utility in Russia, so far). For this purpose the Concern contracts research and design institutes (for example,

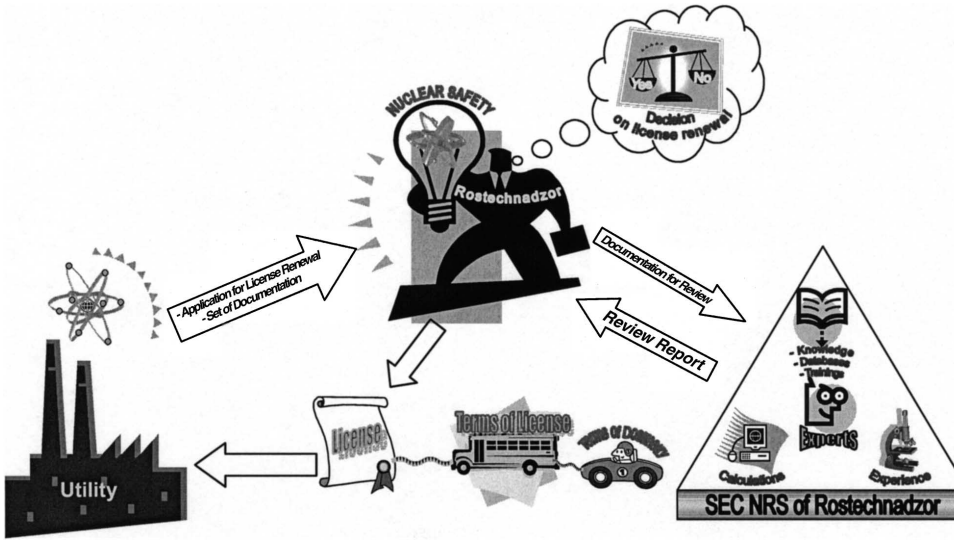

FIG. 2—*Procedure of reviewing the safety justification of NPP operation extension.*

Opytnoe Konstruktorskoe Buro (rus.) (OKB) "Gidropress," Russian Research Center (RRC) "Kurchatov Institute," etc.). Then this application and set of documents are submitted to Rostechnadzor. This set also includes reports with justification of predicted reactor dosimetry parameters at critical points of the equipment. Rostechnadzor reviews this documentation to make a decision on the license renewal. To perform extensive analyses of the Utility's documents, Rostechnadzor forwards this safety justification package to its scientific and engineering support organization—Scientific and Engineering Center for Nuclear and Radiation Safety (SEC NRS). The latter analyzes how requirements of regulatory documents are met in the submitted documentation. Compliance with these requirements is the basic criterion of safety justification evaluation. Afterward, SEC NRS in its review report submits to Rostechnadzor its conclusions and proposals regarding the possibility of extending service life of a given NPP unit. When deciding on the license renewal, Rostechnadzor takes into account the results of the SEC NRS review. If the positive decision is made the license includes an attachment containing certain terms formulated on the basis of the review report comments. The Utility should ensure that these license terms are met during the license validity period. Therefore, in accordance with the process described the reactor dosimetry issues are considered in the review report and reflected in the terms of license.

Approach to Lifetime Evaluation

The approach used for the expert's evaluation of RPV and SS lifetime is applied in accordance with the safety guide of Rostechnadzor [2]. In this approach a residual lifetime of the equipment may be expressed as follows:

$$\tau = \frac{F^a - F_t}{\Phi_{\max}}, \tag{1}$$

where F^a is the allowable neutron fluence ($E > 0.5$ MeV) within the zone determining the equipment safety (the critical point of the equipment), F_t is the current neutron fluence ($E > 0.5$ MeV) in the same point at the moment of the residual lifetime evaluation, and $\Phi_{\max}$ is the accepted fluence rate ($E > 0.5$ MeV) in the same point chosen as maximum value out of all possible fuel cycles in the forecast future.

The implementation of this approach allows understanding of the role of neutron dosimetry and basic principles of management of the VVER pressure vessel lifetime. It proceeds from Eq 1 that the variation

TABLE 1—*Pressure vessel fluence rate reduction (arbitrary units) depending on core pattern of VVER.*

		Full core		Core with DA		Total reduction	
Core loading	Core periphery	30 deg[a]	13 deg	30 deg	13 deg	30 deg	13 deg
Full core	Fresh	1.00	0.61	…	…	1.00	0.61
Full core	BUF	0.94	0.55	…	…	0.94	0.55
Full core	High BUF	0.63	0.44	…	…	0.63	0.44
Core with DA	Fresh	…	…	0.53	1.00	0.14	0.26
Core with DA	BUF	…	…	0.47	0.95	0.12	0.25
Core with DA	High BUF	…	…	0.37	0.73	0.10	0.19

[a]For 30-deg core symmetry.

of parameters in the formula leads to a change of the lifetime evaluation, but in case of a purposeful variation it can contribute to the lifetime management. In accordance with the Safety Guide [2] it is recommended to use conservative margins of Eq 1 parameters. The values of conservative margins are derived from an analysis of uncertainties of these parameters. The margin of F^a is defined by uncertainties of metallurgical factors (for example, factor of radiation embrittlement and critical temperature of embrittlement) and uncertainties of thermal-hydraulic and fracture mechanics calculations results.

The margin of F_t depends on uncertainty of calculated values of neutron fluence at the critical points of the equipment. This uncertainty may be assessed by verification of calculational methods used for this purpose. Such verification is carried out in accordance with the Russian regulatory document [5], which describes the certification procedure of computer codes. The certification of calculational methods being used to evaluate neutron fluence at RPVs of the Russian first generation VVERs is one of the terms of the plant's operation license renewal. Such work has been already initiated by the Utility. It is important to note that the review report prepared by the regulator's experts contains recommendations to perform ex-vessel measurements for validation of calculational results.

A conservative estimation of equipment lifetime depends significantly on the accepted value of Φ_{max} and its uncertainty. It is apparent that the management of the fluence rate (FR) value means the management of the equipment lifetime. For example, dummy assemblies (DA) or burnup fuel (BUF) placed in the core periphery cause a significant decrease of the radiation load on the equipment that consequently leads to the extension of a lifetime. These measures are used now at the first generation VVERs. Results of variation of FR on RPV depending on actual core load pattern in history of operation of one such VVERs are presented in Table 1. It is seen that a possible total decrease of FR on RPV may be fivefold. If the service life extension is sought, the experts recommend placing high burnup fuel at the core periphery; the Utility adopts this approach.

The equipment featuring the neutron spectrum variations at the critical points is studied in respect of the "displacement per atom" parameter (DPA). For the points where attenuation of DPA is more conservative than fast neutron fluence ($E > 0.5$ MeV), it is recommended to perform the lifetime evaluation on the basis of DPA distributions. A correction factor may be used in the following form:

$$K_{DPA} = \frac{\text{DPA}}{F(>0.5\ \text{MeV})}. \tag{2}$$

For example, a study of this factor may be important when analyzing radiation load on the SS of the first generation VVERs. Figure 3 demonstrates a variation of this factor over height of the inner wall of the water tank up to support ring and beyond. It is seen that K_{DPA} starts to grow up to 20 % on the water tank wall in the region above the core and reaches 60 % on the support ring.

An evaluation of how gamma radiation contributes to the total DPA in the upper part of SS (top of the tank and support ring) shows that this value does not exceed 1 % for all positions.

Results of Expert's Analyses

In case of the first generation VVER pressure vessels, the analyses carried out in SEC NRS have showed (Table 2) that the life extension period (15 years) requested by the Utility is not confirmed for some reactors by experts' evaluations based on the conservative approach. Even taking into account thermal annealing of welds and the use of burnup fuel at the core periphery, confidence of the justification of service life extension up to 15 years is under question for some units. Table 2 shows that the 15-year life

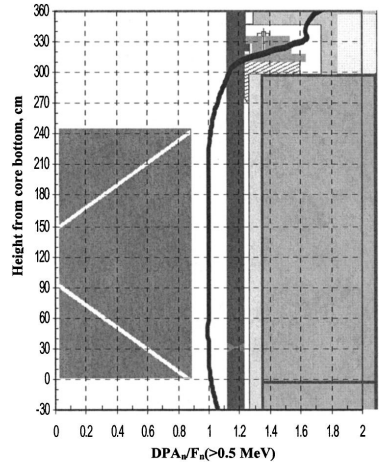

FIG. 3—*Ratio of DPA to neutron fluence (>0.5 MeV) along VVER height through support structures.*

extension period has been granted to Kola-1 only. For other units, there should be an additional justification of their safe operation (to cover the period of 15 years) that takes into account the conservative approach to estimations.

At the same time, as mentioned above, the estimated lifetime can be increased if uncertainties of the influenced parameters are reduced by removing some conservatism in safety margin evaluations. Based on formula 1, the conservative margins of fast neutron fluence and fluence rate directly affect the estimates of the RPV service life extension. However, such reduction of dosimetry parameter uncertainties should be thoroughly validated.

Reactor Dosimetry Research at NPPs with VVERs

The experts' conclusions are drowned out on the basis of the calculated-experimental studies of radiation loads on the NPP equipment. A special calculational procedure involving the three-dimensional neutron fluence and fluence rate evaluation by the method of synthesis has been developed. This procedure named FASTER_230 (Fluence Automatically Synthesized in Thickness of Equipment of Reactor series V-230) is based on the calculations by code DORT. It has been adopted to use macrocross sections obtained from different microdata libraries (e.g., BUGLE96 [6] or BGL440 [7]). Accompanied service codes automatically prepare DORT input files using the core neutronics data, including pin-to-pin neutron source distributions. To evaluate fluence after past fuel cycles, this procedure takes into account the actual parameters of the reactor operation (power history and coolant temperature variation).

Measurements are performed in accordance with Safety Guide [8]. Neutron-activation detectors including reactions ^{54}Fe(n,p), ^{58}Ni(n,p), ^{46}Ti(n,p), ^{63}Cu(n,α), ^{93}Nb(n,n'), ^{237}Np(n,f), ^{238}U(n,f), and ^{63}Cu(n,γ), are irradiated within the cavity near the outer surface of the RPV wall. The calculational procedures are validated through a comparison of calculated and measured activation values.

TABLE 2—*Russian VVER under licensing renewal process.*

Unit	Startup	Annealing	DA	Expiration of design life	Renewal license application	Confirmation by expertise
NV-3	1971	1987 1991	1999	2001	2016	2007
NV-4	1972	1991	no	2002	2017	2010
Kola-1	1973	1989	1985	2003	2018	2018
Kola-2	1974	1989	1985	2004	2019	2009

TABLE 3—*Averaged over core height ratios of Calculated to Experimental Spectral Indexes at ex-vessel cavity.*

Unit	DA[a]	$^{54}Fe(n,p)$	$^{58}Ni(n,p)$	$^{46}Ti(n,p)$	$^{63}Cu(n,a)$	$^{93}Nb(n,n')$	$^{237}Np(n,f)$	$^{238}U(n,f)$
NV-3	Yes	1.00	1.01	0.92	0.99	1.08	1.09	1.01
NV-4	No	1.00	0.97	0.90	0.95	1.07	1.05	0.99
Kola-1	Yes	1.00	1.01	0.95	1.01	0.99	1.04	0.92
Kola-2	Yes	1.00	1.07	1.02	0.97	0.99	1.11	0.99
Uncertainty of experimental SI, %		0	7.1	7.8	7.8	9.4	9.4	8.6

[a]Dummy assembly.

The ex-vessel measurements have been now performed at all Russian VVERs of first generation. Laboratories of SEC NRS, RRC "Kurchatov Institute," and VVER design organization—OKB "Gidropress"—carried out calculational and experimental studies common for Kola-1 and Kola-2.

Tables 3 and 4 present results of comparison of spectral parameters obtained by SEC NRS from studies of the first generation VVERs. The spectral index (SI) representing the ratio of the reaction rate of a separate detector to the reaction rate of the iron detector $[^{54}Fe(n,p)]$ used as monitor one is used as a spectral parameter.

Table 3 shows that the discrepancy between the calculated and experimental SI values is generally coincidental with the uncertainty of the SI experimental values.

A comparison of spectral indexes evaluated at different heights within the cavity of NV-4 (Table 4) shows an even greater disagreement in the point above the top of the core (on the top of the water tank), especially, in the case of the Neptunium reaction. Such disagreement may be explained by the use of the synthesis approximation in respect to the upper part of the reactor. A comparison of absolute calculational and experimental results for this part of the reactor shows an overestimation of calculation data (up to 20–50 %, depending on the unit), whereas there is an agreement of results obtained within the core height.

Dosimetry Issues in the Russian RPV Material Testing Programs

The operation of the first generation VVERs throughout the service life extension period is supported by the testing of RPV material specimens prepared from templates cut out from their RPVs. Additionally a specimen reirradiation procedure is used for prediction of property degradation during the extended operation period. This reirradiation is performed in standard locations of surveillance specimen irradiation program of VVER-440 of V-213 series.

A study of samples prepared from trepans cut out from pressure vessels of decommissioning VVER may be very useful (e.g., RPV of Greifswald NPP units) as to confirm a trend curve of the property degradation. The Russian Regulatory Body (Rostechnadzor) recognizes the importance of such studies and supports activity in this area.

The experimental study of neutron dosimetry of templates is based on measurement of ^{54}Mn and ^{93m}Nb activity in template materials. However, more reliable experimental evaluation of long-term accumulated fluence (over 30 years of operation) is obtained through the analysis of Niobium activity, taking into account low neutron threshold and a long half-life of the appropriate reaction. Moreover, only this reaction is suitable for experimental evaluation of neutron fluence on trepan samples. In this reference, regulatory recommendations concerning neutron dosimetry of material testing with the use of templates and trepans are aimed at improving and using the Niobium analysis technique.

Neutron dosimetry of reirradiation procedure needs improvement of calculational methods (accounting for space and energy distributions of neutron field parameters), increase of reliability of Nb-detector measurements, and adding fissionable detectors (e.g., ^{237}Np and ^{238}U) to the set of accompanied detectors.

TABLE 4—*Ratios of Calculated to Experimental Spectral Indexes at ex-vessel cavity of NV-4.*

Height[a], cm	Position	$^{54}Fe(n,p)$	$^{58}Ni(n,p)$	$^{46}Ti(n,p)$	$^{63}Cu(n,a)$	$^{93}Nb(n,n')$	$^{237}Np(n,f)$	$^{238}U(n,f)$
280	Top of tank	1.00	0.90			1.02	0.78	
124	Midplane	1.00	0.97	0.91	0.92	1.08	1.07	0.99
30	Weld #4	1.00	0.96	0.89	0.97	1.06	1.04	0.99

[a]Account from core bottom.

VVER-1000 Reactor Dosimetry in Aspect of Equipment Lifetime Evaluation

The issues considered above for reactor dosimetry of the first generation VVERs with regard to license renewal have implications for VVER-1000 type reactors. This concerns the computer code verification and certification, improvement of surveillance specimen dosimetry, and regulation of radiation load on the reactor pressure vessel. Investigations performed with regard to VVER-1000s have also shown that uncertainty of neutron fluence on RPV and variations of radiation load depending on neutron-physical characteristics of the reactor core may be of importance in the context of justification of the extended operation. The effect of variations of radiation load is especially important for the case of MOX fuel use at NPPs with this type of VVER. The justification of MOX fuel use at the operated VVER-1000s should be supported by reliable calculations of the radiation load and validation of their results by ex-vessel measurements. In accordance with the regulatory requirements [9], it should be ensured that the use of MOX fuel will not affect the RPV service life extension.

Conclusions

Reactor dosimetry issues have been analyzed with regard to service life extension of non-restorable equipment of the Russian VVERs. This study has focused on reactor pressure vessel and support structures affected by irradiation. When applied to some of the first generation VVERs the conservative margins of neutron dosimetry parameters (neutron fluence and fluence rate) directly influence the estimates of the extended operation period.

Uncertainty of neutron fluence values should be evaluated during verification and certification of calculational methods, used in practice by the Utility for fluence prediction at the critical points of the equipment. It is recommended that ex-vessel measurements are performed at VVERs in order to validate the said calculational methods.

DPA is the recommended approach for the assessment of lifetime extension of support structures because it is more conservative than neutron fluence above 0.5 MeV.

The usefulness of the Niobium-93 technique of fluence measurements as applied to template and trepan specimen dosimetry is especially emphasized in this paper.

The possibility of loading of MOX fuel to the operating VVER-1000s should be thoroughly investigated from the point of view of justification of service life extension in future.

References

[1] "The List of Basic Legal Statements and Regulatory Standards used by Gosatomnadzor of Russia for State Regulation of Safety in the Field of Use of Atomic Energy. P-01-01-2003," GOSATOMNADZOR of Russia, May 2003.

[2] "Safety Guides. Recording of Fast Neutron Fluence at VVER Pressure Vessels and Surveillance Specimens for Ulterior Prediction of RPV Radiation Lifetime (RB-007-99)," *Bulletin of GOSATOMNADZOR of Russia* 3(5), 2–14 (1999).

[3] Rhoades, W. A. and Childs, R. L., "The DORT Two-Dimensional Discrete Ordinate Transport Code," *Nucl. Sci. Eng.* 99(1), 88–89 (1998).

[4] McElroy, R. J., et al., "Low Temperature Embrittlement of LWR RPV Support Structures," *Proc. NEA/CSNI Workshop on Safety Assessment of Reactor Pressure Vessels*, Espoo, Finland, 8–9 October, 1990, Vol. 2, p. 255.

[5] "Regulations on Certification of Software Used at Validation or Ensuring of Safety of Nuclear and/or Radiation Dangerous Objects and Factories (RD-03-17-94)," GOSATOMNADZOR of Russia, July 1994.

[6] White, J. E., et al., *BUGLE-96: Coupled 47 Neutron, 20 Gamma-Ray Group Cross Section Library Derived from ENDF/B-VI for LWR Shielding and Pressure Vessel Dosimetry Applications*, RSIC Data Library Collection, DLC-185, March 1996.

[7] J. Bucholz, Antonov, S., and Belousov, S., *BGL440 and BGL1000 Broad Group Neutron/Photon Cross-Section Libraries Derived from NDF/B-VI Nuclear Data*," IAEA INDC(BUL)-15.

[8] "Safety Guides. Procedure of Neutron Dosimetry on the Ex-Vessel Surface of VVER of NPP (RB-

018-01)," *Bulletin of GOSATOMNADZOR of Russia*, 6(19), 32–47 (2001).

[9] "Rules of Arrangement and Safety Operation of the Equipment and Pipelines of Nuclear Power Installations (PNAE G-7-008-89)," Rules and Norms in Nuclear Power Engineering. GOSATOMENERGONADZOR, Moscow, ENERGOATOMIZDAT, 1990.

Journal of ASTM International, Vol. 3, No. 3
Paper ID JAI13494
Available online at www.astm.org

Sergey I. Belousov,[1] *Krasimira D. Ilieva,*[1] *Desislava L. Kirilova,*[1] *Biser Y. Petrov,*[1] *and Eckhard Polke*[2]

Validation of the Neutron Fluence Calculation on the VVER-440 RPV Support Structure

ABSTRACT: Measurements with activation detectors were carried out on Unit 4 of Kozloduy NPP in order to validate the fluence calculation data for the RPV support structure. Irradiation of iron, copper, and niobium detectors was performed during the 17th fuel cycle. The neutron fluence on the support structure and the activities of irradiated detectors were calculated by the three-dimensional transport code TORT with BGL440 multigroup cross section library. The history of local power distribution in the reactor core was taken into account. The measured and calculated induced activities are in good agreement in the area of the support structure. The calculated fluence evaluation in this area is conservative.

KEYWORDS: validation, neutron fluence, support structure, reactor pressure vessel

Introduction

The evaluation of the neutron fluence on the reactor pressure vessel (RPV) support structure was done in order to assess the rest of the lifetime of NPP equipment and facilities for further development of the aging management program within the scope of the modernization program for Units 1–4 of Kozloduy NPP. This evaluation was performed by neutron transport calculations.

The neutron fluence calculation in the area of the support structure is a very complicated task due to the system geometry complexity with strongly differing characteristics of the materials that makes it difficult to evaluate the calculation accuracy. Simultaneously, the accuracy of the neutron fluence calculation is limited by the uncertainties of the nuclear data. That is why a validation of the neutron fluence calculation based on comparison of calculated and measured induced activities of threshold detectors was done. The ratio of calculated to measured activity values was used as a measure of the calculated neutron fluence uncertainty. The validation was carried out by measured activity of Fe-, Cu-, and Nb-detectors. Three-dimensional calculations of the neutron fluence with energy above 0.5 MeV and of the induced activity of detectors positioned in the vicinity of RPV support structure were carried out for the 17th cycle of Unit 4 Kozloduy NPP. The fluence is used to determine the material irradiation damage according to the Russian standard [1].

Measurements

The choice of the positions suitable for the detectors positioning was an awkward task due to the inaccessibility to places close to the support structure. Furthermore, the determination of the detector position coordinates was related with some uncertainties due to the lack of detailed drawings of the reactor system elements in the area of the support structure.

Foil detectors were placed for irradiation during the 17th cycle in the following positions:

- Position 1: horizontally, in the air cavity over the support structure, over the RPV flange (Figs. 1 and 2).

Manuscript received June 20, 2005; accepted for publication September 29, 2005; published online December 2005. Presented at ASTM Symposium on Reactor Dosimetry, 12th International Symposium on 8–13 May 2005 in Gatlinburg, TN; D. W. Vehar, D. M. Gilliam, and J. M. Adams, Guest Editors.

[1] Senior Researcher, Institute for Nuclear Research and Nuclear Energy, Bulgarian Academy of Sciences, 72 Tsarigradsko shosse blvd., 1784 Sofia, Bulgaria.
[2] Senior Researcher, Framatome ANP GmbH, Freyeslebenstr. 1, 91058 Erlangen, Germany.

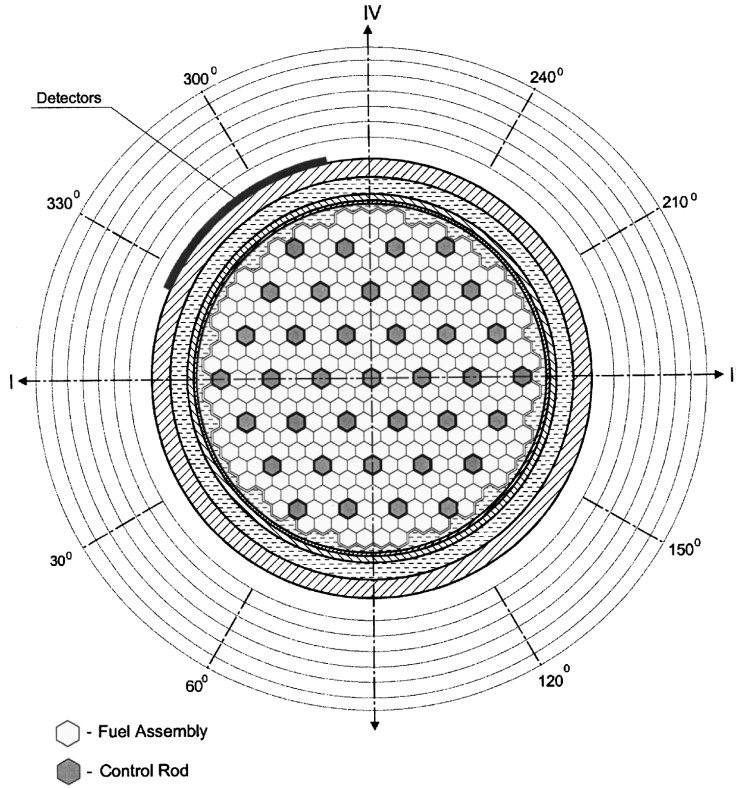

FIG. 1—*The detector position against the reactor core orientation.*

- Position 2: vertically, at the top of the air cavity between the RPV and the water tank, under the support structure (Fig. 1, Fig. 3).

The detectors' characteristics are presented in Table 1.

The determination of the specific activity of the irradiated foils (detectors) was carried out following the ASTM standards [3–5]. The uncertainty of activity measurements did not exceed 15 %. The standard deviation of the measurements of the foils irradiated in Position 2, under the RPV support structure was relatively lower in comparison with those irradiated in Position 1, over the RPV support structure, because the flux level in the vicinity of the Position 2 was significantly higher than in Position 1 region.

Calculations

Codes and Libraries

The relative reactor core power distribution and the fuel local burn up values needed for neutron source definition were calculated in hexagonal three-dimensional geometry by the PYTHIA/DERAB code [6] in pin-by-pin presentation.

The calculation of the neutron fluence and activities induced in foil detectors during the irradiation was carried out by the three-dimensional code TORT [7].

The neutron cross section library BGL440 [8] was applied in neutron transport calculations. The activation cross section data file IRDF-90 [9] was used for detectors' activity calculation.

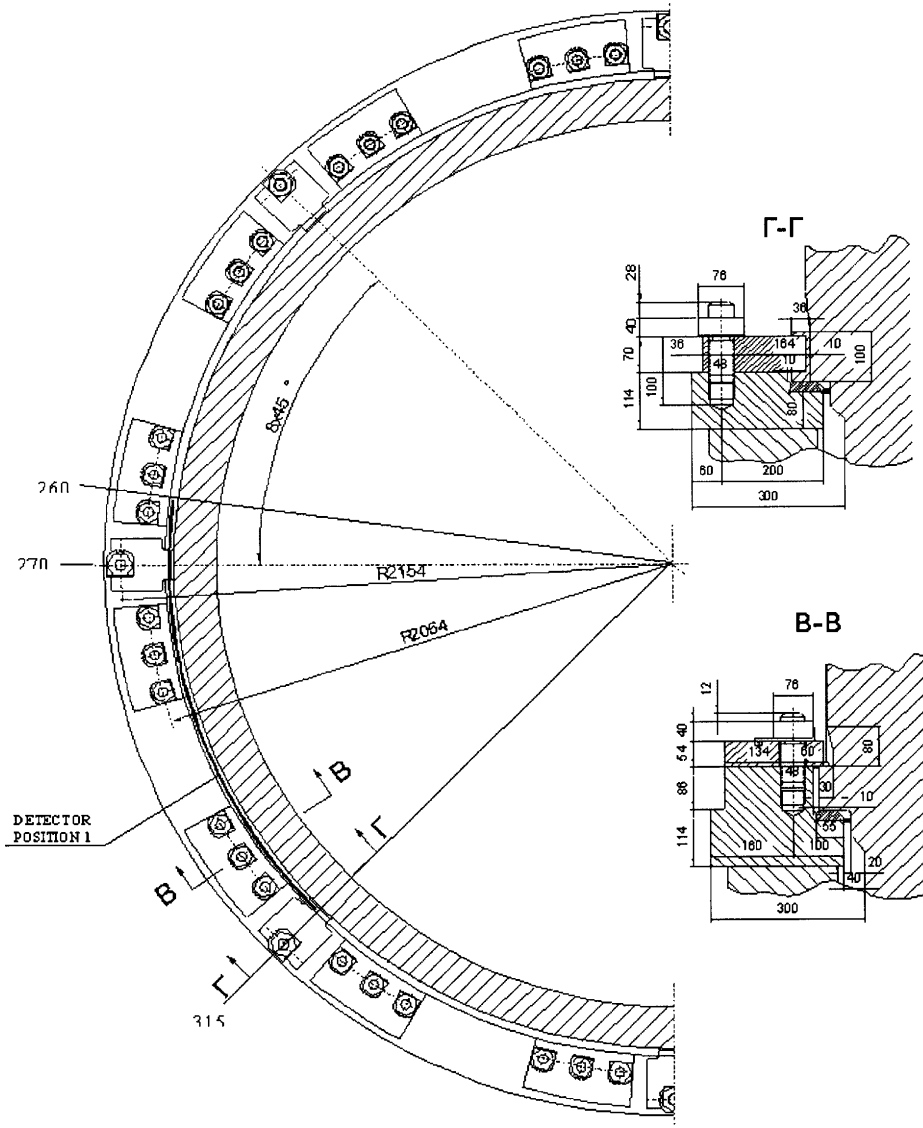

FIG. 2—*Positioning of neutron detectors in Position 1 of the RPV support structure.*

The preparation of the fixed neutron source from reactor core calculation results as well as the transformation from hexagonal to cylindrical (r,θ,z) mesh (the last used in the TORT calculation) was performed by the interface software package DOSRC [10].

Calculational Model

The three-dimensional calculations in (r,θ,z) mesh were performed with the TORT code in P5S12 approximation. The geometry model of the support structure comprises in-vessel and out-of-vessel constructions in radial and axial space limits which correspond to the geometry symmetry of the area (Fig. 4).

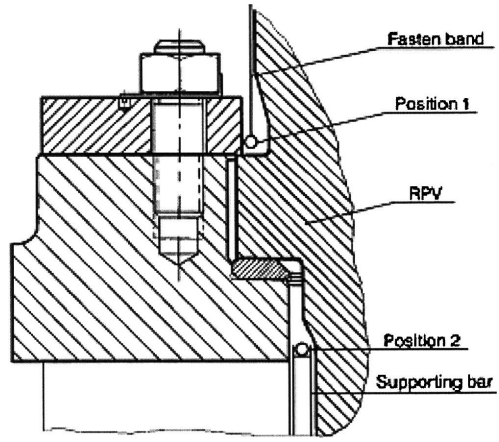

FIG. 3—*Positioning of neutron detectors in Position 1 and Position 2 of the RPV support structure.*

Sensitivity analysis was carried out for determination of the optimal cylindrical coordinates mesh set. On the basis of this analysis the calculations were carried out in 90-deg azimuthal symmetry sector that includes 45-deg symmetry sector of the support structure and 30-deg symmetry sector of the reactor core. The applied boundaries and number of intervals were as follows:

over the radius—from 101 cm to 305 cm, I=141intervals;
over the azimuth—from 0-deg to 90-deg, J=90 intervals;
over the height—from 161.33 cm to 365 cm (from 80.67 cm below the upper edge of the reactor core to 25 cm above the supporting ring), K=142 intervals.

The distribution of neutron fluence, with energy above 0.5 MeV, in the area of the support structure in 30-deg azimuthal direction normalized to the maximal fluence value is presented in Fig. 5.

The induced activity from the reactions: $^{54}Fe(n,p)^{54}Mn$, $^{63}Cu(n,\alpha)^{60}Co$, $^{93}Nb(n,n')^{93m}Nb$ of detectors irradiated in the area of the RPV support structure during the 17th cycle of Unit 4 was calculated by the following formula [11]

$$a = N_0 \int dE\sigma^d(E)L^{-1}\sum_i f_i^d S_i(\vec{r},E) \tag{1}$$

$$f_i^d = [1-\exp(-\lambda_d T_i)]\exp(-\lambda_d \tau_i) \tag{2}$$

where N_0=number of target nuclei in the detector; $\sigma^d(E)$=activation cross section of the detector d; L =operator of neutron transport; S_i=fixed neutron source in point $\vec{r}$ with energy E; λ_d=decay constant; T_i=duration of the ith steady-state; τ_i=time interval after the ith steady-state up to the moment of activity determination. The summation was performed over every steady-state interval i.

Neutron fluence and activity calculations were carried out for the 17th cycle of Unit 4.

Validation of Results

The validation of the neutron fluence calculation was based on comparison of calculated and measured induced ^{54}Mn, ^{60}Co, and ^{93m}Nb activities of threshold detectors. The calculated and measured ^{54}Mn

TABLE 1—*Characteristics of the threshold activation detectors [2].*

Reaction	Threshold Energy, MeV	Decay Half Lifetime $T_{1/2}$
$^{54}Fe(n,p)^{54}Mn$	1.6	312.12 d
$^{63}Cu(n,\alpha)^{60}Co$	6.8	5.2174 y
$^{93}Nb(n,n')^{93m}Nb$	0.5	16.13 y

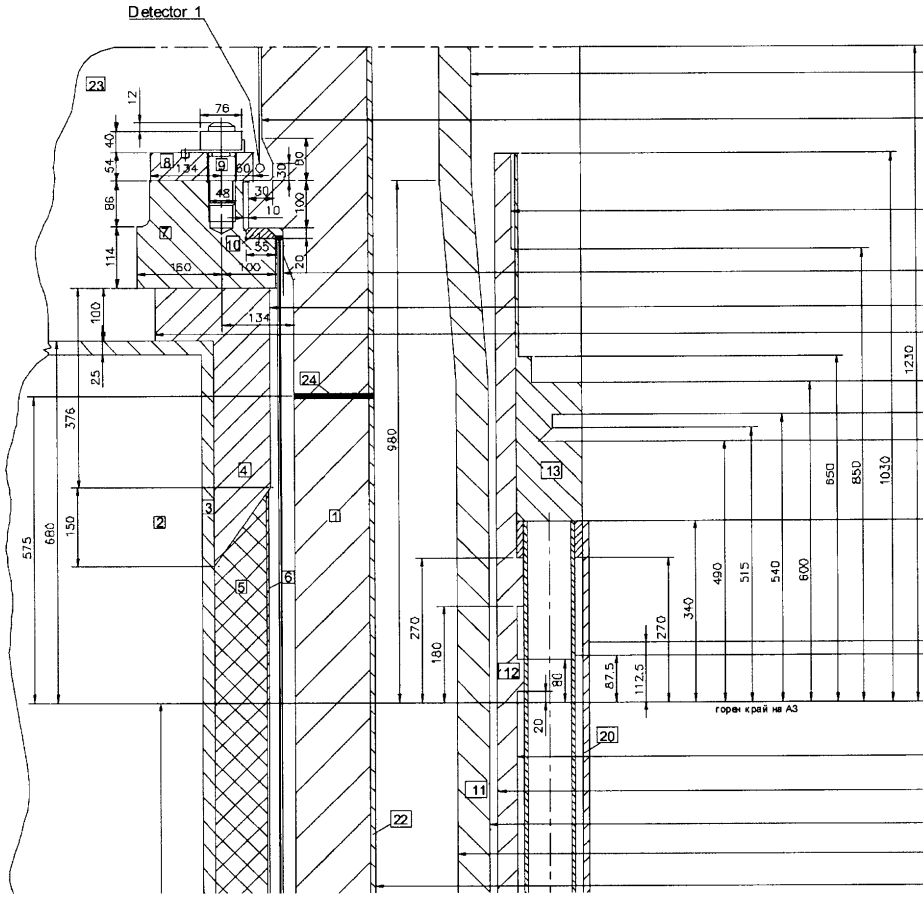

FIG. 4—*Radial-axial geometry of reactor and support structure, Kozloduy NPP Unit 4.*

activities are demonstrated in Figs. 6 and 7 for example. The mean deviation D_{mean}, between calculated Cal, and measured Exp, activities (for N detectors) was determined by the relation:

$$D_{mean} = \frac{1}{N}\sum_{i=1}^{N} (Cal/Exp - 1)_i, \% \quad (3)$$

The D_{mean} values for Position 1 and Position 2 are presented in Table 2.

For the detectors positioned horizontally, above the support structure (Position 1):

- the mean deviation between the calculated and measured Mn and Co activities is less than the uncertainty of measurements;
- the mean deviation of Nb activity is systematically higher, with 6 %, than the uncertainty of measurements.

For the detectors positioned vertically, under the support structure (Position 2):

- the mean deviation of Co activity is less than the uncertainty of measurements;
- the mean deviations of Mn and Nb activities are higher, 5 % and 14 %, respectively, than the uncertainties of measurements.

The calculated activities of copper and niobium detectors irradiated above the support structure as well as activities of niobium detectors irradiated under the support structure are higher than the measured ones.

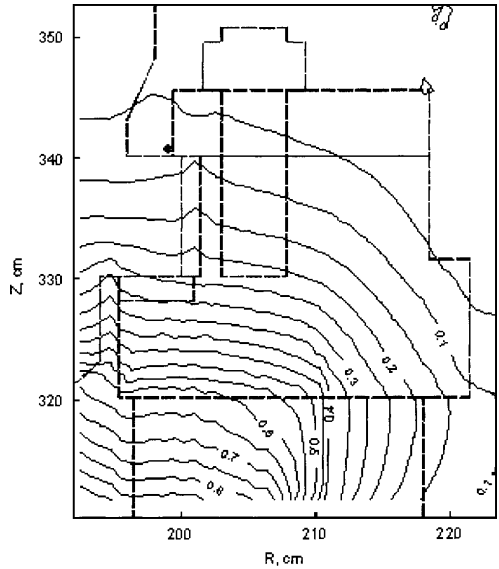

FIG. 5—*Neutron fluence distribution in the area of the support structure normalized to the maximal value (in the bottom left corner).*

Moreover, the mean deviation for all detectors is positive. Consequently, the obtained results show that the fluence evaluation by calculation in the area of support structure is conservative.

Conclusion

The calculation of the neutron fluence in the area of the RPV support structure of Kozloduy NPP with VVER-440/230 type of reactor was validated by activation detectors' measurements.

The comparison between measured and calculated activity data shows that the evaluation of the neutron fluence is conservative with uncertainty that does not exceed the maximum experimental uncertainty of activity measurements that is lower than 15 %.

The results of the performed validation give a confidence in the extrapolation of calculated neutron fluence data for lifetime estimation of Kozloduy NPP Unit 4.

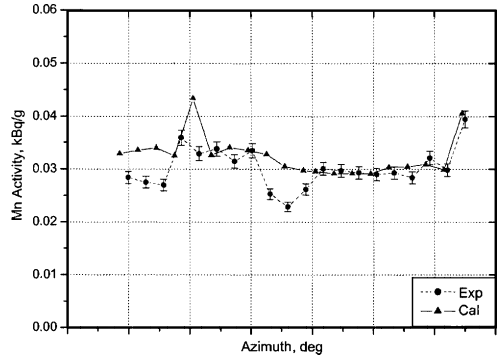

FIG. 6—*Calculated and measured (with uncertainty) ^{54}Mn activity values of detectors irradiated above the support structure, Position 1, during 17th cycle of Kozloduy NPP Unit 4.*

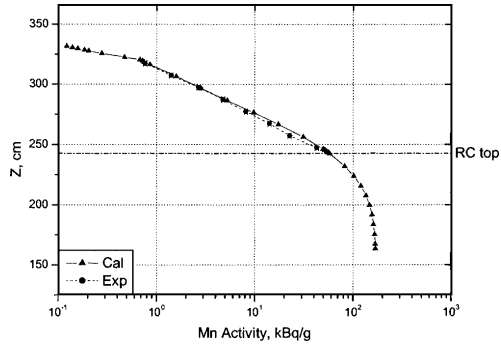

FIG. 7—*Measured and calculated ^{54}Mn activity of detectors irradiated behind the RPV, Position 2, from the technological break up to the end of cycle 17, Kozloduy NPP Unit 4.*

TABLE 2—*Mean deviation D_{mean} [%], in Position 1 and Position 2.*

	^{54}Mn	^{60}Co	^{93m}Nb
Position 1 (horizontal)	7.9	8.9	20.8
Position 2 (vertical)	11.0	0.8	20.8

Acknowledgments

This work was carried out under the contract of the Framatome ANP GmbH "Evaluation of the RLT of Units 1-4 of NPP Kozloduy."

References

[1] *Regulations and Calculation Norms for Equipment and Tubing Strength of the Nuclear Energy Facilities*, PNAE G-7-002-86, PNAE G-7-008-89, Gosatomenergonadzor, Energoatomizdat, 1989.
[2] Erdtmann, G., *Neutron Activation Tables*, Verlag chemie, Weinheim-New York, 1976.
[3] E 263-93, *Test Method for Measuring Fast-Neutron Reaction Rates by Reactivation of Iron*.
[4] E 523-92, *Test Method for Measuring Fast-Neutron Rates by Radoiactivation of Copper*.
[5] E 1297-96, *Standard Test Method for Measuring Fast-Neutron Reaction Rates by Reactivation of Niobium*.
[6] Thomas, S., *Programm PYTHIA zur Berechnung des Makroabbrands in Druckwasserreaktoren vom Typ WWER*, Berlin, K.A.B., 1996.
[7] Rhoades, W. A. and Childs, R. L., *TORT Three-Dimensional Discrete Ordinate Neutron/Photon Transport code with Space-Dependent Mesh and Quadrature*, ORNL-6268, Nov. 1987.
[8] Bucholz, J. A., Antonov, S. Y., and Belousov, S. I., *BGL440 and BGL1000 Broad Group Neutron/Photon Cross-Section Libraries Derived from ENDF/B-VI Nuclear Data*, INDC(BUL)-15, Distrib.:G, Nov. 1996.
[9] IRDF90, v. 2, *The International Reactor Dosimetry File*, IAEA-NDS-141.
[10] Antonov, S., Popova, I., Belousov, S., and Ilieva, K., "Software for Neutron Source Input for Discrete Ordinates Neutron Transport Codes," in Report of IAEA RC 8621/1996; *BgNS Transactions*, Vol. 3, No. 1, 1998, pp. 100–103.
[11] Ilieva, K., Antonov, S., and Belousov, S., "Calculation Modeling of Detector Activity in the VVER/PWR Reactor Pressure Vessel Surveillance," *Nucl. Sci. Eng.*, January 1996, Vol. 122, No. 1.

Journal of ASTM International, Vol. 3, No. 9
Paper ID JAI100341
Available online at www.astm.org

N. E. Holden,[1] *R. N. Reciniello,*[1] *J.-P. Hu,*[1] *J. Leith,*[2] *and T. N. Tehan*[2]

Reactor Dosimetry Study of the Rhode Island Nuclear Science Center

ABSTRACT: The RINSC is a 2 MW light water reactor that has a graphite thermal column, that is used for educational and industrial applications as well as for biological research. A series of measurements and calculations have been performed in this thermal column. Thermoluminescent dosimeter measurements of the neutron dose rate and the gamma-ray dose rate, as well as bare gold foil and cadmium covered gold foil measurements of the thermal and epithermal neutron flux densities are graphically compared to MCNP Monte Carlo calculations.

KEYWORDS: RINSC, neutron dose, gamma dose, MCNP, neutron flux, photon flux, TLD

Introduction

The Rhode Island Nuclear Science Center (RINSC), located on the Narragansett Bay Campus of the University of Rhode Island, is a state-owned and U.S. NRC-licensed nuclear facility constructed for educational and industrial applications [1]. The main building of RINSC houses a 2 MW thermal power critical reactor immersed in demineralized water within a shielded tank. As its original design in 1958 by the Rhode Island Atomic Energy Commission focused on the teaching and research use of the facility, only a minimum of 3.85 kg fissile uranium-235 was maintained in the fuel elements to allow the reactor to reach a critical state. In 1986 when RINSC was temporarily shut down to start a U.S. DOE-directed core conversion project for national security reasons, all the U-Al based Highly-Enriched Uranium (HEU, 93 % uranium-235 in the total uranium) fuel elements were replaced by the newly developed U_3Si_2-Al based Low Enriched uranium (LEU, 20 % uranium-235 in the total uranium) elements [2]. The reactor first went critical after the core conversion was achieved in 1993, and a feasibility study on the core upgrade to accommodate Boron Neutron-Capture Therapy (BNCT) was completed in 2000 [3].

The 2-MW critical reactor at RINSC, which includes six beam tubes, a thermal column, a gamma-ray experimental station and two pneumatic tubes, has been extensively utilized as neutron-and-photon dual source for nuclear-specific research in the areas of material science, fundamental physics, biochemistry, and radiation therapy. After the core conversion, along with several major system upgrades (e.g., a new 3-MW cooling tower, a large secondary piping system, a set of digitized power-level instruments), the reactor has become more compact and thus more effective in generating a high neutron flux in both the in-core and ex-core regions for advanced research. If it had not been limited by the manpower and operating budget in recent years, the RINSC built "in concrete" structure and control systems should have been systematically upgraded to a 5 MW power facility to further enhance its experimental capability while still maintaining its safe margin as designed [2].

In this paper, the theoretical prediction of the flux and dose of neutrons and photons transported from the in-core region to the ex-core irradiation facility (thermal column) is presented, based on Monte Carlo results obtained from the processing of MCNP code [4]. The 5-ft wide 5-ft high and 10-ft long thermal column, which was constructed by piled graphite blocks, has been fully simulated by code to complement an earlier MCNP model that only includes the in-core geometry for the fuel conversion analysis [3].

Manuscript received June 20, 2005; accepted for publication May 18, 2006; published online October 2006. Presented at ASTM Symposium on Reactor Dosimetry, 12th International Symposium on 8–13 May 2005 in Gatlinburg, TN; D. W. Vehar, D. M. Gilliam, and J. M. Adams, Guest Editors.

[1] Guest Physicist, National Nuclear Data Center, and Health Physicist, Radiological Control Division, and NY State Professional Engineer, National Synchrotron Light Source, respectively, Brookhaven National Lab, Upton, NY 11973-5000.
[2] Guest Scientist and Director, respectively, Rhode Island Nuclear Science Center, Narragansett, RI 02882.

Dosimetry data measurements from thermoluminescent dosimeters (TLD badges containing ^{6}LiF or ^{7}LiF chips) and bare and cadmium-covered gold foil measurements are also presented through comparison with the computed results. Details of the code model and dosimeter utilization are described in this paper.

Reactor Core and Irradiation Facility

The RINSC reactor, as shown in Figs. 1(*a*) and 1(*b*), is a 2 MW thermal power, university-type research reactor immersed in a 36 000-gal pool of demineralized water. The pool is contained in an open shielded tank, divided into three sections (low power section, fuel storage section, high power section), that is approximately 22.5-ft long, 8.5-ft wide, and 32-ft deep. The high power section is circular with a diameter of 8.5 ft and a depth of 32 ft. Neutron beam ports, 6 and 8 in. in diameter, penetrate the biological shield and terminate at the core face. Two pneumatic systems confined within 2-in. diameter tubes also terminate at the core face. A 10-ft long thermal column, indicated by the regions A, B, and C in Fig. 1(*a*), extends through the shield to the high power end of the pool.

The reactor core as shown in Fig. 2 is configured from individual fuel elements placed in a core grid box at 26 ft beneath the pool surface. The grid box is attached to the base of a suspension frame, which in turn is attached above the pool surface to a movable bridge that spans the width of the pool. Control of the reactor is achieved through the use of four shim-safety blades and one regulating blade. The safety blades are an alloy of aluminum and boron (B_4C based Boral™); the regulating blade is a hollow, stainless steel, rectangular tube. The shim-safety blades are held up by electromagnets at the ends of aluminum extensions that attached to drive motors above the pool surface. The normal method for shutting down the reactor is insertion of the blades with their drive motors. In the event of an emergency, the electric current can be turned off to the electromagnets and the blades will drop freely into the core.

The reactor's thermal column is a graphite pile, which is 5-ft wide by 5-ft high by 10-ft long within a concrete biological shield. There is a 3-in. thick lead shield and a 2-in. thick aluminum cooling plate (31 in. downstream of the lead shield) between the reactor core and the thermal column, which extends to the outer face of the concrete shield (within a 1-in. steel framing). The thermal column is made up of consecutive graphite blocks, each being 4 in. by 4 in. in cross section. Near the centerline of the thermal column, a 2 in. by 2 in. air beam hole has been designed to accommodate samples and apparatus for experimental usage. During the criticality operation in 1964 at 1 MW power, the ex-core peak flux of thermal neutrons and that of fast neutrons, with HEU fuel elements in the core, were 1.5×10^{8} n/cm^2/s and 1.5×10^{7} n/cm^2/s, respectively, at the cooling plate (the location where the air beam hole starts). In 1996, measurements at 100 kW power with LEU fuel elements in the core, the ex-core peak flux of thermal neutrons, and epithermal neutrons were, respectively, 3.9×10^{9} n/cm^2/s and 1.3×10^{7} n/cm^2/s at the cooling plate.

The name of the thermal column reflects the goal of its design and the property of its constituent, in that most of the core neutrons transported through the long beam path in graphite should be efficiently moderated before being absorbed by the material in the target samples (tallies in the model). Since neutrons in the thermal energy region dominate the spectrum of the neutron flux up to 10 MeV, the counting of the fast neutrons in the thermal column requires the use of the flux-reduction technique (e.g., using cadmium to shield thermal neutrons) to improve the accuracy of the fast neutrons. In the gamma-ray dose rate measurements, due to the presence of a 3-in. lead shield in an aluminum tank (0.25-in. thick wall) next to the reactor core, only the photons with energies >1 MeV can be detected within an acceptable statistical uncertainty ($<10\%$ at the one-sigma level). Since the decay of gamma-rays in the thermal column has been confirmed to follow an exponential curve based on the data obtained from both calculations and measurements, the dose rate at the front-face of the thermal column (6 in. from the core edge, 2.5 in. behind the 3-in. lead shield) will be $\sim7.8\times10^{8}$ mR/h at 1 MW operation. At the aluminum cooling plate (nearly 3 ft from the core edge), the gamma-ray dose rate will be reduced to 8.2×10^{6} mR/h. At 5 ft and at 8 ft from the face of the thermal column, the predicted dose rate will be reduced to 9.2×10^{5} mR/h and 4.3×10^{4} mR/h, respectively.

Computational Model

Simulation of the RINSC reactor for core conversion analysis has been thoroughly performed during 1986–1993 by the use of Monte Carlo particle transport code MCNP [4]. This statistical-based code that

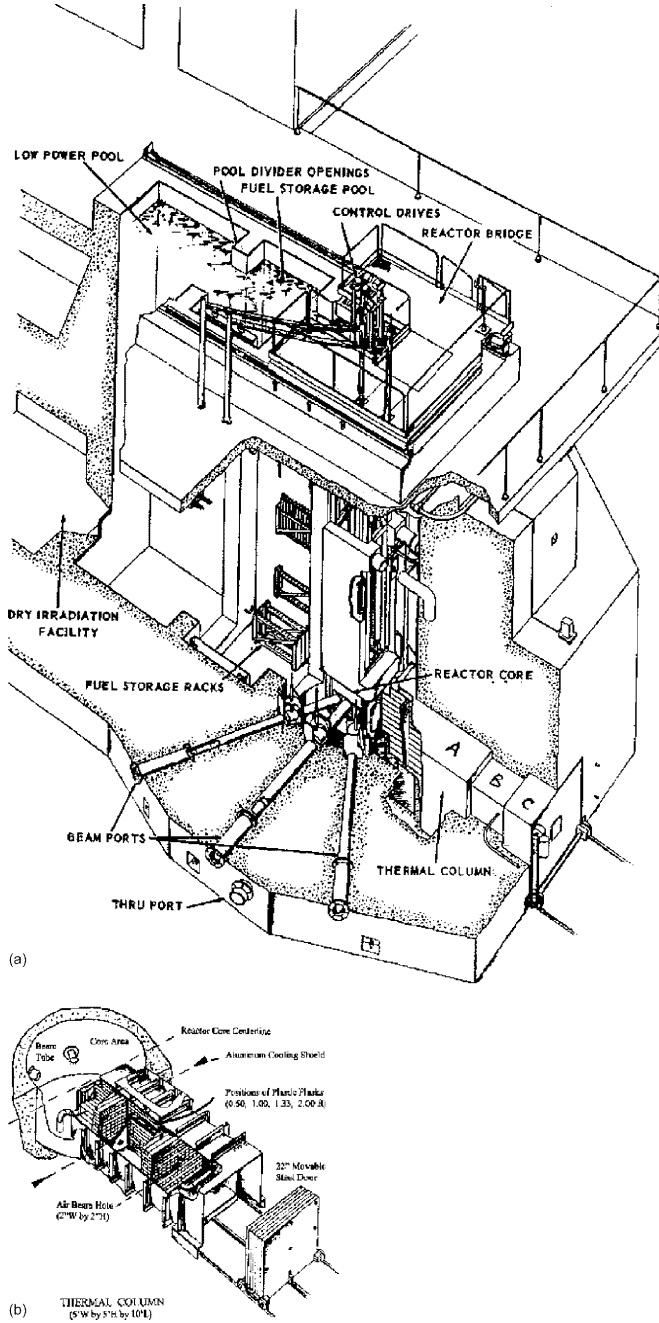

FIG. 1—*(a) The RINSC reactor facility shown above includes the reactor core, horizontal beam ports, control rod system, and graphite thermal column (A-B-C) in the fuel pool. The graphite thermal column (A-B-C) developed for sample irradiation is shown at the right. (b) The graphite thermal column at RINSC is fully modeled for dose estimation.*

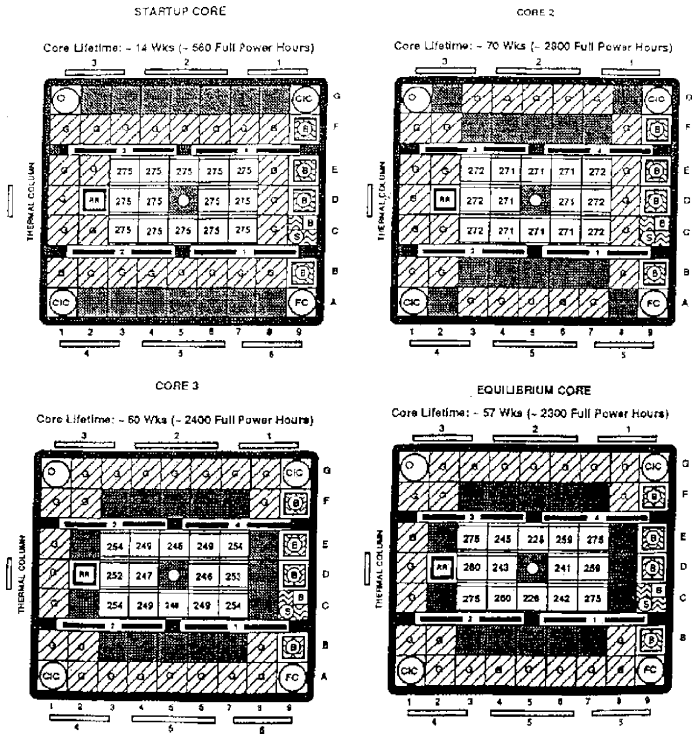

FIG. 2—*The gram amounts of uranium-235 in 14 HEU elements at the 1964 startup, transition (core 2 and 3), and equilibrium core in the RINSC reactor where lifetimes were based on recorded operation of 8 hours per day and 5 days per week.*

has been developed and periodically updated by the Los Alamos National Laboratory is a general purpose Fortran compiled software package, which can be used to model any single particle motion or coupled neutron photon transport in a 3-D geometry consisting of different material regions. For the in-core parameter analysis [3], detailed geometrical configuration of the key elements plus a full set of material cross sections (including the cross section sets for thermal neutron treatment) must be incorporated into the model input for code processing in order to obtain results with high accuracy. For the ex-core irradiation studies, due to the presence of multiple material regions through which most of the core particles, if not absorbed by or leaked out from the system, must have been slowed down via inelastic scattering before reaching samples or TLDs, a homogenized reactor core (diminished angular and distant-effect of point sources in the core to remote tallies) followed by segmented material zones (to orient particle transport in geometry by optional weighting factors) can be set up in the model to expedite the code run while maintaining the source strength to its downbeam areas. To judge the adequacy of the model simplification, checking on the core criticality, and flux distribution based on the present reactor status (e.g., uranium consumed, sample used) are essential.

The MCNP model developed for the in-core and ex-core analysis can be observed from Fig. 3, in which the left one represents a full-core geometry comprising fuel plates (F) and control blades (B) in the central elemental cells (C) surrounded by the reflector (beryllium, R) and moderator (graphite, G) cells, symmetrical to the core midplane. The right two figures, respectively, represent a simplified RINSC core and a full-reactor geometry containing homogenized material regions (in light water, W) and segmented thermal column (including aluminum cooling plate). To expand model geometry from a full core (in-core analysis) to a full reactor (ex-core studies), sets of criticality test-runs according to the actual amount of ^{235}U (3.5 kg in an equilibrium core and 3.85 kg in a fresh core), ^{238}U (four times the amount of ^{235}U in the

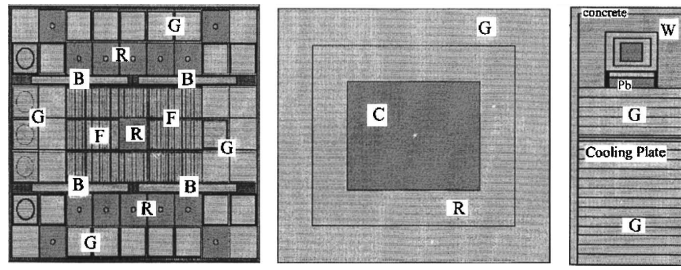

FIG. 3—*The left figure shows the MCNP geometry for in-core parameter analysis and the right two figures show the homogenized core and segmented thermal column for the ex-core tally (flux and dose) estimate.*

LEU fuel), ^{14}Si and ^{27}Al (in atomic ratio of U:Si:Al=3:2:1 for the U_3Si_2–Al fuel), ^{10}B and ^{11}B (in an atom ratio of ^{10}B:^{11}B=1:4 for natural boron in the four control blades), ^{56}Fe (one regulating blade), ^{1}H and ^{16}O (space-filled light water in the ratio of ^{1}H:^{16}O=2:1), ^{12}C and ^{9}Be (reflector elements), concrete (biological shield), and natural Pb (gamma shield) must be performed through adjustment on the boron contents in the core to approach K_{eff}=1.00+an excess reactivity. The term of excess reactivity is reserved to balance the negative worth measured from target samples and irradiated apparatus. In the code input of the material section, the boron alone (^{10,11}B) has been set as adjustable because of the fact that all four safety blades are actually located outside of the fuel elements and thus are less effective in neutron absorption than determined by the uniformly distributed boron in a homogenized core as set in the model. Furthermore, under reactor criticality the four safety blades must have been lifted to a fixed bank position below which the fuel elements are free from blade shielding (i.e., no neutron absorption), thus yielding a nonuniform boron distribution in the core which is different from the material homogeneity setup in code. In addition to the criticality test, the reliability of the calculated flux in the code runs also needs to be checked to ensure the model's adequacy. This can be approached by flux normalization in terms of measured data points along the beam path upstream, from where flux tallies are normally set up. In the RINSC reactor, the reference points are located at the core edge and the cooling plate.

Sample Irradiation

The method for irradiating samples in the thermal column is as follows. The reactor is first brought up to a subcritical point by removing the four safety shim blades. Then the wood pole with the samples on it is inserted into the beam hole of the thermal column, and subsequently the reactor is brought up to power (e.g., 100 kW) for the length of time of the sample irradiation. The reactor was then scrammed for sample removal and counting.

In the latest sample irradiation at RINSC thermal column during November 2004 to January 2005 using the ^{6,7}LiF-based TLD badges, the average dose rates of neutrons and photons obtained from a critical operation of the reactor at 100 to 300 kW power in 2 to 7 min exposure periods are listed in Table 1. Note that due to the initial startup of the reactor by lifting the four safety blades step-wise from criticality at ~10 W until a steady power level of 100 kW is reached, the actual exposure time of the TLD in the thermal column is estimated to be about 1 min longer (~3 to 8 min total irradiation period).

TABLE 1—*Neutron and photon dose rates determined from TLD badges at a reactor power level of 100 kW and for a 3 to 8 min exposure.*

Distance to Cooling Plate (ft)	Neutron Dose (mR/h)	Photon Dose (mR/h)
1.0	1.4E07	1.3E06
2.0	4.8E06	3.7E05
2.5	4.7E06	2.3E05
3.0	3.5E06	1.2E05

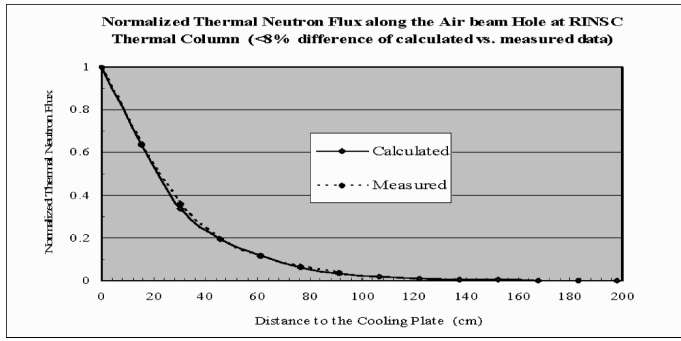

FIG. 4—*Comparison of MCNP calculated versus foil measured thermal neutron flux along the central air beam hole at RINSC thermal column.*

Conclusions

At the RINSC reactor, fission energy neutrons generated from the LEU core are slowed to epithermal energy neutrons through the core edge regions and further slowed down (moderated) into thermal neutrons in the thermal column. When bare and cadmium-covered gold foils were used in the earlier measurements (1993–1996), the measured data compared to MCNP calculated thermal and epithermal flux of neutrons agree within 8 and 20 %, respectively, as shown in Figs. 4 and 5. No photon flux was specifically measured at the time of the neutron flux measurement.

The efforts dedicated to the post core conversion analysis (1993–1996), followed by the major facility upgrade needed for the BNCT project preparation, dominated the limited working time along with the on demand operation of the RINSC reactor. From the neutron-and-photon dual mode MCNP calculations, the flux of photons after normalization with respect to the flux tally obtained at aluminum cooling plate (~3 ft from the core edge) is shown in Fig. 6. For reference regarding future measurements, the flux of photons to a distance of 200 cm (~6.6 ft) down the thermal column is included in the same plot, using exponential decay as a rough estimate.

The use of ^{6,7}LiF-TLDs for dose estimation of the neutrons and photons in the thermal column was recently performed during November 2004 until January 2005. Measured data at 100 to 300 kW power for ~3 to 8-min exposure time (including a 1-min extension for the reactor startup) are presented in Table 1. The normalized curve plotted along the data (with ± uncertainty) from equal-distant TLDs setup in line within the air beam hole is depicted in Figs. 7 and 8, in which the predicted dose by the code MCNP (in solid line) is also included for comparison. In most of the measurements conducted previously and pres-

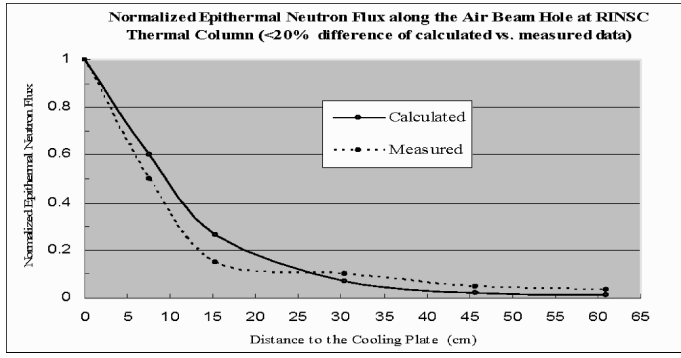

FIG. 5—*Comparison of MCNP calculated versus foil measured epithermal neutron flux along the central air beam hole at RINSC thermal column.*

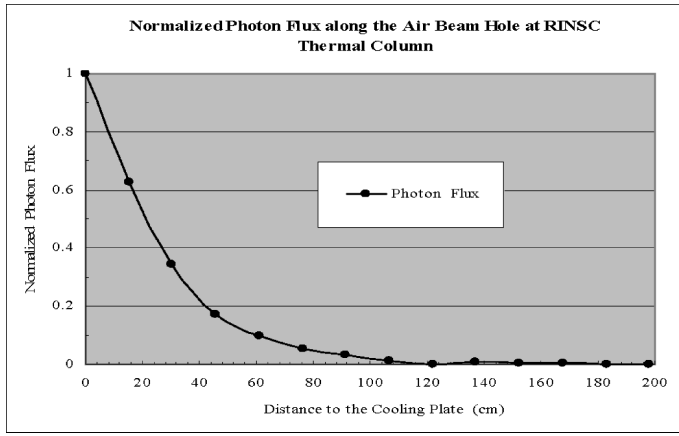

FIG. 6—*MCNP calculated photon flux along the central air beam hole in thermal column.*

ently, the result's uncertainty has been found to be <9 % of the population mean, while the maximum difference has been 23 % which occurred at downstream sample locations (>3 ft) in the thermal column or occurred due to a short irradiation period (of ~2 to 7 min). Compared to the calculated dose from MCNP runs, the maximum discrepancy for the neutron dose is ~23 % and for the gamma dose is ~14 %. Both of these maxima occur at the furthest location from the cooling plate (>3 ft).

The dose discrepancy is larger for neutrons than for photons, since the code embedded flux-to-dose conversion for the epithermal neutrons is up to 30 times higher than that for thermal neutrons, while the variation is much slighter (a factor of 6.73) for conversion of the prompt photons (>1 MeV). To ensure the reliability of radiation dose from the calculations, two sets of conversion factors [5] are recommended for use in the future.

Acknowledgment

This research was partly supported by the U.S.-DOE under the contract DE-ACO2-98CH10886 (BNL) and partly supported by the U.S.-DOE Nuclear Energy Grant (RINSC).

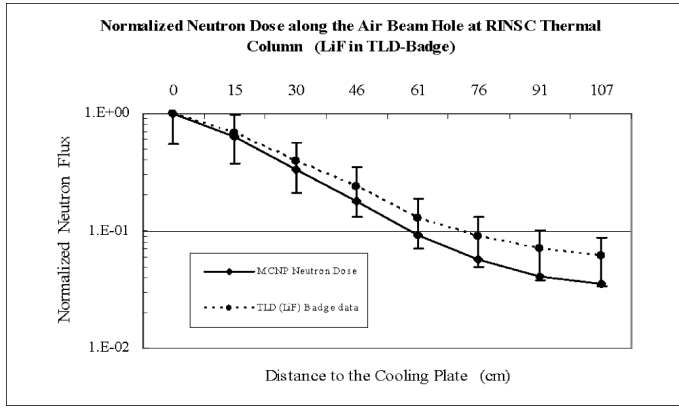

FIG. 7—*Comparison of MCNP calculated versus TLD measured neutron dose along the central air beam hole at RINSC thermal column.*

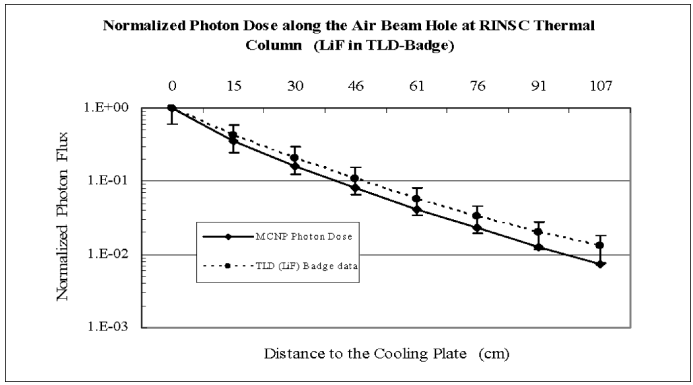

FIG. 8—*Comparison of MCNP calculated versus TLD measured photon dose along the central air beam hole at RINSC thermal column.*

The authors wish to acknowledge the support with reactor operation, sample installation, and data compilation by W. Simoneau, H. Bicehouse, M. Middleton, and M. J. Davis of the RINSC, and the provision of MCNP in-core model by Dr. S. C. Mo of the Argonne National Laboratory.

References

[1] Rhode Island Nuclear Science Center (RINSC), edited in the *Research, Training, Test and Production Reactor Directory*—United States of America, 1st ed., published by the American Nuclear Society, La Grange Park, IL, 1980, pp. 1091–1112.

[2] Tehan, T., "The Rhode Island Nuclear Science Center Conversion from HEU to LEU Fuel," *2000 International Reduced Enrichment for Research and Test Reactors Meeting Program* (*RERTR*, http://www.rertr.anl.gov), Las Vegas, NV, 1–6 October 2000.

[3] Mo, S. C. et al., "Modification of the RINSC LEU Core to Increase Fluxes for BNCT Study," *2000 International Reduced Enrichment for Research and Test Reactors* Meeting Program (*RERTR*, http://www.rertr.anl.gov), Las Vegas, NV, 1–6 October, 2000.

[4] Briesmeister, J. F., Ed., *MCNP—A Monte Carlo N-Particle Transport Code (version 4B2)*, developed by the Los Alamos National Laboratory (LA-12625-M), and distributed by the Oak Ridge National Laboratory (CCC-660), 1997.

[5] ICRP-21 and NCRP-38, ANSI/ANS-6.1.1–1977, "Neutron Flux to Dose Rate Conversion Factors and Quality Factors," published by the American Nuclear Society, La Grange Park, IL1977.

Journal of ASTM International, Vol. 3, No. 8
Paper ID JAI13427
Available online at www.astm.org

Gabor Hordosy,[1] *Gyorgy Hegyi,*[1] *Andras Kereszturi,*[1] *Csaba Maraczy,*[1] *Peter Vertes,*[2] *and Eva M. Zsolnay*[3]

Comparison of the Results of the Calculational and Experimental VVER-440 Pressure Vessel Dosimetry at Paks NPP

ABSTRACT: At Paks NPP, Hungary, a major project was launched to investigate the possibility of lifetime extension up to about 60 years. As a part of this project, detailed calculational and experimental investigation of the pressure vessel neutron radiation load having been performed. A computational procedure was developed earlier for evaluating the fast flux in the pressure vessel. The neutron source is taken from core calculation performed by the code KARATE and it is given in the core boundaries. The neutron transport from the source to and through the pressure vessel is investigated by MCNP4C. This procedure has now been tested against a new set of activation foil measurements. Good agreement was found between the measured and calculated reaction rates for fast reactions. In the case of thermal reactions, the agreement was weaker. The effect of error in nuclear data on fast reaction was studied.

KEYWORDS: reactor dosimetry, pressure vessel calculations, activation measurements

Introduction

Hungary has four units of VVER-440 pressurized water reactor [1] at the Paks Nuclear Power Plant (NPP). Investigation of the possibility of the lifetime extension of these units up to 60 years is going on. The radiation load is to be determined for the past and planned future reactor cycles for this time. The lead factor (defined as the ratio of fast flux at the surveillance test specimen and at the fast flux at the pressure vessel) has values of about 17–20 for the VVER-440 reactors. This high value makes possible the experimental monitoring of the degradation of pressure vessel material, because the test specimens at the surveillance positions receive as much radiation load during a few years as the pressure vessel during the planned extended lifetime.

However, the flux at the pressure vessel may change essentially with time because of the change in loading strategy and operational conditions. Introduction of new fuel will further modify this change. Consequently, for accurate prediction of the fluence of pressure vessel, the change of the neutron source in the core should be followed with sufficient frequency. This implies that the flux in the pressure vessel should be calculated at a great number of times; i.e., a lot of shielding calculations should be performed.

To speed up these calculations, a mixed procedure was developed and applied at KFKI AERI. The neutron source was specified on the boundaries of the core, and this source was used in the subsequent Monte Carlo calculation. In this way, the neutron transport inside the core was investigated by a core design code, saving essential amount of computer time. (Using this procedure, a detailed three-dimensional (3D) fluence distribution was determined in the pressure vessel of all four units.) However, such a procedure requires experimental verification. The first steps of this have already been done and published in [2] for such cases, when foils were irradiated for one cycles. In this paper, the results of further comparison will be shown, where the foils were irradiated for 3, 4, and 5 cycles.

Manuscript received June 20, 2005; accepted for publication May 16, 2006; published online June 2006. Presented at ASTM Symposium on Reactor Dosimetry, 12th International Symposium on 8–13 May 2005 in Gatlinburg, TN; D. W. Vehar, D. M. Gilliam, and J. M. Adams, Guest Editors.

[1] Research scientist, KFKI Atomic Energy Research Institute, H-1525 Budapest 114, P.O.B. 49, Hungary.
[2] Senior research scientist, KFKI Atomic Energy Reserch Institute, H-1525 Budapest 114, P.O.B. 49, Hungary.
[3] Associate professor, Budapest University of Technology and Economics, Institute of Nuclear Techniques, H-1521 Budapest P.O.B. 91, Hungary.

Computational Procedure

The neutron source on the outer surface of the reactor core was evaluated by the help of KARATE code [3]. KARATE is a 3D nodal code with coupled neutron physical-thermohydraulical model developed in KFKI AERI. It solves the neutron transport equation in linearly anisotropic approximation; i.e., the neutron flux and current is calculated on the surfaces of the nodes. It was validated against a number of measurements and benchmarks. It is routinely used at Paks NPP. It consists of four levels of calculations with consistent bi-directional connection between levels via parameterization:

- First level: Multigroup spectral calculations to determine the cross sections for the two- or four-group calculations and the energy spectra of the neutron flux and current. Thirty-five thermal and 35 epithermal groups are used.
- Second level: four-group, two-dimensional fine mesh reflector albedo calculations to evaluate the core-reflector albedo matrices.
- Third level: two-group, two-dimensional fine-mesh calculations, which determine the linear power distribution of the fuel rods. From these calculations the fission source for every level of the fuel rods and for every isotope can be determined.
- Fourth level: core-level, nodal calculations, which calculate the power distribution at the assembly level and the boundary conditions for the third level of the calculations.

Using KARATE for pressure vessel source calculations, the reactor core was divided into nodes by ten horizontal planes. An axial segment of an outer surface of a fuel assembly in the outermost row is called as "page" in the following when this segment corresponds to a node. These "pages" are numbered according to a scheme, and their surface and the outward normal vector is denoted by F_i and $\mathbf{n}_i$. The Monte Carlo source for the pages can be connected by the flux and current evaluated for that surface.

If the angular current and flux is denoted by $\mathbf{J}^*(\mathbf{r},E,\mathbf{\Omega})$, $\Phi^*(\mathbf{r},E,\mathbf{\Omega})$ where $\mathbf{r}$ is the position, E is the energy, and $\mathbf{\Omega}$ is the solid angle, then $\mathbf{J}^*(\mathbf{r},E,\mathbf{\Omega})=\Omega\Phi^*(\mathbf{r},E,\mathbf{\Omega})$. Assuming that the neutron distribution is uniform on a particular page, the Monte Carlo source for that page can be written as

$$S_i = \int_{Fi} \mathrm{d}\mathbf{r}(\mathbf{n_i J}^*) = \int_{Fi} \mathrm{d}\mathbf{r}(\mathbf{n_i \Omega})\left[\frac{1}{4\pi}\Phi(\mathbf{r},E) + \frac{3}{4\pi}\mathrm{J}(\mathbf{r},E)(\mathbf{n_i \Omega})\right] \tag{1}$$

or more conveniently

$$S_i(E,\mathbf{\Omega}) = S_{i,1}(E)(\mathbf{n_i \Omega}) + S_{i,2}(E)(\mathbf{n_i \Omega})^2 \tag{2}$$

where $\Phi(\mathbf{r},E)$ and $\mathrm{J}(\mathbf{r},E)$ are the scalar flux and current, respectively, and the index i refers to a particular page. (Here, the linearly anisotropic approximation of the angular flux was used.) Using this result, the source can be defined for each page as a weighted sum of a linearly and a quadratically anisotropic term. The weights depend on the energy and on the page. MCNP4C [4] cannot handle double dependence of a variable, but the calculation can be performed in two steps, performing one calculation with linearly and one calculation with quadratically anisotropic angular dependence of the source.

Calculations were performed in a "quasi-3D model" to determine the error of the calculated reaction rate due to the uncertainty of nuclear data library of iron. This error was calculated using the covariance data processed by the NJOY code [5] and the sensitivities calculated by the perturbation capabilities of MCNP. Because the trial calculations with ENDF/B-VI library gave unrealistically high error (larger than 100 %), the ENDF/B-V in library was used for steel composition in the neutron transport calculations. The results of these calculations will be shown later on Table 5 in connection with comparison of measured and calculated reaction rates. For evaluation of the reaction rates, the IRDF90 [6] dosimetry library was used.

Comparison of Measurements and Calculations

For the testing of the calculational method, the measurements performed for the 8-11 and 9-11 cycles of Unit II and the measurements performed for the 7-11 cycles of Unit IV were used. Around the core, six irradiation places can be found. At each irradiation place there are 2 irradiation capsule assemblies in capsule holder tubes. A typical assembly consists of 19 or 20 capsules. The detector chains can be found next to the core barrel with a stainless steel cover. They are located at the azimuthal flux maximum. The capsules contain several kinds of activation foils and Charpy impact test specimens made of reactor vessel material. Unfortunately, some of the detectors were damaged during the removal from the capsules.

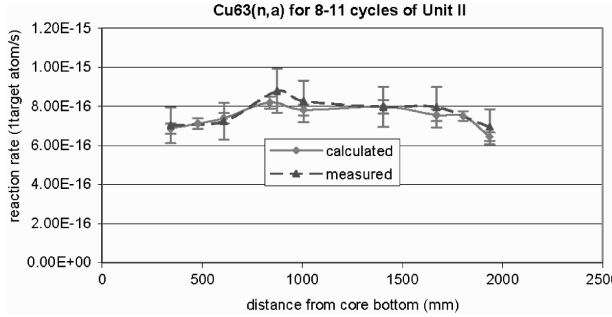

FIG. 1—*Measured and calculated $^{63}Cu(n,\alpha)^{60}Co$ reaction rates for the 8-11 cycles of Unit II.*

The capsule assemblies with the test specimens and activation foils were modeled in detail in the MCNP calculation. Load follow calculations were performed for these cycles to get the correct sources. Generally four MCNP calculations were performed per cycle. The fast reactions $^{54}Fe(n,p)^{54}Mn$, $^{93}Nb(n,n')^{93m}Nb$, $^{63}Cu(n,\alpha)^{60}Co$, and the thermal reaction $^{93}Nb(n,\gamma)$ were measured at different locations. The comparison of calculated and measured values for Unit II is shown in Figs. 1–7 together with their error.

In the case of Unit IV, quite a lot of irradiated foils were damaged during the removal, so that we have measurements at only three different axial positions. Because of this limited number of positions, the comparison is presented only in the tables (see Tables 1–4).

From the inspection of figures and tables shown above, it can be seen that the agreement for the three fast reactions $^{54}Fe(n,p)^{54}Mn$, $^{93}Nb(n,n')^{93m}Nb$, $^{63}Cu(n,\alpha)^{60}Co$ is good. With one exception, the deviation

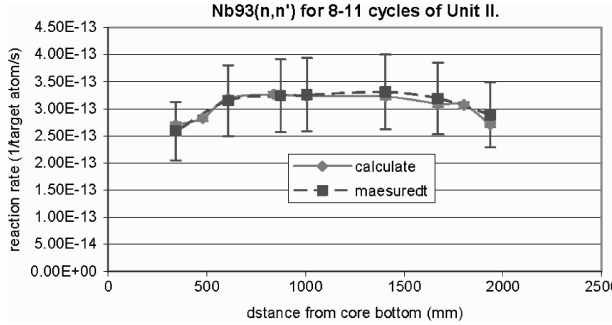

FIG. 2—*Measured and calculated $^{93}Nb(n,n')^{93m}Nb$ reaction rates for the 8-11 cycles of Unit II.*

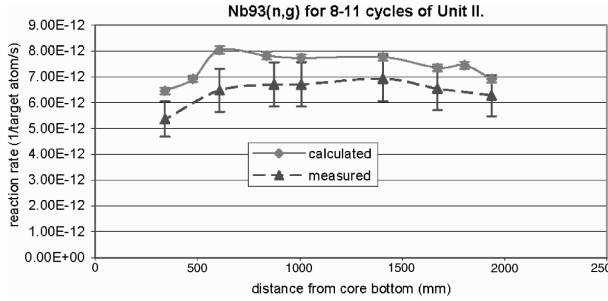

FIG. 3—*Measured and calculated $^{93}Nb(n,\gamma)$ reaction rates for the 8-11 cycles of Unit II.*

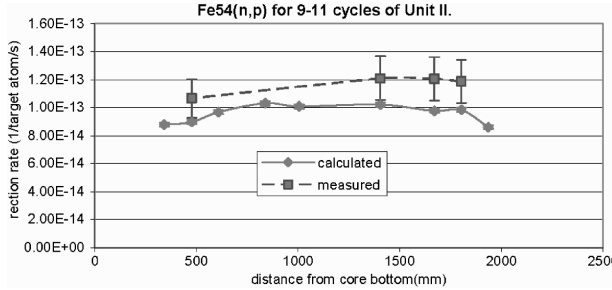

FIG. 4—*Measured and calculated $^{54}Fe(n,p)^{54}Mn$ reaction rates for the 9–11 cycles of Unit II.*

between the measured and calculated values is less, which comes from the measurement error and the statistical error of the computation. The only exception is the case of $^{54}Fe(n,p)^{54}Mn$ for the 9–11 cycles of Unit II, but the deviation here also can be explained by the error due to the uncertainties of nuclear data, which is shown in Table 5. These uncertainties were evaluated using the covariance data and the reaction sensitivities evaluated in 14 energy groups by the perturbation capability of MCNP.

However, the case of thermal reaction $^{93}Nb(n,\gamma)$ is more complicated. In the case of 9–11 cycles of Unit II the agreement is good, the measured and calculated values are agreement within the experimental and statistical error. In the case of 8–11 cycles of Unit II, and particularly in the case of 7–11 cycles of Unit IV the deviation is quite large, in some cases it is above 30 %. Unfortunately, that moment for this reaction the sensitivity analysis of nuclear data has not been performed. Thus, the clarification of this difference needs further work.

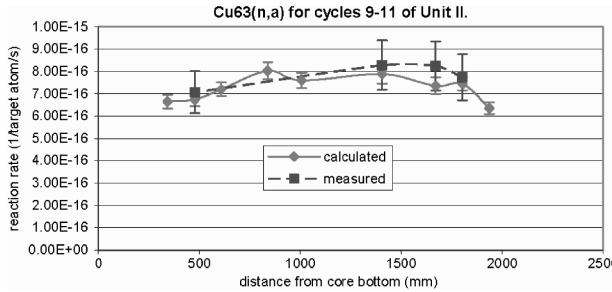

FIG. 5—*Measured and calculated $^{63}Cu(n,\alpha)^{60}Co$ reaction rates for the 9–11 cycles of Unit II.*

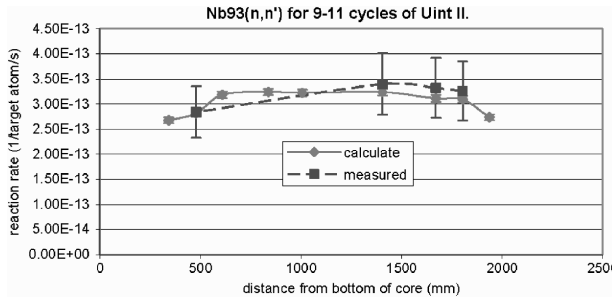

FIG. 6—*Measured and calculated $^{93}Nb(n,n')^{93m}Nb$ reaction rates for the 9–11 cycles of Unit II.*

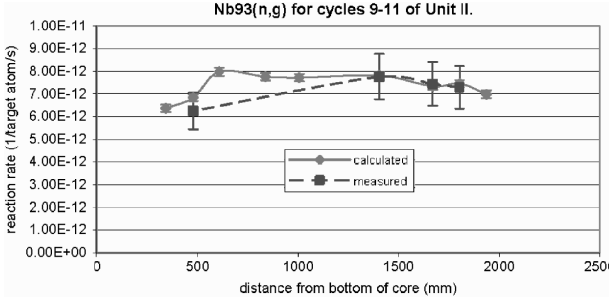

FIG. 7—*Measured and calculated $^{93}Nb(n, \gamma)$ reaction rates for the 9–11 cycles of Unit II.*

Summary

Reaction rates were calculated and measured for different axial positions in surveillance position of Units II and IV of the Paks NPP. Detailed operational history of the reactor was taken into account in deriving the neutron source for the calculations. A surface source was used to accelerate the Monte Carlo calculations. Good agreement was found in the case of the fast reaction, but quite large discrepancies were found in some cases for the thermal reaction $^{93}Nb(n,\gamma)$. The explanation of this deviation needs further examination.

TABLE 1—*$^{54}Fe(n,p)^{54}Mn$ reaction rates for cycles 7-11 of Unit IV.*

h, mm	R_m	σ_m, %	R_c	σ_c, (%)	Δ %
875.6	1.15×10^{-13}	4.8	1.07×10^{-13}	0.47	−7.0
610.2	1.04×10^{-13}	4.8	1.00×10^{-13}	0.48	−3.8
475.3	9.24×10^{-14}	5.8	9.3×10^{-14}	0.49	0.6

TABLE 2—*$^{93}Nb(n,n')^{93m}Nb$ reaction rates for cycles 7-11 of Unit IV.*

h, mm	R_m	σ_m, %	R_c	σ_c, %	Δ, %
875.6	3.18×10^{-13}	5.8	3.13×10^{-13}	0.65	−1.6
610.2	2.96×10^{-13}	5.8	2.99×10^{-13}	0.66	1.0
475.3	2.57×10^{-14}	5.8	2.79×10^{-14}	0.71	8.6

TABLE 3—*$^{63}Cu(n,\alpha)^{60}Co$ reaction rates for cycles 7-11 of Unit IV.*

h, mm	R_m	σ_m, %	R_c	σ_c, %	Δ, %
875.6	8.11×10^{-16}	4.8	8.39×10^{-16}	1.40	3.5
610.2	7.14×10^{-16}	4.7	7.60×10^{-16}	1.26	6.4
475.3	6.64×10^{-16}	4.9	7.14×10^{-16}	1.19	7.5

TABLE 4—*$^{93}Nb(n, \gamma)$ reaction rates for cycles 7-11 of Unit IV.*

h, mm	R_m	σ_m, %	R_c	σ_c, %	Δ, %
875.6	6.03×10^{-12}	4.8	7.55×10^{-12}	0.71	25.2
610.2	5.79×10^{-12}	4.8	7.66×10^{-12}	0.69	32.3
475.3	4.97×10^{-12}	4.7	6.78×10^{-12}	0.72	36.4

TABLE 5—*Uncertainty of the calculated reaction rates due to the iron cross-section error.*

$^{54}Fe(n,p)^{54}Mn$	8 %
$^{63}Cu(n,\alpha)^{60}Co$	9 %
$^{93}Nb(n,n')^{93m}Nb$	6 %

References

[1] Gado, J., Hegedus, Cs. J., Kereszturi, A., Makai, M., Maraczy, Cs., and Telbisz, M., "KARATE—A Code for VVER-440 Core Calculation," *Trans. Am. Nucl. Soc.*, 71, 1994, pp. 485.

[2] Hordosy, G., Hegyi, Gy., Kereszturi, A., Maraczy, Cs., Temesvari, E., Vertes, P., and Zsolnay, E. M., *11th International Symposium on Reactor Dosimetry*, Brussels, Belgium, 2002.

[3] Gado, J., Hegedus, Cs. J., Kereszturi, A., Makai, M., Maraczy, Cs., and Telbisz, M., "KARATE—A Code for VVER-440 Core Calculation," *Trans. Am. Nucl. Soc.*, 71, 1994, pp. 485.

[4] MCNP™—A General Monte Carlo N-Particle Transport Code-Version 4C, LA-13709-M, Breismeister, J., Ed., 2000.

[5] MacFarlane, R. E. and Muir, D. W., The NJOY Nuclear Data Processing System, Version 91, LA-12740-M, 1994.

[6] Kocherov, P. and McLaughlin, P. K., "The International Reactor Dosimetry File IRDF-90, Ver. 2," Report IAEA-NDS-141, Rev. 2, IAEA, Vienna, Oct. 1993.

Journal of ASTM International, Vol. 3, No. 8
Paper ID JAI100361
Available online at www.astm.org

Patrick J. Griffin, Ph.D.,[1] *S. Michael Luker, B.S.,*[2] *Donald B. King, Ph.D.,*[3] *K. Russell DePriest, Ph.D.,*[4] *and Philip J. Cooper, Ph.D.*[5]

Characterizing the Time- and Energy-Dependent Reactor *n*/γ Environment

ABSTRACT: In a reactor pulse, the early radiation has a neutron/gamma component resulting from the prompt fission neutron and gamma radiation and from the neutron-induced secondary gammas. However, after the primary reactor pulse, the radiation environment also includes a time-dependent delayed neutron and gamma component. At even later times, the material activation dominates the source term. When active tests are conducted in the reactor, the radiation environment at a particular time may not be well characterized by the time-integrated spectrum provided by the typical radiation transport calculations. This paper defines the steps that are required to adequately model the time- and energy-dependent radiation environment in the reactor environment. This paper also compares the time-dependent response from a range of active dosimeters in a reactor pulsed environment and shows how the *n*/γ mixed-field response for the dosimeters and the changing radiation field can influence the interpretation of the dosimetry.

KEYWORDS: dosimeter, delayed gamma, PCD, active dosimetry, PIN, calorimeter, radiation rate, flux, activation, fluence rate, fission chamber, ionization chamber, SPND

Introduction

Typical spectrum characterization techniques in reactor environments use integral passive dosimetry metrics (e.g., activation foils or Bonner spheres) to unfold a time-averaged radiation environment. However, the actual reactor radiation environment is more dynamic. In a reactor pulse, the early radiation has a neutron/gamma component resulting from the prompt fission neutron and gamma radiation and from the neutron-induced secondary gammas. However, after the primary reactor pulse, the radiation environment also includes a time-dependent delayed neutron and gamma component. At even later times, the material activation radiation dominates the source term. When active tests are conducted in the reactor, the radiation environment at a particular time may not be well characterized by the time-integrated spectrum provided by the typical radiation transport calculations. When test objects and passive dosimeters are removed from the reactor, they have not only seen the main reactor pulse, but they have also seen the time-dependent delayed fission radiation environment as well as activation gammas. It can be difficult for an experimenter to deconvolute the actual integral radiation environment seen by a test object from the available calculated spectrum characterization data.

The purposes of this paper are (1) to outline a calculational methodology for deconvoluting the time- and energy-dependent radiation environments in a pulsed test reactor field, and (2) to survey the strengths, weaknesses, and consistency of the time-dependent active dosimetry from available monitors that can be

Manuscript received June 20, 2005; accepted for publication May 24, 2006; published online August 2006. Presented at ASTM Symposium on Reactor Dosimetry, 12th International Symposium on 8–13 May 2005 in Gatlinburg, TN; D. W. Vehar, D. M. Gilliam, and J. M. Adams, Guest Editors.

[1] Distinguished Member of the Technical Staff, Applied Nuclear Technologies, Sandia National Laboratories, P.O. Box 5800, MS1146, Albuquerque, NM 87185-1146.

[2] Senior Member of the Technical Staff, Applied Nuclear Technologies, Sandia National Laboratories, P. O. Box 5800, MS 1146, Albuquerque, NM 87185-1146.

[3] Principal Member of the Technical Staff, Advanced Nuclear Concepts, Sandia National Laboratories, P.O. Box 5800, MS1146, Albuquerque, NM 87185-1146.

[4] Senior Member of the Technical Staff, Applied Nuclear Technologies, Sandia National Laboratories, P. O. Box 5800, MS1146, Albuquerque, NM 87185-1146.

[5] Principal Member of the Technical Staff, Applied Nuclear Technologies, Sandia National Laboratories, P. O. Box 5800, MS1146, Albuquerque, NM 87185-1146.

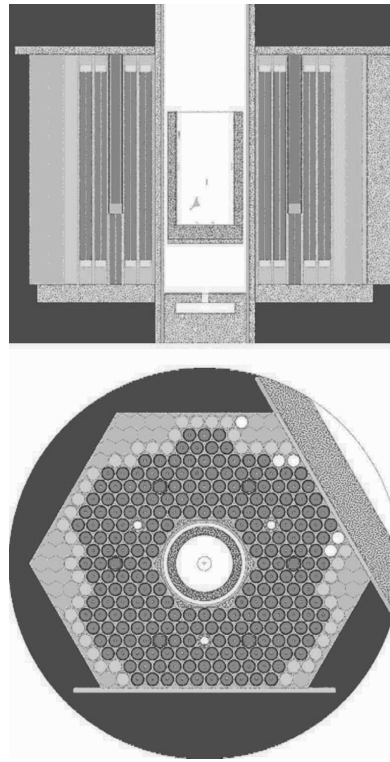

FIG. 1—*ACRR reactor CG model: (a) vertical cut and (b) horizontal cut.*

used to validate the calculational methodology. An inspection of the simultaneous time-dependent response from different types of active dosimeters can also be used to illuminate the difficulties of separating the neutron/gamma response of any dosimeter in the mixed n/γ radiation field of a reactor.

Calculational Approach

Monte Carlo calculations can be used to model the reactor environments. These calculations are typically run in a "kcode" mode where a normal fission distribution in the reactor fuel represents the fission source term, and the prompt fission neutron/gamma radiation is transported to the test locations. In this transport process, the neutrons will interact with the reactor materials and generate secondary gamma radiation. As an example of such a reactor model, Figs. 1(*a*) and 1(*b*) show a vertical and horizontal cut through a combinatorial geometry (CG) model of the pool-type Annular Core Research Reactor (ACRR). This geometry model can be used with Monte Carlo codes such as MCNP, MORSE, TART, and COG.

A typical analysis of the radiation environment stops with this type of radiation transport calculation. However, every fission event has not only prompt neutron and gamma radiation but also delayed neutron and gamma radiation. The delayed gamma radiation is generated at the same fission sites as were responsible for the prompt neutron/gamma radiation, but it has a time-dependent energy spectrum. The time-integrated delayed gamma radiation is nearly equal in magnitude to the prompt fission gamma radiation [1]. The time-dependent emission rate and the energy spectrum for the delayed neutrons have been empirically fit by Spriggs and Campbell [2]. The time-dependent and energy-dependent delayed gammas have not been as well characterized, but some data can be culled from the literature [3]. Figure 2 shows the normalized time dependence of the delayed neutron and gamma radiation from a fission event. Figure 2(*a*) is a composite of data that appears in Ref. [1] and Fig. 2(*b*) is a plot of the functional representation

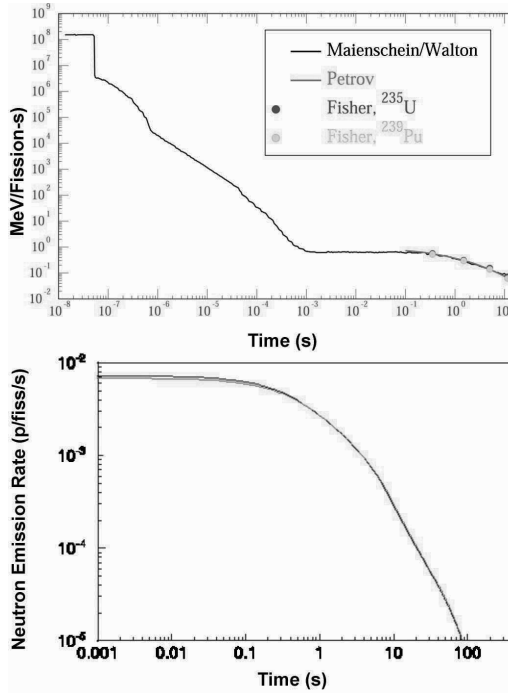

FIG. 2—*Time-dependence of delayed fission radiation: (a) gamma, and (b) neutron.*

recommended in Ref. [2]. The time-integrated delayed neutron fluence from a ^{235}U thermal fission is ~0.0158 neutrons/fission [1] (this corresponds to a delayed neutron fraction of β =0.0065 neutrons/fission). The time-integrated delayed gamma energy from a thermal ^{235}U fission is about ~6.84 MeV/fission and 3.31 photons/fission are emitted in the first 45 s [1]. The time-dependent emission and spectral data that are available in the literature provide a basis for modeling delayed radiation source term that can be coupled into the appropriate radiation transport methodology.

A radiation pulse from a test reactor typically has a pulse width that can vary from 50 μs in a fast burst reactor to 100 ms in a low-energy pulse from a water-moderated test reactor. The radiation transport calculations give the results for an instantaneous prompt fission pulse, essentially using a delta function as the source term. Thus, the prompt fission reactor radiation environment at a test location should be modeled by doing a time-dependent convolution of the calculated radiation over an experimentally measured fission time-dependent source profile while incorporating the delayed radiation contributions. Since the delayed radiation has a different spectral content than the prompt fission radiation, in order to capture the actual radiation spectral distributions at the experiment location, the reactor model radiation transport calculations must be repeated using the proper energy dependence of the delayed source terms in the convolution. Many research reactors use a prompt Cd-based self-powered neutron detector (SPND) as their power indicator. In water-moderated fission reactors, this is an excellent metric to use for the time-dependent source profile in the calculation. The same thermal neutrons that drive the fissions in a water-moderated reactor are responsible for the SPND signal. Note, however, that the SPND signal is delayed by one generation from the actual fission source term. This time delay is estimated to be about 2 μs in a water-moderated reactor such as the ACRR.

At even later times, the radiation environment at a test location may be dominated by activation gammas produced from nearby materials. The activation dose seen by a test object is a combination of the decay gammas from small nearby masses and the more numerous gammas produced by the more massive, but more distant, material. The local material environment can increase the gamma dose seen at a point by

more than an order of magnitude. Even trace quantities of high atomic number elements in nearby materials can dominate the activation dose seen by test objects. For example, the late-time activation component from the walls of an ionization chamber must be considered in any attempt to compare the calculated-to-experimental ratio of the response of an ionization chamber at times as long as 24 h after a reactor pulse.

There are several potential approaches to modeling the activation component of the radiation environment, but each approach also has its potential pitfalls. Radiation transport calculations can give a high fidelity local neutron spectrum, but they are not able to incorporate cross sections to represent the creation of all of the potential activated nuclides. Transport codes also use a fixed material composition, so that the effect of multiple neutron transmutations during long reactor operations is not addressed. Activation codes such as CINDER90 and ANITA can do an excellent job of calculating the types and amounts of activated isotopes in an infinitesimal amount of irradiated material, but they use a few energy group representation that does a poor job in characterizing the activation gamma spectrum. The Browne and Firestone Table of the Radioactive Isotopes (TORI) [4] provides a very detailed-energy resolution description and accurate quantitative metric for all emitted activation gammas from unstable isotopes. The optimal approach to modeling the activation source term is to chain together the tools/codes so as to combine the strengths of each approach and result in the highest fidelity representation of the activation radiation. The recommended methodology is to:

- Use the Monte Carlo codes to calculate a local radiation environment near each distinct mass. Good resolution is used to distinguish masses near the test location. Lumped mass models are sufficient for more distant masses.
- For each identified mass, an activation code is used to identify the time-dependent atom numbers of unstable activated isotopes that are created. The time dependence in the population of unstable nuclides is the result of the decay of short-half-life isotopes as well as the potential further transmutation of intermediate unstable isotopes during an extended irradiation.
- The TORI decay library is then used to produce a high-resolution energy and time-dependent source term at each identified location.
- The above time- and energy-dependent decay gamma source is then used in a source module of a time-dependent radiation transport code, such as MCNP, to calculate a time-dependent dose at the active area of the dosimeter location of interest.

Work is underway to create a prototype implementation of this methodology in support of our radiation effects studies.

Experimental Approach

Survey of Active Dosimeters

There is a wide assortment of active dosimeters used by the experimental community. These dosimeters include prompt Cd-based self-powered neutron detectors (SPNDs), fission chambers, ionization chambers, diamond photoconducting detectors (PCDs), silicon *pin* diodes, Schottky diodes, calorimeters, and more. Figure 3 depicts representative *pin* diodes, PCDs, and silicon calorimeters in use at the Sandia National Laboratory (SNL). These dosimeters are all seen to be small so that they can be fielded with an experiment package and are not likely to perturb the free-field radiation environment. Since the reactor environment is a mixed radiation neutron/gamma environment, it is important to consider the mixed field response for each type of dosimeter. Unfortunately, the literature does not provide a solid foundation for modeling the mixed-field response of most of these active dosimeters.

The dominant Cd-based SPND response is to thermal neutrons. However, high-energy neutrons can induce transmutation reactions in Cd and result in prompt gammas that produce a signal (electrons in a return circuit). In addition, the SPND does have an energy-dependent response to external gammas [5]. For short-time active dosimeters ($<$100 ms) in reactor environments, the SPND is the most frequent power monitor because its response tracks the neutron population. The problem with SPNDs are that they have a small signal and, as a result, are typically large in length ($\sim$0.4 m) and located next to the fuel itself rather

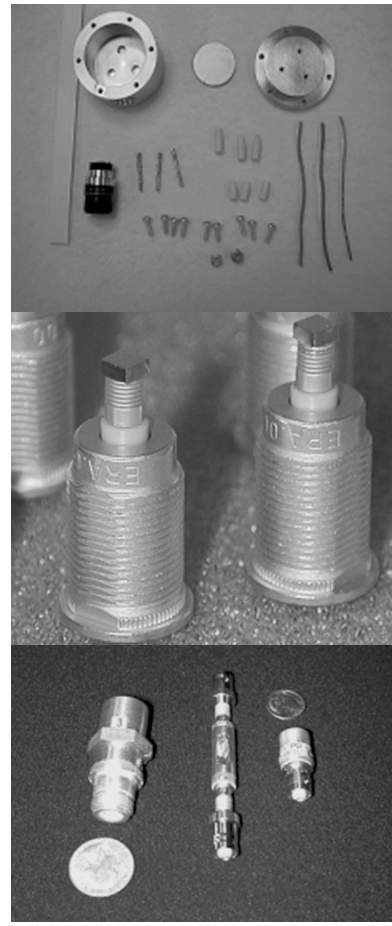

FIG. 3—*SNL active dosimeters: (a) calorimeter components, (b) PCD internal construction, (c) pin, diamond PCD, and ionization chamber.*

than at the experimental locations. Experimenters desire a monitor that can be small relative to the field gradients, will not interfere with their experiment package, and report on the ionizing dose rather than the thermal neutron population.

The fission chambers in use at Sandia include a wide variety of fissile materials. Fission chambers with ^{235}U deposits respond mostly to thermal neutrons, but can also exhibit a photofission response to high-energy photons (energies greater than ~5 MeV) [6]. Chambers with ^{238}U deposits would be expected to respond primarily to high-energy neutrons due to the low cross section for the $^{238}\mathrm{U}(n,f)$ reaction at energies <100 keV, but even high purity ^{238}U has small amounts of ^{235}U. In a water-moderated reactor, dosimetry-quality ^{238}U with 0.2 % atom fraction of ^{235}U has about half of its fissions from the $^{235}\mathrm{U}(n,f)$ impurity reaction as opposed to the $^{238}\mathrm{U}(n,f)$ reaction [7]. ^{237}Np fission deposits are being investigated at Sandia as a way to get a high-energy sensitive fission response without significant low-energy neutron sensitivity. Figure 4 compares the ^{235}U and ^{238}U fission chamber time-dependent response to that from an SPND in two ACRR pulses. The dosimeter response is arbitrarily normalized so that the peak rates match for the various dosimeters. The agreement in the time profile through the main pulse is seen to be excellent. A significant deviation is seen in the tail of the response—about a factor of 2. The ^{238}U fission chamber is seen to have the largest response in the tail while the SPND has the smallest response. This is

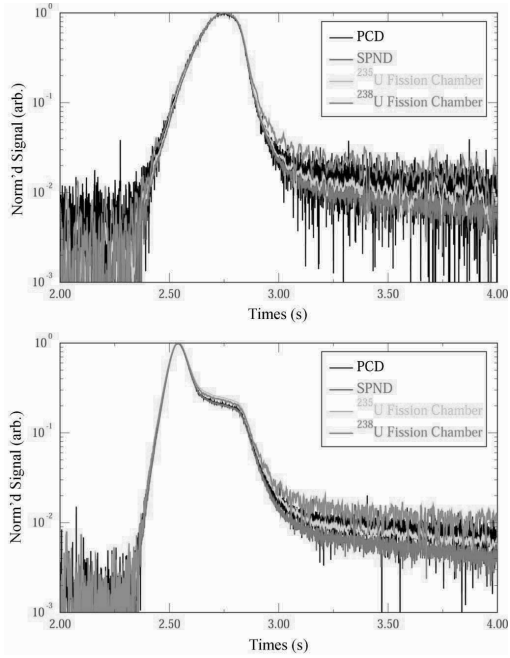

FIG. 4—*Fission chamber response in ACRR: (a) 10 MJ pulse and (b) 20 MJ pulse.*

consistent with the expected gamma response of the ionization chamber of the dosimeters after the main neutron pulse is complete. The SPND has the least gamma sensitivity (relative to its neutron response). The fission chambers have nearly identical ionization chambers—with similar gamma sensitivity, but the normalization of the curves compensates for the increased sensitivity of the ^{235}U fission chamber (despite the fact that it has a thinner uranium deposition). Thus, on a relative basis, the gamma tail is higher in the ^{238}U fission chamber due to its higher normalization and equal gamma sensitivity.

Diamond PCDs respond to the ionization from the residual charged particles resulting from neutron-induced reactions. For elastic and inelastic reactions the residual atom is carbon, while other heavy residual particles result from transmutation particles such as the (n,p) and (n,α) reactions as well as the light proton or alpha particle. There are some questions about the efficiency of this neutron-induced charge collection [8] due to the charged particle energy deposition partitioning between ionization and lattice phonons (which is energy and atomic number dependent) that is reinforced by some observed experimental anomolies. A diamond PCD is a new detector recently used in test reactor environments. This detector is very small and has a very fast response (less than 1 ns). There are two outstanding issues being addressed with the diamond PCDs: (1) a possible rate-dependent gamma response and (2) a neutron response that, when normalized to the ^{60}Co gamma response, is less than the calculated neutron carbon kerma and may exhibit a linear energy transfer (LET) dependence that would translate into a neutron energy-dependent response. If the neutron/gamma response efficiency does not exactly track the carbon kerma, then the response of this detector would show a shift in response when the neutron/gamma ratio in the environment is changed. This means that the PCD conversion factor from measured volts to deduced dose, Gy(carbon), during the main reactor pulse (nominally 28 % from neutrons and 72 % from gammas in the water-moderated ACRR, and 68 % from neutrons and 32 % from gammas in a fast burst reactor (FBR)) would be different in the late times when the delayed gammas dominate the radiation environment. Figure 4 shows that the PCD agrees well with the SPND and fission chambers in the main ACRR reactor pulse. In the tail, the PCD is responding to the delayed gammas. Its position relative to the SPND and fission chambers is consistent with this model of a primary sensitivity to gammas and decreased carbon-kerma energy dependence for the neutron response.

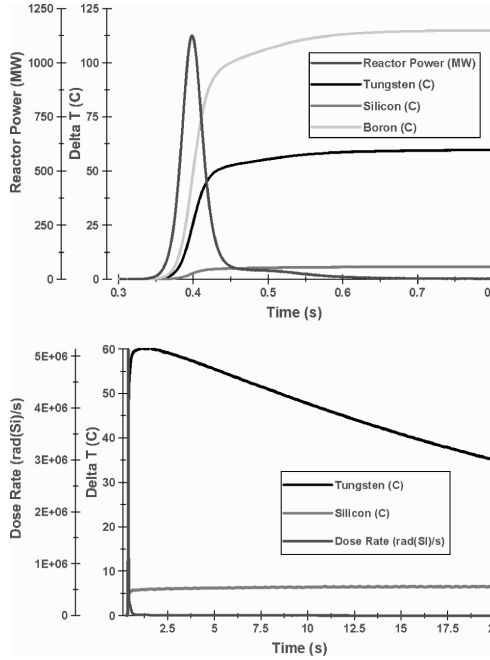

FIG. 5—*Calorimeter thermal behavior: (a) temperature rise and (b) temperature loss.*

Calorimeters have both a neutron and a gamma response. The calorimeter is a direct measure of the total dose in the active calorimeter material. The research reactor experimenter's interest is often in ionizing dose to silicon semiconductor devices. The problem with a silicon calorimeter is its small response. A small 20-MJ pulse in the water-moderated ACRR reactor has a neutron fluence of 1×10^{14} cm^{-2}, but a silicon calorimeter temperature increase of only 5°C. In the White Sands Missile Range Molly-G reactor, a fast pulsed ^{235}U metal assembly, a maximum energy pulse (300°C change in the fuel temperature) has a neutron fluence of 5×10^{13} cm^{-2} and a silicon calorimeter temperature change of only 0.2°C. High atomic number calorimeters, such as tungsten, respond predominantly to gammas and can have temperature changes for a 300-MJ ACRR pulse of 50°C. A ^{10}B calorimeter can be used as a thermal neutron dosimeter and also shows a very large signal, a temperature change of 100°C in a 300-MJ ACRR pulse. Figure 5(*a*) shows representative calorimeter responses for silicon, tungsten, and enriched boron-10 calorimeters in a 300-MJ ACRR pulse. The calorimeter design was similar for all three materials.

Another problem with a calorimeter is that the reactor gamma spectrum is time dependent and not well characterized. When a tungsten calorimeter is used, the metric is Gy(W). The conversion of Gy(W) to the user-requested Gy(Si) must assume a gamma spectrum and can introduce a large uncertainty. Thus, the calorimeter should always be selected to mirror the metric of interest to the user. A problem with the calorimeter is that its signal represents an integral response. One has to differentiate the signal to get an active time profile. Using careful electromagnetic shielding for the signals and fast sampling can permit the acquisition of good derivatives and good time profiles at early times in a reactor pulse. In order to use the calorimeter at moderate times (seconds) after a pulse, careful calorimeter design is required to minimize thermal diffusion effects. The thermal losses in calorimeters in Fig. 5(*b*) are seen to depend on the maximum material temperature (size of radiation environment) as well as the calorimeter design details. This is because, at high material temperatures, radiative heat losses are important.

P-i-n diodes (*pins*) are another common dose rate monitor. These devices consist of a highly resistive intrinsic or *i*-type region with *p*- and *n*-type material on either side. Diodes of silicon and gallium arsenide are available. This is a good dose rate monitor for semiconductor testing in gamma fields, since it intrinsically responds to a dose in silicon or GaAs. A *pin* diode has a fairly strong signal, but one has to take care

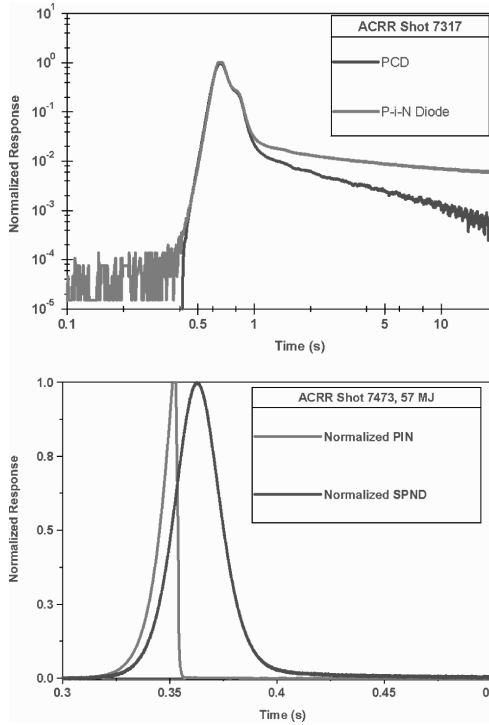

FIG. 6—*Pin degradation: (a) increased leakage current and (b) device failure in ACRR.*

that the *pin* diode does not saturate during the pulse or debiasing of the voltage supply. The design must be checked to ensure that it does not exhibit rate dependence in the radiation fields of interest, but the useful dose rate range is typically $10^3 - 10^8$ Gy(Si)/s $\{10^5 - 10^{10}$ rd(Si)/s$\}$ [9]. The pin diode has issues in a reactor neutron/gamma field. The *p*-type material dopant in silicon *pins* diodes is typically natural boron. The ^{10}B in the dopant has a large thermal neutron cross section and can produce an anomalously large neutron response. In addition, the *pin* diode is a minority carrier device and neutrons easily damage it. This results in the following effects: (1) a change in the diode calibration for small fluence shots in fast burst reactors (2) increased leakage current from intermediate exposures in moderated reactor exposures (see Fig. 6(*a*)), and (3) for large ACRR pulses, a failed diode in the middle of an application as is demonstrated in Fig. 6(*b*). Some of this neutron damage will anneal out, but, since the early-time annealing is device dependent and not well characterized, this can result in a change of dosimeter calibration during a pulse with subsequent recovery before a post-test validation of the calibration.

Ionization chambers are very sensitive active detectors, but most will saturate during a reactor pulse and there may be a delay while the detector comes out of saturation. These detectors are most useful in the late-time portion of the reactor pulse, but the detector responds to ionization from both neutrons and gammas and the mixed field response must be considered. In addition, the activation of the ionization chamber is a concern at late times while reading low dose rates. The low rate gamma calibration of the detector is easily established in ^{60}Co sources, but the neutron calibration is extremely difficult. It is also difficult to preclude a rate-dependent response that would affect the interpretation of the dosimeter in a reactor pulsed environment where the rate is typically 10^8 rd(Si)/s. Without the ability to capture the response during the radiation peak it can be difficult to experimentally establish a consistent normalization to the response from other detectors in a mixed n/γ reactor field.

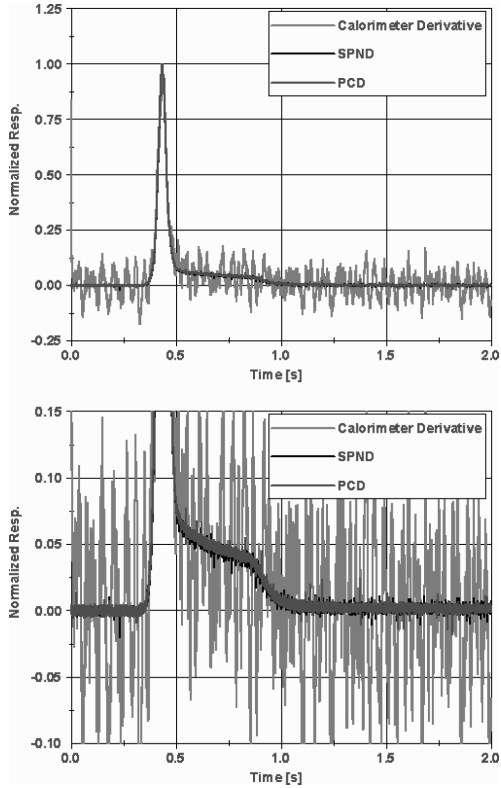

FIG. 7—*Short-term dosimeter agreement. (a) Linear view. (b) Logarithmic view.*

Consistency of Early-time Dosimeter Response

A primary concern is the consistency of the response of various active dosimeters. At early times the primary active dosimeters for use in a reactor environment are a SPND, PCD, fission chamber, and a calorimeter. Figures 7(*a*) and 7(*b*) show that the SPND and PCD responses are virtually indistinguishable. In addition, the derivative of the silicon calorimeter is seen to agree very well with the other active dosimeters at these early times. Figure 4 shows that the ^{235}U and ^{238}U fission chambers also agree very well with the PCD and SPND for these early times. A radiation-hardened silicon *pin* diode from Emerge Semiconductor has also been shown to agree very well with the other active dosimeters for a small single pulse in ACRR. For multiple or large pulses, even radiation hardened *pin* diodes fail or show response degradation, as shown in Figs. 6. These data support a conclusion that the early-time time profiles for most active dosimeters agree with one another.

The main drawback of the silicon calorimeter is its small signal and the intrinsic noise for high bandwidth measurements in the reactor environment. If one is interested in nonsilicon dose in a test object, then a calorimeter constructed from a different material could be considered. Figure 8(*a*) shows that a tungsten calorimeter has a large response and has an excellent match with the SPND and PCD time profile for an ACRR reactor pulse.

The above comparison examined time profiles for arbitrarily normalized dosimeter measurements. The normalization of the various dosimeters in the mixed neutron/gamma reactor environment is an outstanding question. There are questions about the response of most of the candidate active dosimeters that would preclude any conclusion on the dosimeter comparison. Since the calorimeter is a fundamental dosimeter, it represents the highest fidelity indication of the dose at early times after a pulse in the reactor environment. The recommended procedure is to field both a calorimeter as well as an active dosimeter such as an SPND,

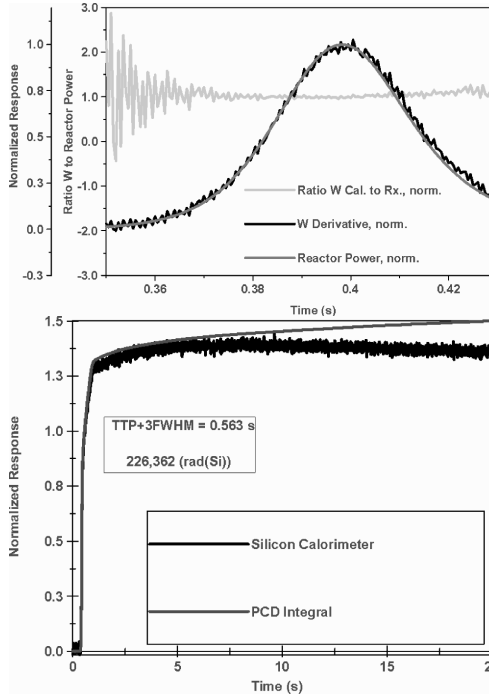

FIG. 8—*Calorimeter: (a) tungsten early-time agreement and (b) silicon late-time deviation.*

PCD, or fission chamber. The time profile from the PCD, SPND, or fission chamber is then normalized to the early-time calorimeter response. A calibration time equal to the peak plus three full widths at half-maximum (FWHM) has been found to be optimal for a water moderated reactor such as ACRR. In a fast burst reactor with a pulse FWHM of 50 μs, early time cable noise is a concern and the optimal calibration time is about 5 ms after the pulse peak. This time represents an early enough time that the calorimeter does not exhibit any heat loss, but late enough that radiation-induced signals on the cable can be ignored. The problem with this time is that the small late-time PCD or SPND signal produced at a FBR makes it difficult to capture their late-time signal, while also not saturating amplifiers during the main reactor pulse. Use of multiple active detectors or dividing the signal between instruments with different amounts of amplification may be required.

Consistency of Late-time Dosimeter Response

At late times, the selection of active dosimeters is much more complex. Figure 8(*b*) shows that a silicon calorimeter begins to experience heat losses and its measure deviates from the integral of a PCD at times beyond about 2 s. Nonsilicon calorimeters have a larger temperature rise and, as seen in Fig. 5(*b*), lose heat at even smaller times. Figure 4 shows that a fission chamber response changes in the tail as its dominant response changes from neutrons to gammas. This same behavior is seen in a SPND. Figure 6(*a*) shows that the *pin* diode experiences, at best, higher leakage current in the late times and a loss of calibration. The conclusion is that, while several active dosimeters will give a late-time signal, the interpretation of the late-time dosimeter response is very difficult.

Calculations of the late-time reactor radiation environment are expected to be useful in selecting which dosimeters to use at late times. As preparation for an eventual comparison of the measured dosimeter response with a calculated response, a comparison was made of the time-dependent measurements from a range of active dosimeters following pulsed and steady-state reactor operations. The test protocol used calls for having a "cold" reactor, one that has not seen an operation for at least 12 h, conducting a

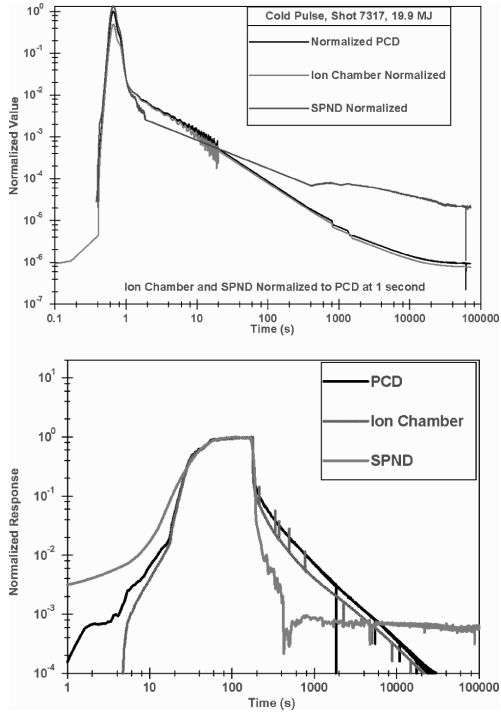

FIG. 9—*Dosimeter comparison: (a) pulsed and (b) steady state.*

predetermined operation with the active dosimeters, and continuing the measurement for 24 h after the operation. Figure 9(*a*) shows some representative data from a small (20-MJ) pulse in the water-moderated Annular Core Research Reactor (ACRR) at Sandia National Laboratories. Figure 9(*b*) shows representative data from a 300-MJ steady-state operation in ACRR. These measured responses exhibit some of the mixed radiation effects enumerated in the previous paragraph. The relative neutron/gamma response of each detector is important in interpreting the late-time response from these various active dosimeters. For example, the SPND is primarily a neutron-sensitive detector. The late-time plateau in the SPND curve of Fig. 9(*b*) represents the noise floor for the dosimeter. Since the ACRR has BeO-UO_2 as fuel, this late-time signal may represent a late-time photoneutron environment induced by the delayed fission gammas and activation gammas. The deviation between the SPND and the PCD or ionization chamber at late times is due to the fact that the PCD and ionization chamber are primarily responding to the gamma radiation and the late-time gamma-to-neutron ratio is much higher than that during the main reactor pulse. The mid-time response of the PCD and ionization chamber in Fig. 9(*a*) fits the $t^{-1.2}$ falloff expected for the delayed gamma environment. At very late times, Fig. 9(*a*) shows a plateau in the PCD dosimeter response. This is attributed to a response dominated by the activation gammas while the delayed fission gamma continues to decay.

Conclusion

This paper has presented a methodology for calculating the time-dependent radiation environment in a reactor. The proposed methodology addresses the prompt fission neutrons and gammas, the reactor environment neutron-induced secondary gammas, the delayed neutrons and gammas, and the activation gammas. The methodology chains together existing tools to accomplish a high fidelity representation of this environment. The paper also surveys the range of available active dosimeters and reports on the strengths and weakness of each type of dosimeter. Data are shown to illustrate these strengths and weaknesses. A

comparison of dosimeters shows that the PCD, SPND, and fission chambers all agree in the early time profile of the reactor pulse. A silicon calorimeter is recommended as the most accurate normalization metric for the early-time dosimeter time profiles. Late-time comparisons are made between active dosimeters for pulsed and steady-state reactor operation. No active dosimeter could be recommended for use at late times and work is continuing to address this need.

Acknowledgments

This work was supported by the United States Department of Energy under Contract DE-AC04-94AL85000. Sandia is a multiprogram laboratory operated by Sandia Corporation, a Lockheed Martin Company, for the United States Department of Energy.

References

[1] Keepin, G. R., *Physics of Nuclear Kinetics*, Addison-Wesley Publishing Co., Reading, MA, 1965.

[2] Spriggs, G. D., Campbell, J. M., and Piksaikin, V. M., "An 8-Group Delayed Neutron Model Based on a Consistent Set of Half-Lives," LA-UR-98-1619, Rev. 3, Los Alamos National Laboratory, Los Alamos, NM; also at URL http://public.lanl.gov/jomc/DN_YOC.html

[3] Maienschein, F. C., Peelle, R. W., Zobel, R., and Love, T. A., *Proceedings of 2nd United Nations International Conference on Peaceful Uses of Atomic Energy*, Geneva, Switzerland, 1958, Vol. 15, p. 366.

[4] Firestone, R. B., Shirley, V. S., Baglin, C. M., Chu, S. Y. F., and Zipkin, J., *The 8th Edition of the Table of Isotopes*, book and CD-ROM, John Wiley & Sons, Inc., New York, 1996; Online version available at URL http://ie.lbl.gov/toi.html

[5] Lee, W. N., Cho, G., Kim, K. H., Kim, H. J., Choi, Y. S., and Park, M. K., "A Study of the Sensitivity of Self-Powered Neutron Detector (SPND)," *IEEE Trans. Nucl. Sci.*, Vol. 48, 2000, pp. 1587–1591.

[6] Dietrich, S. S., and Berman, B. L., "Atlas of Photoneutron Cross-Sections Obtained with Monoenergetic Photons," *At. Data Nucl. Data Tables*, Vol. 38, 1988, pp. 199–338.

[7] Griffin, P. J., Kelly, J. G., Luera, T. F., and VanDenburg, J., "SNL RML Recommended Cross Section Compendium," Sandia National Laboratories Report SAND92-0094, November 1993.

[8] Griffin, P. J., Luker, M. S., King, D. B., DePriest, K. R., Hohlfelder, R. L., and Auo-Anttila, A. J., "Diamond PCD for Reactor Active Dosimetry Applications," *IEEE Trans. Nucl. Sci.*, Vol. 51, 2004, p. 3631—3637.

[9] ASTM Standard E 1894-97, "Standard Guide for Selecting Dosimetry Systems for Application in Pulsed X-Ray Sources," *Annual Book of ASTM Standards*, Vol. 12.02, ASTM International, West Conshohoken, PA, 2005.

Journal of ASTM International, Vol. 3, No. 3
Paper ID JAI13443
Available online at www.astm.org

M. Plaschy,[1] *C. Destouches,*[2] *R. Chawla,*[3] *D. Beretz,*[4] *F. Mellier,*[5] *H. Servière,*[4] *P. Fougeras,*[4] *P. Chaussonnet,*[4] *C. Domergue,*[4] *J.-M. Laurens,*[4] *and H. Philibert*[4]

Determination of Adjusted Neutron Spectra in Different MUSE Configurations by Unfolding Techniques

ABSTRACT: Investigations of spectrum adjustment by unfolding techniques for different locations of critical and driven subcritical MUSE4 configurations are presented. The current analysis is based on the recent accomplishment of specific foil activation measurements and on the use of the unfolding code STAY'SL in conjunction with IRDF-90 and IRDF-2002 dosimetry libraries. Specific developments have been conducted to consider the uncertainties associated with the determination of the experimental absolute reaction rates and the initial calculated spectrum in the most realistic manner. In this context, the iterative adjustment process for the neutron spectrum is established on the basis of variance/covariance matrices defined for the three types of input parameters, i.e., the experimental reaction rates, the initial spectrum, and the dosimetry nuclear data files. The results highlight the spectral variations between different locations of the MUSE4 cores, in particular the characteristic behavior of a subcritical configuration driven by an external $T(d,n)He^4$ (14 MeV neutrons) source.

KEYWORDS: spectrum adjustment, activation measurements, threshold reactions, MUSE, STAY'SL, IRDF

Introduction

The transmutation capabilities of accelerator driven systems (ADSs) as an alternative to conventional reactors have often been mentioned, since these systems avoid safety problems related to the very low β_{eff} values of the minor actinides such as Np and Am. Due to the innovative aspects of such hybrid cores, it is necessary to extend the validation domain of calculation methods and data developed for critical fast reactors to the analysis of such source-driven subcritical systems. For example, accurate knowledge of the energy and spatial dependence of the neutron flux is essential for assessing characteristics such as the impact of the external source on power peaking and irradiation damage effects. In this context, various ADS-representative dynamic and static measurements have been carried out during the experimental MUSE4 program at the MASURCA facility in Cadarache (France), as briefly described in the following section.

In particular, large-scale foil activation experiments have been performed in various critical and subcritical MUSE4 cores, the measured activities providing an important database for the study of spectral effects in different positions. In effect, these activation measurements, which are described in the third section, constitute an important experimental basis for the adjustment of the calculated neutron spectrum by employing appropriate unfolding techniques.

The iterative unfolding process applied currently, and defined concisely in the fourth section, corre-

Manuscript received June 20, 2005; accepted for publication September 29, 2005; published online December 2005. Presented at ASTM Symposium on Reactor Dosimetry, 12th International Symposium on 8–13 May 2005 in Gatlinburg, TN; D. W. Vehar, D. M. Gilliam, and J. M. Adams, Guest Editors.

[1] Reactor Physicist, Laboratory for Reactor Physics and Systems Behaviour (LRS), Paul Scherrer Institute (PSI), CH-5232 Villigen-PSI, Switzerland.

[2] Research Engineer, Commissariat à l'Energie Atomique (CEA), Nuclear Energy Direction, (DER/SPEx/LPE) F-13108 St-Paul-Lez-Durance, France.

[3] Professor, Ecole Polytechnique Fédérale de Lausanne (EPFL), CH-1015 Lausanne, Switzerland; co-affiliation: LRS-PSI.

[4] Experimental Programmes Laboratory Member, Commissariat à l'Energie Atomique (CEA), Nuclear Energy Direction (DER/SPEx/LPE), F-13108 St-Paul-Lez-Durance, France.

[5] MUSE Project Coordinator, Commissariat à l'Energie Atomique (CEA), Nuclear Energy Direction (DER/SPEx/LPE), F-13108 St-Paul-Lez-Durance, France.

sponds essentially to use of the STAY'SL code and the IRDF dosimetry data files. Generally speaking, the employed method allows determination of an adjusted neutron spectrum by minimization of an error function (the χ^2 function in our case) while considering the experimental reaction rates, a calculated input spectrum and appropriate nuclear cross section libraries, as well as, for each of the input parameter types, the associated variance-covariance matrices.

Even though the characterization of neutron spectra by unfolding techniques is basically a well known method applied since the 70s [1], recent developments, such as the release of new dosimetry data files and the availability of improved calculation codes, are promising for the determination of considerably more accurate adjusted spectra. This possibility is reinforced in our studies due to the specific efforts which have been devoted to the determination of the variance-covariance matrices. The relevance of the employed methodology is explained in the fifth section.

On the basis of the above-mentioned developments, various different adjusted spectra are presented and discussed in the sixth section. The reported spectra have been obtained for several different locations in the critical core, as well as for the corresponding locations of one of the subcritical cores driven by an external $T(d,n)He^4$ source. In this context, particularly since the foil activation reactions used cover a wide range of threshold energies (going up to almost 14 MeV ($^{92}Nb(n,2n)$, $\sim$11 MeV threshold)), spectral behaviour specific to the ADS-type heterogeneities considered, as also to the presence of the external neutron source, has been highlighted.

Finally, conclusions are drawn, and certain recommendations made for further investigations.

The MUSE4 Program

The MUSE4 experimental program of the MUSE ("MUltiplication avec une Source Externe") project has been completed recently at the MASURCA facility at Cadarache (France) [2,3]. This research program was conducted on behalf of the MUSE European collaboration in the frame of the European 5th PCRD ("Programme-Cadre pour la Recherche et le Développement technologique").

Objectives of the MUSE4 Program

The extensive MUSE4 experiments, accomplished between the years 2000 and 2004, consist of studies in a reference critical fast-spectrum configuration, followed by the detailed investigation of three different source-driven subcritical modifications of the same. Two major aspects have been analyzed. First, different types of reactor kinetic measurements, aimed at determining the subcriticality level, were developed, tested, and analyzed [4]. Second, classic static measurements were carried out for characterization of the neutron spectrum variations by using a set of miniature fission chambers (^{235}U, ^{238}U, ^{237}Np, ^{239}Pu, ^{240}Pu, ^{241}Am,…) and by irradiating various types of activation foils (indium, iron, nickel, zinc,…) at locations where the spectral variations were particularly significant (mainly near the accelerator/lead interface) [5].

In more general terms, the achieved integral measurements constitute a new and important experimental database for validating the calculation methods employed in the analysis of ADSs, e.g., the deterministic code ERANOS [6–8] and its associated nuclear data library ERALIB [9].

The MUSE4 Configurations

The basic reactor configuration consists of five different regions, set up as an arrangement of tubes of $10.6\times10.6\times230.44$ cm^3, each presenting a different axial-zone structure. It is convenient to describe the individual MUSE4 regions starting from the center of the assembly.

The presence of the accelerator tube at the center creates perturbed regions which go through the reactor along the mid-plane. In front of the accelerator tube, which has a lead/aluminum clad, there is a lead diffusing region which serves mainly to get the power distribution relatively symmetric. Again, the two regions, with their associated heterogeneity effects, represent ADS-specific particularities. The fuel zone consists of about 70 MOX assemblies (PuO_2/UO_2+Na) and is hence characteristic for a standard fast reactor core. Slightly different ^{239}Pu enrichments are employed for the fuel above and below the accelerator tube. The MOX zone is surrounded by a reflector region, constituted by sodium and stainless steel rods. Finally, the external zone of the reactor consists of stainless steel shielding. A horizontal cross-sectional view of the MUSE4 critical configuration (M4CRIT) is given in Fig. 1.

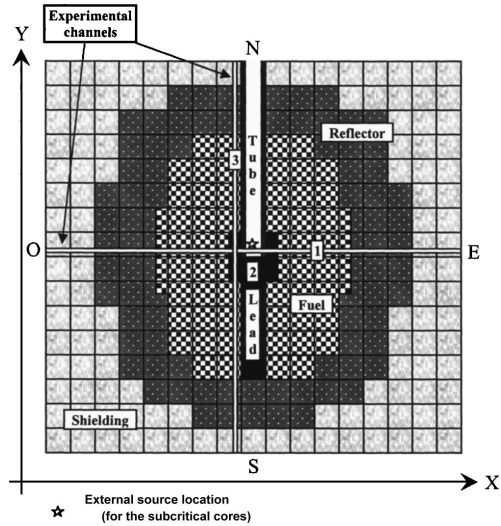

FIG. 1—*Horizontal cross. sectional view of the MUSE4-type configuration, indicating the locations where the spectrum has been adjusted.*

In addition to the M4CRIT configuration, investigations are also reported in the present study for the M4SC0 subcritical configuration. This configuration, defined by a k_{eff} of about 0.995, is similar in layout to the critical loading, except that a small number of fuel assemblies are replaced by reflector assemblies to obtain the desired degree of subcriticality. It should be mentioned that three other subcritical cores were loaded during the MUSE4 program, viz. (a) M4SC2 ($k_{eff} \sim 0.970$), (b) M4SC3 ($k_{eff} \sim 0.950$) and (c) M4SC3-Na/Pb ($k_{eff} \sim 0.960$) [10].

To drive the different subcritical cores, the deuteron accelerator (GENEPI) was used in two different modes, viz. to produce either 2.7 MeV neutrons via the $D(d,n)He^3$ reaction (DD) or 14 MeV neutrons via the $T(d,n)He^4$ reaction (DT). In this paper, the analyzed subcritical driven system corresponds to the configuration M4SC0+DT.

Foil Activation Measurements

During the entire MUSE4 program, more than 350 samples of about 15 different materials were activated and counted from 14 irradiations in total [11]. To introduce activation foils in different locations of the MASURCA facility, experimental radial and axial channels (having a section of 1.27 cm $\times$ 1.27 cm) were provided (see Fig. 1), the samples have been loaded into the reactor using aluminum support rods of cross section 1.00 cm $\times$ 1.00 cm.

Activation Samples and Location

The choice of foils has been guided mainly by the need to cover a range of threshold energy values as wide as possible. The list of activation reactions employed in the current paper is given in Table 1. Most of the high-purity foils used were disk-shaped with a thickness of 0.25 mm and a diameter of 9 mm.

For the reported spectrum adjustment studies, the threshold reaction measurements were carried out at three different locations, indicated by the numbers 1–3 in Fig. 1. Location 1 has been considered as a reference point in an unperturbed region near a calibrated fission chamber. Location 2 permits study of the impact of the lead region, while position 3 provides a useful test of code capabilities to treat streaming effects along the voided accelerator-tube region.

TABLE 1—*List of the activation threshold reactions employed.*

Reaction	Threshold [MeV]
$^{115}In(n,n')^{115m}In$	1.2
$^{58}Ni(n,p)^{58}Co$	2.8
$^{64}Zn(n,p)^{64}Cu$	2.8
$^{54}Fe(n,p)^{54}Mn$	3.1
$^{56}Fe(n,p)^{56}Mn$	6.0
$^{24}Mg(n,p)^{24}Na$	6.8
$^{27}Al(n,a)^{24}Na$	7.2
$^{93}Nb(n,2n)^{92}Nb$	11.0

Correction Factors and Activity Accuracies

The achievement of accurate foil activation measurements requires particular attention giving for the application of necessary corrections and the treatment of experimental uncertainties. The γ-spectrometry measurements have been performed in the Cadarache dosimetry laboratory. The corrections to be applied result from either the irradiation conditions or from physical effects associated with the γ-counting of the irradiated foils.

In particular, due to the constraints associated with the accurate determination of foil activities (radioisotope decay periods, γ-laboratory availability, reactor power level, and irradiation duration), the complete activation campaign had to be carried out during several separate irradiations. In this context, it was necessary to define a calibration factor to normalize each irradiation. For the purpose, twelve fission chambers ("monitors") were introduced into the reactor. The need to use these detectors led to a 1.5 % uncertainty $(1-\sigma)$ on the inter-calibration of the different M4CRIT irradiations, the uncertainty for the M4SC0+DT irradiations being lower than 0.5 % (because power levels were almost constant in this case). Finally, the absolute reactor power was deduced from a calibrated miniature fission chamber (^{235}U or ^{241}Am deposit depending on the power level). The uncertainty associated with the power determination was about 5 % for M4CRIT and about 8 % for M4SC0+DT, the uncertainty of the external source strength has been considered in the latter case as well.

Apart from the corrections mentioned above, self-shielding effects for the different activation foils were assessed numerically with the aid of MCNP-4C Monte Carlo simulations [11]. As expected, the corrections have to be taken into account only in the case of nonthreshold reactions at locations near zones with softer neutron spectra.

Furthermore, there is the need to correct for several different physical effects during the γ-counting of the irradiated foils. First, depending on the disintegration scheme of the activation product and the detector/sample distance (but independent of the activity level), some γ-emission coincidences occur, yielding less counts under the considered peak. Second, particularly in the case of the threshold reactions, the activity of the counted foils is generally low. This induces the use of the closest possible distance between the foil and the HPGe γ-detector in order to achieve acceptable statistical accuracies. Finally, γ-self-absorption effects have been taken into account. This effect is essentially related to the γ-energy, and to the thickness and density of the foil material.

Absolute Reaction Rates

With the help of the correction factors described above, it is possible to determine the saturated activity (A_{sat}) of a given experimental sample in Bq per milligram of the considered target nuclide. Then, as well known, the saturated activity is directly related to the measured reaction rates. Finally, while knowing the power level of the reactor, the absolute experimental reaction rates can be expressed in Bq/mg/Watt (or also 1/mg/Watt/s). The absolute experimental reaction rates used in this paper with their uncertainties (at $1-\sigma$) are given in Table 2.

Description of the Selected Unfolding Method

Since the 70s, various calculation schemes for spectrum unfolding (code+dosimetry nuclear data) exist for the achievement of spectrum adjustment based on experimental reaction rates. In our case, the code

TABLE 2—*Absolute experimental threshold reaction rates (Bq/mg/watt) for different locations of the M4CRIT and M4SC0 + DT configurations (while using the calibration factor given by STAY' SL).*

Reaction	M4CRIT Location 1	M4CRIT Location 2	M4CRIT Location 3	M4SC0+DT Location 1	M4SC0+DT Location 2	M4SC0+DT Location 3
^{115}In(n,n′)	1.14E+06	8.52E+05	8.59E+05	1.13E+06	9.61E+05	7.23E+05
^{58}Ni(n,p)	5.16E+05	2.64E+05	3.70E+05	5.07E+05	3.08E+05	3.63E+05
^{64}Zn(n,p)	1.93E+05	9.38E+05	1.30E+05	⋯	⋯	⋯
^{54}Fe(n,p)	3.78E+05	1.85E+05	2.66E+05	⋯	⋯	⋯
^{56}Fe(n,p)	4.66E+03	1.74E+03	3.34E+03	⋯	2.31E+04	4.17E+03
^{24}Mg(n,p)	6.84E+03	2.63E+03	⋯	8.61E+03	3.45E+04	⋯
^{27}Al(n,a)	3.00E+03	1.17E+03	⋯	6.11E+03	2.31E+04	3.35E+03
^{93}Nb(n,2n)	2.01E+03	⋯	⋯	⋯	8.23E+04	⋯

Remark: The associated uncertainties at $1-\sigma$ are <2 %, not including the uncertainties in assembly power.

STAY'SL [12], developed by ORNL (Oak Ridge National Laboratory), and two different versions of the IRDF (International Reactor Dosimetry Files) data files have been used.

Basic Principles of the STAY'SL Code

In brief, the application of this method requires the definition of a set of stable isotopes which have well known cross sections for neutronic reactions covering a large range of energies and which, in addition, give rise to appropriate radio-nuclides from the viewpoint of emitted γs or X-rays (signal easily measured, well defined peak in energy, adequate yield, convenient decay constant, …). Such a suitably chosen set of materials, as represented by the reactions listed in Table 1, has been irradiated at a constant flux level in locations where the neutron spectrum has to be determined. As outlined in the previous section, experimental reaction rates and their associated uncertainties are then derived from the measured activities and irradiation data. Finally, the adjusted neutron spectrum is deduced by minimization of an error function (χ^2 in our case) using the experimental reaction rates, the calculated spectrum, dosimetry data files and their associated variance-covariance matrices. The χ^2 function is of the following type:

$$\chi^2 = (A^{ex} - A^{ca})^t \cdot (\Gamma_{A^{ex}} + \Gamma_{A^{ca}})^{-1} \cdot (A^{ex} - A^{ca})$$

where A^{ex} is a vector describing the different experimental reaction rates, A^{ca} is a vector describing the different calculated reaction rates, Γ_A^{ex} is the variance/covariance matrix associated with the measured activities, and Γ_A^{ca} is the variance/covariance matrix associated with the calculated activities.

STAY'SL uses an iterative process, based on the least-squares method, to obtain the desired solution. This unique solution corresponds to the adjusted spectrum which leads to the lowest value of the χ^2 function. The result is strongly correlated with the variance/covariance matrices, the latter defining the spectrum adjustment margins in function of the input calculated spectrum. In this context, specific developments have currently been carried out to define the variance/covariance matrices as realistically as possible (see next section).

The IRDF-90v2 and IRDF-2002 Dosimetry Neutron Libraries

In conjunction with the STAY'SL code, the use of recent dosimetry neutron libraries is essential. In the current work, we have used the IRDF-type libraries which result from an important international effort supported by the IAEA (International Atomic Energy Agency). More precisely, the IRDF-90v2 [13] and the recently released IRDF-2002 [14] data files have been employed. The significant improvements achieved in IRDF-2002 are based on the post-evaluation integration of reactor dosimetry cross section data and their uncertainties coming from various libraries including IRDF-90v2, JENDL/D-99, and RRDF-98.

Improvements of the Method

Unfolding methods used to modify the neutron spectrum obtained from a given set of foil irradiations have suffered in the past from technical limitations: activity measurements of many radioisotopes were not possible with enough precision. Also, some of the uncertainty matrices provided with the cross section data files were not realistic, as well as the matrices the calculated spectra themselves. In particular, a sensitive

TABLE 3—*Correlation factors used for the determination of the experimental reaction rates covariances.*

Energy Diff. Between Emitted γ-rays (Δγ)	Correlation Factor
$\Delta\gamma < 10$ keV	1.0
10 keV $< \Delta\gamma <$ 50 keV	0.9
50 keV $< \Delta\gamma <$ 100 keV	0.8
100 keV $< \Delta\gamma <$ 200 keV	0.6
200 keV $< \Delta\gamma <$ 400 keV	0.3
400 keV $< \Delta\gamma <$ 1000 keV	0.1
1000 keV $< \Delta\gamma$	0.0

point is the determination of a nonarbitrary variance/covariance matrix for the input spectrum. As mentioned earlier, specific attention has been given to this point. Generally speaking, the STAY'SL adjustment process is characterized by the following input data:

(a) The experimental absolute reaction rates and their associated uncertainties.
(b) The nuclear data library and its associated uncertainties.
(c) The calculated input spectrum and its associated uncertainties.

The Experimental Reaction Rates and Their Associated Variance/Covariance Matrix

The uncertainties associated with the activation measurements are mainly due to the statistical uncertainty of the γ-counting and the efficiency calibration curve of the γ-detector as a function of the energy of the emitted γ-ray. In this context, the experimental reaction rate covariance matrices have been calculated with the following considerations. First, of course, no correlation is considered for the statistical uncertainty of the γ-counting. For the detector efficiency calibration, a correlation factor between two reaction rates is estimated assuming that this depends on the difference between the energies of the γ-rays emitted by the radio-isotopes concerned: the closer the γ-ray energies are, the stronger is the correlation. This is, of course, due to the fact that the same efficiency calibration curve is used for each measurement. The assumed correlation factors are presented in Table 3. It is worth noting that an additional uncertainty has been accounted for, viz. that associated with the intercalibration of the reactor power during each separate irradiation (as explained previously).

The Nuclear Data Library and Its Associated Variance/Covariance Matrix

The IRDF nuclear cross section data are given in 640 energy groups (SAND-II format). These data are also provided with their associated variance/covariance matrices. Different modifications were necessary to be able to use the IRDF-90 and IRDF-2002 files in conjunction with STAY'SL, a specific format for the data, as also a particular group structure (condensation in 45 energy groups), being employed with the code.

The Calculated Input Spectrum and Its Associated Variance/Covariance Matrix

In the present study, the principal improvements related to the spectrum adjustment technique concern the calculation of suitable input spectra and, specifically, the determination of realistic variance/covariance matrices.

The different input spectra have been calculated in 45 energy groups in 3D with the ERANOS-2.0 (TGV-VARIANT) code [6–8] in conjunction with the ERALIB-1 nuclear data library [9]. These fluxes per group are given in Fig. 2 for each configuration. As expected, the presence of the 14 MeV neutron source in the M4SC0+DT configuration is clearly highlighted for location 2. These input spectra are compared to the adjusted ones in the next section.

To determine the spectrum variance/covariance matrices, the following method has been used:

(a) Definition of a representative, simplified full-core model in RZ-geometry—The basic RZ-model for the MUSE4 configurations has been defined with the help of ERANOS sensitivity and representativity calculations [11], permitting to identify the most important isotopes. In our case, the latter are ^{238}U, ^{238}Pu, ^{239}Pu, ^{240}Pu, ^{241}Pu, ^{56}Fe, ^{23}Na, Pb_{nat}, and ^{16}O. The four-region homogeneous model has been chosen instead of the full-core 3D model in order to achieve reasonable calculation times.

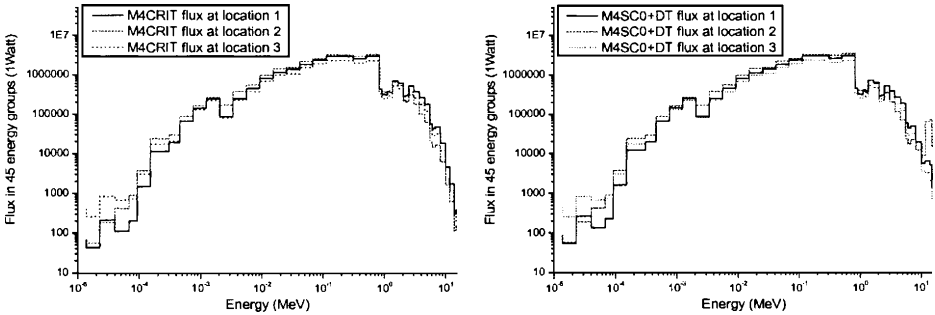

FIG. 2—*Input flux per group calculated with ERANOS. 2.0 in conjunction with ERALIB. 1.*

(b) Use of the ERALIB-1 uncertainty matrix to determine cross section variations—The ERALIB-1 nuclear data library comprises not only cross sections for a large number of isotopes (for detailed calculations of neutron transport), but also the corresponding uncertainties. In the present context, the cross section uncertainties for the principal MUSE-4 isotopes (see previous item) were extracted.

(c) Achievement of 500 spectrum calculations—On the basis of the ERALIB-1 cross section uncertainties, 500 different possible values of each isotope cross section were defined randomly while respecting a normal distribution around the reference value. An analogous stochastic methodology was used to take the composition uncertainties into account. With the help of specific ERANOS developments, the 500 different sets of input values were used to calculate, for each of the three considered locations, the flux per group (i.e., neutron spectrum), 500 times.

(d) Creation of the spectrum variance/covariance matrix—At this point, standard analysis of the 500 calculated spectra allowed the determination of the variance/covariance matrix of the flux for each considered energy group. In our case, this matrix has been established with respect to an energy structure of 45 groups (Table 4). A representative variance/covariance matrix for the high energy groups (>1 MeV) is given for illustration in Table 5.

The following comments need to be made on the above method for determining the variance/covariance matrix for the STAY'SL input spectrum:

(a) The deduced spectrum variance/covariance matrix is characterized by significant non-diagonal terms (see Table 5). This indicates a strong correlation of the uncertainties between the different groups. Additional studies are needed to identify the exact reasons for this phenomenon, which has been also observed in other analyses [15].

TABLE 4—*Description of the 45 energy group structure used.*

Upper energy Limit (eV)	Group Structure	Upper Energy Limit (eV)	Group Structure	Upper energy Limit (eV)	Group Structure
1.964033E+07	1	2.018965E+06	16	1.503439E+04	31
1.733253E+07	2	1.652989E+06	17	9.118820E+03	32
1.491825E+07	3	1.353353E+06	18	5.530844E+03	33
1.384031E+07	4	1.224564E+06	19	3.354626E+03	34
1.161834E+07	5	1.108032E+06	20	2.034684E+03	35
1.000000E+07	6	1.002588E+06	21	1.234098E+03	36
8.187308E+06	7	9.071795E+05	22	7.485183E+02	37
6.703200E+06	8	8.208500E+05	23	4.539993E+02	38
6.065307E+06	9	4.978707E+05	24	3.043248E+02	39
5.488116E+06	10	3.019738E+05	25	1.486254E+02	40
4.493290E+06	11	1.831564E+05	26	9.166088E+01	41
3.678794E+06	12	1.110900E+05	27	6.790405E+01	42
3.011942E+06	13	6.737947E+04	28	4.016900E+01	43
2.465970E+06	14	4.086771E+04	29	2.260329E+01	44
2.231302E+06	15	2.478752E+04	30	1.370959E+01	45

TABLE 5—*Spectrum variance/covariance matrix associated with location 1 for the energy groups of interest (between 1 MeV and 20 MeV).*

Gr.	Std Dev. (%)	1	2	3	4	5	6	7	8	9	10	11	12	13	14	15	16	17	18	19	20	21	…
1	13.4	1.0	1.0	1.0	0.8	0.4	0.3	0.2	0.2	0.2	0.1	0.1	0.1	0.1	0.1	0.1	0.1	0.0	0.0	0.0	0.0	0.0	…
2	9.2		1.0	1.0	0.8	0.5	0.3	0.2	0.2	0.2	0.2	0.2	0.2	0.2	0.1	0.1	0.1	0.1	0.1	0.0	0.0	0.0	…
3	5.6			1.0	0.9	0.6	0.5	0.4	0.4	0.4	0.4	0.4	0.3	0.3	0.3	0.2	0.2	0.2	0.2	0.1	0.0	0.0	…
4	3.2				1.0	0.9	0.8	0.7	0.7	0.7	0.7	0.7	0.7	0.6	0.6	0.5	0.5	0.3	0.3	0.3	0.1	0.1	…
5	2.7					1.0	0.9	0.9	0.9	0.9	0.9	0.9	0.9	0.8	0.8	0.7	0.6	0.5	0.5	0.4	0.1	0.1	…
6	2.6						1.0	0.9	0.9	0.9	0.9	0.9	0.9	0.9	0.8	0.8	0.7	0.6	0.6	0.5	0.2	0.2	…
7	2.6							1.0	0.9	0.9	0.9	0.9	0.9	0.9	0.9	0.8	0.7	0.6	0.6	0.5	0.2	0.2	…
8	2.5								1.0	0.9	0.9	0.9	0.9	0.9	0.9	0.8	0.7	0.6	0.6	0.5	0.2	0.2	…
9	2.5									1.0	0.9	0.9	0.9	0.9	0.9	0.8	0.8	0.6	0.6	0.5	0.2	0.2	…
10	2.6										1.0	1.0	1.0	0.9	0.9	0.8	0.7	0.6	0.6	0.5	0.1	0.1	…
11	2.4											1.0	1.0	1.0	0.9	0.9	0.8	0.6	0.6	0.5	0.2	0.2	…
12	2.0												1.0	1.0	0.9	0.9	0.8	0.7	0.7	0.6	0.3	0.3	…
13	1.6													1.0	1.0	0.9	0.9	0.8	0.7	0.6	0.3	0.3	…
14	1.3						Symmetrical matrix								1.0	1.0	0.9	0.8	0.7	0.7	0.3	0.3	…
15	1.1					1.0	1.0	0.9	0.9	0.8	0.6	0.6	…										
16	1.0																1.0	1.0	0.9	0.9	0.7	0.7	…
17	0.9																	1.0	1.0	1.0	0.8	0.8	…
18	0.9																		1.0	1.0	0.9	0.9	…
19	0.9																			1.0	0.9	0.9	…
20	1.1																				1.0	1.0	…
21	1.1																					1.0	…
…	…	…	…	…	……	…	…	…	…	…	…	…	…	…	…	…	…	…	…	…	…	…	…

(b) As the main isotopes are identical for the critical and subcritical MUSE-4 configurations, the spectrum variance/covariance matrix has been defined only on the basis of calculations for the critical case.

(c) The calculated spectra and their associated variance/covariance matrices have been normalized by fixing the power level at 1 Watt.

Adjusted Spectra and Discussion

Considering the selected threshold reactions, the main objective of the present spectrum adjustment study concerns the high-energy flux component (between 1 MeV and 15 MeV). This choice has been motivated mainly by the need for accurate characterization of the 14 MeV external source effect, the presence of this source in the subcritical MUSE4 configurations being one of the most distinctive aspects of the program. To reach this goal, it was decided to study the spectrum in 45 energy groups of which 21 lie above 1 MeV (see Table 4), this structure having also been used for the ERANOS input spectra (see Fig. 2).

Application of the Spectrum Adjustment Process and Resulting Effects

As stated earlier, the spectrum adjustment process has been applied to locations 1, 2, and 3 of the M4CRIT and M4SC0+DT configurations (see Fig. 1) by considering the experimental absolute reaction rates given in Table 2. Various aspects have been investigated to obtain reference adjusted spectra, as explained below.

First, the STAY'SL adjustment methods assess the consistency between the flux level resulting from the experimental absolute reaction rates and the flux level of the initial calculated spectrum. It can be concluded that the adjustment is optimal (i.e., with the lowest χ^2 function value) for all locations of M4CRIT when a factor of 1.28 is applied to the flux level of the initial spectrum, while the opposite behavior is identified for all positions of M4SC0+DT (adjustment is ideal when a factor of 0.75 is applied to the flux level of the initial spectrum). The origin of this bias can be due either to a systematic error associated with the experimental power determination, or to the intrinsic ERANOS predictions themselves. Further investigations, such as stochastic simulations (MCNP calculations), are recommended to identify the most significant reason of such contradictory normalization needs.

Next, the use of the IRDF-90v2 and IRDF-2002 data files for the spectrum adjustment has been compared. From this viewpoint, the deduced adjusted spectra are very similar in all studied cases. Con-

TABLE 6—*Calculation/Experiment (C/E) for the threshold reaction rates while using IRDF-2002 and IRDF-90v2 for location 1 in M4CRIT and location 2 in M4SC0 + DT.*

C/E Threshold Reactions	M4CRIT IRDF-2002 Location 1	M4CRIT IRDF-90v2 Location 1	M4SC0+DT IRDF-2002 Location 2	M4SC0+DT IRDF-90v2 Location 2
^{115}In(n,n′)	1.01±0.05	0.99±0.05	0.92±0.06	0.90±0.6
^{58}Ni(n,p)	1.04±0.04	1.02±0.04	1.12±0.08	1.13±0.08
^{64}Zn(n,p)	0.98±0.06	0.97±0.06	⋯	⋯
^{54}Fe(n,p)	1.04±0.06	1.04±0.06	⋯	⋯
^{56}Fe(n,p)	1.14±0.04	1.07±0.04	0.82±0.08	0.81±0.08
^{24}Mg(n,p)	1.10±0.04	1.13±0.04	0.93±0.08	0.93±0.08
^{27}Al(n,a)	1.23±0.06	1.23±0.06	0.85±0.08	0.85±0.08
^{93}Nb(n,2n)	1.57±0.05	⋯	0.82±0.08	0.82±0.08

cerning the individual IRDF-90v2 and IRDF-2002 reaction rate predictions, small discrepancies have been seen only for the ^{56}Fe(n,p) reaction rate in the M4CRIT configuration (see Table 6).

Spectrum adjustments have also been done while using a tri-diagonal spectrum variance/covariance matrix instead of the matrix given in Table 5. The resulting effects are a nonnegligible increase of the χ^2 function and a less modified spectrum (i.e., reduction of the adjustment effects).

Finally, certain threshold reactions have been identified as being inappropriate for the spectrum adjustment process. In particular, the ^{93}Nb(n,2n) reaction could not be used to unfold the spectrum in the M4CRIT configuration, the prediction of this reaction rate in M4CRIT (without 14 MeV neutrons) being problematic, as seen in Table 6 (there may be a need to improve the threshold description for this reaction).

The results for two representative adjusted spectra are given in Fig. 3.

The first spectrum is that obtained for location 1 of the M4CRIT configuration, while the other corresponds to the flux per group at location 2 of the M4SC0+DT configuration. The two sets of results presented were obtained using IRDF-2002 data and the experimental reaction rates given in Table 2 (except the ^{92}Nb(n,2n) reaction for M4CRIT). In both cases, the corresponding χ^2 function value is about 6, which is very satisfactory (χ^2 < twice the degree of freedom, which corresponds to the number of experimental reaction rates employed). The adjustments are seen to be more significant for the high-energy groups, the ^{27}Al(n,α) and ^{24}Mg(n,p) high-threshold reaction rates being the most sensitive from the viewpoint of accurate reproduction by the calculation scheme. For all other analyzed spectra, the STAY'SL process led to lower adjustments with similarly satisfactory values for the χ^2 function (between 1 and 6).

Comparisons Between the M4CRIT and M4SC0 + DT Configurations

Figure 4 shows the variation of the normalized adjusted spectra between the critical M4CRIT configuration and the subcritical M4SC0+DT configuration driven by the 14 MeV external source for locations 2 (near the source) and 3 (beside the accelerator tube). For position 2, the presence of 14 MeV neutrons in the case of M4SC0+DT is clearly identified, the corresponding experimental threshold reaction rates being

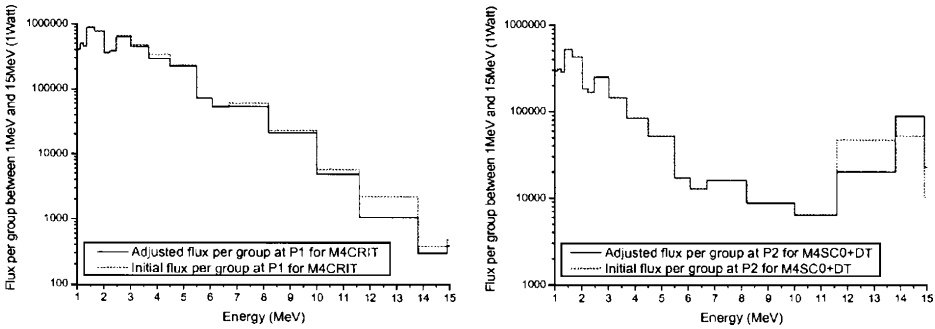

FIG. 3—*Adjusted and initial flux per group at location 1 of the M4CRIT configuration (left) and at location 2 of the M4SC0 + DT configuration (right).*

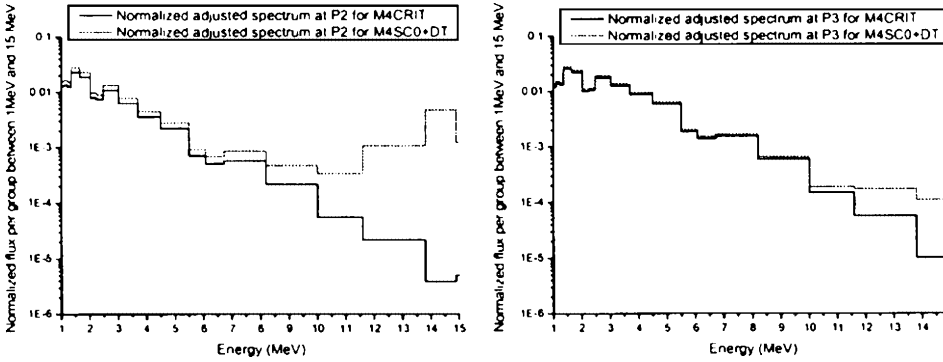

FIG. 4—*Normalized adjusted flux per group at locations 2 (left) 3 (right) for M4CRIT and M4SC0 + DT.*

strongly affected (see Table 2). For position 3, it is interesting to highlight the spectrum discrepancy for the energy groups above ~10 MeV. This spectrum difference may be attributed to streaming effects along the accelerator tube, as this location is at a distance of more than 30 cm from the point of emission of the high-energy source neutrons. It should be mentioned, however, that a slight increase of the high-energy flux component is seen even at location 1.

Conclusion

Investigations of spectrum adjustment by unfolding techniques for different locations of critical and driven subcritical MUSE4 configurations have been presented in this paper. The studies have been based on foil activation measurements and on the use of the STAY'SL unfolding code in conjunction with the IRDF-90v2 and IRDF-2002 data files.

Various improvements have been implemented in the adjustment technique, e.g., the determination of a nonarbitrary variance/covariance matrix for the initial calculated flux per group. More precisely, a realistic assessment of the sensitivity of ERANOS calculations has permitted the quantification of the uncertainties associated with the considered initial spectra. Furthermore, particular care has been taken in estimating the experimental uncertainties of the different measured threshold reaction rates.

In summary, an iterative adjustment process for the neutron spectrum has been developed and applied to three different locations of the M4CRIT and M4SC0+DT MUSE4 configurations. The investigations performed have demonstrated good consistency of the employed methodology. For example, the results obtained clearly highlight the spectral variations between the critical and subcritical configurations, in particular the effects of the external 14 MeV neutron source. It should be mentioned that the need to significantly renormalize the initial flux level has indicated the possibility of systematic errors in the experimental power determination and/or in the ERANOS predictions. Further investigations, e.g., employing MUSE4 models based on the Monte Carlo code MCNP, are recommended in this context. Finally, it is felt that the application of unfolding codes other than STAY'SL, as available in the NMF-90 module [16], should be tested with the aim of qualifying an alternative methodology for spectrum determination in future experimental programs.

Acknowledgments

The MUSE4 project was conducted at the MASURCA facility at CEA-Cadarache. We are grateful to the entire MASURCA staff for the excellent reactor operation and maintenance. Our thanks are also due to O. P. Joneja, R. Früh, J. P. Steudler, and D. Godat for their advice and realization of some of the experimental tools at EPFL. Finally, we acknowledge the support of the LEPh laboratory at CEA-Cadarache and would like to thanks, in particular, C. de Saint Jean.

References

[1] Chiocchio, O. et al., "Measurement of Fast Reactor Type Reactor Spectra by Foil Activation Techniques," *Nucl. Instrum. Methods*, Vol. 91, 1971, pp. 45–56.

[2] Soule, R. et al., "Experimental Validation of the Neutronic Characteristics of the Subcritical Multiplying Medium of an ADS: The MUSE Experiments," *Int. Proceedings of the International Conference on Accelerator Driven Transmutation Technologies and Application (ADTT'01)*, Reno, NV, Nov. 11–15, 2001.

[3] Soule, R. et al., "Neutronic Studies in Support of Accelerator-Driven Systems: The MUSE Experiments in the MASURCA Facility," *Nucl. Sci. Eng.*, Vol. 148, Sept. 2004, pp. 124–152.

[4] Carta, M. et al., "Reactivity Assessment and Spatial Time-Effects from the MUSE Kinetics Experiments," *Int. Proceedings of the International Conference on the New Frontier of Nuclear Technology: Reactor Physics, Safety and High-Performance Computing, PHYSOR*, Chicago, IL, April 25–30, 2004.

[5] Plaschy, M. et al., "Interpretation of Foil Activation and Fission Rate Measurements in Critical and Subcritical MUSE4 Configurations," *Int. Workshop on Partitioning and Transmutation and ADS Development*, SCK-CEN, Belgium, Oct. 6–8, 2003.

[6] Doriath, J. Y. et al., "ERANOS 1: The Advanced European System of Codes for Reactor Physics Calculations," *Int. Proceedings of the Joint Conference on Mathematical Methods and Supercomputing in Nuclear Applications*, Karlsruhe, Germany, April 19–23, 1993.

[7] Rimpault, G. et al., "The ERANOS Data and Code System for Fast Reactor Neutronic Analyses," *Int. Proceedings of the International Conference on the New Frontier of Nuclear Technology: Reactor Physics, Safety and High-Performance Computing, PHYSOR*, Seoul, South Korea, Oct. 7–10, 2002.

[8] Palmiotti, G. et al., "VARIANT: VARIational Anisotropic Nodal Transport for Multidimensional Cartesian and Hexagonal Geometry Calculation," Argonne National Laboratory Report, ANL-95/40, 1995.

[9] Fort, E. et al., "Improved Performances of the Fast Reactor Calculational System ERANOS-ERALIB1 Due to Improved a priori Nuclear Data and Consideration of Specific Additional Data," *Ann. Nucl. Energy*, Vol. 30, 2003, pp. 1879–1898.

[10] Mellier, M. et al., "MUSE-4 Experiment Progress at Subcriticality Levels Representative of ADS Operation," *Int. Proceedings of the International on GLOBAL*, New Orleans, LA, Nov. 16–20, 2003.

[11] Plaschy, M. "Etude Numériques et Expérimentales de Caractéristiques d'un Système Rapide Sous-Critique Alimenté par une Source Externe," Thèse de l'Ecole Polytechnique Fédérale de Lausanne (EPFL) No. 2953.

[12] Perey, F. G., "Least-Squares Dosimetry Unfolding: The Programme STAY'SL," Oak Ridge National Laboratory Report, ORNL/TM-6062, ENDF-254, 1977.

[13] Kocherov, N. P. and McLaughlin, P. K., "The International Reactor Dosimetry File (IRDF-90 Version 2)," IAEA Nuclear Data Section Report, IAEA-NDS-141, IAEA, Oct. 1993.

[14] Griffin, P. J. and Paviotti-Corcuera, R., "Summary Report of the Final Technical Meeting on International Reactor Dosimetry File: IRDF-2002," International Nuclear Data Committee Report, INDC(NDS)-448, IAEA, Oct. 2003.

[15] Boehmer, B. and Manturov, G., "Influence of Input Neutron Spectrum Covariances on Results of Pressure Vessel Neutron Spectrum Adjustments," *Proc. of 9th Int. Symposium on Reactor Dosimetry*, Prague, Czech Republic, Sept. 2–6, 1996.

[16] Kocherov, N. P., "Neutron Metrology File NMF-90," IAEA Nuclear Data Section Report, IAEA-NDS-171, IAEA, Jan. 1996.

Journal of ASTM International, Vol. 3, No. 8
Paper ID JAI100339
Available online at www.astm.org

Shigetaka Maeda,[1] *David W. Wootan,*[1] *and Takashi Sekine*[1]

Characterization of Neutron Fields Using MCNP in the Experimental Fast Reactor JOYO

ABSTRACT: An extensive set of neutron dosimeters ranging from the core center to beyond the reactor vessel were irradiated during the first two operating cycles of the MK-III core to allow a detailed characterization of the neutron spectra and flux distributions for this new core configuration. New analysis methods for predicting the reaction rates for comparison with the dosimetry measurements based on the MCNP code were developed. Analysis of previous MK-II cycle 34-35 dosimetry tests was used to verify the methods. Core models were developed for the different types and locations of dosimetry test subassemblies and biasing schemes were developed. MCNP optimization techniques and the C/E differences were explored. Most of the important parameters that affect the reaction rate calculations and measurements were investigated. In most cases, MCNP provides more accurate estimations of reaction rates and neutron flux than DORT. This indicates that treatment of heterogeneous structure is needed in the predictions for the irradiation test subassembly with no fuel and the irradiation field with large flux gradients.

KEYWORDS: dosimetry, fast reactor, JOYO, Monte Carlo calculation, MCNP, JENDL-3.2

Introduction

One of the primary missions of the JOYO experimental fast reactor is to perform irradiation tests of fuel and structural materials to support the development of fast reactors. Since neutron fluence and spectrum are key parameters in the post irradiation examination (PIE) analysis, their specified accuracies are set for each type of irradiation test. Previous methods applied at JOYO for predicting neutron fields included the three-dimensional diffusion-theory based core management code system for the fuel region and the DORT two-dimensional deterministic transport code for ex-core regions [1]. Recently Monte Carlo transport calculations using the MCNP code [2] have been introduced to account for heterogeneous effects. MCNP can provide accurate geometrical representations and is expected to provide more accurate evaluations than the synthesis of two-dimensional (2-D) calculations.

This paper compares the performance of advanced whole-core Monte Carlo analysis methods and conventional deterministic transport methods in providing accurate calculational predictions for the irradiation conditions of the wide variety of JOYO irradiation test locations. These studies demonstrate the capabilities for providing accurate calculational predictions of performance parameters and irradiation conditions for the wide variety of irradiation tests anticipated in JOYO.

Description of JOYO

The experimental fast reactor JOYO was constructed as the first step in sodium cooled fast reactor development in Japan. Its current missions include improvements in fast reactor safety and operation, and irradiation testing of advanced fuels and materials. The JOYO reactor attained initial criticality in 1977 with the MK-I breeder core. From 1983 to 2000, JOYO was operated at 100 MWt for 35 operational cycles with the MK-II irradiation test bed core.

In 2003 the JOYO reactor upgrade to the 140 MWt MK-III core was completed to increase the irradiation testing capability. The MK-III core [3] incorporates significant changes to the core size and arrangement, fuel enrichment, and reactor power level compared to the MK-II core. This upgraded JOYO

Manuscript received June 20, 2005; accepted for publication June 30, 2006; published online August 2006. Presented at ASTM Symposium on Reactor Dosimetry, 12th International Symposium on 8–13 May 2005 in Gatlinburg, TN; D. W. Vehar, D. M. Gilliam, and J. M. Adams, Guest Editors.
[1] Research Engineer, Japan Atomic Energy Agency, 4002, Narita, O-arai, Ibaraki, 311-1391, Japan.

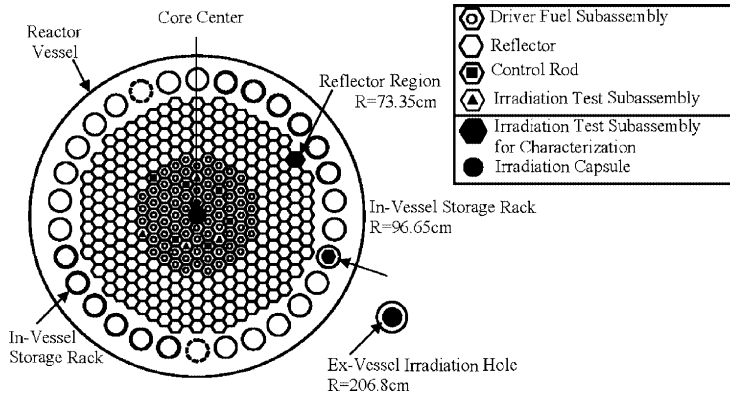

FIG. 1—*Irradiation test subassemblies and capsule position.*

MK-III has been operated since 2003 with the primary mission of developing fuels and materials considered in the feasibility study on commercialized fast reactor cycle systems.

The MK-III core specifications were determined such that the fast neutron flux would be increased and a large number of irradiation rigs could be irradiated simultaneously. The fuel region in the MK-III core is divided into two radial enrichment zones to flatten the neutron flux distribution. The active core is cylindrical and about 80 cm in equivalent diameter and 50 cm in height. There is a radial reflector region of stainless steel surrounding the core that is 25- to 30-cm thick. Shielding subassemblies with B_4C are loaded in the outer two rows of the reactor grid, replacing radial stainless steel reflector subassemblies.

As a result, the fast neutron flux is up to 1.3 times higher than that of the MK-II core, with 140 MWt reactor power. Also, the irradiation test field space with a high neutron flux is approximately double that of the MK-II core. Four neutron environments are available for experiments in the upgraded JOYO MK-III core, ranging from the reactor core to the ex-vessel irradiation hole as follows.

(1) Fuel Region: High temperature and high neutron flux
(2) Reflector Region: Softer neutron spectrum and two orders lower neutron intensity than fuel region
(3) Upper Core Region: Higher temperature and softer spectrum than reflector region
(4) Ex-vessel Region: Lower energy neutron dominated

In the fuel region, the total flux is 4 to 6×10^{15} n/cm$^2\cdot$s and the spectrum index ($\phi_{E>0.1\ MeV}/\phi_{total}$) is approximately 0.6 to 0.7. In the ex-vessel irradiation hole, the total flux magnitude is about 10^{12} and the spectrum index is on the order of 0.01.

Description of Irradiation Test for Benchmark

A number of reactor dosimetry measurements have been conducted in JOYO to assure the reliability and accuracy of the neutron flux calculations [4]. Dosimetry tests irradiated in the MK-II operational cycles 34 and 35 providing a full range of environments were selected to verify the new core calculational methods. Figure 1 shows the loaded position of the irradiation test subassemblies and capsules which contained sets of dosimeter materials.

In-vessel Neutron Reaction Rate Measurement from the Core to the In-vessel Storage Rack

The in-vessel reaction rate distribution was measured by the activation method using a dosimeter set consisting of Fe, Ni, Cu, Ti, Co, Ta, Sc, Np, and ^{235}U which have reactions in different neutron energy ranges. Irradiation test subassemblies with included dosimeters were loaded at the core center, the reflector region (9th row) and the in-vessel storage rack. The structure of the irradiation subassembly is shown in Fig. 2. These test subassemblies were irradiated for 117.1 E.F.P.Ds in the MK-II core from November 1999 to June 2000.

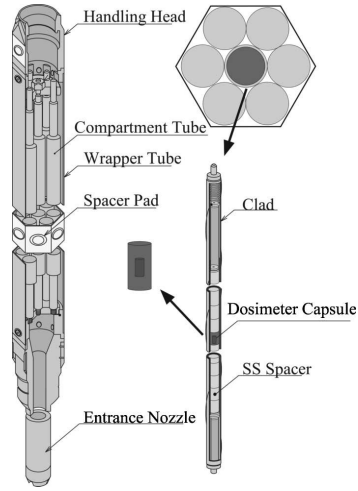

FIG. 2—*Structure of irradiation test subassembly.*

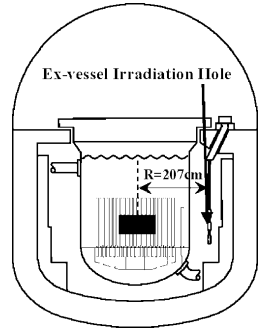

FIG. 3—*Cross section view of JOYO.*

Ex-vessel Neutron Reaction Rate Measurement

Irradiation capsules made of aluminum were placed in the ex-vessel irradiation hole at a radius of 206.8 cm between the reactor vessel and the graphite shield. A dosimeter set consisting of Fe, Ni, Cu, Ti, Co, Ta, Sc, Np, and ^{235}U was used. The measurement location is shown in Fig. 3. The irradiation period was 48.15 E.F.P.Ds.

Measured Reaction Rate and Neutron Flux

Reaction Rate

The reaction rate was determined by analyzing the gamma ray or X-ray spectra as measured from the irradiated dosimeters. The measurements were performed with a high purity Germanium (Ge) gamma-ray detector and a Low Energy Photon Spectrometer (LEPS). Both detectors were calibrated with standard gamma-ray sources whose energies spanned those of the activated nuclides. The accuracy of the gamma-ray measurement system had been confirmed to within 3 % through integral tests in the fast spectrum neutron field in the YAYOI fast neutron source reactor at the University of Tokyo and the reactor dosimetry

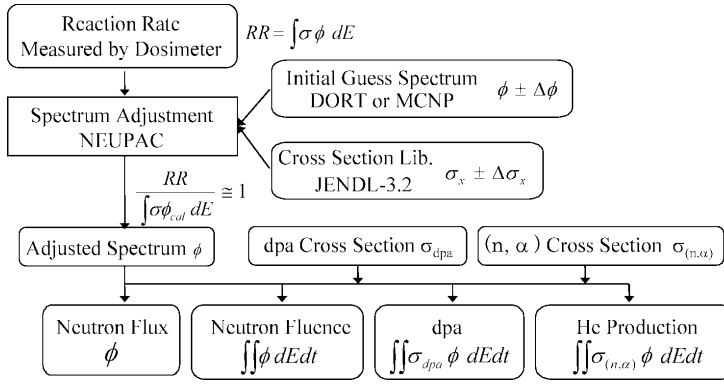

FIG. 4—*Measurement flow and neutron adjustment by NEUPAC.*

intercomparison study between JOYO and EBR-II. Corrections were required for dosimeter masses, impurities, burn-up during irradiation, neutron self-shielding during irradiation, and gamma ray self-absorption.

Neutron Flux Unfolded Using Multi Foil Activation Method

The neutron spectrum at each dosimeter position is adjusted by the measured reaction rates using "NEUPAC," a J-log type spectrum unfolding code package, as shown in Fig. 4. NEUPAC uses 103-group cross sections with error covariances processed from the JENDL dosimetry file based on JENDL-3.2. The neutron flux and relevant irradiation parameters such as displacement per atom (dpa) and helium production were evaluated with the adjusted neutron spectrum.

Discrete Ordinates Calculation Method

The compositions of each core subassembly and neutron source distribution in JOYO are calculated by the core management code system MAGI [5] and were used as input to DORT. The nuclear calculation used in MAGI is based on three-dimensional diffusion theory with seven neutron energy groups. MAGI uses the JFS-3-J3.2 cross section set, which is based on the JENDL-3.2 library [6]. The core configuration is modeled using the three-dimensional Hexagonal-Z geometry for each operational cycle of JOYO MK-II core. The axial extent of the model is 140 cm divided into 20 axial meshes with the fuel region (55-cm high) divided into eleven axial meshes. The MAGI burn-up calculation takes into account the actual core configuration and the reactor power history of each operational cycle. The accuracy of the fuel burn-up and neutron flux calculated by MAGI was previously confirmed to be within 5 % in the fuel region by reactor dosimetry tests and chemical analysis of ^{148}Nd obtained from PIE. A ^{239}Pu fission spectrum was adopted. The DORT calculations were conducted in the RZ and XY-Rθ geometries (shown in Fig. 5). The XY-Rθ results were from connected XY-Rθ calculations. The angular flux calculation in the core represented with X-Y geometry was converted for use as the boundary source for the out of core region represented with R-θ geometry. In calculating the neutron flux distribution in the XY-Rθ geometry, the axial neutron leakage from the core mid-plane was considered as a pseudo-absorption. This leakage term was obtained using the gradient of the neutron flux at 2.5 cm above and below the horizontal surface of the core that was calculated in the RZ geometry. The transport equation is solved as a fixed source problem with P_3 expansion of the angular dependence of the scattering cross sections, and a symmetric S30 (full symmetry S_6) directional quadrature set. The cross section data used in the DORT calculations were JSD-J2/JFT-J2 shielding constants set [7] (100-neutron and 20-gamma groups) made from the nuclear data file JENDL-2. This dataset has been typically used for shielding analysis for FBRs in Japan. The effectiveness of this method had already been confirmed through the experiments in JASPER (the Japanese-American Shielding Program for Experimental Research) [7]. The JSSTDL library [8], which was gener-

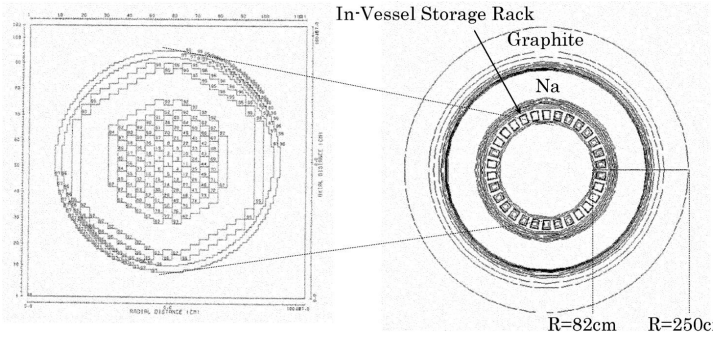

FIG. 5—*DORT 2D-XY and 2D-Rθ calculation model of JOYO.*

ated from JENDL-3.2 and has a 100-neutron and 40-gamma group structure, was also used to evaluate the effect of the cross section library.

Calculation Method Using MCNP

The new analysis strategy involves developing efficient calculational models using the continuous energy MCNP code that are optimized for each unique type of test environment. The advantages of the MCNP code are that it provides transport of both neutrons and gamma rays, includes heterogeneous geometry modeling capability, has many options for optimization in space and energy, and can utilize the JOYO core management fuel compositions.

Geometry, Composition, and Calculation Method

A whole core MCNP model was created for cycle 35 of the MK-II core. This model included the core loading and MAGI core management burned fuel subassembly compositions for the beginning of cycle 35. The main fission products were also included in the fuel compositions. The fuel subassemblies were modeled as discrete pins, while reflectors were homogeneously modeled. The subassemblies were divided into 29 axial zones ranging from 90 cm below core mid-plane to 120 cm above core mid-plane. The model extended radially through the graphite shield to a radius of 320 cm, the same as the RZ and Rθ models used in the DORT calculations. The control rods were adjusted to an axial height corresponding to the end of cycle (EOC) elevation (46.10 cm withdrawn). Cross sections based on JENDL3.2 were used.

Each of the irradiation subassemblies included separate pins containing steel dosimeter capsules. Inside each capsule was a cavity of approximately 1 cm in diameter and 1 cm in height, for a volume of 0.79 cm^3, where the actual dosimeters were located. The MCNP model for each of the subassemblies included a 58-cm high region centered on core mid-plane with heterogeneous representations of the wrapper tube, the seven pins, and the steel dosimeter capsules inside each pin. The small region inside the dosimeter capsule where the dosimeters were located was modeled as a homogenized smear of the dosimeters and vanadium capsules. This allows separate calculations of the perturbing effects of the dosimeters, such as neutron self-shielding. The challenge was to calculate reaction rates with adequate statistical uncertainties inside each of these small dosimeter cavities. Figure 6 shows the details of the irradiation subassemblies geometry models.

MCNP is run in the "kcode" mode, where it generates the fission source by an iterative k_{eff} process. Since MCNP includes both neutron and gamma-ray heating, normalization factors for the tally results were normalized to the total energy deposition in the reactor.

The contribution of the delayed gamma-ray energy from fission products was estimated because MCNP only includes contributions to energy deposition from prompt gamma rays from fission. Values of delayed fission product gamma-ray energy contribution for each of the fissioning isotopes was obtained from ENDF/B-VI data files, and weighted by the global fraction of total fissions. The result was a core-wide average of 6 MeV per fission, or a correction of 3 %.

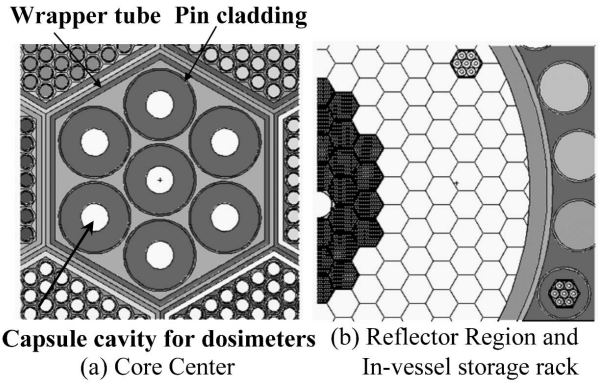

FIG. 6—*Horizontal cross section of the MCNP model at the core mid-plane.*

A total neutron plus photon heat deposition calculation over the entire reactor was made to obtain the power normalization factor for the reaction rate tallies. A neutron+photon MCNP calculation for the MK-II cycle 35 core was made in the kcode mode with neutron and photon importances of 1.0 in the core and decreasing importances in the radial shield regions. The model was extended axially to 150 cm below core mid-plane and to 180 cm above core mid-plane since about 4 % of the neutrons escaped from the original model. Tallies were included for both neutron and photon heating in all components in the model. The normalization factor for the tallies for a total power of 100 MW (including a reduction of 6/200 for delayed gamma energy, so the MCNP calculated total power should be 97 MW) was determined. The total energy deposition and photon energy deposition calculated by MCNP for the MK-II Cycle 35 core loading that includes the delayed gamma heating contribution was consistent with the core management code. The statistical uncertainty on the total heating was 0.06 %. Of the 100 MW total, the total gamma heating component (including the delayed gamma heating) was 12.5 MW. Power deposited in the IVS region, including the contribution of the eight fuel assemblies, was 1.4 MW.

Optimize the Weight Windows

The MCNP weight window specifications were developed by an iterative process, where the MCNP weight window generator was used for starting values, then modifications were made manually to tailor the biasing separately for the ex-vessel irradiation hole, in-vessel storage rack, radial reflector, and core center dosimeter reaction rate calculations. A separate calculation with uniform importances in all regions was used to provide a basis for judging the efficiency of the biasing schemes. The MCNP weight window generator alone was not sufficient for creating directly usable weight windows because of the complexity of the transport problem. The number and relative magnitude of three-dimensional weight window mesh bins were varied radially and azimuthally in an attempt to optimize the calculational efficiency for each dosimeter location. The number of weight window energy bins was also varied. A different optimization scheme was developed for each unique location type, but all involved running MCNP in the "kcode" mode and using three-dimensional mesh based weight windows with three energy bins ($<$1 MeV, 1–3 MeV, $>$3 MeV) biased to higher energies. The optimization scheme developed for the ex-vessel irradiation hole dosimetry used 20 radial regions biased radially outward and point detector tallies. The optimization scheme developed for the reflector region and in-vessel storage rack subassemblies included 14 radial regions biased radially outward, 12 azimuthal regions biased to the vicinity of the reflector region and in-vessel storage rack subassemblies, and flux volume tallies in each of the dosimeter capsule cavities. Varying the weight windows azimuthally to focus on the particular reflector and in-vessel storage locations was found to increase the efficiency of the calculation.

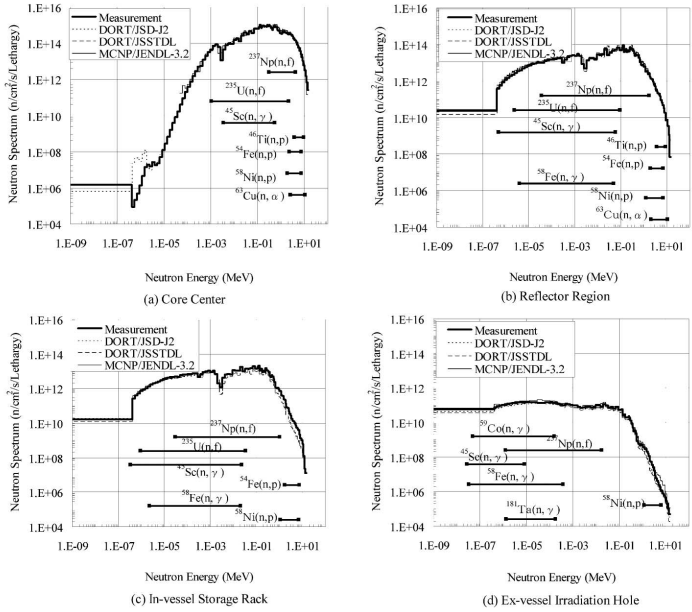

FIG. 7—*Comparison of neutron spectrum.*

Result and Discussion

Neutron Flux and Spectrum

Typical neutron spectra results for the whole core calculations in the individual dosimeter cavities at core mid-plane from the MCNP calculations with JENDL-3.2 cross sections are compared in Fig. 7 with the measurement results for the DORT calculations with the two datasets and also showed 90 % confidence level for each reaction rate. Both neutron spectra from the DORT calculations with different datasets were in good agreement, indicating these datasets give accurate estimations of the neutron spectrum for shielding calculations in a fast reactor. MCNP calculations were in good agreement with the measurements except for the ex-vessel irradiation hole. This is because of a high flux of high energy neutrons in the neutron spectrum calculated by MCNP, due to insufficient neutron histories and a large statistical error. Further investigation about the biasing method for high energies is needed to reduce the statistical uncertainties.

Reaction Rate

Table 1 shows the comparison of measured and the calculated reaction rates for each irradiation location at core mid-plane by MCNP and DORT with two datasets. The optimization results demonstrated that biasing schemes for each location can provide adequate statistical uncertainties for the reaction rates in less than 1 cm^3 volume of the dosimeter capsule cavity in a MCNP calculation. In two DORT calculations a slightly better average C/E ratio and a smaller deviation were observed for the JSSTDL than JSD-J2 datasets. However, calculated values overestimate the measured values, for example in the ^{235}U fission reaction and flux value. It seems that the local flux distribution inside the irradiation test subassembly with no fuel is not fully predicted by DORT. The MCNP ^{235}U fission reaction was in good agreement with the measured value. In most cases, MCNP provides more accurate estimations of reaction rates and neutron flux than DORT. This indicates that treatment of heterogeneous structure is needed in the predictions for the irradiation test subassembly with no fuel and the irradiation field with large flux gradients. But some discrepancy still exists and further investigation will be required to increase the accuracy and to further

TABLE 1—*C/E ratios for dosimetry*

		Reaction Rate								Flux	
		^{54}Fe(n,p)	^{58}Fe(n,g)	^{58}Ni(n,p)	^{63}Cu(n,a)	^{46}Ti(n,p)	^{45}Sc(n,g)	^{237}Np(n,f)	^{235}U(n,f)	Total	E>0.1 MeV
(a) Core Center											
DORT	JSD-J2	1.27	…	1.24	1.32	1.30	1.27	1.36	1.11	1.20	1.20
	JSSTDL	1.28	…	1.25	1.34	1.33	1.25	1.37	1.11	1.20	1.21
MCNP	JENDL-3.2	0.99	…	1.01	1.00	1.06	1.20	1.21	1.04	1.11	1.12
(b) Reflector Region											
DORT	JSD-J2	1.01	1.40	1.10	1.09	1.02	1.26	1.31	1.11	1.21	1.25
	JSSTDL	0.90	1.55	0.99	1.04	1.00	1.35	1.31	1.22	1.24	1.20
MCNP	JENDL-3.2	0.89	1.09	1.05	0.89	1.03	1.23	1.25	1.11	1.16	1.17
(c) In-Vessel Storage Rack											
DORT	JSD-J2	0.37	1.00	0.39	0.93	…	…	0.75	0.82	0.77	0.66
	JSSTDL	0.33	1.05	0.36	0.97	…	…	0.76	0.87	0.77	0.61
MCNP	JENDL-3.2	0.90	0.95	1.01	0.94	…	…	1.03	0.93	1.02	1.03
(d) Ex-Vessel Irradiation Hole											
DORT	JSD-J2	…	0.83	0.47	0.77	0.81	0.82	0.90	…	0.82	0.78
	JSSTDL	…	0.78	0.43	0.71	0.80	0.89	0.95	…	0.84	0.76
MCNP	JENDL-3.2	…	0.95	1.53	0.87	1.03	1.11	1.14	…	1.22	1.11

evaluate the irradiation conditions using MCNP. On the other hand, the calculated values of the Np reaction rate have big discrepancies. The discrepancy appears due to the difficulty of evaluating the burn-up and burn-in correction factor. Further investigation into the correction will be required.

MK-III Core Characterization Test

These same methods will be applied to the MK-III core and predictions made for new MK-III core dosimetry tests. A new extensive set of reactor dosimetry measurements in the fuel, reflector, in-vessel storage, and ex-vessel regions is being irradiated during the first two operating cycles of the MK-III core in order to check the validity of the spectrum calculations using the developed methods. Figure 8 shows the core configuration and location of the special dosimeter characterizer subassemblies for the first and second duty cycles of the MK-III core. A total of 18 characterizer subassemblies were irradiated ranging from core center to IVS locations. In addition, an ex-vessel dosimeter package was irradiated in ex-vessel irradiation hole location.

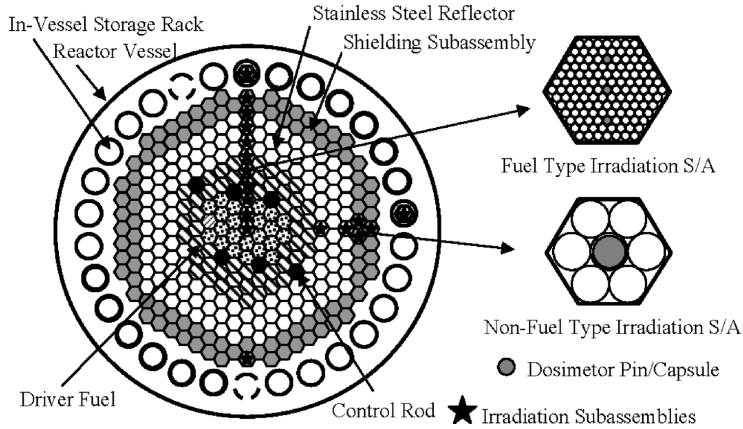

FIG. 8—*MK-III core characterization test.*

Conclusions

An extensive set of neutron dosimeters ranging from the core center to beyond the reactor vessel were irradiated during the first two operating cycles of the MK-III core to allow a detailed characterization of the neutron spectra and flux distributions for this new core configuration. New analysis methods for predicting the neutron flux and the reaction rates for comparison with the dosimetry measurements based on the MCNP code were developed. Analysis of previous MK-II cycle 34-35 dosimetry tests was used to verify the methods. Core models were developed for the different types and locations of dosimetry test subassemblies and biasing schemes were developed. MCNP optimization techniques and the C/E differences were explored. Most of the important parameters that affect the reaction rate calculations were investigated. In most cases, MCNP provides more accurate estimations of reaction rates and neutron flux than DORT. This indicates that treatment of heterogeneous structure is needed in the predictions for the irradiation test subassembly with no fuel and the irradiation field with large flux gradients.

Acknowledgment

The authors would like to note the contribution of Mr. T. Ito of Information Technologies Japan Inc. for the MAGI neutron flux calculation, and Mr. T. Masui and Mr. T. Saikawa of Inspection Development Company for the JOYO dosimetry. We also greatly appreciate the cooperation and valuable comments by Dr. O. Sato of Mitsubishi Research Institute Inc. on the DORT calculation methods.

References

[1] Rhoades, W. A. and Childs, R. L., "DORT Two-dimensional Discrete Ordinates Transport Code," RSIC Code Package CCC-484 (ORNL, November 1989).

[2] Brown, F. B. et al., "MCNP—A General Monte Carlo N-Particle Transport Code Version 5," LA-UR-030-1987 (2003).

[3] Maeda, Y., et al., "Distinguished Achievements of a Quarter Century Operation and a Promising Project Named MK-III in JOYO," *Nucl. Technol.*, Vol. 150, No. 1, 2005, pp. 16–36.

[4] Aoyama, T., et al., "Characterization of Neutron Field in the Experimental Fast Reactor JOYO for Fuel and Structural Material Irradiation Test," *Nucl. Eng. Des.*, Vol. 228, 2004, pp. 21–34.

[5] Ohkawachi, Y., et al., "JOYO MK-II Core Characteristics Database—Update to JENDL-3.2," *Proceedings of the 2002 Symposium on Nuclear Data*, Tokai, Japan 21–22, November 2002, JAERI-Conf. 2003-006, 2003, pp. 294–299.

[6] Nakagawa, T., et al., "Japanese Evaluated Nuclear Data Library Version 3 Revision-2: JENDL-3.2," *J. Nucl. Sci. Technol.*, Vol. 32, No. 12, 1995, p. 1259.

[7] Takemura, M., et al., "JASPER Experiment Analyses—(6) Investigation of Analysis Method," 1987 Fall Meeting of the Atomic Energy Society of Japan, Oct. 1987, A61 (in Japanese).

[8] Hasegawa, A., *Nuclear Data News*, No. 62, 1999 (in Japanese).

Journal of ASTM International, Vol. 3, No. 3
Paper ID JAI13454
Available online at www.astm.org

Do Heon Kim,[1] *Choong-Sup Gil,*[1] *and Jonghwa Chang*[1]

Benchmark on the 3-D VENUS-2 MOX-Fueled Reactor Dosimetry Calculations by DANTSYS Code System

ABSTRACT: The benchmark calculation for the 3-D VENUS-2 MOX-fueled reactor dosimetry has been performed by the TRANSX/DANTSYS code system. The nuclear data from the ENDF/B-VI.8, JENDL-3.3, and JEFF-3.0 have been processed for the MATXS-format 199-group neutron libraries by NJOY99.90. The equivalent fission fluxes at the 34 measurement positions on the core mid-plane have been calculated using the dosimetry reaction rates for the ^{58}Ni(n,p), ^{115}In(n,n'), ^{103}Rh(n,n'), ^{64}Zn(n,p), ^{237}Np(n,f), and ^{27}Al(n,α) detectors. The estimated results by the JENDL-3.3 and JEFF-3.0 have been compared with those by the ENDF/B-VI.8.

KEYWORDS: VENUS-2, DANTSYS, NJOY99.90, ENDF/B-VI.8, JENDL-3.3, JEFF-3.0, IRDF-90 version 2

Introduction

The OECD/NEA has been preparing the physics benchmarks related to the reactors loaded with a form of mixed-oxide (MOX) uranium and plutonium fuel to understand better the behavior of the fuel and to identify any possible improvements in the nuclear data and physics modeling methods. A benchmark exercise based on the VENUS-2 MOX core measurement data has been initiated for this purpose. In 1999, the first benchmark test was set up to verify the power distribution predicted by the 2-D VENUS-2 MOX core measurement data [1,2]. Extensions to the 3-D calculation were launched in 2001 for a more thorough investigation of the calculation methods used for the VENUS-2 MOX-fueled system [3,4]. The main objective of the 3-D calculation was a comparison of the predicted axial fission rates of the six fuel pins with the measured values.

The present benchmark calculation on the 3-D VENUS-2 MOX-fueled reactor dosimetry [5], which follows on from the former 2-D and 3-D tests, has been performed by the TRANSX/DANTSYS code system [6,7]. The equivalent fission fluxes at 34 measurement positions have been calculated from the dosimetry reaction rates for the ^{58}Ni(n,p), ^{115}In(n,n'), ^{103}Rh(n,n'), ^{64}Zn(n,p), ^{237}Np(n,f), and ^{27}Al(n,α) detectors.

VENUS-2 Core

The VENUS (Vulcain Experimental NUclear Study) facility is a zero power critical reactor located at SCK●CEN in Belgium. The core is comprised of 12 "15×15" subassemblies as shown in Fig. 1. The central part of the core consists of UO_2 fuel pins 3.3 wt. % enriched in ^{235}U (i.e., 3.3/0 UO_2) and Pyrex pins. There are UO_2 fuel pins 4.0 wt. % enriched in ^{235}U (i.e., 4.0/0 UO_2) on the periphery of the core and MOX fuel pins enriched 2.0 wt. % in ^{235}U and 2.7 wt. % in high grade plutonium (i.e., 2.0/2.7 MOX) on the most external part of the core.

The measurement positions in VENUS-2 are shown in Fig. 2. The six detectors were placed on the core mid-plane of the reactor at 34 locations in the central hole (1), the core inner baffle (2), the core outer baffle (7), the water reflector (5), the core barrel (8), the water gap (9), and the neutron pad (2).

Manuscript received June 20, 2005; accepted for publication September 29, 2005; published online December 2005. Presented at ASTM Symposium on Reactor Dosimetry, 12th International Symposium on 8–13 May 2005 in Gatlinburg, TN; D. W. Vehar, D. M. Gilliam, and J. M. Adams, Guest Editors.

[1] Senior Researcher and Principal Researchers, respectively, Korea Atomic Energy Research Institute, P.O. Box 105, Yuseong, Daejeon, 305-600, Korea.

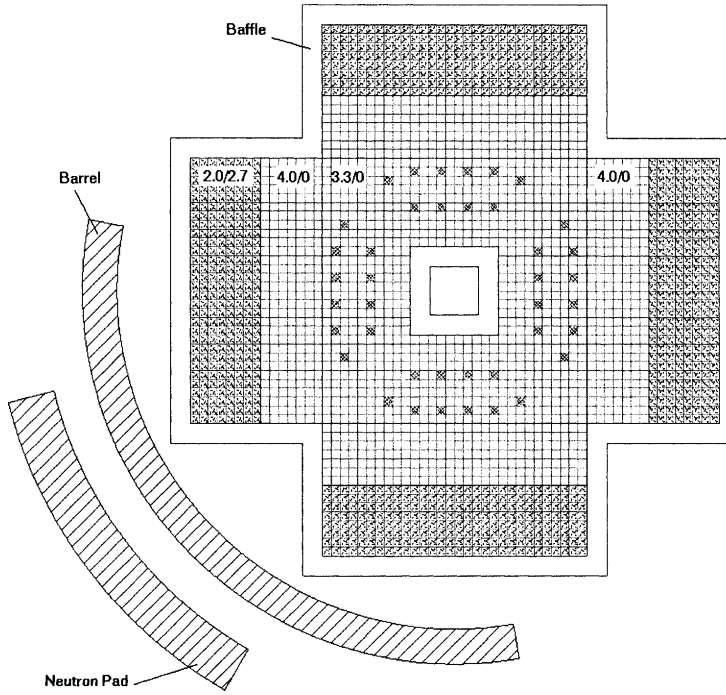

FIG. 1—*VENUS-2 core loading configuration.*

Library Generation

A MATXS-format multi-group neutron library should be provided for the TRANSX/DANTSYS code system. The ENDF/B-VI.8, JENDL-3.3 and JEFF-3.0 were adopted for all the isotopes constituting the VENUS-2 facility except for natural tin, which was taken from the ENDL-84 library. The neutron data library with a 199-group structure of VITAMIN-B6 [8] has been generated by NJOY99.90 [9]. The VITAMIN-B6 neutron group structure can be useful for a broader range of applications such as a variety of reactor designs and shielding problems including thermal and fast reactor systems. The neutron weighting function is of the form typically used for fission reactor shielding problems. The function is composed of a smoothly varying combination of a Maxwellian thermal spectrum, a 1/E slowing down spectrum and a fission spectrum. (IWT=4 in GROUPR module of NJOY) Figure 3 shows the flow diagram of the NJOY99.90 nuclear data processing for the VENUS-2 benchmark calculations.

Benchmark Calculations

The benchmark calculations were carried out using the TRANSX/DANTSYS code system. The 1-D transport calculations for three fuel cells and a Pyrex cell were performed to calculate the region-wise 199-group weighting flux by using the macroscopic cross sections prepared by the TRANSX code. A 1-D cylindrical geometry, mesh widths of ~0.03 cm, and a P_3-S_{16} approximation were applied. The resulting weighting fluxes were utilized to collapse the 199-group data into a 47-group data for the 3-D core calculations. Here, the 47-group data corresponds to the problem-dependent broad-group cross section library, which has a neutron group structure of the BUGLE-96 [8]. For other regions such as the barrel, baffle, plexiglass, stainless steel grids, neutron pad, etc., the group collapse was carried out with the built-in P_0 flux.

For the 3-D core calculation, the VENUS-2 core was modeled up to the neutron pad in the x- and y-directions. It was assumed that the regions beyond the neutron pad were filled with water. In the

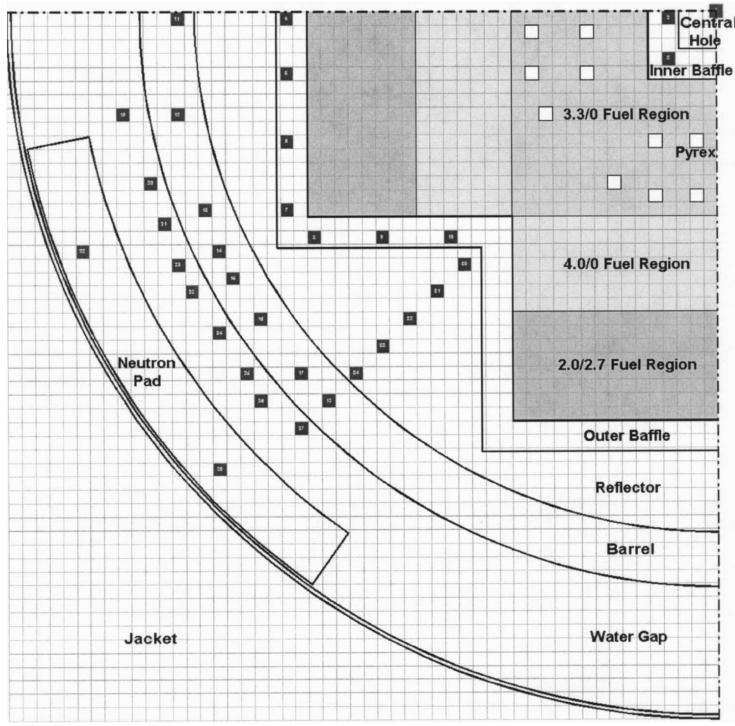

FIG. 2—*Measurement positions in VENUS-2.*

z-direction, the core was modeled explicitly from the bottom to the top with a proper use of the homogenization technique for the regions having a complex geometrical shape such as the bottom, intermediate, and upper grids. The mesh sizes are ~0.63 cm (a half of the fuel cell pitch) up to the outer baffle region

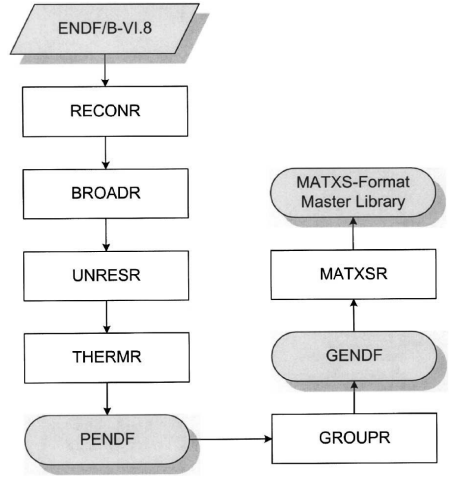

FIG. 3—*Flow diagram of the NJOY99.90 nuclear data processing.*

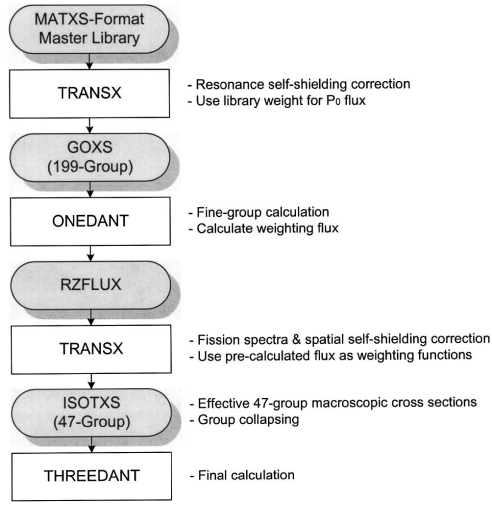

FIG. 4—*Procedures for the 3-D VENUS-2 benchmark calculation.*

and 1.26 cm outside the region in the x- and y-directions. In the z-direction, the mesh widths are 2 cm. Also, the calculation was carried out with the P_3-S_8 approximation. All the procedures for the benchmark calculation are illustrated in Fig. 4.

The equivalent fission fluxes at the 34 positions on the core mid-plane of the reactor were measured using the $^{58}Ni(n,p)$, $^{115}In(n,n')$, $^{103}Rh(n,n')$, $^{64}Zn(n,p)$, $^{237}Np(n,f)$, and $^{27}Al(n,\alpha)$ detectors. The threshold energies of the detectors are 0.5, 0.339, 0.04, 0.5, 0.01, and 5.0 MeV, respectively. The $^{64}Zn(n,p)$ detector is used for a measurement at the energies beyond the barrel and the $^{27}Al(n,\alpha)$ detector is used to observe the performance of the calculation tools at the high energy level. The IRDF-90 version 2 dosimeter cross section data [10] was taken to estimate the dosimetry reaction rates for the detectors. This data was collapsed into 47 groups with the same weighting function as in the library generation.

Results

The 3-D VENUS-2 core calculations have been performed by using the libraries based on the ENDF/B-VI.8, JENDL-3.3 and JEFF-3.0. The effective multiplication factors (k_{eff}) of the core were estimated to be 0.99579, 0.99870, and 0.99698, respectively. Like the other thermal criticality benchmarks [11], the JENDL-3.3 tends to increase the k_{eff} compared with the ENDF/B-VI.8 and JEFF-3.0. The equivalent fission fluxes are the reaction rates divided by the ^{235}U fission spectrum averaged cross sections of the corresponding dosimeter. Tables 1 and 2 show the equivalent fission fluxes with the ENDF/B-VI.8-based library at a 100 % power in the stainless steel zones and in the water zones, respectively. The neutron fluxes at threshold energies $E_{th} > 0.1$ MeV and $E_{th} > 1.0$ MeV are given in the last two columns of the tables.

Figures 5 and 6 show the relative differences (%) of the JENDL-3.3 results from the ENDF/B-VI.8 results in the stainless steel zones and in the water zones, respectively. The differences become greater as the threshold energies of the detectors become larger. For the $^{237}Np(n,f)$, $^{103}Rh(n,n')$, and $^{115}In(n,n')$ detectors, which have relatively small threshold energies, the ENDF/B-VI.8 and JENDL-3.3 provide good agreements to within a difference of $\sim$3 %. In the inner baffle, outer baffle, and reflector regions close to the fuel regions, the differences were estimated to be negative. It implies that the neutron fluxes more than the threshold energies calculated with the JENDL-3.3 are smaller than those with the ENDF/B-VI.8 near the fuel regions.

For the $^{58}Ni(n,p)$ and $^{64}Zn(n,p)$ detectors, which have the same threshold energy of 0.5 MeV, the differences between the JENDL-3.3 and ENDF/B-VI.8 are almost the same while showing a maximum

TABLE 1—*Equivalent fission fluxes at a 100 % power in the stainless steel zones.*

[Unit: neutrons/cm^2/sec]

Measurement Position[a]	^{58}Ni(n,p)	^{115}In(n,n')	^{103}Rh(n,n')	^{64}Zn(n,p)	^{237}Np(n,f)	^{27}Al(n,α)	Flux at E>0.1 MeV	Flux at E>1.0 MeV
Inner Baffle								
(−4.41,−0.63)	1.40E+09	1.77E+09	2.16E+09	1.35E+09	2.39E+09	1.27E+09	3.20E+09	1.33E+09
(−4.41,−4.41)	1.68E+09	2.11E+09	2.55E+09	1.62E+09	2.81E+09	1.51E+09	3.74E+09	1.58E+09
Outer Baffle								
(−39.69,−0.69)	5.68E+08	6.93E+08	8.24E+08	5.50E+08	9.02E+08	5.31E+08	1.18E+09	5.12E+08
(−39.69,−5.67)	5.40E+08	6.59E+08	7.83E+08	5.23E+08	8.57E+08	5.04E+08	1.12E+09	4.87E+08
(−39.69,−11.97)	4.40E+08	5.38E+08	6.40E+08	4.26E+08	7.01E+08	4.13E+08	9.20E+08	3.98E+08
(−39.69,−18.27)	2.56E+08	3.21E+08	3.89E+08	2.47E+08	4.29E+08	2.43E+08	5.72E+08	2.39E+08
(−37.17,−20.79)	2.65E+08	3.32E+08	4.03E+08	2.55E+08	4.46E+08	2.52E+08	5.96E+08	2.48E+08
(−30.87,−20.79)	5.25E+08	6.50E+08	7.82E+08	5.07E+08	8.60E+08	4.87E+08	1.14E+09	4.83E+08
(−24.57,−20.79)	8.34E+08	1.05E+09	1.27E+09	8.05E+08	1.41E+09	7.47E+08	1.88E+09	7.84E+08
Barrel								
(−49.77,−0.63)	7.55E+07	9.05E+07	1.07E+08	7.27E+07	1.17E+08	8.66E+07	1.51E+08	6.72E+07
(−49.77,−9.45)	6.54E+07	7.92E+07	9.44E+07	6.29E+07	1.04E+08	7.57E+07	1.35E+08	5.90E+07
(−47.25,−18.27)	5.97E+07	7.57E+07	9.31E+07	5.71E+07	1.04E+08	6.54E+07	1.40E+08	5.71E+07
(−45.99,−22.05)	4.92E+07	6.39E+07	8.03E+07	4.68E+07	9.02E+07	5.41E+07	1.24E+08	4.86E+07
(−44.73,−24.57)	4.31E+07	5.62E+07	7.07E+07	4.11E+07	7.94E+07	4.67E+07	1.10E+08	4.27E+07
(−42.21,−28.35)	4.02E+07	5.01E+07	6.15E+07	3.84E+07	6.85E+07	4.78E+07	9.21E+07	3.77E+07
(−38.43,−33.39)	3.56E+07	4.18E+07	4.97E+07	3.42E+07	5.45E+07	4.58E+07	7.08E+07	3.11E+07
(−35.91,−35.91)	3.57E+07	4.12E+07	4.84E+07	3.45E+07	5.29E+07	4.72E+07	6.79E+07	3.05E+07
Neutron Pad								
(−58.54,−22.47)	6.09E+06	7.47E+06	9.27E+06	5.80E+06	1.03E+07	8.94E+06	1.39E+07	5.67E+06
(−46.60,−41.95)	4.29E+06	5.12E+06	6.29E+06	4.10E+06	6.99E+06	6.58E+06	9.36E+06	3.86E+06

[a](x,y) in [cm, cm] coordinates with respect to core center.

difference of 7.1 % in the neutron pad region. For the ^{27}Al(n,α) detector, the differences become significantly larger, reaching ~14 %. The accuracy of the equivalent neutron fluxes using the ^{27}Al(n,α) detector may strongly depend on the nuclear data and the methods/tools for calculating the fast neutron fluxes of more than 5 MeV. In the reflector region, the equivalent neutron fluxes by all the detectors tend to decrease with the distance from the fuel regions.

Figures 7 and 8 show the relative differences (%) of the JEFF-3.0 results from the ENDF/B-VI.8 results in the stainless steel zones and in the water zones, respectively. The calculated results using the JEFF-3.0 give a similar trend to the JENDL-3.3. For the ^{58}Ni(n,p) and ^{64}Zn(n,p) detectors, differences of

TABLE 2—*Equivalent fission fluxes at a 100 % power in the water zones.*

[Unit: neutrons/cm^2/sec]

Measurement Position[a]	^{58}Ni(n,p)	^{115}In(n,n')	^{103}Rh(n,n')	^{64}Zn(n,p)	^{237}Np(n,f)	^{27}Al(n,α)	Flux at E>0.1 MeV	Flux at E>1.0 MeV
Central Hole								
(00.00, 00.00)	1.05E+09	1.17E+09	1.33E+09	1.03E+09	1.47E+09	1.10E+09	1.85E+09	8.44E+08
Water Gap								
(−54.36,−9.59)	2.14E+07	2.31E+07	2.64E+07	2.08E+07	2.92E+07	2.96E+07	3.67E+07	1.67E+07
(−52.89,−15.80)	2.56E+07	2.92E+07	3.45E+07	2.48E+07	3.84E+07	3.28E+07	5.02E+07	2.14E+07
(−51.53,−19.78)	2.40E+07	2.76E+07	3.30E+07	2.32E+07	3.70E+07	3.14E+07	4.89E+07	2.03E+07
(−50.03,−23.33)	1.97E+07	2.30E+07	2.76E+07	1.90E+07	3.11E+07	2.54E+07	4.11E+07	1.69E+07
(−48.74,−25.91)	1.82E+07	2.13E+07	2.58E+07	1.76E+07	2.91E+07	2.35E+07	3.88E+07	1.58E+07
(−46.29,−30.06)	1.76E+07	2.01E+07	2.40E+07	1.71E+07	2.68E+07	2.40E+07	3.54E+07	1.48E+07
(−44.08,−33.22)	1.54E+07	1.73E+07	2.04E+07	1.49E+07	2.27E+07	2.14E+07	2.95E+07	1.27E+07
(−42.29,−35.48)	1.38E+07	1.46E+07	1.68E+07	1.34E+07	1.85E+07	2.07E+07	2.33E+07	1.06E+07
(−39.03,−39.03)	1.66E+07	1.78E+07	2.05E+07	1.61E+07	2.26E+07	2.47E+07	2.87E+07	1.29E+07
Reflector								
(−23.31,−23.31)	6.18E+08	7.17E+08	8.35E+08	6.03E+08	9.19E+08	6.11E+08	1.20E+09	5.21E+08
(−25.83,−25.83)	3.42E+08	3.69E+08	4.11E+08	3.36E+08	4.55E+08	3.81E+08	5.54E+08	2.63E+08
(−28.35,−28.35)	1.90E+08	1.95E+08	2.10E+08	1.87E+08	2.34E+08	2.30E+08	2.68E+08	1.37E+08
(−30.87,−30.87)	1.08E+08	1.07E+08	1.13E+08	1.07E+08	1.25E+08	1.43E+08	1.38E+08	7.42E+07
(−33.39,−33.39)	6.34E+07	6.28E+07	6.71E+07	6.24E+07	7.29E+07	8.81E+07	8.33E+07	4.40E+07

[a](x,y) in [cm,cm] coordinates with respect to core center.

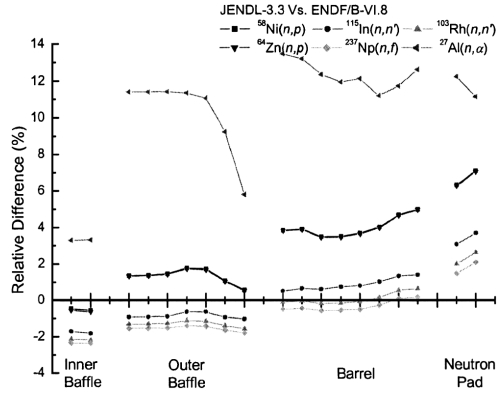

FIG. 5—*Relative differences of the JENDL-3.3 results from the ENDF/B-VI.8 results in the stainless steel zones.*

~0.5 % were maintained between the JEFF-3.0 and ENDF/B-VI.8 unlike the JENDL-3.3. Especially for the $^{27}Al(n,\alpha)$ detector, the differences were attenuated to an extent of less than 7.7 %.

Figure 9 shows the comparisons of the neutron fluxes at the threshold energies $E_{th} > 0.1$ MeV and $E_{th} > 1.0$ MeV. The fluxes at $E_{th} > 1.0$ MeV show a good agreement between the JENDL-3.3 and JEFF-3.0 in most regions. Also, the fluxes at $E_{th} > 0.1$ MeV agree well between them except in the water gap regions.

Summary

The 3-D VENUS-2 MOX-fueled reactor dosimetry calculation has been performed by the TRANSX/DANTSYS code system with the MATXS-format 199-group neutron libraries based on the ENDF/B-VI.8, JENDL-3.3, and JEFF-3.0. The JENDL-3.3 and JEFF-3.0 results show a similar tendency when compared with the ENDF/B-VI.8 results. The JENDL-3.3 provides the largest differences for the equivalent fission fluxes for the $^{27}Al(n,\alpha)$ detector when compared with the ENDF/B-VI.8. Also, the relatively large discrepancies of the neutron fluxes at threshold energies over 0.1 MeV between the JENDL-3.3 and JEFF-3.0 were shown in the water gap regions.

This benchmark exercise was performed as a "blind" test. Because the measured values are not yet open to the participants, a comparative analysis between the calculated and measured values could not be

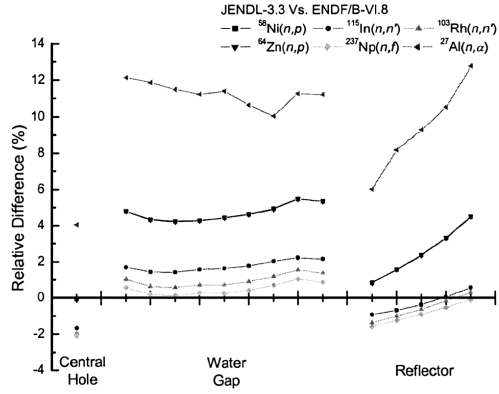

FIG. 6—*Relative differences of the JENDL-3.3 results from the ENDF/B-VI.8 results in the water zones.*

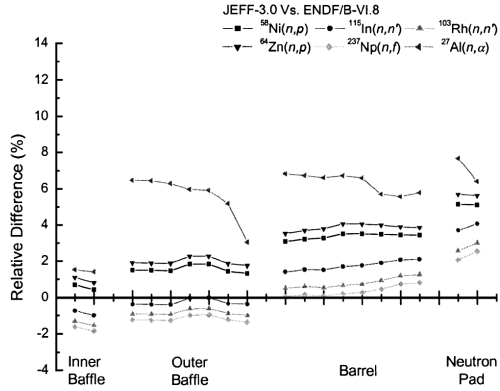

FIG. 7—*Relative differences of the JEFF-3.0 results from the ENDF/B-VI.8 results in the stainless steel zones.*

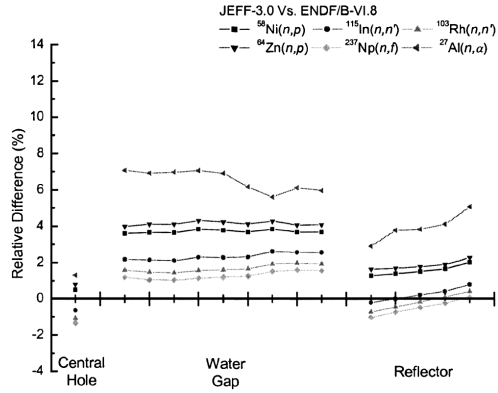

FIG. 8—*Relative differences of the JEFF-3.0 results from the ENDF/B-VI.8 results in the water zones.*

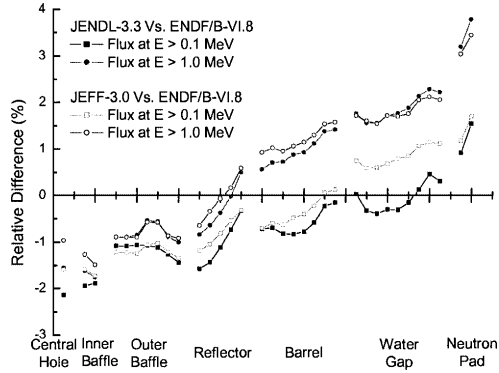

FIG. 9—*Comparisons of the neutron fluxes at the threshold energies $E_{th}>0.1$ MeV and $E_{th}>1.0$ MeV.*

completed. The analysis, ultimately, will become a part of the final report to be issued by the organizers of this exercise.

Acknowledgments

This project has been carried out under the Nuclear Research and Development program by Korea Ministry of Science and Technology.

References

[1] Na, B. C. and Sartori, E., "*Blind Benchmark on the VENUS-2 MOX Core Measurements*," NEA/SEN/NSC/WPPR(99)2, OECD/NEA, 1999.

[2] Na, B. C., "*Benchmark on the VENUS-2 MOX Core Measurements*," NEA/NSC/DOC(2000)7, OECD/NEA, 2000.

[3] Na, B. C. and Messaoudi, N., "*Blind Benchmark on the 3-D VENUS-2 MOX Core Measurements*," NEA/SEN/NSC/WPPR(2001)1, OECD/NEA, 2001.

[4] Na, B. C., "*Benchmark on the Three-dimensional VENUS-2 MOX Core Measurements*," NEA/NSC/DOC(2003)5, OECD/NEA, 2004.

[5] Han, C. Y., Shin, C.-H., Kim, H.-C., Kim, J. K., Messaoudi, N., and Na, B.-C., "*VENUS-2 MOX-Fueled Reactor Dosimetry Calculations: Benchmark Specification*," NEA/NSC/DOC(2004)6, OECD/NEA, 2004.

[6] MacFarlane, R. E., "*TRANSX 2: A Code for Interfacing MATXS Cross-Section Libraries to Nuclear Transport Codes*," LA-12312-MS, Los Alamos National Laboratory, 1992.

[7] Alcouffe, R. E., Baker, R. S., Brinkley, F. W., Marr, D. R., O'Dell, R. D., and Walters, W. F., "*DANTSYS: A Diffusion Accelerated Neutral Particle Transport Code System*," LA-12969-M, Los Alamos National Laboratory, 1995.

[8] ORNL, "*BUGLE-96: Coupled 47 Neutron, 20 Gamma-ray Group Cross Section Library Derived from ENDF/B-VI for LWR Shielding and Pressure Vessel Dosimetry Applications*," DLC-185, RSIC Data Library Collection, Radiation Shielding Information Center, 1996.

[9] MacFarlane, R. E. and Muir, D. W., "*The NJOY Nuclear Data Processing System, Version 91*," LA-12740-M, Los Alamos National Laboratory, 1994.

[10] Kocherov, N. P. and McLaughlin, P. K., "*The International Reactor Dosimetry File (IRDF-90 Version 2)*," IAEA-NDS-141 (Rev. 4), IAEA, 1999.

[11] Kim, D. H., Gil, C.-S., Kim, J.-D., and Chang, J., "*Comparisons of the MCNP Criticality Benchmark Suite with ENDF/B-VI.8, JENDL-3.3, and JEFF-3.0*," ICNC2003: The Seventh International Conference on Nuclear Criticality Safety, p. 304, Tokai, Ibaraki, Japan, 2003.

Journal of ASTM International, Vol. 3, No. 3
Paper ID JAI13481
Available online at www.astm.org

B. Ošmera,[1] *M. Mařík,*[1] *F. Cvachovec,*[2] *V. Tsofin,*[3] *S. Lomakin,*[4] *S. Zaritsky,*[5] *A. Egorov,*[5] *and E. Brodkin*[5]

Experimental and Calculation Investigations of the Space-Energy Neutron and Photon Distribution in the Vicinity of Reactor Pressure Vessel and Surveillance Specimen Box of New Type in the WWER-1000 Mock-Up

ABSTRACT: The radiation field parameters in the vicinity of new type of WWER-1000 surveillance specimens boxes and in RPV simulator have been investigated in the WWER-1000 Mock-up in the reactor LR-0. The neutron and photon spectra have been measured with stilbene cylindrical crystals in the energy range approximately from 0.5 MeV to 10 MeV. The experimental values of integral neutron field parameters (attenuations of integral neutron flux densities between different points of mock-up as well as the spectral indices, i.e., ratios of integral neutron flux densities with different thresholds) were obtained also. The mock-up (LR-0 reactor) power monitoring during measurements was carried out with two fission chambers, one fixed, one moveable axially, so that four orders in power were covered. The experimental data (spectra, attenuation factors, and spectral indices) have been compared with the calculation results. The sensitivity to parameters of calculation model and method was evaluated also.

KEYWORDS: space-energy neutron distribution, photon distribution, reactor pressure vessel, surveillance specimens, WWER-1000 mock-up, LR-0 research reactor

Introduction

Modern WWER-1000 units (Kalinin 3, Temelin 1 and 2, and constructed NPPs in Tianwan, China and Kundankulam, India) are equipped with new type of surveillance specimens boxes (SSB), which look like at containers and are located close to the inner surface of the reactor pressure vessel (RPV). The experimental and calculation investigations were performed in the WWER-1000 mock-up assembled in the LR-0 reactor in order to support the dosimetry of this new type SSB. It was the same mock-up which was used earlier in experiments for a dosimetry of WWER-1000 RPV without SSB [1], Fig. 1. The model of the new SSB was positioned on the inner surface of the LR-0 tank (i.e., close to inner surface of the RPV model, which is located just out of the LR-0 tank) at the symmetry axis of the mock-up (Figs. 2 and 3).

The measurement before the SSB was performed in the displacer tted closely to SSB, positioned at the LR-0 tank. The measurements at the barrel, inside the LR-0 tank were performed in the displacer xed to the barrel. Outside the LR-0 tank the measurements over the RPV simulator thickness were performed with the step 5 cm. The RPV simulator consists of four 5-cm thick segments which can be radially shifted to create an air layer for the detector.

The experimental data were compared with 3D TORT and synthesis calculations with BUGLE96 cross sections library.

Manuscript received June 20, 2005; accepted for publication September 29, 2005; published online December 2005. Presented at ASTM Symposium on Reactor Dosimetry, 12th International Symposium on 8 13 May 2005 in Gatlinburg, TN; D. W. Vehar, D. M. Gilliam, and J. M. Adams, Guest Editors.

[1] Chief Scientist, Senior Engineer, respectively, Nuclear Research Institute Ře plc, 250 68 Ře , Czech Republic.
[2] Professor, University of Defence, 61200 Brno, Czech Republic.
[3] Head of Bureau, EDO GIDROPRESS, 142103 Podolsk, Moscow Region, Russia.
[4] Senior Staff Scientist, SEC of GOSATOMNADZOR, 107140 Moscow, Russia.
[5] Head of Department, Senior Staff Scientist, Senior Staff Scientist, respectively, Russian Research Center Kurchatov Institute, 123182 Moscow, Russia.

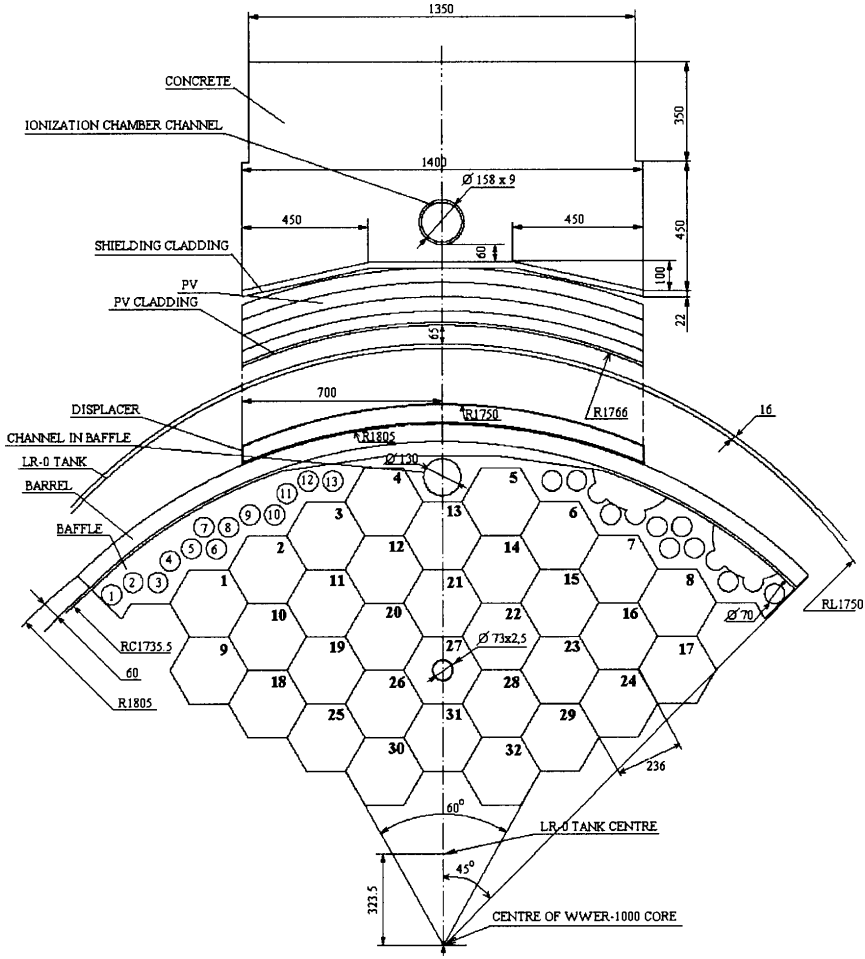

FIG. 1 *The scheme of the WWER-1000 mock-up. The left side corresponds to the plane at z = 122 cm, the right side corresponds to the plane at z = 85 cm (z = 0 at the bottom edge of fuel). R—curvature radius, RL—radius with respect to the LR-0 tank center, RC—radius with respect to the center of WWER-1000 core.*

Experimental Results and Comparison with Calculations

The photon and neutron spectra measurements were carried out with two-parameters spectrometer [2] with stilbene scintilator crystals (cylinders 10×10, 20×20, and 45×45 mm). The 45×45 mm crystal enables simultaneous measurement of photon and neutron spectra in the energy range 0.5 (1.0) MeV 10.0 MeV approximately. All measurements were absolute (absolute neutron and gamma ux densities per monitor unit), the monitoring system covered four orders in relative power. The measurements were performed in the benchmark without (out of mock-up, Fig. 1) surveillance box simulator (at the barrel, before, behind RPV, and over the RPV simulator thickness $\frac{1}{4}$, $\frac{1}{2}$, $\frac{3}{4}$, consisting of four 5-cm thick segments).

In the benchmark with SSB (Fig. 2) simulator the measurements were performed at the barrel, before the SSB, before RPV, and in $\frac{1}{4}$ of RPV simulator.

The spectra were evaluated in ne linearly equidistant (0.1 MeV) energy grid and in the BUGLE format including uncertainties.

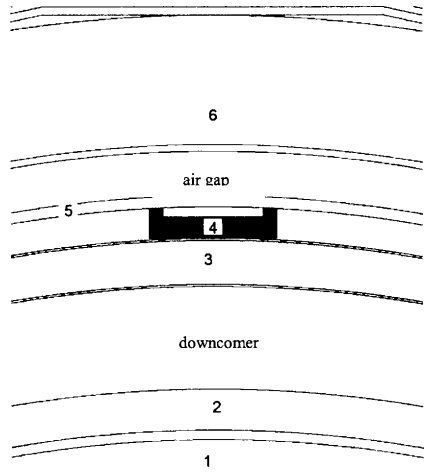

FIG. 2 *Arrangement of the surveillance specimen box simulator in the benchmark–central plane. 1—baffle, 2—barrel, 3—displacer, 4—SSB simulator, 5—LR-0 tank, 6—RPV simulator.*

Additional measurements were performed with Track detector [3] before RPV and in $\frac{1}{4}$ of RPV in the benchmark with SSB model.

Besides the spectra several space and space-energy indices were evaluated too, the data are based on the measured spectra. These integral data are listed below in Tables 1 3 and compared with calculations performed in RRC Kurchatov Institute.

Three-dimensional calculations were performed in P_3S_8 approximation of discrete ordinates method by synthesis method using codes DORT and ANISN and directly using code TORT. Cross sections library BUGLE-96 was used in both cases. The sensitivity to the space grid parameters were studied comparing the spectra calculated with different grids.

The space grid with 345 steps in θ (30 sector) 150 in R (radius) and 25 in Z (axial, one half of mock-up height) was found as optimum, close to asymptotic case (these calculations are labeled as SYNT 1). The SYNT 2 calculations were done using $189 \times 100 \times 25$ grid. The same grid was used in TORT calculations.

In Table 1 the attenuation factors (ratios of integral uxes above given energy in de ned measuring positions) measured in the benchmark with SSB are compared with calculations. The results of SYNT and TORT calculations are very closed comparing them with the experimental uncertainties. A similar situation is in comparison to measured and calculated spectral indices (SI, ratios of integral uxes above 0.5 and 1.0 MeV to uxes above 3 MeV in given spectrum) in Table 2. The gamma calculations are still in the process of evaluation, so that the data in Table 3 are not compared with the calculation.

Due to some technical troubles the reference (xed) monitoring chamber was positioned in two different points in two measurements with and without SSB.

By means of the absolute measurements with stilbene spectrometer at the barrel, before and behind RPV the measured values were reevaluated to one (relative) power so that the absolute measurements with

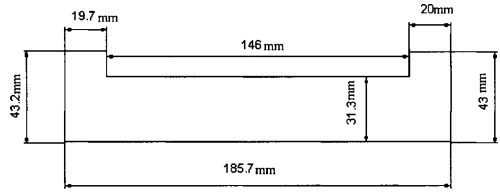

FIG. 3 *Surveillance specimen box simulator. The axial length is 600 mm.*

TABLE 1 *Comparison of calculated and measured attenuation factors (AF) in the mock-up with SSB.*

		AF			
E, MeV		2/24	24/3	2/3	3/4
3.01	Exp.	8.54	2.38	20.3	2.34
	±σ, %	4.6	7.4	6.0	12.3
	SYNT1	8.61	2.50	21.5	2.34
	SYNT2	8.52			
	TORT	8.53	2.45	20.9	2.35
	SYNT1/Exp.	1.008	1.050	1.059	1.000
	SYNT2/Exp.	0.997			
	TORT/Exp.	0.999	1.029	1.030	1.004
1.00	Exp.	17.8	1.83	32.5	2.16
	±σ, %	7.5	8.8	4.9	9.2
	SYNT1	17.2	2.06	35.4	1.82
	SYNT2	16.8			
	TORT	16.7	2.03	33.8	1.83
	SYNT1/Exp.	0.964	1.125	1.089	0.843
	SYNT2/Exp.	0.943			
	TORT/Exp.	0.936	1.109	1.040	0.847
0.498	Exp.	26.2	1.64	42.8	2.04
	±σ, %	6.9	7.9	5.3	10.9
	SYNT1	24.9	1.82	45.3	1.49
	SYNT2	24.2			
	TORT	23.9	1.79	42.9	1.49
	SYNT1/Exp.	0.949	1.110	1.058	0.730
	SYNT2/Exp.	0.923			
	TORT/Exp.	0.913	1.091	1.002	0.730

Point 2 at the barrel, Point 24 before SSB, Point 3 before RPV, Point 4 1/4 of RPV, E energy in MeV.

TABLE 2 *Comparison of calculated and measured spectral indices (SI) in the mock-up with SSB.*

		Point		
SI		24	3	4
0.5/3.0	Exp.	4.58	6.65	7.64
	±σ, %	7.8	7.5	14.6
	SYNT1	4.51	6.18	9.68
	SYNT2	4.55	9.69	
	TORT	4.63	6.33	9.96
	SYNT1/Exp.	0.984	0.929	1.267
	SYNT2/Exp.	0.993	1.268	
	TORT/Exp.	1.011	0.952	1.304
1.0/3.0	Exp.	3.17	4.12	4.47
	±σ, %	8.6	7.5	13.4
	SYNT1	3.24	3.94	5.05
	SYNT2	3.27	5.06	
	TORT	3.30	3.98	5.12
	SYNT1/Exp.	1.023	0.956	1.130
	SYNT2/Exp.	1.030	1.132	
	TORT/Exp.	1.041	0.966	1.145

TABLE 3 *Ratio of integral gamma and neutron fluxes above 1 MeV in the mock-up with SSB.*

Point	$\phi(\gamma > 1$ MeV$)/\phi(n > 1$ MeV$)$	Relative Uncertainty, %
24	34.3	4
3	24.5	3
4	10.5	7

TABLE 4 *Comparison of measured integral data in Point 3—before RPV in the mock-ups with and without SSB.*

Point	Relative Integral Flux >1 MeV		SI 0.5/3.0		SI 1.0/3.0		Ratio of Gamma and Neutron Flux >1 MeV	
3 SSB	13.79		6.65		4.12		24.5	
		4.7 %		7.5 %		7.5 %		3 %
3	11.97		4.73		3.87		32.0	
		3.5 %		6.3 %		5.8 %		3.7 %

Relative integral uxes correspond to the same relative power level.

and without SSB can be compared. In Table 4 the integral data measured before RPV with and without SSB are compared. All spectra were measured several times and the results were averaged. The mean square deviation represents the uncertainties of type A.

Table 4 presents the increase of fast neutron ux density impinging on the RPV inner wall behind the surveillance specimen box.

Conclusions

The experiment and its analysis con rmed usefulness of the study of the radiation eld in the vicinity of the border of the environments with very different parameters like water and iron. The detailed WWER-1000 benchmarking without SSB were performed in the frame of the project REDOS, 5th FP of the EU, reported in Ref. [4].

The work was done under contract with EDO Gidropress; some speci c measurements and evaluations were performed in the frame of the grant MSM 2672244501 of the Czech Ministry of Education, Youth and Sports.

References

[1] WWER-1000 Mock-up Experiment in the LR-0 Reactor, *Mock-up Description and Experimental Data*, REDOS/R(01)/December 2002/Issue 01 (restricted distribution).

[2] Bure , Z., Cvachovec, J., Cvachovec, F., Celeda, P., and O mera, B., Multiparameter Multichannel Analyzer System for Characterization of Mixed Neutron Gamma Field in the Experimental Reactor LR-0, *Proceedings of the 11th International Symposium on Reactor Dosimetry*, Brussels, August 2002.

[3] O mera, B., Po ta, S., Karpunin, N. I., and Lomakin, S. S., Track Detector Measurements in RPV of WWER-1000 Mock-up in the LR-0 Reactor, *Proceedings of the 12th International Symposium on Reactor Dosimetry*, USA, May 2005.

[4] O mera, B., Boehmer, B., Ballesteros, A., Konheiser, J., Kyncl, J., Hordosy, G., Kereszt ri, A., Belousov, S., Ilieva, K., Kirilova, D., Mitev, M., Smutn , V., Polke, E., Zaritsky, S., Tšre, C., and Ortego, P., Accurate Determination and Benchmarking of Radiation Field Parameters, Relevant for Pressure Vessel Monitoring. A Review of Some REDOS Project Results, *Proceedings of the 12th International Symposium on Reactor Dosimetry*, USA, May 2005.

Journal of ASTM International, Vol. 3, No. 7
Paper ID JAI13482
Available online at www.astm.org

Igor Remec,[1] *Thomas M. Rosseel,*[2] *Edward D. Blakeman,*[1] *Charles A. Baldwin,*[1] *Dennis W. Heatherly,*[1] *and Kenneth R. Thoms*[3]

Characterization of the Neutron Field in the HSSI Reusable Irradiation Facility at the Ford Nuclear Reactor

ABSTRACT: The characterization of the neutron environment in a reusable facility for irradiation of metallurgical specimens, located at the Ford Nuclear reactor in Michigan, was performed with a combination of transport calculations, extensive dosimeter measurements, and neutron spectrum adjustment. The average difference between the calculated and "measured" reaction rates was ~7 % (the calculations underpredicted the measurements), and the average absolute difference was ~10 %. Therefore, the calculations and measurements agreed very well. The flexible facility performed excellently during several years of operation but was discontinued when the Ford reactor ceased operation. The heavy-section steel irradiation (HSSI) program is taking the initial steps toward selecting a site for a new irradiation facility, similar to the one described here.

KEYWORDS: neutron irradiation, embrittlement, TORT, dosimetry

Introduction

The heavy-section steel irradiation (HSSI) program sponsored by the U.S. Nuclear Regulatory Commission (NRC) and conducted at the Oak Ridge National Laboratory (ORNL) traces its origins to the initiation of the heavy-section steel technology program in 1967. In 1989 the HSSI program evolved into a distinct effort dedicated to the studies of irradiation effects in steel. The HSSI program objectives are to develop a more thorough and quantitative assessment of the effects of neutron irradiation on the fracture toughness of typical reactor pressure vessel (RPV) materials, to develop data to reduce uncertainties in embrittlement predictions for RPV life extensions, and to incorporate insights gained by the systematic assessment of margins into codes and standards applicable to resolving major regulatory issues that involve irradiation embrittlement. The ongoing projects include studies of (1) the fracture toughness transition and Master Curve methodology with an emphasis on curve shift and shape for highly embrittled materials, (2) irradiation effects on high-nickel welds and high-copper, low-upper-shelf welds, (3) the effects of dynamic testing, intergranular fracture, and subsize specimens on fracture toughness and an evaluation of the bias term, (4) the irradiation embrittlement of the heat-affected zone, (5) the validation of the assessment of irradiated and aged materials, and (6) the microstructural basis for radiation-induced damage using microcharacterization methods, modeling, and database analysis. The results of the HSSI program provided a basis for many U.S. regulations, such as ASTM Standards for Fracture-Toughness Testing, Surveillance Monitoring and Radiation Embrittlement Prediction; PTS Rule Reevaluation, Resolution of Generic Issue 15 (Radiation Effects on RPV Supports), as well as data for NRC Reg. Guide 1.99.

Throughout its existence, the HSSI program has performed irradiation of steel samples at several test reactors using different irradiation facilities. The latest facility was operated at the University of Michigan's Ford Nuclear Reactor (FNR) in Ann Arbor, Michigan. This paper will briefly describe that facility and focus on the neutron characterization.

Manuscript received June 20, 2005; accepted for publication April 19, 2006; published online May 2006. Presented at ASTM Symposium on Reactor Dosimetry, 12th International Symposium on 8–13 May 2005 in Gatlinburg, TN; D. W. Vehar, D. M. Gilliam, and J. M. Adams, Guest Editors.

[1] S&T Staff Member, Oak Ridge National Laboratory, Oak Ridge, TN, 37831.
[2] Manager, Heavy-Section Steel Irradiation (HSSI) Program, Oak Ridge National Laboratory, Oak Ridge, TN, 37831.
[3] Subcontractor, Oak Ridge National Laboratory, Oak Ridge, TN, 37831.

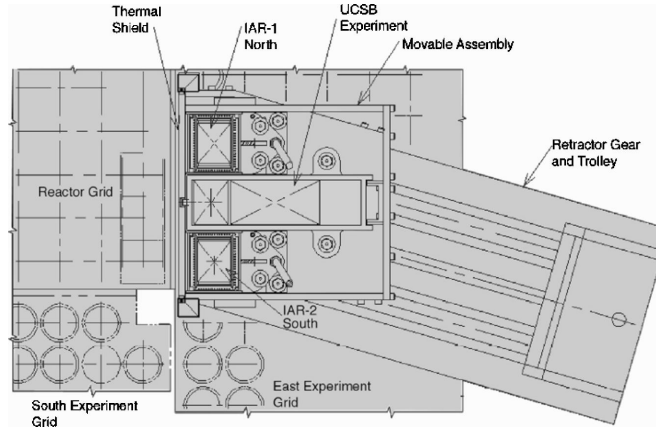

FIG. 1—*Horizontal (XY) cross section of the HSSI irradiation facility at the FNR.*

HSSI Reusable Irradiation Facility

The HSSI Reusable Irradiation Facility (RIF) consisted of low- and high-flux irradiation capsules used primarily by the University of California in Santa Barbara (UCSB) and two HSSI program capsules. The capsules were designed to quickly and easily permit the removal and exchange of metallurgical specimens. A variety of specimens could be accommodated such as 1T, Charpy V-notch, full-size tensile, and smaller specimens. A detailed description of the facility can be found in Ref. [1].

The horizontal cross section of the facility is shown in Fig. 1. The facility was located adjacent to the southeast side of the reactor core. The central part of the facility was occupied by the UCSB capsules. Closer to the core was the "high-flux" UCSB capsule, followed in the direction away from the core by the "low-flux" UCSB capsule. On each side of the UCSB capsules was an HSSI capsule—the "North" and "South" HSSI capsule, respectively. The dimensions of the specimen compartments in the x and y directions were approximately 5.2 cm $\times$ 2.6 cm in the high-flux UCSB capsule, 5.2 cm $\times$ 12.8 cm in the low-flux UCSB capsule, and 7.6 cm $\times$ 6.1 cm in each of the HSSI capsules.

Characterization of the Facility

Since the capsules were reusable, the dosimetry measurements for the characterization of the facility were performed with the actual capsules. It was not necessary to use special "dummy" capsules as was done in previous HSSI irradiation experiments. The characterization of the neutron field in the facility was performed using the state-of-the-art methodology, which consisted of irradiation of neutron dosimeters inside the capsules, the calculation of the neutron field with neutron transport theory, and least-squares adjustment of the calculated multigroup neutron spectra and measured reaction rates to determine the best-estimate neutron-exposure parameters. For ease of use, the exposure-parameter distributions were fitted with three-dimensional analytical functions. Details on the neutronic characterization of the facility are given in Ref. [2].

Neutron Dosimetry Measurements

Neutron dosimeters, used for the characterization of the facility were irradiated in three experiments: the UCSB capsule dosimetry experiment (102 measurements); the HSSI (north and south) capsule dosimetry experiment (134 activities measured), and the CVN packet experiment irradiated at the top of the high-flux UCSB capsule (10 measurements).

The neutron dosimeters consisted of Fe, Ni, and Co "gradient wires" (the Co dosimeter was actually Co/Al alloy with 0.100 wt % Co), which were irradiated bare, and fission radiometric dosimeter sets (FRDs). After irradiation the wires were cut in several pieces and the activity of each piece was measured

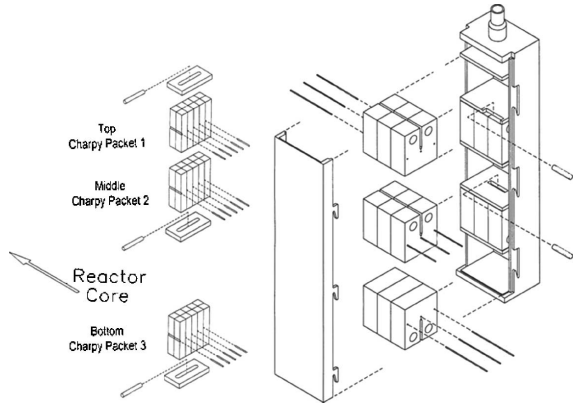

FIG. 2—*Locations of dosimeter wires and FRDs in the Charpy V-notch samples irradiated in the UCSB high-flux capsule (left) and in the HSSI capsule (right).*

separately, providing information about the change in neutron field along the wire. The gradient wires usually extended throughout the specimens compartment from one side to the other or from the front to the back.

A standard FRD contained Co, Fe, Ni, Ti, Cu, NpO_2, and UO_2 wires. The NpO_2, and UO_2 wires were encapsulated in vanadium. The dosimeter wires were packed in a gadolinium vial with a ~0.89-mm (0.035-in.)-thick wall. The gadolinium vial was put in a stainless steel tube, with an outer diameter of 0.58 cm (0.23 in.) and a wall thickness of ~0.038 cm. After the irradiation, the FRDs were opened and the activity of each dosimeter was measured separately.

The arrangement of gradient wires and FRDs in the HSSI capsule is shown in Fig. 2. Both North and South capsules used an identical arrangement. The FRDs were placed in holes machined in the capsule spacer plates. All gradient wires in the HSSI capsules were Fe wires. Since dummy metallurgical specimens were used for the neutronic characterization, gradient wires were placed in holes drilled through the specimens. The capsules were not rotated during the irradiation. After the irradiation, the gradient wires were cut in five pieces each and the activity of each piece was measured separately.

The arrangement of dosimeters in the Charpy packets, which were irradiated in the high-flux UCSB capsule, is also shown in Fig. 2. Here the gradient wires were located in the aligned notches of the Charpy specimens. This was not only convenient but also very effective, because the measurement was performed in the immediate vicinity of the point of interest in the Charpy specimen. The arrangement of Fe and Co wires is shown in Fig. 2. The Charpy packets were rotated during the irradiation; consequently these gradient wires were not sectioned but rather measured as a whole.

In the low-flux UCSB capsule the dosimeters were put inside dummy steel blocks within drilled holes. The locations not used for dosimeters were filled with aluminum, so that ~50 % of the volume of the "dummy" block was filled with aluminum and ~50 % with steel. The dummy blocks with Ni, Fe, and Co dosimeters were placed in 16 compartments of the UCSB capsules. In addition, four dummy blocks with FRDs were placed inside the UCSB capsules and three FRDs were placed in the spacer plates adjacent to the Charpy packets in the high-flux UCSB capsule.

Neutron Transport Calculations

Portions of the RIF capsules extend above the top of the active fuel (top of the UCSB high-flux capsule) and slightly to the south of the southeast corner of the reactor core (the South HSSI capsule; see Fig. 1). In such regions, the neutron flux changes quickly with all three spatial coordinates and it is more challenging to determine its spatial distribution. Approximate methods of calculation—like flux synthesis, which was used in the analyses of previous HSSI experiments—are not reliable in such regions and explicit three-dimensional transport calculations are preferred. Other circumstances that favor the three-

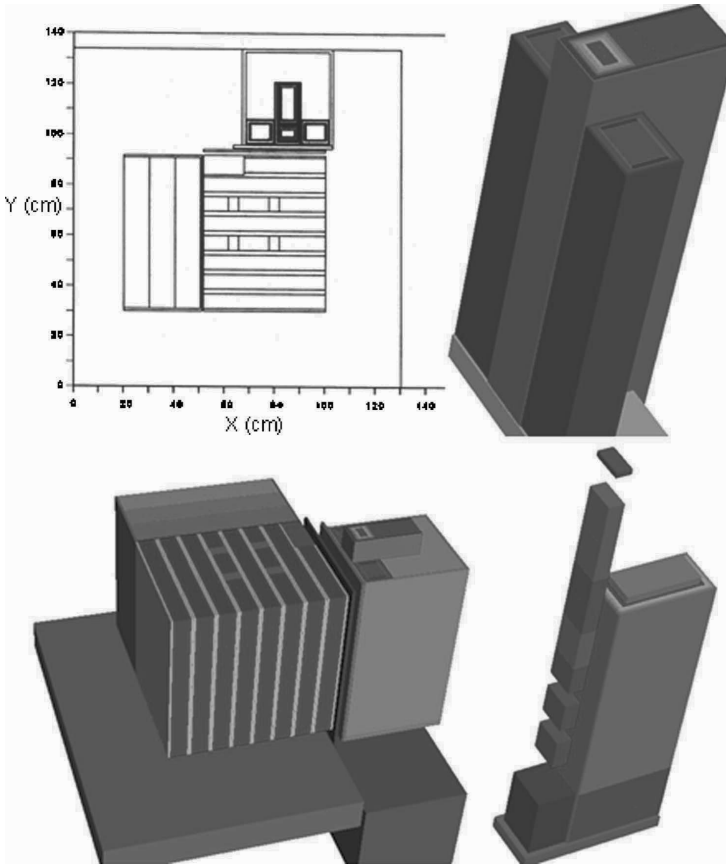

FIG. 3—*TORT model, clockwise from the upper left corner: horizontal cross section of the model, HSSI and UCSB capsules, and UCSB capsule with the cover removed from the front part, and three-dimensional view of the reactor core and HSSI Reusable Irradiation Facility.*

dimensional calculations are the presence of void regions in the capsules and differences in thickness between the HSSI and UCSB capsules; the UCSB low-flux capsule extends much further away from the side of the core than the HSSI capsules (see Fig. 1). An analysis of this geometry with the synthesis method would require several models for different parts of the facility. It was therefore concluded that performing the neutron transport calculations with the three-dimensional TORT code [3] should result in an analysis with higher efficiency and greater accuracy.

The geometry model for the TORT calculation is shown in Fig. 3. The water pool in which the reactor core and irradiation facility were submerged was included in the calculations but is not shown on the picture. The TORT model was built using Cartesian *XYZ* geometry. The reactor and UCSB/HSSI capsules were modeled as two separate sections of the model, using the TORT discontinuous mesh option. The horizontal cross section of the model was described with 10 808 geometric cells, and in the vertical direction 50 planes were used, so a total of 540 400 space cells were used. The cells formed 217 rectangular "bodies" and 53 material zones. The calculation was performed in 47 neutron energy groups. The cross sections were taken from the modified SAILOR library.[4] The P_3 approximation to the angular

[4]The modified SAILOR library was prepared by H. M. Manohara and M. L. Williams, Louisiana State University, Nuclear Science Center; personal communication to I. Remec, ORNL, 1994.

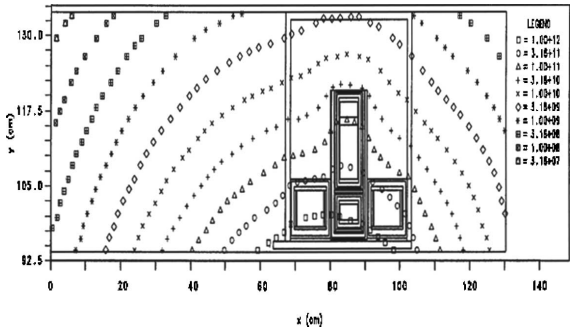

FIG. 4—*The horizontal cross section of the facility, with superimposed isoflux contours of the fast flux ($E > 1$ MeV; $cm^{-2}\,s^{-1}$).*

dependence of the anisotropic scattering cross sections (i.e., the P_0 to P_3 Legendre components) was applied, and a S_{10} "directional quadrature set" was used. The calculation was performed as a fixed neutron source calculation. The fixed neutron source for the TORT calculation was prepared from the core power distributions for three core cycles of the Ford reactor.[5]

The transport calculation provided multigroup neutron fluxes at the center of each space cell of the model; interpolation was used when the locations at which the fluxes were required did not coincide with the centers of the model cells.

The results of the transport calculations are illustrated in Figs. 4 and 5. Figure 4 shows the horizontal cross section of the irradiation facility with superimposed isoflux contours of the fast flux ($E > 1$ MeV). Figure 5 shows the closeup of the irradiation facility from Fig. 4. The figures show that the flux distribution is not symmetric across the irradiation facility's symmetry plane perpendicular to the core side. This is, of course, caused by the asymmetric placement of the irradiation facility adjacent to the corner of the core. More interestingly, the figures also show a strong perturbation in the fast-flux distribution in the water pool, caused by the steel capsules. The isoflux contours, which resemble concentric arcs in the water pool far away from the capsules, change shape in the vicinity of the capsules. Inside and around the capsules higher fast flux values are found further away from the core than in the water. This is caused

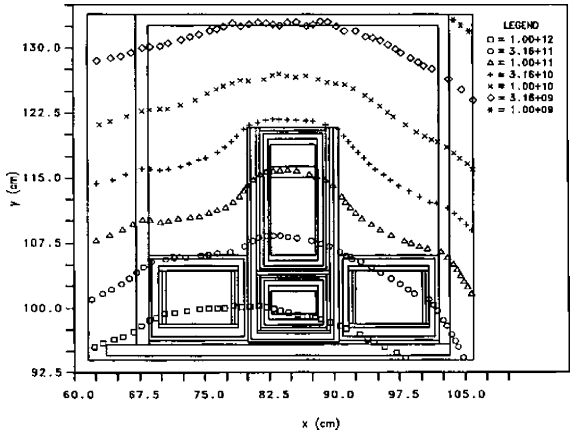

FIG. 5—*The closeup of the horizontal cross section of the irradiation facility, with superimposed isoflux contours of the fast flux ($E > 1$ MeV; $cm^{-2}\,s^{-1}$).*

[5]The core power distributions were calculated by J. C. Lee, University of Michigan; personal communication to I. Remec, ORNL, 1998.

TABLE 1—*The ranges of fast neutron fluxes and dpa rates at the HSSI RIF.*

HSSI RIF Capsule	Fast neutron flux ($E>1$ MeV) ($cm^{-2}\,s^{-1}$)		dpa rate in Iron (s^{-1})	
	Minimum	Maximum	Minimum	Maximum
HSSI/UCSB low flux	6.07×10^{10}	3.85×10^{11}	9.67×10^{-11}	5.93×10^{-10}
HSSI/UCSB high flux	1.51×10^{11}	9.83×10^{11}	2.16×10^{-10}	1.45×10^{-9}
HSSI-South	3.93×10^{11}	4.81×10^{11}	5.90×10^{-10}	7.30×10^{-10}
HSSI-North	6.80×10^{11}	8.32×10^{11}	1.02×10^{-9}	1.25×10^{-9}

mainly by the differences in neutron scattering in the water and steel. The irregular shape of the fast flux distribution offers further support for the decision to perform the analysis with a three-dimensional transport calculation.

Comparison of the Calculations and the Measurements

To compare the calculations and measurements, the calculated multigroup fluxes were folded with reaction cross sections, taken from Ref. [4], to obtain calculated reaction rates. The impact of the gadolinium cover was approximately accounted for by reducing the multigroup cross sections by the flux attenuation factor derived from the thickness of the cover and the gadolinium total cross section at the corresponding energy.

The conversion of the measured specific activities to "measured" reaction rates was performed separately for each of the three experiments (i.e., UCSB and HSSI dosimetry experiments and Charpy packets) and the specific reactor power history for each of the experiments was taken into account. Since the top Charpy packet was removed before the middle packet, the conversion was actually performed separately for each of the two Charpy packets also. The Charpy packets were rotated during the irradiation to obtain a more even fluence distribution throughout the packets. This was accounted for in the conversion from specific activities to the reaction rates by using two sets of fluxes—one set for the original location of the dosimeters and the other set for the rotated positions. The conversion was done with the computer code ACT from the LSL-M2 code package [5].

The average difference between the calculated and measured reaction rates was ~7 % (the calculations underpredicted the measurements), and the average absolute difference was ~10 %. Therefore, the calculations and measurements agreed very well.

Neutron-Spectrum Adjustment and the Results of the Characterization

The least-squares neutron-spectrum adjustment calculations were performed with the computer code LSL-M2. The reaction rates obtained from all three experiments were applied simultaneously to adjust the calculated neutron fluxes. A total of 256 reaction rates at 129 locations was used. The adjusted neutron spectrum at each location and the best-estimate neutron exposure rates were determined at all locations of the dosimeters. The exposure parameters selected were the neutron fluence rates with energies greater than 1 MeV, 0.5 MeV, and 0.1 MeV, and the displacement per atom (dpa) rate in iron. For the dpa rate calculations, the cross sections from ASTM Standard E 693 [6] were folded with the group fluxes and summed.

These exposure parameters were determined for each dosimetry location. The ranges of the fast fluxes and dpa rates are listed in Table 1. Fast fluxes at selected locations are also shown in Fig. 6. On average (over all the locations of dosimeters), the adjustment increased the fast flux ($E>1$ MeV) by 5.7 %. The maximum increase of the fast flux at any location, due to adjustment, was about 20 %, and the maximum decrease was about 11 %.

The exposure parameters obtained from the adjustment runs were also fitted to three-dimensional analytical functions, so that values at any desired location inside the facility could be easily determined. In addition to the "global" fits for the entire facility, "local" fits for each of the HSSI capsules and high- and low-flux UCSB capsules were also calculated.

Uncertainties of the best-estimate exposure-parameter rates obtained from the adjustment calculations at the locations of the dosimeters were in the range of 2.9–to 5.7 % (1 sigma). When irradiation exposure

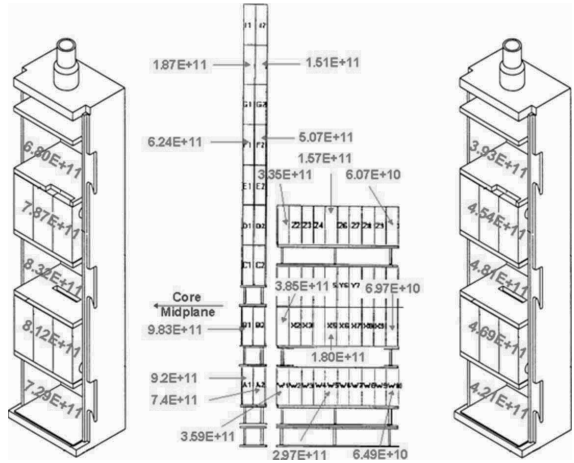

FIG. 6—*Fast neutron flux ($E > 1$ MeV; $cm^{-2}\,s^{-1}$) at center of compartments in North HSSI capsule (left), South HSSI capsule (right), and UCSB high- and low-flux capsules (middle); (not to scale).*

rates are calculated from analytical fitting functions, uncertainties arising from the fitting should be considered. These resulted in the total estimated uncertainty of ~7 % (1 sigma).

Conclusions: HSSI Reusable Irradiation Facility Experience and Future Plans

The neutron field in the HSSI RIF facility was thoroughly characterized with the three-dimensional neutron transport calculations, extensive dosimetry measurements, and the neutron spectrum adjustment calculations. The results of the transport calculations agreed well with the measurements. The neutron fluxes and dpa rates were accurately and reliably determined throughout the facility. The characterization method used was found very satisfactory.

The HSSI facility operated from March 1997 to July 3, 2003, when the Ford Nuclear Reactor was shut down. More than 20 000 effective full power hours of operation were accumulated, and various irradiation campaigns were completed in a well-characterized neutron field and with excellent temperature stability. The facility operated very reliably and exceeded expectations. The transport of capsules to the hot cell and the removal of metallurgical specimens (without any cutting or grinding) were executed smoothly, and the amount of radioactive waste was minimized since the capsules were reusable. Also, the amount of irradiated material shipped from the reactor site over public highways was minimized since only the specimens were transported.

Currently the HSSI program is not irradiating specimens; however, work is under way to establish a new capability. Information has been gathered about potential sites for a new facility, similar to the one discussed in this paper. Four reactors in North America and four in Europe are being considered. The HSSI staff and other experts visited several of these sites and gathered information for feasibility evaluations. Pending an agreement between the U.S. Nuclear Regulatory Commission and the Department of Energy for a Joint Irradiation Facility (JIF) to be used by the HSSI and Generation IV Materials program, a request for proposals for the operation of the new facility will be issued. It is anticipated that the dosimetry and temperature calibration studies will start about 9 to 12 months after the start of construction and that the new facility will be operational within 18 months after the NRC/DOE agreement is in place. The current plan calls for a minimum 5-year period of operation with an option for another 5 years at the discretion of the U.S. federal agencies.

References

[1] Heatherly, D. W., Thoms, K. R., Hurst, M. T., and Giles, G. E., "Heavy-Section Steel Irradiation Program's Reusable Irradiation Facilities," *ORNL/TM-2002/77*, Oak Ridge National Laboratory, Oak Ridge, Tenn., 2005.

[2] Remec, I., Baldwin, C. A., and Blakeman, E. D., "Characterization of the Neutron Field in the HSSI/UCSB Irradiation Facility at the Ford Nuclear Reactor," *ORNL/TM-1999/140*, Oak Ridge National Laboratory, Oak Ridge, Tenn., 2005.

[3] Rhoades, W. A. and Simpson, D. B., "The TORT Three-Dimensional Discrete Ordinates Neutron/Photon Transport Code (TORT Version 3)," *ORNL/TM-13221*, Oak Ridge National Laboratory, 1997.

[4] Remec, I., "An Update of the Dosimetry Cross-Section Data Base for the LSL-M2 Adjustment Code," *ORNL/TM-13409*, Oak Ridge National Laboratory, October 2004.

[5] Stallmann, F. W., "LSL-M2: A Computer Program for Least-Squares Logarithmic Adjustment of Neutron Spectra," *NUREG/CR-4349 (ORNL/TM-9933)*, Oak Ridge National Laboratory, 1986.

[6] ASTM Standard E 693, "Standard Practice for Characterizing Neutron Exposures in Ferritic Steels in Terms of Displacements Per Atom (DPA)," *Annual Book of ASTM Standards*, ASTM International, West Conshohocken, PA.

Journal of ASTM International, Vol. 3, No. 8
Paper ID JAI100355
Available online at www.astm.org

K. Russell DePriest[1]

Benchmark Experiments/Calculations of Neutron Environments in the Annular Core Research Reactor

ABSTRACT: Benchmark experiments using spherical test objects were performed in the central cavity of Sandia National Laboratories' Annular Core Research Reactor. The experiments were performed with 10.16 cm and 17.78 cm diameter aluminum (Al6061) and high-density polyethylene spheres that were essentially solid with cavities scrolled out along the equator to allow the insertion of activation foils and/or sulfur pellets. The neutron monitor foils were selected to cover a wide range of reaction energies. The reactor environments were modeled in detail using Monte Carlo N-Particle eXtended (MCNPX). The experimental results were compared to the Monte Carlo calculations of the reaction rates of each of the foils at various depths in the spheres produced by MCNPX. The comparison includes a complete treatment of the uncertainties.

KEYWORDS: ACRR, MCNPX, reactor benchmarks, neutron environments, reactor test facilities

Nomenclature

Abbreviations

SNL	=	Sandia National Laboratories
ACRR	=	Annular Core Research Reactor
HDPE	=	high-density polyethylene
MCNPX	=	Monte Carlo N-Particle eXtended
C/E	=	calculation to experiment
RML	=	Radiation Metrology Laboratory
RXNs	=	reactions
KCODE	=	k_{eff} calculation in MCNPX

Symbols

n	=	neutron
p	=	proton
γ	=	gamma ray (photon)
X	=	any exiting particle from nuclear reaction
MeV	=	1.602×10^{-13} joules
MJ	=	1.0×10^{6} joules
$\bar{\Phi}_V$	=	average particle flux in a volume
V	=	volume of cell
E	=	particle energy
t	=	time
$\Psi(\vec{r},\hat{\Omega},E,t)$	=	angular particle flux
$\vec{r}$	=	position vector
$\hat{\Omega}$	=	vector direction

Manuscript received June 20, 2005; accepted for publication May 18, 2006; published online June 2006. Presented at ASTM Symposium on Reactor Dosimetry, 12th International on 8–13 May 2005 in Gatlinburg, TN; D. W. Vehar, D. M. Gilliam, and J. M. Adams, Guest Editors.

[1] Ph.D., Senior Member Technical Staff, Applied Nuclear Technologies Department, Sandia National Laboratories, P.O. Box 5800, MS 1146, Albuquerque, NM 87185-1146.

$RXNs/cm^3$ = reaction density
C = constant scaling factor
$R(E)$ = energy-dependent response function
$\varphi(E)$ = energy-dependent particle fluence
λ = radioactive decay constant
N = atom density
ρ = mass density
$\sigma^2_{C/E}$ = statistical variance of C/E ratio
Δ = test statistic

Introduction

A series of benchmark experiments using spherical test objects were performed in the central cavity of Sandia National Laboratories' Annular Core Research Reactor (ACRR). The ACRR is a pool-type reactor that is equipped with a large 22.86 cm diameter dry central cavity suitable for fielding experimenter test objects. The ACRR facility also has the capability of inserting spectrum-modifying buckets into the dry cavity for tailoring the neutron/gamma environment that a test object will encounter. The experiments were performed with 10.16 cm and 17.78 cm diameter aluminum (Al6061) and high-density polyethylene (HDPE) spheres that were essentially solid with cavities scrolled out along the equator to allow the insertion of activation foils and/or sulfur pellets. The cavities in the spheres were configured such that there were no streaming paths for radiation or large void volumes. In addition to the foils located in the interior of the spheres, an external nickel (Ni) activation foil was attached to the equator on the exterior of each sphere. The external Ni foil provides normalization back to the free-field reactor spectrum characterization and allows comparison from one reactor operation to another. The neutron monitor foils were selected to cover a wide range of reaction energies. Table 1 shows the neutron monitors that were used in the irradiations. The effective energy response range found in Table 1 corresponds to approximately 90 % of the neutron energies found in the ACRR Central Cavity [1].

The irradiation environments were selected to provide a "clean" geometry for modeling the experiments. Additionally, the materials for the spheres were chosen to provide a baseline calculation (Al6061) and a stressing calculation (HDPE). The reactor environments were modeled in detail using Monte Carlo N-Particle eXtended (MCNPX) [2]. The MCNPX model includes the ability to move control rods to match the experiment positions so that the neutron flux profile within the reactor will be calculated more accurately [3].

This paper presents the results of benchmark experiments in the spherical test objects for ACRR irradiations of neutron monitors in 10.16 cm and 17.78 cm diameter spheres composed of Al6061 and HDPE. The experimental results are compared to the Monte Carlo calculations of the reaction rates of each of the foils at various depths in the spheres produced by MCNPX. The comparison between calculation and experiment includes a calculation-to-experiment (C/E) ratio and a complete treatment of the calculation uncertainties.

TABLE 1—*Neutron monitors used for benchmark experiments.*

Monitor reaction	Effective energy response range, MeV
$^{58}Ni(n,p)^{58}Co$	1.9–7.4
$^{32}S(n,p)^{32}P$	2.0–7.2
Cd-covered $^{197}Au(n,\gamma)^{198}Au$	5.4×10^{-7}–1.0
$^{45}Sc(n,\gamma)^{46}Sc$	6.3×10^{-9}–5.75×10^{-6}
Cd-covered $^{59}Co(n,\gamma)^{60}Co$	5.4×10^{-7}–1.35×10^{-4}
$^{nat}Ti(n,X)^{47}Sc$	1.6–7.5
$^{nat}Ti(n,X)^{48}Sc$	6.0–12.5

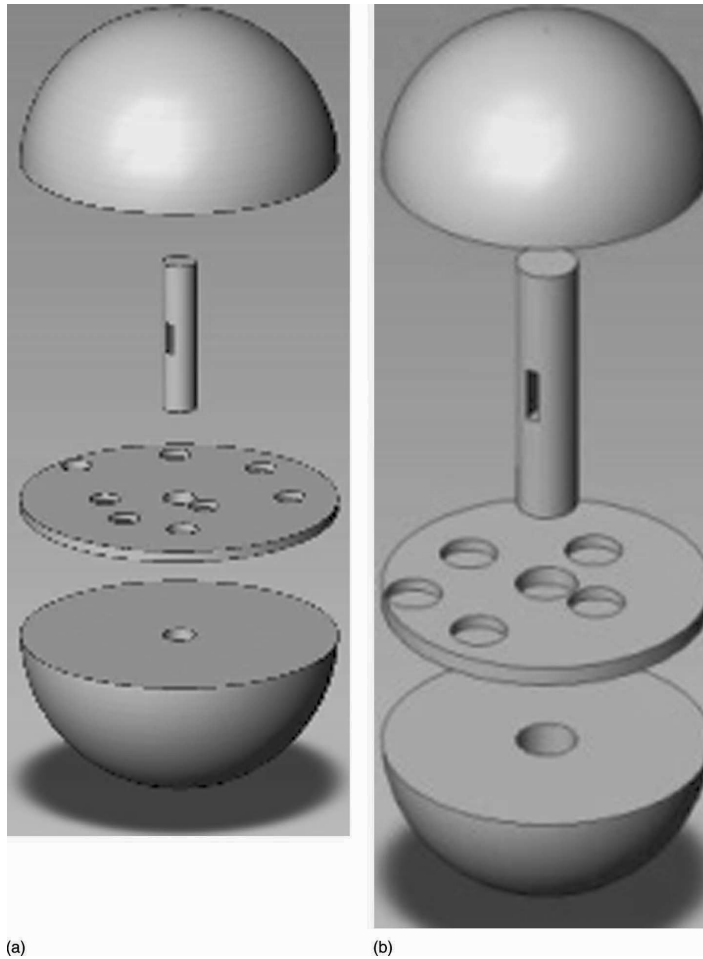

FIG. 1—*Schematics of Spheres: (a) 17.78 cm diameter; (b) 10.16 cm diameter.*

Experiment Description

The experiment spheres were disassembled into their four components (see Fig. 1 for schematics of the spheres). The four components of a sphere are a 0.6 cm thick center plate with a threaded hole in the center, two near-hemisphere portions (upper and lower) with threaded holes to match the center plate, and a slotted threaded central rod used to assemble the sphere. All the components are manufactured from the same material. An activation foil was inserted into the slot in the central threaded rod of each sphere and the rod was screwed into the lower hemisphere. This location is identified as Position 0, and the foil in this location is in a vertical orientation at the fuel centerline when the spheres are placed in the reactor. After inserting the center foil, the center plate of the sphere is screwed onto the lower portion of the sphere. Additional activation foils are then placed in the void regions of the center plate. These locations are identified as Positions 1–8 in the 17.78 cm spheres or Positions 1–5 in the 10.16 cm spheres (see Table 2). Finally, the top portion of the sphere was attached to the other components, and an activation foil was attached to the exterior of the sphere at the equator. In addition, a Sandia National Laboratories (SNL) custom Ni foil (0.0254 cm thickness) was attached to the exterior of the sphere at the equator. The location

TABLE 2—*Positions in 17.78 cm and 10.16 cm diameter spheres.*

Location	Radius from center of sphere (cm)	Angle from reference (deg)
	17.78 cm diameter spheres	
Position 1	1.9050	0
Position 2	4.1402	225
Position 3	4.5720	270
Position 4	5.1054	315
Position 5	6.1722	45
Position 6	6.7056	90
Position 7	7.2390	135
Position 8	7.8486	180
	10.16 cm diameter spheres	
Position 1	1.9050	0
Position 2	2.4384	90
Position 3	2.9718	180
Position 4	3.5052	270
Position 5	4.1402	225

of the external Ni foil is identified as Position 9 in the 17.78 cm sphere or Position 6 in the 10.16 cm sphere.

After assembly, a sphere was placed in an aluminum bucket used for dosimetry irradiations. The dosimetry bucket contains a centering mechanism with standoffs (see Fig. 2) that ensure that the activation foils are located at the fuel centerline (oriented horizontally). The dosimetry bucket was placed in the central cavity of the ACRR. The experiment package was then irradiated at 5 % steady state power for 40 MJ (irradiation time was approximately 5.5 min). The experiment package was removed from the reactor as soon as possible after the irradiation (usually within 20 min). The spheres were disassembled to remove the activation foils, and the foils were delivered to the SNL-Radiation Metrology Laboratory (RML) for assay. (For additional information on the experimental procedures see Ref. [4].)

Experimental Uncertainties

The experimental results that were obtained during the test series included uncertainties associated with the processing of the dosimetry foils. The RML performs multiple counts on each dosimetry foil using different detectors, so an uncertainty based on multiple measurements is provided. The RML also provides an additional uncertainty quantity based on the statistical nature of the measurement. These two uncertainties are added in quadrature to establish a total experimental uncertainty for each of the foils irradiated during the experiment series.

Calculation Description

A full model of the ACRR was used for the calculations [3]. The calculations were performed using a multiprocessor version of MCNPX VERSION 2.5E [2] in the "KCODE" mode. The standard tallies in MCNPX

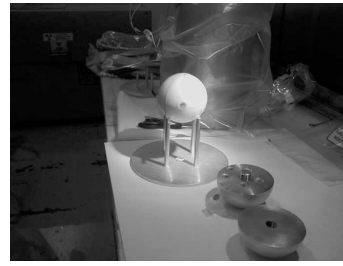

FIG. 2—*10.16 cm diameter spheres with standoff for dosimetry bucket.*

calculate the particle flux (particles/cm^2). The tallies that were used in these calculations correspond to a track length estimate of the cell (volume) flux. The track length estimate of the cell flux in physical terms is

$$\bar{\Phi}_V = \frac{1}{V}\int dE \int dt \int dV \int \Psi(\vec{r},\hat{\Omega},E,t)d\Omega \tag{1}$$

where $\bar{\Phi}_V$ is the average particle flux in a cell or volume (particles/cm^2), V is the volume (cm^3) of the cell, E is the particle energy (MeV), t is the time (sec), $\Psi(\vec{r},\hat{\Omega},E,t)$ is the angular flux (particles/cm^2/sec/MeV/steradian), $\vec{r}$ is the position vector, and $\hat{\Omega}$ is the vector direction.

However, foil activation calculations are not simple particle fluxes. The energy-dependent neutron flux must be used to calculate a reaction density (RXNs/cm^3) for the production of the activation products. MCNPX provides a relatively simple method of correctly calculating these reaction rates. The calculation performed by MCNPX is the equivalent of the following:

$$\text{RXNs/cm}^3 = C\int R(E)\varphi(E)dE \tag{2}$$

where C is a constant scaling factor (atoms/barn-cm), $R(E)$ is the energy-dependent response function (i.e., dosimetry cross section in barns/atom/particle/cm^2), and $\varphi(E)$ is the energy-dependent particle fluence (particles/cm^2). The experimental results are given in terms of specific activity (Bq/g) for all the activation foils except sulfur tablets. The activity (Bq) of a radioactive sample is given by the following equation:

$$\text{Activity} = \lambda N \tag{3}$$

where λ is the decay constant of the radioactive isotope (1/sec) and N is the atomic density of the radioactive isotope (atoms/cm^3). To compare to the experiment results, the following equation is used for the calculation results:

$$\text{Specific activity} = (\text{RXNs/cm}^3)(\lambda)\left(\frac{1}{\rho}\right)\left(\frac{\text{fissions}}{\text{MJ}}\right)\left(\frac{\text{neutrons}}{\text{fission}}\right)(\text{reactorMJ}) \tag{4}$$

where ρ is the mass density (g/cm^3) and the "reactor MJ" is the integrated reactor power from the ACRR.

Many Monte Carlo calculations use variation reduction techniques to reduce the number of histories required to achieve statistically significant results. In this series of calculations, only the default variance reduction technique in MCNPX (i.e., implicit capture) was used. Since variance reduction was not utilized, the calculations described above used 1×10^6 neutrons per cycle for 2002 cycles for a nominal total of 2×10^9 fission neutrons for each calculation. The first two cycles were used to establish the proper distribution of fission sites in the reactor model, so those cycles were not included in the neutron tally calculations.

Calculation Uncertainties

There are several components that factor into the overall calculation uncertainty associated with this experiment series. These uncertainties include the following: (1) the Monte Carlo statistical uncertainty; (2) the uncertainty in the experimental configuration and integrated reactor power; (3) the uncertainty in the nuclear data for the radiation transport and dosimetry reactions; and (4) uncertainties associated with the values used for the physical quantities.

Monte Carlo Statistical Uncertainty

The Monte Carlo calculations include a statistical uncertainty. The calculations have a statistical uncertainty for each reaction and position in the spheres. In general, the Monte Carlo statistical uncertainty is less than 5 %, but the actual value determined by the calculation is used in the uncertainty analysis.

Experiment Configuration

Geometry—The geometry of the experiment was established to provide benchmark data for both cross-sectional evaluations and radiation transport calculation. The geometry is well defined, so many of the issues that often make variance reduction difficult are not found in this experiment. Thus, the geometry and positioning uncertainties in the MCNPX calculations are quite low. Using SNL historical values for this uncertainty (derived from experimental experience), the uncertainty in the experiment configuration was assumed to be 3 % for all locations in the spheres.

Integrated Reactor Power—The integrated reactor power is typically reported in MJ. For "identical" reactor operations, the external Ni foil will vary because the reactor uses a different detector (i.e., other than a Ni foil) for its power diagnostic. This uncertainty must be considered in the total calculation uncertainty. This uncertainty was determined for all reactor configurations and spheres used in the test series.

Uncertainty in the Nuclear Data

Radiation Transport Cross Sections—When analyzing the uncertainty in the calculation of these reactions, the transport cross sections for the materials of interest should be a starting point. The transport cross sections are used when developing both the reactor and test object models. In these calculations, the large size of the reactor model and the use of KCODE mode of calculations minimize the effects of uncertainties in the transport cross sections of all the materials in the model. When comparing k_{eff} calculations (a metric for transport accuracy) to experimental measurements of delayed critical positions, the calculated k_{eff} values are generally within 1 % of the measurement (see [3]). Thus, 1 % will be used for the transport cross-sectional uncertainty. (Note: Intuition indicates that 1 % is too low for this uncertainty. However, it is not apparent at this time what metric provides a better means of estimating the uncertainty in the transport cross sections for a large system such as the ACRR.)

Dosimetry Cross Sections—The uncertainty in the dosimetry cross section is an element in the overall uncertainty in the nuclear data. Dosimetry cross section must include an estimate of the energy-dependent uncertainty associated with the reaction. If this is not included in the cross-sectional evaluation, the evaluation is generally discarded from use in neutron spectra unfolds, etc. A covariance matrix is the general form that is used for these energy-dependent cross-sectional uncertainties. To produce the integral uncertainties in the dosimetry cross sections for each of the ACRR operations, the neutron energy spectrum was folded with the covariance matrices.

Uncertainty in the Physical Quantities

Fission Energy Released—The amount of energy released per fission (MeV/fission) has an effect on the number of neutrons that are used for normalizing the calculated reaction rates. Typically, the energy released includes the energy from fission product decay. Since these calculations are not interested in the energy associated with the decay of fission products, the uncertainty in this quantity is greater. A value of 180 MeV/fission was used in the calculations, but values that range from 170 Mev/fission to 190 MeV/fission are reasonable. Therefore, an uncertainty of 5.57 % was used for this quantity.

Radioactive Half-life—The equation for calculating the activity of a radioactive material is shown above in Eq 3. The atom density (N) is calculated by MCNPX (this is the reaction rate for producing the dosimetry reaction), but λ is obtained by using the radioactive half-life in the *Nuclear Wallet Cards* [5]. The values for the half-life in the *Nuclear Wallet Cards* include the uncertainty.

Atom Fraction—The atom fraction of the "reacting" nucleus is used to produce the proper dosimetry reaction rate. This value is also found in the *Nuclear Wallet Cards* along with an uncertainty.

Overall Calculation Uncertainty

The overall calculation uncertainty is obtained by combining the individual uncertainties defined above taking into consideration the degree to which the individual uncertainties are correlated. The uncertainties

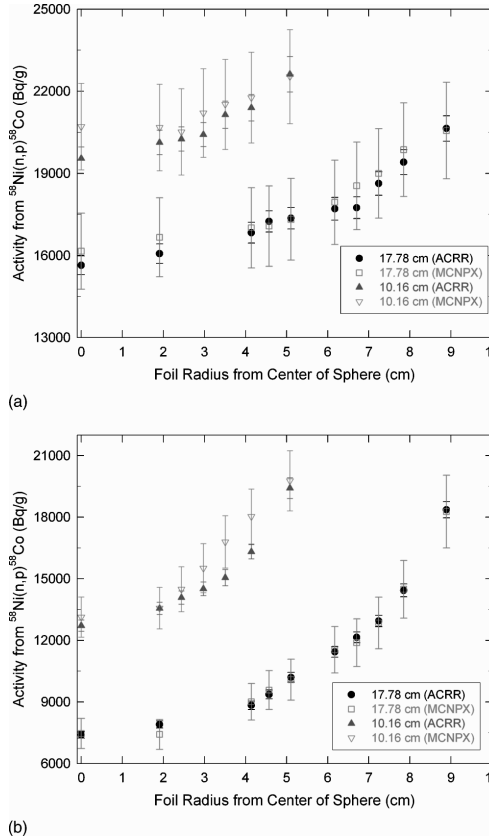

FIG. 3—*Ni Activity Comparison: (a) Al6061 spheres; (b) HDPE spheres.*

considered in this analysis are all assumed to be uncorrelated. Thus, the components of the uncertainty were added in quadrature to produce a total calculation uncertainty for each ACRR reactor configuration and foil location.

Results

There were 31 separate ACRR operations (central cavity neutron irradiations) in the test series. The amount of data associated with both the experiments and calculations makes it impossible to present the entire test series comparison in this paper. In an effort to provide a standard for future benchmark experiments and calculations in reactor environments, examples of the calculation to experiment comparisons performed and the statistical metrics used to assess the success/failure of the benchmark activity are presented in this paper. The full analysis of each of the ACRR operations can be found in DePriest [6].

Nickel (Ni) foils are often used at SNL as a monitor that gives experimenters the ability to perform ACRR power normalization. The reaction of interest for the Ni foils responds only to fast neutrons (neutrons with kinetic energies greater than 2 MeV, see Table 1). The comparisons of the raw experimental data for Ni activation with the MCNPX calculation of the same quantity are found in Fig. 3. Scandium (Sc) foils are often utilized as thermal neutron monitors because of their strong 1/v neutron absorbing behavior (see Table 1 for the effective neutron energy response of Sc foils). The comparisons of the raw experimental data for Sc activation with the MCNPX calculation of the same quantity are found in Fig. 4. In Figs. 3 and 4, the data from the two Al6061 spheres are found in Figs. 3(*a*) and 4(*a*) while the data from the two

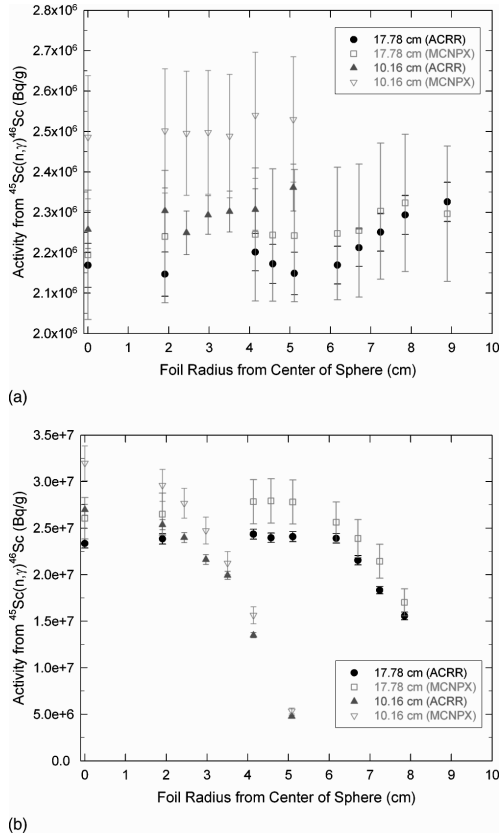

FIG. 4—*Sc Activity Comparison: (a) Al6061 spheres; (b) HDPE spheres.*

HDPE spheres are found in Figs. 3(*b*) and 4(*b*). The error bars seen in Figs. 3 and 4 are 1σ and correspond to the uncertainties described in the sections above.

The above figures present both the experiment and calculation on the same scale and also include the best estimate of the uncertainties in both quantities. Such figures are often seen in viewgraph presentations when code calculations are compared to experiments. While the comparisons show qualitative agreement, the conclusions that can be drawn from the data set are limited by the lack of quantitative analysis of the quality of the comparisons. (For further details on the inadequacies of comparisons that conclude with Figs. 3 and 4, see Trucano et al. [7].) In order to produce more quantitative comparisons of the data, the C/E ratio is examined. For perfect agreement between calculations and experiment results, the C/E ratio is equal to 1.0. However, without including both the experiment and calculation uncertainties, the statistical value of such a C/E comparison is dramatically reduced [7]. In order to calculate the uncertainty in a C/E ratio, Eq 5 is used. Equation 5 is a standard error propagation formula [8].

$$\sigma^2_{\mathrm{C/E}} \approx \left|\frac{\partial}{\partial C}(\mathrm{C/E})\right|^2 \cdot \sigma^2_C + \left|\frac{\partial}{\partial E}(\mathrm{C/E})\right|^2 \cdot \sigma^2_E = \left|\frac{1}{E}\right|^2 \cdot \sigma^2_C + \left|\frac{C}{E^2}\right|^2 \cdot \sigma^2_E \tag{5}$$

Plots of the C/E ratios for the Ni and Sc activation experiments are found in Fig. 5. The error bars in Fig. 5 are computed using Eq 5. The figure clearly shows how well the calculation predicts the experiment because most (if not all) of the points have uncertainty bars that cross a C/E ratio equal to 1.0. In addition, the quantitative comparisons in Fig. 5 provide the ability to statistically determine how well the benchmark

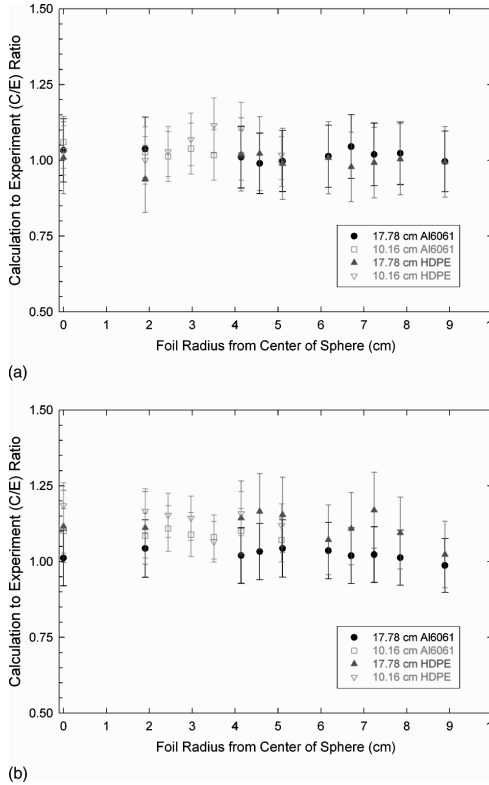

FIG. 5—*C/E ratio comparisons: (a) Ni activation; (b) Sc activation.*

calculations match the experimental results and quantitatively determine if any bias exists in the calculations.

Based on the data obtained in the ACRR operations, Fig. 6 presents side-by-side boxplots of the C/E ratios (using normalized model predictions) for the various foil types in the 17.78 cm sphere configurations. The bottom (top) of each shaded box establishes the 25th (75th) percentiles of each distribution. The line through the middle of the box establishes the median of each distribution. The "whiskers" and "asterisks" extending above and below the boxes show the range of each distribution. The asterisks identify observations that are inconsistent with the rest of the distribution. Ideally, each boxplot should be tightly distributed around C/E equal to 1.0. Situations where the boxplots are located away from C/E equal to 1.0 may indicate a systematic model error that affects predictions across the range of depths.

Based on the results of the boxplot analysis, a test statistic was developed to compare the deviation between C/E and 1.0 and address the validity of the ACRR model used for the benchmark calculations. The test statistic (Δ) is defined in Eq 6.

$$\Delta = \frac{(\mathrm{C/E}) - 1.0}{\sigma_{\mathrm{C/E}}} \tag{6}$$

In each of the ACRR operations, the magnitude of σ_C dominates the magnitude σ_E (σ_E is typically assessed at 2–5 % while σ_C is typically found to be 10–15 %) because they are added in quadrature. Assuming that Δ is normally distributed with mean zero and variance one (i.e., no fundamental model error), then it would be unusual to observe $|\Delta|$ greater than 3. (In essence, we are examining the normalized data to see if we find differences that are greater than 3 standard deviations from 1). A valid model is considered to be one that is accurate to within the uncertainties due to the experimental error and model

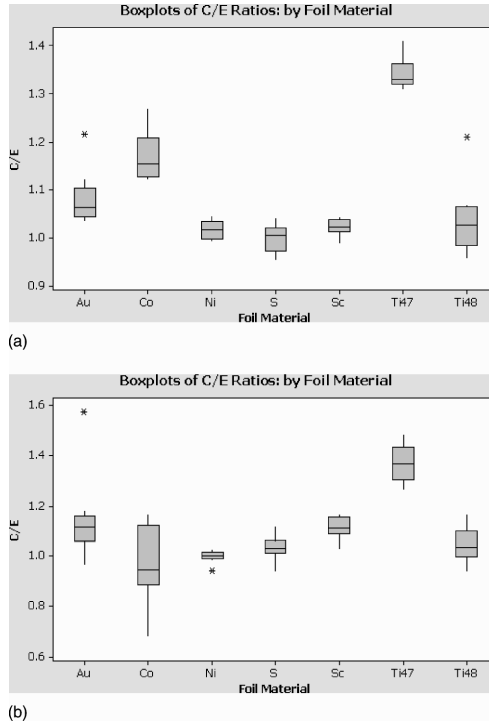

FIG. 6—*Boxplots of C/E ratios for 17.78 cm diameter spheres: (a) Al6061; (b) HDPE.*

error (i.e., $|\Delta|$ is not too large) over the entire space over which the model is to be applied.

For modeling conditions involving Ni, Sc, Cd-covered Au, Cd-covered Co, ^{47}Ti, and ^{48}Ti foils, the relative modeling error is approximately 10 %. However, the modeling error is approximately 20 % for modeling conditions involving S tablets. Using the test statistic and examining the boxplots, the model seems to be quite accurate over the complete range of conditions for all of the dosimetry foils presented here except ^{47}Ti (other exceptions are identified in [6]). The ^{47}Ti reaction rate calculation was performed with the ENDF/B-VI Rel. 0 dosimetry cross section.

Conclusions

A large series of benchmark quality experiments were conducted at Sandia National Laboratories' ACRR facility. In addition to the production of experimental data, the benchmark setup was modeled with high fidelity using the MCNPX Monte Carlo radiation transport code. The limited space of this forum prevents the full presentation of the results of the benchmark comparison. However, examples of the multiple comparisons performed during the benchmark activity were presented. These examples were intended to be a reference for the type of comparisons that should be completed when evaluating future benchmark calculations. The treatment of the benchmark data, both experiments and calculations, included a comprehensive assessment of the uncertainty components. Quantitative comparisons without the uncertainty metrics associated with them lack the robustness that is needed to draw meaningful conclusions.

The standard comparisons were determined to be inadequate for quantitative evaluation of benchmark calculation models. The calculation-to-experiment (C/E) ratio was recommended for quantitative comparison of benchmark calculations with the experimental data. The proper treatment for the uncertainty associated with the C/E ratio was presented. A test statistic (Δ) was developed and utilized to evaluate the adequacy of the benchmark calculation model. Using the test statistic, the MCNPX model of the ACRR was

determined to be adequate over the wide range of conditions examined during the benchmark comparison activity. Finally, SNL plans to perform additional benchmark experiment in the ACRR Central Cavity with spheres of different materials. The current plans include the use of spheres of a high Z material (high purity lead) and a structural material (stainless steel 304).

Acknowledgments

Work supported by the United States Department of Energy under Contract No. DE-AC04-94AL85000. Sandia is a multiprogram laboratory operated by Sandia Corporation, a Lockheed Martin Company, for the United States Department of Energy.

References

[1] Griffin, P. J., Kelly, J. G., and Vehar, D. W., "Updated Neutron Spectrum Characterization of SNL Baseline Reactor Environments, Vol. 1: Characterization," SAND Report No. SAND93-2554, Sandia National Laboratories, Albuquerque, NM, 1994.

[2] "MCNPX User's Manual, Version 2.4.0" Los Alamos Report No. LA-CP-02-408, Los Alamos National Laboratory, L. S. Waters, Ed., Los Alamos, NM, 2002.

[3] DePriest, K. R., Cooper, P. J., and Parma, E. J., "MCNP/MCNPX Model of the Annular Core Research Reactor," SAND Report No. SAND2006-3067, Sandia National Laboratories, Albuquerque, NM, 2006.

[4] DePriest, K. R., "Experiment Summary for n/γ Attenuation Through Materials (Environments 1A)," SAND Report No. SAND2006-3066, Sandia National Laboratories, Albuquerque, NM, 2006.

[5] Tuli, J. K., *Nuclear Wallet Cards, National Nuclear Data Center (for the U.S. Nuclear Data Program)*, Brookhaven National Laboratory, Upton, NY, 2000.

[6] DePriest, K. R., "Summary of NuGET Validation Activities for n/γ Attenuation Through Materials (Environments 1A)," SAND Report No. SAND2006-3068, Sandia National Laboratories, Albuquerque, NM, 2006.

[7] Trucano, T. G., Pilch, M., and Oberkampf, W. L., "General Concepts for Experimental Validation of ASCI Code Applications," SAND Report No. SAND2002-0341, Sandia National Laboratories, Albuquerque, NM, 2002.

[8] Knoll, G. F., *Radiation Detection and Measurement*, 2nd ed., John Wiley & Sons, New York, 1989.

Journal of ASTM International, Vol. 4, No. 1
Paper ID JAI100342
Available online at www.astm.org

F. A. Garner,[1] *B. M. Oliver,*[2] *L. R. Greenwood,*[1] *D. L. Porter,*[3] *and T. Allen*[4]

Measurement of Helium Generation in AISI 304 Reflector and Blanket Assemblies after Long-term Irradiation in EBR-II

ABSTRACT: Five hexagonal ducts constructed from AISI 304 stainless steel in the annealed state were removed from rows 8–14 of the EBR-II fast reactor after many years of irradiation to study the effect of atomic displacement rate on void swelling. For this objective it was important to assure that the observed differences in void swelling were not strongly influenced by variations in helium/dpa ratio. The two major contributions to helium production arise from the nickel and boron content of the steel. However, the boron content was unspecified and therefore unknown, but it was determined from an unirradiated archive duct by converting a well-defined fraction to helium and then measuring the helium content using isotopic dilution mass spectrometry. The same technique was used to measure the total helium in the irradiated duct specimens. After separating the boron contribution from the total measured helium it was possible to determine the contribution from various fast and thermal neutron interactions with the other major elements in the steel and compare the helium generation with predicted values. One important conclusion of the study is that the range of He/dpa ratios over the five subassemblies was not very large, allowing the observed changes in swelling to be attributed primarily to variations in displacement rate and temperature.

KEYWORDS: stainless steel, helium, fast reactors, boron, neutron flux-spectra

Introduction

Far from the active core regions of a small fast reactor it becomes somewhat more difficult to calculate the helium generation in stainless steel components of the reflector and blanket regions. This is particularly true for components that served many years in EBR-II while the core and reflector regions underwent many modifications, or for components which were moved and sometimes rotated during their lifetime.

In an experiment directed toward determination of the effect of displacement rate on void swelling of annealed AISI 304 stainless steel, it was important to ensure that observed differences in void swelling were primarily in response to displacement rate and not other important variables such as the helium/dpa ratio that might exhibit time-dependent or position-dependent variations [1–3]. Helium is well known to accelerate the nucleation of voids and shorten the transient regime of swelling. However, since there are helium sources associated with both low and high energy neutrons, one cannot confidently assume that lower flux regions with their inherently softer spectra will lead to consistent decreases or increases in helium generation per dpa. As the high energy source of helium declines, the low energy source tends to increase and the net change can move in either direction.

Rather than relying only on calculations of expected helium content for such complicated histories, the helium content was measured directly using an isotopic dilution mass spectrometry method known to be very accurate. Since some significant fraction of the helium in these relatively soft spectral regions arises from transmutation of boron it was necessary to determine the unknown boron content using an archive duct of the same heat of steel.

Manuscript received June 20, 2005; accepted for publication October 25, 2006; published online December 2006. Presented at ASTM Symposium on Reactor Dosimetry, 12th International Symposium on 8–13 May 2005 in Gatlinburg, TN; D. W. Vehar, D. M. Gilliam, and J. M. Adams, Guest Editors.

[1] Laboratory Fellow, Pacific Northwest National Laboratory, Richland, WA 99354.
[2] Scientist, Pacific Northwest National Laboratory, Richland, WA 99354.
[3] Materials Scientist, Idaho National Laboratory, Idaho Falls, ID 83403.
[4] Assistant Professor, University of Wisconsin, Madison, WI 53706.

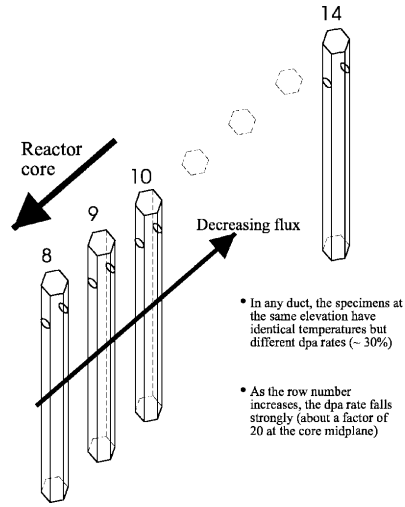

FIG. 1—*Schematic representation of flux-effects experiment in EBR-II.*

Experimental Details

The width of the face of these hexagonal ducts is 2.9 cm and the duct is 1-mm thick. Four of the five ducts employed in this study were constructed from the same heat of steel designated 772864 and were irradiated for the majority of their lifetime in Rows 8, 9, and 10 of EBR-II, as schematically shown in Fig. 1. The two ducts that were irradiated in Row 10 were on opposite sides of the core. The fifth duct was much older and spent most of its residence time in Row 14 but was constructed from an earlier different heat of steel prepared to the same specification but without an available archive, but analyses conducted after irradiation showed that the composition of the two heats was quite similar, as shown in Table 1.

As shown in Table 2 and also in Fig. 2, these ducts remained in the reflector and blanket regions of EBR-II for different periods spanning many years, with only the two Row 10 ducts remaining in the same position and orientation throughout their residence. However, while the Row 10 ducts (U9007 and U9009 at 32 and 27 dpa, respectively) were not moved, the core, reflector, and blanket regions underwent many

TABLE 1—*Composition of Heat 772864 in wt %.*

	N_2	Mn	Cr	Ni	Co	Cu	Si	Mo	Nb	P	C	S
Vendor specification	…	0.8	18.56	9.05	…	…	0.51	…	…	0.027	0.07	0.003
Measurements at EBR-II	0.05	0.832	…	8.20	0.016	0.02	…	0.011	0.001	…	…	…

…=Not specified or measured.

TABLE 2—*Run history and temperature assignments.*

Assembly	EBR-II Row	MWD in this Row[a]	Time Fraction	dpa (max)	Temperature Assignment
U9007	10	187 505	1.00	32.0	Average
U9009	10	184 463	1.00	27.0	Average
U8972	9	91 166	0.41	33.0	Time average
	15	133 785	0.59	1.4	In Row 9 only
U9807	8	60 165	0.36	32.0	Time average
	16	107 495	0.64	0.9	In Row 8 only
U1603	8	5951	0.02	2.4	Time average
	14	348 584	0.98	7.6	In Row 14 only

[a]MWD=megawatt-days.

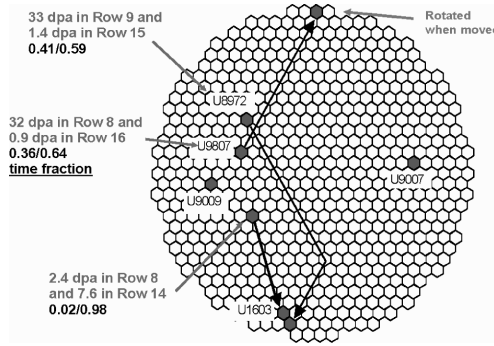

FIG. 2—*Schematic representation of assembly location history. Only the two Row 10 assemblies remained in the same position and orientation throughout the irradiation. The other three assemblies were moved one time and sometimes rotated during the irradiation.*

significant modifications during this period. During the Liquid Metal Reactor Program the core was expanded to include many lower worth assemblies, with many changes made from run-to-run.

Twenty 2.0-cm diameter specimens spanning a large axial range about the core centerplane were removed from each of the inboard and outboard faces of each duct. The faces examined were defined by the orientation and row where the majority of the dose was accumulated, with inboard-outboard defined relative to the core centerline to maximize the dose difference. The average density of each 2.0-cm disk was measured using an immersion density technique and the results are reported elsewhere [1–3]. After density measurements were completed, smaller specimens averaging ranging from ~2 to ~4 mg were produced from 5 of the 20 disks from each of the inboard and outboard sides of each duct and used for determination of helium content. A total of 50 specimens were measured, taken from two opposing flats of each assembly.

The time-averaged values of temperature and dpa relevant to each duct and individual specimen were determined at the EBR-II facility of Argonne National Laboratory. These calculations are reported in Ref. [3] and the dpa and methods of temperature assignments are shown in Table 2.

An archive duct of the production heat used for ducts in Rows 8–10 was obtained and a ~30 mg sample was cut from one of the faces of the duct. For the helium analyses, specimens were prepared from each supplied sample by sectioning using small diagonal cutters. Before each use, the cutters were cleaned by wiping several times with a dry paper wipe. Prior to analysis, each specimen was cleaned in acetone and air-dried. The mass of each specimen was then determined using a calibrated microbalance traceable to the National Institute of Standards and Technology (NIST). Mass uncertainty is estimated to be ±0.002 mg. Sample etching to remove at least 0.013 mm was performed to remove sufficient material to avoid errors associated with α-recoil across specimen surfaces, or surface contamination. Two separate measurements were made on specimens cut from each sample.

Helium analyses were conducted using isotope-dilution gas mass spectrometry following vaporization in a resistance-heated tungsten-wire crucible in one of the helium mass spectrometer system's high-temperature vacuum furnaces [4]. The absolute amount of ^{4}He released was measured relative to a known quantity of added ^{3}He "spike." Each helium spike was obtained by expanding and partitioning a known quantity of gas through a succession of calibrated volumes [5]. Additionally, the mass spectrometer was calibrated for mass sensitivity during each series of runs by analyzing known mixtures of ^{3}He and ^{4}He.

The results of the gas analyses are presented in Figs. 3 and 4 as gas concentrations in atomic parts per million (10^{-6} atom fraction). Conversion from total gas atoms released to gas concentration was based on a calculated value of 1.097×10^{22} atoms/gram for the 304 stainless steel material. It should be noted, however, that this conversion value, and the gas concentrations obtained using it, are not very sensitive to small changes in material composition. Uncertainty in the individual helium analysis results, determined from the cumulative uncertainties in the sample mass, the isotope ratio measurement, and the spike size, is estimated to be ~1 %.

The boron content in the hex-can sample was determined using a method similar to neutron activation.

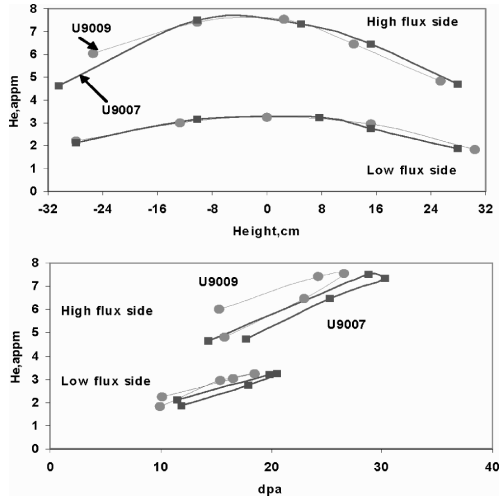

FIG. 3—*Helium measurements of the two Row 10 assemblies versus axial location and dpa level. Note the very clear separation in generation rate between the low and high flux sides.*

The sample was exposed to a known dose of thermal neutrons in order to convert a known fraction of the ^{10}B isotope to helium via the ^{10}B (n,α) ^{7}Li reaction. After irradiation, the helium generated was measured in several smaller specimens (~3.5 mg) cut from the sample, and used to determine the boron content,

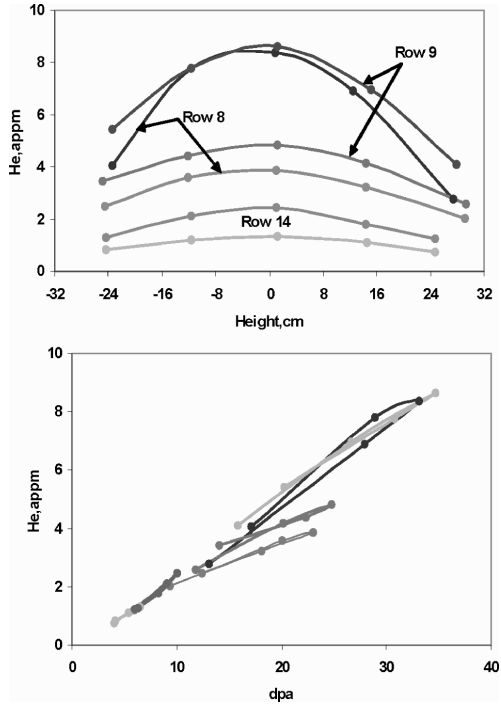

FIG. 4—*Helium measurements of assemblies in Rows 8, 9, and 14 versus axial location and dpa level.*

assuming an isotopic abundance of 19.9 % for ^{10}B. Neutron dosimetry samples, in the form of a well characterized Al-^{6}Li alloy wire, were included in the irradiation assembly to accurately determine the thermal neutron fluence via the $^{6}Li\ (n,\alpha)\ ^{3}H$ reaction. The thermal neutron cross sections for the ^{10}B and ^{6}Li samples are well known.

The irradiation of the archive specimens was conducted in the research reactor at McMaster University in Canada. The irradiation time and thermal fluence were 160 hours and 2.04×10^{19} n/cm^2, respectively. The thermal-to-fast neutron ratio in this spectrum was approximately six, ensuring that >99 % of the helium was generated from the boron with no significant amount of helium generated from the major elements, Ni, Fe, Cr, etc.

Results and Discussion

As discussed in Refs. [1,2] there was a very clear and consistent effect of flux on void swelling in AISI 304 stainless steel at every temperature studied, providing that some other unrecognized variable did not contribute strongly. For void swelling the helium generation rate is known to often be a strong contributor to the onset of swelling, especially when the steel initially resists swelling [6]. While annealed 304 stainless steel is known not to be very resistant to swelling [2,7], it was prudent to check the possibility that the helium/dpa generation rate might be varying strongly. After measuring the total helium content the first step in assessing its origin lies in the determination of the boron content. The natural boron content in the archive samples was determined in this study to be 1.4 wt. ppm, corresponding to 0.25 wt. ppm ^{10}B, or 1.4 appm ^{10}B with an uncertainty calculated to be about ±3 %. Therefore, even at complete burnup the maximum helium arising from the ^{10}B source could not exceed 1.4 appm. Most measured helium levels are significantly larger, at minimum a factor of ~2 higher, indicating that the primary helium contributions at higher exposures came from Ni, Fe, and Cr.

The results of the helium measurements on the irradiated specimens are shown versus both position and versus dpa in Figs. 3 and 4. Note that the two Row 10 assemblies have remarkably similar profiles even though the total exposures of the two assemblies are ~16 % different. The helium generation rate per dpa on the high flux side of the Row 10 assemblies is measurably larger than that of the low flux sides. There is also some small variation in total helium generation between the upper and lower portions of the Row 10 assemblies with slightly more helium produced in the lower portion of the assembly. This difference is not so pronounced in the other assemblies and may reflect some influence of their movement during residence. For all subassemblies, however, the He/dpa ratio is relatively independent of axial location as shown in Fig. 5.

When all He concentration data are plotted versus dpa, it is seen in Fig. 6 that the helium generation rate averages about ~0.25 appm/dpa. While some assemblies lie above or below this average rate, the variations are not large enough or systematic enough to significantly impact the conclusion of a strong dependence of dpa rate on swelling. Together with the finding that the total helium concentration never exceeds 10 appm this allows us to conclude that the range of He/dpa ratios over the five subassemblies is not very large, allowing the observed changes in swelling to be attributed primarily to variations in displacement rate and temperature, with helium playing at most a second-order role.

When the components have experienced a complicated history in neutron flux-spectra the need for measurements of time-integrated helium generation can be demonstrated using calculated flux-spectra that were available early in the life of EBR-II. Detailed flux-spectra derived from the EBR-II reactor low power dosimetry run designated 78C were available for comparison [8] and the total integrated time were used to make comparisons between 78C-based calculations and our measurements. However, the core has undergone numerous changes in local experimental loading over the lifetime of these assemblies. With the exception of U1603 (in the core from run 25 to 170), all assemblies were put into the reactor during runs 95-118, and stayed through runs 166-170. During the lifetime of these assemblies EBR-II underwent significant expansion to accommodate a growing number of experimental subassemblies. This expansion tended to reduce the local neutron flux over time.

As shown in Fig. 7 the 78C-based predictions of dpa are indeed significantly larger than those calculated for the mid-point of the assemblies, with the magnitude of over-prediction increasing strongly at lower row numbers. Note that significantly more helium was measured in Row 10 than was predicted.

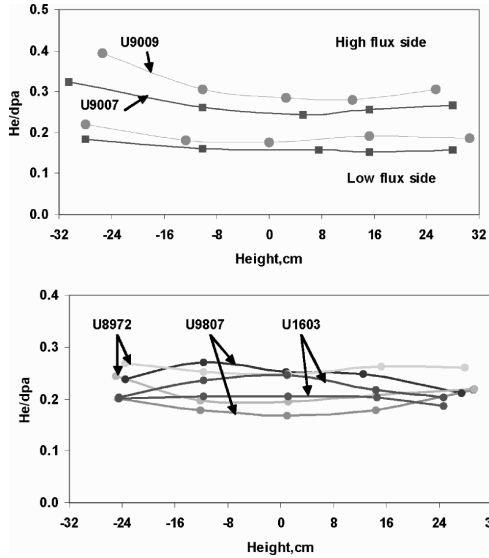

FIG. 5—*Helium/dpa ratios of assemblies in Row 10 (top) and Rows 8, 9, and 14 (bottom) versus axial location.*

Figure 8 shows that the predicted helium for Row 8 is also significantly lower than measured in Row 8, but also for Rows 9 and 14.

This apparently contradictory set of conclusions is a reflection of the fact that helium is generated primarily by nickel in a Fe-Cr-Ni alloy, but there are two competing reactions [9–14]. The first helium contribution arises from a high-energy reaction (n,α) with threshold energy of ~1 MeV. As the core expanded the average neutron flux and energy both tended to decrease in the reflector region. On the other hand, the low-energy two-step ^{58}Ni (n,γ) ^{59}Ni (n,α) ^{56}Fe reaction sequence increases in importance in softer spectra and dominates the helium production in this experiment. In addition the ^{10}B (n,α) ^{7}Li reaction also becomes more important in softer spectra.

These Run 78C predictions confirm two aspects of the measured behavior. First, Fig. 7 shows that there is indeed a tendency for slightly higher helium generation rates in the lower portion of the core compared to the upper portion. Second, Fig. 8 shows that the He/dpa rate is relatively constant along the axial direction of a given assembly, both in agreement with the results of the current study.

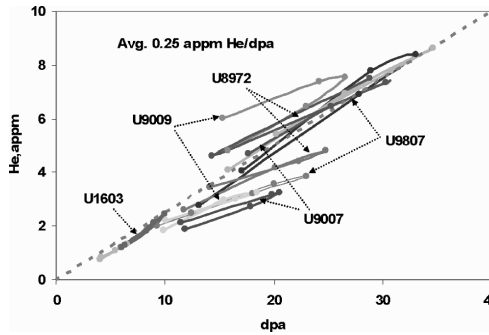

FIG. 6—*Compilation of helium measurements for all assemblies versus dpa level, showing an average generation rate of ~0.25 appm/dpa.*

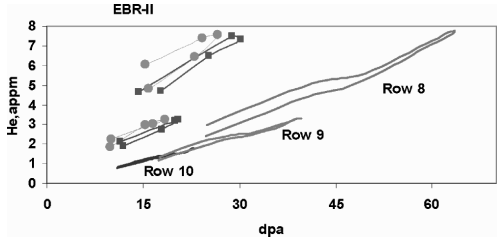

FIG. 7—*Comparison of measured values of helium for the two Row 10 assemblies versus predicted values (calculated at assembly center) for Rows 8, 9, and 10. Note that the measured values of helium for Row 10 assemblies are significantly larger than predicted.*

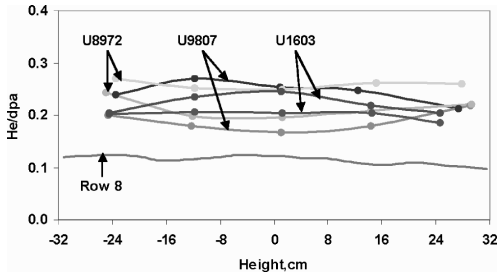

FIG. 8—*Comparison of measured values of helium/dpa versus axial location for assemblies in Rows 8, 9, and 14 versus prediction for Row 8. Note that significantly more helium is generated in Row 8 than was predicted.*

Conclusions

The helium generated in AISI 304 stainless steel during irradiation in the EBR-II fast reactor is a sensitive function of neutron flux-spectra. When the flux-spectra vary over the residence time of a long-lived component it becomes more difficult to predict the accumulated helium, especially when the time history of the component is complicated and when the components reside in the blanket and reflector regions of the reactor.

In such cases the helium is best measured using techniques such as isotope-dilution gas mass spectrometry. If it is desirable to predict the relative contributions of high-energy (n,α), low energy $^{58}Ni\ (n,\gamma)\ ^{59}Ni\ (n,\alpha)\ ^{56}Fe$ and low energy $^{10}B\ (n,\alpha)\ ^{7}Li$ reactions, then the detailed composition of the steel must be known. When the boron concentration has not been measured then the $^{10}B\ (n,\alpha)\ ^{7}Li$ reaction can be used with archive material to determine its concentration and contribution to helium production. In a complicated time-history experiment where it was important to know the relative roles of He/dpa ratio and dpa rate, it was demonstrated in this report that the He/dpa ratio did not vary strongly among the experimental samples and was most likely only a variable of second-order importance compared to the effect of dpa rate on void swelling of AISI 304 stainless steel.

References

[1] Bond, G. M., Sencer, B. H., Garner, F. A., Hamilton, M. L., Allen, T. R., and Porter, D. L., "Void Swelling of Annealed 304 Stainless Steel at ~370–385°C and PWR-Relevant Displacement Rates," *9th International Conference on Environmental Degradation of Materials in Nuclear Power Systems–Water Reactors*, 1999, pp. 1045–1050.

[2] Garner, F. A., Edwards, D. J., Bruemmer, S. M., Porollo, S. I., Konobeev, Y. V., Neustroev, V. S.,

Shamardin, V. K., and Kozlov, A. V., "Recent Developments Concerning Potential Void Swelling of PWR Internals Constructed from Austenitic Stainless Steels," *Proceedings, Fontevraud 5, Contribution of Materials Investigation to the Resolution of Problems Encountered in Pressurized Water Reactors*, 23–27 September 2002, paper #22, on CD format, no page numbers.

[3] Garner, F. A., Hamilton, M. L., Porter, D. L., Allen, T. R., Tsutsui, T., Nakajima, M., Kido, T., and Ishii, T., "Determination of Damage Rate Dependence of Void Swelling of Solution-Annealed 304 Stainless Steel Using Irradiated EBR-II Reflectors," manuscript in preparation.

[4] Oliver, B. M. and Farrar, H., "Mass Spectrometer System to Determine Very Low Levels of Helium in Small Solid and Liquid Samples," *J. Vac. Sci. Technol. A*, Vol. 4, 1986, p. 1740.

[5] Oliver, B. M., Bradley, J. G., and Farrar, H., "Helium Concentration in the Earth's Lower Atmosphere," *Geochim. Cosmochim. Acta*, Vol. 48, 1984, p. 1759.

[6] Garner, F. A., "Chapter 6: Irradiation Performance of Cladding and Structural Steels in Liquid Metal Reactors," *Materials Science and Technology: A Comprehensive Treatment*, Vol. 10A Nuclear Materials, B. R. T. Frost, Ed., VCH Publishers, 1994, pp. 419–543.

[7] Garner, F. A., and Porter, D. L., "A Reassessment of the Swelling Behavior of AISI 304L Stainless Steel," *International Conference on Dimensional Stability and Mechanical Behavior of Irradiated Metals and Alloys*, Brighton, England, 1983, pp. 41–44.

[8] Franklin, F. C., Ebersole, E. R., and Heinrich, R. R., "Analysis of EBR-II Low-Power Dosimetry Run 78C," *Argonne National Laboratory Report*, Vol. ANL-77-76, 1977.

[9] Greenwood, L. R., Garner, F. A., and Oliver, B. M., "Helium Generation Rates in Isotopically Tailored Fe-Cr-Ni Alloys Irradiated in FFTF/MOTA," *J. Nucl. Mater.*, Vol. 191-194, 1992, pp. 1051–1055.

[10] Garner, F. A., Greenwood, L. R., and Harrod, D. L., "Potential High Fluence Response of Pressure Vessel Internals Constructed from Austenitic Stainless Steels," *6th International Symposium on Environmental Degradation of Materials in Nuclear Power Systems—Water Reactors*, San Diego, CA, 1993, pp. 783–790.

[11] Greenwood, L. R., Garner, F. A., and Oliver, B. M., "An Assessment of the Ni-59 Isotopic Tailoring Technique to Study the Influence of Helium/dpa Ratio," *J. Nucl. Mater.*, Vol. 212–215, 1994, pp. 492–497.

[12] Garner, F. A., Greenwood, L. R., and Oliver, B. M., "A Reevaluation of Helium/dpa and Hydrogen/dpa Ratios for Fast Reactor and Thermal Reactor Data Used in Fission-Fusion Correlations," *Effects of Radiation on Materials: 18th International Symposium*, ASTM STP 1325, ASTM International, West Conshohocken, PA, R. K. Nanstad, M. L. Hamilton, F. A. Garner, and A. S. Kumar, Eds., 1999, pp. 794–807.

[13] Garner, F. A., Oliver, B. M., and Greenwood, L. R., "The Dependence of Helium Generation Rate on Nickel Content of Fe-Cr-Ni Alloys Irradiated at High dpa Levels in Fast Reactors," *J. Nucl. Mater.*, Vol. 258–263, 1998, pp. 1740–1744.

[14] Garner, F. A. and Greenwood, L. R., "Survey of Recent Developments Concerning the Understanding of Radiation Effects on Stainless Steels Used in the LWR Power Industry," *10th International Conference on Environmental Degradation of Materials in Nuclear Power Systems—Water Reactors*, 2003, pp. 887–909.

Journal of ASTM International, Vol. 3, No. 3
Paper ID JAI13433
Available online at www.astm.org

P. Kotiluoto[1]

Verification of MultiTrans Calculations by the VENUS-3 Benchmark Experiment

ABSTRACT: The MultiTrans software has been developed at VTT Technical Research Centre of Finland for 3D radiation transport problems. Adaptive tree multigrid technique is used as a deterministic solution method. This enables local refinement of the calculation grid combined with the use of effective multigrid acceleration on tree-structured nested grids: starting from a fast solution on coarse grid, successive solutions are obtained on finer and finer grids. In the MultiTrans code, simplified spherical harmonics (SP_3) radiation transport approximation is used. In order to test the applicability of the new MultiTrans code to reactor dosimetry problems, light water reactor pressure vessel steel (LWR-PVS) benchmark experiment VENUS-3 (with partial length shielded assemblies) was chosen. The results show good agreement to the experimental reaction rates of the VENUS-3 benchmark, demonstrating the applicability of the new MultiTrans code in reactor dosimetry.

KEYWORDS: MultiTrans, radiation transport, reactor dosimetry, tree multigrids, VENUS-3 benchmark

Introduction

Advanced 3D radiation transport methods allow detailed calculation of neutron flux distributions and related quantities for internal parts of nuclear reactors. For instance, DPA (displacement per atom) rates are important for estimation of embrittlement of reactor materials.

In reactor dosimetry, computational methods of radiation transport give important complementary information to measurements. For such positions where dosimeters simply cannot be placed, one is enforced to rely on calculated quantities. Furthermore, dosimeters usually respond to some reaction-specific neutron energies and therefore will not give complete information about the whole neutron spectrum. On the other hand, in deterministic solution of the radiation transport, some approximations usually have to be made—not only for the radiation transport equation, but also for the geometry and for the transport cross sections—before numerical solution of the problem becomes feasible. Measured values give valuable information about the accuracy of the computational (approximative) method and some estimate of the general uncertainty of the calculated values.

MultiTrans is a deterministic radiation transport software developed at VTT Technical Research Centre of Finland [1–3]. Multigroup simplified spherical harmonics (SP_3) approximation of the Boltzmann transport equation has been used to describe the transport process of neutrons through a host medium [4,5]. Adaptive tree multigrid technique has been utilized as an efficient numerical method to solve these SP_3 equations.

Obviously there is a strong need to verify that any new code is performing as expected and suitable for the intended scope of application. In order to test the applicability of the MultiTrans code to reactor dosimetry problems, light water reactor pressure vessel steel (LWR-PVS) benchmark experiment VENUS-3 (with partial length shielded assemblies) was chosen [6]. Comparison between the calculated and experimental $^{58}Ni(n,p)$, $^{115}In(n,n')$ and $^{27}Al(n,\alpha)$ reaction rates for all the measured detector positions of the 3D VENUS-3 benchmark is presented in this paper.

Manuscript received June 20, 2005; accepted for publication September 29, 2005; published online December 2005. Presented at ASTM Symposium on Reactor Dosimetry, 12th International Symposium on 8–13 May 2005 in Gatlinburg, TN; D. W. Vehar, D. M. Gilliam, and J. M. Adams, Guest Editors.
[1] Research Scientist, VTT Technical Research Centre of Finland, P.O. Box 1608, FI-02044 VTT, Finland.

Materials and Methods

Simplified P_3 Approximation

The spherical harmonics P_N approximation is well established for the Boltzmann radiation transport equation [7]. However, P_N equations are very complicated in 3D. In 1960 simplified P_N approximation was introduced by Gelbard ad hoc [8], but did not gain much popularity due to lack of solid theoretical background. At present, it has been shown that SP_N equations can have asymptotic and variational derivations [4,5], and therefore the SP_N approximation has attracted growing attention.

In the MultiTrans code SP_3 radiation transport approximation is used [1]. The angular flux in 1D Boltzmann equation is expanded as a series of Legendre polynomials up to order 3, and the orthogonality of the base functions (when integrating over the space) is used to get a coupled set of diffusion like equations for the expansion coefficients. The within-group equations for these coefficients are given in Eqs 1–4.

$$\frac{d}{dx}\Phi_1^g(x) + \sigma_{a0}^g \Phi_o^g(x) = S^g(x) \tag{1}$$

$$\frac{1}{3}\frac{d}{dx}\Phi_0^g(x) + \frac{2}{3}\frac{d}{dx}\Phi_2^g(x) + \sigma_{a1}^g \Phi_1^g(x) = 0 \tag{2}$$

$$\frac{2}{5}\frac{d}{dx}\Phi_1^g(x) + \frac{3}{5}\frac{d}{dx}\Phi_3^g(x) + \sigma_{a2}^g \Phi_2^g(x) = 0 \tag{3}$$

$$\frac{3}{7}\frac{d}{dx}\Phi_2^g(x) + \sigma_{a3}^g \Phi_3^g(x) = 0 \tag{4}$$

$S^g(x)$ in the above equations is scalar source term in energy group g, and $\Phi_n^g(x)$ are the Legendre expansion coefficients of the angular group flux. $S^g(x)$ and $\Phi_n^g(x)$ are components of $1 \times G$ vector functions, where G is the total number of energy groups in multigroup approximation. The group transport cross sections are defined by subtraction of the corresponding Legendre component of the group scattering cross section from the group total cross section: these group transport cross sections are given in Eq 5.

$$\sigma_{an}^g = \sigma_t^g - \sigma_{sn}^{g \to g} \tag{5}$$

Generalized 3D equations, with a formal substitution of the 1D derivative with ∇ operator, can be written in second order form by solving odd-moments from Eqs 2 and 4, and then by substituting these odd-moments into Eqs 1 and 3. If one defines the unknown by Eq 6

$$\hat{\Phi}_0^g(\vec{r}) \equiv \Phi_0^g(\vec{r}) + 2\Phi_2^g(\vec{r}) \tag{6}$$

where $\Phi_0^g(\vec{r})$ is the scalar flux and $\Phi_2^g(\vec{r})$ is the P_2 moment term of the group flux, the within-group SP_3 approximation in second-order matrix form (with superscript i as a material and superscript g as an energy group index) is given by Eq 7.

$$\begin{bmatrix} -D_0\nabla^2 + \sigma_{a0} & -2\sigma_{a0} \\ -\frac{2}{5}\sigma_{a0} & -D_2\nabla^2 + \sigma_{a2} + \frac{4}{5}\sigma_{a0} \end{bmatrix}^{i,g} \begin{bmatrix} \hat{\Phi}_0(\vec{r}) \\ \Phi_2(\vec{r}) \end{bmatrix}^{i,g} = S^{i,g}(\vec{r}) \begin{bmatrix} 1 \\ -\frac{2}{5} \end{bmatrix} \tag{7}$$

The diffusion coefficients depend on transport cross sections and are given in Eqs 8 and 9.

$$D_0^{i,g} = \frac{1}{3\sigma_{a1}^{i,g}} \tag{8}$$

$$D_2^{i,g} = \frac{9}{35\sigma_{a3}^{i,g}} \tag{9}$$

The scalar group source including fixed source, group-to-group scattering and fission source term is given by Eq 10.

$$S^{i,g}(\vec{r}) = Q^{i,g}(\vec{r}) + \sum_{g'=1,g'\neq g}^{G} \sigma_{s0}^{i,g'\to g}[\hat{\Phi}_0^{g'}(\vec{r}) - 2\Phi_2^{g'}(\vec{r})] + \frac{\chi^g}{k}\sum_{g'=1}^{G} \nu^{g'}\sigma_f^{i,g'}\Phi_0^{g'}(\vec{r}) \tag{10}$$

Standard multi-group neutronics notation has been used above.

Tree Multigrid Technique

In the adaptive tree multigrid technique used in MultiTrans software, tree structured nested grids of different coarseness are generated from the computer-aided design (CAD) model. The grid adapts to the surface triangulation of each solid part of the CAD model by recursive subdivision of cubic cells. Each cubic cell is conditionally divided into eight sub-cubes, which become the children cells of the parent cell. Every children cell can become a parent and have their own children cells. This procedure is continued until the desired accuracy in the geometry description is achieved. As a result, finest grid is obtained at material borders.

The resulting cell system has a tree structure, in which the subdivisions form the branches and the leaves are the children, which are not divided further. Two cells are said to be neighbors if their boundaries are not disjoint but none of them contains the other. Neighbor cells are called face neighbors if they share a common surface, side neighbors if they share a common line, and corner neighbors if they have a common corner only.

The created nested grid structure, which is called an octree grid, is nonuniform. Therefore it is important to construct a proper difference scheme that works on this nonuniform grid structure but is also as simple as possible for inexpensive numerical solution. In order to simplify the construction of the difference scheme, an additional constraint has been used in octree grid subdivision procedure: the ratio of the size of every face neighbor cells is restricted to be at most 2, which makes the grid regular. This adds up to the amount of cells to some extent, depending on the geometry, and therefore increases the problem size, but on the other hand might also reduce the truncation error farther away from the material borders.

For the SP_3 radiation transport approximation in MultiTrans, an integrated difference scheme is utilized [1]. In the integrated difference scheme the flux derivatives are approximated over each side of a cell C by applying the Green's first identity, Eq 11.

$$\int_C \nabla\Phi dV = \int_{\partial C} (\vec{n}\cdot\nabla)\Phi dA \tag{11}$$

In Eq 11 $\vec{n}$ is the normal vector of the cell surface. When the face neighbor cells are same size, flux over side of the cell can be approximated by using central difference, Eq 12.

$$(\vec{n}\cdot\nabla)\Phi \approx \frac{1}{h}(\Phi_N - \Phi_C) \tag{12}$$

In Eq 12 above, h is the mesh size and Φ_C and Φ_N are the flux values in cell and it's neighbor, respectively. Otherwise, parent of the smaller cell is used, and the difference is given by Eq 13.

$$(\vec{n}\cdot\nabla)\Phi \approx \begin{cases} \frac{1}{2h}(\Phi_N - \Phi_{P(C)}), & \textit{neighbor N is bigger than C} \\ \frac{1}{2h}(\Phi_{P(N)} - \Phi_C), & \textit{neighbor N is smaller than C} \end{cases} \tag{13}$$

In Eq 13 the value of the parent cells $\Phi_{P(C)}$ and $\Phi_{P(N)}$ is the average of their children's values. The discretized within-group SP_3 approximation solved by MultiTrans code in iterative diagonal form is then finally given by Eq 14.

$$\begin{bmatrix} -D_0h^2(\vec{n}\cdot\nabla) + h^3\sigma_{a0} & 0 \\ 0 & -D_2h^2(\vec{n}\cdot\nabla) + h^3\sigma_{a2} \end{bmatrix}_h^{i,g} \begin{bmatrix} \hat{\Phi}_0 \\ \Phi_2 \end{bmatrix}_h^{i,g,l+1} = h^3\sigma_{a0}\begin{bmatrix} 2\Phi_2 \\ \frac{2}{5}\hat{\Phi}_0 - \frac{4}{5}\Phi_2 \end{bmatrix}_h^{i,g,l} + h^3 S_h^{i,g}\begin{bmatrix} 1 \\ -\frac{2}{5} \end{bmatrix} \tag{14}$$

For a fixed source, multigroup flux solution is obtained by first solving the above equation by MultiTrans for the first energy group (with the highest energy), and then using the obtained solution to calculate

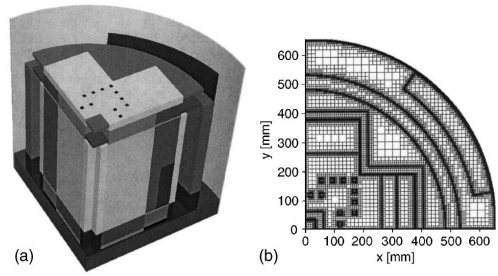

FIG. 1—*VENUS-3 benchmark geometry: (a) CAD model (water regions transparent), (b) horizontal cross section of the octree grid 10 cm below the core mid-plane (with PLSA).*

the source on next lower energy group. This procedure is continued in one sweep through all the groups from highest energy to the lowest, taking group-to-group down-scattering into account at every step. If up-scattering exist, however, several sweeps are required in order to get the correct converged solution. It is also possible to solve a problem with fissile material without defining any fixed source, but doing a criticality eigenvalue search instead. This procedure has been outlined in an earlier paper [3].

The octree algorithm automatically produces all the coarser grids. The sequence of nested fine and coarse grids enables the use of multigrid acceleration method [9]. In a multigrid cycle, the solution strategy recursively leads the discrete problem back to a similar one defined on the next coarser grid. On the coarser grid the solution requires less iteration. The coarse grid solution interpolated to the finer grid can then be used to accelerate the fine grid solution. In the MultiTrans code, all grid levels from coarsest (the root cube) to the finest (the leaf cell representation) are used in nested iteration, producing solution on all grid levels. The multigrid method in connection with the SP_3 equations is described in more detail elsewhere [1].

VENUS-3 Benchmark

The VENUS Critical Facility is a zero power reactor located at SCK●CEN, Mol, Belgium. It has been used to study LWR core designs and to provide experimental data for nuclear code validation. LWR-PVS benchmark experiment VENUS-3 (with partial length shielded assemblies) is a computational 3D radiation transport exercise of the OECD NEA based on the measured data in the experimental program conducted in 1988 [6]. Nuclear Science Committee (NSC) expert group launched the computational VENUS-3 benchmark in 1997: about 14 independent benchmark calculations were supplied by eight institutions. The results of this benchmark have been published by NEA [10]. The well-documented experimental and computational data with detailed material and geometry specifications offers a good resource to verify the calculations with any new transport code, such as MultiTrans.

In order to be able to generate the octree grid for the MultiTrans code, the VENUS-3 benchmark geometry was first constructed with commercially available CAD software based on benchmark specifications [6], see Fig. 1(*a*). All material regions were modeled in detail, except that fuel pin, fuel cladding, and water regions were homogenized over each fuel zone. The external regions outside the jacket inner wall (air, jacket outer wall, reactor vessel, water, and reactor room) were left away from the model, as they can be assumed to have no significant effect to the responses at the measurement points.

The geometry of each material region of the model was exported from the CAD software as a stereolitography (STL) file. A three-dimensional tree multigrid (octree grid) was generated directly from these STL-files, resulting in over 2.46 million cells. A horizontal cross section of the generated octree grid is illustrated in Fig. 1(*b*), showing also the partial length shielded assemblies (PLSA) fuel region below the core mid-plane.

The venus3.src file from NEA-1517/69 SINBAD-VENUS-3 distribution CD was used to generate a fixed-source for MultiTrans calculation. Fission spectrum for ^{235}U was taken from BUGLE-96 library [11]. BUGLE-96 library (version without up-scattering) was also used in generation of the material transport cross sections in 47 neutron groups by MultiTrans for 26 different elemental material compositions involved.

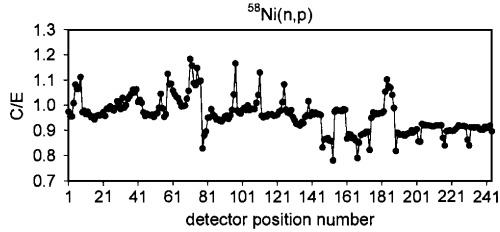

FIG. 2—*Ratio of calculated and experimental $^{58}Ni(n,p)$ reaction rate in 244 detector positions.*

For calculation of the reaction rates, $^{58}Ni(n,p)$, $^{115}In(n,n')$, and $^{27}Al(n,\alpha)$ cross sections were condensed into the 47 BUGLE groups from IRDF-90 version 2 dosimetry library in SAND II energy group structure by using X333 utility program from the neutron metrology file NMF-90 [12] with combined Maxwell, 1/E, and fission weighting spectrum. Resulting fission spectrum averaged dosimetry cross sections were 105.7, 186.3, and 0.726 mbarn for Ni, In, and Al, respectively.

Results

Comparison of calculated and experimental reaction rates for VENUS-3 detector positions is given in Figs. 2–4.

In general, reaction rates agree well with the experimental values: the majority of the values are within 5 % for Ni and Al and within 7 % for In. The deviation is larger than 20 % only in 2 detector positions of Ni in uppermost PLSA region, and in one detector position of In and Al in core barrel near the corner of the PLSA. According to the final NEA report of the VENUS-3 computational benchmark, a systematic overestimation of measurements (more than 5 %) occurs at the extreme top and bottom locations of the active core region [10]. This can partly explain the large deviation of the C/E values for the two Ni detector positions (−22 % for position 153 and −21 % for position 167). However, the overestimation of the calculated In and Al reaction rates near the corner of the PLSA is probably due to the SP_3 approximation, which does not produce accurate results when the solution behaves more transport-like.

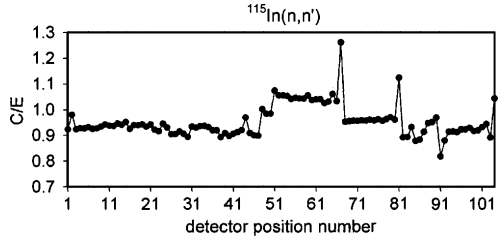

FIG. 3—*Ratio of calculated and experimental $^{115}In(n,n')$ reaction rate in 104 detector positions.*

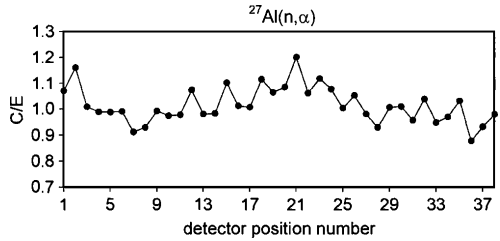

FIG. 4—*Ratio of calculated and experimental $^{27}Al(n,\alpha)$ reaction rate in 38 detector positions.*

The MultiTrans calculations were performed on desktop PC running Windows XP with 3.0 GHz P4 CPU and with 3.62 GB of RAM. Calculation time was 70 min for 47 BUGLE neutron groups.

Conclusions

The MultiTrans results show good agreement to the experimental reaction rates of the VENUS-3 benchmark, demonstrating the applicability of the new MultiTrans code in reactor dosimetry.

Acknowledgments

I wish to acknowledge my colleague, Tom Serén, for help with the dosimetry cross sections and related utility programs, as well as for other valuable guidance.

References

[1] Kotiluoto, P., "Fast Tree Multigrid Transport Application for the Simplified P_3 Approximation," *Nucl. Sci. Eng.* Vol. 138, 2001, pp. 269–278.

[2] Kotiluoto, P., Hiismäki, P., and Savolainen, S., "Application of the New MultiTrans SP_3 Radiation Transport Code in BNCT Dose Planning," *Med. Phys.* Vol. 28, 2001, pp. 1905–1910.

[3] Kotiluoto, P., "Application of the New MultiTrans SP_3 Radiation Transport Code in Criticality Problems and Potential Use in Dosimetry," in *Reactor Dosimetry in the 21st Century*, World Scientific, Singapore, 2003, pp. 580–587.

[4] Larsen, E. W., Morel, J. E., and McGhee, J. M., "Asymptotic Derivation of the Multigroup P_1 and Simplified P_N Equations with Anisotropic Scattering," *Nucl. Sci. Eng.* Vol. 123, 1996, pp. 328–342.

[5] Brantley, P. S. and Larsen, E. W., "The Simplified P_N Approximation," *Nucl. Sci. Eng.* Vol. 134, 2000, pp. 1–21.

[6] Leenders, L., "LWR-PVS Benchmark Experiment VENUS-3 (with Partial Length Shielded Assemblies)," FCP/VEN/01, SCK/CEN, September 1988.

[7] Davison, B., *Neutron Transport Theory*, Oxford University Press, London, 1957.

[8] Gelbard, E. M., "Application of Spherical Harmonics Methods to Reactor Problems," Bettis Atomic Power Laboratory, WAPD-BT-20, 1960.

[9] Wesseling, P., *An Introduction to Multigrid Methods*, Wiley, New York, 1992.

[10] Prediction of Neutron Embrittlement in the Reactor Pressure Vessel, OECD Nuclear Energy Agency, NEA/NSC>/DOC(2000) 5, 2000.

[11] White, J. E., Ingersoll, D. T., Wright, R. Q., et al., "Production and Testing of the Revised VITAMIN-B6 Fine-Group and the BUGLE-96 Broad-Group Neutron/Photon Cross-Section Libraries," Oak Ridge National Laboratory, ORNL-6795, NUREG/CR-6214, Rev. 1, 1995.

[12] Zsolnay, É. M., Szondi, E. J., and Nolthenius, H. J., "The Neutron Metrology File NMF-90," IAEA-NDS-171, Rev. 1, January 1999.

Journal of ASTM International, Vol. 3, No. 4
Paper ID JAI13474
Available online at www.astm.org

Craig R. Heimbach[1]

The Neutron Spectrum of NBS-1

ABSTRACT: A proposed set of photonuclear cross sections was used to calculate the neutron spectrum of a RaBe photoneutron source. The calculation used the gamma rays from ^{226}Ra in equilibrium as a driver, transported the gamma rays through the materials of the source, calculated neutron production, and subsequent neutron scattering. The calculation produced 27 % more neutrons than measured, and predicted relatively more low-energy neutrons.

KEYWORDS: calibration, neutron, NBS-1, spectrum, photoneutron

Introduction

NBS-1 is the United States national neutron reference. Although the National Bureau of Standards (NBS) has changed its name to the National Institute of Standards and Technology (NIST), the source has kept its NBS designation. It was developed in the late 1940s as a stable, precisely defined neutron source capable as serving as a calibration reference [1]. The source is driven by the gamma rays emitted from one curie of radium. A photoneutron (as opposed to an alpha-neutron) reaction was chosen to avoid unknowns in the emission rate due to radium-beryllium mixing, and to avoid an increase in neutron emission as alpha-emitting polonium-210 built up over the years.

Figure 1 shows the ^{226}Ra decay chain [2]. Full equilibrium will occur only after the 22.3 year ^{210}Pb comes into equilibrium. Even now, over 50 years after the source was constructed, the second part of the decay chain is still 15 % short of equilibrium. On the other hand, there are no gamma rays above the beryllium photoneutron threshold in the latter portion of the chain, so the Ra(γ)Be source equilibrated within a month of construction.

A disadvantage of the photoneutron source is the high gamma-ray background. This is due to two causes. There is a reaction threshold of 1.665 MeV, so that almost all the gamma rays produce no neutrons. In addition, the reaction cross section for the gamma rays above threshold is on the order of millibarns.

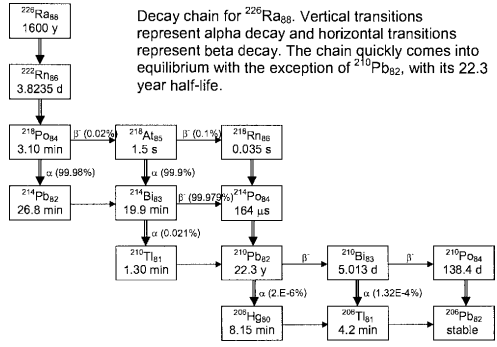

FIG. 1—*^{226}Ra decay chain.*

Manuscript received June 20, 2005; accepted for publication October 25, 2005; published online January 2006. Presented at ASTM Symposium on Reactor Dosimetry, 12th International Symposium on 8–13 May 2005 in Gatlinburg, TN; D. W. Vehar, D. M. Gilliam, and J. M. Adams, Guest Editors.

[1] Physicist, National Institute of Standards and Technology, Gaithersburg, MD 20899.

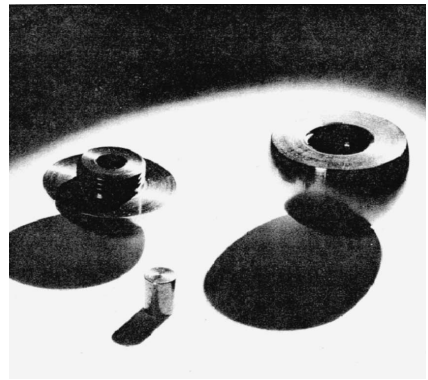

FIG. 2—*40 mm diameter NBS-1 disassembled.*

This gamma-ray background presents health physics concerns and makes active spectroscopy difficult, but does not interfere with the normal source use as a comparison source in a manganese sulfate bath [3]. The gamma-ray field is over 7 msv/h at one metre, even though the neutron emission rate is only 1.234E6 ± 0.8 %-n/s. The neutron/gamma fluence ratio is 0.0000 24 and the dose (sv) ratio is 0.000 54.

Figure 2 shows the construction of NBS-1. It consists of radium ($RaBr_2$) inside a PtIr cylinder which is inserted into the center of a beryllium sphere. The gamma rays from the radium interact with the beryllium to produce neutrons. The beryllium photoneutron threshold energy is 1.665 MeV.

The usual implementation of a National Institute of Standards and Technology (NIST) neutron source calibration is to compare the unknown source against NBS-1 in their ability to activate manganese in a $MnSO_4$ sphere. The NIST sphere is sufficiently large that virtually no neutrons escape before capture. This makes the system insensitive to the neutron spectrum. NIST is exploring the use of a smaller sphere, and this might add some sensitivity to the neutron spectrum.

Measured Spectrum

The neutron spectrum of NBS-1 was measured by Eggler (Fig. 3) [4], using proton-recoil techniques with a hydrogen-based bubble chamber. Eggler found a spectrum with distinct neutron peaks corresponding to the gamma-ray energies of radium decay products.

Based on the kinematics of the $^{9}Be(\gamma,n)^{8}Be$ reaction, one would expect the neutron energy to follow the relation [5]

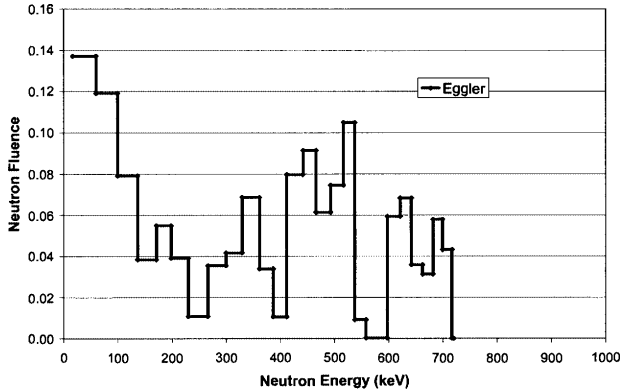

FIG. 3—*Measured neutron spectrum.*

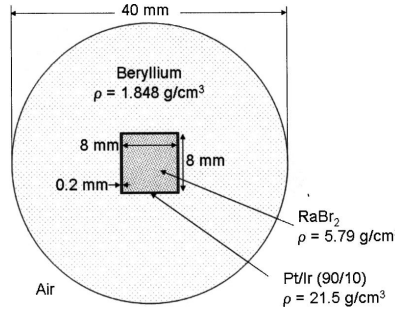

FIG. 4—*Drawing of NBS-1.*

$$E_n = \frac{A-1}{A}\left(E_\gamma - E_t - \frac{E_\gamma^2}{1862(A-1)}\right) + E_\gamma\left(\frac{2(A-1)(E_\gamma - E_t)}{931A^3}\right)^{1/2}\cos\theta$$

where E_γ and E_n are the incident gamma and exiting neutron energies, E_t is the threshold energy, A is the ratio of the target nuclear mass to the neutron mass, and θ is the angle between the incident gamma and the exiting neutron. For RaBe, $E_t = 1.665$ MeV, $A = 8.935$, and the cos(θ) term averages to zero since neutrons are detected in all directions. Thus the prominent Ra-equilibrium gamma rays of 1.76, 2.21 (two close gamma rays), and 2.45 MeV should give rise to neutron peaks of 84, 484, and 697 keV. These correspond reasonably with the peaks in the measurement.

Calculated Spectrum

The International Atomic Energy Agency (IAEA) has recently [6] developed a set of photonuclear reaction cross sections. These are available in Monte Carlo N-particle (MCNP) format (http://t2.lanl.gov/data/photonuclear.html). The cross sections come with a warning that "they are provided for purposes of testing and validation, and they should be treated with caution." Due to the separation of radium from beryllium in NBS-1 and the simple geometry, this neutron source provides a good test of the photonuclear data. Also, any improvement in the knowledge of the neutron spectrum assists NIST in establishing its error budget for neutron fluence calibration.

A straightforward calculation would allow a complete description of the problem. Cross sections would be available for all the materials in NBS-1 and all reactions. Unfortunately, for the materials of NBS-1, photonuclear cross sections are available only for the beryllium. In addition, neutron cross sections were not available for radium.

The lack of photonuclear cross sections was not a severe constraint in the calculation because the other materials have photoproduction reaction thresholds higher than the available gamma rays from the radium decay chain. MCNP has the option of turning off photoproduction in selected materials. This was used to turn off photoproduction for all materials except beryllium.

There were no neutron cross sections available for radium. This was addressed by using bromine cross sections for radium. Density was adjusted to have the correct value. Other techniques discussed below investigate possible problems with this approach.

The equilibrium radium gamma-ray emissions of Sadari and MacMahon [7] were used as gamma-ray input to drive the photonuclear process. MCNP calculates per source particle. Normalization was provided by using the ^{214}Bi absolute yields from Ref. [8]. The normalization of 2.08 gamma rays per disintegration provided the scaling for the calculation.

The source geometry is relatively simple and is shown in Fig. 4. Figure 5 lists the MCNP geometry and materials input for a typical run.

Figure 6 shows how the radium-equilibrium gamma rays line up with the beryllium photoneutron cross section. The rapid change in cross section makes the neutron yield a strong function of the exact gamma ray energy.

```
20   2 -5.79      -40 -44  +46          imp:n=1 imp:p=1 $ inner bromine cylinder
40   3 -21.5      -30 -34 36 #20        imp:n=1 imp:p=1 $ cylinder shell
50   4 -1.848     -20 #20 #40           imp:n=1 imp:p=1 $ beryllium sphere
60   1 -1.293E-3 -50 20                 imp:n=1 imp:p=1 $ outside air
70   0            50                    imp:n=0 imp:p=0 $ dump

c  surfaces
20    so    2.0          $ 4 cm outer diameter of berylium
c
30    cz    0.42         $ 0.84 cm outside of pt/ir capsule
34    pz    0.43         $ top plane of capsule
36    pz   -0.43         $ bottom plane of capsule
c
40    cz    0.40         $ 0.80 cm inside of pt/ir capsule
44    pz    0.41         $ top plane of capsule (inside)
46    pz   -0.41         $ bottom plane of capsule
c
50    so  200.           $ Problem limits

phys:p 10. 0 0 1           $ 1 allows biased photoneutron production
phys:n  20.00 20.0         $ 20 MeV is high energy.
mode n p                   $ neutron and gamma only
c
m1    7014.60c 0.789985   8016.60c 0.210015   $ air
c m2    88000.04p 0.334 35000.04p 0.666       $ radium-dibromide (no neutron)
m2    35079.55c 0.5069 35081.55c  0.4931      $ bromine only (no photo-
neutrons)
mpn2      0                0
m3    78000.42c  0.90 77000.55c  0.10         $ platinum/iridium 90/10
mpn3      0                0                  $ no photoneutrons
m4    4009.26u   1.00                         $ beryllium
```

FIG. 5—*Portion of MCNP input describing geometry and cross sections.*

The calculated neutron spectra reported here represent the neutron fluence at 200 cm. Figure 7 shows the calculated Ra(γ)Be neutron spectrum. The spectra are normalized to one neutron.

The measured and calculated spectra are quite different. The measured spectrum shows substantially more neutrons above 200 keV. Peaks apparent in the measured spectra are absent in the calculated spectra. The measurement provided no absolute normalization; however, the calculation may be normalized to the decay-corrected curie of radium present within NBS-1. The gamma peak data of Ref. [7] is not absolutely normalized; however, Ref. [8] provides absolute gamma ray yields, and so the neutron fluence rate could

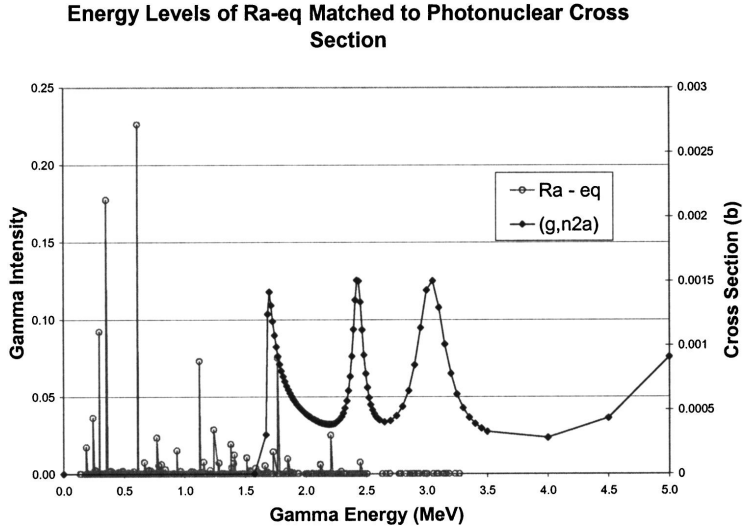

FIG. 6—*Gamma rays from radium aligned with photoneutron cross section.*

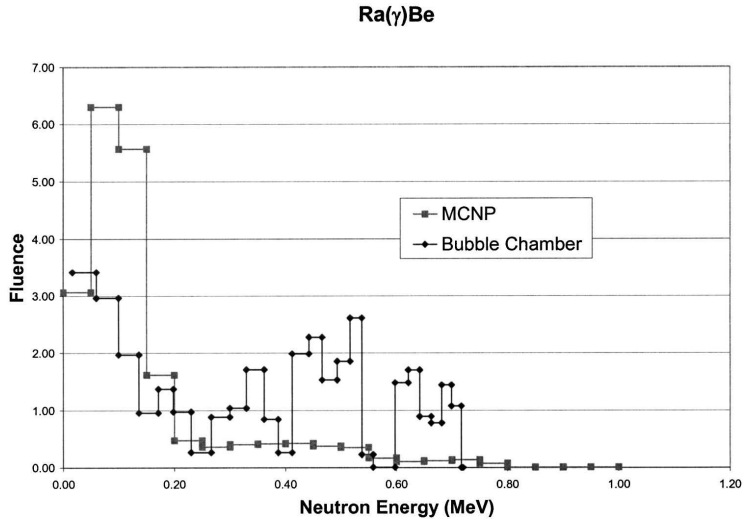

FIG. 7—*Calculated and measured Ra(γ)Be neutron spectrum.*

be calculated to compare against NIST calibrations. The comparison shows the calculation predicting 27 % more neutrons than NIST measures.

Two sets of calculations were performed to investigate scattering effects which may affect the neutron spectrum. In the first case, monoenergetic neutrons were assumed to be generated inside the inner $RaBr_2$ cylinder. The extent to which they maintained their energy can be used as an indicator of the extent of neutron scattering as they pass through the beryllium. Figure 8 shows spectra outside the beryllium for four monoenergetic neutron sources. In each case, the original spectrum retained its shape. This implies that, if neutron peaks were generated by the photoneutron process, distinguishable peaks would still be seen on leakage.

A second investigation looked into photon scattering as the gamma rays pass through the source. As with the neutrons, the photon spectrum outside the beryllium sphere for a monoenergetic source of gamma

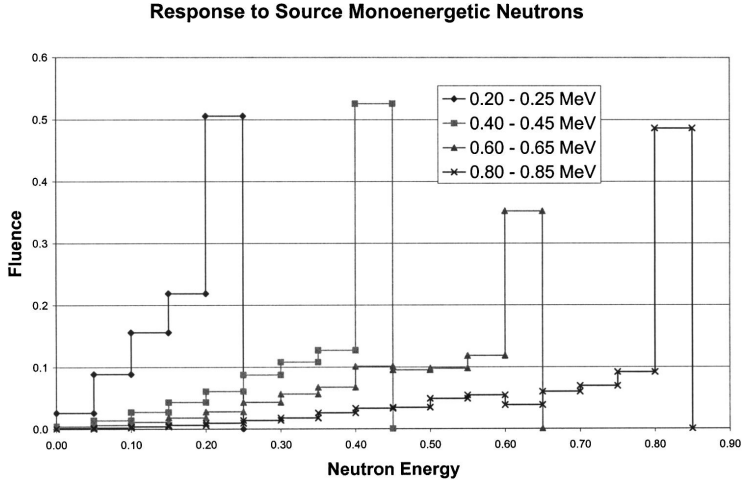

FIG. 8—*Neutrons exiting beryllium sphere for monoenergetic neutron sources.*

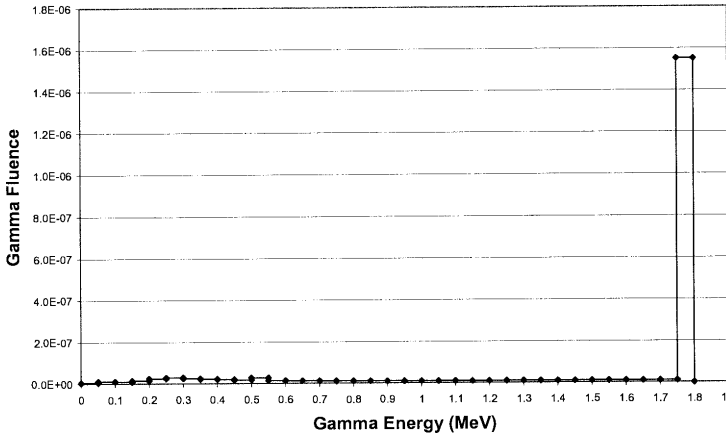

FIG. 9—*Gamma rays exiting beryllium sphere for 1.76 MeV gamma-ray source.*

rays shows minimal down scattering (Fig. 9). There was about a 10 % attenuation of the gamma-rays fluence due to absorption within the $RaBr_2$. Otherwise, there was no effect. The sphere is not sufficiently large for either neutron or gamma-ray scattering effects to significantly affect the neutron spectrum.

A further set of calculations investigated the effects of not having neutron cross sections available for radium. Gamma-ray cross sections were available for all the materials, so a gamma-only calculation could be run with all materials correctly described. This was done, and all photon diagnostics showed that there were no errors in the gamma-ray portion of the problem due to cross section. In particular, a photonuclear-production-weighted MCNP flux (F4) diagnostic was compared for two calculations. The diagnostic consisted of the gamma-ray flux weighted by the photoneutron production cross section. A comparison was made of the photoneutron production reaction rates in the beryllium with and without the correct radium in the center region. The same photoneutron production rate was observed, to within 1 %.

Neutron interactions within the interior of the $RaBr_2$ source cylinder were investigated by quantifying the number of neutrons, generated within the beryllium, that passed back through the inner cylinder. One calculation adjusted the density of the $RaBr_2$ to zero, in an attempt to determine the neutron loss within the cylinder. The zero-density case would eliminate any neutron loss. Neutron loss was negligible. Another calculation made the inner cylinder a zero-importance region, killing any neutrons that entered it. MCNP did not allow doing this for only the neutrons, so the importance was zeroed for both neutrons and gamma rays. A surface-source write/read set of calculations was performed, since the gamma rays could not be generated in a zero-importance cell. Only about 10 % of the neutrons generated within the beryllium pass back through the radium cylinder. These effects are sufficiently small that, neutron interactions with the radium are unlikely to explain the differences between measured and calculated spectra, or discrepancies in overall neutron fluence.

Conclusions

A MCNP calculation was performed for the NIST national neutron reference NBS-1, a RaBe source driven by the gamma rays from radium-226 and its daughters. The calculation used a proposed photoneutron production cross section developed under an IAEA effort. The calculation gave a neutron flux 27 % higher than the NIST calibration value, and a neutron spectrum with significantly more low-energy neutrons than a reported measurement.

The calculation did not show well-defined peaks in the neutron spectrum, as might be expected for specific gamma-ray lines incident on beryllium. Neither neutron nor gamma-ray scattering within the various materials was sufficient to broaden the peaks into a continuum. Cross-section approximations, mainly due to not having a neutron cross section for radium, also are not large enough to explain the discrepancies.

The intense gamma-ray background of the source makes neutron spectral measurement difficult.

One would expect peaks to appear in the neutron spectrum based on the kinematics of the two-body breakup of ^{9}Be into a neutron and ^{8}Be. Any mixing of a three-body breakup (neutron plus two alpha particles) would tend to smooth the neutron peaks. The discrepancy between calculation and measurement implies too high a mixing of three-body breakup in the cross section used for calculation.

[1] DeJuren, J. A., Padgett, D. W., and Curtiss, L. F., "Absolute Calibration of the National Bureau of Standards Photoneutron Standard: I," *J. Res. Natl. Bur. Stand.* 55(2), 63–69 (1955).

[2] Kogan, A. V. and Rusinov, L. I., "Neutron Emission by Excited RaD Nuclei," *Sov. Phys. JETP*, 5, 365–371 (1957) reports neutron emission from RaD (^{210}Tl). It would produce about 0.3 % of the total neutron fluence. Since it equilibrates with ^{226}Ra, and the neutron energy ⩽0.5 MeV is similar to the other neutrons, the effect on neutron calibration is negligible. Its effects are not included in the calculated spectra.

[3] McGarry, E. D. and Boswell, E. W., *Neutron Source Strength Calibrations*, Natl. Bur. Stand. (U.S.), Spec. Publ. 250–18, March 1988.

[4] The Neutron Spectrum of a Radium Beryllium Photo Source, ANL-4476, 1950. This spectrum may also be found in *Fast Neutron Physics, Part I: Techniques*, edited by J. B. Marion and J. L. Fowler, Interscience, New York, 1960.

[5] Price, B. T., Hortom, C. C., and Spinney, K. T., *Radiation Shielding*, Pergamon Press, Elmsford, NY (1957).

[6] Handbook on Photonuclear Data for Applications, IAEA TECDOC 1178, Final Report, Oct. 2000.

[7] Sadari D. and MacMahon, T. D. "Gamma-ray emission probabilities in the decay of ^{226}Ra and its Daughters," *J. Radioanal. Nucl. Chem.* 244(2) 463–469 (2000).

[8] Ekström, L. P. and Firestone, R. B., WWW Table of Radioactive Isotopes, database version 2/28/99 from URL http://ie.lbl.gov/toi

Journal of ASTM International, Vol. 3, No. 7
Paper ID JAI13475
Available online at www.astm.org

N. E. Holden,[1] *R. N. Reciniello,*[2] *and J.-P. Hu*[3]

Radiation Dosimetry in the BNCT Patient Treatment Room at the Brookhaven Medical Research Reactor

ABSTRACT: The BMRR was a 3 MW light water reactor that had an epithermal neutron beam that was used to perform clinical trials on patients with malignant brain tumors. A series of measurements and calculations had been performed in the treatment room both prior to the trials and during the trials. The details of the measurements and the Monte Carlo calculations are presented and compared.

KEYWORDS: BNCT, BMRR, neutron dose, gamma dose, epithermal neutrons

Introduction

The Medical Research Reactor at the Brookhaven National Laboratory (BMRR) was a heterogeneous, tank type, light water cooled and moderated, graphite re ected reactor, which was operated on demand at a power level up to 3 MW for medical and biological research [1]. The reactor rst went critical on March 15, 1959, with 17 fresh fuel elements (2.52 kg uranium-235 in a total of 2.7 kg uranium) in the center core. The BMRR had two treatment rooms on opposite sides of the core. It had a predominately thermal neutron beam in the Thermal Neutron Irradiation Facility (TNIF) on the west side of the core. By early 1990, a redesigned beam line had a predominately epithermal neutron beam in the Epithermal Neutron Irradiation Facility (ENIF) on the east side of the core [2].

The ENIF was approximately 11 ft. by 21 ft. in size with its focal point consisting of a bismuth plate mounted in the wall adjacent to the reactor shield about 36 in. above the oor. The beam originated at a shutter constructed of 0.75 in. steel lled with concrete and weighing ~21 tons. Access to the ENIF was through a pair of hand operated steel shielding doors, each 42 in. wide, 84 in. high, and 5 in. thick. The inner door had a 4 in. thick layer of paraf n on the side facing the reactor. The doors weighed 5000 lb each. Additional shielding material had been added to the entire beam port at reactor wall within the ENIF. The shielding material consisted of 2 in. thick polyethylene sheets, which were impregnated with 95 % enriched ^{6}Li in lithium carbonate (Li_2CO_3). The shielding sheets around the port face were designed to allow the insertion of a variety of different beam collimators.

The ENIF, as described in Ref. [1], served as the Patient Treatment Room, where the epithermal neutron beam was primarily used to perform clinical trials on patients with malignant brain tumors (glioblastoma multiforme). Boron neutron capture therapy (BNCT) was the treatment used in the clinical trials. In 1936, Locher proposed that medical research could be advanced, by destroying cancerous cells using neutrons [3]. He suggested the injection of a soluble, nontoxic compound of boron into super cial cancer, followed by bombardment with slow neutrons, in order to liberate the ionization energy. The minor isotope of boron ^{10}B has an abundance of 19.8 %. The $^{10}B(n,\alpha)^{7}Li$ reaction, as shown in Fig. 1, has a thermal neutron cross section of 3.838×10^{-21} cm^2. For the 94 % reaction branch as depicted in Fig. 1, the released ^{4}He, has an energy of 1.47 MeV, with a range of 10.1 μm (in water) and an average linear energy transfer of 150 keV/μm. The residual nucleus ^{7}Li has an energy of 0.85 MeV with a range of 4.9 μm and an average LET of 170 keV/μm. Due to the short range of both of these tracks, almost all of the energy released is deposited within a distance of a cell diameter of where the reaction takes place. If the boron can

Manuscript received June 20, 2005; accepted for publication April 19, 2006; published online June 2006. Presented at ASTM Symposium on Reactor Dosimetry, 12th International Symposium on 8 13 May 2005 in Gatlinburg, TN; D. W. Vehar, D. M. Gilliam, and J. M. Adams, Guest Editors.

[1] Guest Physicist, National Nuclear Data Center, Brookhaven National Lab., Upton, NY 11973-5000.
[2] Health Physicist, Radiological Control Division, Brookhaven National Lab., Upton, NY 11973-5000.
[3] NY-State Professional Engineer, National Synchrotron Light Source, Brookhaven Lab., Upton, NY 11973.

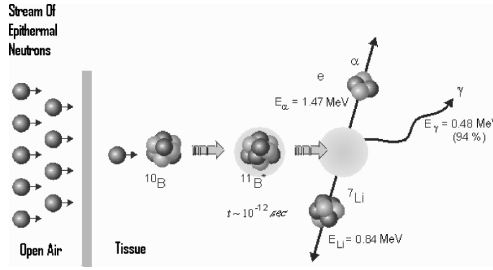

FIG. 1 *The BNCT mechanism and energy release from reaction of $^{10}B(n, \alpha)^7Li$ in tissue.*

be selectively targeted in a cancerous cell, only the cancerous cell would be destroyed, while the nearby healthy cells would be relatively unaffected.

In the BNCT treatment, the patient is initially injected with a boron compound (the boron compound that was initially used was sulfhydryl borane ($Na_2B_{12}H_{11}SH$), while the last compound of boron that was used was boronophenylalanine-fructose (BPA-F) [4]). After the level of the boron in the blood was sampled and determined by prompt photon analysis, the patient was subsequently irradiated with epithermal neutrons. In the earliest measurements performed at the BNL Graphite Research Reactor in the 1950s, thermal neutrons were used. When the initial treatments were performed at the BMRR, thermal neutrons were still being used. The treatments were not successful for a few reasons. The boron compound originally used was not preferentially absorbed in the cancerous cells and the tumors were deep seated (anywhere from 1 to 3 in. beneath the scalp surface with an average depth of ~2.375 in.) and the thermal neutrons were found to be absorbed in the hydrogenous material of the head, before they could reach these tumor cells.

With the development of the new epithermal neutron beam and a new boron compound, BPA-F, BNCT clinical trials were again begun at the BMRR on September 13, 1994 [5]. From that time, until the trials were suspended after May 20, 1999, a total of 54 patients had undergone such clinical BNCT trials at the BMRR. These patients were treated under a series of protocols in which the reactor power was first limited to 2 MW and later raised to 3 MW and the patients were initially irradiated in one session and later they were irradiated in a series of sessions to adjust the irradiation time to the level of boron concentration in the blood, to obtain the required dose for each session (boron was remeasured between sessions). The injected boron compound, BPA-F, was found to be preferentially absorbed in the tumor cells rather than normal cells with a ratio of up to 4 to 1. To be conservative, this ratio was assumed to be ~3.5 to 1. Non-BNCT medical and biological experiments continued at the BMRR until it finally ceased operations. The final shutdown of the BMRR occurred at 12:19 PM on December 28, 2000. The reactor fuel and all of the spent fuel in the BMRR has since been removed and shipped off-site.

Measurement Program

The original critical BMRR core contained 17 fuel elements, which were enriched to 93% in ^{235}U. The core, during the last of the BNCT trials, had 32 enriched fuel elements. To control the total amount of neutron and gamma-ray dose that a patient would receive during the clinical trials, a series of measurements were performed before, during, and after the treatment irradiations. Bare gold foils, cadmium covered gold foils, and various threshold detector foils were used to determine the neutron flux values. Thermoluminescent dosimeter (TLD) badges with ^6LiF and ^7LiF chips were used to provide experimental data on the neutron dose rates and the gamma-ray dose rates. TLD test badges used $^{6,7}LiF:Mg, Ti$ as the thermoluminescent material in the form of solid chips. Three of the chips used were TLD-700 material (chips enriched in ^7Li to 99.93 %), while one chip was TLD-600 material (chips enriched in ^6Li to 95.6 %). These badges also had filters of plastic, copper, and thin aluminized Mylar® film of various thicknesses to separate and measure mixed fields of neutrons, electrons, and gamma rays.

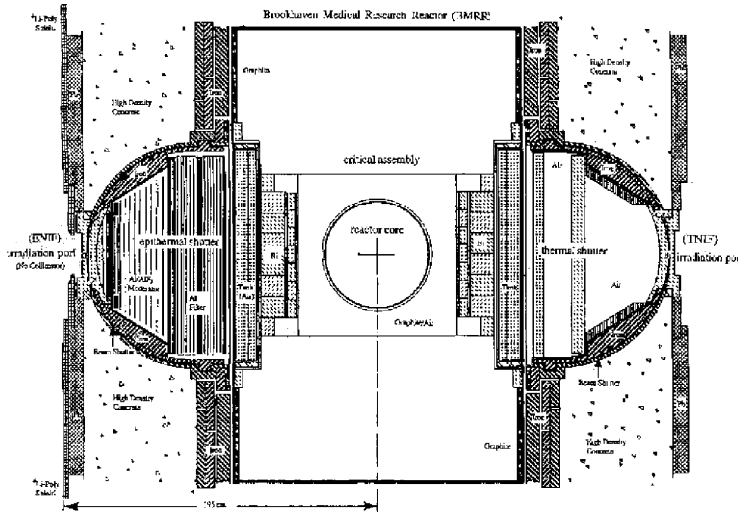

FIG. 2 *Simulation of ENIF and TNIF by the MCNP code shows the symmetry of circular shutter and concrete shield to the critical assembly at reactor center, where homogenized core, moderator, and reflector areas are setup in model.*

The Monte Carlo Program

To calculate the ux of thermal and epithermal neutron in the beam through a simulated BMRR core, the shutter assembly, and the beam irradiation port, a computational technique and an experimental method to validate these computations were required. We used the Monte Carlo based code, MCNP-4B2 [6], to calculate the neutron and gamma-ray uxes and absorbed doses, while measurements of the uxes and doses at the core-shutter interface and at the irradiation port were made using gold foils and TLDs. The MCNP code is a general-purpose FORTRAN-compiled software package, which can be utilized to model any single-particle motion or coupled neutron-photon-electron transport in a three-dimensional geometry consisting of different material regions. We used continuous cross sections for neutron and photon transport and reaction rate calculations and appropriate thermal neutron scattering function $S_{\alpha\beta}$ to treat neutron interactions with light materials such as H_2O, D_2O, graphite, and polyethylene in the MCNP package. To expedite particle tracking, a newer version of the program (MCNP-4C) was used, allowing the data processing to be performed on a parallel computing platform. The continuous-run option increased the particle history and reduced the tally s statistical uncertainty.

The measured neutrons varied from thermal neutron energies (0.001 to 0.4 eV) up to fast neutron energies (0.1 to 10.0 MeV). The MCNP program was used to mock up the geometry of the reactor core down to the polyethylene and lithium carbonate collimator on the port face and the patient treatment room, as shown in Fig. 2. For ef ciency, the heterogeneous reactor core with fuel elements, control rods, water coolant, graphite moderator, and aluminum llers was replaced by a homogeneous cylinder with U, H, O, Al, C, and B in the appropriate nuclide composition. The use of randomly distributed sources rather than point sources in this region increased the number of particle histories and the reaction rate in the entire MCNP geometry, thus expediting statistical sampling for the tallies. Core peripheral llers and their surrounding coolant were simulated by an Al-H_2O- lled cylindrical shell, which was enclosed within an aluminum pressure vessel wall. To properly simulate the homogenized critical core under different operational conditions, the weight percentage of the nuclides in the model input had to be adjusted according to the recorded fuel inventory and critical rod bank position.

For the shutter-closed case, the BMRR basic design feature of $K_{\text{eff}}=1$ maintained in the graphite re ected critical assembly alone (1.7 m cube) was utilized for the source term check-up. Criticality calculations using the shutter-opened con guration were also performed in order to compare the computed thermal neutron ux with the measured ux at the core-shutter interfacial air gap. In this location, most of

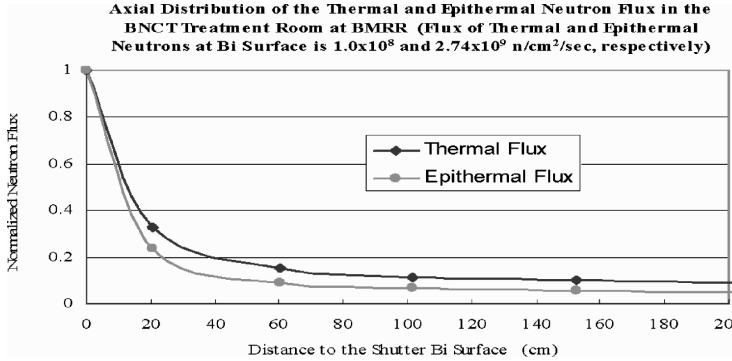

FIG. 3 *Axial distribution of the thermal and epithermal neutron flux along the beam path starting from the shutter Bi surface and passing through the Li_2CO_3-based collimator in the BNCT patient treatment room at ENIF of the BMRR*

the neutrons have been thermalized into the energy region at or below 100 keV, as they move downstream (into the epithermal shutter region) for use in the BNCT treatment.

The Patient Treatment Room

In the ENIF, the neutron beam was located three feet above the oor in the center of the reactor wall. Radiation shielding in the beam port ended with a bismuth shield. For the BNCT treatment, experimental comparisons were made with the patient in place, with a tissue equivalent head phantom in place to mock up the patient s head position and with the room empty to study the impact of the patient on the background ux and dose rate values. At 4 in. downstream of the bismuth shutter apex along the beam path, a removable six in. thick collimator of polyethylene and Li_2CO_3 (95 % ^{6}Li-enriched, to increase thermal neutron absorption) is located. The collimator had a concave cavity with an 8 in. diameter on the reactor side tapering to a 4.75 in. diameter on the treatment room side, for optimal beam focusing. When the collimator is in place, the axial distribution of the thermal and epithermal neutron uxes can be shown by the two curves in Fig. 3. Note that although the epithermal neutron ux decreases relatively faster than the thermal neutron ux, its absolute value is 27 times larger (see the note on the normalized ux values above the curves). Note also in Fig. 3, the rapid fall-off in the rst 20 cm from the bismuth surface of the thermal and epithermal neutron ux values is due to the effect of the Li_2CO_3 collimator, which absorbs most neutrons that are not focused straight down the center of the collimator.

Neutron and Gamma-ray Dosimetry

Before the BNCT clinical trials began in 1994, there was a concern about the response to a patient emergency and the magnitude of the gamma-ray dose rate that would be received by personnel in responding. To obtain an estimate of the gamma-ray dose rate, an ion chamber (Eberline RO2) measured the dose rate at both the port face and at one foot from the port face (the approximate position of a patient). Under the scenario that the reactor went critical and reached a power level of 10 kW, the measured gamma-ray dose rates were 400 μGy/h (40 milli-Rem/h, mR/h) and 180 200 μGy/h (18 20 mR/h), respectively. When the reactor power was raised to 3 MW and operated for 20 min and the power was dropped to 10 kW, these two dose rates were measured to be 1 and 0.4 mGy/h, respectively. After a subsequent 20 min reactor shutdown, the gamma-ray dose rates remained at the same levels of 1 and 0.4 mGy/h, primarily due to the decay gamma radiation from the core. The two dose rate readings at 10 kW operation and during the subsequent shutdown give approximately equal readings because the decay gamma radiation component was generated during the 3 MW operation, while the core prompt gamma radiation component was generated during the 10 kW operation and is now 300 times lower (rather than equal) in

TABLE 1 *Epithermal room neutron & gamma-ray dose rates measured by TLD at 3 MW.*

Location in Patient Treatment Room	Empty Room N (Sv/h)	Empty Room γ (Gy/h)	Phantom in Place N (Sv/h)	Phantom in Place γ (Gy/h)	Patient in Place N (Sv/h)	Patient in Place γ (Gy/h)
Door	0.21	0.015	0.13	0.008	0.14	0.013
North Window	0.32	0.032	0.19	0.025	0.18	0.037
South Window	0.20	0.017	0.11	0.009	[a]	
3 ft high (Opp. Wall)	0.45	0.055	0.13	0.032	0.13	0.047
8 ft high (Opp. Wall)	0.41	0.041	0.15	0.032	0.15	0.040
2 ft right (3 o clock)	0.35	0.048	0.29	0.048	0.52	0.068
2 ft down (6 o clock)	0.45	0.045	0.28	0.030	0.65	0.085
2 ft left (9 o clock)	0.32	0.064	0.24	0.051	0.27	0.094
2 ft up (12 o clock)	0.26	0.150	0.23	0.230	0.30	0.240
4 ft right (3 o clock)	0.29	0.025			0.14	0.078
Collimator Center	2.66	1.380				

[a] indicates no measurement was taken at this location

intensity. The loss of the prompt gamma component from the 300 times larger decay gamma component is not discernible by the instruments.

Another early concern was raised about whether radiation workers would be subject to a signi cant gamma-ray dose rate from the normal work (nonemergency) with patients who were being irradiated. Gamma-ray dose rates, received by the key staff personnel involved in the care during the treatment, were measured. These workers prepared the room and the patient, operated the shutter, located the patient in the proper position in the room, and moved the patient in and out of the room during the treatment. The reactor power was kept at relatively low level ($\sim$10 kW versus 3 MW operation), whenever these workers were in the treatment room. These workers would include the responsible physician, the radiation oncologist, the nurse, the medical physicist, and the health physicist. Results of the measurements, which were taken during the treatment of the rst 12 patients undergoing BNCT in the clinical trials, gave average gamma-ray doses received by these staff members that varied from 14 μGy or (1.4 mrad) to 32 μGy (3.2 mrad) per individual. The highest gamma-ray dose reading recorded during treatment of any individual patient was 70 μGy (7 mrad), which was received (for separate patients) by the radiation oncologist and by the medical physicist.

The neutron ux was measured and calculated at the 4.75 in. opening of the epithermal beam port collimator. The thermal neutron ux was $\sim 3 \times 10^7$ n/cm^2/s, the epithermal neutron ux was $\sim 6 \times 10^8$ n/cm^2/s and the fast neutron ux was $\sim 2 \times 10^7$ n/cm^2/s. There was reasonable agreement ($\leq$15 % discrepancy) between the MCNP calculations and the various bare gold foil, cadmium covered gold foil and threshold foil measurements used to determine the neutron ux values.

In October 1995, a measurement of the neutron dose rate, at a power level of 3 MW and at a distance of 1 ft from the collimator, was performed in the ENIF using an Eberline ASP1 rem-ball (a neutron sensitive instrument). The resulting dose rate was 1.0 Sv/h (100 rem/h). At the same power level, a measurement of the gamma-ray dose rate at one foot from the collimator was 1.0 Gy/h (100 rad/h), using an NRC ADM multipurpose gamma sensitive instrument. In November 1997, neutron and gamma-ray dose rates were measured at the collimator face using monitoring badges with ^{6}LiF and ^{7}LiF chips. The results were 2.66 Sv/h (266 rem/h) and 1.38 Gy/h (138 rad/h). Both of these measurements at the collimator face should be larger than those made at 30 cm away due to the geometric factor, which may have a $1/r$ or $1/r^2$ dependence. This is indeed the case.

A series of experiments [7] on neutron and gamma-ray dose rates were performed in the ENIF between October 1997 and January 1998. The results measured at 3 MW operating power using the TLD personnel monitoring badges with ^{6}LiF and ^{7}LiF chips are given in Table 1. It can be noted from Table 1 that the neutron and gamma-ray dose rates fall off rapidly as one moves out from the center of the beam. For the empty room, there is a reduction in the neutron dose rate at the reactor face by a factor of 5 to 10 in all directions (3, 6, 9, and 12 o clock) at a distance of 2 ft from the beam center, compared to the collimator center results. There is a similar reduction of 10 to 30 in the gamma-ray dose rates. For the area above the collimator, there appears to be much less gamma-ray shielding, resulting in a much larger gamma-ray dose rate under all conditions.

By comparing the data with the patient in place to the data for the empty room, there is obviously

neutron scattering back from the patient to the face of the reactor. However, the scattering of the gamma radiation back to the reactor face is larger. Although there is a signi cant reduction in the neutron dose rate at the 3 ft beam center position on the wall opposite the patient, there appears to be much more absorption of neutrons than gamma radiation by the patient, which is the preferred situation. It might be noted that the head phantom absorbs more gamma radiation than does the patient. More of the average physical dose to the patient s brain (~1.6 times) came from the gamma-ray radiation rather than from the boron-10 neutron capture reaction [8], since much of the larger neutron component of the radiation at the surface was absorbed in penetrating the scalp to reach the tumor and not as much of the gamma radiation component had the same reduction.

A question that has frequently been asked is, What was the status of the patient treatment? Clinical BNCT trials of patients with malignant brain tumors were carried out at the BMRR for half a decade (1994 1999), with encouraging results obtained on 54 patients infused with the then recently developed BPA-F compound, followed by irradiation of the high-intensity epithermal neutron beam. The patients selected for these clinical trials had pretrial survival rates estimated at from 3 to 9 months. The mean post-treatment survival time for all 54 glioblastoma multiforme patients, who were treated under these BNCT protocols, was ~22 months. The survival rate for two of these patients (3.7 %) was greater than 5 years. Another patient (1.9 %) still survives today (May 2005). The combined 5.6 % survival rate of greater than 5 years, and the mean survival time post-BNCT treatment, indicates that BNCT, coupled with the use of the BPA-F compound and an epithermal neutron beam, is a promising treatment for glioblastoma multiforme.

Conclusions

The above data indicate a well-characterized neutron beam in the BMRR facilities, where the desired epithermal neutron ux predominates over both fast and thermal neutron uxes in the ENIF. The residual gamma dose-rate is insigni cant at the BNCT treatment room, in which the gamma dose is about one tenth of the neutron dose to the skin of treated patient. Through the use of TLDs, it is also con rmed that gamma dose to the attending personnel is minimal, at a level close to the background radiation. The dose-rate, which drops rapidly during post shutdown, indicates that emergency access of the facility with no speci c body protection would not result in any radiation hazard to response personnel. Good agreement is obtained from various measurement techniques such as TLD and gold foil irradiation, and collected data from measurements agree with the theoretical results from MCNP calculations. When a patient is located in front of the beam port during shutter opening, the scattering of gamma rays back to the reactor face has been found to be larger than that of neutrons; however, since the dose decreases with $1/r^2$, the effect from beam scattering is very limited. Based on consistent results from particle transport in the ENIF, it is concluded that during the process of BNCT the dose that deposits at the tumor cell (^{10}B tagged) is much larger than that accumulated from the whole body of the patient, which is, in turn, much larger than that absorbed by the attending personnel to the treatment room.

The conclusions from the measurements and the impact on the patient treatment indicated that although the beam at BMRR was well collimated and concentrated for the patient treatment, there was still a need to improve the beam to maximize the epithermal neutron beam compared to the gamma radiation and the fast neutron components of the beam. Work had already begun on the improvement of the epithermal beam with the design of a new beam using a ssion converter plate in the shutter [9] at the time that the BMRR was permanently shut down.

The recommendations from the BMRR BNCT clinical trials [8] called for an increase in the boron compound dose and in its time of delivery. These recommendations have since been followed up by the Studsvik s group [10]; a total of 900 mg of BPA-F per kg of body weight compared to a maximum of 330 mg of BPA-F per kg of body weight at BMRR and 6 h of BPA-F infusion compared to 2 h of BPA-F infusion at BMRR. Efforts worldwide on nding a successor boron compound to BPA-F, which would have an improved tumor cell to normal cell absorption ratio in the body, is still continuing.

Acknowledgment

This research was supported by the US-DOE under the Contract No. DE-ACO2-98CH10886.

References

[1] Godel, J. B., Description of Facilities and Mechanical Components (MRR), BNL-600 (T-173), Brookhaven National Laboratory, February 1960.

[2] Liu, H. B. et al., Upgrades of the Epithermal Neutron Beam at the Brookhaven Medical Research Reactor, *Cancer Neutron Capture Therapy* Y. Mishima, Ed., Plenum Press, NY, 1996.

[3] Locher, G. L., Biological Effects and Therapeutic Possibilities of Neutrons, *Am. J. Roentgenol. Radium Ther.*, Vol. 36, 1936, pp. 1 13.

[4] Coderre, J. A. et al., Biodistribution of Boronophenylalanine in Patients with Glioblastoma Multiforme: Boron Concentration Correlates to the Tumor Cellularity, *Radiat. Res.*, Vol. 149, 1998, pp. 163 170.

[5] Chanana, A. D. et al., Boron Neutron Capture Therapy for Glioblastoma Multiforme: Interim Results from Phase I/II Dose Escalation Studies, *Neurosurgery*, Vol. 44, No. 6, 1999, pp. 1182 1193.

[6] MCNP A Monte Carlo N-Particle Transport Code, (version 4B2), J. F. Briesmeister, Ed., developed by the US-DOE Los Alamos National Laboratory (LA-12625-M), and distributed by the US-DOE Oak Ridge National Laboratory (CCC-660), 1997.

[7] Holden, N. E. et al., Radiation Dosimetry for the NCT Facilities at the Brookhaven Medical Research Reactor, *Frontiers in Neutron Capture Therapy*, (M. F. Hawthorne et al., Eds.), Kluwer Academic/Plenum Press, NY, 2001.

[8] Diaz, A. Z. Assessment of the Results from the Phase I/II Boron Neutron Capture Therapy Trials at the Brookhaven National Laboratory from a Clinician s Point of View, *J. Neuro-Oncol.*, Vol. 62, 2003, pp. 101 109.

[9] Hu, J.-P. et al., Optimization of the Epithermal Neutron Beam for Boron Neutron Capture Therapy at the Brookhaven Medical Research Reactor, *Operational Radiation Safety*, Vol. 86, No. 2, 2004, pp. 103 109.

[10] Capala, J. et al., Boron Neutron Capture Therapy for Glioblastoma Multiforme: Clinical Studies in Sweden, *J. Neuro-Oncol.*, Vol. 62, 2003, pp. 135 144.

Journal of ASTM International, Vol. 3, No. 8
Paper ID JAI100358
Available online at www.astm.org

B. Khorsandi,[1] *T. E. Blue,*[2] *W. Windl,*[3] *and J. Kulisek*[1]

TRIM Modeling of Displacement Damage in SiC for Monoenergetic Neutrons

ABSTRACT: Although silicon carbide is a very good semiconductor material for the fabrication of diode detectors for use as neutron power monitors in nuclear reactors, the electrical properties of the diodes may be altered because of interactions between energetic neutrons and SiC atoms. If the energy that is transferred from a neutron to an atom in a collision exceeds some threshold value, the atom will be moved from its original position, creating displacement damage. Accurately modeling displacement damage is a first step to finding ways to eliminate or decrease the amount of damage the displacements induce. The methodology that we have used to estimate the number of displacements per atom per fluence, using two codes (MCNP and TRIM) is presented in this paper, along with examples of the results of our calculations.

KEYWORDS: displacement damage, MCNP, TRIM, PKA

Introduction

Silicon carbide (SiC) semiconductor diode detectors that are operated in the pulse mode may prove to be useful as neutron power monitors for Generation IV nuclear reactors. As a semiconductor material, SiC has very good thermal, chemical, neutronic, and electrical properties, particularly at high temperatures. Compared to Si, SiC is a radiation hard material; however, like Si, the properties of SiC are changed by irradiation by a large fluence of energetic neutrons, as a consequence of displacement damage. Since predictions of displacement damage and the concomitant radiation effects are important for deciding where the SiC detectors should be placed, we discuss below our efforts to quantify the displacement damage that may be expected to occur as a consequence of neutron irradiation of SiC diode detectors.

In studies of displacement damage, one attempts to estimate the number and configuration of displacements created by projectile particles [1]. The study of displacement damage does not deal specifically with the effects of radiation, the impact of time or temperature, or the recovery of defects. These are considerations in the study of radiation effects; however, the accurate prediction of displacement damage is a first step in the accurate prediction of radiation effects.

In a classic paper, Kinchin and Pease introduced a simple model to estimate the number of displacements per primary knock-on atom (PKA) [2]. Later, Norgett et al. proposed a method to approximate the number of Frenkel pairs that are created by energetic particles more accurately [3]. Because of the importance of these analytic formulations, later in this paper, predictions of displacement damage that we have obtained using detailed Monte Carlo modeling are compared with predictions of displacement damage made using these simple models. Coulter and Parkin formulated the displacement damage methodology for polyatomic materials [4,5].

Most modeling of neutron induced displacement damage, until recent times, has been focused on structural materials, especially iron. Notable among the papers that are not focused on iron is the paper by Lee and Farnum [6] that used SPECTER [7] and TRIM [8] to estimate the number of vacancies per neutron in alumina. The methods that we have used in this paper are similar to the methods that Lee and Farnum have used in that both we and they have predicted PKA source distributions with a computer code and used the resultant PKA source distributions as input to TRIM. However, our methods are different in that

Manuscript received June 20, 2005; accepted for publication May 5, 2006; published online June 2006. Presented at ASTM Symposium on Reactor Dosimetry, 12th International Symposium on 8–13 May 2005 in Gatlinburg, TN; D. W. Vehar, D. M. Gilliam, and J. M. Adams, Guest Editors.

[1] Graduate Student, Ohio State University, Nuclear Engineering Program, Columbus, OH 43202.
[2] Professor, Ohio State University, Nuclear Engineering Program, Columbus, OH 43202.
[3] Professor, Ohio State University, Department of Materials Science and Engineering, Columbus, OH 43210.

our calculations of the PKA source have been generated using the Monte Carlo code MCNP5 [9] with cross sections that are continuous in energy, whereas their PKA source has been generated by using SPECTER. As an additional point of reference, Weber et al. at PNNL have estimated the number of displacements per PKA [10] for SiC as a function of the PKA energy.

In this paper, we describe the methods that we have used to estimate the number of C- and Si-displacements, using two powerful computer codes—MCNP5 and SRIM/TRIM 2003—in combination. Our focus is to determine the displacements per atom (DPA) per fluence. This term (DPA/fluence) is useful for comparing the number of displacements created by various fluences of various projectiles irradiating various target materials.

Displacement Damage Equations

Transferred Energy to PKA

Based on binary collision theory, if a neutron, with energy E_n, collides with an atom in the target, the energy transfer in the elastic collision is given by the expression

$$T = \frac{1}{2}\Lambda E_n(1 - \cos\theta) \tag{1}$$

where T is the kinetic energy of the PKA and θ is the neutron scattering angle. Λ can be calculated as

$$\Lambda = \frac{4m_1m_2}{(m_1 + m_2)^2} \tag{2}$$

where m_1 is the mass of a neutron, and m_2 is the atomic mass of the PKA. ΛE_n is the maximum energy that can be transferred from a neutron to the PKA atom in a collision (and occurs for $\cos(\theta) = -1$).

For elastic isotropic scattering in the center of mass system, the average energy, $\bar{T}$, transferred from a neutron of energy E_n to a nucleus of the target atom can be determined using

$$\bar{T} = \frac{1}{2}\Lambda E_n \tag{3}$$

If we know the kinetic energy of a neutron before and after a collision (E_n and E_n', respectively),the kinetic energy of the PKA, i.e., T, can be simply calculated using Eq 4, for an elastic collision:

$$T = E_n - E_n' \tag{4}$$

For inelastic scattering, the corresponding equation to find the energy of the PKA is more complex. Since in this article we restrict our attention to neutron energies below those for which inelastic scattering occurs for SiC, equations that describe energy transfer in inelastic scattering events are not reviewed here, but can be found in, e.g., Ref. [1].

Number of Displacements

As stated previously, the purpose of this article is to introduce a method to estimate the number of displacements. Displacement damage theories are based on the assumption that the target atom must receive a minimum amount of energy (E_d) in the collision in order to be removed from its original position. For PKA energies that are much larger than E_d, the number of displaced atoms that are produced by the PKA is proportional to the PKA energy. Based on the Nogrett-Robinson-Torrens (NRT) model and the Linhard method, the following equations can be used to approximate the number of defects that are produced per PKA ($\nu(T)$) [1,2,11]:

$$\nu(T) = \xi(T)\left(\frac{\kappa T}{2E_d}\right) \tag{5}$$

where κ is the damage efficiency and is equal to 0.8, independent of the PKA energy, and $\xi(T)$ accounts for the effects of inelastic energy loss by the PKA. $\xi(T)$ can be determined using

$$\xi(T) = \frac{1}{1 + k\ g(\varepsilon)} \tag{6}$$

where

$$k = \frac{0.13372\ Z^{2/3}}{A^{\frac{1}{2}}} \tag{7}$$

and

$$g(\varepsilon) = 3.48008\varepsilon^{1/6} + 0.40244\varepsilon^{3/4} + \varepsilon \tag{8}$$

where

$$\varepsilon = \frac{T}{86.931Z^{7/3}} \tag{9}$$

where the unit of ε is eV. In the above equations, Z and A are the atomic number and atomic mass of the target atom, respectively.

The DPA can be calculated as

$$DPA = \frac{\nu(T)n_{\mathrm{PKA}}}{VN_{\mathrm{SiC}}} \tag{10}$$

where n_{PKA} is the total number of PKAs in the simulation, V is the volume of the detector (the irradiated volume) in cm^3, and N_{SiC} is the atom density of SiC in cm^{-3}.

DPA Estimating Process

In this paper, we suggest to estimate displacements that are created by neutrons in SiC diode detectors by using the outputs of the MCNP and TRIM codes in series. In order to use TRIM to determine the number of displacements resulting from neutrons, TRIM requires as input the types, energies, initial positions and direction cosines of the PKAs. We receive these input parameters by modeling the transport of neutrons through SiC with MCNP.

In our case, we are concerned with displacement damage in Schottky SiC semiconductor diode detectors. These diodes are very thin (~300 μm). Consequently, the majority of neutrons, which are incident upon the surface of the SiC diode, pass through the SiC without interacting. The PTRAC card in MCNP5 was used to determine the probability that a neutron that enters the SiC volume will interact with a Si or C atom therein. Furthermore, a C-program was written to extract neutron characteristics (energy, position, and direction cosines), before and after each collision, as well as the type of the PKA that is created in a collision, from the PTRAC files that were created by MCNP5. Based on conservation of energy and momentum, the PKA characteristics (atomic species, energy, position, and direction cosines), were determined for elastic collisions.

The output of the C-program was used as an input for the TRIM code, which was used to estimate the number of displacements that are created, including the number of C- and Si-vacancies, and replacements. Based on SRIM/TRIM definitions, if both the energies of the projectile after collision and the target atom are more than E_d (the minimum energy that is required to move an atom from its original site), a vacancy will be created in the original position of the target atom. For the case where the projectile and the target atom are of the same atomic species (such as a Si projectile atom striking a Si target atom), and the post-collision energy of the projectile is less than, then there will be a replacement. In the worst case, the statistical error of this process, because of uncertainties in the sampling of MCNP and TRIM, was below 2 %.

The thickness of the semiconductor was assumed to be 310 μm (the active volume was assumed to have a thickness of 10 μm and the substrate was assumed to have a thickness of 300 μm). TRIM treats a solid as being amorphous. In other words, the target properties are assumed to be isotropic, including E_d. The directionally averaged values of E_d were set equal to 20 and 35 eV for C and Si, respectively, to be consistent with Weber et al. [12]. However, there is some uncertainty in these numbers, since—in addition to the isotropic approximation—supposedly more reliable ab initio simulations found that E_d might be

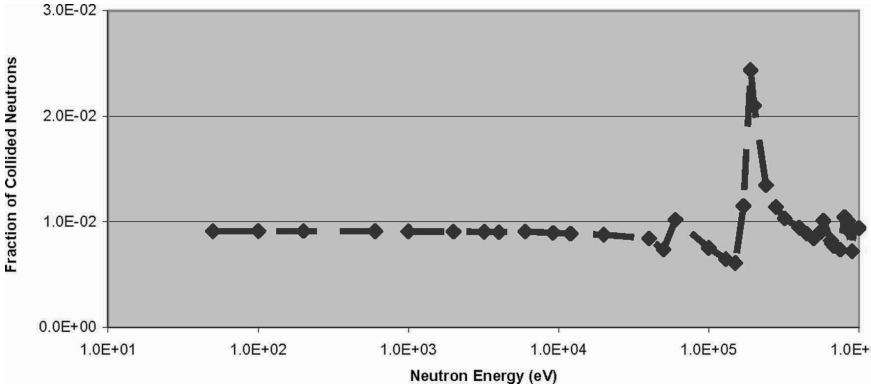

FIG. 1—*Fraction of neutrons that collide while passing through a 310-μm-thick SiC detector.*

higher for C, around 25 eV, and lower for Si, around 31 eV [13]. The experimental E_d values for Si in SiC vary between 35 and 85 eV, as a function of the Si orientation. For C, the experimental E_d values are 22 eVor smaller [14]. The SiC density was set to be 3.2 g/cm^3.

Results and Discussion

We used MCNP5 to determine the fraction of neutrons that collide while passing through the SiC detector. Figure 1 shows the fraction of neutrons that collide while passing through a 310-μm-thick SiC detector versus E_n, assuming the neutrons are isotropically directed.

Except at resonance energies, only a small fraction (about 0.6 %) of the neutrons that are incident upon the detector interact with Si or C atoms within the detector. Consequently, the probability that a particular neutron interacts two times within the SiC detector, before leaving the detector, is approximately 0.004 %. This probability (i.e., the probability that a particular neutron interacts twice within the SiC detector) is an important parameter in distinguishing between thin and thick SiC layers, since the thickness of the layer affects the dependence of the volume-averaged displacement damage on E_n. As an illustration of the effect, assume a neutron with energy E_n interacts within a SiC target that is thick enough that a neutron is likely to interact twice within the target. In this case, if a neutron scatters on a C atom, after the scattering event, the energy of the neutron decreases to $E'_{n,C}$; if a different neutron with the same energy, E_n, interacts with a Si atom, the energy of the neutron decreases to $E'_{n,Si}$. Since on average, $E'_{n,C} < E'_{n,Si}$, the dependence of the volume-averaged displacement damage on E_n would be less dramatic for a thick SiC target than for a thin SiC target; because, for the thick SiC target, the neutron that interacts first with a C atom, and in so doing deposits more energy in the SiC on average than a neutron which interacts first with a Si atom, would have less energy available on average to create additional displacements, if it were to interact a second time within the detector. Conversely, a neutron that interacts first with a Si atom, and in so doing deposits less energy in the SiC on average than a neutron which interacts first with a C atom, would have more energy available on average to create additional displacements, if it were to interact a second time within the detector. Therefore, as stated above, the dependence of the volume averaged displacement damage on E_n would be less dramatic for a thick SiC target than for a thin SiC target, because of the balancing of greater and lesser energy losses that occurs between the first and second collisions in a thick target. For our case, where the SiC target is very thin, the probability of interaction between neutrons and SiC atoms is very small, on a per neutron basis, and the dependence of the displacement damage on E_n is most pronounced.

The elastic scattering cross sections for Si and C are presented in Fig. 2 [15]. As can be seen, for E_n less than approximately 50 keV, the elastic scattering cross section of C is about 2 times greater than the elastic scattering cross section of Si. For E_n greater than 50 keV, the elastic scattering cross section for Si is comparable to, or slightly larger than, that of C.

Figure 3 presents the ratio of C-PKAs to the total number of PKAs (the ratio of the C scattering cross

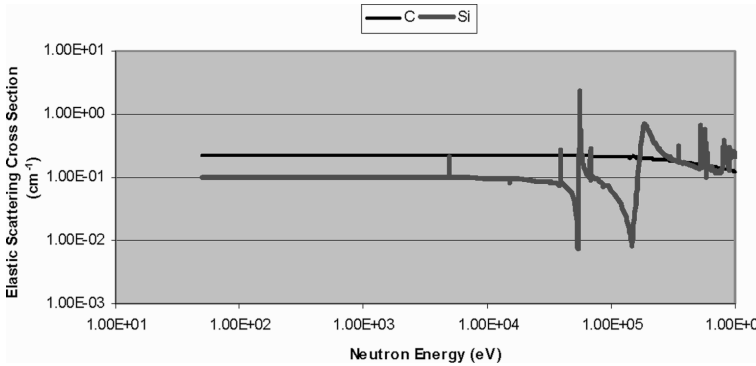

FIG. 2—*The elastic scattering cross sections for Si and C.*

section to the SiC scattering cross section) as a function of neutron energy. For low neutron energies, this fraction is 0.70. For larger neutron energies, this fraction varies due to variations in the scattering cross sections of C and Si.

Figure 4 shows the maximum and average C- and Si-PKA energies as a function of E_n. Theoretically, the ratio of the average PKA energy to the maximum PKA energy should be 0.5 for elastic and isotropic scattering. Our calculations show that this ratio is 0.50, for E_n less than 50 keV for C and for E_n less than

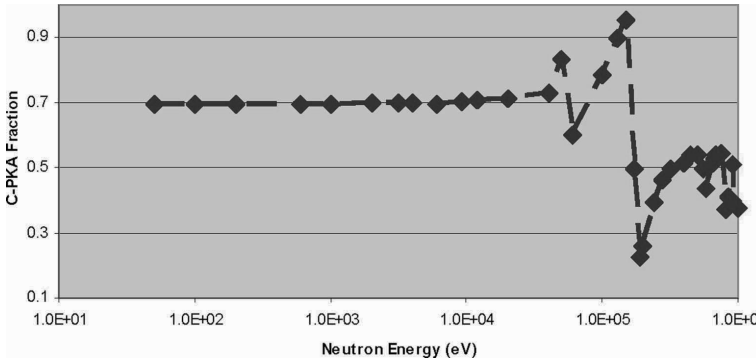

FIG. 3—*Fraction of C-PKAs as a function of neutron energy.*

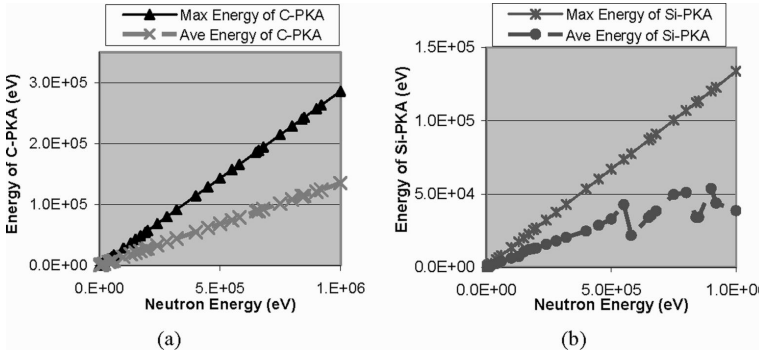

FIG. 4—*Maximum and average PKA energies versus neutron energy for (a) C-PKAs and (b) Si-PKAs.*

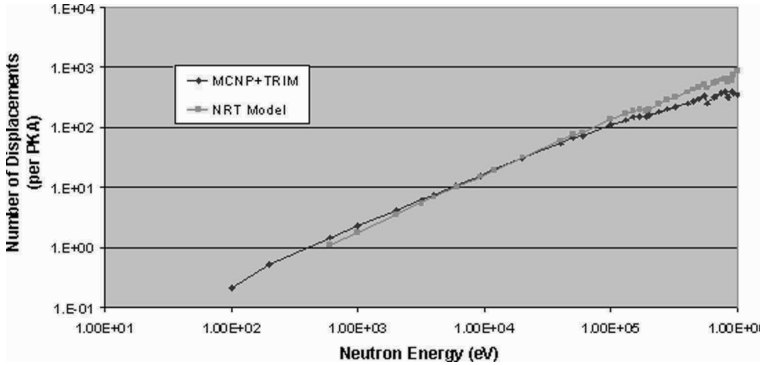

FIG. 5—*Number of displacements per PKA, determined by two methods: our method (MCNP+TRIM) and the NRT model.*

20 keV for Si. For greater than 50 keV for C, our calculations show that this ratio is slightly less than 0.5, because the scattering is not purely isotropic. For E_n ranging from 20 to 1 MeV for Si, our calculations show that this ratio varies between 0.29 and 0.58. Since the atomic mass of C is less than the atomic mass of Si, for equal E_n, the average C-PKA energy is greater than the average Si-PKA energy. Theoretically, the ratio of the average-C-PKA energy to the average-Si-PKA energy should be 2.13 for elastic and isotropic scattering. Our calculations reveal that the ratio of these two average energies is 2.14 for low E_n (where collisions are elastic and isotropic), but that due to anisotropic scattering, this ratio changes dramatically as E_n increases.

Figure 5 shows the number of displacements per PKA determined by our method as a function of E_n. For comparison, the number of displacements per PKA calculated by the simple NRT model is plotted as well. As it can be seen in the figure, these two results are in good agreement, particularly for small E_n. For larger E_n, the difference between the two methods is a little greater, since in the NRT model it is assumed that the neutron scattering angle is isotropic and that it is not a function of E_n. This assumption is not very accurate for large E_n, depending on the type of PKA. In addition, the NRT model was originally developed to estimate the number of displacements for elements, not compounds.

The results of our calculations of DPA/fluence from the previous results are presented as a function of E_n in Fig. 6, along with calculations of the DPA/fluence that we determined using SPECTER. One interesting point is that, according to both, the MCNP+TRIM calculations and the SPECTER calculations, the DPA/fluence is almost a constant, for E_n greater than 200 keV but less than 1 MeV.

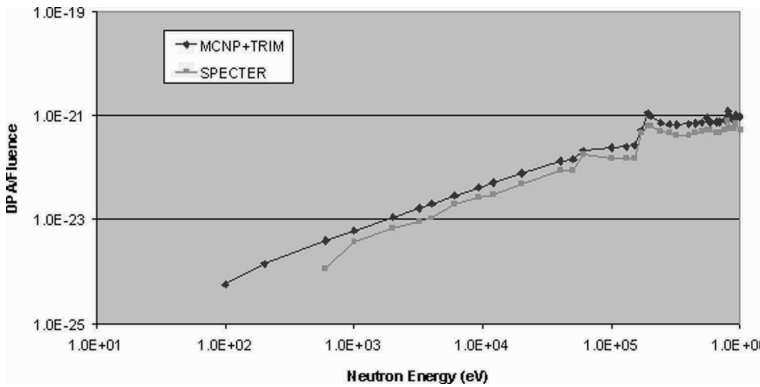

FIG. 6—*DPA/fluence as a function of neutron energy, determined by two methods: the MCNP+TRIM method as suggested in the present paper and SPECTER.*

As can be seen in Fig. 6, the results of the MCNP+TRIM and SPECTER calculations are comparable, except for low E_n. We believe that the main reason for the differences between the code calculations for low E_n is that the codes SPECTER and TRIM use different formalisms to predict the number of displaced atoms per PKA as a function of the kinetic energy of the PKA. The authors refer interested readers to the SPECTER and TRIM manuals [7,8] for details regarding the differences in the formalisms.

One advantage of using MCNP+TRIM is that MCNP+TRIM uses cross sections that are continuous functions of energy. Another advantage of using MCNP+TRIM, compared to SPECTER, is that MCNP+TRIM yields additional information; including, for example, the number of Si- and C-vacancies and replacements, the fraction of collided neutrons and the fraction of C-PKAs. Furthermore, when necessary, the spatial distribution of displacements can be studied. Finally, since TRIM is a code that was developed principally to study displacement damage resulting from ions, the MCNP+TRIM approach allows one to compare, in a consistent manner, the displacement damage caused by neutrons with the displacement damage caused by ions (for example protons to determine the effect of adding Coulomb interaction into the picture).

Conclusions

Our final goal is to be able to predict the operational lifetime of SiC detectors as neutron monitors, as a function of their flux and temperature histories. Towards this goal, we have developed a method to estimate the DPA/fluence using two well-known codes: MCNP and TRIM. From knowledge of the DPA/fluence, we are able to determine the DPA for any fluence. For the next step, we will calculate the resulting concentrations of C- and Si-antisites, vacancies, and interstitials. We will use these results combined with the results of ab initio modeling as input to kinetic diffusion equations that we will solve to study annealing of SiC defects as a function of time and temperature. Finally, we are modeling the influence of point defects on the electrical properties of SiC diodes to predict how these properties would change over time for various relevant time periods for reactor operation, such as a refueling cycle.

Acknowledgments

This material is based upon work supported by the US Department of Energy under the NERI program Award No. DE-FG-07-02SF22620 and NERI Project Number 02-207. Any opinions, findings, and conclusions or recommendations expressed in this material are those of the authors and do not necessarily reflect the views of the Department of Energy.

References

[1] Olander, D. E., "Radiation Damage," *Fundamental Aspect of Nuclear Reactor Fuel Elements*, Technical Information Center, Energy Research and Development Administration, USA, 1976.

[2] Gittus, J., *Irradiation Effects in Crystalline Solids*, Applied Science Publishers LTD, London, 1978.

[3] Norgett, M. J., Robinson, M. T., and Torrens, I. M., "A Proposed Method of Calculating Displacement Dose Rates," *Nucl. Eng. Des.*, Vol. 33, 1975, pp. 50–54.

[4] Coulter, C. A., and Parkin, D. M., "Damage Energy Functions in Polyatomic Materials," *J. Nucl. Mater.*, Vol. 88, 1980, pp. 249–260.

[5] Parkin, D. M., and Coulter, C. A., "Total and Net Displacement Functions for Polyatomic Materials," *J. Nucl. Mater.*, Vol. 101, 1981, pp. 261–276.

[6] Lee, M. B., and Farnum, E. H., "The Effect of Neutron Energy on Defect Production in Alumina," *Nucl. Instrum. Methods Phys. Res. B*, Vol. 102, 1995, pp. 113–118.

[7] Greenwood, L. R., and Smither, R. K., "SPECTER: Neutron Damage Calculations for Materials Irradiations," ANL/FPP/TM-197, Jan. 1985.

[8] Ziegler, F. J., "SRIM-2003," *Nucl. Instrum. Methods Phys. Res. B*, Vol. 219-220, 2004, pp. 1027–1036.

[9] Forster, R. A. et al., "MCNP Version 5," *Nucl. Instrum. Methods Phys. Res. B*, Vol. 213, 2004, pp. 82–86.

[10] Weber, W. J. et al., "The Efficiency of Damage Production in Silicon Carbide," *Nucl. Instrum. Methods Phys. Res. B*, Vol. 218, 2004, pp. 68–73.

[11] Fukahori, T. et al., *Reactor Dosimetry: Radiation Metrology and Assessment*, G. W. Williams et al., Ed., ASTM, International, West Conshohocken, PA, 2001.

[12] Gao, F., Weber, W. J., and Devanathan, R., "Defect Production, Multiple Ion-Solid Interactions and Amorphization in SiC," *Nucl. Instrum. Methods Phys. Res. B*, Vol. 191, 2002, pp. 487–496.

[13] Windl, W. et al., "First-Principle Investigation of Radiation Induced Defects in Si and SiC," *Nucl. Instrum. Methods Phys. Res. B*, Vol. 141, 1998, pp. 61–65.

[14] Zinkle, S. J., and Kinoshita, C., "Defect Production in Ceramics," *J. Nucl. Mater.*, Vol. 251, 1997, pp. 200–217.

[15] Korea Atomic Energy Evaluation Lab., 2000, http://atom.kaeri.re.kr/

Journal of ASTM International, Vol. 4, No. 4
Paper ID JAI101141
Available online at www.astm.org

W. P. Voorbraak,[1] *W. E. Freudenreich,*[1] *G. P. Leendertse,*[2] *and J. K. Aaldijk*[1]

Thermal and Epithermal Fluence Rate Measurements in Multipurpose Reactors: Application of a Least-Squares Fitting Code RESDET to Obtain Thermal and Epithermal Fluence Rates from Measured Reaction Rates

ABSTRACT: A generalized least-squares, two group neutron spectrum adjustment code is presented that uses measured reaction rates of activation foils and thermal and epithermal energy cross-section data to calculate the thermal and epithermal fluence rates in case of well-moderated neutron spectra. The code uses the covariance matrices of the measurements and cross sections to produce the covariance matrix of the calculated thermal and epithermal fluence rates. The report also gives some application examples of the code.

KEYWORDS: thermal fluence rate, epithermal fluence rate, activation foils, covariance matrix

Introduction

Material Test Reactors are more and more transformed to multipurpose reactors. Production of medical isotopes, silicon doping, even direct treatment of patients with thermal neutrons, epithermal neutrons, or both, play an increasingly important role besides the original objective, i.e., testing of materials. This means also a growing interest for an accurate characterization of the thermal and epithermal neutron field as an important parameter for the estimate of the amount of product isotope.

Nowadays, two- or three-dimensional deterministic or Monte Carlo neutron transport codes are in common use. Unfortunately, detailed information on the accuracy of the neutron spectra obtained from these codes is mostly not available. To have confidence in the spectrum and to improve the accuracy of the calculated spectra, a spectrum adjustment is often executed with aid of measured reaction rates of neutron activation foils. To get a good estimation of the quality of the adjusted spectrum, it is necessary to take into account all the uncertainties and correlations of the measurements, the cross sections, and the calculated spectrum. Here, often a covariance matrix of the calculated neutron spectrum is missing.

In and around nuclear reactors, especially research reactors, there are many irradiation positions where it is not necessary to have a fine-group neutron spectrum at one's disposal. In general, these are well-moderated irradiation positions and often the user is only interested in the thermal and epithermal part of the neutron spectrum in these positions. In these cases, a two-group representation of the thermal and epithermal part of the neutron spectrum is satisfactory. On the other hand information on the accuracy of the spectrum parameters should be always presented. Therefore a code, RESDET, has been developed that delivers a two-group neutron spectrum including uncertainty data.

Resdet

A two-group neutron spectrum is composed of a thermal Maxwellian distribution and a $1/E$-shaped distribution for the epithermal energy range. In this simple model, the neutron spectrum can then be

Manuscript received June 20, 2005; accepted for publication March 28, 2007; published online May 2007. Presented at ASTM Symposium on Reactor Dosimetry, 12th International Symposium on 8–13 May 2005 in Gatlinburg, TN; D. W. Vehar, D. M. Gilliam, and J. M. Adams, Guest Editors.

[1] Senior Scientist, MMI-Monitoring, Netherlands Research and Consultancy Group NRG, P.O. Box 25, 1755ZG Petten, The Netherlands.
[2] Senior Scientist, Energy Research Foundation ECN, P.O. Box 1, 1755 ZG, Petten The Netherlands.

characterized by only two parameters: the thermal fluence rate ϕ_0 and the epithermal fluence rate per unit lethargy ϕ_{epi}. These two parameters can easily be obtained from measurements with, e.g., at least two activation materials that have different response distributions in the thermal and epithermal energy range. For this simple situation (a small number of activation foils) the user is interested in a good specification of the uncertainty of the obtained spectrum parameters ϕ_0 and ϕ_{epi}.

For this case, a code, RESDET (an improved version of RESDETLINE and RESDET2 [1,2]), has been developed that calculates the parameters ϕ_0 and ϕ_{epi} and also the covariance matrix of these parameters from measured reaction rates of activation materials and the covariance matrix based on these reaction rates. The code needs the thermal cross section σ_0 and the resonance integral I, and covariance matrix of the considered reactions. These data are available for the code in the accompanying library RESDET.lib. The cross-section data have been taken from [3] and the covariances from [4].

Model

Physical Model—Locations in nuclear reactors, especially the irradiation positions in research reactors in use for the production of medical isotopes or the doping of silicon, often have well-moderated neutron spectra with few fast neutrons. The same holds for the neutron spectrum in simulations of the human body by tissue equivalent materials. These so-called "phantoms" are used to prepare irradiation of patients, for instance, as part of boron neutron capture therapy. In these cases, the neutron spectra can be represented by a Maxwell distribution in the thermal energy region and a $1/E$ distribution in the epithermal energy region. The reaction rate R_i for a specific nuclide i can be expressed in an approximate way as the sum of the activation due to thermal and epithermal neutrons, taking into account the self-shielding for thermal and epithermal neutrons separately (ASTM E 262-97, 1997)

$$R_i = A_i/N_i = G_{th,i} g \phi_0 \sigma_{0,i} + G_{epi,i} \phi_{epi} I_i \tag{1}$$

in which

A_i = the number of activated atoms of nuclide i,
N_i = the total number of atoms of nuclide i,
g = a correction factor that accounts for the departure from the ideal $1/v$ cross section in the thermal energy range (Westcott factor),
ϕ_0 = the equivalent 2200 m/s thermal fluence rate,
ϕ_{epi} = the fluence rate of epithermal neutrons per unit lethargy,
σ_0 = the cross section for 2200 m/s neutrons,
I = the resonance integral defined as follows

$$I = \int_{0.55\ \text{eV}}^{\infty} \frac{\sigma(E)}{E} dE \tag{2}$$

The factors G_{th} and G_{epi} are, respectively, corrections for the self-shielding of thermal and epithermal neutrons. These factors depend on the material, the dimensions of the materials, and their composition. Materials such as gold and silver with a high resonance peak in the cross section are strongly diluted in aluminum in order to reduce the self-shielding correction to a factor close to 1. Gold-aluminum and silver-aluminum have been used.[3] For most activation reactions the Westcott-factor g is equal to 1 or at least close to 1. Activation due to fast neutrons has been neglected: the number of fast neutrons is low as well as the cross section for fast neutrons.

Under these conditions, Eq 1 may be transformed to the more simple form

$$R_i = \sigma_{0,i} \phi_0 + I_i \phi_{epi} \tag{3}$$

Measurement of the reaction rates (R_i) of at least two different activation reactions enables the determination of the thermal fluence rate (ϕ_0) and the epithermal fluence rate per unit lethargy (ϕ_{epi}) from a set of type 3 equations. The quality of the solution for ϕ_0 and ϕ_{epi} of course depends on the uncertainties

[3] ≤1 % gold or silver.

of the measured reaction rates and the cross sections; however, it also strongly depends on the difference of the ratio of the cross sections (I_i/σ_0) of the activation reactions used (a larger difference leads to a better defined solution). The quality of the solution can also be improved by using more than two activation reactions. In such cases, the set of type 3 equations is over determined and there exist several solutions. However, only one of these solutions is "best" in the sense of least squares. Because the (generalized) cross sections and the measured reaction rates in Eq 3 involve uncertainties with correlations a generalized least-squares adjustment code should be used to solve a set of type 3 equations. The disadvantage of frequently used generalized least-squares adjustment codes such as LSL-M2 or STAY'SL (for a compilation of such codes, see Ref. [5]) is, that these codes also need information from a spectrum calculation (fluence rates with uncertainties and correlations). The code RESDET, presented here, does not need this type of calculated spectrum data, but determines the spectrum parameters ϕ_0 and ϕ_{epi} from measured reaction rates only.

Mathematical Solution—The generalized least-squares method, which is used in RESDET, delivers a solution for the spectrum parameters ϕ_0 and ϕ_{epi} that is "best" in the sense that the sum of squared differences between measured reaction rates and reaction rates calculated with type 3 equations is minimized [6].

The set of equations for the differences δ_i (residuals) between measured reaction rates $R_{i,m}$ and calculated reaction rates $R_{i,c}$ by equation 3

$$\delta_i = R_{i,m} - R_{i,c} = R_{i,m} - \sigma_{0,i}\phi_0 - I_i\phi_{epi} \tag{4}$$

can be written in vector notation, giving

$$\mathbf{\Delta} = \mathbf{Y} - \mathbf{B} \cdot \mathbf{X} \tag{5}$$

with

$\mathbf{\Delta}$ = $(n \times 1)$ vector of residuals δ_i,
$\mathbf{Y}$ = $(n \times 1)$ vector of measured reaction rates R_i,
$\mathbf{B}$ = $(n \times 2)$ matrix of cross sections $\sigma_{0,i}$ and I_i,
$\mathbf{X}$ = (2×1) vector of unknown spectrum parameters ϕ_0 and ϕ_{epi}.

One then gets for the sum of squares of the residuals χ^2

$$\chi^2 = \mathbf{\Delta^T} \cdot \mathbf{V}^{-1}(\mathbf{\Delta}) \cdot \mathbf{\Delta} \tag{6}$$

with

$\mathbf{V}(\mathbf{\Delta})$ = $(n \times n)$ covariance matrix of the residuals.

From the requirement of a minimum for χ^2, one gets the solution for the spectrum parameters ($\mathbf{X}$) and their covariance matrix ($\mathbf{V}(\mathbf{X})$)

$$\mathbf{X} = [\mathbf{B^T} \cdot \mathbf{V}^{-1}(\mathbf{\Delta}) \cdot \mathbf{B}]^{-1} \cdot [\mathbf{B^T} \cdot \mathbf{V}^{-1}(\mathbf{\Delta}) \cdot \mathbf{Y}] \tag{7}$$

$$\mathbf{V}(\mathbf{X}) = [\mathbf{B^T} \cdot \mathbf{V}^{-1}(\mathbf{\Delta}) \cdot \mathbf{B}]^{-1} \tag{8}$$

The covariance matrix $\mathbf{V}(\mathbf{\Delta})$ of the residuals applied in RESDET consists of the covariance data of the measured reaction rates R, which are given in the input file, and the covariance data of the cross sections σ and I, which are available in the library file RESDET.lib.

Applications

The procedure is demonstrated for irradiations in the High Flux Reactor, a 45 MW multipurpose reactor in Petten, the Netherlands. The examples deal with the determination of the thermal fluence rate in medical isotope production experiments. Such experiments contain piles of aluminum capsules filled with target material. A few capsules contain a monitor set instead of target material (see Fig. 1). Monitor sets of different composition have been irradiated and used to determine the thermal- and epithermal fluence rate

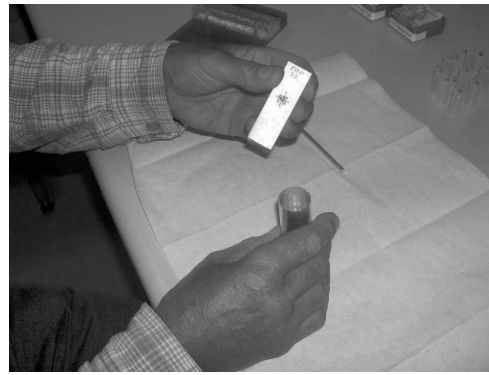

FIG. 1—*Monitor set consisting of cobalt, silver and iron foils used for the determination of the thermal and epithermal fluence rate in isotope production facilities.*

using RESDET. Different pairs of reaction rates have been investigated with RESDET, and results and uncertainties have been compared. The activated foils have been measured with a calibrated HPGe gamma ray spectrometer.

RESDET with Two Activation Reactions—First RESDET is applied to a set of two activation reactions. In this case, a unique solution is obtained for ϕ_0 and ϕ_{epi}. The additional value of a calculation with RESDET compared to a simple algebraic solution is the availability of the covariance matrix for ϕ_0 and ϕ_{epi}. Three activation foils have been irradiated together in the neutron field mentioned above. Two calculations have been performed with RESDET:

1. the reaction $^{59}Co(n,\gamma)^{60}Co$ is combined with the reaction $^{58}Fe(n,\gamma)^{59}Fe$,
2. the reaction $^{59}Co(n,\gamma)^{60}Co$ is combined with the reaction $^{109}Ag(n,\gamma)^{110\ m}Ag$.

Table 1 shows results obtained with RESDET for the combinations 1) and 2).

Large differences are observed between the calculated values ϕ_0 and ϕ_{epi} and their uncertainties. The set comprising the reactions $^{59}Co(n,\gamma)^{60}Co$ and $^{58}Fe(n,\gamma)^{59}Fe$ yields very large uncertainties. The reason is the small difference between the values I_i/σ_0 for both activation reactions (see Table 2). This small difference in I_i/σ_0 leads to a mathematical solution that converges slowly with accompanying large uncertainties.

This difference in I_i/σ_0 values is much larger for the combination $^{59}Co(n,\gamma)^{60}Co$ and $^{109}Ag(n,\gamma)^{110\ m}Ag$ (see Table 2). This results in a much better defined solution for this pair of activation

TABLE 1—*RESDET results for different combinations of activation reactions with uncertainties between ().*

Set	Reaction rate, s^{-1}	ϕ_0, $m^{-2}\ s^{-1}$	ϕ_{epi}, $m^{-2}\ s^{-1}$	Correlation coefficient
^{59}Co+	8.158×10^{-9} (0.6 %)	1.77×10^{18} (29 %)	2.09×10^{17} (120 %)	−1.00
^{58}Fe	2.586×10^{-10} (2.7 %)			
^{59}Co+	8.158×10^{-9} (0.6 %)			
^{59}Ag	1.934×10^{-9} (1.0 %)	1.85×10^{18} (2.4 %)	1.72×10^{17} (11 %)	−0.90

TABLE 2—*Cross sections and cross-section ratio of different activation reactions.*

Reaction	σ_0, m^2	I_i, m^2	I_i/σ_0
$^{59}Co(n,\gamma)^{60}Co$	37.18×10^{-28} (0.7)	75.55×10^{-28} (0.8)	2.03
$^{58}Fe(n,\gamma)^{59}Fe$	1.300×10^{-28} (13)	1.368×10^{-28} (9)	1.05
$^{109}Ag(n,\gamma)^{110m}Ag$	4.172×10^{-28} (5)	67.84×10^{-28} (7)	16.3
$^{55}Mn(n,\gamma)^{56}Mn$	13.4×10^{-28} (6.3)	11.8×10^{-28} (8)	0.88
$^{63}Cu(n,\gamma)^{64}Cu$	4.51×10^{-28} (2)	4.97×10^{-28} (1.4)	1.10
$^{97}Au(n,\gamma)^{198}Au$	98.94×10^{-28}(0.14)	1566×10^{-28}(0.17)	15.8

TABLE 3—*Reproduction of RESDET output using reaction rates of six reactions.*

Reaction	Calculated reaction rate	Measured reaction rate	Coeff of var. measured reaction rate, %	Relative difference, %	Weighted residual
SC45GJ	3.894×10^{-11}	4.079×10^{-11}	0.60	4.52	4.45
		Result rather unlikely			
FE58GJ	2.177×10^{-12}	2.240×10^{-12}	2.60	2.81	0.25
CO59GJ	7.661×10^{-11}	7.641×10^{-11}	0.40	−0.27	−0.33
NB93GI	5.366×10^{-12}	5.678×10^{-12}	0.60	5.49	0.60
AG109GJ	3.199×10^{-11}	3.394×10^{-11}	1.10	5.76	0.93
U235FI	8.453×10^{-10}	8.359×10^{-10}	0.50	−1.13	−2.11

	Calculated value	Coefficient of variation	Correlation matrix	
Thermal fluence rate	1.2600×10^{-16}	0.77	1.000	
Epithermal fluence rate	3.9401×10^{-15}	2.67	−0.758	1.000
Ratio fluence rate sub cadmium/epithermal	3.06	3.20		
CHISQ	25.64			
Degrees of freedom	4			

reactions.

For short irradiations (a few hours) a combination of gold, manganese, and copper is recommended, resulting in the activation reactions $^{197}Au(n,\gamma)^{198}Au$, $^{55}Mn(n,\gamma)^{56}Mn$, and $^{63}Cu(n,\gamma)^{64}Cu$. Gold-aluminum and manganese-aluminum alloys are used to reduce the correction for self-shielding. For this combination of reactions, the ratio I_i/σ_0 for gold is relatively high. Thus, gold has the same role as silver in the last example. In both cases, a well-moderated spectrum is required for a proper calculation, so a neutron spectrum that also contains epithermal neutrons.

RESDET with Six (Later Five) Activation Reactions—When more than two activation reactions are used, RESDET will determine a solution for ϕ_0 and ϕ_{epi} that is "best" in the sense of least squares. In this case, RESDET results can also be used to check the consistency of the input data. An example is shown in the RESDET output in Table 3. The computer output indicates for the reaction $^{45}Sc(n,\gamma)^{46}Sc$ (coded "SC45GJ"): "Result rather unlikely." This is due to the relatively large difference between calculated and

TABLE 4—*Reproduction of RESDET output using reaction rates of five reaction (discarding the reactions $^{45}Sc(n,\gamma)^{46}Sc$).*

Reaction	Calculated reaction rate	Measrued reaction rate	Coeff of var. measured reaction rate, %	Relative difference, %	Residual weighted
FE58GJ	2.163×10^{-12}	2.240×10^{-12}	2.60	3.44	0.31
CO59GJ	7.659×10^{-11}	7.641×10^{-11}	0.40	−0.24	−0.30
NB93GI	5.445×10^{-12}	5.678×10^{-12}	0.60	4.11	0.44
AG109GJ	3.261×10^{-11}	3.394×10^{-11}	1.10	3.93	0.62
U235FI	8.354×10^{-10}	8.359×10^{-10}	0.50	0.06	0.11

	Calculated value	Coefficient of variation	Correlation matrix	
Thermal fluence rate	1.2381×10^{16}	0.86	1.000	
Epithermal fluence rate	4.0449×10^{15}	2.67	−0.759	1.000
Ratio fluence rate sub Cadmium/epithermal	3.06	3.36		
CHISQ		0.78		
Degrees of freedom		3		

measured reaction rate for this reaction in relation to the relatively low uncertainties in the measured reaction rate and in the cross sections (given in RESDET.lib). The output obtained after discarding the reaction $^{45}Sc(n,\gamma)^{46}Sc$ as input is shown in Table 4.

Comparison of the two output sets shows that this action has very limited influence on the results (in this case). The only value that shows a large change is the value of χ^2 ("CHISQ"). A χ^2 value close to unity indicates consistency of the data set.

Conclusions

The code RESDET allows determination of the thermal and epithermal fluence rates ϕ_0 and ϕ_{epi} and their covariance matrix from measured reaction rates of a set of at least two activation foils in an easy way. The application of the code is limited to well-moderated neutron spectra (spectra composed of a thermal Maxwellian and a $1/E$-shaped distribution in the epithermal energy range). This implies that no calculated input spectrum is needed. Self shielding corrections can be neglected as long as strongly diluted material is used for the materials with substantial response in the epithermal neutron energy region. The only extra data needed are the thermal cross sections σ_0, and the resonance integrals I, and the covariance matrix of the considered activation reactions given in the library RESDET.lib.

References

[1] Rieffe, H. Ch., "Program Description of RESDETLINE," RCN Report, R.M.G. Note 72/08, Petten, June 1972.

[2] "RESDET2, A Computer Program for Solving Linear Activation Equations for Resonance Detectors," Aaldijk, J. K., Ed., NRG, Report 20901/02/51120/I, March 2003.

[3] Freudenreich, W. E., "Neutron Activation Cross Section Library DOSCROSS 2001," NRG Report 20689/01.40537/I.

[4] Kocherov, N. P., and Mclaughlin, P. K., The International Reactor Dosimetry File (IRDF90), IAEA, NDS-141, Rev. 2, IAEA, Vienna, October, 1993.

[5] Zijp, W. L., Zsolnay, É. M., Nolthenius, H. J., and Szondi, E. J., "Final report on the REAL-84 Exercise," Report ECN-212, BME-TR-RES-18/88, IAEA-NDS-212, ECN Petten, 1988.

[6] Perey, F. G., "Spectrum Unfolding by the Least Squares Method," Proc. of an IAEA Technical Committee Meeting, Oak Ridge, October 10–12, 1977.

Journal of ASTM International, Vol. 3, No. 3
Paper ID JAI13438
Available online at www.astm.org

Ana C. Fernandes,[1] *Evžen Novák,*[2] *João Cardoso,*[3] *Luis Santos,*[3] *José G. Marques,*[1] *and Vojtěch Rýpar*[2]

Neutron and Photon Dosimetry at the LR-0 Reactor Using Paired Detectors

ABSTRACT: Paired thermoluminescence dosimeters and ionization chambers were used for characterizing mixed (neutron and photon) radiation fields at the LR-0, a zero power model of VVER reactors. Detector responses were investigated in standard photon and thermal neutron fields. A good agreement was obtained among the doses measured with the two methods. Furthermore, the measured photon and neutron attenuation values are consistent with those from evaluated, independent data.

KEYWORDS: reactor dosimetry, mixed fields, ionization chambers, thermoluminescence dosimeters

Introduction

Neutron and photon doses in mixed radiation fields are frequently determined using two detectors with different neutron sensitivities, one of them being insensitive to neutrons. The complex radiation spectra and discrepancies in detector sensitivities reported in the literature are often responsible for a poor agreement between the results obtained.

In the present work, ionization chambers and thermoluminescence dosimeters (TLDs) are used to measure neutron and photon doses at the LR-0 reactor (Nuclear Research Institute, Czech Republic), at points located in the barrel and inside and outside the reactor pressure vessel (RPV). A thorough investigation of dosimeter responses using standard photon fields and the RPI reactor of ITN (Nuclear and Technological Institute, Portugal) is reported. Finally, the dose measurements at LR-0 are compared and interpreted on the basis of independent, reference data.

Materials and Methods

The LR-0 Reactor

The zero power reactor LR-0 is a unique experimental tool which allows to model VVER cores in 1:1 radial scale and is particularly suitable to perform various neutronics determinations and experiments connected with compact fuel storage (VVER-440, VVER-1000, PWR). Mock-up experimental and theoretical investigations have produced a complete set of revised neutron [1] and photon [2] data. The evaluated data are represented in the BUGLE group structure, restricted to the 100 keV 10 MeV energy range. A schematic view of the LR-0 is presented in Fig. 1(*a*), which also identifies the measurement positions (position 2: in the barrel; position 3: before the RPV; position 4: after 5 cm of RPV). Fig. 1(*b*)

Manuscript received June 20, 2005; accepted for publication September 29, 2005; published online December 2005. Presented at ASTM Symposium on Reactor Dosimetry, 12th International Symposium on 8 13 May 2005 in Gatlinburg, TN; D. W. Vehar, D. M. Gilliam, and J. M. Adams, Guest Editors.

[1] Postdoctoral Fellow and Auxiliary Researcher, respectively, Reactor Sector, Nuclear and Technological Institute, Estrada Nacional 10, P-2686-953 Sacav m Portugal and Members of the University of Lisbon Nuclear Physics Centre, Av. Prof. Gama Pinto, 2, P-1649-003 Lisbon, Portugal.

[2] Engineer and Senior Researcher, respectively, Nuclear Power and Safety Division, Nuclear Research Institute Ře plc. Husinec Ře 130, 250-68 Ře u. Prahy Czech Republic.

[3] Laboratory Head and Technician, respectively, Department of Radiological Protection and Nuclear Safety, Nuclear and Technological Institute, Estrada Nacional 10, P-2686-953 Sacav m Portugal.

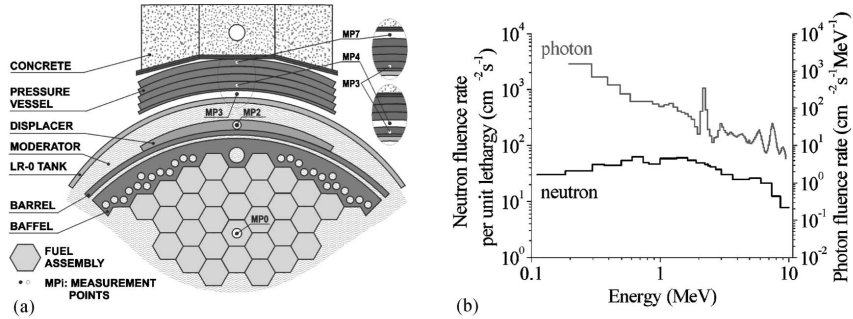

FIG. 1 *The LR-0 reactor: (a) schematic cross view; (b) evaluated neutron and photon spectra in measurement position 3.*

presents the reference LR-0 neutron and photon data at position 3. The power level of LR-0 is monitored by a xed monitoring system. In the present paper, values are normalized to a reference count rate (60000 cps) in the monitoring system.

Ionization Chambers

In the twin chamber technique, neutron and photon doses are determined through the formalism developed by the ICRU [3], expanded to the case where the neutron eld contains a thermal and a fast neutron component [4]. The reading of a detector in a mixed eld relative to its response to the gamma-rays used for calibration can be described as

$$R_u = h_u D_g + k_u D_f + k'_u \Phi_{th}$$

$$R_t = h_t D_g + k_t D_f + k'_t \Phi_{th} \quad (1)$$

where D_g is the photon dose, D_f is the dose from intermediate and fast neutrons (fast neutron dose) and Φ_{th} is the thermal neutron uence; subscript u refers to detectors with a low sensitivity to neutrons and subscript t to detectors with similar sensitivity to neutrons and photons. The quantities h and k are the neutron and photon responses of the detectors relative to the gamma-rays used in the calibration (also called relative sensitivities); k' is the detector reading per unit thermal neutron uence, relative to the response to the gamma-rays used for calibration.

Tissue equivalent (TE) and nonhydrogenous Mg gas ow ionization chambers (0.53 cm^3 volume) were used for measuring neutron and photon absorbed doses, applying the twin chamber technique. Technical characteristics of the ionization chambers are presented in Table 1.

In radiotherapy neutron beams it is frequently assumed that the relative chamber responses to photons is 1.00±1 % [4,5], which in practice corresponds to neglecting their photon energy dependence. As the M2 chamber is not tissue-equivalent, this approximation may not be correct in photon elds with an important low-energy component. Still, as no information is available about the X-ray component of the mixed- elds in LR-0, a relative photon sensitivity equal to 1 will be considered.

The relative fast and thermal neutron sensitivity of the M2 chamber is normally considered as zero. This means that the M2 chamber is supposed to be absolutely insensitive to neutrons, yielding therefore a direct measurement of the photon dose. Authors [4,6] have reported variations in k'_u among different M2

TABLE 1 *Technical characteristics of the ionization chambers.*

Model	Manufacturer and Chamber Type	Wall and Build-up Cap Material and Thickness, mm	Gas
M2	Exradin, thimble Mg(Ar)	Magnesium, 1+2	Argon 99.9999 % purity
T2	Exradin, thimble TE(TE)	A 150 plastic, 1+4	Tissue equivalent gas mixture $N_2$3.2 vol %, $CO_2$32.4 vol %, $CH_4$64.4 vol %

chambers and an increase of the values with time, probably due to contamination and ageing of the chamber materials. In the present study, the consistency of the $k_u = k'_u = 0$ relation will be checked against the TLD measurements.

The relative neutron sensitivity of the T2 chamber has been calculated as a function of the neutron energy, for tabled wall, gas, and tissue parameters [5] and measured in reference neutron beams [4,7]. The results indicate that k_t is negligible for neutron energies in the 10 eV 1 keV range, after which a rapid increase occurs to an almost constant value of 0.9 ± 10 % for energies higher than 10 keV. This means that the response of the T2 chamber, subtracted by the photon and thermal neutron contributions, gives a direct measure (± 10 %) of the fast neutron dose. As for thermal neutrons, a value of $k'_t = 0.43 \pm 1$ % pGy·cm^2 (^{60}Co) is normally used [4,5]. This value is approximately 50 % higher than the thermal neutron kerma factor of A-150 plastic, which indicates the contribution of other interaction processes to the total signal.

To avoid accumulation of gas in the measurement position, similar inlet and outlet Te on tubes (1-mm diameter × 8-m length) were used. The gas ow through the chambers was controlled by a valve and a pressure measuring device at the inlet side of the tube. The difference between inlet and outlet pressure was kept constant at 30 kPa during measurements and calibrations, which corresponds to a ow rate of approximately 2 and 4 cm^3·s^{-1} of argon and methane, respectively (according to the Poiseuille formula). The gas is assumed to be at room temperature. The gas pressure inside the chamber was estimated as the atmospheric pressure plus half of the applied pressure difference. Using this estimation, normal temperature and pressure corrections for the gas volume in the chamber were applied [8].

The chambers were biased at +300 V (with the guard at ground-level) and pre- ushed for approximately 1 h. Electric charge and current intensities were measured with an electrometer (Keithley 6514) in a non oating con guration. Background readings were performed before and after irradiations.

Thermoluminescence Detectors

Thermoluminescence detectors (chips $3.1 \times 3.1 \times 0.9$ mm manufactured by Harshaw, OH) of ^{nat}LiF:Mg,Ti (TLD-100) and ^{7}LiF:Mg,Ti (TLD-700) were used to characterize the thermal neutron and the photon eld, respectively. The sensitivity of LiF to thermal neutrons originates from the high Linear Energy Transfer (LET) alpha particles originating from the thermal neutron capture in ^{6}Li. For this reason, TLD-100 is used in mixed- eld dosimetry as a detector of thermal neutrons while TLD-700, depleted in ^{6}Li for reduced thermal neutron sensitivity, is used as photon dosimeter. Both dosimeters have a good photon energy response ($h_u = h_t = 1$). Large discrepancies are found in the literature for the thermal neutron sensitivities, which to a large extent depend on the ^{6}Li content, dosimeter thickness and evaluation method [9]. In this work, the dosimeter responses to thermal neutrons were investigated in the thermal column of the RPI, for the actual detectors and evaluation conditions. At higher energies a 1/v decrease in the relative sensitivity is observed up to 100 keV. Above this energy, a constant increase occurs from 0.1 up to 5 pGy·cm^2 (^{60}Co) at 20 MeV [10]. A value of 0.5 pGy·cm^2 (^{60}Co) [11] was assumed for both TLD-100 and TLD-700, since the fast neutron kerma arises mainly from the recoiling Li and F ions.

The detectors were evaluated at least 24 h after irradiation, using a Harshaw 3500 reader. Detector responses were measured at a heating rate of 5 C·s^{-1}, by integrating the glow curve between 135 C and 250 C. The annealing procedure consisted of a 1 h treatment at 400 C, cooling down period of 40 min and nally keeping the detectors at 100 C for 2 h.

For irradiations, the detectors were encapsulated in 3 mm Te on, which provides suf cient thickness for establishing electronic equilibrium with a minimum perturbation of the mixed radiation eld. Each measurement was made with ve dosimeters of each material (TLD-100 and TLD-700). Individual calibrations were performed. Control dosimeters irradiated with 5 mGy ^{137}Cs were applied to correct for the sensitivity variations of reader and dosimeters.

Detector Responses

Ionization Chambers

The chamber responses as a function of applied high voltage, dose rate, photon energy, gas temperature and pressure were investigated in the standard photon elds available at ITN.

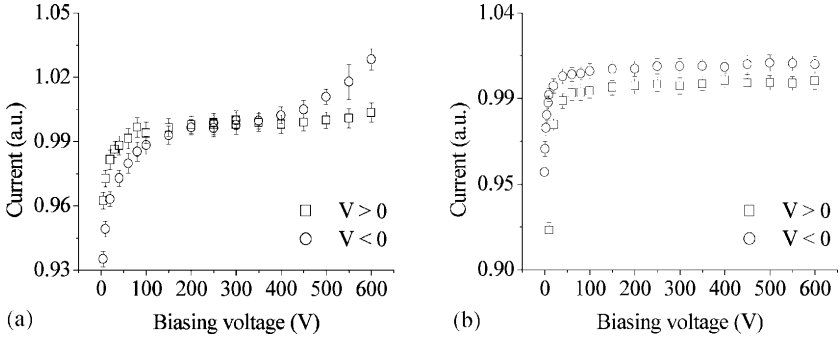

FIG. 2 *Saturation curve of (a) M2; (b) T2 chambers. Values are normalized to the measured response at +300 V.*

Saturation Curve Figure 2 shows the saturation curves of the chambers irradiated with ^{60}Co photons (air kerma rate ~4 mGy·s^{-1}). Chamber M2 exhibits a strong polarity effect; furthermore, no plateau region is observed for collection of negative charge, indicating an overlap between the regions where recombination and electron multiplication occur. Other authors [6] suggest that this effect may be related to the fact that electron attachment does not take place in argon, i.e., there are only positive Ar ions and free electrons having quite different mobilities in the applied electric field. Electron multiplication is more prominent for electrons being collected at the central electrode, where the local electric field strength is generally higher than near the chamber wall. A positive voltage of +300 V was therefore selected for biasing both chambers.

Dose Rate Dependence The response dependence on the dose rate was investigated using ^{137}Cs sources of different intensities, at the same source-detector distance (1 m). This approach was preferred to a variation of the distance to the source, as the application of similar irradiation set-ups allows to reduce the influence of spectral modifications from scattering in collimators and air. The measured chamber responses are presented in Table 2. No significant variation was observed.

Photon Energy The chamber responses as a function of photon energy are represented in Fig. 3. Standard sources of ^{60}Co (1250 keV), ^{137}Cs (661 keV) and various X-ray qualities of the narrow series 24 keV (N30), 33 keV (N40), 48 keV (N60), 65 keV (N80), 83 keV (N100) and 100 keV (N120) were used for this purpose. Both chamber responses exhibit an increased energy dependence for photon energies smaller than 100 keV. The energy dependences roughly follow the ratio of mass energy absorption coefficients between the chamber wall material and air. The response variation of M2 is particularly important and may limit the accuracy of photon dose measurements in fields with an intense contribution of low energy photons. This energy dependence is reduced by the application of the buildup cap, which attenuates the low-energy incident photons.

Pressure Figure 4(*a*) shows the chamber response of M2 as a function of the gas pressure inside the chamber, prior and after the normal pressure correction. This correction was able to normalize the chamber responses to a standard deviation of 0.26 % (M2) and 0.39 % (T2). The results demonstrate that the pressure correction applied to a free gas in an open ionization chamber is adequate for the gas flow ionization chambers, over the gas pressure range considered.

TABLE 2 *Chamber sensitivity at various dose rates, normalized to the highest dose rate measurement.*

Dose rate, mGy·s^{-1}	M2	T2
1.09×10^{-3}±2 %	0.993±2.8 %	0.964±4.9 %
1.05×10^{-2}±2 %	0.993±2.5 %	1.02±1.5 %
1.09×10^{-1}±2 %	1.00±1.9 %	1.00±1.1 %

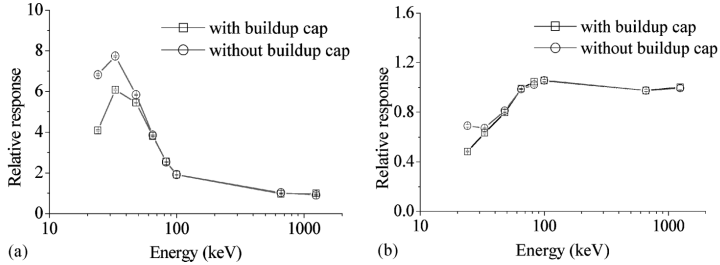

FIG. 3 *Energy response of (a) M2 and (b) T2 chambers for a constant air kerma. The values are normalized to the response for ^{60}Co photons using the buildup cap.*

Temperature The temperature effect on chamber responses was studied by irradiating the chambers at room temperatures between 17 and 23 C. The temperature of both gas bottle and chambers was stabilized during more than 6 h before measurements. Figure 4(*b*) shows the response of M2 as a function of temperature, with and without the normal temperature correction. The results demonstrate the ability of the normal temperature correction to compensate the reduced response occurring from a smaller amount of gas as the temperature increases.

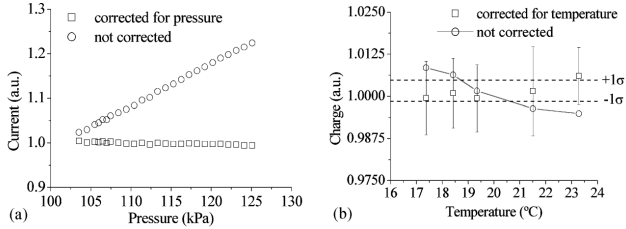

FIG. 4 *Chamber response as a function of (a) gas pressure and (b) gas temperature (normalized to the corrected measurements at 105 kPa and 20°C, respectively).*

Thermoluminescence Dosimeters

Glow Curve Figure 5 shows the glow curves obtained after pure photon (air kerma: $K_{air}=1$ Gy ^{60}Co) and mixed- eld (thermal neutron uence: $\Phi_{th}=3\times10^{11}$ cm$^{\bullet 2}$; $K_{\gamma,air}=400$ mGy) irradiations. The glow curve of LiF:Mg,Ti is composed of various peaks; the relative intensity of the high temperature peaks increases with the radiation LET. Modi ed glow curves are observed for TLD-100 irradiated in the mixed- eld, compared to irradiations in a pure photon eld. For TLD-700, a smaller modi cation is observed as a result of the reduced production of alpha particles.

Linearity The dose response of the dosimeters was investigated for photon and mixed- eld irradiations. Figure 6 shows that the low temperature peaks (III to V) of LiF:Mg,Ti exhibit a linear response for photon doses up to 2 Gy, while the high temperature peaks (VI to VIII) always have a supralinear response (i.e., their sensitivity increases with the photon dose). In the mixed- eld, the low temperature peaks of TLD-100 also have a supralinear response, but the same does not occur for TLD-700, whose main response is due to the photon component. The supralinear response of TLD-100 requires careful calibration procedures, in which the calibration neutron uence should be similar to that expected in the measurements. The high temperature peaks were not used for neutron detection due to their higher supralinear character.

Thermal Neutron Sensitivity The dosimeter sensitivities to thermal neutrons have been measured via an irradiation in the thermal column of RPI ($\Phi_{th}=8\times10^{10}$ cm$^{\bullet 2}$; $K_{\gamma,air}=100$ mGy). The neutron uence

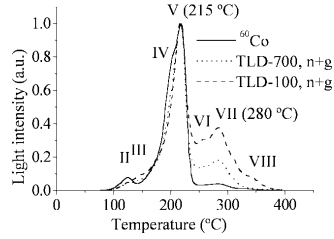

FIG. 5 *Glow curve of TLD-100 and TLD-700 after photon (^{60}Co) and mixed-field (n + g) irradiations. Peak number and temperature are given for the most important peaks.*

was monitored with gold activation foils and the photon dose was measured with hypersensitive LiF (^{7}LiF:Mg,Cu,P), which is one of the least sensitive materials to thermal neutrons [12]. The measured relative thermal neutron sensitivities were 110 and 2.0 pGy á cm^2 (^{60}Co) for the low temperature peaks of TLD-100 and TLD-700, respectively. As a consequence of the supralinear response of TLD-100, the determined thermal neutron sensitivities actually depend on the thermal neutron uence. An uncertainty of 30 % is therefore estimated for these results.

Calculations of Neutron Doses in LR-0

Fast neutron absorbed doses were calculated applying the neutron kerma factors of ICRU [13] to the neutron reference spectra of LR-0.

Due to sparse energy resolution of the BUGLE structure, spectrum-weighted kerma factors were used in the neutron dose calculations, as follows: (i) a reference spectrum consisting of a Maxwellian thermal neutron spectrum (293 K) up to 0.5 eV, a 1/E epithermal shape up to 100 keV, the evaluated LR-0 spectrum at position 3 up to 10 MeV and a Watt-Cranberg shape until 17.3 MeV was de ned as weighting spectrum; (ii) the weighting spectrum was expanded to the 640-group SAND-II structure, applying computer code POTOFINE [14] to the evaluated data; (iii) the ICRU neutron kerma factors were also converted to the 640-group SAND-II structure, using POTOFINE and extending the ICRU data at the lower end assuming a 1/v dependence; (iv) the FLXPRO program [15] was used to condense the expanded ICRU kerma factors into the BUGLE structure; (v) nally, average kerma factors were nally determined for various energy ranges, namely that covered by the LR-0 data.

In principle, an individual weighting spectrum at each measurement position should be obtained from the LR-0 data. However, as the data do not cover the complete energy range, a simpli ed procedure in which a common weighting spectrum closely resembling the evaluated data in the given energy region and having a physical meaning elsewhere was considered suf ciently accurate. Table 3 shows the average neutron kerma factors in various energy ranges and at the measurement positions of LR-0.

The analysis of the weighting spectrum yields the following contribution of each energy group to the total neutron dose at position 3, considering that the thermal neutron uence (group 1) is equal to that in

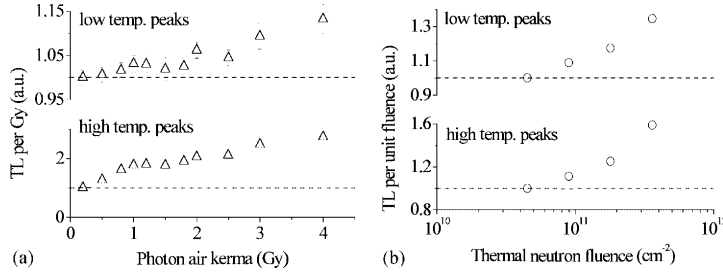

FIG. 6 *Dose response of TLD-100 (normalized to the response at the lowest dose level) in (a) photon and (b) mixed radiation fields.*

TABLE 3 *Average neutron kerma factors of A-150 plastic (fGy·m²).*

Group No.	Energy Range	Position 0	Position 2	Position 3	Position 4
1	0.01 meV 0.414 eV		2.10×10^{-2}		
2	0.414 eV 100 keV		7.06×10^{-2}		
3	100 keV 10 MeV	2.51	1.94	2.42	2.09
4	10 MeV 17.3 MeV		5.93		

group 3 [16]: 0.4 % (group 1); 5.8 % (group 2); 92.6 % (group 3); 1.2 % (group 4). According to these results, most of the neutron dose absorbed in tissue originates from fast neutrons, with energies higher than 100 keV.

Dose Measurements at LR-0

Thermoluminescence Dosimeters

Absorbed dose measurements using TLDs were performed in positions 2, 3 and 4. The reactor power during irradiations was monitored with a xed monitoring system. Table 4 shows the measured equivalent photon doses at the reference reactor power.

The thermal neutron uence rate was estimated from the equivalent photon dose measured with TLD-100 and its measured thermal neutron sensitivity. The measured thermal neutron uence rate and the evaluated fast neutron uence rate were further used to correct the photon dose measurements with TLD-700. An absorbed thermal neutron dose in A-150 tissue equivalent plastic was calculated as the product of the thermal neutron uence rate and the average thermal neutron kerma factor.

Ionization Chambers

Photon and fast neutron dose measurements were performed in positions 2, 3, 4 and 7 of LR-0. The photon equivalent dose obtained with each chamber is shown in Table 5. From the thermal neutron sensitivity of the T2 chamber, the thermal neutron dose (which was estimated with thermoluminescence dosimeters)contributes with twice its value to the neutron signal of the T2 chamber. Such correction has been considered in the fast neutron dose evaluation. As the fast neutron dose calculation is based in the difference between the T2 and M2 chambers (according to Eq 1), neutron dose uncertainties at positions 4 and 7 are too high to be reliable. The results obtained with the two chambers provide consistent measurements of photon dose rates at these positions. Comparing to the results obtained with TLDs, discrepancies lower than 30 % were obtained for the measured photon doses. The results presented in Tables 4 and 5 con rm that the neutron dose absorbed in tissue has a large contribution from fast neutrons, in the order of 1 %.

TABLE 4 *Dose measurements using thermoluminescence dosimeters.*

Position	TLD-700 ^{60}Co, nGy·s^{-1}	TLD-100 ^{60}Co, nGy·s^{-1}	D_g, nGy·s^{-1}	Φ_{th}, cm^{-2}·s^{-1}	D_{th}, pGy·s^{-1}
2	135.3±5 %	1395±9 %	111±6 %	1.2×10^{4}±30 %	2.4×10^{3}±30 %
3	32.2±4 %	40.7±6 %	32.0±4 %	77±30 %	16±30 %
4	8.9±6 %	9.3±9 %	8.9±6 %	3.5±30 %	0.73±30 %

TABLE 5 *Photon dose equivalent, measured with ionization chambers.*

Position	M2, ^{60}Co nGy·s^{-1}	T2, ^{60}Co nGy·s^{-1}	D_f ^{60}Co nGy·s^{-1}
2	131.8±4 %	280.3±5 %	144±14%
3	32.4±4 %	35.6±4 %	3.1±60 %
4	6.4±9 %	6.5±9 %	···
7	2.3±34 %	2.2±18 %	···

TABLE 6 *Ratio of photon (g) and neutron (n) doses between various positions.*

	Evaluated			TLD		Ion chamber	
Ratio	n_{th}	n_f	g	n_{th}	g	n_f	g
Position 2/Position 3	···	47	8.0	149±62	3.5±0.2	46±28	4.1±0.2
Position 3/Position 4	27	1.6	4.2	22±9	3.6±0.3	···	5.1±0.5

Conclusions

Table 6 shows the photon and neutron attenuation, given by the LR-0 evaluated data [1,2,16] and measured in the present work. A good agreement is obtained concerning the photon dose, among the various results. The discrepancy between the evaluated and measured photon attenuation from position 2 (in the barrel) to 3 (in the pressure vessel) is justi ed by the increased contribution of low-energy photons in the RPV, which is not included in the evaluated data. As for neutrons, the different attenuation of thermal and fast neutrons has been characterized using TLDs and ionization chambers, respectively. A good agreement was also achieved relatively to the evaluated data.

The present experiment was therefore able to provide additional information to the LR-0 data, concerning the thermal neutron component. Furthermore, it demonstrated the applicability of independent methods ion chambers and TLDs for consistent dose measurements in reactor-based mixed- elds. Thermal neutron measurement uncertainties in the order of 30 % re ect those from the estimation of thermal neutron uence rate using TLDs. In principle, this dif culty may be overcome by performing TL irradiations at neutron doses as low as those involved in the present study. Such low dose rates are further responsible for the high uncertainties in the measured fast neutron doses at the RPV.

Acknowledgments

The authors thank the LR-0 operators for their assistance in the irradiations, Dr. Martin Grantz (Hochschule, Zittau, Germany) for the support concerning the TL evaluations and Dr. Bohumil O mera for providing the evaluated data. This work was partly funded by the 5th Framework Programme of the Euratom (Project FIR1-CT-2002-40157). A. C. Fernandes acknowledges the Foundation for Science and Technology, Portugal, for a post-doctoral scholarship (SFRH/BPD/16664/03).

References

[1] O mera, B. and Zaritsky, S., WWER-1000 Mock-up Experiment, JV č. 12036-R (Rev. 1), Nuclear Research Institute Ře plc (Czech Republic), May 2002.

[2] O mera, B., Cvachovec, F., and Mař'k, M., The Results of Photon Spectra Measurements Over the Reactor Pressure Vessel Simulator in WWER-100 Model in the LR-0 Experimental Reactor, REDOS-R(06), Issue 1, Nuclear Research Institute Ře plc, March 2004.

[3] *Clinical Neutron Dosimetry Part 1: Determination of Absorbed Dose in a Patient Treated by External Beams of Fast Neutrons*, ICRU Report 45, International Commission on Radiation Units and Measurements, Bethesda, MD, 1989.

[4] Raaijmakers, C. P. J., Watkins, P. R. D., Nottelman, E. L. et al., The Neutron Sensitivity of Dosimeters Applied to Boron Neutron Capture Therapy, *Med. Phys.*, Vol. 23, 1996, pp. 1581 1589.

[5] Kosunen, A., Kortesniemi, M., YIŠ-Mella et al., Twin Ionisation Chambers for Dose Determinations in Phantom in an Epithermal Neutron Beam, *Radiat. Prot. Dosim.*, Vol. 81, No. 3, 1999, pp. 187 194.

[6] Zoetlief, J., Schlegel-Bickmann, D., Schraube, H., and Dietze, G., Characteristics of Mg/Ar Ionisation Chambers Used as Gamma-Ray Dosemeters in Mixed Neutron-Photon Fields, *Phys. Med. Biol.*, Vol. 3, No. 12, 1986, pp. 1339 1351.

[7] Waterman, F. M., Kuchnir, F. T., and Skaggs, L. S., Energy Dependence of the Neutron Sensitivity of C CO_2, Mg Ar and TE-TE Ionisation Chambers, *Phys. Med. Biol.*, Vol. 24, No. 4, 1979, pp. 721 733.

[8] *Absorbed Dose Determination in Photon and Electron Beams*, Technical Reports Series No. 277, International Atomic Energy Agency, Vienna, 1987.

[9] Horowitz, Y. S., Neutron Dosimetry, in *Thermoluminescence and Thermoluminescent Dosimetry Vol. II*, CRC Press, Boca Raton, FL, 1984, pp. 90 114.

[10] Hahn, T., Fellinger, J., Henniger, J. et al., Neutron Response of LiF TL Detectors, *Radiat. Prot. Dosim.*, Vol. 44, No. 1-4, 1992, pp. 297 300.

[11] A•t Abderrahim, H., McGarry, E. D., and Spiegel, V., Assessment of the Fast Neutron Sensitivity of Thermoluminescent Gamma Dosimeters, in *Proc. 7th ASTM Symp. Reactor Dosimetry, Strasbourg, 1990*, Kluwer Academic Publishers, Dordrecht, 1992, pp. 529 536.

[12] Wang, S. S., Cai, G. G., Zhou, K. Q., and Zhou, R. X., Thermoluminescence Response of ^{6}LiF (Mg,Cu,P) and ^{6}LiF (Mg,Cu,P) TL Chips in Neutron and Gamma Ray Mixed Fields, *Radiat. Prot. Dosim.*, Vol. 33, No. 1-4, 1990, pp. 247 250.

[13] *Photon, Electron, Proton and Neutron Interaction Data for Body Tissues*, Report 46, International Commission on Radiation Units and Measurements, Bethesda, MD, 1992.

[14] Ser n, T., PC Programs for the Conversion of Neutron Spectra and Cross Sections Between Different Group and Point Representations, in *Proc. 7th ASTM Symp. Reactor Dosimetry, Strasbourg, 1990*, Kluwer Academic Publishers, Dordrecht, 1992, pp. 239 246.

[15] Stallmann, F. W., LSL-M2: A Computer Program for Least-Squares Logarithmic Adjustment of Neutron Spectra, NUREG/CR-4349, ORNL/TM-9933, Oak Ridge National Laboratory, 1986.

[16] O mera, B., Kyncl, J., Mařik, M. et al., The Gamma Ray Spectra Measurement in Reactor Pressure Vessel Simulator in WWER-1000 Engineering Benchmark, in *Proc. 11th Intl. Symp. Reactor Dosimetry, Brussels, 2002*, World Scienti c, Singapore, 2003, pp. 512 518.

Journal of ASTM International, Vol. 3, No. 7
Paper ID JAI13484
Available online at www.astm.org

N. E. Holden[1]

Survey of the Latest Evaluated Nuclear Data

ABSTRACT: The results of a review and evaluation of nuclear data published in the scientific literature are presented. The status of new chemical elements that have been discovered and officially named and the latest data for new elements that have been claimed are examined. Half lives of very long-lived nuclides are presented. Data on the very heavy elements are tabulated. The problems presented by the attempt to estimate errors for the various nuclear data are considered as well as the psychological aspect of error estimation are also discussed.

KEYWORDS: half lives, new chemical elements, superheavy elements, errors

Introduction

The published scientific literature is scanned and periodically evaluated for neutron and non-neutron nuclear data and the resulting recommendations are published [1,2]. After the literature has been scanned and appropriate data collected, there are often problems with regard to the treatment of the various types of data during this evaluation process and with regard to the method by which the recommendations are drawn from the assessment of the collection of individual measurements. Some problems with uncertainties are presented.

Periodic Table of the Chemical Elements

There have been recent measurements reported in the literature that have claimed discovery of two new chemical elements [3] with proton numbers Z=113 and Z=115. There is a process in place by which that type of information is reviewed and conclusions drawn as to which set of reported data on a new element has a priority claim on the discovery and identification of a new chemical element and whether or not there has been verification of that claim. The resulting conclusion of the review process would allow one group to claim the discovery and be given the privilege of supplying the name of this new element.

In earlier centuries, the basis for the claim of discovery of a chemical element used the properties of the new substances, the colors of their compounds, the shapes of their crystals, and their reactivity to determine the existence of new elements. The honor of discovery has often been accorded not to the person who first isolated the element but to the person who discovered the original mineral, even when the ore was impure and that ore actually contained many elements. The atomic weight of an element and a spectral analysis of an element were not available in the early days, but both of these elemental properties would be required before discovery of the element would be accepted by the latter part of the 19th century.

The requirements for discovery claims have tightened through the years and claims that were previously accepted would no longer meet the minimum constraints imposed today.

There are also cases where the honor of discovery is not given to the first person to actually discover the element but to the first person to claim the discovery in print. If a publication was delayed, the discoverer has often been "scooped" by another scientist.

There were claims and counter-claims between American and Russian scientists 30 years ago and there are similar problems between German and Russian scientists today. Not all problems are of recent vintage. Over the past three centuries, there has been a long list of false claims for elements. The following

Manuscript received June 20, 2005; accepted for publication May 17, 2006; published online June 2006. Presented at ASTM Symposium on Reactor Dosimetry, 12th International Symposium on 8–13 May 2005 in Gatlinburg, TN; D. W. Vehar, D. M. Gilliam, and J. M. Adams, Guest Editors.
[1] Guest Physicist, National Nuclear Data Center, Brookhaven National Laboratory, Upton, NY, 11973.

is a partial list of names proposed in some of these false claims: austrium, berzelium, carolinium, celtium, columbium, damarium, davyum, decipium, demonium, denebium, didymium, donarium, dubhium, eurosamarium, euxenium, glaucodymium, ilmenium, incognitium, ionium, junonium, kosmium, lucium, masurium, metacerium, monium, mosandium, moseleyum, neokosmium, neptunium, nipponium, pelopium, philippium, polonium, rogerium, russium, sirium, thorine, vestium, victorium, wasmium, welsium, and ytterbium.

The above names of ytterbium, columbium, ionium, neptunium, and polonium are not the same as the presently accepted names for those existing elements of those names, nor even the controversial columbium/niobium element with proton number Z=41, or the older name that was assigned to ^{230}Th.

At the turn of the 20th century, the International Committee on Atomic Weights (ICAW) was formed. Although ICAW did not set internationally approved names, a name with an atomic weight value in their table lent support for the adoption of that name by the chemical community. Twenty years later, the ICAW became part of IUPAC, the International Union of Pure and Applied Chemistry, when it was formed. In 1949, the responsibility for acceptance of the name of a chemical element was given by IUPAC to its Commission on Nomenclature of Inorganic Chemistry (CNIC). The CNIC did not deny the right of a discoverer to propose a name for a new chemical element. However, the general criteria were that the approved name should differ as little as possible in different languages; the name should be based on practicality and prevailing usage; and finally the choice of the name carries no implication at all about the priority of discovery. The names of the chemical elements are determined by the acceptance of that name by the chemical community, the priority rights of the discoverer not withstanding. In the latest reorganization of IUPAC, the CNIC no longer exists. The IUPAC Inorganic Chemistry Division Committee now has responsibility for acknowledging new elements.

Previously, chemical elements were discovered in nature. For more than half a century now, new chemical elements are not being discovered in nature but are being synthesized using nuclear reactions. As a result, a joint committee has been formed by IUPAC and by IUPAP (the International Union of Pure and Applied Physics). This joint IUPAC/IUPAP committee has the responsibility to review the claims of discovery of a new element and to investigate whether or not there has been a verification of each discovery. As a result, the element with proton number Z=110, Darmstadtium, has now been added to the Periodic Table [4]. A second element with proton number Z=111, Roentgenium, has also been reviewed [5] and approved.

Radioactive Decay Constants

The radioactive half life of a nuclide (the reciprocal of the radioactive decay constant) is of interest to reactor dosimetry because the half life of the product nucleus in a nuclear reaction has a direct impact on the determination of the reaction rates. For a given count rate, the reaction rate is inversely proportional to the half life of the measured product nucleus. Problems often arise in connection with the estimation of the systematic component of the error in the half life or decay constant measurement. Because of their use in dating samples, there are some long-lived nuclides whose half lives are of interest to the geological community. In many cases, these nuclides have reported half lives, which completely disagree with each other.

^{176}Lu results from counting experiments report half-life values of 3.69 (.02) $\times 10^{10}$ years [6] and also 4.08 (0.03) $\times 10^{10}$ years [7], where the value in parentheses represents the uncertainty. If one accepts the reported uncertainty as one standard deviation, these two measurements differ between 13 and 19 standard deviations and could not be considered to be estimating the same physical quantity. In a similar manner, the data reported for ^{187}Re (a liquid scintillation counting measurement) of 3.51 (0.37) $\times 10^{10}$ years [8] and (a cryogenic microcalorimeter) of 6.2 (0.6) $\times 10^{10}$ years [9], are significantly different estimates of this half life. These problems will be discussed in a later section of this paper.

There has been a significant interest in the possible decay modes of the stable isotopes of the chemical elements. For the very long-lived nuclides (many of which have always been considered stable isotopes) there have been attempts to determine the decay rate for exotic reactions such as proton decay, long-lived alpha decay, long-lived beta decay, and double beta decay. Previously [10], attempts to discover violations to the principle of charge conservation were discussed. There have been no new measurements since the

TABLE 1—*Radioactive half lives and decay modes of long-lived (quasistable) nuclides.*

Nuclide	Decay	Years	Nuclide	Decay	Years	Nuclide	Decay	Years
$^{1}H^{*}$	proton	$>35\cdot10^{27}$	^{40}Ca	ec-ec	$59\cdot10^{20}$	^{48}Ca	$\beta^-\beta^-$	$43\cdot10^{18}$
$^{50}Cr^{*}$	β^+-ec	$13\cdot10^{17}$	^{58}Ni	β^+-ec	$>4\cdot10^{19}$	^{64}Zn	ec-ec	$>23\cdot10^{17}$
$^{71}Ga^{*}$	β^-	$35\cdot10^{25}$	$^{76}Ge^{*}$	$\beta^-\beta^-$	$18\cdot10^{20}$	$^{82}Se^{*}$	$\beta^-\beta^-$	$12\cdot10^{19}$
$^{78}Kr^{*}$	$\beta^+\beta^+$	$>20\cdot10^{20}$	^{94}Zr	$\beta^-\beta^-$	$>1\cdot10^{17}$	$^{96}Zr^{*}$	$\beta^-\beta^-$	$21\cdot10^{18}$
$^{92}Mo^{*}$	β^+-ec	$>19\cdot10^{18}$	$^{100}Mo^{*}$	$\beta^-\beta^-$	$82\cdot10^{17}$	^{96}Ru	$\beta^+\beta^+$	$>31\cdot10^{15}$
$^{106}Cd^{*}$	$\beta^+\beta^+$	$>24\cdot10^{19}$	$^{108}Cd^{*}$	ec-ec	$10\cdot10^{17}$	^{114}Cd	$\beta^-\beta^-$	$>6\cdot10^{17}$
^{116}Cd	$\beta^-\beta^-$	$38\cdot10^{18}$	^{124}Sn	$\beta^-\beta^-$	$>22\cdot10^{17}$	^{128}Te	$\beta^-\beta^-$	$2\cdot10^{24}$
^{130}Te	$\beta^-\beta^-$	$8\cdot10^{20}$	^{124}Xe	ec-ec	$>1\cdot10^{17}$	^{134}Xe	$\beta^-\beta^-$	$>11\cdot10^{15}$
^{136}Xe	$\beta^-\beta^-$	$>8\cdot10^{20}$	^{130}Ba	ec-ec	$2\cdot10^{20}$	^{132}Ba	ec-ec	$13\cdot10^{20}$
$^{136}Ce^{*}$	$\beta^-\beta^-$	$>18\cdot10^{15}$	^{138}Ce	ec-ec	$>9\cdot10^{13}$	$^{150}Nd^{*}$	$\beta^-\beta^-$	$7\cdot10^{18}$
$^{160}Gd^{*}$	$\beta^-\beta^-$	$>19\cdot10^{18}$	$^{176}Yb^{*}$	$\beta^-\beta^-$	$>16\cdot10^{16}$	^{180}W	ec-ec	$7\cdot10^{16}$
$^{186}W^{*}$	$\beta^-\beta^-$	$37\cdot10^{17}$	^{209}Bi	α	$19\cdot10^{18}$	^{238}U	$\beta^-\beta^-$	$20\cdot10^{20}$

study of the ^{73}Ge beta decay to ^{73}As, which is energetically forbidden. The measurement [11] led to a lower half-life limit $>2.6\times10^{23}$ years.

A few years ago, half lives and decay modes of long-lived nuclides were presented [10]. A latest revision [1] of these data is presented in Table 1. There have been changes marked by asterisks, particularly in the case of the double beta decay ($\beta\beta$) mode nuclides. Only decay modes that involve the emission of two neutrinos are listed in the table, since ($\beta\beta$) decay modes, without the emission of neutrinos (0v) have not been detected. Their lower limits are one or more orders of magnitude larger than (2v $\beta\beta$) decay modes.

The claim [12] by Klapdor-Kleingrothaus et al. that they have measured a (0v $\beta\beta$) decay in ^{76}Ge, which would imply lepton number nonconservation, has not yet been substantiated, in spite of the very large number of publications on the subject, both by the original authors and others.

Data on the Very Heavy Chemical Elements

For the very heavy elements, there are other modes of decay (determining factors in stability), spontaneous fission (sf) decay, and cluster decay. In sf decay, the nucleus breaks up into two approximately equal reaction products, both of which have very large masses (some 15 to 40 times larger than an alpha particle). Cluster decay is radioactive decay in which the emitted particle has a much smaller mass than a fission product but it is still larger than the alpha particle (some three to eight times larger). For very heavy chemical elements, a path to the super-heavy elements is being explored. In the process of this investigation, new nuclides and elements are being discovered. The present list [1] of the highest Z elements ($Z > 109$) and their nuclides is shown in Table 2 below.

Note that in Tables 1 and 2, the uncertainty is five or less in the last digit quoted, unless the value is preceded by an approximate sign ($\sim$) in which case the uncertainty is greater than six and could be two digit, e.g., 34 ± 10 would be listed as ~34.

The Problem of Error Estimation

Absolute certainty is a privilege of uneducated minds and fanatics. It is for scientific folk, an unattainable ideal [13]. Most scientists would agree with the above assessment. However, in practice, all too often we assume that with a little effort, we can easily reduce all of our experimental errors to the level of insignificance. There has been an increased emphasis on uncertainties in measurements with the development of computerized programs to handle sensitivity analysis using variance-covariance matrices to treat the correlation among data. However, if input uncertainties have been poorly estimated, computer programs merely enable you to determine the wrong answer much more quickly. There has been a tendency with the advent of hand-held calculators for users to believe that all of the digits listed on the display screen are significant.

In spite of the importance of consistency in working with uncertainties, there was no international consensus on these matters until the mid-1990s. The International Committee for Weights and Measures (Comité International des Poids et Mesures, CIPM) initiated the development of a guide that would

TABLE 2—*Nuclear data on the very heavy chemical elements.*

Nuclide	Half life	Mode decay	Energy (MeV)	Nuclide	Half life	Mode decay	Energy (MeV)
^{267}Ds	3 μ-sec	α	11.6	^{269}Ds	0.17 ms	α	11.1
^{270m}Ds	~6 ms	α	11.0–12.2	^{270g}Ds	~10 μs	α	11.0
^{271m}Ds	~1.1 ms	α	10.7	^{271g}Ds	~56 ms	α	10.7
^{273m}Ds	0.76 ms	α	11.8	^{273g}Ds	118 ms	α	9.73
^{279}Ds	0.18 s	sf 90 % α 10 %	9.70	^{281}Ds	~9.6 s	sf	
^{272}Rg	1.5 ms	α	11.0	^{274}Rg	9.26 ms	α	11.15
^{279}Rg	~0.17 s	α	10.4	^{280}Rg	~3.6 s	α	9.8
^{277}112	0.48 ms	α	11.2–11.7	^{282}112	0.5 ms	sf	
^{283}112	~4 s	α 100 % sf ⩽ 10 %	9.54	^{284}112	0.10 s	sf	
^{285}112	~34 s	α	9.16	^{278}113	0.34 ms	α	11.7
^{283}113	~0.1 s	α	10.1	^{284}113	~0.5 s	α	10.0
^{286}114	0.16 s	sf 60 % α 40 %	10.2	^{287}114	0.5 s	α	10.02
^{288}114	0.8 s	α	9.95	^{289}114	~2.7 s	α	9.8
^{287}115	0.03 s	α	10.6	^{288}115	~87 ms	α	10.5
^{290}116	~15 ms	α	10.9	^{291}116	~6 ms	α	10.74
^{292}116	~18 ms	α	10.66	^{293}116	~0.05 s	α	10.5
^{294}118	~1.8 ms	α	11.7				

establish and promote general rules for calculating and expressing uncertainty. This guide is titled "Guide to the Expression of Uncertainty in Measurement [14]. It is usually referred to by its abbreviation "GUM." GUM introduces a new method for categorizing uncertainties, depending upon how they are evaluated.

"Type A uncertainties" are those uncertainties evaluated by the application of standard statistical methods to a series of observations. The standard deviation of the mean is termed a "standard uncertainty obtained by a type A evaluation" according to GUM. "Type B" evaluations of uncertainty apply methods other than statistical analysis of a series of observations in order to determine a standard uncertainty. "Type B uncertainties" can include those previously referred to as systematic uncertainties. The determination of a quantity may require use of other sources of information, such as data of a calibration standard, data taken from a reference document, or data taken from a manufacturer's specification. Whatever the source, a type B evaluation requires that a standard uncertainty be extracted from the information by a careful consideration of the way in which the uncertainty has been expressed by the source. If the source indicates a stated level of confidence, such as 95 % or 99 %, convert that uncertainty to a standard uncertainty by treating the quoted uncertainty as if a normal probability distribution had been used to calculate it and dividing by the appropriate factor for such a distribution. This would imply factors of 1.96 and 2.576 in the level of confidence stated above.

Eisenhart [15] noted that a reported value, whose accuracy is entirely unknown, is worthless. A measurement result is complete only when accompanied by a quantitative statement of its uncertainty. This uncertainty is required in order to decide if the result is adequate for its intended purpose and to ascertain if it consistent with other similar results.

A reported value whose accuracy is significantly overestimated is extremely misleading, particularly if a truly honest effort has not been made to identify and quantify the various sources of type B uncertainty. Most present day measurements rely on the measured values of various other parameters as so-called, auxiliary constants, and if all of these parameters had unknown sources of type B uncertainty, which biased their results, we would have an enormous problem.

Usually, recommended values and uncertainties are based on the averages obtained by weighting each measurement by the reciprocal square of the quoted standard deviation, which is called variance weighted averaging. Occasionally, recommendations may be based on selecting the one good recent measurement. There are times when a discrepancy in values and uncertainties quoted by a given technique require that the techniques be averaged to produce a more reasonable recommendation.

There are measurements, where the authors quote uncertainties that are orders of magnitude smaller than all other measurements of that quantity. As a result, if variance weighting of the results is applied indiscriminately, these measurements would both disagree with and would exclude many other good recent

measurements from consideration in determining the average value of the parameter. Undoubtedly, the "type B uncertainties" have not been carefully considered in these publications.

When experiments are performed at the level of five % to ten % accuracy, the total number of counts recorded is an important consideration. However, when the quoted overall accuracy reaches the level of one-half percent or better, the estimate of all "type B uncertainties" begin to become a controlling influence on the total accuracy. Continuing to improve the statistical precision by collecting more raw data points does not significantly improve the total error, except superficially, in the absence of any effort to estimate the type B uncertainties. Using variance weighting indiscriminately in such cases penalizes the authors who attempt the difficult task of estimating their "type B uncertainties," while benefiting the authors who make no such attempt to determine all of their sources of uncertainty.

If one has a choice in designing the ideal experiment to measure a physical quantity such as a half life, one would choose to make measurements on many different samples, using a number of duplicate instruments and utilizing a variety of different methods or techniques. This procedure should help to provide the necessary information to correctly estimate the "type B uncertainties" in the measurement.

Psychological Factors in Estimating Error

We now consider the psychological factor, which is involved with the treatment of type B uncertainties, as noted by both Birge [16] and Bridgman [17]. Individual authors search for all sources of error involved in their work, which would bring their result into agreement with all of the earlier measurements of their particular quantity. Whenever the authors' renormalized result agrees with all other measurements of the quantity, the author ceases to investigate their errors any further. In addition, if their measured value is too large, compared to other measurements, the authors do not look for any factors, which would cause their result to increase, but merely for factors that result in the reduction of their measured value.

Consider the following two examples of psychological factors. For a large number of years, the value for the charge on the electron had been based on a set of measured values that were all consistent with one another. When Rutherford measured a value that was reported to be 60 % larger than all of the previous results, all of the measurements made subsequent to Rutherford were suddenly found to be consistent with his new higher value.

In a similar manner, all of the early measurements of Planck's constant clustered about the same value until Birge [16], in 1941, raised that value by one and one-quarter percent in his analysis of the fundamental constants. After this breakthrough, all subsequent measurements of Planck's constant clustered around this "new" estimate.

Finally, consider the evaluation of the half life for ^{239}Pu. In 1974, a best estimate [18] was reported of 24,395 (29) years, where the uncertainty was quoted at the confidence level corresponding to three standard deviations (3σ). Thus, the probability would be 99.7 % that the real value should fall within those uncertainty limits. This half-life result was obtained from experiments that used the alpha particle counting technique. All of these early alpha-counting experiments were consistent. However, there had been one calorimetric measurement [19], which reported a half-life value that was some 300 years lower. More recent measurements on the ^{239}Pu half life (including alpha counting measurements) all now agree with the lower half-life estimate. The presently recommended value is now 30 standard deviations (30σ) away from the 1974 recommendation.

Conclusions

It can be concluded from this survey of nuclear data in the above discussions that both nuclear data and the methods for treating uncertainties are very robust fields. All of the above areas are included in the review of nuclear data that is performed for the annual publication of the *Handbook of Chemistry and Physics* [2].

New chemical elements continue to be discovered and to be named. There are many long-lived nuclides that were considered to be stable but whose radioactive decay has now been observed. For the very heavy chemical elements, data have been presented in the scientific literature, for which the verification will be necessary before the claim can be verified and a name can be proposed and accepted. Finally, it can be seen that the so-called type B uncertainties are very difficult to estimate but they are

extremely important to identify and to either eliminate them or to at least account for them in the quoted result for experiments.

Acknowledgments

This research was supported by the US DOE under Contract No. DE-ACO2-98CH10886. Helpful discussions with R. N. Reciniello and J.-P. Hu (BNL) are gratefully acknowledged.

References

[1] Holden, N. E., "Table of the Isotopes (Revised 2002)," *Handbook of Chemistry and Physics*, 85th ed., edited by D. R. Lide, CRC Press, Boca Raton, FL, 2004, Sec. 11, pp. 50–201, and updates.
[2] Holden, N. E., "Neutron Scattering and Absorption Properties (Revised 2003)," *Handbook of Chemistry and Physics*, 85th ed., edited by D. R. Lide, CRC Press, Boca Raton, FL, 2004, Sec. 11, pp. 202–217, and updates.
[3] Oganessian, Yu. Ts. et al., *Phys. Rev. C*, Vol. 69, 2004, p. 021601.
[4] Holden, N. E. and Coplen, T. B., *Chemistry International*, Vol. 26, 2004, pp. 8–9.
[5] Karol, P. et al., *Pure Appl. Chem.*, Vol. 75, 2003, pp. 1601–1611.
[6] Nir-El, Y. and Lavi, N., *Appl. Radiat. Isot.*, Vol. 49, 1998, pp. 1653–1655.
[7] Nir-El, Y. and Haquin, G., *Phys. Rev. C*, Vol. 68, 2003, p. 067301.
[8] Cosulich, E. et al., *Phys. Lett. B*, Vol. 295, 1992, pp. 143–147.
[9] Naldrett, S. N., *Can. J. Phys.*, Vol. 62, 1984, pp. 15–20.
[10] Holden, N. E., "Radiation Dosimetry in the 21st Century," *Proc. 11th International Symposium Reactor Dosimetry*, Brussels, Belgium, Aug. 18–23, 2002, World Sci. Publ. Co., PTE, Ltd, Singapore, 2003, pp. 646–653.
[11] Klimentov, A. A. et al., *Phys. Lett. B*, Vol. 535, 2002, pp. 77–84.
[12] Klapdor-Kleingrothaus, H. V. et al., *Mod. Phys. Lett. A*, Vol. 16, 2001, pp. 2409–2420.
[13] Keyser, C. J., *Mathematical Philosophy*, E.P. Dutton & Co., New York, 1922, p. 120.
[14] ISO, "Guide to the Expression of Uncertainty in Measurement," *International Organization for Standardization*, Geneva, Switzerland, 1993.
[15] Eisenhart, C., *Science*, Vol. 160, 1968, pp. 1201–1204.
[16] Birge, R. T., *Nuovo Cimento, Suppl.*, Vol. 6, 1957, 39–67.
[17] Bridgman, P. W., *Proc. Natl. Acad. Sci. U.S.A.*, Vol. 46, 1960, pp. 1394–1400.
[18] Deruytter, A. J. and Becker, W., *Nucl. Sci. Eng.*, Vol. 1, 1974, pp. 311–322.
[19] Oetting, F. L., *Dow Chemical Co. Report*, RFP-1469, 1970.

Journal of ASTM International, Vol. 3, No. 2
Paper ID JAI13485
Available online at www.astm.org

Lawrence R. Greenwood[1]

Gas Production in Reactor Materials

ABSTRACT: This paper presents an overview of the principal nuclear reactions that are known to produce hydrogen and helium in irradiated materials and a summary of the comparison of measurements with predictions in various reactors. Hydrogen and helium are produced in all reactor materials by fast neutron reactions which typically have thresholds above 4 MeV. Selected elements also have thermal neutron gas production reactions that can be quite prolific, such as ^{6}Li, ^{10}B, and ^{14}N, and there are a number of elements which produce transmutation products that have high thermal neutron gas production cross sections, most notably ^{59}Ni produced by irradiation of Ni and ^{65}Zn produced by irradiation of Cu or Zn. Since gas production cross sections are isotope-specific, gas production rates can change during irradiation due to transmutation effects or initial rates can be modified by isotopic tailoring of reactor materials.

KEYWORDS: helium, hydrogen

Introduction

Helium and hydrogen are produced in reactor materials by a combination of thermal and fast neutron reactions on the elements and impurities in the materials. Transmutation products may also have significant nuclear cross sections for gas production. In order to calculate the gas production accurately, it is necessary to understand all of these gas production source terms and sum over all such reactions. Helium is generally not found as an impurity in unirradiated materials and helium mobility is so low that it is possible to predict helium concentrations quite accurately. However, hydrogen is found as an impurity in virtually all materials and at reactor operating temperatures, hydrogen diffusion from the large reservoir of free hydrogen in the reactor water or surrounding materials is so large that these environmental sources of hydrogen may swamp any hydrogen produced by nuclear reactions, especially at lower neutron fluences. At higher neutron fluences, ^{59}Ni is the major source of both helium and hydrogen in reactor materials that contain nickel.

Thermal Neutron Reactions and Transmutation

The most important source of helium at low neutron fluences in reactor materials is the presence of a boron impurity since the $^{10}B(n,\alpha)\,^{7}Li$ reaction has a very high thermal neutron cross section of 3837 barns, as shown in Fig. 1. The natural boron content of reactor steels is typically 1 to 10 wppm (weight part per million) and the boron content of Inconel is typically higher at 5 to 20 wppm and has been found to have much higher concentrations in some samples. Although not so well known, there are many other stable isotopes that have significant thermal neutron cross sections that produce hydrogen or helium, as shown in Table 1, including ^{3}He, ^{6}Li, ^{10}B, ^{14}N, ^{17}O, ^{33}S, ^{35}Cl, ^{36}Ar, ^{39}K, ^{40}K, ^{54}Fe, and a few weaker cross sections for a number of other isotopes. Except for O, N, S and Fe most of these isotopes are not common in reactor materials except as impurities and are thus not very important gas producers. However, they may be more important for materials that are irradiated in reactors.

The isotopes listed above are the most important thermal neutron sources of gas at low fluences. However, at higher neutron fluences, they may burn out and cease to produce additional gas. At higher neutron fluences, there are a number of radioactive transmutation products that have significant thermal neutron gas-production cross sections, as shown in Table 1, including ^{7}Be, ^{22}Na, ^{36}Cl, ^{37}Ar, ^{41}Ca, ^{55}Fe,

Manuscript received June 20, 2005; accepted for publication September 29, 2005; published online January 2006. Presented at ASTM Symposium on Reactor Dosimetry, 12th International Symposium on 8–13 May 2005 in Gatlinburg, TN; D. W. Vehar, D. M. Gilliam, and J. M. Adams, Guest Editors.
[1] Laboratory Fellow, Pacific Northwest National Laboratory, Richland, WA 99354.

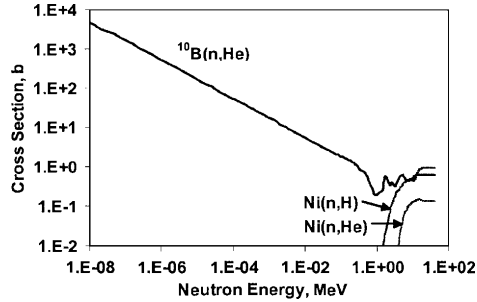

FIG. 1—*Comparison of thermal and fast neutron cross sections for reactor irradiations.*

^{59}Ni, ^{65}Zn, and a few higher mass isotopes. The most important radioactive isotope for reactor materials is ^{59}Ni, which is known to be the major source of helium and hydrogen above neutron fluences of about 1 $\times 10^{21}$ n/cm^2 [1]. The ^{59}Ni evaluated thermal neutron cross sections are shown in Fig. 2 and the production of helium is shown as a function of thermal neutron fluence and compared to He measurements in High Flux Isotope Reactor (HFIR) in Fig. 3. Hydrogen production from ^{59}Ni is a factor of six lower than He production, as discussed later. The transmutation of several of the Ni isotopes is compared to measurements in Fig. 4.

Most of the other isotopes in Table 1 are not commonly seen in reactor materials except for ^{54}Fe and ^{55}Fe produced by transmutation [2]. However, they may be very important in material irradiation experiments such as the production of ^{65}Zn produced during irradiations of Cu [3].

Gas Production by Fast Neutrons

Almost all elements have significant fast neutron cross sections for the production of hydrogen and helium. For reactor steel or Inconel, the main elements of Fe, Ni, Cr, and Mn all have (n, p) cross sections with

TABLE 1—*Stable and radioactive isotopes with significant thermal neutron gas production cross sections (2200 m/s values are listed).*

Stable Isotopes	Helium, barns	Hydrogen, barns	Radioactive Isotopes	Helium, barns	Hydrogen, barns
3He	5330		7Be	0.14	39000
6Li	941		22Na	260	28000
10B	3837		36Cl		0.047
14N		1.83	37Ar	2000	70
17O	0.24		41Ca	0.17	
33S	0.14	0.002	55Fe	0.009	
35Cl		0.48	59Ni	14	2
40K	0.42	4.4	65Zn	2	
54Fe	0.01 mb				

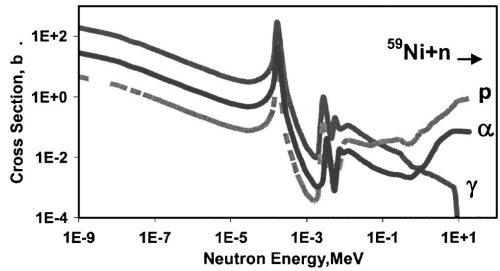

FIG. 2—*Evaluated thermal neutron cross sections for ^{59}Ni.*

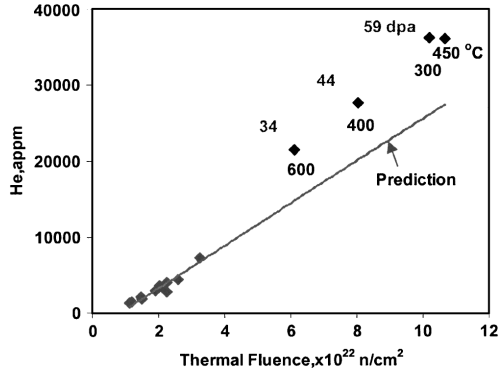

FIG. 3—*Comparison of measured and calculated helium production in Ni irradiated in HFIR. The calculations underpredict the He at high neutron fluences.*

thresholds of about 1 MeV and (n,α) cross sections with thresholds of about 4 MeV, as shown for Ni in Fig. 1. Ni has the highest fast neutron cross sections in reactor materials and is additionally important due to the ^{59}Ni reactions at high fluences [4]. Whereas gas production from thermal neutrons can be easily estimated from the well known thermal neutron cross sections, adjusted for the reactor temperature as necessary, fast neutron gas production cross sections must be calculated from the neutron spectra and are thus subject to significant spectral changes according to the specific location in a reactor. If the neutron spectra are not known, then pressure vessel spectra tend to provide a conservative estimate of the fast gas production since the cross sections tend to decrease at locations nearer to the reactor core, as shown for various locations in a BWR [5].

It is also very important to note that in order to accurately calculate fast neutron gas production, the fast neutron fluences must be determined in a consistent manner as the gas cross sections. If a neutron spectral calculation is available, then it is straightforward to calculate the spectral-averaged gas production cross sections and the calculated fast neutron fluence, taking care to use the same energy threshold such as 1 MeV for both calculations. However, if fast neutron cross sections are measured by reactor dosimetry or retrospective dosimetry techniques, then it is essential to use the same neutron spectrum to calculate the spectral-averaged gas production and fast activation cross sections. Otherwise, considerable errors can be introduced into the calculations.

Hydrogen and helium can be produced by a number of different threshold nuclear reactions and in order to accurately predict the gas production, all possible reactions must be considered. The ENDF/B-V Gas Production File 533 was specially constructed to take into account all known reactions for a number of elements, thus saving the considerable effort required to add up all of the various reactions for each element. In this evaluated nuclear data file, the H and He isotopes are calculated separately and must be summed in order to include ^{2}H and ^{3}H in the total H production and ^{3}He in the total He production. The

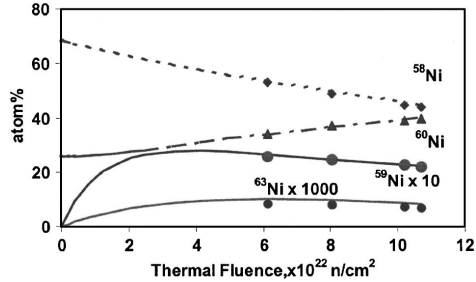

FIG. 4—*Transmutation of Ni isotopes as a function of thermal neutron fluence.*

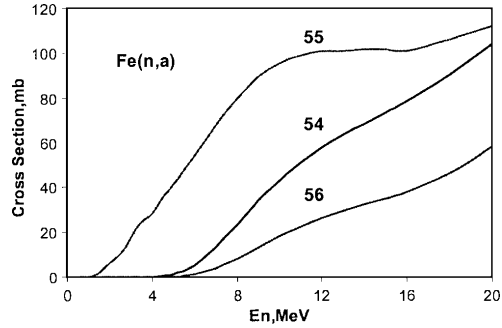

FIG. 5—*Helium production cross sections for various Fe isotopes. Transmutation or isotopic tailoring can significantly affect fast neutron gas production.*

helium cross section for Be is an interesting case since the $^{9}Be(n,2n)^{8}Be(2\alpha)$ reaction leads to two helium atoms such that the nuclear reaction cross sections must be doubled to get the total helium production from Be [6]. This reaction has a very low threshold such that beryllium produces a great deal of helium in a typical reactor spectrum. Beryllium also has a significant photonuclear cross section for the $^{9}Be(\gamma,n2\alpha)$ reaction and can be used to help determine the gamma fluence at reactor location where the gamma flux exceeds the neutron flux.

The accuracy of helium and hydrogen calculations has been tested by direct comparisons with measurements in a variety of reactor materials [4,7].

Isotopic Tailoring and Transmutation

Since different isotopes of an element have different thermal or fast neutron gas production cross sections, isotopic tailoring can be used to alter the gas production in various materials. This effect is illustrated for the iron isotopes in Fig. 5. If an iron or steel sample is enriched in ^{54}Fe, then the helium production can be increased up to a factor of six or more, depending on the reactor spectrum. As ^{55}Fe is produced by transmutation (or if it is doped into samples), the helium production may increase up to a factor of ten over natural iron, as shown in Fig. 6 [8]. Hydrogen production will similarly be accelerated, as shown in Fig. 7. Isotopic tailoring of materials can thus be used to study the effects of gas generation on material properties by simultaneously irradiating materials that only differ in their isotopic composition. Such studies have shown surprisingly large generation of helium and hydrogen in Ni at high neutron fluences. Contrary to expectations, hydrogen can be retained in samples even at high temperatures that also have high levels of helium, presumably by trapping of hydrogen in the helium bubbles, as shown in Fig. 8. The trapped hydrogen may thus affect the material properties more than might be anticipated [9].

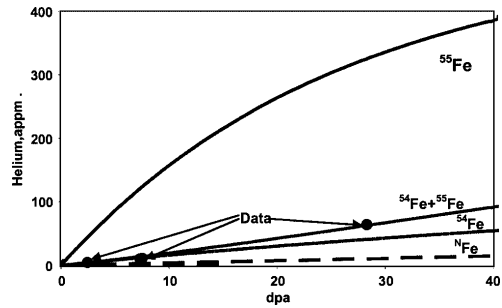

FIG. 6—*Comparison of measured (dots) and calculated (lines) helium for iron isotopically enriched in ^{54}Fe and irradiated in HFIR. The data are fit using the ^{54}Fe and ^{55}Fe cross sections in Table 1.*

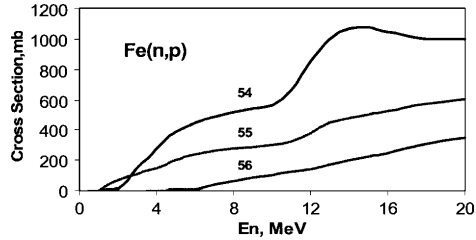

FIG. 7—*Hydrogen production cross sections for various Fe isotopes. Transmutation or isotopic tailoring can significantly affect fast neutron gas production.*

Transmutation will eventually change the isotopic mix of a given element as well as introducing different elemental transmutation products. These changes also affect the gas production rate, most notably if the transmuted isotopes have high gas production cross sections, such as the production of ^{59}Ni and ^{65}Zn.

Additional Radiation Damage from Gas Production Reactions

The thermal neutron gas production reactions listed in Table 1 can significantly increase the displacement damage in reactor materials. Whereas thermal neutron radiation damage from neutron capture gamma reactions is generally much less than radiation damage from fast neutron reactions, the gas production thermal neutron reactions can produce much higher damage rates due to the very large recoil energies that can be produced. For example, the $^{10}B(n,\alpha)^{7}Li$ reaction produces alpha energies of 1.47 and 1.78 MeV and corresponding ^{7}Li recoil energies of 0.84 and 1.02 MeV. A simple calculation shows that using the standard dpa model for boron in steel, one additional dpa will be produced for every 4950 appm of He. For the $^{6}Li(n,\alpha)t$ reaction, the damage rate is 1 dpa per 11 680 appm of He. The $^{59}Ni(n,\alpha)$ reaction similarly leads to a 340 keV ^{56}Fe recoil and an energetic alpha that produces 1 dpa per 552 He appm [1]. Such additional damage effects can be quite substantial for high fluence irradiations above 1×10^{12} n/cm^2.

Future Work

Gas production cross sections are not well known for all elements, especially heavier elements and radioactive isotopes, and integral testing in reactors or accelerator-based neutron sources has only been performed for some elements and isotopes. In both cases, further work is needed to improve our ability to predict gas production in reactor materials. In the case of ^{59}Ni, more work is needed to explain the discrepancy with measurements at high neutron fluences. Hydrogen retention mechanisms are not well understood and have only been measured for a few materials. Transmutation and gas production from

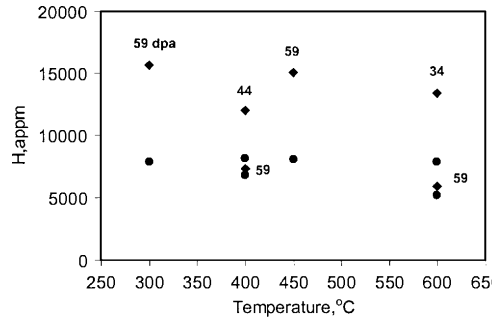

FIG. 8—*Comparison of measured (diamonds) and calculated (circles) hydrogen in nickel samples irradiated to high neutron fluences in HFIR. Note that hydrogen is retained even at elevated temperatures.*

radioactive isotopes have not been studied for all materials and both effects may be significant contributors to our understanding of gas production and radiation damage in irradiated materials.

References

[1] Greenwood, L. R., "A New Calculation of Thermal Neutron Damage and Helium Production in Nickel," *J. Nucl. Mater.*, Vol. 116, 1983, 137.

[2] Greenwood, L. R., Graczyk, D. G., and Kneff, D. W., "A New Technique for Enhancing Helium Production in Ferritic Materials," *J. Nucl. Mater.*, Vol. 155–157, 1992, pp. 1335–1339.

[3] Kneff, D. W., Greenwood, L. R., Oliver, B. M., Skowronski, R. P., and Callis, E. L., "Enhanced Helium Production in Copper," *Radiat. Eff. Defects Solids*, Vol. 92–96, 1985, 553.

[4] Greenwood, L. R., Kneff, D. W., Skoronski, R. P., and Mann, F. M., "A Comparison of Measured and Calculated Helium Production in Nickel Using Newly Evaluated Neutron Cross Sections for ^{59}Ni," *J. Nucl. Mater.*, Vol. 122–123, 1984, 1002.

[5] Greenwood, L. R. and Oliver, B. M., "Comparison of Predicted and Measured Helium Production in US BWR Reactors," *J. ASTM Int.*, Vol. 3(3), 2006.

[6] Greenwood, L. R., Oliver, B. M., Gelles, D. S., Baldwin, D. L., Dalle Donne, M., Kawamura, H., and Scaffidi-Argentina, F., "Measurement and Calculation of Helium Generation in Beryllium Pebbles Irradiated in EBR-II," *Effects of Radiation on Materials*, *ASTM STP 1366*, M. L. Hamilton, A. S. Kumar, S. T. Rosinski, and M. L. Grossbeck, eds., ASTM International, West Conshohocken, PA, 2000, pp. 1062–1074.

[7] Kneff, D. W., Greenwood, L. R., Oliver, B. M., and Skowronski, R. P., "Helium Production in HFIR-Irradiated Pure Elements," *J. Nucl. Mater.*, Vol. 141–143, 1986, pp. 824–828.

[8] Greenwood, L. R., Oliver, B. M., Ohnuki, S., Shiba, K., Kohno, Y., Kohyama, A., Robertson, J. P., Meadows, J. W., and Gelles, D. S., "Accelerated Helium and Hydrogen Production in ^{54}Fe Doped Alloys—Measurements and Calculations for the FIST Experiment," *J. Nucl. Mater.*, Vol. 283–287, 2000, pp. 1438–1442.

[9] Greenwood, L. R., Garner, F. A., Oliver, B. M., Grossbeck, M. L., and Wolfer, W. G., "Surprisingly Large Generation and Retention of Helium and Hydrogen in Pure Nickel Irradiated at High Temperatures and High Neutron Exposures," *J. ASTM Int.*, Vol. 1, No. 4, 2004, pp. 529–539.

Journal of ASTM International, Vol. 3, No. 3
Paper ID JAI13455
Available online at www.astm.org

H. Carcreff,[1] *A. Alberman,*[1] *L. Barbot,*[1] *F. Rozenblum,*[1] *D. Beretz,*[2] *and Y. K. Lee*[3]

Dosimetry Requirements for Pressure Vessel Steels Toughness Curve in the Ductile to Brittle Range

ABSTRACT: As part of PWR life-time assessment project, a large R&D program, PV-CT50, has been carried out from 1995 to 2004, to assess pressure vessel (PV) steel's toughness curve using very large compact tension (CT) specimens ($50 \times 125 \times 120$ mm^3) allowing measurements in the ductile to brittle transition range. A new high capacity irradiation rig was designed to meet the specific CT50 specimens loading requirements in the 70 MWth OSIRIS material testing reactor operated by CEA's Nuclear Energy Division at the Saclay Research Center. This paper presents the measurement and calculation developments required in these particular conditions. Spectrum characteristics and neutron flux levels were determined by a comprehensive dosimetry on mock-ups featuring activation foils and damage monitors. At the same time, a new calculation methodology based on the TRIPOLI-4.3 Monte Carlo code and IRDF-2002 dosimetry files was validated against calorimetric and neutron activation measurements.

KEYWORDS: toughness, CT50 specimens, damage dosimetry, irradiation rig, OSIRIS reactor, TRIPOLI 4.3 Monte Carlo code

Introduction

Many pressure vessel (PV) steel irradiation experiments were devoted to toughness curve establishment. Toughness is the resistance of the material to fast fracture in the presence of a defect. Various steel irradiation programs have been carried out in the 70 MWth OSIRIS reactor ex-core area to plot the toughness evolution. However, previous experiments established only the first part of the toughness curve, corresponding to low temperature of the material because they were restricted to irradiations of CT12.5 and CT25 specimens. Related toughness values did not exceed 60 to 80 MPa$\sqrt{\text{m}}$ and they are not included in the ductile to brittle transition.

In order to reach higher values of toughness, up to around 100 MPa$\sqrt{\text{m}}$ and more, it is necessary to perform mechanical tests with bigger specimens like the CT50 type. As part of the French utility EDF reactor pressure vessel lifetime assessment project, the CT50 type steel irradiation program (PV-CT50), was performed featuring the OSIRIS reactor at CEA-Saclay. Feasibility studies began in 1995. Started in April 2002, the irradiation run was completed in July 2004.

An irradiation of CT50 specimens requires a sample holder and a specific irradiation rig significantly larger than usual ones. The large dimensions of the water box containing the irradiation rig and CT50 specimens could induce a softer neutron spectrum compared with a standard material experiment. Therefore, it is important to keep the spectral characteristics as close as possible to those of previous steels irradiations in OSIRIS reactor dedicated to toughness evaluation and to keep a significant fast neutron flux level leading to an appropriate irradiation time. In addition, such a massive loading of steel creates high gamma energy deposition and introduces constraints in the design of the suitable experimental rig in order to reach the adequate control of temperatures at each CT50 level.

Comprehensive dosimetry on mock-ups featuring activation foils and damage monitors was performed. At the same time, a new calculation methodology based on the continuous-energy TRIPOLI-4.3 Monte Carlo code was validated versus calorimetric and neutron activation measurements.

Manuscript received June 20, 2005; accepted for publication September 29, 2005; published online December 2005. Presented at ASTM Symposium on Reactor Dosimetry, 12th International Symposium on 8–13 May 2005 in Gatlinburg, TN; D. W. Vehar, D. M. Gilliam, and J. M. Adams, Guest Editors.

[1] Commissariat à l'Energie Atomique, Saclay, DEN/DRSN, 91191 Gif sur Yvette, France.
[2] Commissariat à l'Energie Atomique, Cadarache, DEN/DER, 13108 St Paul Lez Durance, France.
[3] Commissariat à l'Energie Atomique, Saclay, DEN/DM2S, 91191 Gif sur Yvette, France.

This paper presents the irradiation program, measurement, and calculation developments required in these particular conditions for the feasibility studies of the irradiation.

We describe first the irradiation requirements, the specificity of the rig and the method for the determination of the irradiation location fulfilling the specifications. Then, mock-ups and calculation methods will be detailed. Finally, the experimental and calculation results will be presented, compared, and discussed.

Irradiation Program

Specimens

Four CT50 specimens (50 mm in thickness) were specially manufactured for the experiment. They were taken from the heat of a PV shell ring. The material called 16 MND5 is an Mn Ni Mo steel alloy.

Considering their dimensions ($50 \times 120 \times 125$ mm^3), the sample holder is limited to a four specimens capacity. The whole loading weight (21 kg) represents the heaviest experimental loading ever irradiated in the OSIRIS reactor. The stacked specimens are 520 mm in height and do not exceed the fissile height of the core which is the most important condition in the design to control the neutron flux and temperature all along the loading.

Main Irradiation Requirements

- The target temperature at the CT50 notch level is 294°C for each specimen and the gradient along the thickness (50 mm) must be monitored.
- The temperature discrepancy must not exceed ±6°C between the specimens during the whole irradiation period.
- Specimens must be irradiated in helium atmosphere.
- The target fast neutron fluence ($E > 1$ MeV) is 7.5 10^{19} n·cm^{-2} at the notch level and loading mid-height.
- The ratio dpa/$\phi_{E>1\ MeV}$, at notch level must be kept in the range 1400–2000 dpa·barn (the ESTEREL program [1], carried out between 1989 and 1995, clearly showed that there is no spectrum effect on steel embrittlement while spectral characteristics are included in that range, and $\phi_{E>1\ MeV}$ proved to be the most appropriate exposure parameter).
- The irradiation run is based upon to two calendar years and therefore it requires at least an average neutron fast flux of about 2.2 10^{12} n·cm^{-2}·s^{-1}, taking into account the reactor operating mode.

Design of the Irradiation Rig

The loading is composed of the stacked specimens separated by five spacers. These spacers are designed to host neutron flux monitors (1 fissile and 37 activation foils). The whole column is located between aluminum shields and centered inside a sleeve (Fig. 1). Heating elements are inserted in the lateral and back shields whereas the front part holds in position thermocouples dedicated to notches monitoring (four thermocouples for each notch).

In addition to the rig itself (15.9 cm in diameter and roughly 4 m height), installation outside the core requires a specific stainless steel water box to hold the rig in position and to ensure its external cooling. The loaded irradiation rig weights 260 kg. These characteristics lead to the biggest and heaviest experimental device ever irradiated in the OSIRIS reactor.

The whole device needs nine elementary experimental locations of the ex-core grid instead of a single one for a standard experiment, involving significant constraints for a multipurpose material testing reactor and for its operating management.

Irradiation Location Study

Apart from neutron spectral considerations, the major problem is to optimize the ex-core location to reduce the gamma heating while preserving a fast neutron flux level.

For simple devices the gamma heating in the irradiation devices of the OSIRIS reactor is currently

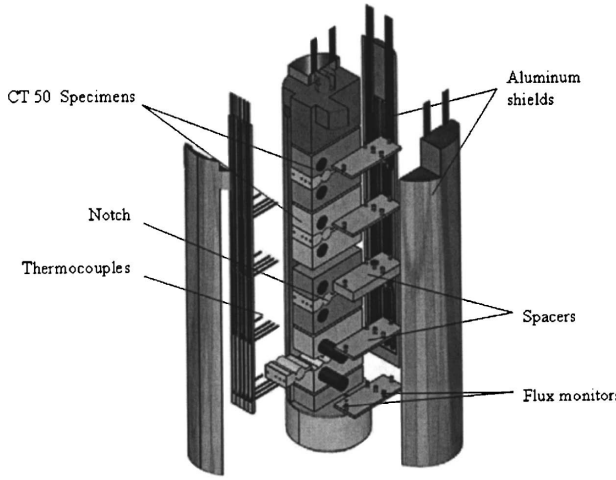

FIG. 1—*CT50 specimens loaded in the sample holder.*

evaluated using a calculation scheme which computes capture γ-rays production from the neutron flux given by a diffusion code and calculates γ-rays attenuation in materials by a point-kernel code. This method is not efficient when a large and complex facility is irradiated outside the core because the perturbed neutron flux is not easily determined by a diffusion code, and γ-ray multi-layer buildup factors are difficult to evaluate leading to a large uncertainty.

Therefore, a new gamma heating calculation methodology based on the continuous-energy TRIPOLI-4 Monte Carlo code [2] has been developed and was applied on this experiment to estimate the distribution of gamma heating inside the whole device considering the irradiation configurations and ex-core location. This heat deposition evaluation is essential for further thermal calculations used to determine the best ex-core location fitting with temperature requirements.

According to iterative core management, shielding calculations and availability of the ex-core irradiation grid, the irradiation facility is found to be best located in the northwest ex-core corner. Cooling channels in the water box are designed on the hot sides and an additional shielding plate can be inserted inside the cooling water channel facing the core, as shown in Fig. 2.

A first benchmark between TRIPOLI-4 gamma heating calculation and calorimetric measurement has been carried out inside the central hole of the water box (Fig. 2). The calorimeter, manufactured and calibrated at CEA-Saclay, is based on a differential measurement. Composed of four aluminum cells, two being equipped with a graphite kernel, the temperatures difference between graphite cells and empty ones leads to the evaluation of the nuclear heating deposit in graphite.

Benchmark results showed that the gamma heating level was too high (about 0.5 $W/g_{graphite}$ at the core mid-plane) to accommodate the PV-CT50 rig at full power in that position. The axial variations were in

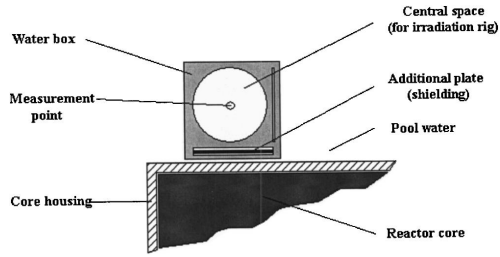

FIG. 2—*First configuration (close to the core housing).*

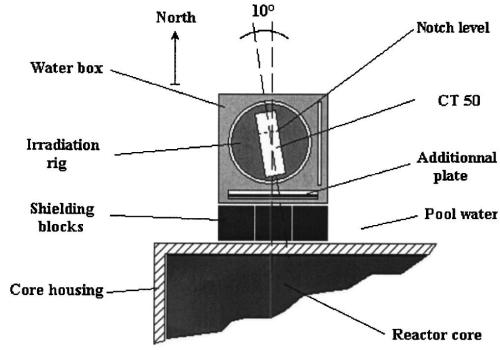

FIG. 3—*Final ex-core configuration.*

good agreement between calculated and measured values [3]. To further reduce the gamma heating, it was decided to move the water box 8.8 cm north, leaving one row of the ex-core grid from the core housing. In that new position shown in Fig. 3, four different shielding configurations were studied without the rig, both by TRIPOLI-4 culations and calorimeter measurements:

- The row between the water box and the core housing filled with water and the large cooling channel of water box equipped with an additional plate (1.1-cm thick) made of aluminum (config. 1) or stainless steel (config. 2).
- The row between the water box and the core housing filled with three shields blocks ($7 \times 7 \times 86$ cm^3) and the cooling channel of water box equipped with the additional plate. The blocks and the plate are both made of aluminum (config. 3) or stainless steel (config. 4).

To keep a fast neutron flux high enough while leading to an acceptable gamma heating level, the best compromise is found with both additional plate and shielding blocks of aluminum. This move to the north position and the introduction of aluminum shielding led to a gamma heating decrease of 35 % compared with the previous configuration (Fig. 2). The calculations show agreement with the measurements at this location.

The validated TRIPOLI-4 calculation scheme was applied to evaluate gamma heating all over the water box and the loaded rig with the new configuration. Using the calculated heating distribution, control of temperatures matches with expected values. In addition, first assessment of ^{58}Ni(n,p) reaction rates and fast flux by measurements and by TRIPOLI-4 calculation showed that the fast flux ($E > 1$ MeV) at the notch level was satisfactory (up to 2.5 10^{12} n·cm^{-2}·s^{-1}, at full reactor power).

Mock-up Measurements with the Complete Device

Thermal Mock-up

Temperature distribution in the whole sample holder and validation of the thermal gradient along the specimen thickness were obtained through a thermal mock-up irradiation run, featuring dummy steel loading especially manufactured for that purpose. Preliminary to any measurement, the temperature gradient was defined like the parameter that would dictate the angular position of the irradiation rig in regard to core axis. The lowest west-east temperature gradient makes a rotation of 10° necessary for CT50 samples as displayed in Fig. 3. This angle is a key data for the neutron mock-up, related TRIPOLI-4 calculation and specimens irradiation.

Neutron Mock-up

PV-CT50 program requires a comprehensive dosimetry with neutron mock-up considering the size of the irradiation facility. The objective is to measure neutron flux, damage levels, spectrum index, and related gradients in the whole loading volume. Damage monitors, 12 GAMIN and 8 tungsten [4–7], are located at

the notch level whereas activation foils (In, Ni, Fe, Cu, Co) are distributed all over the simulated CT50 loading to evaluate spectrum indices and neutron flux gradients between block faces. Two hundred thirty-two foils irradiated in two mock-ups (two operated power levels for two groups of dosimeters) were used to ensure the measurements. Damage versus activation ratios were achieved through GAMIN and tungsten damage monitors, based on electrical resistivity measurements. The GAMIN monitor response is very close to $\phi > 0.1$ MeV whereas tungsten monitor responds closer to dpa_{Fe} [6]. The damage dosimetry with GAMIN and tungsten damage monitors is consistent with previous steels irradiation programs in OSIRIS reactor [7].

TRIPOLI-4 Calculation with the Complete Device

The continuous-energy neutron transport calculation was carried out with TRIPOLI-4 Monte Carlo code, which is developed at CEA-Saclay and validated against international reactor dosimetry benchmarks [8,9]. Important features of TRIPOLI-4 used in this study include the combinatorial and lattice geometry to deal with the complex reactor core and irradiation facilities, the point-wise data library from ENDF/B-VI.4 to avoid the self-shielding treatments of cross sections in reactor core and in large CT50 steel specimens, the automatic biasing schemes to reduce the computer running time, and parallel calculation.

Reactor Core and Irradiation Device Modeling

The repeated structures of OSIRIS fuel were exactly considered in modeling so as to take into account the transport of neutrons through water layers between fuel plates, cooling channels in the fuel rack and annular channels in the reactor core housing. Stainless steel water box, aluminum shield blocks, and associated cooling channels were also correctly described. Inside the water box, the cylindrical aluminum rig and the large CT blocks were modeled in detail.

The rotation modeling was carried out for the CT blocks and the associated dosimeters by using rotation operator and fictive volumes in TRIPOLI-4. Eighty-three activation foils and 20 damage monitors were modeled on the rotated CT specimens with 22 axial and seven horizontal positions.

Neutron Source Modeling

The OSIRIS core power map in the TRIPOLI-4 calculations was prepared by a 2D diffusion code using the loading data of the operation cycle F164. The cosine-shaped vertical power density distribution was taken from measurements. The gradient of the neutron source emitted from the fuel meat in the northwest of the core was calculated in detail. Taking into account the local power distribution is important for the present study.

To simplify the TRIPOLI-4 fixed source simulation, the fresh fuel composition was taken all over the reactor core; the nickel absorber in the upper part of the fuel plates was neglected and the hafnium control plates in control elements were removed.

As two operating power levels were used during the irradiation for two groups of activation foils (first group: $^{58}Ni(n,p)$, $^{115}In(n,n')$ and damage monitors for 3 h at a low power irradiation, and second group: $^{63}Cu(n,\alpha)$, $^{58}Ni(n,p)$ and $^{54}Fe(n,p)$ for 30.5 h at a high power irradiation), the neutron source intensity in the TRIPOLI-4 calculations was determined by assuming a fixed power of 70 MWth. A ^{235}U Watt fission spectrum was used with thermal fission spectrum parameters [8,9].

Automatic Biasing Schemes

To speed up the simulation of TRIPOLI-4 calculations on neutrons transport, the automatic multi-group INIPOND biasing scheme was applied [2]. In gamma heating studies and fast flux estimation, only the axial maximum flux area were calculated so the biasing scheme based on discrete point detectors was used in order to push the neutrons and gamma from the reactor core and the reflector to the tally area [3].

In the CT50 complete device mock-up calculation, the 22 axial levels of the dosimeters have been prepared in order to check the axial variation of the fast flux. To obtain the axial calculation results in a single simulation with the regular calculation errors, a new biasing dataset has been established using a cylindrical surface detector of TRIPOLI-4.3 [9].

In fact, the spatial importance information of this biasing scheme is calculated with the cylinder

biasing meshes, with setting the cylinder axe of biasing on the central dosimeters of the CT blocks. As the cylindrical surface detector of biasing is set with a small radius, the neutrons from the reactor core and the reflector are pushed to the dosimeters on the four CT50 blocks.

Tally and Simulation

Using the IRDF-2002, IRDF-90.V2 files [10] and damage cross sections from CEA for GAMIN and tungsten damage monitors [5], the reaction rates of $^{63}Cu(n,\alpha)$, $^{58}Ni(n,p)$, $^{54}Fe(n,p)$ and $^{115}In(n,n')$, and the damage results of graphite, tungsten and iron were calculated. Neutron spectra and integral neutron fluxes for the energies above 0.1 and 1 MeV were also analyzed.

Parallel calculations of TRIPOLI-4 were run with a cluster of PCs. For a calculation using the automatic biasing scheme described above and track-length estimators, six processors of 3 GHz for 14 h were necessary to produce acceptable converged results in the 103 small dosimeter volumes.

Experimental and Calculation Results of Neutron Mock-up

Table 1 presents the measured and calculated reaction rates at the notch level (corresponding to 8 cm in CT50 specimen depth and −1 cm from core mid-plane). Calculated reaction rates are given using IRDF-2002 files. When using IRDF-90.V2, results are slightly lower (−3.6 % for $^{58}Ni(n,p)$, −5.4 % for $^{63}Cu(n,\alpha)$ and −1.5 % for $^{115}In(n,n')$) and the correlation with measurements is degraded. For $^{54}Fe(n,p)$ detector, calculation results are identical with both IRDF files.

TABLE 1—*Reaction rates comparison between experiment and TRIPOLI-4.3 calculation (Reactor power: 70 MWth).*

Nuclear Reactions	Dosimetry	Uncertainty [1σ]	Calculation	Uncertainty [1σ]	Ratio (C-M)/M
$^{58}Ni(n,p)^{58}Co$ [$\times 10^{-13}$ s^{-1}]	2.18	±1.2 %	2.11	±0.7 %	−3.2 %
$^{54}Fe(n,p)^{54}Mn$ [$\times 10^{-13}$ s^{-1}]	1.55	±1.5 %	1.50	±0.8 %	−3.2 %
$^{115}In(n,n')^{115m}In$ [$\times 10^{-13}$ s^{-1}]	6.62	±5.3 %	6.04	±0.4 %	−8.8 %
$^{63}Cu(n,\alpha)^{60}Co$ [$\times 10^{-15}$ s^{-1}]	1.01	±1.6 %	0.94	±2.3 %	−6.9 %

The (C-M)/M ratios in Table 1 show that calculation values are in close agreement with experimental ones. For $^{115}In(n,n')$ detector, the experimental uncertainty is 5.3 % due to the high uncertainty of the ^{115m}In decay scheme leading to inaccuracies in activity measurements.

These reaction rate results depend on the uncertainty of OSIRIS reactor power during irradiation but they are obtained with low uncertainties in the dosimetry field. To be independent of reactor power normalization process in measurement and in TRIPOLI-4.3 calculations, Table 2 presents the comparison in terms of axial averaged spectrum indices at the notch depth.

Spectrum index, ρ x/y, is defined as the ratio of two fission fluxes (ϕ^f). Fission flux is calculated by dividing the reaction rate by an averaged cross section over the fission spectrum. In the present work the following values are used: 101 mb for $^{58}Ni(n,p)$ detector, 78.8 mb for $^{54}Fe(n,p)$, 0.44 mb for $^{63}Cu(n,\alpha)$ and 168 mb for $^{115}In(n,n')$. Calculated spectrum indices in Table 2 are obtained with IRDF-2002. When using IRDF-90.V2, results of ρ Ni/Cu, ρ Fe/Ni and ρ In/Ni are higher (respectively, +1.9, +3.6 and +2.2 %) and they improve the correlation with the measurements except for ρ Fe/Ni.

Damage to activation spectrum indices, ρ G/Ni and ρ W/Ni, are obtained from GAMIN (graphite) and tungsten damage monitors calibrated with previous studies [4–6].

Ratios in the third part of Table 2 are derived from GAMIN and tungsten damage dosimetry methodology explained in Fig. 4. The calculated ratios, $\phi_{>1\ MeV}/\phi^f_{Ni}$ and $dpa_{Fe}/\phi_{>1\ MeV}$, are found to be in good agreement (within 3.5%) with the experiment at the specimens notch level.

Table 3 presents fast flux and iron dpa results at the notch level near core mid-plane. Both experimental fast flux $\phi_{>1\ MeV}$ and iron damage flux results are obtained with the early established correlations between damage measurements (ρ G/Ni) and (ρ W/Ni), and calculated ($\phi_{>1\ MeV}/\phi^f_{Ni}$) and ($\phi_{Fe(dpa)}/\phi^f_{Ni}$) (see Fig. 4).

TABLE 2—*Spectrum ratios comparison between experiment and TRIPOLI calculation (axial averaged values at the notch depth).*

Spectrum Index Activation Measurement	Measurement (M)	Uncertainty [1σ]	Calculation (C)	Uncertainty [1σ]	Ratio (C-M)/M
$\rho\frac{Ni}{Cu}$	0.96	±4.8 %	0.94	±2.9 %	−2.1 %
$\rho\frac{Fe}{Ni}$	0.89	±3.8 %	0.92	±1.6 %	+3.4 %
$\rho\frac{In}{Ni}$	1.76	±6.4 %	1.71	±1.3 %	−2.8 %
Spectrum Index Damage Measurement	Measurement (M)	Uncertainty [1σ]	Calculation (C)	Uncertainty [1σ]	Ratio (C-M)/M
$\rho\frac{G}{Ni}$	4.64	±3.5 %	3.81	±2.5 %	−17.9 %
$\rho\frac{W}{Ni}$	3.40	±7.6 %	3.13	±2.3 %	−7.9 %
Spectrum Index	Measurement (M)	Uncertainty [1σ]	Calculation (C)	Uncertainty [1σ]	Ratio (C-M)/M
$\rho\frac{\phi_{E>1\ MeV}}{\phi^{f}_{Ni}}$	1.21	±6.1 %	1.17	±1.7 %	−3.3 %
$\rho\frac{dpa_{Fe}}{\phi_{E>1\ MeV}}$	1 780	±7.8 %	1 720	±0.6 %	−3.4 %

TABLE 3—*Fluxes evaluation at the notch level (reactor power: 70 MWth; −10 mm/core mid-plane).*

Flux	Measurement (M)	Uncertainty [1σ]	Calculation (C)	Uncertainty [1σ]	Ratio (C-M)/M
ϕ^{f}_{Ni} [$\times 10^{12}$ n·cm^{-2}·s^{-1}]	2.16	±1.2 %	2.09	±0.8 %	−3.2 %
$\phi_{E>1\ MeV}$ [$\times 10^{12}$ n·cm^{-2}·s^{-1}]	2.65	±6.5 %	2.47	±0.5 %	−6.8 %
dpa_{Fe} [$\times 10^{-9}$ s^{-1}]	4.8	±5.6 %	4.35	±0.3 %	−9.4 %

The calculated fast flux fits well with the experiment (within 6.8 %, 1σ of measurement 6.5 %). The experimental iron damage result, with an uncertainty of 5.6 %, is obtained using a damage cross section (835 barns) of iron recommended by EURATOM (EUR 5274) [7]. The calculated iron dpa is obtained with IRDF-2002 damage files. The EURATOM and ASTM iron damage files produced similar results but they lead to a (C-M)/M ratio of 9.4 %.

Discussion

Typical values measured in steel experiments located outside the OSIRIS core are usually about 0.8 for $\phi_{>1\ MeV}/\phi^{f}_{Ni}$ and 1500 dpa·barn for $dpa_{Fe}/\phi_{>1\ MeV}$. A primary analysis of Table 2 shows that the spectrum is slightly distorted compared to those of previous steel experiments. The $\phi_{>1\ MeV}/\phi^{f}_{Ni}$ (1.21) and the $dpa_{Fe}/\phi_{>1\ MeV}$ (1780) are significantly higher.

However, the ESTEREL program demonstrated that there is no spectrum effect on steel's embrittlement in the range of spectra found in PWR (surveillance capsules, internal surface, 1/2 thickness) which is covered by an iron $dpa/\phi_{>1\ MeV}$ ratio ranging from about 1400 to 2000 dpa·barn. Despite of the steel volume, the axial averaged value is found to be 1780 and meets clearly the initial requirement. In addition, this value is in the range covering French PWR spectra between the internal surface to 1/2 thickness of PV (approximately between 1500 and 2000 dpa·barn). That result ensures the program relevance with the previous ones dedicated to toughness evaluation.

Characteristics of different spectra are presented in Fig. 4 to show the correlation between spectrum indices ($\phi_{>1\ MeV}/\phi_{Ni}$ and ϕ_{dpa}/ϕ_{Ni} with regard to ϕ_{W}/ϕ_{Ni}). Some data points, calculated by the TRIPOLI Monte Carlo code, correspond to the French PWR vessel spectra (surveillance position, 1/4 thickness, 1/2

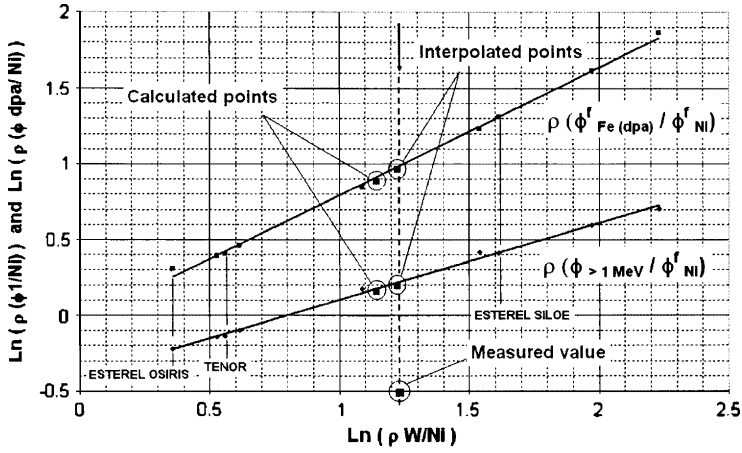

FIG. 4—*PV-CT50 spectrum compared with other experiments.*

thickness). Three previous material experiments, ESTEREL and TENOR (dedicated to toughness study with CT25) with a complete damage dosimetry achieved in OSIRIS and SILOE reactors in the 90s, are also indicated on Fig. 4.

The figure shows that $\phi_{>1\ MeV}/\phi_{Ni}$ and $\phi_{Fe(dpa)}/\phi_{Ni}$ spectrum indices can be derived from a $(\rho\ W/Ni)^n$ dependence. These mathematical correlations are used in fast flux ($\phi_{>1\ MeV}$) and iron damage flux estimations at CEA-Saclay. These indices allow us to appreciate the PV-CT50 spectral characteristics. The measured value of the ϕ_W/ϕ_{Ni} spectrum index is located in the middle of the index range covered by the two irradiations of the ESTEREL program, carried out in OSIRIS and SILOE reactors (see Fig. 4). In addition, the TRIPOLI-4.3 calculation scheme and IRDF-2002 library fit very well with these correlations and are consistent with previous evaluations.

Conclusion

As part of the PV lifetime assessment project, an extensive irradiation program was carried out in OSIRIS reactor to evaluate steel toughness in the ductile to brittle range. A new high-capacity irradiation rig has been developed to welcome four CT50 specimens taken and manufactured from the heat of a vessel ring.

In order to fulfill the objectives in terms of spectrum characteristics and fast neutron flux level, extensive damage dosimetry was performed to keep a consistent process with previous steel irradiation programs carried out in OSIRIS reactor. In addition, a new TRIPOLI-4.3 calculation methodology was developed and applied for that purpose.

Despite of the significant steel volume located in the ex-core area involving high gamma heating and a soft neutron spectrum, an optimized location and an irradiation environment were found in the northwest ex-core area to meet the initial requirements.

Irradiation temperature accuracy was part of the rig design and a very careful control has been successfully observed during all of the irradiation run. The correlation between neutron mock-ups measurements and 3D Monte Carlo calculations emphasized the possibility of the new calculation scheme to predict neutron characteristics in such distorted spectrum. Results can be summarized as:

- Calculated reaction rates in the range $E > 1$ MeV (with the exception of the $^{63}Cu(n,\alpha)$ and $^{115}In(n,n')$ reactions), spectrum index $\phi_{>1\ MeV}/\phi_{Ni}$ and iron dpa/$\phi_{>1\ MeV}$ were found within 4% of the experiment.
- The results were very consistent with the previous ESTEREL program, a reference program in damage dosimetry. The target spectrum was determined to be in the middle of the spectrum range covered by the ESTEREL program. In that range, no spectrum effect on steel embrittlement was observed.

References

[1] Alberman, A., Carcreff, H., Ermont, G., Soulat, P., Beretz, D., and Brillaud, C., "Neutron Spectrum Effect and Damage Analysis of Pressure Vessel Steels Irradiations," *Proceedings of the 9th International Symposium on Reactor Dosimetry*, 1996, pp. 524–534.

[2] Both, J. P., "A Survey of TRIPOLI-4," *Proc. of the 8th Int. Conf. on Radiation Shielding*, Arlington, TX, Apr. 24–28, 1994, Vol. I, No. 373 1994. TRIPOLI-4 version 4.3 http://www.nea.fr/abs/html/nea-1716.html 2004.

[3] Lee, Y. K., David, J. C., and Carcreff, H., "A Gamma Heating Calculation Methodology for Research Reactor Application," *Trans. 5th Int. Topical Meeting on Research Reactor Fuel Management*, RRFM2001, Aachen, Germany, Apr. 1–3, 2001, p. 147.

[4] Genthon, J. P., "Les Travaux du Sous-group Dommage d'Irradiation du group de travail d'EURATOM sur la Dosimétrie en Réacteur de Recherche," *Nucl. Eng. Des.*, Vol. 33, 1975, pp. 7–9.

[5] Alberman, A., and Genthon, J. P., "Nouveau Développement de la Dosimétrie de Dommages par la Technique Tungstène," *4th Symposium ASTM-EURATOM sur la Dosimétrie des Réacteurs. Washington NUREG CP-0029*, 1982, p. 331.

[6] Alberman, A., "Expérience de Dosimétrie «DOMPAC» Simulation Neutronique de l'Epaisseur de la Cuve d'un Réacteur PWR Caractérisation des Dommages d'Irradiation," *3ème Symposium ASTM-EURATOM sur la Dosimétrie des Réacteurs. Ispra, EUR 6813*, 1980, p. 407.

[7] Alberman A., Beretz, D., Bourdet, L., and Carcreff, H., "Neutron Spectrum Effect on Pressure Vessel Embrittlement: Damage and Qualification of Irradiation Locations in OSIRIS and SILOE Reactors," *Proceedings of the 8th International Symposium on Reactor Dosimetry*, 1993, pp. 472–479.

[8] Lee, Y. K., "Analysis of the NRC PCA Pressure Vessel Dosimetry Benchmark Using TRIPOLI-4.3 Monte Carlo Code and ENDF/B-VI.4, JEF2.2 and IRDF-90 Libraries," *Nuclear Mathematical and Computational Sciences: A Century in Review, A Century Anew*, M&C 2003, Gatlinburg, TN, April 6–10, 2003, on CD-ROM, ANS, LaGrange Park, IL, 2003.

[9] Lee, Y. K., "Analysis of the VENUS-3 PWR Pressure Vessel Surveillance Benchmark Using TRIPOLI-4.3 Monte Carlo Code," *Current proceedings*, 2005.

[10] IRDF2002, http://www-nds.iaea.org/ 2005.

Journal of ASTM International, Vol. 4, No. 5
Paper ID JAI101090
Available online at www.astm.org

P. D. Ferguson,[1] *F. X. Gallmeier,*[1] *L. K. Mansur,*[1] *and M. S. Wechsler*[2]

Mesh Tally Radiation Damage Calculations and Application to the SNS Target System

ABSTRACT: A new method for the calculation of radiation damage parameters in large geometries encompassing multiple materials using the MCNPX mesh tally has been developed. The method has been tested against previously published calculations of the displacement rate for protons and neutrons at the center of the SNS 316LN stainless steel target vessel nose. Displacement rates for neutrons, protons, and the total using the mesh tally method are shown to agree with previous work. The mesh tally method is also applied to the SNS aluminum moderator vessels and to the SNS inner reflector plug composed of aluminum, beryllium, and stainless steel. Results are given for displacement, helium, and silicon production rates.

KEYWORDS: displacements, helium production, MCNPX, mesh tally method, neutron irradiation, proton irradiation, radiation damage, silicon production, SNS

Introduction

The Spallation Neutron Source (SNS) [1] at Oak Ridge National Laboratory is scheduled to begin operation in June 2006. The SNS is designed to be a 1.4 MW pulsed neutron scattering facility with 1-GeV protons incident on a flowing liquid mercury target [2]. Directly above and below the target are four moderators, three containing supercritical hydrogen at 20 K and one containing ambient water. Surrounding the moderators is a heavy water cooled beryllium reflector, with a radius of 32 cm, followed by a heavy water cooled stainless steel reflector. The beryllium, stainless steel, and heavy water are contained in an aluminum vessel. A schematic of the SNS target system is shown in Fig. 1.

When calculating radiation damage parameters in accelerator driven systems, it is customary to create small tally cells near the region of interest and calculate damage rates inside the cell. However, for complex systems such as the SNS and the Japanese Spallation Neutron Source (JSNS), the region of peak damage rate may not be easily identified. It can also be useful in the design process to understand how radiation damage parameters vary throughout the target system since design decisions for the extent of replaceability for various components are determined partly on this basis. For these reasons, the calculation of radiation damage parameters was studied and improvements were implemented.

The purpose of this paper is to present an improved method for calculating radiation damage parameters in large target systems. The results of the method are confirmed by comparing a recent calculation with previous published work using the older methods. Finally radiation damage parameters are calculated for the SNS target system using the improved method.

Calculation Method

All calculations for the SNS target system were completed assuming a beam power of 2 MW to accommodate future upgrade paths. Radiation damage calculations for the SNS were completed using the MCNPX [3] mesh tally feature. The mesh tally is a way of calculating flux, dose, etc., in a rectangular or cylindrical grid superimposed over the standard computational geometry. The resolution of the calculation is controlled by the spacing of the superimposed grid and not the geometry. As a result, geometry modi-

Manuscript received March 1, 2007; accepted for publication April 26, 2007; published online May 2007. Presented at ASTM Symposium on Reactor Dosimetry, 12th International Symposium on 8–13 May 2005 in Gatlinburg, TN; D. W. Vehar, D. M. Gilliam, and J. M. Adams, Guest Editors.

[1] Oak Ridge National Laboratory, Oak Ridge, TN37831-6475.
[2] Department of Nuclear Engineering, North Carolina State University, Raleigh, NC27695-7909.

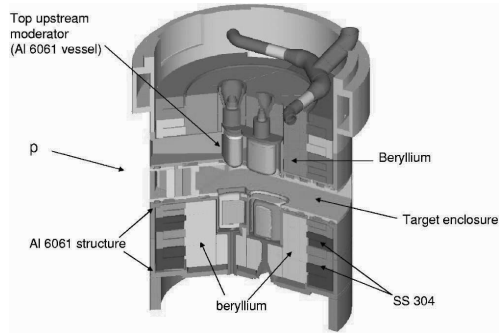

FIG. 1—*Schematic of the SNS target station.*

fications are not required to search for the peak or to develop a reasonable trend curve for the quantity of interest. Using this method of tallying, prior knowledge of the location of the peak flux, dose, etc., is not required. One important issue with the standard mesh tally is the fact that the superimposed meshes typically do not conform to the geometry boundaries. Therefore, each of the superimposed mesh cells may consist of multiple materials, making it impossible to use a materials specific response function, such as a displacement or gas production cross section.

For these calculations, the mesh tally capability of MCNPX was modified to allow material specific cross section folding with neutron or proton fluxes. With the modified mesh tally, any reaction rate for which a cross section exists can be calculated over a large region of interest in a complex geometry. For regions containing multiple materials, one modified mesh tally is performed for each material within the region with the appropriate cross section specified and the tally histograms can be added together to make the final plot over the entire region. It should be noted that the modified mesh tally performs like the energy multiplier card (em card) in MCNPX with some limitations and additional complexity due to the multiple materials within a tally region. The energy multiplier card can be used, in both MCNPX and MCNP, to multiply a tally by a response function as a function of energy. The benefits of the modified mesh tally over the energy multiplier card are: (1) with a mesh tally, results are obtained for the entire geometry instead of at a single point, and (2) the modified mesh tally allows the separation of materials with different response functions, such as steel and aluminum structure within a single tally region. It is planned to submit the modified mesh tally patch to the MCNPX team for possible inclusion in a future MCNPX release.

The modified mesh tally was accomplished by introducing a new keyword, *mater*, into the mesh tally input line. The *mater* keyword is used to specify the material, using the MCNPX material card numbers, for which the tally is being completed. For the material specified, the *dose* keyword is used to input the appropriate cross section for the calculation.

For the SNS target system, radiation damage cross sections were defined as follows:

(1) Displacement cross sections used SPECTER [4] (ENDF/B-V) for neutron energies $E < 20$ MeV, MCNPX models for $E > 20$ MeV.
(2) Gas production cross sections used SPECTER (ENDF/B-V) for neutron energies $E < 20$ MeV, LA150 libraries for neutrons with $20\ \text{MeV} < E < 150$ MeV and protons with $E < 150$ MeV, MCNPX models for neutron and protons with $E > 150$ MeV.
(3) Silicon production cross sections from ENDF/B-VI were used for neutrons with $E < 20$ MeV for aluminum 6061.

It should be noted that any set of cross sections can be used with the modified mesh tally, including the new NCSU Radiation Damage database [5] which has been presented in another paper at this conference.

Verification of the Calculation Method; SNS Target Vessel Nose

A set of detailed calculations was performed by Barnett et al. [6,7] for the nose of the SNS target. They calculated the peak displacement rate in the nose of the SNS target vessel to be 36 dpa/year using previous

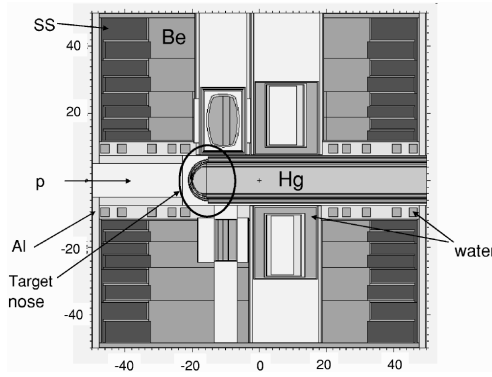

FIG. 2—*MCNPX model of the SNS target station. The vertical and horizontal scales are in units of cm.*

methods of tallying in a small cell in the center of the target. It is important to note that this calculation is for a 365-day year and not a typical 5000-hour operational year at SNS. Barnett et al. broke the total displacement rate down as 23 and 13 dpa/yr for neutrons and protons, respectively. Translating to one SNS year, those rates become 13.1 dpa/SNS yr for neutrons and 7.4 dpa/SNS yr for protons.

An MCNPX model of the SNS target system was created and an elevation view is shown in Fig. 2. This model was used for all calculations in this paper. Protons are incident on the double-walled stainless steel 316LN target vessel containing mercury. Structural aluminum alloy 6061 surrounds the target vessel followed by beryllium and stainless steel 304. To compare with the earlier calculations [6,7], a mesh tally was completed for the center of the nose of the 316LN SS target vessel. Figure 3 shows the modified mesh tally plots for protons and neutrons, with peak values of 13 dpa/SNS yr for neutrons and 7.4 dpa/SNS yr for protons. The mesh tally displacement calculations for neutrons, protons, and the total are thus in essential agreement with the earlier calculations. This result gives confidence in the accuracy of the modified mesh tally calculation method.

Calculations for the SNS Moderator and Reflector

The modified mesh tally was applied to the top, upstream SNS moderator vessel, which is in the region of highest neutron flux, to calculate the dpa rate, the helium production rate, and the silicon production rate in the aluminum. Over 17 cross section sets are required to account for proton and neutron incident particles for each of the reactions (displacement, He production, Si production) and each of the materials of interest for the SNS target system. In the interest of brevity, an example of the cross sections used are shown in Fig. 4, where the aluminum alloy 6061 displacement and He production cross section for incident neutrons and protons is shown. Above ~100 MeV, where physics models are used to calculate the cross sections, little difference is seen between proton and neutron cross sections, although the difference is present upon close inspection. Discontinuities can be seen in the data depending on the energy at which

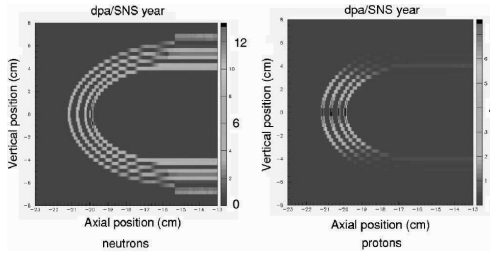

FIG. 3—*Displacement per atom mesh plots for the SNS target vessel nose using the modified mesh tally.*

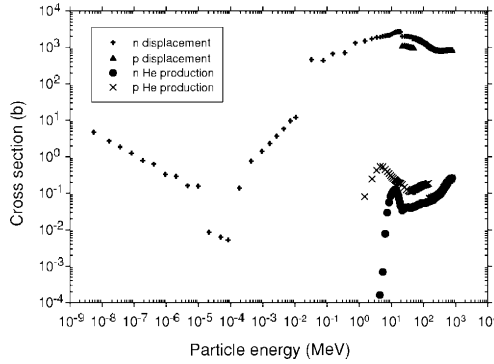

FIG. 4—*Displacement and helium production cross sections for protons and neutrons incident on aluminum alloy 6061.*

the transition from evaluated data to physics models takes place. In general, this transition occurs at 20 MeV for ENDF data or at 150 MeV for the limited number of nuclides in the LANL 150 MeV library.

As an example of the mesh tally capability, Fig. 5 shows the SNS moderator geometry on the left and the displacement rate for the aluminum moderator vessel on the right, with a maximum displacement rate of ~7 dpa/SNS year. The vertical gradient in the displacement is indicative of the rate at which the neutron flux drops away from the target, while the relatively constant displacement rate in the horizontal direction indicates that the neutron flux distribution is relatively flat over the dimensions of the moderator. The helium and silicon production rates are shown in Fig. 6, with maxima of ~50 appm He/SNS year and ~170 appm Si/SNS year. The helium production rate shows gradients similar to the displacement plot

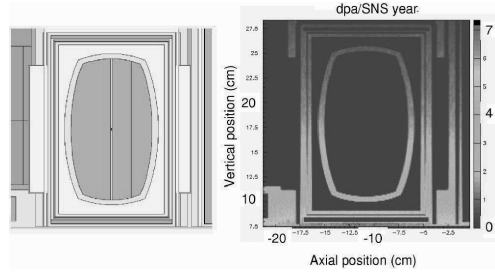

FIG. 5—*An elevation view of the top upstream SNS moderator with the displacement rate mesh plot on the right. The maximum displacement rate in the aluminum moderator vessel is 7 dpa/SNS year.*

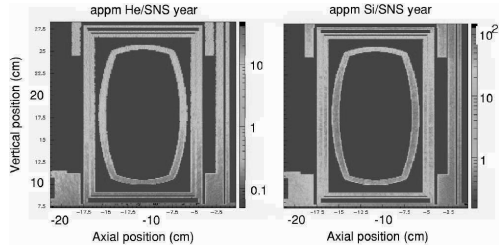

FIG. 6—*Helium (left) and silicon (right) production rates for the top upstream SNS aluminum moderator vessel. The maximum helium production rate is ~50 appm He/SNS year and the maximum silicon production rate is ~170 appm Si/SNS year.*

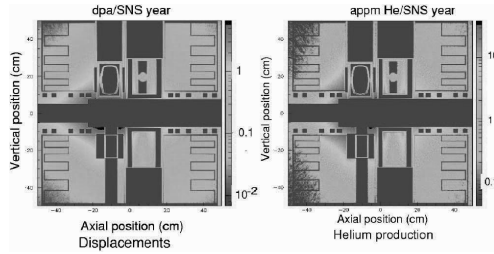

FIG. 7—*Displacement rate (left) and helium production rate (right) for the SNS reflector system, including aluminum structure, beryllium reflector material, and SS 304 outer reflector/shield. The maximum displacement rate is ~7 dpa/SNS year in the aluminum while the maximum helium production rate is ~40 appm He/SNS year. There is no evidence of elevated helium generation in the beryllium reflector.*

shown in Fig. 5. However, the silicon production rate is much more homogeneous even in the vertical direction. The displacements, which are typically dominated by neutrons in the 0.1–10 MeV range, and the helium production, typically driven by neutrons above ~10 MeV, show the steep gradient in the vertical direction, while the silicon production, which is dominated by thermal neutron capture in aluminum, is relatively flat, showing how the neutron spectrum changes as the neutrons leave the target and interact with the moderator and the beryllium reflector.

The modified mesh tally was applied, through a series of calculations, to the entire SNS inner reflector plug. The displacement rates and the helium production rates are shown in Fig. 7. The maximum displacement rate is again ~7 dpa/SNS year in the aluminum near the top upstream moderator, as should be expected from the moderator calculations. The maximum helium production rate occurs in the aluminum and not in the beryllium, indicating that the average neutron energy in the beryllium is not high enough to result in significant helium production via the (n,α) and the $(n,2n)2\alpha$ channels. The modified mesh tally was used to plot the flux-averaged neutron energy in the entire reflector, as shown in Fig. 8, to validate this assumption. The average neutron energy in the beryllium near the upstream moderator, where the displace-

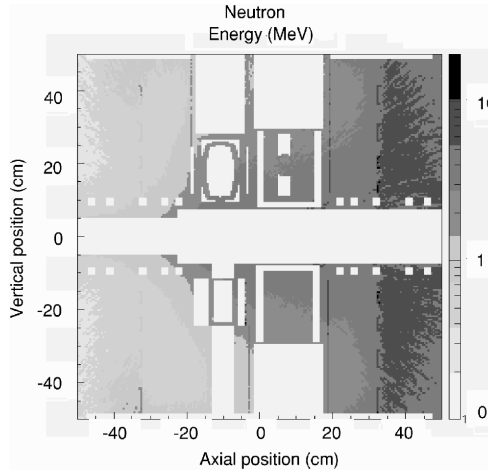

FIG. 8—*Average neutron energy in the SNS reflector system, including aluminum structure, beryllium reflector material, and SS 304 outer reflector/shield. The high-energy component of the spallation process results in average neutron energies near 10 MeV in the downstream region of the target system. Near the upstream moderators, where the displacement rates and helium production rates are highest, the average neutron energies are ~4 MeV in the aluminum, ~1 MeV in the beryllium, and less than 1 MeV in SS 304.*

ment rate and helium production rate are the highest, is ~1 MeV. The peak in the (n,α) cross section occurs near 4 MeV according to ENDF/B-V data [8].

Summary

An improved mesh tally method of radiation damage calculations for large systems and multiple materials has been developed and presented. The method was tested using the SNS target vessel nose as a baseline and good agreement with previous published work was obtained. Finally, the method was applied to the SNS moderator vessels and the SNS inner reflector plug. Displacement, helium, and silicon production rates are presented. In particular, an increase in the helium production rate in beryllium was searched for and was not found due to the energy of the neutron flux in the beryllium being well below the peak in the (n,α) cross section.

Acknowledgments

SNS is managed by UT-Battelle, LLC, under contract DE-AC05-00OR22725 for the U.S. Department of Energy.

SNS is a partnership of six national laboratories: Argonne, Brookhaven, Jefferson, Lawrence Berkeley, Los Alamos, and Oak Ridge.

References

[1] Appleton, B. R., Conceptual Design Report, National Spallation Neutron Source, Vols. 1 and 2, ORNL/M-6063 and -6064, Oak Ridge National Laboratory, Oak Ridge, TN 37831, 1997. Also, NSNS/CDR-2/V1 and NSNS/CDR-2/V2, Oak Ridge National Laboratory, Oak Ridge, TN 37831, May 1997.

[2] SNS Parameters List, SNS 100000000-PL0001-R13, Spallation Neutron Source Report, Oak Ridge National Laboratory, Oak Ridge, TN 37831, June 2005, available online at http://www.sns.gov/documentation/pubs.htm.

[3] MCNPX, Version 2.4.0, the MCNPX Team, LA-UR-02-5253, Los Alamos National Laboratory, Los Alamos, NM 87545, August 2002.

[4] Greenwood, L. R. and Smither, R. K., SPECTER: Neutron Damage Calculations for Materials Irradiations, ANL/FPP/TM-197, Argonne National Laboratory, Argonne, IL, 60439, 1985.

[5] Lu, W., Wechsler, M. S., Ferguson, P. D., and Pitcher, E. J., "Spallation Radiation Damage Calculations and Database; Cross-Section Discrepancies Between the Codes," *Proceedings, Reactor Dosimetry, 12th International Symposium*, May 8–13, 2005, Gatlinburg, TN.

[6] Barnett, M. H., Wechsler, M. S., Dudziak, D. J., Corzine, R. K., Charlton, L. A., and Mansur, L. K., "Calculations of Radiation Damage at SNS," *Proceedings, 3rd International Topical Meeting on Nuclear Applications of Accelerator Technology (AccApp99)*, American Nuclear Society, La Grange Park, IL, 1999, pp. 555–559, (ANS Winter Meeting, Long Beach, CA, Nov. 14–18, 1999).

[7] Barnett, M. H., Wechsler, M. S., Dudziak, D. J., Mansur, L. K., and Murphy, B., "Radiation Damage to the 316 Stainless Steel Container Vessel at SNS," *J. Nonlinear Opt. Phys. Mater.*, Vol. 296, 2001, pp. 54–60, *Proceedings, 4th International Workshop on Spallation Materials Technology*, Schruns, Austria, Oct. 8-13, 2000.

[8] Fisher, H. M., *A Nuclear Cross Section Data Handbook, LA-11711-M Manual*, Los Alamos National Laboratory, Los Alamos, NM 87545, Patricia W. Mendius, Ed., Group IS-11; prepared by Helen Byers, Group X-6, 1989.

Journal of ASTM International, Vol. 3, No. 5
Paper ID JAI13487
Available online at www.astm.org

Milan Brumovsky,[1] *Milan Marek,*[1] *Ladislav Zerola,*[1] *Ladislav Viererbl,*[1] *Victor N. Golovanov,*[2] *V. V. Lichadeyev,*[2] *B. M. Raetsky,*[2] *and A. L. Petelin*[2]

Attenuation of Radiation Damage and Neutron Field in Reactor Pressure Vessel Wall

ABSTRACT: In the paper the large-scale irradiation experiment is described. It is aimed at the experimental assessment of the effect of reactor pressure vessel wall on neutron flux, neutron energy spectrum as well as irradiation embrittlement through the vessel wall. The experiment was realized within the IAEA Technical cooperation project. The irradiation was performed in the RIAR, Dimitrovgrad, Russian Federation, under the coordination by the Nuclear Research Institute Rez plc, Rez, Czech Republic. Mechanical testing and neutron dosimetry will be performed in both organizations with the larger part in the coordinating institute.

KEYWORDS: surveillance, RPV spectrum, neutron dosimetry

Introduction

Nowadays, no official guidance for predicting the behavior of VVER reactor pressure vessel (RPV) materials through a wall thickness exists even though such information is required for the assessment of RPV integrity mainly during pressurized thermal shock emergency events. Attenuation of the neutron field through the RPV wall thickness is connected not only with the decrease of neutron flux but also with substantial changes in the neutron spectrum. All irradiation experiments as well as surveillance specimen programs are evaluated with respect neutron fluence above a specific energy limit (0.5 or 1 MeV or both) and practically all such irradiations are performed in one very similar neutron spectrum. Thus, no experimental data exist for an evaluation taking into account the neutron spectrum change. Only few data from mock-up experiments and calculations of neutron flux and neutron spectra exist but they are not connected with any real irradiation experiments.

Predictive formulas proposed for PWR cannot be fully applied as they have been evaluated for a different type of RPV materials and also for different neutron flux energy criterion and different determinations of material transition temperatures and their shifts. In addition to this, these formulas are not under a strong discussion due to a lack of experimental data.

Description of the Project

The IAEA Technical Cooperation project "Radiation Damage Attenuation in VVER Reactor Pressure Vessels" was proposed by the Nuclear Research Institute (NRI) and finally approved to be realized in cooperation with the RIAR (Scientific and Research Institute for Nuclear Reactors) in Dimitrovgrad, Russian Federation, where the irradiation experiment was performed.

Purpose of the Experiment

Radiation damage in a reactor pressure vessel wall is usually determined on the basis of neutron field calculations and experiments from surveillance specimen program testing. However, it is known that the neutron spectrum is changing through the RPV wall but no direct correlation exists between neutron

Manuscript received June 20, 2005; accepted for publication September 29, 2005; published online April 2006. Presented at ASTM Symposium on Reactor Dosimetry, 12th International Symposium on 8–13 May 2005 in Gatlinburg, TN; D. W. Vehar, D. M. Gilliam, and J. M. Adams, Guest Editors.
[1] NRI Rez plc, Husinec-Rez 130, 25068, Czech Republic.
[2] FSUE "SSC RF RIAR", 433510, Dimitrovgrad-10, Ulyanovsk region, Russia.

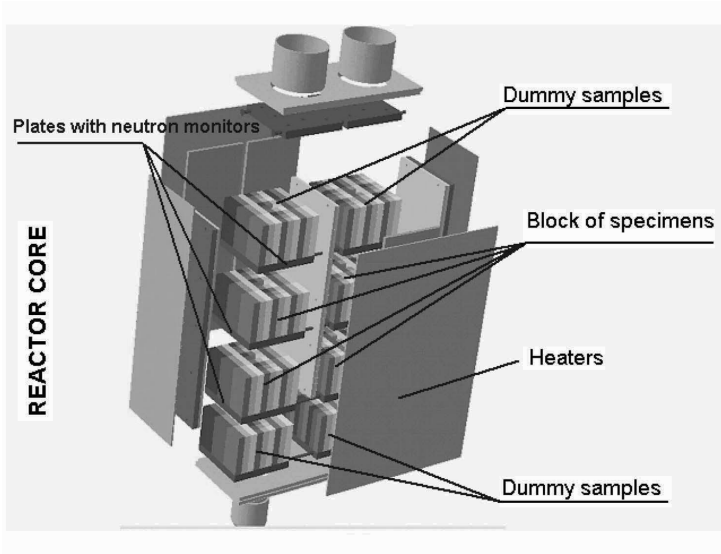

FIG. 1—*Scheme of the large-scale experiment in the KORPUS facility of RIAR. Blocks of specimens B and C were arranged in the capsule CZR-1, while A and D in CZR-2.*

damage and neutron spectrum. Thus, real radiation damage through RPV wall can be determined by a large-scale experiment of the mock-up type only where changes in material properties through the vessel wall are determined and connected simultaneously with changes of the neutron field at the specimen positions.

Technical Specification of the Experiment

Irradiation of a block of specimens (minimum dimensions: height, 100 mm; width, 80 mm; depth 200 mm) representing the full RPV VVER-1000 wall of 200-mm thickness was performed under conditions corresponding to real RPV conditions of temperature and neutron field. The irradiation rig should not affect the neutron field in test specimens of this block. The temperature monitoring through the block and neutron dosimetry must be sufficient for a full characterization of both fields within test specimens (i.e., this block must be surrounded by an additional steel shielding playing the role of a vessel in both inner surface directions to ensure that the neutron field in the block in both these directions will be as close to the real conditions in the RPV wall as possible.

The scheme of the irradiation experiment in the KORPUS facility in RIAR [1] is shown in Fig. 1.

Target Irradiation Conditions

The target neutron fluence on the inner mock-up surface was approximately 6×10^{23} m^{-2} ($E_n > 0.5$ MeV); in the location of the test specimens (i.e., in one specimen layer) the required maximum difference was less than 15 % in neutron flux between the layer center and the layer sides/boundaries.

The required irradiation temperature was 288 ± 10°C throughout all the specimen blocks. The irradiation rig was located in the reactor reflector to approach the inner RPV wall neutron spectrum.

Neutron Dosimetry

Neutron dosimetry should characterize neutron field (fluence and spectrum) in the whole specimen block in all three directions. Two sets of neutron monitors were recommended—one set was supplied, fully measured, and evaluated by the RIAR, the second set was be supplied, and evaluated by the NRI. Both the sets should be evaluated in such a way to enable determination of fast neutron fluence values based on the

combination of neutron transport calculation results and fluence monitors measurement results. The neutron spectrum adjustment procedure is based on American Society for Testing and Materials (ASTM) recommendation [2] and either the SAND II code or codes explicitly based on statistical principle (STAY'SL, BASACF [3,4]) are applied.

Temperature Measurements

The temperature field through the specimens block was measured by a set of thermocouples located at typical positions: outer surfaces as well as in the block centers. The temperature was continuously measured and recorded in agreed time intervals.

Specimens Irradiated

Mainly specimens from VVER-1000 RPV materials (base metals and weld metals) were irradiated. In addition to those, several sets of specimens from the IAEA reference steel JRQ were added for a comparison with the PWR radiation damage data. In both cases, two cutting schemes were used: First, specimens for irradiation were cut from the middle part of the vessel wall in the same way as they are usually chosen for surveillance specimens programs and also for the acceptance tests of RPV materials during their manufacturing to characterize these materials; second, specimens were cut from the whole thickness of the wall and located in the same way in the irradiation experiment—in this way, the real distribution of irradiation embrittlement/transition temperatures through the vessel wall after irradiation will be determined and compared with the data obtained by a standard procedure using specimens from the middle of the thickness and initial material characterization from the 1/4 of thickness.

Additionally, two US PWR materials were also selected for inclusion in the IAEA program. The first one was a high copper weld metal, and the second material was a low copper base metal. The selection of the US materials resulted from comparisons of the predicted results using mechanistically guided correlations to estimate projected changes.

All specimens/plates were supplied by the NRI in accordance with the irradiation design. The specimens of plate or rectangular shape were arranged into blocks to assure a good contact between the individual layers. Detailed design of specimen/plate arrangement and position was finalized in cooperation between RIAR and NRI dependent upon neutron monitor and thermocouple locations.

Types of Specimens

From irradiated plates/inserts, the following types of specimens were manufactured and tested by the NRI:

- Charpy V-notch impact specimens
- Precracked Charpy size static fracture toughness specimens
- Hardness specimens

Most of the tests will be carried out in NRI; some comparison will also be performed in RIAR.

Specimens were arranged into four blocks A, B, C, and D. The B and C blocks were installed in one capsule CZR-1 and the others, A and D in the second capsule CZR-2.

Expected Output

The immediate output of the project should be an elaboration of a guidance/procedure for an improved and corrected evaluation of radiation embrittlement through RPV wall thickness. The procedure will help to evaluate the whole RPV lifetime and will also increase the precision and reliability of such assessments as it will take into account the real conditions and real neutron fields in RPVs. In addition to this, it will help to compare the calculated and experimentally verified neutron field distributions through a RPV wall thickness.

Detailed and experimentally verified knowledge on real radiation embrittlement through RPV wall will also put more precisely the level of safety margins used in RPV integrity evaluation and thus will improve the reliability of the whole assessment.

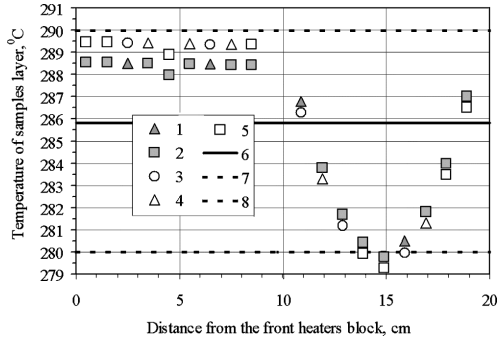

FIG. 2—*Temperature changes over thickness of sample blocks B (1,2) and C (3,4,5). 6, average irradiation temperature value; 7 and 8, bounds of the range 280 < T < 290 °C.*

Preliminary Results

Irradiation was performed between April and December 2004 and some preliminary results have been already obtained in two parts (CZR-1, CZR-2), where two columns of specimens of thickness 200 mm were irradiated in one capsule.

The irradiation temperature was measured continuously by the set of thermocouples in several locations of the experiment. The temperature distribution within the thickness of the experimental facility is shown in Fig. 2. It is seen that the irradiation temperatures were within the required limits; somewhat lower temperatures were measured in the outer part of the simulated wall but still within the required limits (±10 °C).

First results from the neutron dosimetry are shown in Fig. 3 for different locations through the simulated vessel wall thickness. Preliminary reaction rates of the NRI monitor set measured at NRI are presented in Table 1.

Conclusions

The large-scale irradiation experiment for the simulation of the reactor pressure vessel wall during irradiation has been successfully performed.

The experiment will give information about changes of neutron flux and neutron energy spectrum through the reactor pressure vessel wall and also about changes of transition temperatures characterizing irradiation embrittlement of reactor pressure vessel materials—VVER-1000 base and weld metal, and PWR base and weld metals.

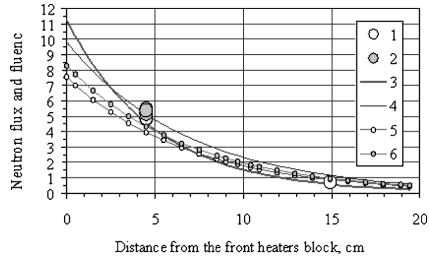

FIG. 3—*Change of neutron flux and fluence though the blocks A and D. 1, 2: experimental values of neutron flux of energy E > 3.0 MeV, 10^{11} cm^{-2} s^{-1}. 3: results of the previous measurements for neutrons with energy E > 3.0 MeV, 10^{11} cm^{-2} s^{-1}. 4: results of the previous measurements for neutrons with energy E > 0.5 MeV, 10^{12} cm^{-2} s^{-1}. 5 and 6: average neutron fluence of energy E > 0.5 MeV, 10^{19} cm^{-2}, for ampoules CZR-2 and CZR-1, respectively*

TABLE 1—*Reaction rates obtained by NRI measurements*

Level	Distance (cm)	Reaction Rates (1/s)				
		Cu63(n,a)Co60	54Fe(n,p)54Mn	93Nb(n,n)93mNb	58Ni(n,p)58Co	46Ti(n,p)46Sc
Above block B	2	1.40E-15	1.96E-13	6.19E-13	2.61E-13	2.62E-14
	4	8.57E-16	1.24E-13	4.26E-13	1.67E-13	1.60E-14
	6	6.11E-16	8.86E-14	3.47E-13	1.20E-13	1.14E-14
	8	4.12E-16	6.16E-14	2.70E-13	8.41E-14	7.74E-15
	10	2.77E-16	4.10E-14	1.84E-13	5.71E-14	5.13E-15
	12.5	1.87E-16	2.69E-14	1.35E-13	3.79E-14	3.31E-15
	14.5	1.13E-16	1.75E-14	9.55E-14	2.46E-14	2.12E-15
	16.5	8.66E-17	1.31E-14	7.24E-14	1.88E-14	1.58E-15
	18.5	5.71E-17	9.27E-15	5.66E-14	1.31E-14	1.08E-15
	20.5	4.06E-17	6.16E-15	3.92E-14	8.88E-15	7.45E-16
Between blocks B and C	2	1.69E-15	2.29E-13	7.18E-13	3.10E-13	3.10E-14
	4	1.01E-15	1.47E-13	5.32E-13	1.99E-13	1.92E-14
	6	7.07E-16	1.03E-13	3.85E-13	1.43E-13	1.35E-14
	8	4.85E-16	7.30E-14	3.11E-13	1.01E-13	9.16E-15
	10	3.23E-16	4.82E-14	2.26E-13	6.73E-14	6.02E-15
	12.5	1.93E-16	3.14E-14	1.52E-13	4.41E-14	3.86E-15
	14.5	1.33E-16	2.02E-14	1.12E-13	2.87E-14	2.44E-15
	16.5	1.04E-16	1.52E-14	8.22E-14	2.15E-14	1.83E-15
	18.5	6.66E-17	1.06E-14	6.40E-14	1.51E-14	1.24E-15
	20.5	5.38E-17	7.17E-15	4.37E-14	1.02E-14	8.55E-16
Below block C	2	1.53E-15	2.22E-13	6.68E-13	3.05E-13	2.92E-14
	4	9.56E-16	1.37E-13	4.55E-13	1.96E-13	1.80E-14
	6	6.73E-16	9.71E-14	3.56E-13	1.41E-13	1.26E-14
	8	4.50E-16	6.42E-14	2.79E-13	9.86E-14	8.56E-15
	10	3.11E-16	4.50E-14	2.06E-13	6.60E-14	5.68E-15
	12.5	2.01E-16	2.98E-14	1.40E-13	4.35E-14	3.61E-15
	14.5	1.30E-16	1.90E-14	1.13E-13	2.84E-14	2.31E-15
	16.5	9.63E-17	1.44E-14	7.40E-14	2.13E-14	1.72E-15
	18.5	6.40E-17	1.00E-14	6.04E-14	1.51E-14	1.17E-15
	20.5	4.73E-17	6.78E-15	4.24E-14	1.01E-14	8.18E-16
Above block A	2	1.26E-15	1.77E-13	5.29E-13	2.35E-13	2.38E-14
	4	7.48E-16	1.09E-13	3.76E-13	1.49E-13	1.43E-14
	6	5.48E-16	7.96E-14	3.03E-13	1.08E-13	1.03E-14
	8	3.85E-16	5.59E-14	2.33E-13	7.76E-14	6.98E-15
	10	2.45E-16	3.68E-14	1.68E-13	5.11E-14	4.62E-15
	12.5	1.61E-16	2.43E-14	1.17E-13	3.41E-14	3.02E-15
	14.5	9.86E-17	1.57E-14	7.93E-14	2.19E-14	1.85E-15
	16.5	7.71E-17	1.17E-14	6.17E-14	1.66E-14	1.44E-15
	18.5	5.29E-17	8.27E-15	5.15E-14	1.18E-14	9.95E-16
	20.5	3.88E-17	5.51E-15	3.42E-14	7.89E-15	6.73E-16
Between blocks A and D	2	1.53E-15	2.14E-13	6.51E-13	2.85E-13	2.86E-14
	4	9.57E-16	1.28E-13	4.70E-13	1.89E-13	1.72E-14
	6	6.48E-16	9.55E-14	3.71E-13	1.38E-13	1.23E-14
	8	4.52E-16	6.68E-14	2.69E-13	9.20E-14	8.46E-15
	10	2.97E-16	4.39E-14	1.98E-13	6.43E-14	5.48E-15
	12.5	1.95E-16	2.85E-14	1.37E-13	4.06E-14	3.50E-15
	14.5	1.35E-16	1.79E-14	9.68E-14	2.58E-14	2.17E-15
	16.5	9.18E-17	1.35E-14	7.71E-14	1.99E-14	1.65E-15
	18.5			5.73E-14	1.37E-14	1.16E-15
	20.5	4.33E-17	6.33E-15	3.99E-14	9.05E-15	7.59E-16
Below block D	2	1.41E-15	2.01E-13	6.10E-13	2.83E-13	2.70E-14
	4	8.65E-16	1.24E-13	4.57E-13	1.79E-13	1.64E-14
	6	6.17E-16	8.86E-14	3.45E-13	1.30E-13	1.17E-14
	8	4.23E-16	6.32E-14	2.57E-13	9.10E-14	8.00E-15
	10	2.75E-16	4.10E-14	1.86E-13	6.05E-14	5.17E-15
	12.5	1.77E-16	2.67E-14	1.30E-13	3.95E-14	3.27E-15
	14.5	1.10E-16	1.65E-14	9.52E-14	2.52E-14	2.06E-15
	16.5	8.67E-17	1.27E-14	6.58E-14	1.92E-14	1.58E-15
	18.5	5.80E-17	8.97E-15	5.29E-14	1.37E-14	1.07E-15
	20.5	3.93E-17	5.97E-15	3.52E-14	9.01E-15	7.19E-16

The results of the experiment will help us understand the irradiation embrittlement attenuation through the reactor pressure vessel walls in relation to the neutron spectrum changes.

Acknowledgements

This work was supported by the research project MSM 2672244501.

References

[1] Brodkin, E. B., Egorov, A. L., Golovanov, V. N., Markina, N. V., Raetsky, V. M., Sulaberidze, V. S., Tsikanov, V. A., Zaritsky, S. M., "The Irradiation Facility KORPUS for Irradiation of the Reactor Structure Materials, "*Reactor Dosimetry, ASTM STP 1228*, American Society for Testing and Materials, H. Farrar IV, P. Lippincott, J. G. Williams, and D. W. Vehar, eds., Philadelphia, 1994, pp. 480–489.

[2] ASTM Standard E 944-02, Standard Guide for Application of Neutron Spectrum Adjustment Methods in Reactor Surveillance, E 706 (IIA), *Annual Book of ASTM Standards*, Vol. 12.02, ASTM International, West Conshohocken, PA.

[3] Perey, F. G., "Least Squares Dosimetry Unfolding: The Program STAY'SL," Report ORNL/TM-6062, ENDF254, Oak Ridge National Laboratory, October 1977.

[4] Tichy, M., "The Program BASACF," Report UDZ-254/88, Institute of Radiation Dosimetry, 1990.

Journal of ASTM International, Vol. 3, No. 3
Paper ID JAI13422
Available online at www.astm.org

A. D. Carlson,[1] *S. A. Badikov,*[2] *Z. Chen,*[3] *E. V. Gai,*[2] *G. M. Hale,*[4] *F.-J. Hambsch,*[5] *H. M. Hofmann,*[6] *T. Kawano,*[7] *N. M. Larson,*[8] *S.-Y. Oh,*[9] *V. G. Pronyaev,*[10] *D. L. Smith,*[11] *S. Tagesen,*[12] *and H. Vonach*[12]

An International Evaluation of the Neutron Cross Section Standards

ABSTRACT: Work is reported here on the process and present results of an international evaluation of the neutron cross section standards. The evaluations include the H(n,n), ^{3}He(n,p), ^{6}Li(n,t), ^{10}B(n,α), ^{10}B(n,$\alpha_1\gamma$), ^{197}Au(n,γ), ^{235}U(n,f), and ^{238}U(n,f) standard reactions as well as the ^{238}U(n,γ) and ^{239}Pu(n,f) reactions. This evaluation was performed to include new experiments on the standards that have been made since the ENDF/B-VI evaluation was completed and to improve the evaluation process. Evaluations have been completed for the ^{6}Li(n,t), ^{197}Au(n,γ) and ^{238}U(n,γ) cross sections. Also below 20 MeV the H(n,n), ^{235}U(n,f), ^{238}U(n,f) and ^{239}Pu(n,f) cross sections are completed. Many of the cross sections being evaluated are used in neutron dosimetry for fluence determination. The general trend observed for the evaluations is an increase in the cross sections for most of the reactions from fractions of a percent to several percent compared with the ENDF/B-VI results.

KEYWORDS: neutron cross section standards, fission standards, capture standards, R-matrix, evaluation

Introduction

The standards are the basis for the neutron reaction cross section libraries. The dosimetry cross sections are measured relative to these standards. Many of the neutron cross section standards are used for neutron dosimetry applications. Significant improvements have been made in the standard cross section database since the last complete evaluation of the neutron cross section standards, almost 20 years ago. It is important to re-evaluate these cross sections taking into account new experimental data and improved evaluation techniques. In response to requests for improvements in the standards, the Cross Section Evaluation Working Group (CSEWG) formed a task force, the Working Party on International Evaluation Cooperation of the Nuclear Energy Agency Nuclear Science Committee formed a subgroup and the International Atomic Energy Agency (IAEA) formed a coordinated research project (CRP). These groups have worked cooperatively to improve the evaluation process. The emphasis has been on the H(n,n), ^{10}B(n,α), and fission standards. Table 1 shows the standards and the expected energy ranges that should result from the new evaluation. Extended energy ranges compared with the ENDF/B-VI results are expected for the cross sections for H(n,n), ^{235}U(n,f) and ^{238}U(n,f) from 20 MeV to $\sim$200 MeV; and for

Manuscript received June 20, 2005; accepted for publication September 29, 2005; published online December 2005. Presented at ASTM Symposium on Reactor Dosimetry, 12th International Symposium on 8–13 May 2005 in Gatlinburg, TN; D. W. Vehar, D. M. Gilliam, and J. M. Adams, Guest Editors.

[1] Physicist, National Institute of Standards and Technology, Gaithersburg, MD, 20899.
[2] Physicist, Institute of Physics & Power Engineering, Obninsk, Russia.
[3] Physicist, Tsinghua University, Beijing, China.
[4] Physicist, Los Alamos National Laboratory, Los Alamos, NM.
[5] Physicist, Institute for Reference Materials and Measurements, Geel, Belgium.
[6] Physicist, Erlangen-Nürnberg University, Erlangen, Germany.
[7] Physicist, Los Alamos National Laboratory, Los Alamos, NM, formerly at Kyushu University, Kasuga, Japan.
[8] Physicist, Oak Ridge National Laboratory, Oak Ridge, TN.
[9] Physicist, Korean Atomic Energy Research Institute, Yuseong, Daejeon, Republic of Korea.
[10] Physicist, Institute of Physics & Power Engineering, Obninsk, Russia, formerly at the IAEA, Vienna, Austria.
[11] Physicist, Argonne National Laboratory, Argonne, IL.
[12] Physicist, Vienna University, Vienna, Austria.

TABLE 1—*Neutron cross section standards.*

Reaction	Proposed Energy Range
H(n,n)	1 keV to 200 MeV
^{3}He(n,p)	0.0253 eV to 50 keV
^{6}Li(n,t)	0.0253 eV to 1 MeV
^{10}B(n,α)	0.0253 eV to 1 MeV
^{10}B(n,$\alpha_1\gamma$)	0.0253 eV to 1 MeV
C(n,n)	0.0253 eV to 1.8 MeV
Au(n,γ)	0.0253 eV, 0.2 MeV to 2.5 MeV
^{235}U(n,f)	0.0253 eV, 0.15 to 200 MeV
^{238}U(n,f)	2 MeV to 200 MeV

^{10}B(n,α) and ^{10}B(n,$\alpha_1\gamma$) from 250 keV to 1 MeV. Changes in the energy ranges of the other standards may occur depending on the results of the evaluation process.

The ^{238}U(n,f) cross section, which is an NEANDC/INDC standard, was accepted as an ENDF standard at the Fall 2004 CSEWG meeting. However, 2 MeV was recommended as the lower bound for use of this cross section as a standard. The use of this cross section from threshold to 2 MeV is discouraged as a standard due to the very rapid change of this cross section in that energy range and the very small cross section in the threshold energy region. The present evaluation of this cross section does extend down to 0.3 MeV so it can be used at the lower energies needed for dosimetry applications.

Evaluation Efforts

The largest contribution to the evaluation has been made by the IAEA CRP. The CRP has included membership from Austria, Belgium, China, Germany, Japan, the Republic of Korea, Russia, and the USA. The main objectives of the evaluation are the following: Improve the methodology for determination of the covariance matrix used in cross section evaluations; upgrade the computer codes using this methodology; study the reasons for uncertainty reduction in R-matrix and model independent fits; evaluate cross sections and covariance matrices for the light elements, H(n,n), ^{3}He(n,p), ^{6}Li(n,t), ^{10}B(n,$\alpha_1\gamma$), and ^{10}B(n,α); establish the methodology and computer codes for combining the light element with the heavy element evaluations leading to a final evaluation of the neutron cross section standards. The evaluation efforts [1] have led to many results and this work is ongoing. The work includes improvements to the experimental data in the standards database and methods for handling discrepant data; R-matrix evaluation of the hydrogen scattering cross section and conversion of measurements relative to the hydrogen cross section to the new standard; studies of the effect of Peelle's Pertinent Puzzle (PPP) and its effect on the standards; evaluation work on microscopic calculations leading to independent determinations of R-matrix poles; studies of the small uncertainties resulting from evaluations; smoothing procedures; and results provided for the ENDF/B-VII standards.

Database Studies

The status of the standards database [2] has been discussed recently. For each experiment in the database, the documentation was investigated for possible corrections that may need to be made and for errors or missing information. This investigative procedure in many cases led to estimates of the uncertainties and correlations within an experiment and correlations with other experiments. This information was used to obtain covariance matrices for the measurements that were used in the evaluation process. The database also includes data involving the ^{238}U(n,γ) and ^{239}Pu(n,f) cross sections. There are many very accurate measurements of these cross sections. The use of these additional data improves the database as a result of ratio measurements of those cross sections to the traditional standards. Also scattering and total cross section data have been included for ^{6}Li and ^{10}B since they provide information on the standard cross sections. No evaluation of the C(n,n) cross section is planned because very little new data have been obtained subsequent to the ENDF/B-VI evaluation and the data obtained since then are in good agreement with that evaluation.

Significant improvements were obtained for the thermal constants used in the evaluation. This was largely due to the very accurate coherent scattering measurements for ^{235}U obtained by Arif [3] that were

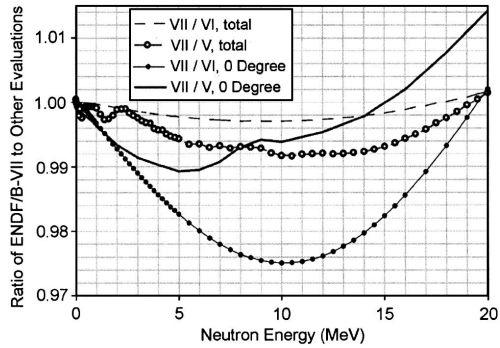

FIG. 1—*Comparison of the present hydrogen evaluation to other evaluations. The present results are the ENDF/B-VII standard. The ENDF/B-VI and ENDF/B-V total cross sections are compared with the present results. Also the zero degree differential cross sections for the ENDF/B-VI and ENDF/B-V evaluations are compared with the results of this evaluation.*

used to provide a more accurate scattering cross section and an improved analysis of the Gwin [4] ν bar uncertainties.

A large database of measurements, a significant portion of which were assembled by Poenitz [5] for the ENDF/B-VI standards evaluation, was used for the evaluation. In addition to the datasets introduced after the ENDF/B-VI evaluation and before the initiation of this evaluation, more than 30 datasets have been added to the standards database. Work has been done to understand the experiments and possible problems with them that may cause discrepancies to exist. During the ENDF/B-VI evaluation process, unusual results [6] were observed with the code GMA [7] when correlated discrepant data were used. To remove problems associated with these discrepancies, data greater than three standard deviations away from the output results were down weighted in the ENDF/B-VI GMA evaluation. This had the effect of making χ^2 per degree of freedom essentially one. It would be better if the sources of the discrepancies could be found, then the evaluation could be done with consistent datasets. This is a very difficult task since there are thousands of data points. For the present evaluation a medium energy range correlation component was added to the experimental data that were discrepant. This component is added if the difference from the evaluation is more than two sigma for a single point or more than one sigma for two or more consecutive energy points. The data are then consistent with the evaluation within the modified experimental uncertainty. This results in a much better χ^2 per degree of freedom and larger uncertainty in the evaluated results. The change in the cross section from this procedure is small.

Hydrogen Evaluation

The hydrogen scattering cross section below 30 MeV neutron energy has been evaluated at Los Alamos National Laboratory (LANL) using the R-matrix code EDA [8]. Calculations of the angular distribution using these R-matrix parameters are in much better agreement with recent measurements [9] than the ENDF/B-VI evaluation. Comparisons of the new hydrogen evaluation with other evaluations are shown in Fig. 1. With the availability of the new hydrogen standard, all data in the database relative to hydrogen cross sections were converted so they are relative to the new standard.

The database contained measurements relative to several different versions of total cross sections. Also a number of experiments were in the database that used different laboratory angles, and different versions of the differential cross section. The effect of the change in the hydrogen standard cross section causes, for example, a change as large as 0.5 % for the evaluated ^{235}U(n,f) cross section in the 10 MeV energy region. The hydrogen evaluation will be extended to 200 MeV neutron energy. When that work has been completed, the data in the database at those higher energies that are relative to the hydrogen cross section will be converted to the new standard.

Peelle's Pertinent Puzzle (PPP) Problems

Problems associated with PPP were observed early in the evaluation process [10]. A test run using a model independent least squares code fitting the logarithm of the cross section produced higher cross sections than a run fitting the cross section. There were discrepant data in the test run. The problem appears to be largely a result of using discrepant data but it also is caused by the existence of data correlations. This is the maxi-PPP versus mini-PPP effect. The EDA R-matrix analysis uses only statistical uncertainties for the cross sections, but also includes a procedure for fitting normalizations that takes into account the normalization uncertainties; this procedure does not suffer the PPP problem, as it is equivalent to the Propagated-Uncertainty-Method [11]. Analyses using the RAC R-matrix code [12] (Tsinghua University) that includes medium range correlations do suffer this problem to some degree. A number of methods for reducing PPP have been employed such as using percent uncertainties, using a logarithmic transformation, or the Box-Cox transformation. The GMA code was modified by adding the Chiba-Smith [13] option to handle PPP problems. This option, called GMAP, renormalizes the experimental absolute errors on the assumption that it is the fractional error that actually reflects the accuracy the experimenter has provided. This approach appears to have reduced the effect of PPP significantly. Comparisons using the Chiba-Smith, Box-Cox, and logarithmic transformation are in good agreement for a number of test cases. To improve the quality of evaluations, special care should be exercised to reduce the effect of discrepant data.

Theoretical Model Calculations

Theoretical calculations are being made to help describe some of the light-nuclei standard cross sections. Since there are relatively few nucleons involved for the ^{4}He compound nucleus, it is possible to use the Refined Resonating Group Model (RRGM), to obtain information about the ^{3}He(n,p) cross section. This model allows realistic nuclear interactions to be used; however, it requires very large computer resources. Using effective NN potentials allows heavier nuclei to be studied such as the A=7 case which leads to the ^{6}Li(n,t) standard. Using effective potentials allows the calculations to be done with a standard personal computer. The work on these two standards has progressed well. The calculations produce results that are rather close to those given by R-matrix analyses. Transforming the RRGM results to R-matrix poles gives guidance for initial values in R-matrix analyses. This work should lead to improved values of the parameters and more realistic uncertainties in the cross sections. In some cases the information on the poles allows an evaluator to recognize limitations in an experimental dataset.

The Small Uncertainty Problem

The small uncertainties obtained in the ENDF/B-VI evaluation process [6] are of great concern. An important task for this effort is to try to understand in detail how standard error propagation in model independent or R-matrix analyses can result in such small uncertainties, and whether there are more reasonable corrections or algorithms to employ. Work has been done on the small uncertainty problem through comparisons of several tests of model independent and R-matrix codes using a common database. The R-matrix codes being used in this study are EDA (LANL), SAMMY [14] (ORNL), and RAC (Tsinghua University). The generalized least squares codes being used are GLUCS [15] (University of Vienna), GMAP (IAEA and IPPE), and SOK [16] (LANL). A code based on an analytical approximation model, PADE2 [17] (IPPE) was also used. It is necessary to select a database containing measurements that can be properly used in the comparison. For example, some of the codes cannot handle certain types of input data correlations. For the comparison tests, it was assumed that no correlations exist between the datasets. The only correlations within the datasets are assumed to be short energy range (statistical) and long energy range (normalization). The results of the generalized least squares codes were in good agreement. Comparisons of the R-matrix codes proved to be more difficult since the input conditions were difficult to standardize. New R-matrix comparisons are now being made using an improved database that is the same for each code with an effort to standardize the analysis procedure. The chi-square expressions used in EDA, SAMMY, and RAC are also being investigated. An important result of the present work is that it is essential to consider the covariances, not just the variances, in applications of cross sections to practical systems.

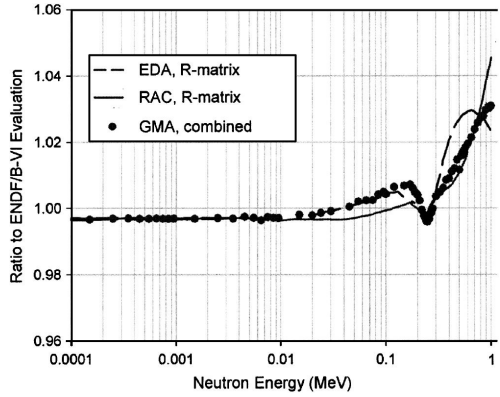

FIG. 2—*Comparison for the ^{6}Li(n,t) cross section of the ENDF/B-VI evaluation with the EDA R-matrix analysis, the RAC R-matrix analysis, and the combination result. The combination result is the ENDF/B-VII standard.*

Evaluation Procedure

The need for standards for the upcoming ENDF/B-VII evaluation has been an important motivating factor for this work. It was decided that a combination procedure somewhat similar to that used for the ENDF/B-VI standards evaluation would be used to obtain those standards. All the standards except the H(n,n), ^{3}He(n,p), and C(n,n) cross sections will be evaluated using the GMAP code with input from the RAC and EDA R-matrix analyses and a thermal constants evaluation. The Axton evaluation [18] of the thermal constants with the associated variance-covariance data for ^{233}U, ^{235}U, ^{239}Pu, and ^{241}Pu was used as input to the GMAP code since it includes accurate cross sections which have been measured relative to the neutron cross section standards. Thus this evaluation will have an impact on the determination of the standards.

The R-matrix analyses will be using charged-particle data and the entire lithium and boron neutron databases, including total and scattering cross section data for these nuclides. The only lithium and boron data for direct use in the GMAP code will be the ratio measurements. Thus the R-matrix and GMAP datasets have no common or correlated datasets. For the ^{6}Li(n,n) R-matrix work, the cross sections obtained from the RAC and EDA analyses were not identical. The cross sections from the RAC and EDA analyses were averaged (unweighted) and used as the R-matrix input to GMAP. The covariance matrix used with these central values was that from the RAC code since its results appeared more physically reasonable. The R-matrix input and thermal constants data were treated like the additions of other datasets to the GMAP code. At each energy point, half the difference between the RAC and GMAP results was treated as a model uncertainty that was added to the RAC covariance of uncertainties. This then takes into account the small differences obtained between the RAC and EDA analyses. The results of these analyses are shown in Fig. 2.

Unfortunately, only the RAC analysis for boron was available in time for the release of the standards for the ENDF/B-VII library, so the boron cross sections have not been released. The RAC boron results alone were used as input to GMAP to provide data for the impact on the other cross sections from the R-matrix boron analysis. The effect was found to be small.

Smoothing of the Evaluation

The results of the combination procedure will not be smooth. For the ^{6}Li(n,t), ^{10}B(n,$\alpha_1\gamma$), and ^{10}B(n,α) cross sections, smoothing will not be required since the highest weight will go to the cross sections used in the R-matrix analyses. For the heavy element standards, there are some models that could provide insight on how to define the curves. It was determined that a simple smoothing algorithm would be satisfactory for most cases. It was used sparingly for the heavy element cross sections. A patch using the

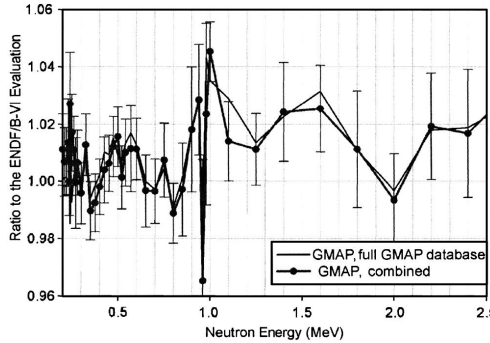

FIG. 3—*Comparison for the Au(n, γ) cross section of the ENDF/B-VI evaluation with the combination result and the results obtained with the GMAP code using the entire neutron database.*

shape of the Maslov [19] evaluated curve was applied in the 50–60 MeV region for the ^{235}U(n,f) cross section where a rather large fluctuation, assumed to be statistical, occurred.

Results of the Evaluation

The cross sections obtained for the ^{6}Li(n,t), Au(n,γ), ^{235}U(n,f), and ^{238}U(n,f) standard cross sections as well as for the ^{238}U(n,γ) and ^{239}Pu(n,f) cross sections are shown in Figs. 2–7 as ratios to the ENDF/B-VI results.

For Figs. 3–7, results are given for the combination procedure and that obtained using the GMAP code with the entire neutron database (i.e., including the data normally only used for the R-matrix analyses). All uncertainties shown are one standard deviation values. The combination results are the final cross sections. The combination results and the H(n,n) results, up to 20 MeV, were given to the CSEWG in November as the proposed standards for the ENDF/B-VII library.

Some benchmark data testing has been done using these data. The quantity K1 calculated from the evaluation is 721.6 b. This should be compared with the "preferred" value of 722.7 b determined by Hardy [20]. The agreement is quite good when one considers that the uncertainty in the Hardy value is 3.9 b. Preliminary criticality calculations for a large range of criticals using these data [21] are generally in better agreement than those obtained with the ENDF/B-VI standards.

It is anticipated that the additional work being done on the hydrogen cross section to extend it to 200 MeV will have only a very small effect on the hydrogen cross section below 20 MeV. Only the cross sections were released for use in the ENDF/B-VII library. The covariances are still under investigation.

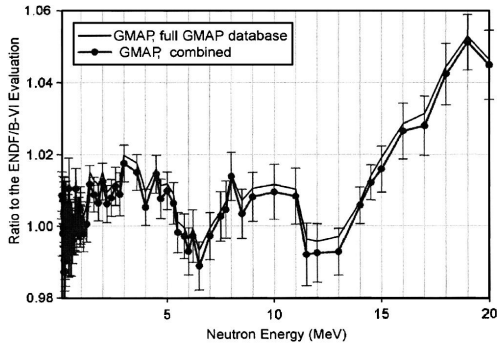

FIG. 4—*Comparison for the ^{235}U(n,f) cross section of the ENDF/B-VI evaluation with the combination result and the results obtained with the GMAP code using the entire neutron database.*

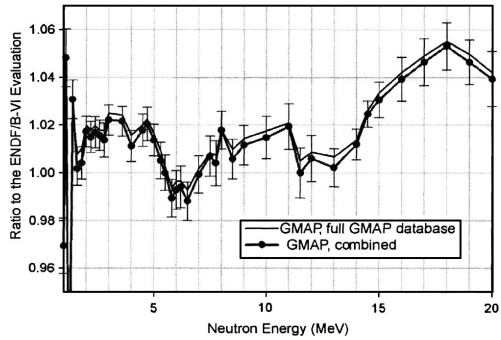

FIG. 5—*Comparison for the $^{238}U(n,f)$ cross section of the ENDF/B-VI evaluation with the combination result and the results obtained with the GMAP code using the entire neutron database.*

When both boron R-matrix results are available, the boron input will be obtained in a manner similar to that used for the lithium case described above. The boron cross sections will then be obtained from the GMAP program using the lithium and boron R-matrix data from EDA and RAC and the thermal constants input. The $^{3}He(n,p)$ cross section is being evaluated independently by Hale. It is anticipated that the boron

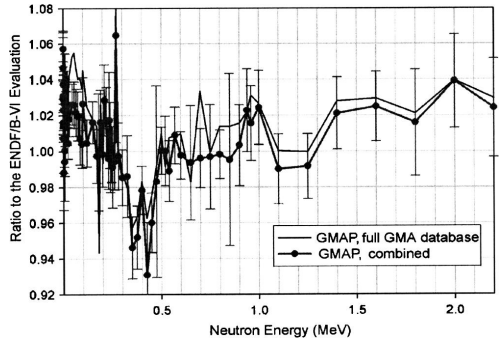

FIG. 6—*Comparison for the $^{238}U(n,\gamma)$ cross section of the ENDF/B-VI evaluation with the combination result and the results obtained with the GMAP code using the entire neutron database.*

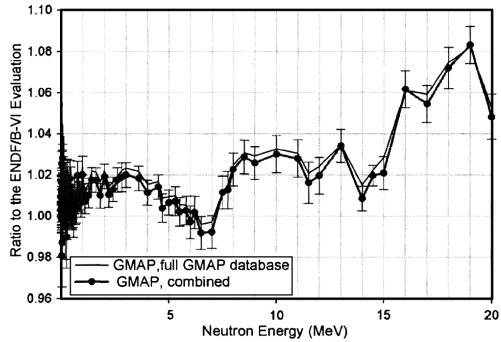

FIG. 7—*Comparison for the $^{239}Pu(n,f)$ cross section of the ENDF/B-VI evaluation with the combination result and the results obtained with the GMAP code using the entire neutron database.*

cross sections, the ^{3}He(n,p) cross section, and the extension of the H(n,n), ^{235}U(n,f), ^{238}U(n,f), and ^{239}Pu(n,f) cross sections to 200 MeV will be released later this year.

Conclusions

The work reported here has been a successful international effort. The evaluated neutron standards data from this work are available for use, internationally, in any nuclear data activity. A pressing need was satisfied since the most important standards were supplied for the new ENDF/B-VII library. However, the remaining standards and the detailed uncertainty information must be provided. Work continues to provide that information. A new IAEA Data Development Project has been approved that is focused on the maintenance of the neutron cross section standards. This project could provide a method for obtaining standards evaluations that will be up to date when they are needed by the various nuclear data evaluation projects.

References

[1] Pronyaev, V. G., Badikov, S. A., Chen, Z., Carlson, A. D., Gai, E. V., Hale, G. M., Hambsch, F.-J, Hofmann, H. M., Larson, N. M., Smith, D. L., Oh, S.-Y., Tagesen, S., and Vonach, H., "The Status of the International Neutron Cross Section Standards File," *Proceedings, International Conference on Nuclear Data for Science and Technology*, Sept. 26–Oct. 1, 2004, Santa Fe, NM, pp. 808–815.

[2] Hambsch, F.-J., Carlson, A. D., Vonach, H., "Status of the Neutron Cross Section Standards Database," *Proceedings, International Conference on Nuclear Data for Science and Technology*, Sept. 26–Oct. 1, 2004, Santa Fe, NM, pp. 826–829.

[3] Arif, M., Kaiser, H., Werner, S. A., and Willis, J. O., "Precision Measurement of the Bound-Coherent-Neutron Scattering Length of ^{235}U," *Phys. Rev. A*, Vol. A35, 1987, pp. 2810–2814.

[4] Gwin, R., Spencer, R. R., and Ingle, R. W., "Measurements of the Energy Dependence of Prompt Neutron Emission from ^{233}U, ^{235}U, ^{239}Pu and ^{241}Pu for E_n=0.005 to 10 eV Relative to Emission from Spontaneous Fission of ^{252}Cf,&#x2 *Nucl. Sci. Eng.*, Vol. 87, 1984, pp. 381–404.

[5] Poenitz, W. P. and Aumeier, S. E., "The Simultaneous Evaluation of the Standards and Other Cross Sections of Importance for Technology," *ANL/NDM-139*, 1997.

[6] Carlson, A. D., Poenitz, W. P., Hale, G. M., Peelle, R. W., Dodder, D. C., Fu, C. Y., and Mannhart, W., "The ENDF/B-VI Neutron Cross Section Measurement Standards," *ENDF-351*, 1993.

[7] Poenitz, W. P., "Data Interpretation, Objective, Evaluation Procedures and Mathematical Technique for the Evaluation of Energy-Dependent Ratio, Shape and Cross Section Data," *Proceedings of the Conference on Nuclear Data Evaluation Methods and Procedures*, B. A. Magurno and S. Pearlstain, Eds., BNL-NCS-51363, Vol. I, 1981, pp. 249–289.

[8] Hale, G. M., "Use of R-Matrix Methods for Light Element Evaluations," *Proceedings of the Conference on Nuclear Data Evaluation Methods and Procedures*, B. A. Magurno and S. Pearlstain, Eds., BNL-NCS-51363, Vol. II, 1981, pp. 509–531.

[9] Boukharouba, N., Bateman, F. B., Brient, C. E., Carlson, A. D., Grimes, S. M., Haight, R. C., Massey, T. N., and Wasson, O. A., "Measurement of the n-p Elastic Scattering Angular Distribution at E=10 MeV," *Phys. Rev. C*, Vol. C65, 2002, p. 014004.

[10] Carlson, A. D., Hale, G. M., and Pronyaev, V. G., "Summary Report of the First Research Coordination Meeting on Improvement of the Standard Cross Sections for Light Elements," INDC(NDS)-438, IAEA, 2003.

[11] Larson, N. M., "Treatment of Data Uncertainties," *Proceedings, International Conference on Nuclear Data for Science and Technology*, Sept. 26–Oct. 1, 2004, Sante Fe, NM, pp. 374–377.

[12] Chen, Z. P., "Reduced R-Matrix Analysis for ^{17}O System," *Atomic Energy Science and Technology* (*Yuanzineng Kexue Jishu*), Vol. 29, No. 4, 1995, pp. 366–371.

[13] Chiba, S. and Smith, D. L., "A Suggested Procedure for Resolving an Anomaly in Least-Squares Data Analysis Known as "Peelle's Pertinent Puzzle" and the General Implications for Nuclear Data Evaluation," *ANL/NDM-121*, 1991.

[14] Larson, N. M., "Updated Users' Guide for SAMMY Multilevel R-matrix Fits to Neutron Data Using

Bayesian Equation," *ORNL/TM-9179/R5*, 2000.

[15] Tagesen, S. and Hetrick, D. M., "Enhancements to the Generalized Least-Squares Cross-Section Evaluation Code GLUCS," *Proceedings of International Conference on Nuclear Data for Science and Technology*, Gatlinburg, USA, May 9–13, 1994, Am. Nucl. Soc., Inc., LaGrange Park, IL, J. K. Dickens, Ed., 1994, Vol. 1, pp. 589–591.

[16] Kawano, T., Matsunobu, H., Murata, T., Zukeran, A., Nakajima, Y., Kawai, M., Iwamoto, O., Shibata, K., Nakagawa, T., Ohsawa, T., Baba, M., and Yoshida, T., "Evaluation of Fission Cross Sections and Covariances for ^{233}U, ^{235}U, ^{238}U, ^{239}Pu, ^{240}Pu, and ^{241}Pu," *JAERI-Research-2000-004*, 2000.

[17] Badikov, S. A., Gai, E. V., Guseynov, M. A., and Rabotnov, N. S., "Nuclear Data Processing, Analysis, Transformation and Storage with Pade-approximants," *Proceedings of International Conference on Nuclear Data for Science and Technology*, May 13–17, 1991, Jűlich, Germany, Springer-Verlag, 1991, pp. 182–187.

[18] Axton, E. J., "Evaluation of the Thermal Constants of ^{233}U, ^{235}U, ^{239}Pu and ^{241}Pu, and the Fission Neutron Yield of ^{252}Cf," *CBNM (IRMM) Report GE/PH/01/86*, 1986.

[19] Maslov, V. M., "Uranium Symmetric/Asymmetric Nucleon-Induced Fission Up to 200 MeV," *Eur. Phys. J. A*, Vol. 21, 2004, pp. 281–286.

[20] Hardy, J., private communication, Memo dated 18 June 1985.

[21] MacFarlane, R. E., private communication, 2005.

Journal of ASTM International, Vol. 3, No. 8
Paper ID JAI13424
Available online at www.astm.org

O. Gritzay,[1] *V. Kolotyi,*[2] *N. Klimova,*[3] *O. Kaltchenko,*[2] *M. Gnidak,*[2] *and P. Vorona*[2]

Precision Neutron Total Cross-Sectional Measurements for Natural Carbon at Reactor Neutron-Filtered Beams

ABSTRACT: An experimental investigation of the total neutron cross section for natural carbon was made at Kyiv Research Reactor using neutron-filtered beams with energies 24, 59, and 148 keV. The intense neutron beams formed by composite neutron filters at reactor horizontal channels)had fluxes of about 10^6 to 10^7 neutron/cm^2 s at the fixed neutron energies, which enabled us to measure the neutron cross sections with accuracy better than 1 %. Transmission method was used in these measurements. The results of the measurements are presented together with the analysis of the known previous experimental data and the evaluated nuclear data from ENDF libraries. Sample thickness dependence of the observed neutron cross section, measured at the 148-keV filter, has been detected which hypothetically may be connected with existence of a very strong resonance in the ^{13}C neutron cross section in the energy range 119 to 157 keV.

KEYWORDS: carbon, research reactor, neutron filtered beam, total neutron cross section, transmission method

Introduction

This investigation is devoted to the precise measurements of total neutron cross section for natural carbon. This element is well known as reactor structure material and at the same time as one of the most important scattering standards, especially at energies of less than 2 MeV, where the neutron total and elastic scattering cross sections are essentially identical. The best experimental data in the area 1 to 500 keV have the uncertainty 1 to 4 % [1,2]. However, the difference between these data and those obtained from the *R*-matrix analysis and used to obtain the ENDF evaluations is evident (Fig. 1) especially in the energy range 1 to 60 keV. The use of the technique of neutron filtered beam developed at the Kyiv Research Reactor makes possible to reduce the uncertainty of the experimental data to 1 % and less [3,4]. These high precision data on natural carbon could stimulate a new run of the *R*-matrix analysis for carbon.

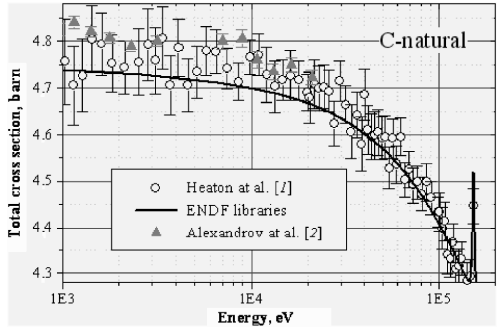

FIG. 1—*Natural carbon neutron total cross sections.*

Manuscript received June 20, 2005; accepted for publication May 18, 2006; published online July 2006. Presented at ASTM Symposium on Reactor Dosimetry, 12th International Symposium on May 8–13, 2005 in Gatlinburg, TN; D. W. Vehar, D. M. Gilliam, and J. M. Adams, Guest Editors.

[1] Head of Neutron Physics Department, Institute for Nuclear Research, Kyiv, 03680, Ukraine.
[2] Senior Scientist of Neutron Physics Department, Institute for Nuclear Research, Kyiv, 03680, Ukraine.
[3] Research Engineer of Neutron Physics Department, Institute for Nuclear Research, Kyiv, 03680, Ukraine.

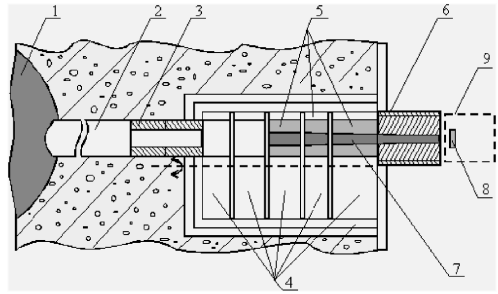

FIG. 2—*Construction of neutron filtered beam to receive the quasi-mono-energetic neutron flux. 1—Beryllium reflector; 2—horizontal channel tube; 3—preliminary collimator; 4—beam shutter disks; 5—filter-collimator assembles; 6—outside collimator; 7—filter components; 8—sample for activation (optionally); 9—device for samples removing.*

Experimental Setup and Measurements

Experimental investigation of the total neutron cross section for natural carbon was made on the eighth and ninth horizontal channels at the Kyiv Research Reactor. Experimental installations on horizontal reactor channels (Fig. 2) include the systems for forming of filtered neutron beams, neutron detector and counting systems, sample management systems, and systems of radiation shielding.

The forming system includes the elements of beam collimation and neutron filtration on the way from reactor core to detector. The preliminary forming of necessary beam geometry is realized with two iron and boron carbide collimators. Further beam forming takes place in the first three disks of shutter and in outer collimator. In the order lead, textolite and mixture of paraffin with H_3BO_3 are used as material for these collimators. The collimation system provided beam narrowing to 12 mm/m, which corresponded to a beam diameter at the sample of 10 mm.

The elements of neutron filtration system take place in the first three disks of shutter and in the outer collimator. To receive the quasi-mono-energetic beams with average energies of 24, 59, and 148 keV, we used the composite neutron filters that consisted of Fe, Al, S, and ^{10}B for the first, of ^{58}Ni, S, V, Pb, Al, and ^{10}B for the second, and of Si, Ti, and ^{10}B for the third one. The filter component optimization, to obtain the largest possible intensity of the main energy line at the most optimal impurity of the parasitic energy lines in the neutron spectrum, was carried out by means of calculation using our code FILTER_L [5].

The detection and neutron counting systems included: the proportional hydrogen recoil counters CHM-38 (Gas Filling: 90 % H_2+9.56 % CH_4+0.44 % $^3He_2$, gas pressure 2280 Torr) or LND 281 (Gas Filling: H+CH_4+N_2, gas pressure 3240 Torr), electronic components, personal computer IBM 286/287 and communication lines.

The management system for experimental samples provides the establishment of the samples in the neutron beam. Simultaneously three samples can be loaded into the system and placed in the beam in any sequence and combination.

Tree type of carbon samples were used in these measurements: (1) solid samples from reactor graphite (C 99.9 %); (2) powder samples, loaded into aluminum container (C 99.9 %); (3) carbon disks; each of them has thickness 1 mm and diameter 30.4 mm (C 99.997 %).

For determination of background counting rate, polyethylene samples with thickness 4.730 to 0.550 g/cm^2 were used. For high statistics accuracy, the measurements were carried out for 30 to 40 h for each sample. To remove the influence of instability factors, the samples in the neutron beam were replaced every minute.

Sample transmission was calculated for each carbon sample measurement series with formulae:

$$T = \frac{N_{\mathrm{SMP}} - N_{\mathrm{SMP+PE}}}{N_{\mathrm{DB}} - N_{\mathrm{DB+PE}}} \tag{1}$$

where

N_{SMP}—beam after sample,

TABLE 1—*24-keV filter components.*

^{10}B (85 %)	Al	S	Fe
1.0	112.81	62.1	236.22

N_{SMP+PE}—beam after sample+polyethylene,
N_{DB}—direct beam,
N_{DB+PE}—direct beam+polyethylene.

The transmission was then averaged over 50 to 500 channels of 1024 channels of proton recoil counter data. These averaged values then were averaged over all series of measurements. The total cross section for sample was determined as

$$\sigma_x = -\frac{1}{n_x}\ln\langle T\rangle \tag{2}$$

The total uncertainty included the statistical inaccuracy of measurements, sample weight and dimensions inaccuracies:

$$\Delta\sigma_x = -\frac{1}{n_x}\sqrt{\left(\frac{d\langle T\rangle}{\langle T\rangle}\right)^2 + (\sigma_x dn_x)^2} \tag{3}$$

24-keV *Filter*

We used here the composite neutron filter that consisted of Fe, Al, S, and 10B to receive the quasi-mono-energetic beam with the average energy 24.01±1.74 keV and neutron flux about 4.4×10^5 n/cm^2 s. The purity of beam was about 99.8 %, other additions to the main spectra were negligible: 73 keV, 0.14 %; 351 keV, 0.02 %.

The filter components (g/cm^2), used in these experiments for the forming of filtered neutron beam at the energy 24 keV, are presented in Table 1.

Figure 3 shows the calculated neutron spectra with peak energy 24.01 keV for filter used in experiment. The limits of 95 % response function for 24-keV filter spectrum were defined as 19.3 to 25.8 keV.

Three samples of reactor carbon (99.9 %) were used in these measurements. The sample thickness and the total neutron cross section, obtained on each sample, are presented in the Table 2. The final value of total neutron cross section, averaged over all samples, was 4.680±0.020 barn (relative accuracy 0.42 %).

59-keV *Filter*

We used here the composite neutron filter consisted of ^{58}Ni, S, V, Pb, Al, and ^{10}B to obtain the quasi-mono-energetic beam with the average energy 58.98±2.60 keV. The purity of beam was about 98.4 %, other additions to the main spectra were: 83 keV, 0.02 %; 366 keV, 1.6 %.

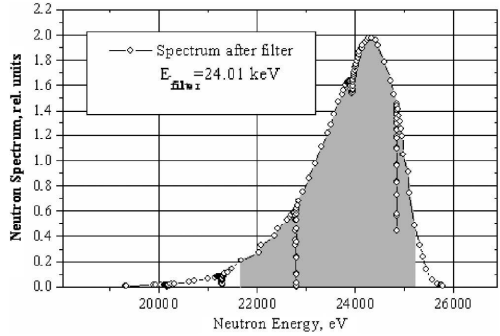

FIG. 3—*Calculated neutron spectrum after filter with energy 24.01 keV. The shaded area corresponds to 95 % response function.*

TABLE 2—*Sample thickness and total neutron cross sections for the 24-keV filter.*

#	Sample thickness, atom/barn	σ_{tot}, barn	$\Delta\sigma_{tot}$, barn	$\Delta\sigma_{tot}/\sigma_{tot}$,%
1	0.12759±0.00006	4.655	0.008	0.17
2	0.17520±0.00009	4.712	0.009	0.19
3	0.30344±0.00015	4.677	0.029	0.62

The filter components (g/cm^2), used in these experiments for filtered neutron beam forming at the energy 59 keV, are presented in the Table 3.

Figure 4 shows the calculated neutron spectra with peak energy 58.98 keV for the filter used in experiment. The limits of 95 % response function for 59-keV filter spectrum were defined as 51.92 to 60.22 keV.

Three samples of reactor carbon (99.9 %) were used in these measurements. The sample thickness and the total neutron cross section, obtained for each sample, are presented in the Table 4. The final value of total neutron cross section, averaged over all samples was 4.507±0.052 barn (relative accuracy 1.15 %).

148-keV *Filter*

We used here the composite neutron filter consisted of Si, Ti, and ^{10}B to obtain the quasi-mono-energetic beam with the average energy 148.09±17.60 keV. The purity of beam was about 95.4 %, contribution of higher energy lines is negligible: 0.6 %. The low-energy lines in the region of (0.1 to 2) keV and 54 keV make more considerable contributions (about 0.18 % and 4.2 %), but in the data analysis they may be separated due to the proton recoil counter spectroscopic capability. The intensity of this filter was very large and we used additional Pb to reduce the counting rate to the reasonable value to avoid large dead-time corrections.

The filter components (g/cm^2), used in these experiments for forming of filtered neutron beam at the energy 148 keV, are presented in the Table 5.

TABLE 3—*59-keV filter components.*

^{10}B (85 %)	^{58}Ni (99.3 %)	S	V	Al	Pb
0.2	83.3	133.0	18.33	5.4	28.34

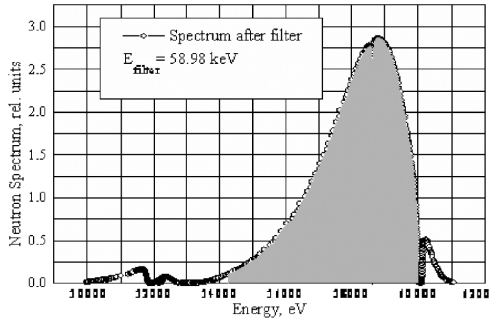

FIG. 4—*Calculated neutron spectrum after filter with energy 58.98 keV. The shaded area corresponds to 95 % response function.*

TABLE 4—*Sample thickness and total neutron cross sections for the 59-keV filter.*

#	Sample thickness, atoms/barn	σ_{tot}, barn	$\Delta\sigma_{tot}$, barn	$\Delta\sigma_{tot}/\sigma_{tot}$, %
1	0.008880±0.000012	4.497	0.100	2.23
2	0.17520±0.00026	4.729	0.110	2.35
3	0.017760±0.000012	4.480	0.039	0.87

TABLE 5—*148-keV filter components.*

^{10}B (85 %)	Si	Ti
1.0	197.18	12.3

Figure 5 shows the calculated neutron spectra with peak energy 148.09 keV for filter used in experiment. The limits of 95 % response function for 148-keV filter spectrum were defined as 118.71 to 157.01 keV.

Ten samples of carbon with thickness from 0.008888 to 0.24788 atoms/barn were used in these measurements: seven solid samples from reactor graphite (C 99.9 %), two powder samples, loaded into aluminum container with internal diameter 31.75 mm (C 99.9 %) and one sample in the form of carbon disk with thickness 1 mm (C 99.997 %).

Our experimental results, obtained for carbon samples with different thicknesses, are shown in Fig. 6. As is obvious, the observed total neutron cross sections depend on the sample thickness. Linear extrapolation to zero thickness, obtained by means of the least-squares method using experimental results for the seven thinnest carbon samples, gives an unshielded value of the total neutron cross section for carbon of 4.630±0.068 barn.

Discussion of Results

Figure 7 represents our results for C-nat. total neutron cross sections at energies in the intervals 19.3 to 25.8 keV, 51.9 to 60.2 keV, and 118.7 to 157.0 keV together with the known experimental data from database EXFOR/CSISRS [1,2,6–11] and ENDF evaluations.

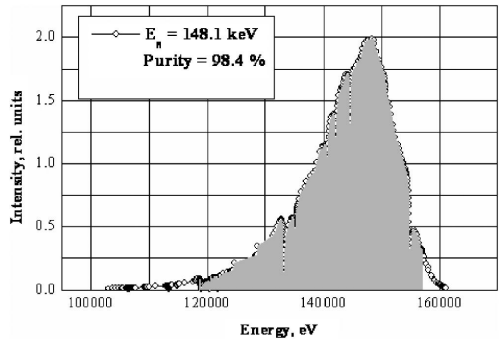

FIG. 5—*Calculated neutron spectrum after filter with energy 148.1 keV. The shaded area corresponds to 95 % response function.*

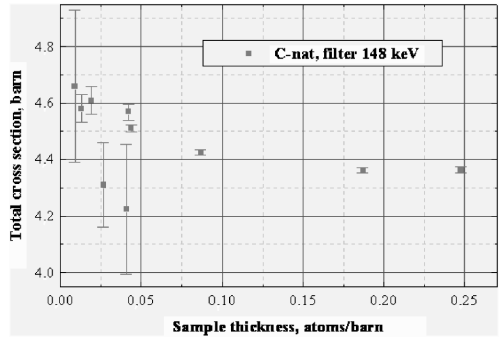

FIG. 6—*The observed experimental total neutron cross sections for natural carbon, obtained at the filter beam with energy 148 keV.*

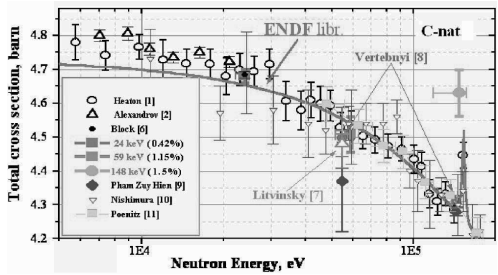

FIG. 7—*Our results for C-nat. total neutron cross sections for the 148-keV filter, experimental data from database EXFOR/CSISRS and ENDF libraries.*

For 24 keV, our result is in good agreement with the result of Block [6], i.e., 4.684±0.009 barn, measured with a Fe–Al filter and time-of-flight at the Linac spectrum.

Previous measurements at our reactor with a somewhat different filter based on Si (energy 55 keV) gave the values 4.48±0.039 barn [7] and 4.497±0.089 barn [8]; rather close to our result for the 59-keV filter. The value of total cross section, obtained for the 55-keV filter in [9] 4.37±0.15 barn lies significantly below, but its measurement accuracy is low: 3.4 %.

The value of the C-nat. total cross section, measured in our experiments with neutron filter at the energy 148 keV and corrected for the self-shielding effect, is considerably higher than ones obtained with the same Si filter by Vertebnyj [8] (4.309±0.018 barn) and by Hien [9] (4.280±0.013 barn). They are rather close to our results, obtained for carbon samples with thicknesses 0.12759 to 0.24788 atoms/barn. Unfortunately, information about the thickness of samples used in [8,9] is not available.

As it follows from the last edition of BNL-325 [12], the isotope ^{13}C, part of which has an abundance of only 1.1 % in natural carbon, has strong *p*-wave resonance with energy 152.9±1.4 keV (J=2, Γ_n =3.7±0.7 keV, Γ_γ=4.0±1.6 eV). The resonance parameters for the ^{13}C, given in the most recent work of Moxon et al. [13] and tabulated in the EXFOR data library with ENTRY 22184, are very close to BNL-325 data: resonance energy 152391.1±0.12 eV, Γ_n=3629±250 eV.

Thus, dependence of total neutron cross section on sample thickness, observed in our experiments, can be explained by a self-shielding effect. However, unshielded value of C-nat. cross section 4.630±0.068 barn, estimated by us as averaged neutron cross section for energy range 118.71 to 157.01 keV, points out that in this energy range there is very strong resonance. Its neutron width may be much more than 3.7 keV. We consider our result as preliminary. Investigation will be continued.

Acknowledgments

This research was supported by LLNL under Contract No. B513819.

References

[1] Heaton, H. T., Menke, J. L., Schrack, R. A., and Schwartz, R. B., "Total Neutron Cross Section of Carbon from 1 keV to 15 MeV," *Nucl. Sci. Eng.*, 56, 1975 pp. 27–31.

[2] Alexandrov, Yu. A., Guseva, I. S., Laptev, A. B., Nikolenko, N. G., Petrov, G. A., and Shcherbakov, O. A., "Measurement of the Neutron Total Cross Sections for Bi, C, Si, Pb," Reprint JINR-E3-213, 1997, Dubna, Russia.

[3] Gritzay, O., Kolotyi, V., Kalchenko, O., Vorona, P., and Gnidak, M., "High Precision Measurements of Cr Total Cross Section at Neutron Filtered Beams," *J. Nucl. Sci. Technol.*, Supp. 2, 1, 2002, pp. 389–392.

[4] Gritzay, O., Libman, V. A., Murzin, A. V., Nikolenko, V. G., Popov, A. B., Samosvat, G. S., and Waschkowski, W., "Preliminary Measurements of the Neutron Total Cross Section of ^{208}Pb at 24 keV

and the Neutron Polarizability," *Proceedings of the 8th International Seminar on Interaction of Neutrons with Nuclei: Neutron Spectroscopy, Nuclear Structure, Related Topics*, JINR, Dubna, Russia 2000, p. 165.

[5] Gritzay, O. O., Kolotyi, V. V., and Kalchenko, O. I., "Neutron Filters at Kyiv Research Reactor," Reprint KINR-01-6, 2001, Kyiv, Ukraine.

[6] Block, R. C., Fujita, Y., Kobayashi, K., and Oosaki, T., "Precision Neutron Total Cross Section Measurements Near 24 keV," *J. Nucl. Sci. Technol.*, 12, 1975 pp. 1–11.

[7] Litvinsky, L., Libman, V., and Murzin, A., "Elastic and Inelastic Scattering Neutron Angular Distributions on the Neutron Filter Facility," KINR-85-35, 1985, Kyiv, Ukraine.

[8] Vertebnyj, V. P., Murzin, A. V., Pshenichnyj, V. A., Litvinskij, L. L., Libman, V. A., and Pak-En-Men, "Determination of Elastically and Inelastically Scattered Neutrons Angular Distributions on the Neutron Filter Facilities," *Proceedings of an Advisory Group Meeting on Properies of Neutron Sources*, Leningrad, USSR, 9–13 June 1986.

[9] Hien, P. Z., Tang, V. H., and Xuan, N. P., "Total Neutron Cross Section of U-238 as Measured With Filtered Neutrons of 55 keV and 144 keV," IAEA Nuclear Data Section report to the I. N. D. C. No. 265, 1992.

[10] Nishimura, K., Yamanouchi, Y., Kikuchi, S., and Nakagawa, T., "Total Cross-Section Measurement for Carbon, Lanthanum and Praseodymium," JAERI Tokai Reports, No. 6883, 1977.

[11] Poenitz, W. P., Whalen, J. F., and Smith, A. B., "Total Neutron Cross Sections of Heavy Nuclei," *Nucl. Sci. Eng.*, 78, 1981 p. 333.

[12] Brookhaven National Laboratory, "Neutron Cross Sections," Vol. 1, BNL-325, Academic Press, New York, 1984.

[13] Moxon, M. C., Bond, J. B., and Brisland, J. B., "The Measurement of the Total Cross Section of Sodium and Carbon," *Processdings of the Int. Conf. on the Physics of Reators: Operation, Design, and Computation*, Marseille, France, 23–27 Apr 1990, I, p. 32.

Journal of ASTM International, Vol. 3, No. 7
Paper ID JAI13467
Available online at www.astm.org

Wei Lu,[1] *Monroe S. Wechsler,*[2] *Phillip D. Ferguson,*[3] *and Eric J. Pitcher*[4]

Spallation Radiation Damage Calculations and Database: Cross-Section Discrepancies between the Codes

ABSTRACT: A radiation damage database at NCSU is described that contains, at present, cross sections for damage energy, displacements, helium, and hydrogen. For neutrons and protons at 20–3200 MeV energies, the targets include 23 target elements from Mg to U and eight practical alloys. The underlying calculations employ Bertini, ISABEL, and CEM2k intranuclear cascade models as provided within MCNPX, three level-density formulations (GCCI, HETC, and Jülich), and multistage pre-equilibrium model (MPM) on and off. The database also includes radiation damage cross sections for lower-energy neutrons and protons, as obtained from LA150, SPECTER, ENDF, and SRIM. Examples of the database contents are provided with regard to damage energy and displacement cross sections for neutrons on Al, Fe, and W. Also, neutron flux and displacement rate calculations are described for neutrons on Fe and the 316 stainless steel mercury container vessel at SNS. In addition, discrepancies between the codes are discussed.

KEYWORDS: aluminum, codes, damage energy, cross sections, database, displacements, flux, iron, neutron irradiation, proton irradiation, radiation damage, spallation, tungsten

Introduction

There has been, in recent years, a special interest in accelerator-driven spallation neutron sources with applications that include neutron scattering and diffraction research, accelerator transmutation of nuclear waste, accelerator-aided electric power, and accelerator production of tritium. These nuclear systems accelerate protons at energies extending up to 1–3 GeV onto heavy-element targets such as Ta, W, Hg, Pb, Bi, and U. The de Broglie wavelengths of protons at these energies is so short that the protons are able to interact with individual nucleons within the heavy target nuclei, so as to produce neutrons in sufficient quantity to be useful in the above-mentioned systems. Early in the nuclear age, the term coined for this type of interaction was "spallation" [1]. Thus, by "spallation radiation damage" we mean damage due to protons energetic enough to produce spallation neutrons and due to those spallation neutrons, which have energies that extend up to the energy of the incident protons.

Radiation damage due to fission neutrons (average energy about 1–2 MeV) or even fusion neutrons (about 14 MeV) is largely due to damage energy transferred to lattice atoms. By "damage energy" we mean energy transferred by interactions with target nuclei, excluding energy delivered to electrons. These fission and fusion energy transfers are mostly elastic interactions, in which no new particles are produced. By contrast, spallation radiation damage at much higher energies is largely nonelastic, producing many new light particles (in particular helium and hydrogen) and also new heavier species in the form of transmutation products. In all three areas, fission, fusion, and spallation, the major damaging entities are displacements, and, as is shown below, the damage energy and displacement cross sections can be quite high at spallation energies. Furthermore, the larger amounts of helium, hydrogen, and heavier transmutation products may exacerbate the displacement radiation damage.

The purpose of this paper is to describe a project at NCSU to establish a radiation damage database and to present results that indicate some discrepancies between codes used to calculate radiation damage. One objective of the database is to move toward designating a standard method of calculating the radiation

Manuscript received June 20, 2005; accepted for publication April 19, 2006; published online June 2006. Presented at ASTM Symposium on Reactor Dosimetry, 12th International Symposium on 8–13 May 2005 in Gatlinburg, TN; D. W. Vehar, D. M. Gilliham, and J. M. Adams, Guest Editors.

[1] Research Associate, Dept. of Nuclear Engineering, North Carolina State University, Raleigh, NC 27695-7909.
[2] Adjunct Professor, Dept. of Nuclear Engineering, North Carolina State University, Raleigh, NC 27695-7909.
[3] Neutronics Team Leader, Spallation Neutron Source, Oak Ridge National Laboratory, Oak Ridge, TN 37830.
[4] Deputy Group Leader for Nuclear Physics, Los Alamos National Laboratory, Los Alamos, NM 87545.

damage cross sections. The standard method may change as newer calculation codes are developed and newer experimental determinations become available. However, the standard method at a particular time will provide a basis for comparison between various values and to elucidate the issues most important in a proper evaluation of radiation damage. An end product of the database project is intended to be a library of damage cross sections and other information that can be accessed by interested parties in a user-friendly and convenient way.

The NCSU Radiation Damage Database

Damage energy, displacement, helium, hydrogen, and transmutation product cross sections are compiled in three categories, depending on energy range, source, and projectile.

(A) **20–3200 MeV,** Monte Carlo intranuclear codes (INC), neutrons and protons. The codes include MCNPX [2], which contains the Bertini and ISABEL INC's (formerly within LAHET [3]) and the cascade-exciton model CEM2k [4]. The target materials investigated are 23 elemental targets in five groups of increasing atomic number (and eight alloys, not discussed here):

Group1: $_{12}$Mg, $_{13}$Al, $_{14}$Si
Group2: $_{22}$Ti, $_{23}$V, $_{24}$Cr, $_{25}$Mn, $_{26}$Fe, $_{27}$Co, $_{28}$Ni, $_{29}$Cu
Group3: $_{40}$Zr, $_{41}$Nb, $_{42}$Mo, $_{47}$Ag, $_{50}$Sn
Group4: $_{73}$Ta, $_{74}$W, $_{79}$Au, $_{80}$Hg, $_{82}$Pb, $_{83}$Bi
Group5: $_{92}$U

For the 23 elemental targets, cross sections were calculated embracing the following items:

- Three intranuclear cascade (INC) models (Bertini, ISABEL, and CEM2k)
- 1E6 histories for Bertini and ISABEL INC's; 1E5 histories for CEM2k INC
- Damage energy, displacement, He, and H production cross sections
- Three level-density formulations (GCCI, HETC, and Jülich)
- Multistage pre-equilibrium model on and off
- For He and H, comparisons with experimental values
- Transmutation production cross sections for all products for neutron and proton energies of 100, 500, and 1000 MeV

(B) **20<E<150 MeV,** LANL LA150 library [5]

Neutrons

Damage energy, displacement, He, and H cross sections for 11 elemental targets (Al, Si, Cr, Fe, Ni, Cu, Nb, W, Hg, Pb, and Bi).

Protons

He and H for 11 elemental targets (same as for neutrons).

(C) **E<20 MeV**

Neutrons

SPECTER [6]:

Damage energy and displacement cross sections for 19 elemental targets (Mg, Al, Si, Ti, V, Cr, Mn, Fe, Co, Ni, Cu, Zr, Nb, Mo, Ag, Ta, W, Au, and Pb)

He and H cross sections for 16 elemental targets (Mg, Al, Si, Ti, V, Cr, Mn, Fe, Co, Ni, Cu, Zr, Nb, Ag, W, and Au)

ENDF-6 [7]:

Damage energy and displacement cross sections for 11 targets (Al, Si, Cr, Fe, Ni, Cu, Nb, W, Hg, Pb, and Bi)

He and H cross sections for 20 targets (Mg, Al, Si, Ti, V, Cr, Mn, Fe, Co, Ni, Cu, Zr, Nb, Ag, Ta, W, Au, Hg, Pb, and Bi)

Protons, 23 targets, as shown in (A), above

Rutherford scattering: damage energy and displacement cross sections

SRIM [8]: damage energy and displacement cross sections.

In this brief paper, we concentrate on damage energy and displacement cross sections for neutrons on Al, Fe, and W, as representative of light, medium-weight, and heavy target elements, respectively.

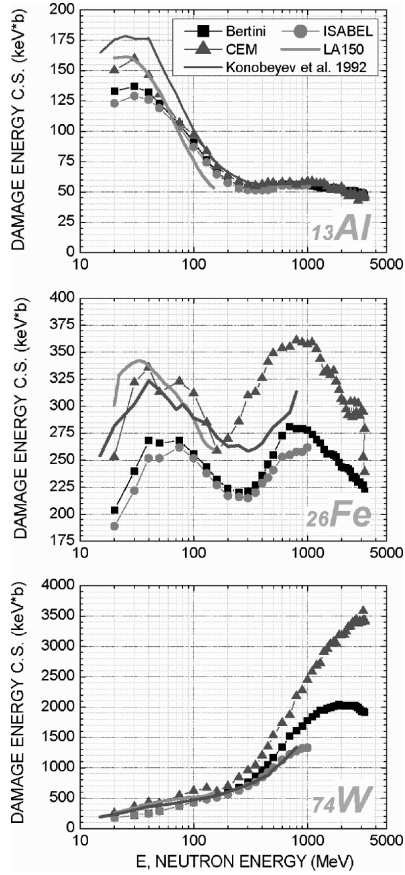

FIG. 1—*Neutron induced damage energy cross sections by Bertini, ISABEL, CEM2k (20 MeV<nE <3200 MeV), LA150 (20 MeV<nE<150 MeV), and Konobeyev et al. [9] (15 MeV<nE<800 MeV) for Al, Fe and W.*

Damage Energy and Displacement Cross Sections for Neutrons on Al, Fe, and W

The INC-based codes provide damage energies (T_{dam}) delivered to the nuclei of target atoms per incident neutron or proton of energy E. The damage energy cross section is then given by

$$\sigma_{\mathrm{dam}} = \frac{T_{\mathrm{dam}}}{xN_V} \tag{1}$$

where x is the target thickness=0.1 cm and N_V is the atomic density=6.0, 8.5, and 6.3 $\times 10^{22}$ atoms/cm^3 for Al, Fe, and W, respectively. Damage energies for Al, Fe, and W are shown versus neutron energy in Fig. 1 based on calculations using the Bertini, ISABEL, and CEM2k INC's within MCNPX and also based on the LA150 library [5] and BISERM data from Konobeyev, Korovin, and Sosnin [9]. We see the characteristic different shapes of damage energy curves for light, medium-weight, and heavy targets. The codes also furnish separate data for elastic and nonelastic interactions, as shown in Fig. 2 for CEM2k calculations. It is clear from Fig. 2 that the relative nonelastic contribution increases with increasing target weight. Concerning the two peaks for Fe in Fig. 1, it appears from Fig. 2 that the lower- and higher-energy peaks are due to elastic and nonelastic interactions, respectively, but the lower-energy peak occurs in addition to a large nonelastic contribution. A similar behavior for Ni was described

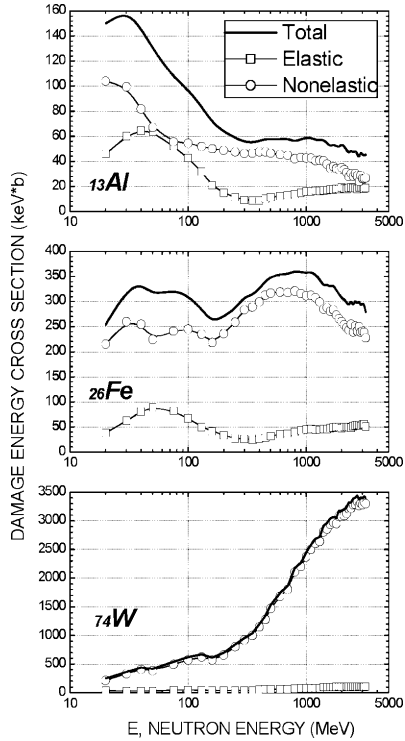

FIG. 2—*Damage energy cross section by CEM2k vs neutron energy for Al, Fe, and W showing elastic, nonelastic, and total contributions.*

earlier by Pitcher et al. [10] based on LAHET2.8. This behavior probably applies to all the medium-weight targets from Ti to Cu.

Displacement cross sections σ_d are based on the damage energy cross sections. According to ASTM Standard Practice E 521-96 [11], σ_d is given by

$$\sigma_d = \frac{0.8}{2T_d}\sigma_{\text{dam}} \tag{2}$$

where T_d is the threshold displacement energy. In [11], T_d is given as 25, 40, and 90 eV, respectively, for Al, Fe, and W; in [6] and [12], the values are 27, 40, and 90 eV, respectively.

Neutron Flux and Displacement Production Rates at SNS

The SNS spallation neutron source is an accelerator-based neutron scattering facility that employs 1000 MeV protons at 2 mA, directed on a mercury target contained in a 316 stainless steel vessel [13]. Figure 3 shows differential neutron flux and spectrum versus neutron energy, as averaged over a 13.1 cm^3 volume known as TV1 at the nose or upstream end of the mercury container vessel [14]. The flux of neutrons of energies between E_0 and 1000 MeV is 6.78×10^{14} n/cm^2 s, where E_0=0.57 keV (the neutron energy that produces a 40 eV PKA in a head-on collision in iron). The average neutron energy in this flux is about 6.2 MeV. The shape of the neutron flux shown in Fig. 3 is similar to neutron flux reported for the SINQ spallation neutron source [15–17]. Figure 3 also shows the proton flux at the SNS target vessel nose, which is strongly dominated by the 1000-MeV energy of the incident protons.

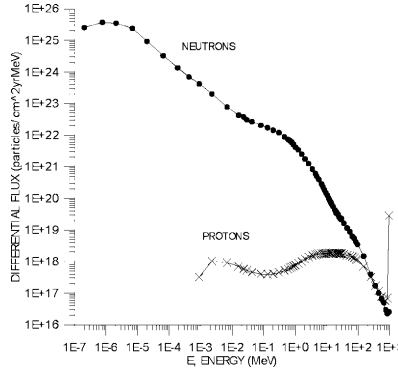

FIG. 3—*Differential neutron and proton flux at tally volume TV1 for the SNS nose region. After [14].*

The displacement production rate is obtained by folding the differential neutron flux (Fig. 3) into the displacement cross section, as obtained from the damage energy cross section in accord with Eq. 2. The damage energy cross section for Fe, for example, is shown from 0.01 to 150 MeV in Fig. 4. We see the wide swings in damage energy cross section due to resonance reactions based on ENDF-6 information. The SPECTER points appear to give average values through the ENDF-6 fluctuations. In addition, we note the good match between SPECTER and LA150 at the 20 MeV boundary energy. By contrast, the Bertini and CEM2k values are quite a bit lower than LA150 and SPECTER at 20 MeV, although the CEM2k cross sections are in fairly good agreement with LA150 above about 40 MeV. LA150 is an evaluated code, where the evaluations are based on a combination of nuclear model calculations and experimental observations. On the whole, a reasonable approach may be to use SPECTER below 20 MeV, LA150 between 20 and 150 MeV, and CEM2k (or perhaps Bertini) above 150 MeV. This combination of codes and the neutron flux of Fig. 3 were used to calculate displacement rate in Fe. The result (Fig. 5) indicates 16 dpa/year for the total displacement rate due to neutrons. For neutrons in the three energy ranges, $E < 20$, $20 < E < 150$, and $150 < E < 1000$ MeV, the fractional contributions are 78, 19, and 3%, respectively. Since the relative contribution above 150 MeV is so small, the effect of cross-section differences between Bertini and CEM2k above 150 MeV is negligible. A total displacement rate of 16 dpa/year was also reported earlier [14] for 316 stainless steel. This rate refers to the average displacement rate in the 13.1 cm^3 TV1 tally volume. Later, several series of flux determinations were done using smaller and smaller tally volumes. This permitted an estimate of the maximum displacement rate, i.e., the rate at the center of the proton beam and at the upstream tip of the SNS vessel nose [18]. The resulting maximum displacement rate was 23 dpa/year for neutrons and 13 dpa/year for protons. These values refer to time at

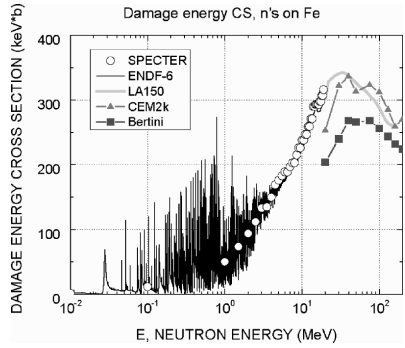

FIG. 4—*Damage energy cross section for neutrons on Fe from 0.01 to 150 MeV.*

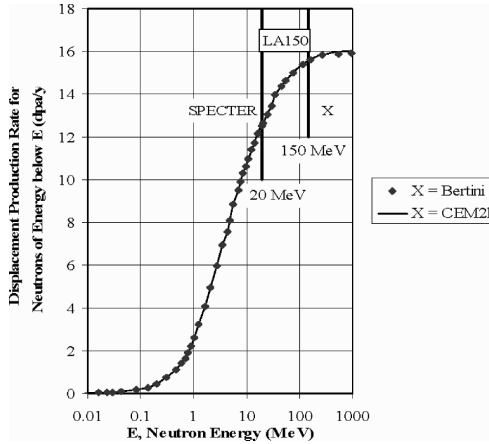

FIG. 5—*Displacement production rate in Fe due to neutrons of energy below E versus neutron energy E as calculated using SPECTER + LA150 + Bertini and using SPECTER + LA150 + CEM2k. The two curves are almost identical.*

full power, whereas SNS is expected to be at full power for about 5000 h per calendar year of 8760 h. Thus, the accumulated exposure at SNS is predicted to produce a maximum of 13 and 7 dpa per calendar year due to neutrons and protons, respectively.

Discrepancies Between the Codes

As discussed in [10], it has been known for some time that the INC-based codes, such as Bertini and CEM2k, give lower displacement cross sections near 20 MeV than are given by ENDF and SPECTER, which is based in part on ENDF-5 [6]. In Fig. 6, we express for various targets the relative difference from SPECTER. We define the relative difference from SPECTER (RDS) as $(S-X)/S$; where S is the SPECTER cross section value at 20 MeV and X is the L, B, C, LA, or E value (L=LAHET2.82, B =Bertini/MCNPX, *C*=CEM2k/MCNPX, LA=LA150, and E=ENDF-6). The following may be noted from Fig. 6: (1) RDS is essentially absent for X=E=ENDF, as expected; (2) RDS is quite small for X =LA=LA150. This is probably reasonable since ENDF and LA150 are both evaluated libraries based partly on experimental observations; and (3) RDS for X=C=CEM2k is lower than for X=Bertini (within MCNPX) or X=L=LAHET (Bertini within LAHET), particularly for higher-Z targets.

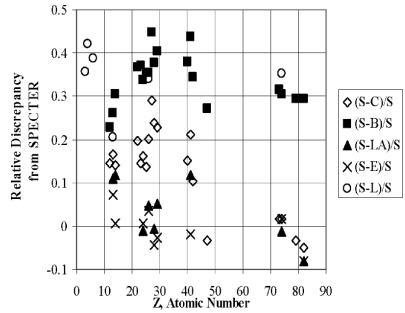

FIG. 6—*Relative discrepancy at 20 MeV from SPECTER (S) values of damage energy or displacement cross section from CEM2k (C), Bertini (B), LA150 (LA), ENDF-6 (E), and LAHET 2.82 (L). The data for LAHET were taken from Pitcher et al. [10].*

The reason for low cross sections near 20 MeV from Bertini and CEM2k as compared to ENDF and LA150 is still a matter of discussion. Chadwick et al. [5] have suggested that the INC model may be valid at energies above 150 MeV where semiclassical approximations can be used, but for energies below 150 MeV it may be deficient, since it does not take nuclear structure and quantum effects sufficiently into account.

Acknowledgments

This work was performed under contract between NCSU and LANL, and supported by the Advanced Fuel Cycle Initiative under the Office of Nuclear Energy, Department of Energy.

References

[1] Seaborg, G. T., "Nuclear Transformations in the New High Energy Ranges," *Chem. Eng. News*, Vol. 25, 1947, pp. 2819–2822.

[2] Waters, L. S., "MCNPX User's Manual," Version 2.3.0, Report LA-UR-02-2607, Los Alamos National Laboratory, Los Alamos, New Mexico, 2002, see also, http://mcnpx.lanl.gov/main.html

[3] Prael, R. E. and Lichtenstein, H., "User Guide to LCS: The LAHET Code System," LA-UR 89-3014, Radiation Transport Group, Los Alamos National Laboratory, Los Alamos, New Mexico, 1989.

[4] Mashnik, S. G., Sierk, A. J., Bersillon, O., and Gabriel, T., "Cascade-Exciton Model Detailed Analysis of Proton Spallation at Energies from 10 MeV to 5 GeV," *Nucl. Instrum. Methods Phys. Res. A* Vol. 414, 1998, p. 68; also, Report LA-UR-97-2905, Los Alamos National Laboratory, Los Alamos, NM, 1997. In addition, see http://t2.lanl.gov/publications/publications.html.

[5] Chadwick, M. B., Young, P. G., Chiba, S., Frankle, S. C., Hale, G. M., Hughes, H. G., Koning, A. J., Little, R. C., MacFarlane, R. E., Prael, R. E., and Waters, L. S., "Cross Section Evaluations to 150 MeV for Accelerator-Driven Systems and Implementation in MCNPX," *Nucl. Sci. Eng.*, Vol. 131, 1999, pp. 293–328; see also, LA-UR-98-1825, Los Alamos National Laboratory, 1998.

[6] Greenwood, L. R., and Smither, R. K., "SPECTER: Neutron Damage Calculations for Materials Irradiations," ANL/FPP/TM-197, Argonne National Laboratory, Argonne, Illinois, 60439, 1985.

[7] "ENDF-102, Data Formats and Procedures for the Evaluated Nuclear Data File ENDF-6," BNL-NCS-44945-01/04-Rev., V. McLane, Ed., National Nuclear Data Center, Brookhaven National Laboratory, Upton, New York, 2001.

[8] Ziegler, J. F., Biersack, J. P., and Littmark, U., *The Stopping and Range of Ions in Solids*, Pergamon Press, New York, 1985, see also, www.srim.org

[9] Konobeyev, A. Y., Korovin, Y. A., and Sosnin, V. N., "Neutron Displacement Cross Sections for Structural Materials Below 800 MeV," *J. Nucl. Mater.* Vol. 186, 1992, pp. 117–130.

[10] Pitcher, E. J., Ferguson, P. D., Russell, G. J., Prael, R. E., Madland, D. G., Court, J. D., Daemen, L. L., and Wechsler, M. S., *The Effect of the New Nucleon-Nucleus Elastic Scattering Data in LAHET Version 2.8 on Neutron Displacement Cross Section Calculations, Materials for Spallation Neutron Sources*, The Minerals, Metals, and Materials Society (TMS), Warrendale, PA, 1998, pp. 15–22; *Proceedings of the Symposium on Materials for Spallation Neutron Sources*, Orlando, Florida, 9–13 February 1997.

[11] ASTM Standard E 521-96, "Standard Practice for Neutron Radiation Damage Simulation by Charged-Particle Irradiation," Annual Book of ASTM Standards, American Society for Testing and Materials, West Conshocken, PA, Vol. 12.00, 1996, pp. 1–20.

[12] Lucasson, P., "The Production of Frenkel Defects in Metals," pp. 42–65, in Fundamental Aspects of Radiation Damage in Metals, Proceedings of an International Conference, Gatlinburg, TN, 6–10 October 1975, edited by M. T. Robinson and F. W. Young, Vol. I, CONF-751006-P1, U. S. Energy Research and Development Administration, Washington, DC, 1975.

[13] Mansur, L. K., "Materials Research and Development for the Spallation Neutron Source Mercury Target," *J. Nucl. Mater.* Vol. 318, 2003, pp. 14–25.

[14] Barnett, M. H., Wechsler, M. S., Dudziak, D. J., Corzine, R. K., Charlton, L. A., and Mansur, L. K., "Calculations of Radiation Damage at SNS," in *Proceedings, Third International Topical Meeting on Nuclear Applications of Accelerator Technology (AccApp99)*, American Nuclear Society, La Grange

Park, Illinois, 1999, pp. 555–559.

[15] Dai, Y., Foucher, Y., James, M. R., and Oliver, B. M., "Neutronics Calculation, Dosimetry analysis, and Gas Measurements of the first SINQ Target Irradiation Experiment, STIP-I," *J. Nucl. Mater.*, Vol. 318, 2003, pp. 167–175.

[16] Lu, W., Wechsler, M. S., and Dai, Y., "Calculations of Radiation Damage at SINQ Target 5," in *Proceedings, Sixth International Meeting on Nuclear Applications of Accelerator Technology* (AccApp'03), American Nuclear Society, La Grange Park, IL 60526, 2004, pp. 438–446.

[17] Lu, W., Wechsler, M. S., and Dai, Y., "Radiation Damage at the Aluminum Entrance Window of the SINQ Target 3," *J. Nucl. Mater.*, Vol. 318, 2003, pp. 176–184.

[18] Barnett, M. H., Wechsler, M. S., Dudziak, D. J., Mansur, L. K., and Murphy, B., "Radiation Damage to the 316 Stainless Steel Container Vessel at SNS," *J. Nucl. Mater.* Vol. 296, 2001, pp. 54–60.

Journal of ASTM International, Vol. 3, No. 7
Paper ID JAI13469
Available online at www.astm.org

Igor Remec,[1] *David C. Glasgow,*[2] *John R. Haines,*[3] *and Jeffrey O. Johnson*[4]

Proton Induced Activation in Mercury: Comparison of Measurements and Calculations

ABSTRACT: Measurements and simulations of the proton beam interaction with the mercury target were performed to support Spallation Neutron Source design. Due to the abundance of isotopes produced in mercury, the long delay between the irradiation and the measurements, and the self-shielding of the mercury sample, the measurements were difficult to perform and the activities of several isotopes have large uncertainties. Calculations predicted the activities of the most reliably measured isotopes within 20 %–40 %; however, some large discrepancies were observed for some isotopes for which the measurements were considered less reliable. Predicted dose rates were in very good agreement with the measurements.

KEYWORDS: proton beam, mercury, activation, MCNPX, gamma rays, dose rate

Introduction

The Spallation Neutron Source (SNS) construction began at the Oak Ridge National Laboratory (ORNL) in 1999. SNS will deliver a 1.4-MW pulsed beam of 1-GeV protons to a mercury target. The neutrons are produced in the target mostly through spallation reactions. These high-energy neutrons are slowed down in the room-temperature or cryogenic moderators, which are located above and below the target, and are delivered through beam tubes to the experimental stations. When SNS is completed in 2006, at a total cost of $1.4 billion, it will be the most powerful spallation source in the world for neutron-scattering research and development. The SNS project is a partnership involving six Department of Energy national laboratories (Argonne, Brookhaven, Jefferson, Lawrence Berkeley, Los Alamos, and Oak Ridge).

The SNS will be the first scientific facility to use pure mercury as a target for a proton beam. Mercury was chosen for the target because it is not damaged by radiation, as solids are; it has a high atomic number, making it a good source of neutrons; and, since it is a flowing liquid, it directly transports the time-averaged power deposited by the beam to the heat exchanger located in a hot cell far away from the beam interaction region.

To develop the SNS target design, several experiments were conducted at the Los Alamos Neutron Science Center (LANSCE) at Los Alamos National Laboratory (LANL). In an early experiment [1], a stainless steel container filled with mercury was exposed to a series of proton pulses. The objective was to study the pressure waves in the mercury and the strains in the container induced by the neutron pulses and to gather information about the mercury activation in order to assess the accuracy of predictions. This paper will briefly describe the experiment, discuss the calculations of proton-beam-induced activation in mercury, and provide a comparison of the measurements and calculations.

Experiments

While two targets were used in the experiment, mercury activation measurements were performed on the samples from the "Target A" only, which was a bullet-shaped container built from 316-type stainless steel, instrumented with optical strain and pressure sensors, and a thermocouple. The target was fabricated by

Manuscript received June 20, 2005; accepted for publication April 19, 2006; published online May 2006. Presented at ASTM Symposium on Reactor Dosimetry, 12th International Symposium on 8–13 May 2005 in Gatlinburg, TN; D. W. Vehar, D. M. Gilliam, and J. M. Adams, Guest Editors.

[1] S&T Staff Member, Oak Ridge National Laboratory, Oak Ridge, TN 37831-6172.
[2] Research Staff Member, Oak Ridge National Laboratory, Oak Ridge, TN 37831-6387.
[3] SNS EDF Target Group System Group Member, Oak Ridge National Laboratory, Oak Ridge, TN 37831-6474.
[4] Group Leader, Oak Ridge National Laboratory, Oak Ridge, TN 37831-6172.

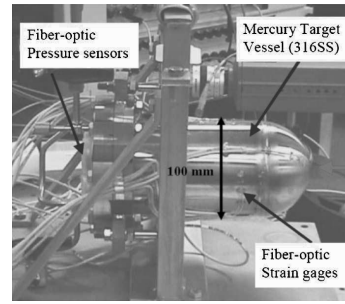

FIG. 1—*Target A before the experiments.*

welding a 100-mm-diameter dome to a cylindrical body with a 100-mm-diameter and a length of 150 mm. The target was supported by the three tabs attached to the flange at the back of the target. The tabs reached through the holes in the support plate, which was screwed to the base plate. Mercury (a total of ~20.6 kg) was loaded and unloaded into the target through the stainless steel valves inserted in the cover flange. Figure 1 shows Target A as it was being prepared for the experiments. The target was enclosed in a secondary container (not shown in Fig. 1) in order to mitigate any leakage of mercury from the primary container.

The tests were conducted in Target 2 (Blue Room) of the LANSCE Weapons Neutron Research Facility (WNR) at LANL on January 30 and 31, 1999. The target, which was placed at the center of the beam, received 35 proton beam pulses. Each pulse of 800 MeV protons was ~300 ns long and consisted of 5.3×10^{12} to 2.3×10^{13} protons; a total of 5.85×10^{14} protons was delivered to the target during the experiments.

By selecting the beam size and intensity, thermal expansion pressure waves of the same magnitude as expected in SNS could be produced. The intensity and distribution of the beam were modified by changing the number of protons incident on the target or by inserting stainless steel plates to scatter the beam and broaden the beam profile on the target. The peak beam intensity produced an energy deposition of 2 kJ in the target and induced a peak pressure of ~40 MPa in the mercury. The beam intensity was measured by the current transformer (pick-up coil) and it was also deduced from the activation foils placed in the proton beam directly in front of the target. The activation foils—pure Cu foils, 152.4 mm×152.4 mm (6 in. ×6 in.) in size were also used to determine the beam profile. After the irradiation they were cut in 36 25.40 mm×25.40 mm (1 in.×1 in.) square foils and the activity of each foil was measured separately. The activities of the reaction products listed in Table 1 were measured in the copper foils and the results were quite consistent. The ^{57}Co was found to allow the most accurate measurements due to low energy of emitted gamma rays and consequently higher detector efficiency. While Al activation foils were also irradiated, the resulting ^{24}Na, having a 15-h half life, decayed below the measurable level by the time the measurements on the foils were attempted at ORNL.

Besides the activation foils, the proton beam profiles were also measured with phosphor plate fluorescence. A phosphor plate was placed in the proton beam in front of the target, and the proton-induced fluorescence was observed by a video camera. The recorded images were digitized and analyzed to determine relative beam profiles. The fluorescence and activation measurements showed good consistency;

TABLE 1—*Proton-induced reactions in natural copper suitable to determine proton fluence.*

(p,x) Reaction product and half life (d)	Gamma-ray energy (keV)	Cross section for 800-MeV protons (mb)
^{59}Fe, 44.5	1099, 1292	1.86
^{56}Co, 77.3	846, 1238	9.9±0.73
^{57}Co, 271.8	122	27.7±2.1
^{54}Mn, 312.1	834	24.3±1.8
^{51}Cr, 27.7	320	31.1±2.3

TABLE 2—*Proton beam pulse characteristics.*

Run number	Number of pulses	Number of protons		Percent difference (%)	Scattering plates
		Cu activation foil	Current transformer		
1	4	3.86E+13	4.26E+13	−9.4	None
2	3	4.52E+13	4.35E+13	3.8	0=None
3	7	1.53E+14	1.58E+14	−3.3	2×12.7 mm
4	17		2.50E+14		1×12.7 mm
5	4	9.08E+13	9.08E+13	0.0	None

however, the resolution of the activation measurements was better. The analysis led to the description of the beam profile as a "double Gaussian" of the form

$$I = I_1 e^{-r^2/2\sigma_1^2} + I_2 e^{-r^2/2\sigma_2^2} \tag{1}$$

The fitting parameters depended on the presence or absence of the steel scattering plates, which were positioned about 1.5-m (5 ft) upstream of the target. The typical values of the parameters were 1.56×10^{11} to 7.00×10^{10} protons/mm^2 for I_1; 7.45×10^8 to 1.01×10^9 protons/mm^2 for I_2; 8.9 to 17.2 mm for σ_1; and 52.7 to 57.7 mm for σ_2. The values given first are for the beam without scattering plates, and the values given second are for the 12.7-mm-0.5-in.-thick scattering plate in the proton beam. The center of the beam was also found to be slightly off center of the activation foils (at $x=-3.95$ mm, $y=0.72$ mm for the beam without a scattering plate, and at $x=-3.1$ mm, $y=2.3$ mm for the beam with 12.7-mm-thick scattering plate.)

A detailed list of the proton beam pulses delivered to the target is given in Table 2. A comparison of the pulse intensities as determined by the activation foils and the current transformer coil is also given in Table 2.

A small sample of mercury was withdrawn from the target following the experiments and retained for gamma spectroscopy measurements.

The gamma spectroscopy was performed at ORNL about 24 days after the end of irradiation, which limited the measurements to longer-lived isotopes. Nevertheless, due to numerous isotopes still present, the measurement was difficult. A 1-mL sample of mercury was placed in a glass vial inside a plastic container and mounted on a counting card placed at 50 mm from the detector end cap. Counting lasted 1.5×10^5 s, with very low dead time. A high-resolution germanium-detector gamma-ray spectrometer was used; the resolution of the detector was better than 1.7 keV at the 1332-keV gamma line of ^{60}Co.

The detector efficiency calibration would normally require a mercury-based calibrated source, with a geometry identical to the sample in order to correctly account for the self-shielding in the sample. Such a source was not available; therefore, the detector calibration was performed with a mixed-radionuclide certified standard, which is a water solution, with three radioactive sources emitting seven gamma rays. Every effort was made to match the geometry of the mercury sample. The task to correct for the self-shielding was left to the analysis.

Figure 2 depicts the measured gamma-ray spectrum emitted from the mercury sample. Some of the identified gamma-ray peaks are indicated on the spectrum. The gamma-ray spectrum was quite complicated and contained about 75 gamma peaks, of which less than half were positively identified. Generally the spectrum suffered from a large number of peaks and from a small number of counts in the many peaks of interest. Significant uncertainty exists in the cases with large background structure and small number of counts in the peak emerging from the background. This situation arises most often in the lower-energy part of the spectrum because of Compton scattering background contributions. Unfortunately, many of the intense gamma rays belonging to the candidate radionuclides appeared in this region. Choosing a clean, interference-free gamma ray representative of a particular nuclide was extremely difficult. Normally the agreement between different gamma peaks emitted by a radionuclide is the most important and useful measure of the level of interference and confidence in estimating the activity. However, because the self-shielding correction depends on gamma-ray energy, and the self-shielding corrections for mercury were not available when the measurements were performed, such a comparison was impossible. Lastly, each gamma ray was searched for potential interference using a web-based gamma-ray library maintained by the Lawrence Berkeley Laboratory and each was examined to verify that the automatic (software-based) analysis was performed adequately.

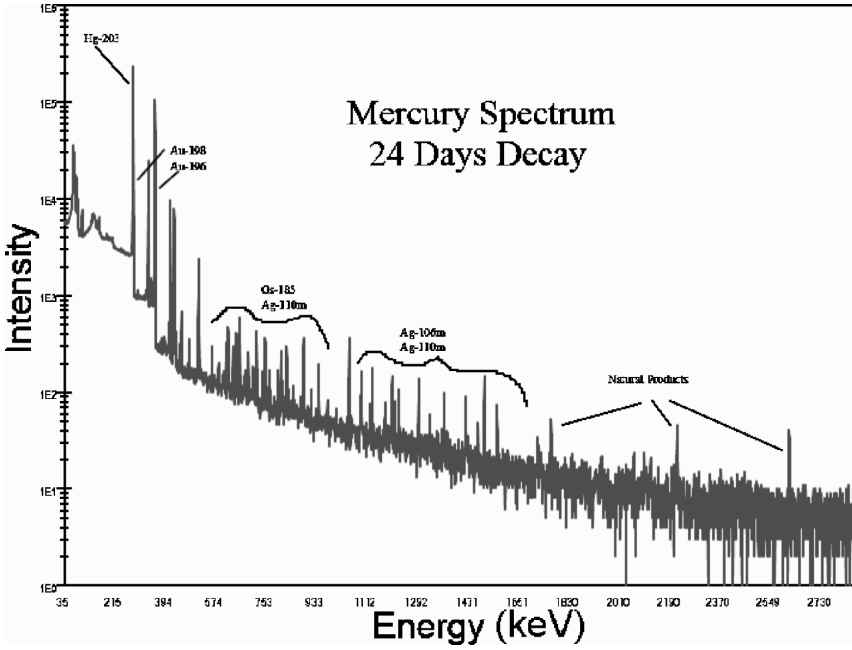

FIG. 2—*Spectrum of gamma rays emitted from mercury.*

The isotopes ^{195}Au, ^{196}Au, ^{198}Au, ^{203}Hg, and ^{110m}Ag were identified with high confidence, because they were less affected by the problems discussed above. The ^{105}Ag measurement was considered of medium quality, somewhat less reliable than the activities of the previous group. Isotopes ^{106m}Ag, ^{188}Ir, ^{185}Os, ^{194}Au, and ^{199}Au exhibited many problems (including poor counting statistics for ^{194}Au, ^{188}Ir, and ^{185}Os), which make the measured activity less reliable and may even question the presence of these nuclides. However, the presence of this latter group is supported by the spectrum (except for ^{194}Au). The activities of ^{194}Au and ^{188}Ir were severely reduced due to their relatively short half lives compared to the decay time of 24 days. The measured specific activities are listed in Table 3. All activities are corrected to the beginning of the measurements. The uncertainty (1-sigma) listed is based on the counting statistics only and is not the total uncertainty of the measurements.

TABLE 3—*Measured and calculated activities of the isotopes identified in the mercury sample. The self-shielding correction factors and the ratios of the calculated and measured activities are also given.*

Nuclide	Half life (days)	Gamma-ray energy (keV)	Measured activity (Bq/g)	Standard deviation[a] (%)	Calc.self-shielding correction	Corrected measured activity (Bq/g)	Calculated activity (Bq/g)	C/M
^{203}Hg	46.61	279.19	29.64	0.1	3.827	113.4	158.0	1.39
^{199}Au	3.14	158.38	0.26	7.7	13.389	3.481	9.579	2.75
^{198}Au	2.6952	411.80	1.51	1.3	2.177	3.287	4.176	1.27
^{196}Au	6.18	355.60	14.64	0.2	2.580	37.77	46.79	1.24
^{195}Au	186.12	98.90	1.72	4.7	45.810	78.79	76.45	0.97
^{194}Au	1.58	328.50	0.06	33.3	2.901	0.1741	0.2225	1.28
^{188}Ir	1.72	155.00	0.15	20.0	13.991	2.099	180.2	85.87
^{185}Os	93.6	874.80	0.18	38.9	1.400	0.2520	53.60	212.7
^{110m}Ag	249.8	657.76	0.12	5.8	1.564	0.1877	0.01019	0.05
^{106m}Ag	8.28	451.00	0.27	7.4	1.997	0.5391	0.1292	0.24
^{105}Ag	41.3	344.57	0.3	7.7	2.696	0.8087	0.5301	0.66

[a]Standard deviation due to counting statistics only.

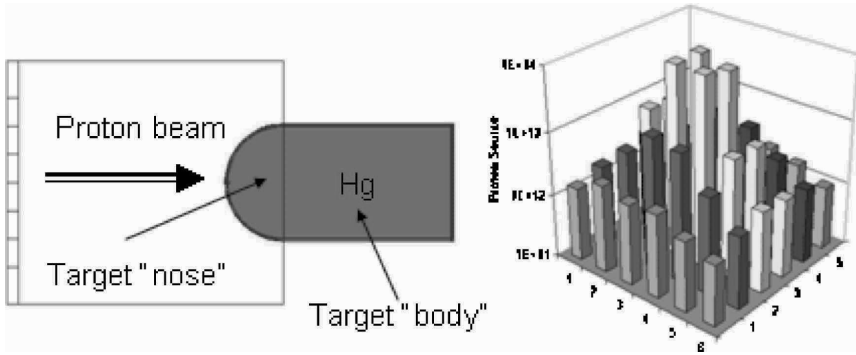

FIG. 3—*Cross section of the MCNPX model (left) and the schematic diagram of the proton beam spatial profile, as used in the MCNPX calculation (right).*

Calculation of Mercury Activation

The simulation of the proton beam interaction with mercury target was performed with the MCNPX code (Version 2.1.5) [2]. The target was modeled as a simple steel cylinder with hemispherical top and flat bottom, as shown in Fig. 3.

The proton beam was modeled as a monodirectional (collinear with the *Z* axis) beam of 800-MeV protons, since the angular divergence and energy spread of the proton beam were not measured in the experiment. The beam profile was constructed from the measured activation profiles for the beam without a scattering plate and the beam with two scattering plates, while the profile for the beam with one scattering plate (for which the Cu plate activation measurement was not performed) was obtained as the average of the beam profiles with two plates and without a plate. The three profiles were normalized by the total number of protons delivered in each beam configuration (as measured by the current transformer coil) and combined in a single profile. This profile was input in MCNPX as a surface source, defined on a 152.4 mm × 152.4 mm (6 in. × 6 in.) square grid, which was identical to that used for measuring the Cu plate activities. Within each 25.4 mm × 25.4 mm rectangle of the grid, the source profile was flat. Schematic representation of the proton beam distribution used in MCNPX is shown in Fig. 3; some of the grid cells used for beam profile specification are also shown on the left side in Fig. 3.

The MCNPX calculation used neutron cross sections up to 20 MeV (data for Hg isotopes were from the special cross-sectional library file "aptn2," e.g., 80198.23c) and the Bertini intranuclear cascade physics model for the higher energies. For protons, the Bertini model was used for all energies. Track length tallies were used to calculate neutron flux in the mercury. The calculated neutron spectra in mercury, both in the "nose" and "body" of the target, are shown in Fig. 4.

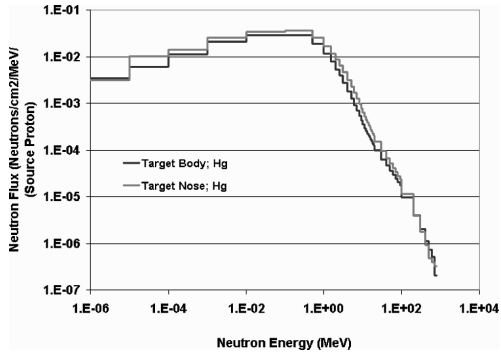

FIG. 4—*Calculated neutron spectra in the nose and body of the mercury target.*

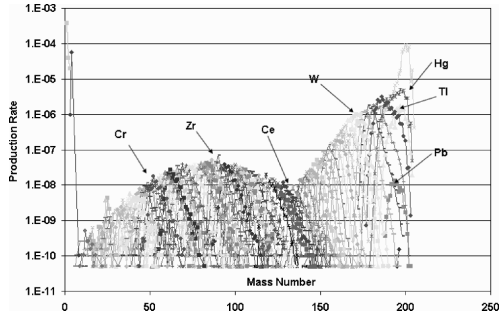

FIG. 5—*Production rates of isotopes in mercury bombarded with 800-MeV proton beam.*

The collision data for neutrons above 20 MeV and for protons were written to a "history" file created by MCNPX; the productions rates of the isotopes, obtained by analyzing this tape are shown in Fig. 5. The figure shows the probability of the isotope production per proton hitting the target as a function of mass number. Different colors denote different elements. All isotopes of an element are connected with a line of the same color. All elements from hydrogen to bismuth are present and more than 1900 isotopes are represented.

The Activation Analysis System (AAS) [3] was used to process the history file with the HTAPE3X [4] code and extract the production rates of the isotopes. AAS was also used to process the neutron-induced reaction cross sections for mercury isotopes from the FENDL [5] library into the energy bin structure used for neutron flux tallies in MCNPX, to fold the cross sections with fluxes below 20 MeV; to combine the isotope production rate with the isotope production rates from protons and neutrons above 20 MeV, and, finally, to run the ORIHET [6] code to calculate the buildup of the isotopes during the proton beam irradiation period and subsequent decay until the beginning of the gamma spectroscopy measurement. While the proton beam irradiation was performed in 35 short (~300-ns) pulses, the activation calculations assumed only one short period of irradiation, followed by the decay. Since the measured isotopes are relatively long lived, this approximation was considered adequate.

The activation calculations were performed separately for the nose and the body of the target and the specific activities were from ~60 % (^{203}Hg) to a factor of ~2.7 (^{105}Ag) higher in the nose than in the body of the target. However, it was assumed that the complete mixing occurred before the sample was removed; therefore, the average concentrations are compared with the measurements in Table 3.

Calculation of Self-Shielding Correction

In the gamma-ray spectrum measurements, the source consisting of a water solution was used to calibrate the detector efficiency. However, the sample was mercury, which has about ten times higher electron density than water and consequently attenuates gamma rays more. Because of the larger self-shielding of the mercury sample with respect to the water sample, the counting efficiency was overestimated, particularly at lower gamma-ray energies.

To determine the self-shielding corrections, a series of MCNPX calculations was performed in which the sample-to-detector geometry was modeled. The gamma-ray source was specified as an isotropic spatially uniform source within the measured sample with energy equal to the characteristic gamma ray of the selected isotope. Two calculations were performed: The first calculation contained the mercury sample and the second calculation had the mercury replaced with water. The gamma-ray current at the detector surface facing the sample was tallied. The self-shielding correction factor was determined as the ratio of the gamma-ray currents in the energy bin corresponding to the gamma-ray peak from the calculation with water and with mercury. For the 99-keV gamma rays emitted by ^{195}Au, the correction factor is ~46. With increasing energy, the correction factor decreases rapidly and is only ~1.4 at the 875-keV gamma ray emitted by ^{185}Os. The correction factors are listed in Table 3.

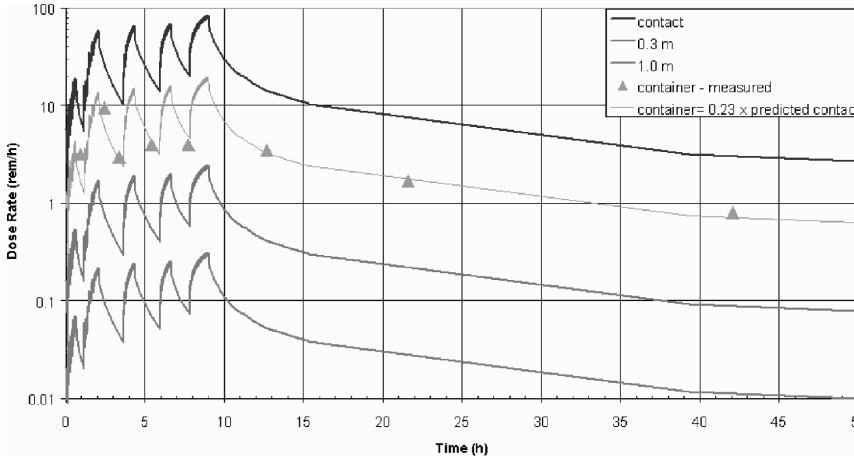

FIG. 6—*Dose rates in the vicinity of mercury target versus time. Colored lines show predicted values, and the triangles denote measured dose rates.*

Comparison of Calculated and Measured Specific Activities

The isotopes identified in the measured gamma-ray spectrum of the mercury sample are listed in Table 3. Their half lives and energies of the gamma-ray peaks used to determine activity are given, together with the measured specific activity and the corresponding standard deviation (due to counting statistics only). The calculated gamma-ray self-shielding correction is also listed, followed by the measured activity corrected for self-shielding, the calculated specific activity, and the ratio of calculated and measured specific activities.

For six of the measured isotopes (e.g., ^{203}Hg, ^{198}Au, ^{196}Au, ^{195}Au, ^{194}Au, and ^{105}Ag), the calculated and measured activities agree within 40 %. Four out of five isotopes for which the measurements were considered reliable (i.e., ^{203}Hg, ^{198}Au, ^{196}Au, and ^{195}Au) are in this group and, therefore, in reasonable agreement with the calculations; the ^{105}Ag measurement was considered of medium quality, while the ^{199}Au measurement was considered less reliable.

For ^{199}Au and ^{105m}Ag, the calculations are ~3 times higher and 4 times lower, respectively, than the measurements; for ^{105m}Ag, the measurement was of medium reliability while for the ^{199}Au the measurement was less reliable. For the remaining three isotopes (^{188}Ir, ^{185}Os, and ^{110m}Ag), there is no agreement since the calculated-to-measured activity ratios are between 0.05 and ~210. The ^{188}Ir measurement is questionable because of the lack of its parent ^{188}Pt in the spectrum. The ^{185}Os measurement also suffered from potential interferences from other nuclides while for the ^{110m}Ag measurement, no concerns were identified and the measurement was considered reliable.

For most of the nuclides, for which the measurements were considered reliable, the agreement with calculations is relatively good—within 20 % to 40 %; however, some large discrepancies were observed for some isotopes for which the measurements were considered less reliable.

Dose Rate Prediction for the Mercury Target

For another experiment, similar to the one described above, the calculations were used to predict the dose rate near the target after a series of proton beam pulses. The first part of the calculations was performed as described for the activation experiment with MCNPX and AAS and the gamma sources at several times after a single proton pulse were determined. The target was modeled as an equivalent volume sphere, and a deterministic discrete ordinates calculation with the ANISN code was performed for each selected time. Finally, the actual time sequence and strength of the pulses were factored in and the dose at any given time was determined as the sum over the contributions from all completed pulses. Figure 6 shows the predicted dose on the surface of the target at 0.3 m and 1 m from the surface of the target.

During the experiment, the dose rate was measured at the surface of the secondary container several centimeters away from the target (exact distance from the target was not recorded). The measured dose rates were found to be between the predicted dose at the surface and at 30 cm away, as expected. The calculated time-dependent dose rate at the surface, scaled to ~13 cm from the surface (i.e., reduced by a factor of 0.23), was found to match the measured dose rates quite well, as is show in Fig. 6. The target received ~200 pulses with $\sim 2.8 \times 10^{13}$ protons per pulse. Pulses were delivered in groups with "no-beam" time between them which resulted in the "saw-like" shape of the buildup and decay of the radioisotopes in the target and the resulting dose rate as shown in Fig. 6.

Conclusion

The simulation of the 800-MeV proton beam interaction with the mercury target was performed with the MCNPX code and AAS was used for the activation calculations. Out of 11 radioisotopes measured, 6 were predicted to within 20–40 % or better. Two were predicted within a factor of 4 or better, and for three isotopes there was no agreement. Due to the abundance of isotopes produced in mercury, the long delay between the irradiation and the measurements, and the self-shielding of mercury sample, the measurements were difficult to perform and activities for several isotopes have large uncertainty. In light of this, the comparison of activities is considered encouraging; however, additional experiments would be desirable to improve the verification of the simulations.

For the dose rate, which is a function of the total activation gamma-ray source rather than a function of an individual isotope, very good agreement between the predictions and measurements was observed.

References

[1] Haines, J. R., Allison, S. W., Cates, M. R., Earl, D. D., Glasgow, D. C., Jerde, E., McManamy, T. J., and Tsai, C. C., "Mercury Target Tests at the LANCSE-WNR Facility-FY99," Spallation Neutron Source Target Systems Report SNS/TSR-0146, 1999.

[2] Waters, L. S., ed., *MCNPX User's Manual, Version 2.1.5*, TPO-E83-G-UG-X-00001, Revision 0, 1999.

[3] McNeilly, G. S., and Remec, I., "Activation Analysis System," personal communication, ORNL, 2000.

[4] Prael, R. E., "HTAPE3X for Use with MCNPX," LA-UR-99-1992, April 16, 1999.

[5] Pashchenko, A. B., and McLaughlin, P. K., *FENDL/A-1.1, Neutron Activation Cross Section Data Library for Fusion Applications*, IAEA-NDS-148, Rev. 2 (1995).

[6] Atchison, F., "ORIHET for the VAX," December 1984; also P. Cloth et al., "HERMES, A Monte Carlo Program System for Beam Material Interaction Studies," KFA Juelich, Report Juel-2203 (1988).

Journal of ASTM International, Vol. 3, No. 8
Paper ID JAI13457
Available online at www.astm.org

Bertram Boehmer,[1] *Joerg Konheiser,*[1] *Klaus Noack,*[1] *Anatoli Rogov,*[1] *Ingrid Stephan,*[1] *Wolfgang Hansen,*[2] *Dietmar Hinke,*[2] *Siegfried Unholzer,*[2] *Martin Grantz,*[3] *and Hans-Christoph Mehner*[3]

Measurements and Monte Carlo Calculations of Gamma and Neutron Flux Spectra Inside and Behind Iron/Steel/ Water Configurations

ABSTRACT: Gamma and neutron flux spectra were measured inside and behind various combined iron, steel, and water slabs, which were set up in the radial beams of the zero-power training and research reactors Ausbildungskernreaktor of the Technical University Dresden and Zittauer Lehr- und Forschungsreaktor of the University of Applied Sciences Zittau/Goerlitz. The measurements were carried out with a liquid NE-213 scintillation spectrometer in the energy ranges 0.23–10 MeV for photons and 1–20 MeV for neutrons. These experiments were simulated with the Monte Carlo transport codes MCNP-4C2 and TRAMO. With MCNP the point-wise energy representation of the nuclear data from ENDF/B-VI library, release 8, was used. For TRAMO effective group cross sections were prepared by means of NJOY from the same data library. The paper describes the experiments and calculations and presents and compares some results.

KEYWORDS: neutron/gamma flux spectra, NE-213 scintillation spectrometer, neutron/gamma transport calculations, Monte Carlo method, MCNP, TRAMO

Introduction

The "surveillance specimen story" at the High Flux Isotope Reactor (HFIR) of the Oak Ridge National Laboratory revealed the following two facts: first, that gamma radiation can substantially contribute to the embrittlement of reactor structural components and, second, that the calculation methods and nuclear data available at that time were not in a sufficiently good state, which would have been necessary for a fast clearing up of the observed phenomenon [1,2]. Pushed by the unexpected results of the material investigations of the surveillance specimen material scientists evolved several theoretical models with the help of which the observations should be explained. Among them the model of the "freely migrating defects" permitted even a considerable enhancement of the embrittlement far over the DPA (displacements per atom) standard by high-energy gamma rays [3]. In the middle of the 1990s, the Nuclear Science Committee of the Nuclear Energy Agency analyzed the state of the art in computing radiation doses to reactor components. There the difference of the verification conditions of calculation methods and nuclear data applied for neutron and gamma dose calculations was pointed out [4,5]. Those used for gamma dose calculations were assessed to be at a considerably lower level than those for neutron doses. The verification of numerical methods and nuclear data for gamma dose calculations is still an actual issue of reactor dosimetry research. This statement is independent on the final answer to the question about a possible enhancement of the material embrittlement by gamma irradiation. It is also supported by new concepts for light water reactors (LWR) designed with an enlarged water gap between core and reactor pressure vessel (RPV). For instance, in the case of the advanced boiling water reactor (ABWR) the gamma-induced embrittlement will amount nearly to the same value as that of the neutrons and this even when estimated on the DPA base [6,7]. So, concerning the reactor exploitation time the gamma embrittlement becomes just as important as the neutron embrittlement.

Manuscript received June 20, 2005; accepted for publication May 17, 2006; published online June 2006. Presented at ASTM Symposium on Reactor Dosimetry, 12th International Symposium on 8–13 May 2005 in Gatlinburg, TN; D. W. Vehar, D. M. Gilliam, and J. M. Adams, Guest Editors.

[1] Research Engineer, Research Center Rossendorf, 01314 Dresden, Germany.
[2] Research Engineer, Technical University Dresden, 01062 Dresden, Germany.
[3] Graduate Research Assistant and Professor, respectively, University of Applied Sciences Zittau/Goerlitz, 02763 Zittau, Germany.

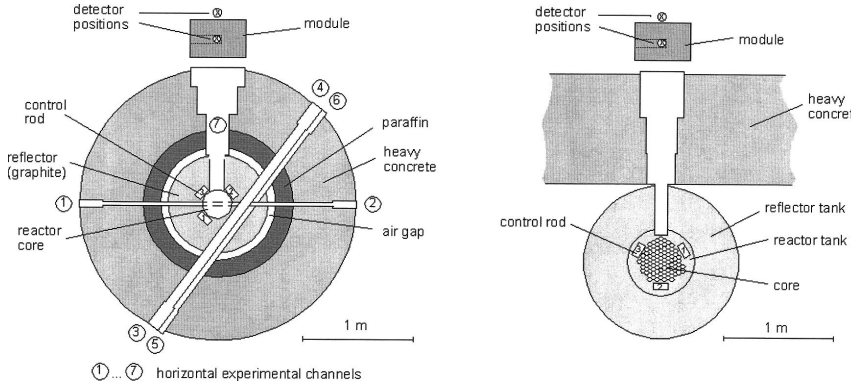

FIG. 1—*Horizontal cross section of the reactors AKR (left) and ZLFR (right).*

From the shortly outlined situation as it was some years ago we took the motivation for a research project, the focus of which was primarily directed to the verification of the Monte Carlo codes TRAMO [8] and MCNP-4C2 [9] regarding the calculation of gamma fluence spectra in reactor environments. The Monte Carlo transport code MCNP is capable to calculate coupled neutron/gamma problems and is widely used together with nuclear data based on ENDF/B data libraries. But, a systematic verification for gamma spectra calculations in this field has not yet been reported. The Monte Carlo transport code TRAMO, which has been developed by Forschungszentrum Rossendorf especially for reactor dosimetry flux/fluence calculations, now has been extended for coupled neutron/gamma and gamma transport calculations. The code, which uses nuclear data in an energy group representation prepared by means of the NJOY code [10], has also to be verified by comparing with experimental data. For that purpose, neutron/gamma transmission experiments were carried out at two zero-power training and research reactors. Gamma and neutron flux spectra were measured inside and behind various combined iron, steel, and water slabs, which were set up in the radial beams of the reactors.

In the following chapters this contribution provides information on some of the performed experiments, describes the calculations, and presents and compares results of measurements and calculations. Since the assessment of all results is not yet finished the presented results are to be considered preliminary.

Experiments

The experiments were carried out at the zero-power training and research reactors AKR (Ausbildungskernreaktor) of the Technical University Dresden and ZLFR (Zittauer Lehr- und Forschungsreaktor) of the University of Applied Sciences Zittau/Goerlitz. Figure 1 shows schematic drawings of the horizontal cross sections of both reactors.

The AKR of the Technical University Dresden has a small compact core consisting of a homogeneous mixture of 20 % enriched uranium oxide and polyethylene as solid moderator [11]. The core has a height of 27 cm and a diameter of 25 cm. Its nominal power is 2 W. A graphite reflector of 15 cm thickness surrounds the reactor core. The biological shield consists of two cylindrical walls of thickness 15 cm and 60 cm made of paraffin and heavy concrete, respectively. The radial irradiation channel used for the transmission experiments leads from the core surface through the reflector and biological shield.

The ZLFR of the University of Applied Sciences Zittau/Goerlitz is a small, light water moderated and reflected reactor of tank type with a nominal power of 1 W [12]. Its core consists of 94 fuel elements arranged in hexagonal geometry. The fuel is a mix of uranium oxide and aluminum. The enrichment of uranium is 36 %. The height of the core is 57 cm. The reactor tank has a diameter of 61 cm and is surrounded by a reflector tank with a diameter of 140 cm. Both tanks are filled with light water. The radial channel starts directly from the core tank.

The various transmission modules were composed by plates of iron and stainless steel (SS, X5CrNi18.19), each 1 cm thick, and by water tanks of thickness 4 cm, 10.2 cm, and 12.6 cm. The cover

of the tanks was made of 0.3 cm thick SS. The lateral dimensions of the plates and water tanks were 65×50 cm^2. So, the modules were considerably wider than the channel exits. In order to enable spectrum measurements inside the modules, some of the SS and iron plates had specific cuttings. They could be arranged in such a way to build a quadratic horizontal channel with an area of 6×6 cm^2 for the insertion of the scintillation detector. With the plates and water tanks various combinations of iron, steel, and water slabs were realized. These modules were set up in the radial reactor beams at a distance of 10 cm from the beam exit.

As main measurement technique a liquid NE-213 scintillation spectrometer was applied for the simultaneous measurement of neutron and gamma energy spectra [13]. The response of the spectrometer covers the range between 1 MeV and 20 MeV for neutrons and between 0.23 MeV and 10 MeV for gamma rays. The cylindrical scintillator had a diameter and a length of 3.8 cm each. For the measurements inside the transmission modules the scintillator was coupled to the photo-multiplier by means of a 50 cm long light guide with an outer diameter of 4.5 cm. The neutron and gamma energy spectra were unfolded from the registered primary data by means of the code DIFBAS [14]. The energy spectra were obtained as absolute fluxes because the spectrometer had been absolutely calibrated. Unfortunately, a higher energy resolution than the group structure of the BUGLE-96 cross section set [15] could not be achieved. Also, the three very narrow neutron groups between 2.23 MeV and 2.47 MeV had to be unified to one interval. Attempts to obtain a better resolution by means of the available unfolding routine failed up to now.

A special goal of the experiments consisted of relating the measurement results to an absolute scale of the reactor power. Aactivation detectors, which were located near to the center of the cores, were irradiated during reactor operations at different power levels and their activations were measured afterwards. In addition, for monitoring the reactor power during the measurements a miniature fission chamber FC-4A from CENTRONIC was installed in the core center of the AKR and at the top of the core in case of the ZLFR [16]. The mass of the fissile material in the fission chamber was known from calibration experiments in well-defined neutron fields. On the other hand, criticality calculations were performed by means of MCNP-4C2 with detailed models of the reactor cores while the fission rate and the activations were computed in relation to one average fission source neutron, which is the standard normalization of the results of the code. Then, assuming the measured and computed rates as the true values of these quantities one could determine the actual reactor power during the experiments. The power measuring instrumentations of both reactors showed good proportionality with the FC-4A chamber.

The uncertainty of the measurements was mainly determined by the errors of the reactor normalization and of the measurement itself that comprises the detection of the particles and the unfolding procedure with an uncertain response function. The maximum 1σ error of the normalization was estimated to be about 10 %. The total measurement uncertainties of the integrated fluxes above 1 MeV were assessed to be 4 % and 3 % for neutrons and gammas, respectively [17]. So, the total errors of the measured integrated fluxes amounted to about 11 %. As will be shown and discussed below the measured neutron flux at the lower edge of the energy interval had to be excluded as a runaway value that was produced by a systematic error of the used measurement/unfolding technique. The 1σ errors of the other group-wise integrated fluxes were assessed to amount to 15–23 % for neutrons and 12–16 % for gammas. The higher relative errors result for lower group fluxes at higher energies. To keep the errors on that level the experiments were carried out at higher reactor power and with longer measurement time, up to some hours for the thick transmission modules.

Calculations

The transmission experiments described in the previous section had to be simulated by the Monte Carlo codes MCNP and TRAMO. To do this in reactor criticality calculations would be very inefficient. To get an efficient calculation scheme the task was reformulated so that the transmission calculations could be done with effective surface sources located between reactor exit and transmission module both for neutrons and for gammas. A size of 70×90 cm^2 for the source was sufficient. The source distributions for neutrons and gammas were represented as a product of discrete distributions in space, energy, and flight direction. The surface was divided in subareas of 10×10 cm^2 and the energy range was divided in a fine-group structure (118 neutron groups, 95 gamma groups). The angular distribution turned out to be very narrow around the normal vector of the surface. It was represented as a product of an one-step function of the cosine between

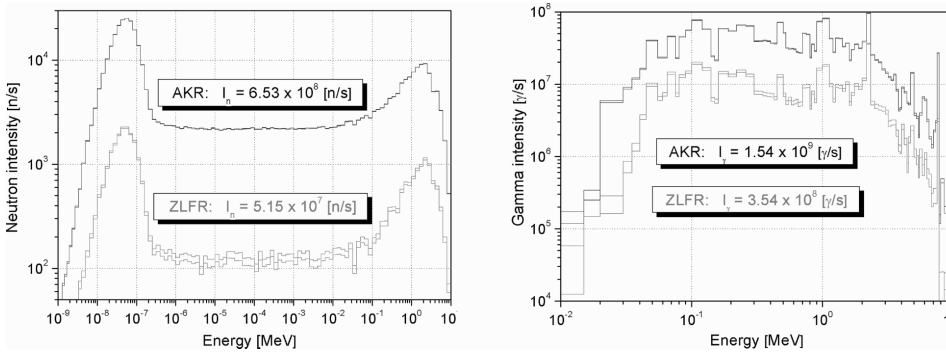

FIG. 2—*Energy spectra of neutron and gamma source intensities for AKR and ZLFR.*

flight direction and normal vector with an uniform distribution in the azimuthal angle. In a criticality calculation done with MCNP all information that was necessary for the construction of these effective surface sources representing the out-streaming neutron/gamma reactor beams was collected. The gamma source was not subdivided in the two components consisting of photons emitted by fissions and by other neutron-induced reactions, respectively. Finally, the suitability of the built surface sources for both reactors was cross checked by calculating particle fluxes behind the surface source in vacuum in a criticality calculation and in a simulation with the surface source. For the fine adjustment of the sources the lower boundary of the polar angle interval was slightly varied.

Figure 2 shows for both reactors operated with the same power of 2 W, the group-wise integrated intensities as calculated by MCNP for the fine-group structure and gives the total neutron and gamma emission intensities. The doubled curves represent the 1σ-error band around the mean value. The gamma spectra turned out to be practically the same but the neutron spectra differ to some degree.

The neutron/gamma transport simulations of the transmission experiments, which were done by means of MCNP and TRAMO, used the same model of the system. The geometry consisted of the reactor, the transmission module, and the NE-213 scintillator including the light guide. The scintillator also served as the detector volume for the flux estimation. Two types of transport calculations had to be carried out for each measured module composition: A coupled neutron/gamma calculation starting with the neutron source gave the neutron flux Φ_n and the flux $\Phi_{\gamma,n}$ of secondary gammas emitted from neutron reactions. The second calculation was a pure gamma transport calculation beginning with the gamma surface source and estimating the flux of gammas $\Phi_{\gamma,\gamma}$ directly coming from the reactor. Then, the total gamma flux Φ_γ is the sum of both gamma flux components: $\Phi_\gamma = \Phi_{\gamma,n} + \Phi_{\gamma,\gamma}$. To get an acceptable efficiency of the Monte Carlo calculations the splitting/roulette technique had to be applied, especially, for thick modules. Generally, the statistical errors of the neutron/gamma fluxes integrated above 1 MeV were less than 1 % whereas those of the group fluxes were in the range up to few percent with the exception of the two energy groups above 8 MeV for gammas.

The background situation of the experiments was studied by means of MCNP calculations. The results proved that for the modules measured the high-energy neutron background was negligible in each case. However, the situation changes when considering the high-energy gamma flux. Its background is mainly determined by thermal neutrons moving in the surroundings, being captured and that way generating highly energetic gamma radiation. This background turned out to be of the same order as the transmitted gamma flux only in the case of very thick modules.

Results and Discussion

All experimental and numerical results that are presented in the following sections are normalized to a reactor power of 1 W.

TABLE 1—*Ratios of calculated and measured high-energy neutron and gamma fluxes behind water modules (ZLFR).*

	Neutron flux ($E_n > 1$ MeV)		Gamma flux ($E_\gamma > 1$ MeV)	
Thickness (cm)	TRAMO/Exp.	TRAMO/MCNP	TRAMO/Exp.	TRAMO/MCNP
3.4	0.99	0.97	0.85	0.85
8.0	1.06	0.99	0.97	0.86
20.0	0.88	1.09	1.14	1.02

Water Modules

Three water modules were measured at the ZLFR reactor: one water container with the inner width of 3.4 cm; one water container with the inner width of 8.0 cm; and two containers close together with the inner widths of 8.0 cm; and 12.0 cm. The NE-213 detector was centrally located on the beam axis in a distance of 0.5 cm from the back of the last container. Table 1 gives the ratios of the measured and calculated high-energy neutron and gamma fluxes integrated over the energy range above 1 MeV. Figure 3 shows the measured and calculated absolute energy spectra of the neutron and gamma fluxes behind the two combined water tanks. The neutron group fluxes are divided by the lethargy width of the groups.

Comparing numerical and experimental results one can find the following facts. Concerning the high-energy gamma flux: The TRAMO results maximally differ from the measurements by about 15 % where both thinner modules are underestimated but the thick one is overestimated. The MCNP results for the two thinner modules are higher than the TRAMO results by about 15 %, but both calculations agree well for the 20 cm water thickness. For this thickness, the gamma flux spectra in Fig. 3 indicate that the slight overestimation is caused by a greater simulated capture rate of thermal neutrons at hydrogen than it really appears. Also, both calculations show that the portion of the neutron-induced gammas amounts to about 6 % only. Concerning the high-energy neutron flux, the comparison shows a good agreement between the calculations for the two thinner modules, but they differ by about 10 % for the thickest one. Comparing TRAMO and MCNP results with the measurements one observes the greatest deviation for the 20 cm thickness as an underestimation by 10 % and 20 %, respectively. The neutron flux spectra in Fig. 3 indicate that just the transmission of neutrons with energies between 1 MeV and 3 MeV is underestimated. Also, the spectra show a considerable difference in the lowest energy group (1.0–1.35 MeV) between the measurement and both numerical results by a factor of about two. Unfortunately, this discrepancy had to be interpreted as a consequence of the weak point of the measuring/unfolding technique at the low energy edge of the measuring range rather than being a real effect.

Iron Modules

Measurements were carried out with four modules of iron at the AKR reactor. The modules had the thickness 5 cm, 10 cm, and 18 cm. In addition, one measurement was also performed inside the 18 cm thick module where the centers of the measuring channel and of the NE-213 detector were at a depth of 13 cm. Table 2 gives the ratios of calculated and measured high-energy neutron and gamma fluxes and Fig. 4 shows the absolute flux spectra for the 18 cm thick module.

The comparison of numerical and experimental results reveals the following findings. Concerning the

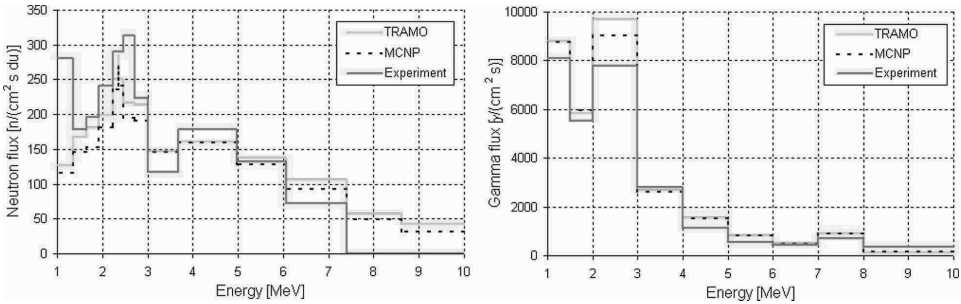

FIG. 3—*Absolute neutron and gamma flux spectra behind 20 cm of water (ZLFR).*

TABLE 2—*Ratios of calculated and measured high-energy neutron and gamma fluxes behind and inside iron modules (AKR).*

	Neutron flux ($E_n > 1$ MeV)		Gamma flux ($E_\gamma > 1$ MeV)	
Thickness (cm)	TRAMO/Exp.	TRAMO/MCNP	TRAMO/Exp.	TRAMO/MCNP
5.0	0.82	1.05	0.76	0.90
10.0	0.92	1.07	0.90	0.98
13.0[a]	0.73	0.95	0.73	0.79
18.0	0.91	1.06	1.08	1.19

[a]Measurement inside the module of 18 cm thickness.

high-energy gamma flux: The TRAMO results show a similar dependence on the iron thickness as in case of water—the thinner modules are underestimated up to 25 % and the thickest module is slightly overestimated. However, the measurement inside the 18 cm module is clearly out of this tendency. The MCNP results underestimate all measurements with a maximal deviation of about 15 % in the case of the 5 cm thickness. Both codes give a ratio of the neutron-induced gamma flux to the total gamma flux continuously increasing with the module thickness, starting from about 25 % up to 40 %. The consequence is visible in the gamma flux spectrum shown in Fig. 4—the remarkable increase in the energy group between 7 MeV and 8 MeV resulting from the capture of thermal neutrons. Also, the spectrum illustrates the underestimation of the MCNP results compared with TRAMO as well as with the measurement, particularly in the range below 3 MeV. Concerning the high-energy neutron flux, one can observe only a marginal underestimation of the measurement by both calculations, which is restricted to the energy interval between 2 MeV and 3 MeV. As in the case of the water module, the lowest energy group shows again the abnormal deviation of the measurement from both calculations.

Steel/Water/Iron Module

This section presents the results of four measurements, which were carried out with a module composed of steel, water, and iron slabs at the AKR reactor. The composition of the module in the beam direction was as follows: 21.1 cm steel; two water tanks with inner widths of 8.0 and 9.6 cm; and 18 cm iron. Four measurements were performed inside the module. The detector positions were at the following depths: M1—–9.7 cm; M2—18.2 cm; M3—42.9 cm; M4—44.9 cm. In addition, one measurement was made behind the module. However, in this experiment the background of the high-energy gammas turned out to be greater than the gamma flux transmitted through the module.

Table 3 presents ratios of calculated and measured high-energy neutron and gamma fluxes. The analysis of these results reveals the following findings. Concerning the high-energy gamma flux: The TRAMO results underestimate the measurements M1, M2, and M3 in a range up to 15 %, but overestimates M4 by about 10 %. The MCNP results give an underestimation of all measurements, maximally by about 20 %. The deviation becomes smaller with increasing depth inside the module. Both codes give a maximal relative portion of the neutron-induced gamma flux for the positions M3 and M4, where in the latter case the values 0.84 and 0.72 were calculated by MCNP and TRAMO, respectively. For the case of measurement M4, the gamma flux spectrum shown in Fig. 5 illustrates the consequences: The group fluxes between 2 MeV and 3 MeV and between 7 MeV and 8 MeV are strongly raised, what is obviously caused by the

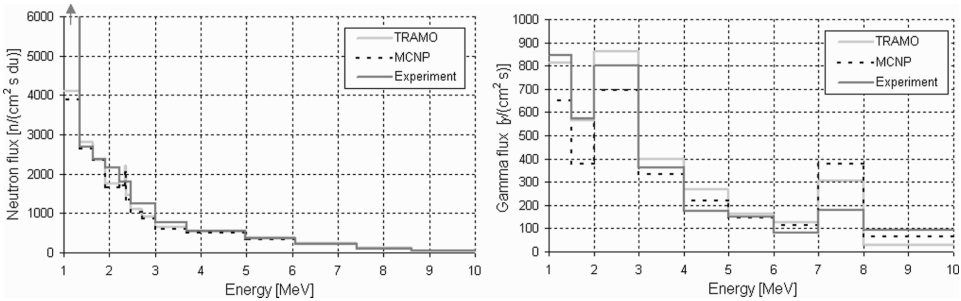

FIG. 4—*Absolute neutron and gamma flux spectra behind 18 cm of iron (AKR).*

TABLE 3—*Ratios of calculated and measured high-energy neutron and gamma fluxes inside and behind a module composed of steel, water, and iron slabs (AKR).*

	Neutron flux ($E_n > 1$ MeV)		Gamma flux ($E_\gamma > 1$ MeV)	
Measurement	TRAMO/Exp.	TRAMO/MCNP	TRAMO/Exp.	TRAMO/MCNP
M1	0.82	1.02	0.85	1.05
M2	0.83	1.04	0.95	1.08
M3	0.81	1.07	0.95	1.07
M4	0.91	1.08	1.09	1.13

capture of thermal neutrons in hydrogen and in iron nuclei, respectively. Both calculated spectra are relatively close to the measured one. Concerning the high-energy neutron flux, one observes from Table 3 that the TRAMO results underestimate all measurements within 20 %. The MCNP results show the same dependence on the detector position, but are always lower, maximally by about 10 %.

Summary

Neutron and gamma transmission experiments were carried out in the radial beams of two zero power training and research reactors. The transmission modules were composed of water containers, steel, and iron slabs. Absolute neutron and gamma flux spectra above 1 MeV were measured by means of a liquid NE-213 scintillator at positions behind and inside the transmission modules. The experiments were calculated by means of the MCNP-4C2 and the TRAMO Monte Carlo codes using the data library ENDF/B-VI, release 8, directly (MCNP) or preparing group data (TRAMO) by means of the NJOY code. The paper presented the results of some measurements and calculations. The comparison of these results reveals the following observations.

- Measurements behind water modules of different thickness: The TRAMO results for the total high-energy gamma flux vary in the range of ±15 % around the measured values. They are lower than the MCNP results by 15 % with the exception of the 20 cm thickness where both calculations agree well. The gamma flux spectrum indicates an overestimation of secondary gammas produced by the capture of thermal neutrons in hydrogen. The results of both codes for the total high-energy neutron flux agree within 10 %. The maximal deviation from the measurements of −(10−20) % was observed for the water thickness of 20 cm.
- Measurements behind and inside iron modules of different thickness: The high-energy gamma flux calculated by TRAMO is up to almost 30 % lower than the measured values with the exception of the greatest thickness of 18 cm where an overestimation of about 10 % is observed. For this thickness, the TRAMO result maximally differs from the MCNP result by about 20 %. The spectrum shows a clear underestimation by MCNP in the range below 3 MeV. Concerning the high-energy neutron flux: TRAMO underestimates the measured values up to about 30 %, but both calculations deviate by less than 10 %.

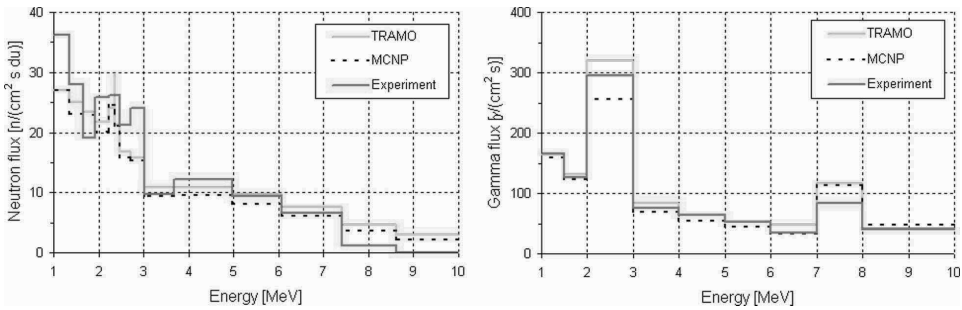

FIG. 5—*Absolute neutron and gamma flux spectra at the measurement position M4 inside a heterogeneous module composed of steel/water/iron slabs (AKR).*

- Measurements inside a heterogeneous module composed of steel, water, and iron slabs: The results of both codes show nearly the same course of the deviations from the measured results in dependence on the detector position, and this is true for the high-energy neutron and for the gamma flux. However, in all cases TRAMO calculates greater fluxes than MCNP by up to about 15 %. In general, the calculations underestimate the measurements, maximally up to 25 % with the only exception of the TRAMO result for the deepest detector position.

Acknowledgment

The authors gratefully acknowledge support of this work from Deutsche Forschungsgemeinschaft.

References

[1] Cheverton, R. D. et al., "Evaluation of HFIR Pressure-Vessel Integrity Considering Radiation Embrittlement," *Report No.* ORNL/TM-10444, Oak Ridge National Laboratory, 1988.

[2] Remec, I. et al., "Effects of Gamma Induced Displacements on HFIR pressure Vessel Materials," *J. Nucl. Mater.*, Vol. 217, 1994, pp. 258–268.

[3] Alexander, D. E. and Rehn, L. E., "The Contribution of High Energy Gamma Rays to Displacement Damage in LWR Pressure Vessels," *J. Nucl. Mater.*, Vol. 209, 1994, pp. 212–214.

[4] NEA/NSC/DOC/ (96) 5, 1996.

[5] Rulko, R. P., Kodeli, I., and Sartori, E., "Review of the Status of Reactor Vessel Embrittlement Prediction," *Proceedings, 9th International Symposium on Reactor Dosimetry*, Prague, Czech Republic, 2–6 September, 1996, pp. 535–546.

[6] Alexander, D.E. and Rehn, L. E., "Gamma-Ray Displacement Damage in the Pressure Vessel of the Advanced Boiling Water Reactor," *J. Nucl. Mater.*, Vol. 217, 1994, pp. 213–216.

[7] Garner, F. A., Greenwood, L. R., and Roy, P., "An Assessment of Potential Gamma Ray Enhancement of Embrittlement in ABWR Pressure Vessel Walls," *18th International Symposium, ASTM STP 1325*, West Conshohocken, PA, 1999, pp. 52–74.

[8] Barz, H.-U., "TRAMO—A Flexible Multi-Group Neutron Transport Code on the Basis of the Monte Carlo Method for Flux Calculations," *Report No.* ZfK-705, Rossendorf, 1990.

[9] Briesmeister, J. F., Ed., "MCNP™—A General Monte Carlo N-Particle Transport Code, Version 4C," *LA-13709-M*, Los Alamos, 2000.

[10] MacFarlane, R. E., "NJOY99.0—Code System for Producing Pointwise and Multigroup Neutron and Photon Cross Sections from ENDF/B Data," PSR-480, Los Alamos, 2000.

[11] Adam, E. et al., "Der Ausbildungs- und Forschungsreaktor der TUD," *Kernenergie*, Vol. 22, 1979, pp. 320–326.

[12] Mehner, H.-C., "Der Zittauer Lehr- und Forschungsreaktor," *Atomwirtschaft*, Vol. 43, 1998, pp. 83–86.

[13] Unholzer, S. et al., "The Measurement of Neutron and Neutron Induced Photon Spectra in Fusion Related Assemblies," *Nucl. Instrum. Methods Phys. Res. A*, Vol. 476, 2002, pp. 160–164.

[14] Tichy, M., "The DIFBAS Program—Description and User's Guide," *Report* PTB-7.2-193-1, Braunschweig, 1993.

[15] White, J. E. et al., *Proceedings ANS Topical Meeting on Radiation Protection & Shielding*, April 21–25, 1996, No. Falmouth, MA, pp. 1071–1079, RSIC package: DLC-0185/01.

[16] Boehmer, B. et al., "Investigation of Gamma and Neutron Energy Fluences in Iron-Water Benchmark Configurations for the Verification of Monte Carlo Calculations and their Application in Reactor Material Dosimetry," *J. Nucl. Sci. Technol.*, Supplement Vol. 2, 2002, pp. 947–950.

[17] P., Batistoni et al., "Neutronics Experiment on a Mock-up of the Frascati Neutron Generator," *Fusion Eng. Des.*, Vol. 47, 1999, pp. 25–60.

Journal of ASTM International, Vol. 3, No. 3
Paper ID JAI13458
Available online at www.astm.org

E. P. Lippincott[1] *and M. P. Manahan, Sr.*[2]

Advances in Calculation of Fluence to Reactor Structures

ABSTRACT: Accurate calculation of fluence to reactor structures involves integration of exposure over time taking into account changes in operating conditions and also estimation of the uncertainty in the calculation process. This paper reports on recent improvements we have made in calculation techniques and also on validation of those techniques by benchmarking against measurements in operating boiling water reactors (BWRs). Results and discussion of calculations in regions that fall outside the reactor beltline and thus require 3-D calculations to produce accurate results are presented.

KEYWORDS: neutron fluence determination, reactor structures, exposure, boiling water reactor, benchmarking

Introduction

Recently, concerns over exposure levels in boiling water reactor (BWR) structural components have arisen. Of particular interest are the shroud, top guide, and grid beam structures, which lie close to the core region and thus attain very high exposures of fast neutrons. Analysis of the exposure to these structures is complicated because of changing coolant densities axially within the core as steam is produced, because of changing power distributions due to control rod repositioning and fuel burnup, and because of geometrical considerations that do not lend themselves to analysis using standard 2-D calculational methods. This paper discusses investigations of these calculational concerns and benchmarking of the results.

Figures 1 and 2 illustrate a typical BWR geometry. This geometry is that chosen for the BWR calculational benchmark [1]. In Fig. 1, the fuel region extends from just above the core support plate to just below the top guide. The closest structures are the shroud, top guide, and core plate, and exposures to these structures are calculated to assess the material damage level, especially for the welds holding these structures together. Figure 2 shows a plan view at the core midplane. The surveillance capsule location is adjacent to the vessel inner radius and most measurement data for validation of calculational fluence levels are from this region. Significant structures for assessment of vessel exposure include the jet pumps, which lie between the shroud and vessel.

Time Integration

Operating conditions are continuously changing in power reactors and this is especially true for BWR fuel cycles where significant changes in both power distribution and water density occur during a fuel cycle. To obtain suitable average conditions over a fuel cycle, we have investigated the changing operating conditions to divide the cycle into subparts with consistent parameters. The approach used is to average the calculational input based on significant power and void changes within each fuel cycle. The control rod sequence exchanges are of interest since they result in significant changes in the distribution of power and void fraction within the core. Therefore, typically 6–10 subcycles for transport analysis were defined at each of the cycle sequence exchanges. It must be recognized that core flow and control rod adjustments are made during the subcycles, but it has been assumed that these control adjustments do not have a large effect on the reactor nodal power and void distributions, particularly for the outer fuel bundles. These edge bundles (outer two rows) dominate the fast neutron flux at the shroud and vessel in the beltline region. This

Manuscript received June 20, 2005; accepted for publication September 29, 2005; published online December 2005. Presented at ASTM Symposium on Reactor Dosimetry, 12th International Symposium on 8–13 May 2005 in Gatlinburg, TN; D. W. Vehar, D. M. Gilliam, and J. M. Adams, Guest Editor.
[1] 1776 McClure Road, Monroeville, PA 15146.
[2] MPM Technologies, Inc., 2161 Sandy Drive, State College, PA 16803-2283.

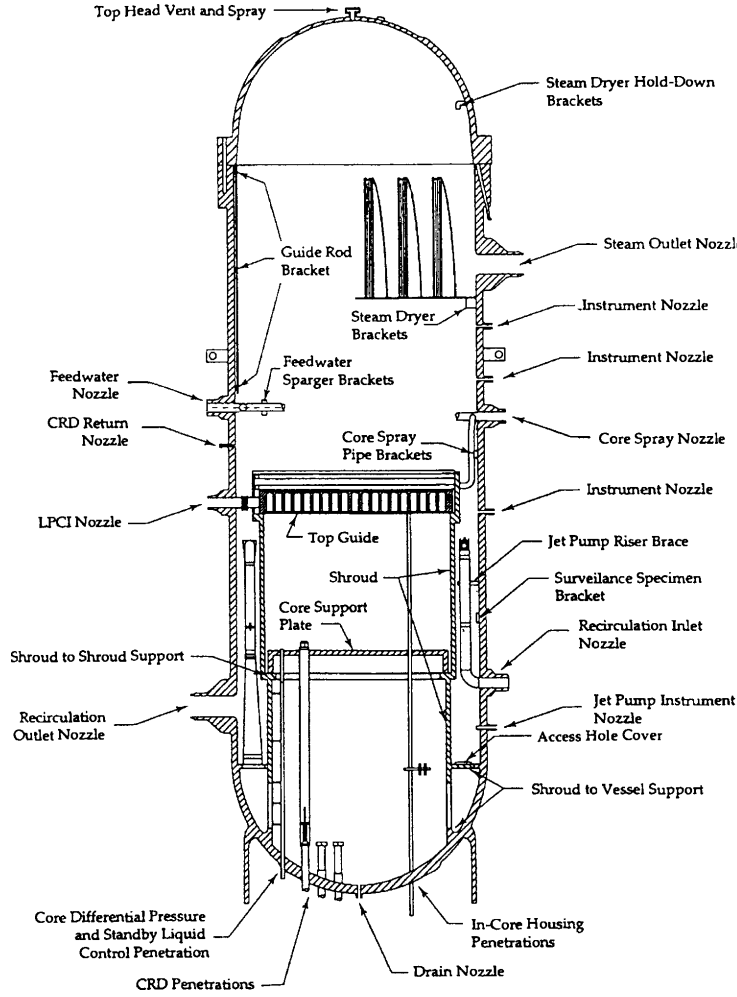

FIG. 1—*Typical BWR geometry.*

approach is reasonable since peripheral bundles are not typically controlled and control rod adjustments made during a subcycle have only a small impact on power and void distributions within these bundles. In order to check this assumption, plots of pin power linear heat generation rate as a function of burnup were evaluated. As expected, the variations over the individual segments are continuous and the average power is well represented by selecting the middle of the segment.

By the suitable averaging of the water density over the cycle, and taking the average power from the cycle burnup, we have shown in multiple cases that the cycle can be well represented by a single cycle statepoint calculation. Results for the single statepoint calculation have been compared with more detailed analyses that separately calculate the 6–10 subparts, and these comparisons indicate that using our averaging process gives results that agree within 1–2 % with the detailed time analysis. Of course, the detailed time analysis is required for accurate dosimetry analysis of the shorter-lived dosimetry products such as Co-58 or Mn-54, since flux levels during a cycle can vary by as much as ±20 % around the mean value during the length of a fuel cycle.

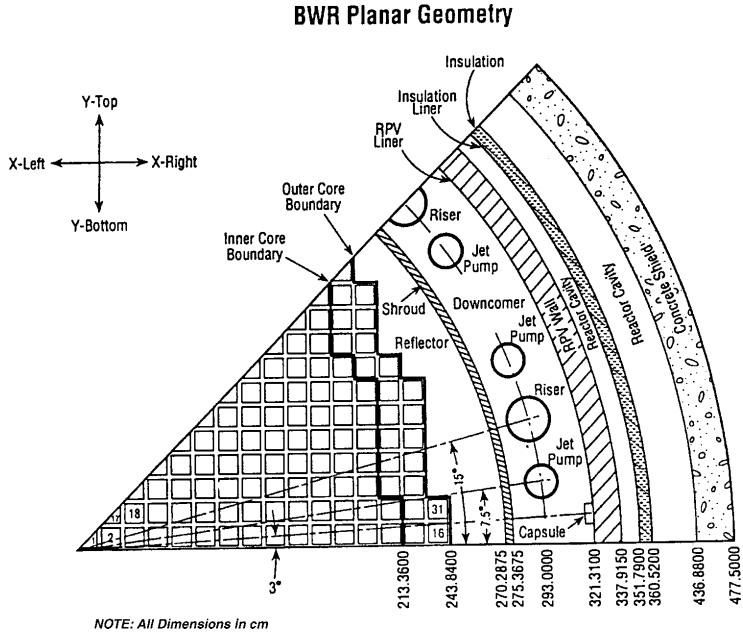

FIG. 2—*Cross section view of typical BWR geometry at core axial midplane.*

Benchmarking Calculational Results in Operating Plants

To establish the accuracy of the cross sections and calculational methods used for evaluation of fluence to BWR structures, we have compared the calculated results with measured dosimetry data in all the plants we have analyzed. We have benchmarked our BWR calculational results against dosimetry measurements from operating plants for nine cases and achieved excellent results as shown in Table 1. The average calculated-to-measured (C/M) ratio for these cases is 1.01 with a standard deviation of 6 %. This result indicates that present models and calculational methods produce accurate results, and also indicates consistency of analysis and measurement.

TABLE 1—*Tabulation of dosimetry results for operating BWR plants.*

Reactor	Dosimeter Measurement Description	Dosimeter Types Analyzed	Average C/M Ratio
Plant 1	Wires Removed from Capsule Holder after Cycle 1	Fe, Cu	0.94
	Surveillance Capsule	Fe, Cu	1.00
	Surveillance Capsule	Fe, Ni, Cu	1.07
	Surveillance Capsule	Fe, Ni, Cu	1.00
	Shroud Retrospective Dosimetry	Fe, Ni	1.11
Plant 2	Surveillance Capsule	Fe, Cu	1.02
Plant 3	Wires Removed from Capsule Holder after Cycle 1	Fe	0.92
Plant 4	Wires Removed from Capsule Holder after Cycle 1	Fe	1.04
	Surveillance Capsule	Fe, Cu	0.94
	Overall Average		1.01

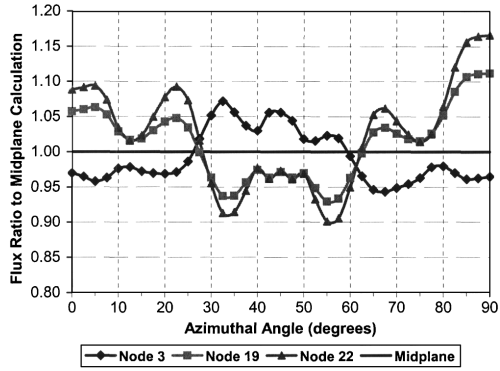

FIG. 3—*Comparison of fluence rate vs. azimuthal angle at the shroud inner radius for several off-midplane fuel nodes vs. the midplane fluence rate.*

Three-Dimensional Evaluations

Most surveillance analyses and benchmarking have been performed at locations lying radially outside the core and axially in the beltline region between the top and bottom of the fuel. For some applications, most noteworthy for determinations of BWR shroud and top guide weld exposures, it is necessary to calculate fluence in regions where simple symmetries are no longer valid. Although 3-D calculations are now practical with modern computer workstations, transport calculations of neutron fluence to reactor structures are still typically made using 2-D S_n calculations. The use of 2-D models is convenient for calculation of the effects of changing fuel loadings and changes in other conditions that may occur with changes in fuel burnup. In order to estimate the fluence in the 3-D geometry, the following synthesis equation may be used to evaluate the flux φ for each case:

$$\varphi(R,\theta,Z) = \varphi(R,\theta) * \varphi(R,Z)/\varphi(R) \tag{1}$$

In this equation, $\varphi(R,\theta)$ is taken from an R,θ calculation (normalized to the power at the core axial midplane in the model region), and $\varphi(R,Z)$ is from an R,Z calculation normalized to the power in the entire core. A third calculation determines $\varphi(R)$ using a 1-D cylindrical model normalized at the core midplane. This synthesis equation is recommended in the NRC Regulatory Guide 1.190 [2].

Within the axial region the deviations from the synthesis formulation will occur in BWR reactors due to shifts in the azimuthal distribution of power and coolant density with height in the core. The effects of these shifts have been investigated and results are shown in Fig. 3. This figure shows the difference in azimuthal flux shape at three fuel nodes compared to the core axial midplane. Node 3 is centered 15 in. (38 cm) from the core bottom, node 19 is 36 in. (48 to 91 cm) above the midplane, and node 22 is 15 in. (38 cm) below the top of the fuel. In most cases, the neglect of these changes results in less than a 10 % error, but at a few angles and for locations near the top of the core, the effect can be greater.

In regions above and below the core, the separability of the azimuthal flux shape from the axial flux shape does not hold. An indication of the region where Eq 1 will fail is shown in Fig. 4. This figure shows the fraction of the fluence rate at the shroud inner radius due to radial leakage from the core, which has a symmetry close to that from the core midplane calculation. The greater the deviation of this value from 1.0, the greater the error in application of the synthesis method. Therefore, obtaining accurate fluence estimates in these regions ruires a more complicated analysis. We have performed 3-D calculations using the TORT code [3], and we have also developed an extension of the simple synthesis method in order to evaluate fluence to structures above and below the active fuel using data as illustrated in Fig. 4. The calculations were done for a BWR geometry similar to that described for the BWR benchmark calculation [1]. Comparisons were made between the TORT results and 2-D synthesis results using Eq 1 within the beltline region. An example is shown in Fig. 5, which illustrates the generally good agreement between the 3-D and 2-D synthesis results in this region.

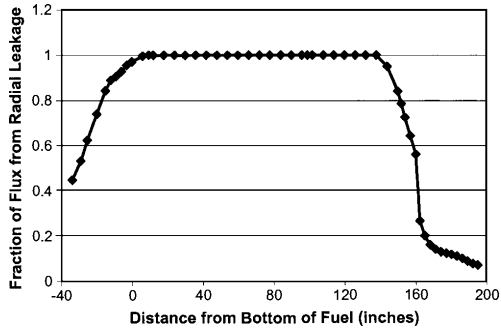

FIG. 4—*Calculated fraction of fast fluence at the shroud inner radius due to radial leakage from the core.*

An example of the results from calculations performed outside of the beltline region is shown in Fig. 6. In this figure, the fluence rate at the shroud inner radius at a point about 12.5 in. (32 cm) above the core is derived from the 2-D calculations using both the standard and extended synthesis methods, and these are compared with the 3-D result. It is seen that the standard synthesis greatly overpredicts the maximum fluence, but also underpredicts the fluence at the minimum. The agreement between the extended synthesis method and the 3-D calculation is seen to be excellent. Similar results are obtained at other axial heights. Based on the results obtained it is concluded that the extended synthesis method can be applied to determine reasonable estimates of the neutron fluence to structures outside the beltline region. While we have only applied this method to BWR geometries, it may be anticipated that equally good results may be obtained in PWR applications.

Conclusions

Calculations of fluence to BWR structures are complicated by power and water density variations during operation and by the need to assess fluence in regions where 2-D calculations are not adequate. The studies summarized in this paper have shown that accurate results can be obtained in these calculations by suitable averaging over time. Benchmarking of calculations against surveillance measurements in four different plants with differing geometries have produced average C/M ratios very close to unity. Investigations of 3-D effects have shown that the TORT code produces results that are reasonably accurate. An expanded

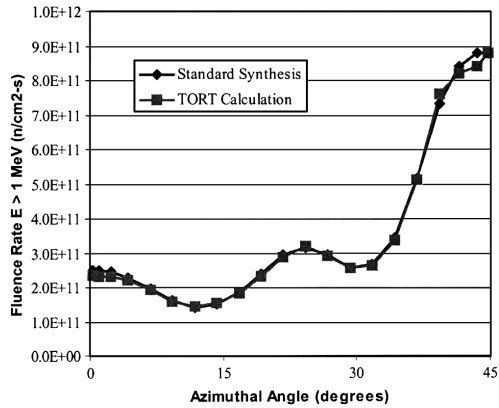

FIG. 5—*Fluence rate vs. azimuthal angle at the shroud inner radius at a location 21 in. (53 cm) below the top of the fuel.*

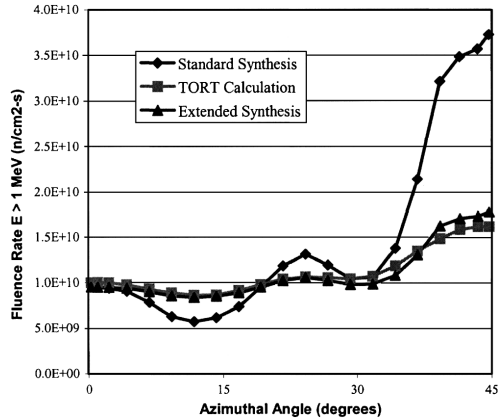

FIG. 6—*Fluence rate vs. azimuthal angle at the shroud inner radius at a location 12.5 in. (32 cm) above the top of the fuel.*

2-D synthesis technique was developed and was also shown to produce good results. The expanded 2-D synthesis technique is much faster to set up and run, and can be used for detailed investigations of time-dependent effects when multiple runs with a 3-D code are impractical.

References

[1] Carew, J. F., Hu, K., Aronson, A., Prince, A., and Zamonsky, G., "PWR and BWR Pressure Vessel Fluence Calculational Benchmark Problems and Solutions, NUREG/CR-6115 (BNL-NUREG-52395)," Draft completed May 20, 1997.

[2] *Regulatory Guide 1.190, Calculational and Dosimetry Methods for Determining Pressure Vessel Neutron Fluence*, U.S. Nuclear Regulatory Commission, March 2001.

[3] RSICC Computer Code Collection, CCC-650, "DOORS3.2a, One, Two- and Three-Dimensional Discrete Ordinates Neutron/Photon Transport Code System," available from the Radiation Safety Information Computational Center, Oak Ridge National Laboratory, Oak Ridge, TN, Updated Oct. 2003.

Journal of ASTM International, Vol. 3, No. 4
Paper ID JAI13460
Available online at www.astm.org

G. Borodkin,[1] *N. Khrennikov,*[1] *B. Böhmer,*[2] *K. Noack,*[3] *and J. Konheiser*[3]

Deterministic and Monte Carlo Neutron Transport Calculation for Greifswald-1 and Comparison with Ex-vessel Measured Data

ABSTRACT: The results of a study of neutron and gamma field functionals derived by deterministic S_n and Monte Carlo calculation methods and by neutron activation measurements in application to the ex-vessel cavity of the VVER-440 reactor Greifswald-1 are presented. A good agreement of deterministic and stochastic calculation results with each other as well as with measurement results was found for neutron threshold detector reaction rates at ex-vessel positions. The influence of different numbers of cross-sectional groups on the calculation results is demonstrated.

KEYWORDS: VVER, neutron-gamma transport calculation, ex-vessel activation measurements

Introduction

The VVER-440/230-type reactor of Greifswald NPP, Unit 1 (Greifswald-1), was shut down in 1990. The near-core basic reactor equipment (reactor pressure vessel, support constructions, and internals) irradiated during 15 fuel cycles is available for structural material research at trepans to be cut out at positions of interest [1]. The analysis of material property degradation under irradiation is urgent due to the need to confirm the safety of operating VVER units of similar type, and also in connection with investigations of the possibility of operation prolongations, for example, of Russian NPP Units with VVER-440/230.

A necessary condition for the reliability of results of material property studies, particularly on radiation embrittlement of the reactor pressure vessel (RPV), is the validity of neutron and gamma dosimetry of relevant reactor equipment. In this connection, calculation methods used to predict end-of-life neutron fluence in the VVER-440 equipment need to be validated and upgraded, if necessary. The purpose of this work is to study neutron and gamma field functionals obtained for the near-RPV area by different calculation methods and to compare calculation results with ex-vessel cavity measured data.

The paper deals with the results of a comparison of independent calculations by deterministic (DORT [2] and BUGLE-96 [3]) and MonteCarlo (TRAMO [4] and ENDF/B-VI) codes. The comparison was made for neutron and gamma fluence rates (FR) and additionally for neutron and gamma DPA (displacement per atom) rates.

The experimental results unpublished up-to-now were available from an internal report [5] and data files of the predecessor institute of the Forschungszentrum Rossendorf. They were obtained in the late 1980s under participation of one of the authors. The comparison of experimental and calculational results is based on analysis of C/M (calculated to measured) ratios of dosimetry reaction rates (RR). The analyzed threshold detector reactions were $^{58}\mathrm{Ni}(n,p)$, $^{54}\mathrm{Fe}(n,p)$, $^{46}\mathrm{Ti}(n,p)$, and $^{63}\mathrm{Cu}(n,\alpha)$.

Manuscript received June 20, 2005; accepted for publication September 29, 2005; published online January 2006. Presented at ASTM Symposium on Reactor Dosimetry, 12th International Symposium on 8–13 May 2005 in Gatlinburg, TN; D. W. Vehar, D. M. Gilliam, and J. M. Adams, Guest Editors.

[1] Head of Reactor Dosimetry Group (Borodkin), Head of Department (Khrennikov), Scientific and Engineering Centre for Nuclear and Radiation Safety (SEC NRS) of Rostechnadzor, Malaya Krasnoselskaya ul., 2/8, bld. 5, 107140 Moscow, Russia.
[2] Guest Scientist at the Forschungszentrum Rossendorf e.V. (FZR), Postfach 510119, D-01314 Dresden, Germany.
[3] Head of Department (Noack), Research Scientist (Konheiser), Forschungszentrum Rossendorf e.V. (FZR), Postfach 510119, D-01314 Dresden, Germany.

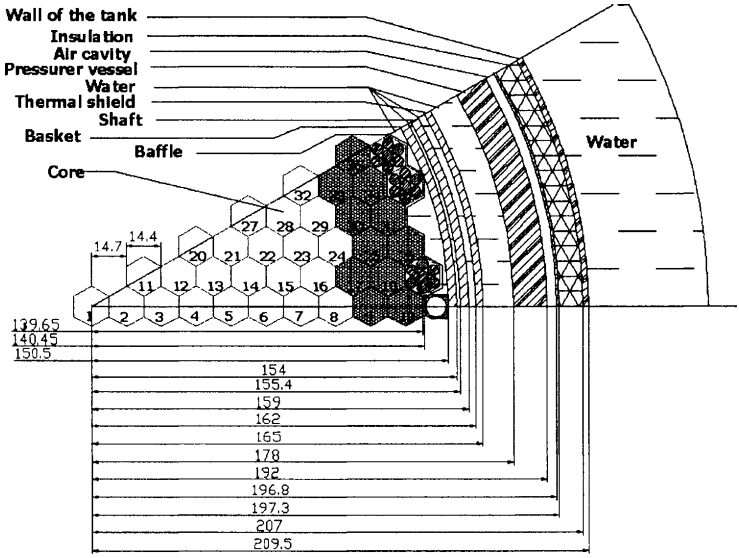

FIG. 1—*Thirty-degree midplane sector of symmetry of Greifswald-1 reactor model used in DORT calculations.*

Greifswald-1 Dosimetry Study

Reactor Description

The Greifswald-1 reactor is a first generation VVER-440, where a water tank is used as a biological shield (Fig. 1) contrary to the concrete shield used in later VVER-440-type reactors.

As the neutron activation measurements were carried out during the 12th fuel cycle, the calculation study was done for the same cycle. The operation during 314 effective full power days in this cycle is characterized by a reduced reactor core resulting from the installation of 36 dummy assemblies on the core periphery—three dummy assemblies per 30-deg sector as shown in Fig. 1. A full set of three-dimonsional (3D) time-dependent reactor core data including pin-to-pin neutron source distributions was obtained from detailed neutron-physical core calculations. This set was used for preparation of reactor models for discrete ordinate S_n and Monte Carlo neutron-gamma transport calculations. The core periphery (last row), the most important part of the reactor for the ex-core fluence rate study, was loaded with fresh (unburned) fuel assemblies.

The air cavity behind the RPV (see Fig. 1) was used for ex-vessel neutron activation measurements. With the help of the available power history during the 12th fuel cycle average experimental reaction rates for nominal power were evaluated.

Calculation Methods

Neutron and gamma fluences were calculated using the DORT code for a grid of positions covering the whole reactor. As a cross-sectional set, the BUGLE-96T library (47 neutron/20 gamma groups) with upscattering in the thermal region was used. The two peripheral assembly rows (see Fig. 1) were modeled taking into account pin-wise source distributions. The 3D fluence rate distributions were synthesized from results of three 2D calculations as was proposed in [6].

Pure 3D calculations were carried out with the Monte Carlo code TRAMO. Two group libraries with largely differing numbers of energy groups were used: 47 neutron/20 gamma groups (BUGLE-96 energy scale) in the first and 640 neutron/94 gamma groups in the second case. Both libraries were derived in the same way from ENDF/B-VI by the NJOY code [7]. The flux weighting spectrum used for group library

preparation consists of three adjoining spectrum parts: in the thermal region—a Maxwell spectrum with temperature 0.0253 eV, in the epithermal and medium part (0.215 eV to 0.8208 MeV)—a 1/E spectrum, in the fast region—a fission spectrum with maximum energy of 1.4 MeV. The inelastic scattering cross sections were represented by Legendre polynomials. Equiprobable angular intervals were generated for a number of energy points in case of the elastic scattering and the scattering in the thermal region. Alpha/beta factors were employed for the thermal scattering on hydrogen, and the other nuclides were computed relying on the free gas model. For the resonance self-shielding the F-factors formalism was used.

The dosimetry cross-sectional library used for calculation of the reaction rates was IRDF-90, rev. 2 [8]. Radiation damage parameters for neutrons were obtained on the basis of the ASTM evaluation of DPA cross sections available from IRDF-90, rev. 2. Gamma DPA rates were evaluated on the basis of cross section data from [9].

In both S_n and Monte Carlo calculations, a 60-deg periodicity sector was modeled taking into account detailed 3D neutron source distributions (pin wise in peripheral assemblies) and the dependence on the burnup of neutron-physical properties of fuel assemblies.

TRAMO calculations were performed for the ex-vessel cavity midplane, and calculation results are fluence rates integrals over three degrees azimuth intervals.

Experiment Description

During the 12th reactor cycle neutron-activation detectors were irradiated in the ex-vessel cavity at five azimuthal positions: 26.6, 40, 53.4, 66.8, and 80.2 deg relative to the main axis I in the anticlockwise direction. These azimuths correspond to 6.8, 20.2, 26.6, 40, and 53.4 deg in the 60-deg symmetry sector. For each azimuth, detector sets were placed at ten height levels evenly distributed over the core height. Reaction rates were derived from measured end-of-irradiation activities and decay factors calculated on the basis of total thermal power history. All analyzed dosimetry reactions—^{58}Ni$(n,p)^{58}$Co, ^{54}Fe$(n,p)^{54}$Mn, ^{46}Ti$(n,p)^{46}$Sc, and ^{63}Cu$(n,\alpha)^{60}$Co—are functionals of the fast neutron field and can be characterized by effective threshold energies 2.5, 3.0, 4.5, and 6 MeV, respectively.

Comparison of Results and Discussion

The influence of cross-sectional group structures on calculation results is shown in Table 1, presenting relations between broad group (47 n/20 g) and fine group (640 n/94 g) TRAMO calculation results for neutron and gamma fluence rate (FR) integrals and DPA. The mean difference for neutron FR and DPA is not higher than 2 % except for thermal neutrons (11 %) and fluence rate above 3 MeV (4 %). In the latter case, the difference may be partly caused by increased statistical error relative to other functionals. The average statistical errors are 4.5 % for 640 n/94 g and 2 % for 47 n/20 g calculations. The mean difference for gamma FR and DPA is near that observed for neutrons (~2 %). The larger differences for thermal neutrons can be explained by the very coarse description of the thermal region by the broad group cross-sectional set.

A comparison of DORT and TRAMO (47 n/20 g groups) results is presented in Table 2. In average, the DORT results are 1–6 % lower than the TRAMO results for all neutron functionals except for thermal neutrons FR. In the last case the underestimation is near 20 %.

For gammas, DORT calculation results are systematically lower than the TRAMO results by an average over all analyzed functionals of about 10—12 %.

In the case of thermal neutrons and gamma calculations, the upscattering effect plays a significant role, as shown in a comparison of the two last rows of Table 2. Taking into account upscattering in DORT calculations results in a 60 % reduction of the deviation from the results obtained without consideration of upscattering for thermal neutrons and near 45 % for gamma functionals.

Results of DORT calculations were compared with measured data in all experimental positions and for every detector.

Figure 2 demonstrates a comparison of calculated and measured RR along axial direction on 54.3 deg (experimentally defined azimuth maximum). A coincidence of shapes of axial distributions of calculated and experimental data can be observed for all detectors. Moreover, it can be seen that within the core height the agreement of absolute calculated and experimental values is within the limits of experimental uncertainties with total σ values of 5–6 %.

TABLE 1—*Ratios of 47 n/20 g to 640 n/94 g TRAMO calculated functionals for azimuthal intervals at ex-vessel cavity on midplane of Greifswald-1.*

Azimuth interval, deg	Neutron FR and DPA							Gamma FR and DPA			
	>3 MeV	>1 MeV	>0.5 MeV	>0.1 MeV	Therm.	Total	DPA	>3 MeV	>1 MeV	Total	DPA
0-1.5	1.01	1.05	1.03	1.01	0.91	1.02	1.02	1.02	1.03	1.02	1.02
1.5-4.5	1.11	1.02	1.02	1.00	0.93	1.00	1.00	1.00	1.00	0.98	1.01
4.5-7.5	1.00	1.01	1.02	0.99	0.92	0.99	0.99	1.00	0.99	1.03	1.05
7.5-10.5	1.03	1.00	1.01	0.98	0.91	0.98	0.98	1.02	0.98	1.04	1.02
10.5-13.5	1.00	0.99	1.00	0.98	0.89	1.00	0.98	0.97	1.01	1.03	1.03
13.5-16.5	0.95	0.99	1.00	0.96	0.91	0.99	0.96	0.98	0.99	1.03	1.03
16.5-19.5	0.93	0.99	1.02	0.99	0.92	1.00	0.98	0.96	0.99	1.02	1.03
19.5-22.5	0.90	1.00	1.01	1.00	0.90	1.00	0.98	1.03	1.01	1.02	1.05
22.5-25.5	0.84	0.97	0.98	0.98	0.86	1.00	0.96	1.01	0.99	1.00	1.05
25.5-28.5	0.86	0.96	1.01	0.97	0.89	0.99	0.96	0.98	1.00	1.04	1.05
28.5-31.5	0.87	0.96	1.00	0.96	0.85	0.98	0.95	0.96	0.98	1.03	1.04
31.5-34.5	0.95	0.97	0.96	0.96	0.86	0.99	0.96	0.99	0.98	1.00	1.01
34.5-37.5	1.06	0.99	1.00	0.97	0.86	0.99	0.98	0.93	0.95	1.00	1.02
37.5-40.5	0.95	0.98	0.99	0.97	0.88	0.99	0.96	0.94	0.94	1.00	1.02
40.5-43.5	1.02	1.00	1.02	0.99	0.88	1.00	0.99	0.97	0.96	0.99	1.03
43.5-46.5	0.98	1.01	1.01	0.97	0.90	0.99	0.98	0.96	0.97	1.02	1.05
46.5-49.5	1.01	0.95	0.99	0.97	0.88	0.99	0.96	1.02	0.99	1.03	1.02
49.5-52.5	1.02	1.01	1.00	0.97	0.89	0.99	0.98	0.98	0.99	1.03	0.98
52.5-55.5	0.88	0.97	0.99	0.97	0.85	0.99	0.96	0.99	0.99	1.03	1.03
55.5-58.5	0.90	1.00	1.00	0.98	0.90	0.99	0.97	0.97	0.99	1.01	1.01
58.5-60	0.99	1.01	0.99	0.98	0.82	0.99	0.97	0.90	0.91	0.97	1.04
Mean	**0.96**	**0.99**	**1.00**	**0.98**	**0.89**	**0.99**	**0.98**	**0.98**	**0.98**	**1.02**	**1.03**

TABLE 2—*Ratios of DORT to TRAMO (47 n/20 g) calculated functionals for azimuthal intervals at ex-vessel cavity on midplane of Greifswald-1.*

Azimuth interval, deg	Neutron FR and DPA							Gamma FR and DPA			
	>3	>1	>0.5	>0.1	Therm.	Total	DPA	>3	>1	Total	DPA
0-1.5	0.98	0.94	0.93	0.98	0.78	0.95	0.96	0.85	0.87	0.88	0.84
1.5-4.5	0.95	0.93	0.93	0.99	0.79	0.95	0.96	0.87	0.89	0.90	0.86
4.5-7.5	0.99	0.94	0.93	0.99	0.77	0.95	0.96	0.86	0.89	0.90	0.85
7.5-10.5	0.96	0.93	0.93	0.98	0.77	0.95	0.96	0.90	0.91	0.90	0.89
10.5-13.5	0.95	0.94	0.93	0.98	0.77	0.95	0.95	0.89	0.90	0.90	0.88
13.5-16.5	0.98	0.93	0.93	0.99	0.79	0.95	0.96	0.91	0.92	0.91	0.90
16.5-19.5	0.99	0.95	0.94	0.99	0.77	0.96	0.97	0.88	0.91	0.90	0.88
19.5-22.5	1.06	0.96	0.95	1.00	0.79	0.96	0.98	0.90	0.91	0.92	0.89
22.5-25.5	1.03	0.97	0.96	1.01	0.80	0.97	0.98	0.87	0.89	0.90	0.86
25.5-28.5	1.03	0.97	0.95	1.01	0.79	0.97	0.99	0.88	0.90	0.91	0.87
28.5-31.5	1.02	0.98	0.96	1.03	0.83	0.99	1.00	0.89	0.91	0.91	0.87
31.5-34.5	0.98	0.99	0.97	1.03	0.84	1.00	1.01	0.89	0.91	0.92	0.88
34.5-37.5	1.00	0.97	0.96	1.02	0.81	0.98	0.99	0.90	0.91	0.91	0.89
37.5-40.5	1.03	0.97	0.95	1.00	0.80	0.97	0.99	0.91	0.93	0.92	0.90
40.5-43.5	1.01	0.95	0.94	1.00	0.80	0.96	0.97	0.90	0.92	0.91	0.90
43.5-46.5	0.96	0.93	0.92	0.98	0.78	0.95	0.95	0.91	0.91	0.91	0.90
46.5-49.5	0.93	0.93	0.91	0.97	0.79	0.94	0.94	0.91	0.91	0.91	0.89
49.5-52.5	0.94	0.92	0.91	0.97	0.78	0.94	0.94	0.88	0.90	0.90	0.87
52.5-55.5	0.98	0.94	0.92	0.98	0.79	0.95	0.95	0.88	0.90	0.89	0.87
55.5-58.5	0.97	0.91	0.91	0.97	0.78	0.94	0.94	0.88	0.89	0.89	0.87
58.5-60	0.97	0.93	0.92	0.98	0.80	0.94	0.95	0.89	0.90	0.90	0.88
Mean	**0.99**	**0.95**	**0.94**	**0.99**	**0.79**	**0.96**	**0.97**	**0.89**	**0.90**	**0.90**	**0.88**
Mean (DORT no upscat.)	**0.99**	**0.95**	**0.93**	**0.99**	**0.29**	**0.93**	**0.97**	**0.51**	**0.50**	**0.53**	**0.43**

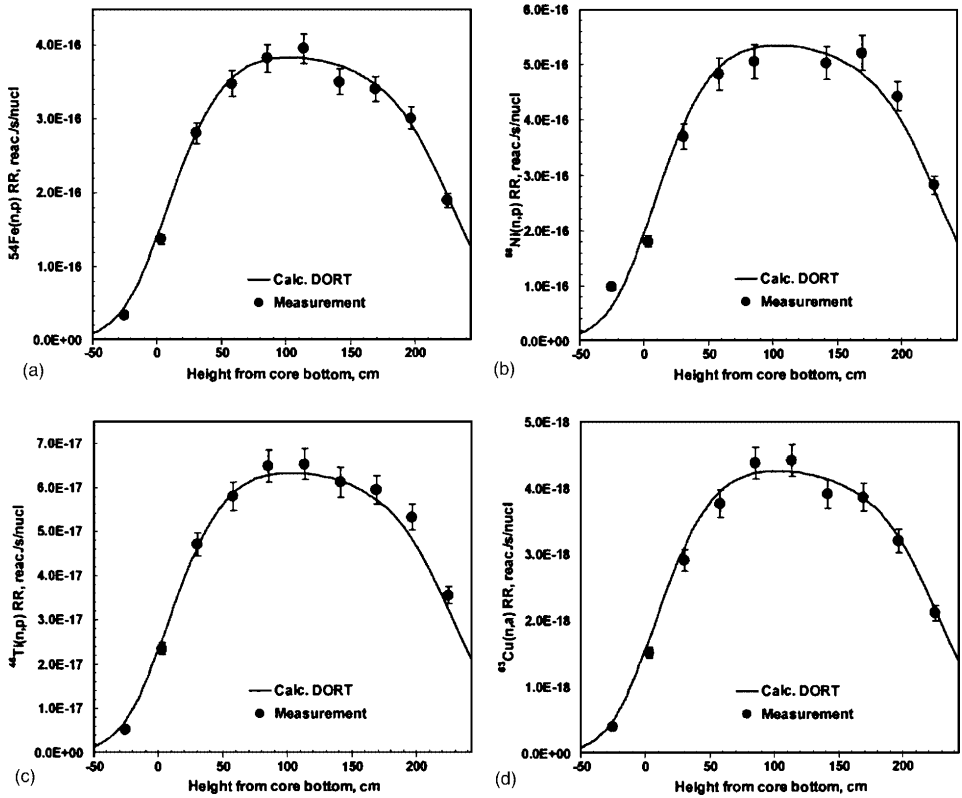

FIG. 2—*Comparison of calculated and measured* $^{54}Fe(n,p)$ *(a),* $^{58}Ni(n,p)$ *(b),* $^{46}Ti(n,p)$ *(c), and* $^{63}Cu(n,\alpha)$ *(d) reaction rates along the axial direction at 54.3 azimuth degrees in ex-vessel cavity of Greifswald-1.*

Comparisons of azimuthal distributions of reaction rates on the midplane level (124 cm from core bottom) in absolute units for two types of calculations are shown in Fig 3. The experimental data measured at the height nearest to the midplane (114 cm) were also presented in this diagram. It is possible to compare the measured results with results calculated at the midplane because the axial variation of the RR in this interval (from 124 to 114 cm) is less than 1 %.

It can be noted that maximum TRAMO calculated values in azimuth distributions are higher than the DORT ones. Nevertheless, agreement of calculated distributions with each other and with measured distributions is within reasonable limits for all analyzed reactions.

In Table 3 summarized results of the analysis of data calculated by DORT and of experimental data obtained in the ex-vessel cavity of Greifswald-1 are presented. The table displays C/M ratios averaged over five azimuthal points and their standard deviations (SD) for every axial experimental position and every detector.

Excepting the position below core bottom (−25 cm level), averaged C/M data are near unity with a scatter of ±11 %. It may be seen that C/M value increases near and below core bottom. Possible reasons are inaccuracy of the synthesis method used in DORT ($R\Theta$ model was created for reactor core midplane geometry and neutron source), or possible inaccuracy of axial positions of detectors. The C/M value averaged over all detector positions and detectors within the core height is 1.00±0.04, which indicates good agreement of measured and calculated data.

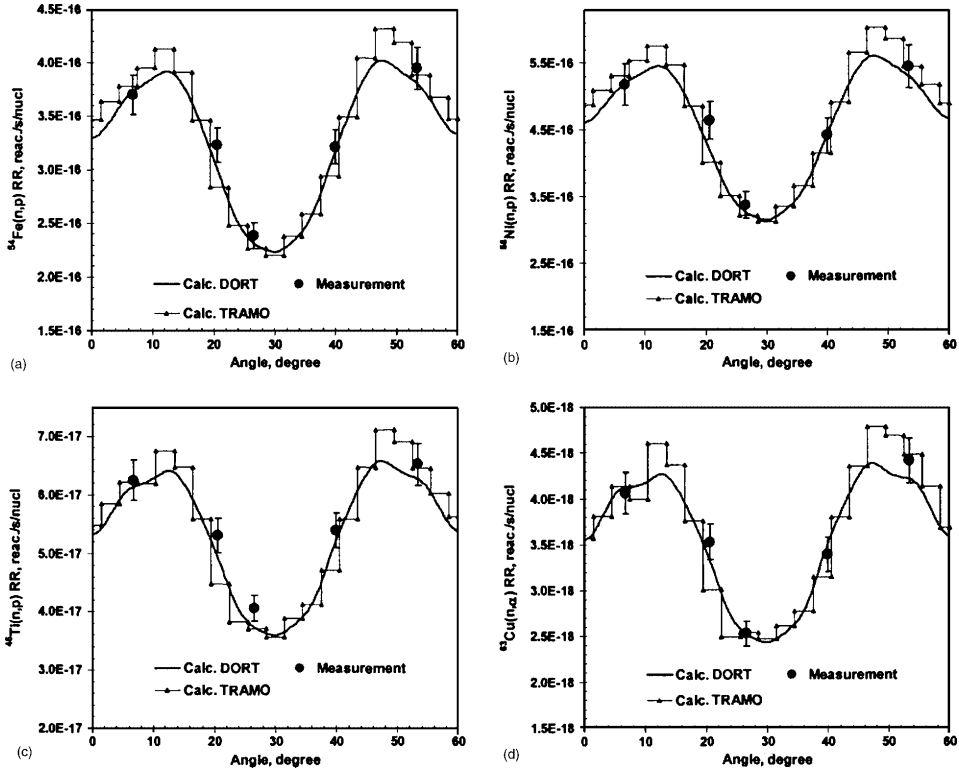

FIG. 3—*Comparison of calculated and measured $^{54}Fe(n,p)$ (a), $^{58}Ni(n,p)$ (b), $^{46}Ti(n,p)$ (c) and $^{63}Cu(n,\alpha)$ (d) reaction rates along ex-vessel azimuthal direction on midplane of Greifswald-1.*

Conclusions and Recommendations

Deterministic calculations by DORT, and Monte Carlo calculations by TRAMO were analyzed and compared with each other and with measured data for midplane ex-vessel positions at the Greifswald-1 reactor. On average, DORT results for fast neutrons including DPA evaluations are less than TRAMO ones by 1–6 %.

TABLE 3—*Azimuthally averaged C/M values (DORT calculated only) and their SD for ex-vessel cavity height positions of Greifswald-1.*

Height from core bottom, cm	Reactions								Mean over all reactions	
	^{54}Fe(n,p)		^{58}Ni(n,p)		^{46}Ti(n,p)		^{63}Cu(n,α)			
	C/M	SD	C/M	SD	C/M	SD	C/M	SD	C/M	SD
225.2	1.01	±0.05	0.89	±0.10	0.95	±0.10	1.00	±0.04	**0.96**	**±0.06**
197.4	0.98	±0.02	0.93	±0.02	0.91	±0.03	1.02	±0.03	**0.96**	**±0.05**
169.6	1.00	±0.07	0.95	±0.05	0.92	±0.07	1.00	±0.06	**0.97**	**±0.04**
141.8	1.02	±0.05	1.01	±0.05	0.98	±0.04	1.01	±0.05	**1.01**	**±0.02**
114	0.98	±0.02	0.98	±0.03	0.96	±0.02	1.00	±0.04	**0.98**	**±0.02**
86.2	1.01	±0.04	1.02	±0.06	0.98	±0.04	0.99	±0.04	**1.00**	**±0.02**
58.4	1.03	±0.05	1.03	±0.08	1.01	±0.06	1.01	±0.05	**1.02**	**±0.01**
30.6	1.00	±0.04	1.00	±0.11	1.00	±0.03	1.03	±0.07	**1.01**	**±0.02**
2.8	1.11	±0.07	1.08	±0.12	1.08	±0.04	1.08	±0.07	**1.09**	**±0.01**
−25	1.28	±0.19	1.02	±0.32	1.31	±0.24	1.19	±0.22	**1.20**	**±0.13**
Mean over all heights (without −25 cm)									**1.00**	**±0.04**

Thermal neutron and gamma fluences are systematically underestimated by DORT calculations by about 20 and 10 %, respectively.

The analysis of the influence of different cross-sectional group structures (640 n/94 g versus 47 n/20 g) shows unsystematic scatter for neutron and gamma fluence and DPA rates of about 2 % with exception of thermal neutron data for which the 640 neutron group calculation gives on average 11 % higher results.

The comparison of ex-vessel measurements of axial distributions of different threshold reaction rates with DORT calculations resulted in good coincidence of distribution shapes. Absolute values agreed within ±11 % over the core height. The C/M value averaged over measurement positions and detectors in the core height region equals 1.00 ± 0.04 in case of DORT calculations.

The TRAMO calculations performed for the reactor midplane agree reasonably with DORT results and measurements.

On the whole, the agreement of results of the neutron and gamma dosimetry research performed at the Greifswald-1 confirms the reliability of calculation methods used in this work for analysis and prediction of properties of reactor material under irradiation during reactor operation.

Acknowledgments

This study was performed as a result of Russian-German scientific-technical cooperation with the support of the German Federal Ministry of Economy and Labor. The authors also wish to express their gratitude to the leaders of the Institute of Safety Research of the FZR, Professor F.-P. Weiss and Professor U. Rindelhardt, and to the Director of the SEC NRS Professor B. Gordon for their support of this work.

References

[1] Rindelhardt, U., Böhmer, B., and Böhmert, J., "*RPV Integrity Assessment by Operational Feedback: Post Service Investigations of VVER-type NPPs*." *Transactions of ANS*, 88 (2003). p. 547.

[2] Rhoades, W. and Childs, R., *TORT/DORT: Two-and Three Dimensional Discrete Ordinates Transport* (CCC-543, RSIC, ORNL, TN, 1991).

[3] Ingersoll, D. T., et al., *Production and Testing of the VITAMIN-B6 Fine-Group and the BUGLE-93 Broad-Group Neutron/Photon Cross Section Libraries Derived from ENDF/B-VI Nuclear Data*, (ORNL-6795, NUREG/CR-6214, January 1995).

[4] Barz, H.-U. and Konheiser, J., FZR-245, *Forschungszentrum Rossendorf A*, 1998.

[5] Mehner, H.-C., Böhmer, B., and Stephan, I., Neutronendosimetrie an der Druckgefäßauβenwand des Blocks 1 im KKW Greifswald bei Einsatz von Abschirmkassetten, Arbeitsbericht ZfK - RPM 6/88, Zentralinstitut für Kernforschung Rossendorf (December 1988).

[6] Borodkin, G. and Boehmer, B., *Validation of 3D Synthesis RPV Neutron Fluence Calculations using VVER-1000 Ex-Vessel Reference Dosimetry Results*, 2000 ANS Annual Meeting, June 4-8, 2000, San Diego California, *Transactions of the ANS*, Vol. 82, 2000, pp. 223-225.

[7] MacFarlane, R. E. and Muir, D. W., *The NJOY Nuclear Data Processing System (Version 91)*, Los Alamos, LA-12740-M (1994).

[8] Kocherov, N. P. and McLaughlin, P. K., The International Reactor Dosimetry File (IRDF-90) (Report IAEA-NDS-141, Rev.2, IAEA, Vienna, October 1993).

[9] Kwon, J. and Motta, A. T., *Ann. Nucl. Energy* 27 (2000) 1627.

Journal of ASTM International, Vol. 3, No. 7
Paper ID JAI13488
Available online at www.astm.org

R. E. Pevey,[1] *L. F. Miller,*[1] *W. J. Marshall,*[1] *L. W. Townsend,*[1] *and B. Alvord*[2]

Coarse-Mesh Adjoint Biasing of a Monte Carlo Dose Calculation

ABSTRACT: Deep penetration radiation transport calculations have been performed to determine the dose rates at a positron emission tomography (PET) facility in China. The radiation source is a cyclotron that is used for the production of the PET isotopes, with a labyrinthine concrete wall arrangement to minimize dose to operation personnel. Since directionally biased Monte Carlo calculations did not reach an acceptably low standard error after a week of CPU time, approximate adjoint fluxes were calculated for each of four detector locations using coarse-mesh adjoint discrete ordinates calculations and were used to bias the Monte Carlo calculations. This biasing resulted in improved computational efficiency of a factor of one to three orders of magnitude. This result shows the value of even approximate adjoint flux biasing to speed up Monte Carlo calculations.

KEYWORDS: isotope production, Monte Carlo, discrete ordinates, adjoint biasing

Introduction

Deep penetration Monte Carlo calculations have been performed to determine the operation personnel dose rates at a positron emission tomography (PET) facility in China. The radiation source is a cyclotron built by CTI, Inc. that is used for the production of isotopes necessary for PET scans. For the protection of operation personnel, the room containing the cyclotron is separated from the control area by a labyrinthine arrangement of corridors. Plan and elevation views of the building are shown in Figs. 1 and 2.

The radiation source is the cyclotron target (located on the outer rim of the cyclotron midplane), in which positron-emitting fluorine-18 is produced by the irradiation of oxygen-18 with 11 MeV protons

$$^{18}_{8}\mathrm{O} + ^{1}_{1}\mathrm{H} \rightarrow ^{18}_{9}\mathrm{F} + ^{1}_{0}n$$

$$^{18}_{9}\mathrm{F} \rightarrow ^{18}_{8}\mathrm{O} + ^{0}_{+1}\beta$$

The reaction yields approximately 10^{10} neutrons/second/(microamp of proton beam current). Predicted dose rates were needed for four locations in the building at which personnel might be located. Because of the importance of the geometrical arrangement of the cyclotron itself, it was decided to utilize a three-dimensional Monte Carlo calculation of the radiation transport.

Modeling of the Facility

Development of Neutron Source Terms

Energy dependent neutron source spectra were obtained by calculations with the ALICE91 code [1] and are shown in Fig. 3. For comparison purposes, the figure shows spectra for various initial proton energies, although the calculations for this paper used only the 11 MeV proton beam values, corresponding to the actual cyclotron installed in the facility. This source spectrum was used directly in the Monte Carlo calculations and was integrated into the 28n-18g SCALE [2] energy group structure for the discrete ordinates calculations. (Although the cyclotron source emits both neutrons and photons, previous cyclotron

Manuscript received June 20, 2005; accepted for publication April 19, 2006; published online May 2006. Presented at ASTM Symposium on Reactor Dosimetry, 12th International Symposium on 8–13 May 2005 in Gatlinburg, TN; D. W. Vehar, D. M. Gilliam, and J. M. Adams, Guest Editors.

[1] The University of Tennessee, Pasqua Engineering Bldg., Knoxville, TN 37996
[2] CTI, Inc., 810 Innovation Dr., Knoxville, TN 37932

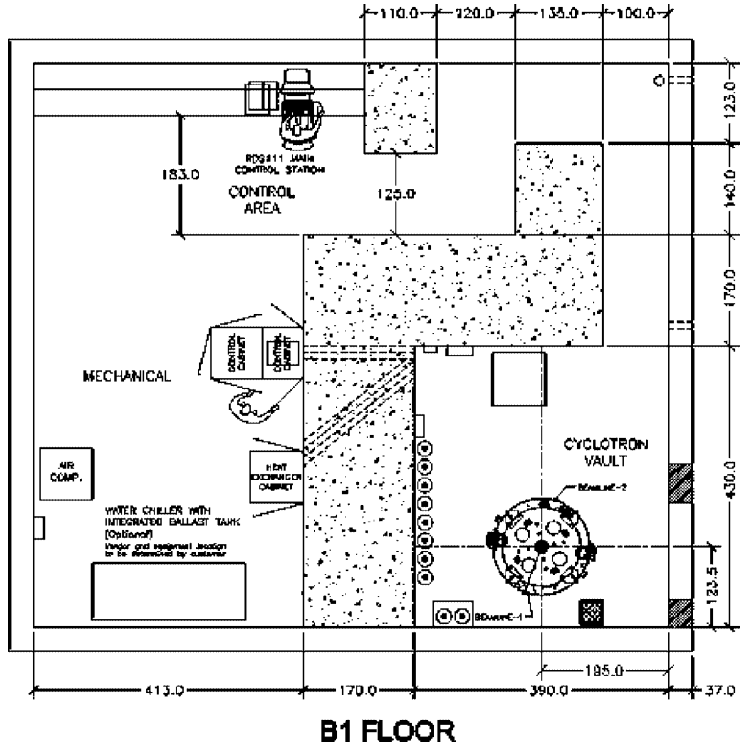

FIG. 1—*Plan view of the PET facility B1 floor.*

design calculations indicate that a negligible number of original photons contribute to the external dose, so the photon source was ignored in this study.)

Development of the Three-Dimensional Monte Carlo Model

The three-dimensional (3D) Monte Carlo computer code used in this analysis was MCNP [3], developed at the Los Alamos National Laboratory. The geometrical modeling capabilities of the code allow for very complicated three-dimensional material arrangements. Figures 4 and 5 show two slices (*x*-*y* and *y*-*z*) of the resulting MCNP model through the source point at the edge of the cyclotron.

The cyclotron is modeled as concentric cylinders of air, copper, and iron. The central air-filled cylinder has a radius of 45.7 cm and a height of 41.14 cm. This is surrounded by an annulus of copper of the same height and a thickness of 11 cm. The outer wall of the cyclotron is an iron annulus 16.2 cm thick. The top and bottom of the cyclotron are iron disks with a radius of 72.9 cm and a thickness of 24.39 cm.

The outer walls, floors, and ceilings of the two facility floors (which we will refer to as the B1 floor and first floor) were modeled as shown in Figs. 4 and 5. (Note that the outer walls are not shown in Fig. 1, but were included in the model.) On the B1 floor, the shielding walls and the walls of the serpentine access hall are the only internal walls modeled. On the first floor, the walls of the radiochemistry lab and the wall between the upper control and scanner rooms are modeled. All other internal walls and fixtures are ignored.

To determine the dose at representative locations where personnel might be located, phantoms were placed at the four locations denoted by the letters A through D on Figs. 4 and 5. Detectors A and B are located on the B1 floor level at positions corresponding to operations personnel workstations; Detector D was also placed on the B1 level, at the closest potentially accessible location to the cyclotron. Detector C was located at the closest accessible location on the first floor, directly above the cyclotron.

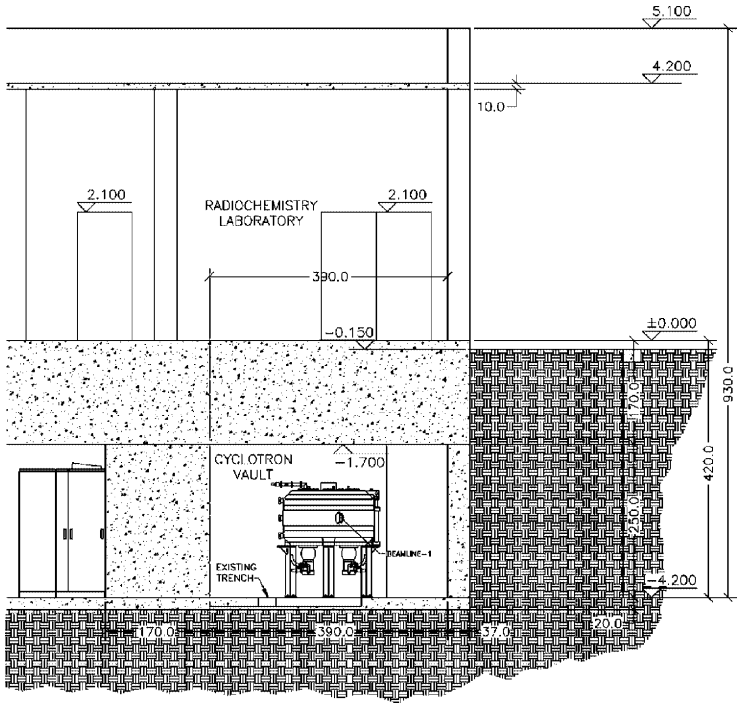

FIG. 2—*Elevation view of the PET facility showing both B1 and first floor.*

Each dose rate calculation was performed using the average flux inside a cylindrical phantom (23 cm in radius and 0.9 m tall) composed of standard International Commission on Radiation Units and Measurements (ICRU) tissue. The flux-to-dose conversion factors were the ANSI/ANS-6.1.1-1977 values obtained from Appendix H of the MCNP manual [3,4]; for the discrete ordinates calculations, these were integrated over the SCALE 27n-18g group structure.. The phantoms were placed vertically (as if in a chair) for detectors A, B, and D, with the phantom for Detector C positioned horizontally (as if lying on the floor).

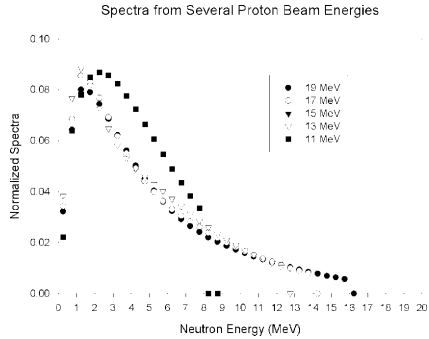

FIG. 3—*Normalized neutron spectra for several proton beam energies.*

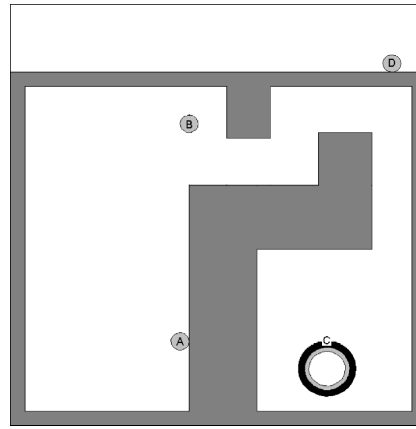

FIG. 4—*X-Y view of the MCNP model (through midplane of cyclotron).*

Results of Original Direction-Biased Monte Carlo Calculation

The original MCNP calculations (utilizing the MCNP4B version of the code [3]) were performed with only a simple directional biasing of the neutron source, with a preferred direction toward the upper right in Fig. 4 (toward the entrance to the serpentine corridor), which was believed to be the path of highest contribution.

The dose rate values obtained for the four detectors (after almost seven days of computation) are shown in the rightmost column of Table 1. The resulting dose rates range from a high of 19.4 mrem/h at the exposed Detector D location to a low of 0.0143 mrem/h for the first floor location of Detector C. The results indicate that personnel should not be allowed at the location of Detector D, but that the other three locations represent acceptable dose rates for work locations (with acceptability set at 1 mrem/h since the cyclotron will not be operated continuously).

The only problem with the results is the unacceptably high uncertainty on the dose rates for two of the four detectors. According to the MCNP manual [3,4], Monte Carlo results should not be considered reliable if the fractional standard deviation is greater than 10 %, with a value of 5 % or lower preferred. Both Detectors A and C fail this test, with fractional standard deviations of almost 20 % and 40 %, respectively, for their total dose rates (neutron plus gamma ray).

In practice, since the high standard deviations correspond to dose rates that are well below the 1 mrem/h limit, it would be our normal practice to accept the low dose rate/high uncertainty results as indicating that the actual dose rates will be acceptably low even though the formal statistical test is not met.

Because of the long computation time required to solve for these dose rates, it was decided to continue

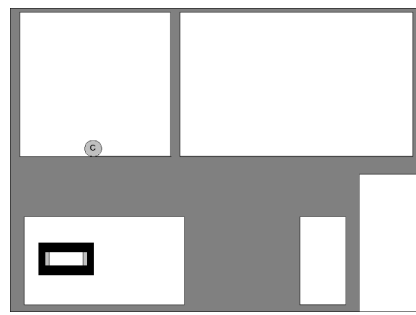

FIG. 5—*Y-Z view of MCNP model (through centerline of cyclotron).*

TABLE 1—*Comparison of adjoint-biased MCNP results with original MCNP results.*

Case		Dose rates (mrem/h) [% standard deviation] Detector A Adjoint biasing	Detector B Adjoint biasing	Detector C Adjoint biasing	Detector D Adjoint biasing	Original (direction biasing)
Detector A	*n*	0.0412	0.0342	0	0	0.0516
		[6.13]	[15.84]	[0]	[0]	[20.5]
	γ	0.00183	0.000215	0	0	0.00151
		[10.75]	[67.41]	[0]	[0]	[36.6]
	Total	**0.043**	0.034	0	0	**0.053**
		[5.34]	[15.7]	[0]	[0]	**[19.9]**
Detector B	*n*	0.664	0.680	0	0.476	0.676
		[7.85]	[1.98]	[0]	[70.41]	[4.9]
	γ	0.00352	0.00976	0	0	0.01004
		[66.47]	[6.23]	[0]	[0]	[23.4]
	Total	0.668	**0.690**	0	0.476	**0.686**
		[7.82]	**[1.95]**	[0]	[70.4]	**[4.84]**
Detector C	*n*	0	0	0.0201	0	0.01235
		[0]	[0]	[1.82]	[0]	[41.53]
	γ	0	0	0.00167	0	0.001948
		[0]	[0]	[8.89]	[0]	[57.50]
	Total	0	0	**0.0218**	0	**0.0143**
		[0]	[0]	**[1.81]**	[0]	**[36.7]**
Detector D	*n*	19.60	18.64	15.28	19.4	19.04
		[20.21]	[5.32]	[57.82]	[3.62]	[1.7]
	γ	0	0.2296	0	0.2692	0.3176
		[0]	[34.18]	[0]	[6.40]	[3.2]
	Total	19.6	18.87	15.28	**19.67**	**19.36**
		[20.21]	[5.27]	[57.8]	**[3.57]**	**[1.67]**
Number of histories		6.13 million	0.97 million	5.18 million	1.39 million	428 million
CPU time (min)		120	120	120	120	9950
Relative figure of merit		1450	503	17363	17	1

to adapt the MCNP model to increase the efficiency of the calculation. There were two reasons for this. The first reason is that CTI has multiple cyclotron placements each year, each of which are unique and some of which will require calculational confirmation of dose rates; therefore, any efficiency gains will pay off in future analyses. The second reason is that a new version of MCNP was released which included a new feature of cell importance biasing that we thought might be effectively used in this type of problem.

Development and Results of 3D Discrete Ordinates Calculations of the System

It has long been recognized that accurate adjoint fluxes (i.e., solutions to the adjoint form of the radiation transport equation) can be effectively used by Monte Carlo calculations as importance profiles to bias radiation transport random walks. Unfortunately, in MCNP versions to date the importance profile has had to be specified cell-by-cell for each of the many uniquely shaped 3D spatial elements that make up the model. These adjoint fluxes were extremely difficult to obtain and translate into the data format needed by the code (which the MCNP manual refers to as the WWINP format).

Beginning with version 5.0 of the code [4], it is now possible to specify the importance profiles on a regular Cartesian grid that is unrelated to the actual geometric layout of the 3D cells in the model. This capability has opened up the potential of using the results of a simplified 3D Cartesian discrete ordinates calculation to bias the more accurate Monte Carlo model calculation. What is not so clear is how accurate the discrete ordinates model has to be to speed up the Monte Carlo calculation.

To test this capability, it was decided to utilize a very crude three-dimensional Cartesian code (referred to as CARTER [5]) that is used for instructional purposes in graduate level radiation transport and reactor theory classes at the University of Tennessee. Although the code is undocumented, unvalidated, and typically used only for methods demonstration purposes, it has the extreme advantages of being very simple and completely under the control of the first author. A new version of the code was written with the following features:

1. Geometric input read from the MCNP input file;
2. Cross sections read from SCALE multigroup working libraries;
3. Adjoint or forward calculation performed;
4. Isotropic (P_0) scattering assumed;
5. Step spatial differencing used to guarantee non-negative fluxes; and
6. Resulting fluxes stored in the WWINP format required by the MCNP5 code.

Although for normal discrete ordinates runs, this meshing of space, direction, and energy would be ridiculously coarse, we were interested in seeing if even this coarse tool could increase the MCNP efficiency.

Forward and Adjoint Calculations

The MCNP model described above was reduced to a 3D Cartesian model by constructing a uniform mesh cell grid and assigning the material for each mesh cell based on the material at the cell midpoint in the original MCNP model. In addition to a forward calculation using a 27-group approximation to the source spectrum, four separate adjoint calculations were performed—one for each detector, with the flux-to-dose conversion factor serving as the adjoint source. For each of the values, the CARTER code used an S_4 quadrature, a (13 cm) × (13 cm) × (13 cm) calculational mesh, the SCALE 27n-18g group working library [2], and a convergence criterion of only 10 %. Both forward and adjoint calculations were run on this coarse mesh and each of the calculations took about 20 min of CPU time (without any acceleration of the iterations).

Development of Spatial Channel Plots

From the resulting scalar fluxes from the CARTER runs, a (forward scalar flux)*(adjoint scalar flux) data file was created and used to produce two-dimensional "spatial channel theory" [6] plots. Spatial channel theory uses the product of the forward angular flux (representing where particles actually exist) and the adjoint angular flux (representing the future expected contribution of particles as a function of space, energy, and direction) to approximate the density of ***contributing*** particles as they travel from the source to the detector.

The resulting data approximates the energy and spatial "paths" of particles that actually reach to the detector (while ignoring those that do not). For design purposes, this information can be used to locate places in the geometry where more or less shielding should be placed. For Monte Carlo analysis, these plots can also be used to identify areas of the problem geometry and spectrum where sampling effort should be concentrated.

For our purposes, the energy dependence and z axis dependence were integrated out to produce one number for each (x,y) cell location ij using

$$\text{Value}_{ij} = \sum_k \sum_{g=1}^{45} \phi_g^*(x_i, y_j \,.\, z_k)\phi_g(x_i, y_j \,.\, z_k)$$

(Note that using the scalar fluxes instead of angular fluxes probably reduces the accuracy of the results.)

Figures 6–9 show the resulting (so-called) "contributon" fluxes for each of the four detectors. For these plots all (x,y) mesh points were darkened in proportion to the logarithm of the cell contributon density, with values ignored if less than one millionth of the maximum cell (which in this problem will always be the source cell). Outlines of the walls, cyclotron, and detectors are included in the plots for orientation purposes.

Several notable features of these plots are as follows:

1. Figure 6 shows that the predominant paths for particles reaching Detector A are those straight through the wall that separates the source and the detector. It is also true that particles can successfully reach the detector even if they start in the wrong direction, probably by bouncing off the cyclotron room walls. (Note that the "shadow" of contributons behind the detector is most likely an unphysical artifact of using scalar fluxes instead of angular fluxes in computing the contributon fluxes. That is, the forward fluxes are most likely higher in directions away from the detector and the adjoint fluxes have important flux directions toward the detector; therefore, an

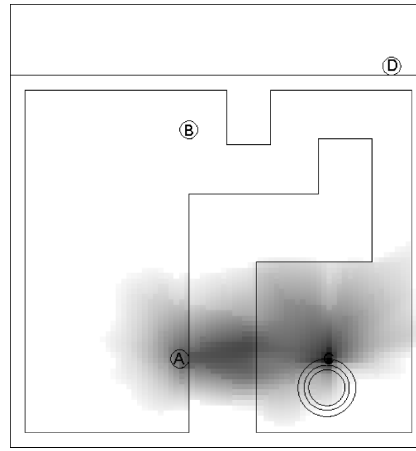

FIG. 6—*Relative contributon density for Detector A (plan view, z averaged).*

integration over direction would most likely be much smaller than the product of scalar fluxes used here.)

2. Figure 7 shows that the predominant paths for particles reaching Detector B include both paths through the walls (in a straight line from source to detector) and paths through the corridor. Of the two, the corridor paths seem to be a little more prominent. Therefore, the most effective dose reduction design change would probably be the addition of vault doors in the corridor or redesign of the corridor layout.
3. Figure 8 shows that the predominant paths for particles reaching Detector C are those that (as would be expected) go straight up through the ceiling. Few particles exiting the cyclotron room subsequently reach this detector.
4. Figure 9 shows that the predominant paths for particles reaching Detector D go down the corridor that provides an almost straight path from source to detector. Again, the "shadow" behind the detector is most likely an unphysical calculational artifact (as described in feature (1) above.)

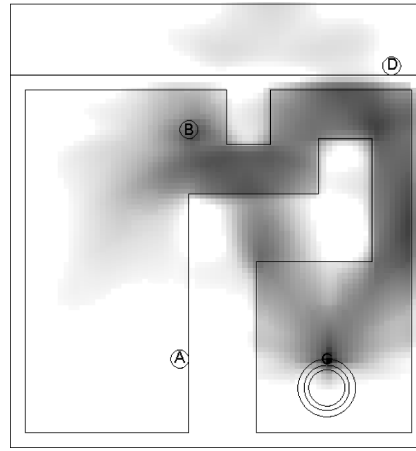

FIG. 7—*Relative contributon density for Detector B (plan view, z averaged).*

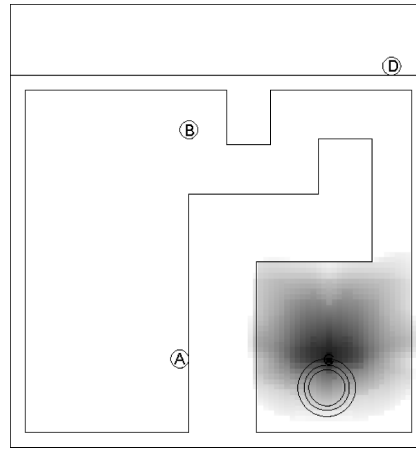

FIG. 8—*Relative contributon density for Detector C (plan view, z averaged).*

Biased 3D Monte Carlo Calculations of the System

The fluxes from the four CARTER adjoint runs were converted into WWINP files of three-dimensional mesh-wise, energy-group-dependent importance values. The original (forward) MCNP input deck was then rerun four times for two hours each, using the four CARTER-produced WWINP files for the space- and energy-dependent importance profile. The effect of using an importance file in this way is that the Monte Carlo random walks are "steered" toward the particular detector that the adjoint was calculated from, maybe at the expense of paths that lead in other directions. The net result of this (if all goes well) is that the particular detector should be more efficiently calculated, but perhaps at the expense of the other detectors.

The results, compared to the original results from the CTI study, are also shown in Table 1. Each of the first four columns of results corresponds to the detector readings for a particular detector-based adjoint. For convenience in reading the table, the total dose (and % standard deviation) for the detector for which the adjoint was made is listed in **BOLD** for easy comparison to the original results. Some notable features of the table are as follows:

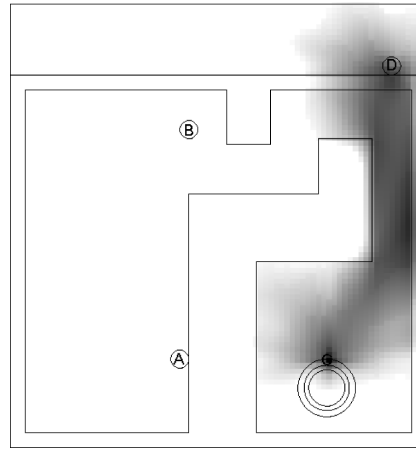

FIG. 9—*Relative contributon density for Detector D (plan view, z averaged).*

1. For all four detectors, the use of the adjoint for the particular detector improves the efficiency of the calculation. For each of them, two hour runs give acceptable results (i.e., less than 10 % standard deviation). Also, the adjoint biasing results seem to statistically agree with the original run's results (based on overlap of their +/−1 sigma ranges), except for Detector C where the original run's standard error was 36.7 %, which is too high to be reliable.
2. The figures of merit (i.e., the inverse relative computer time required for a given fractional standard deviation) versus the original calculation are given for the four detectors in the last row of the table. Even the easiest calculation (Detector D) showed a factor of 17 improvement in efficiency. The other improvements were even larger.
3. As expected, for the cases with adjoint importance functions steering particles toward a particular detector, the other detectors were not as efficiently calculated. For the case of the Detector C importance function, for example, the other detectors hardly received any contribution at all. It is interesting to note, though, that use of the Detector A adjoint resulted in acceptable results for Detector B as well (although the reverse was not as effective). Also, using the Detector B adjoint resulted in acceptable results for Detector D, but, again, not the reverse.
4. For each detector adjoint, the results for both the neutron and gamma dose rates were less than 10 % (except for Detector A's gamma ray value slightly above it at 10.75 %). This ability to estimate the gamma dose rate was much improved over the original case, for which only one gamma ray dose rate calculation (i.e., for Detector D) was less than 10 %.

Conclusions

It is apparent that computational efficiencies can be improved by one to three orders of magnitude through the use of adjoint biasing techniques, with the greater gains coming from the deeper penetration detector positions. Although this benefit would most likely be dependent on the particle transport characteristics and geometry for particular problems, this approach is shown to be of significant value for Monte Carlo shielding calculations, even with approximate adjoint flux calculations.

In addition, the spatial channel theory plots of contributon density are also shown to be an effective graphical tool for visualizing the important particle paths, which should prove useful for shielding design projects.

For future analyses similar to the present one, we plan to automate the steps that link the MCNP and CARTER codes to more readily take advantage of this analysis strategy.

References

[1] *ALICE91: Particle Spectra from Compound Nucleus Decay*, RSICC package PSR-0146 (1996).
[2] *SCALE: A Modular Code System for Performing Standardized Computer Analyses for Licensing Evaluation*, NUREG/CR 0200, Rev. 7 (ORNL/NUREG/CSD 2/R7), Vols. I, II, and III (2004).
[3] J. F. Briesmeister, ed., *MCNP—A General Monte Carlo N-Particle Transport Code—Version 4C*, Los Alamos National Laboratory Report No. LA-13709-M (2000).
[4] X 5 Monte Carlo Team, *MCNPA General Monte Carlo N Particle Transport Code, Version 5, Volume II: Users Guide*, LA CP 03 0245 (2003, revised 2004).
[5] Pevey, R. E., "Class notes for NE571: Graduate Reactor Theory," http://web.utk.edu/~rpevey/NE571/SCALE7.htm (2004).
[6] Williams, M. L. and Engle, W. W. Jr., *The Concept of Spatial Channel Theory Applied to Reactor Shielding Analysis*, ORNL/TM-5467, (1976).

Journal of ASTM International, Vol. 3, No. 10
Paper ID JAI100338
Available online at www.astm.org

Y. K. Lee[1]

Analysis of the VENUS-3 PWR Pressure Vessel Surveillance Benchmark Using TRIPOLI-4.3 Monte Carlo Code

ABSTRACT: This paper presents the analysis of the VENUS-3 PWR Pressure Vessel Surveillance Dosimetry Benchmark using the three-dimensional (3D) continuous-energy Monte Carlo code TRIPOLI-4.3. VENUS-3 benchmark specifications are taken from the 2004 release of the International Database for Integral Shielding Experiments (SINBAD) of OECD/NEA. Pointwise nuclear data library for TRIPOLI-4.3 transport calculations were prepared from ENDF/B-VI.4. Detector cross sections for $^{27}Al(n,\alpha)$, $^{58}Ni(n,p)$, and $^{115}In(n,n')$ from IRDF-2002, IRDF-90.v2, and ENDF/B-VI.4 have been investigated. Two ^{235}U fission spectra, continuous Watt spectrum and 581 group ENDF/B-VI.4 spectrum have been compared. To speed up the simulation and to predict the axial (50-cm) and azimuthal (0°–90°) variation of the reaction rates for core barrel measurement points, variance reduction techniques using cylindrical surface detector and cylindrical biasing meshes have been applied and demonstrated. C/E values at 160 different locations have been evaluated. Without taking into account the uncertainty of the nuclear data in transport calculation and the uncertainty of the 3D neutron source distribution, a 10 % C/E tolerance margin should be accepted.

KEYWORDS: VENUS-3, PWR, reactor dosimetry, benchmark, TRIPOLI-4, Monte Carlo code, variance reduction

Introduction

High-energy neutron bombardment causes hardening, embrittlement, and dimensional instability of the reactor component steels and degrades the structure integrity of reactor pressure vessel (RPV). Improving the calculation methodology and reducing the uncertainty in RPV fast neutron fluence estimation have a direct impact on design pressure water reactor (PWR) lifetime, operation safety margins and potential plant lifetime extension [1].

PWR pressure vessel dosimetry calculations at CEA/Saclay were analyzed using three-dimensional (3D) TRIPOLI-3 Monte Carlo code with multigroup ENDF/B-VI library and International Reactor Dosimetry File IRDF-85 [2]. Recently, the continuous-energy TRIPOLI-4 code has been introduced for reactor dosimetry applications. The pointwise ENDF/B-VI.4 library has been used for transport calculations and the IRDF-90.v2 file for reaction rates and iron damage evaluations [3,4]. Lattices geometry, automatic variance reduction, and parallel computing in TRIPOLI-4 make the detail core modeling and the RPV dosimetry calculations to be more accurate and practical.

RPV dosimetry benchmarks, ASPIS (1-m-thick iron), PCA-REPLICA (water/iron, 12/13 cm), NESDIP-3 (water/iron, 18/20 cm), Winfrith water (50-cm-thick water) [5,6], and Saint-Laurent B1 PWR RPV surveillance results, were calculated before each release of TRIPOLI-4 code. These benchmarks validate not only the nuclear data but also the transport calculations and the variance reduction schemes. To develop the database of benchmarks for TRIPOLI-4 code, more international certificated RPV dosimetry benchmarks and CEA internal PV-CT50 steel dosimetry measurements are currently investigated [7].

VENUS RPV dosimetry benchmarks were organized by OECD/NEA Nuclear Science Committee based on VENUS PWR mock-ups. The purpose was to apply 3D Monte Carlo and Sn codes on the analysis of the exposure of reactor structure components to neutron fluence [8]. The VENUS-3 benchmark has been reformulated in the 2004 released SINBAD database and the measured reaction rates of Al, Ni, In detectors are now available [9].

Compared with PCA and NESDIP benchmarks, the VENUS-3 experiment presents four interesting

Manuscript received June 20, 2006; accepted for publication July 27, 2006; published online October 2006. Presented at ASTM Symposium on Reactor Dosimetry, 12th International Symposium on 8-13 May 2005 in Gatlinburg, TN; D. W. Vehar, D. M. Gilliam, and J. M. Adams, Guest Editors.
[1] Commissariat à l'Energie Atomique, CEA/Saclay, DEN/DM2S/SERMA, 91191 Gif sur Yvette, France.

aspects: (1) core, baffle, and core barrel mock-ups are closer to a real PWR, (2) 3D power map is prepared in detail, (3) many axial and azimuthal measurements are available on core barrel, and (4) a partial length shielded assembly (PLSA) is designed at the core periphery.

This paper reports on calculations made on VENUS-3 benchmark using TRIPOLI-4.3 code. Detector cross sections for $^{27}Al(n,\alpha)$, $^{58}Ni(n,p)$, and $^{115}In(n,n')$ reactions from IRDF-2002, IRDF-90.v2 [10], and ENDF/B-VI.4 have been tested. ^{235}U Watt fission spectrum and the 581 group ENDF/B-VI.4 spectrum have been applied separately. To speed up the simulation and to predict 160 axial and azimuthal (from 0.7° to 89.3°) variations of results in a single run, new variance reduction techniques using cylindrical surface detector and cylindrical biasing meshes have been applied. C/E values at different locations presented in trend curves are useful to validate the simulations and to appreciate detector cross sections and ^{235}U fission spectra.

VENUS-3 Pressure Vessel Benchmark

VENUS PWR Mock-ups

The Venus Criticality Facility is a zero-power reactor with a cruciform-shaped core located at SCK/CEN, Mol, Belgium. From 1983 to 1988, the VENUS mock-ups simulated the RPV internals, including reflector geometry and core boundary shape, of a generic three-loop PWR reactor.

Three core loading configurations were made in VENUS PWR mock-ups: VENUS-1, simulating a fresh UO_2 core loading; VENUS-2, simulating a low-leakage core loading including MOX fuel pins in the eight outermost rows; and VENUS-3, simulating the PLSA concept in the outermost fuel rows in order to study a low-leakage core and the lead factor. In PLSA pins, the lower half of the axial length of fuel is replaced by steel. The RPV internal structures, including the core baffle, core barrel, and thermal shield (neutron pad), are presented for the three mock-ups.

VENUS-3 Experiment Configuration

The VENUS-3 core is made up of twelve 15×15 subassemblies. The pin-to-pin pitch (1.26 cm) remains typical of the 17×17 PWR fuel assembly. The core was built with a central 4 % enriched UO_2 rods in stainless steel clad (4/0 fuel) and a peripheral 3.3 % enriched UO_2 rods in Zircaloy clad (3/0 fuel). The length of 4/0 and 3/0 fuels is 50 cm. The outermost five rows of two diametrically opposite arms of the cross core were replaced by the PLSA pins made of stainless steel and 3/0 fuel. Several Pyrex absorber rods surrounding the core inner baffle were arranged. A whole core-quadrant is composed of 639 fuel rods and 11 Pyrex pins (Fig. 1).

Pressure vessel internal components of VENUS-3 mock-up include: (1) the core outer baffle (2.858 cm thick), (2) the water reflector (minimum thickness 2.169 cm and 45° thickness 17.5 cm), (3) the core barrel (4.99 cm), (4) the first water gap (5.8 cm), and (5) the thermal shield (average thickness 6.72 cm). Except for the baffle and the reflector minimum-thickness, the thicknesses have been somewhat reduced to fit the VENUS reactor geometry.

The second water gap and the RPV were not simulated. A validation of the calculation up to the thermal shield was considered as acceptable and the complete simulation in the radial direction was already investigated in a slab geometry with the PCA mock-up [4].

The angular shape of the core barrel has a quadrant symmetry achieved with acceptable reflecting conditions (in stainless steel) at 0° and 90°, respectively. The angular shape of the thermal shield was limited by the available space; the quadrant symmetry is also achieved with reflecting conditions in water at 0° and 90°. The exact quadrant symmetry dimensions, the different axial regions and the material compositions are defined in Ref. [9].

VENUS-3 Experiment Measurements

The relative power map was measured through gamma scanning. The relative uncertainty of the neutron fission source with regard to the absolute power is below 4 % and the uncertainty of source space distribution is between 1.5 % and 4 %. The missing measured points were determined by an interpolation procedure so as to obtain a 3D power map with 30×30×14 meshes.

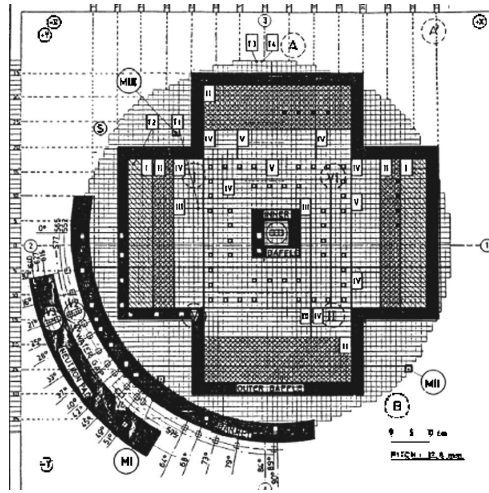

FIG. 1—*VENUS-3 core (4/0 fuel in zones III, IV, and V, 3/0 fuel in zone II, PLSA pins in zone 1; from core center to neutron pad: inner baffle, fuel, outer baffle, water reflector, core barrel, and water gap; azimuthal measurement locations on baffles and core barrel: 0.7° to 89.3°).*

The total fission rate value per quadrant was obtained from absolute measurements at several locations using ^{235}U miniature fission chambers; this measurement yielded a value of 5.652×10^{12} fissions per second per core quadrant which is used as a multiplication factor for converting the 3D power map to the source at 100 % power.

$^{27}Al(n,\alpha)$ $^{58}Ni(n,p)$, and $^{115}In(n,n')$ detectors were used at several points. Measurement locations for the 21° and 45° angles, which correspond to the maximum and minimum fast fluxes, respectively, were provided. The measurement locations are given in Fig. 1 and the measured results are given in terms of reaction rates.

The 14 axial measurement locations, corresponding to the 50-cm fuel length, make possible the study of the impact of the PLSA pins. The ten azimuthal locations (0.7° to 89.3°) enable the verification of the transport of neutron through different thicknesses of water reflector between outer baffle and core barrel. The estimated measurement uncertainties are 5 % [9].

TRIPOLI-4.3 Monte Carlo Calculations

The quadrant symmetry modeling of VENUS-3 benchmark has been made with TRIPOLI-4.3 code according to the specifications of Ref. [9]. The lattice geometry has been used to deal with the reactor core. The 3D power maps with two different fission spectra have been separately applied. The automatic variance reduction and the parallel calculation have been performed to speed up the simulation. Different dosimetry files have been tested and compared.

VENUS-3 Core and Reactor Vessel Internal Components Modeling

The repeated structures of fuel were exactly considered in TRIPOLI-4 modeling so as to take into account the transport of neutrons through water, fuel rods, Pyrex absorber rods, and PLSA region. The core-quadrant was defined with six lattices. One central mixed lattice was used to model the 15×15 4/0 fuel array and the 11 Pyrex absorber array [11]. Five other lattices were used to describe two 4/0 fuel zones (arrays 6×15 and 15×6), two 3/0 fuel zones, and one PLSA region (5 × 15 array). Reactor vessel internal components including baffles, core barrel, thermal shield, and VENUS-3 reactor vessel, were also correctly described using boundary surfaces.

The detector was modeled by a small cylinder volume (radius 0.4 cm and height 1 cm). Totally, more

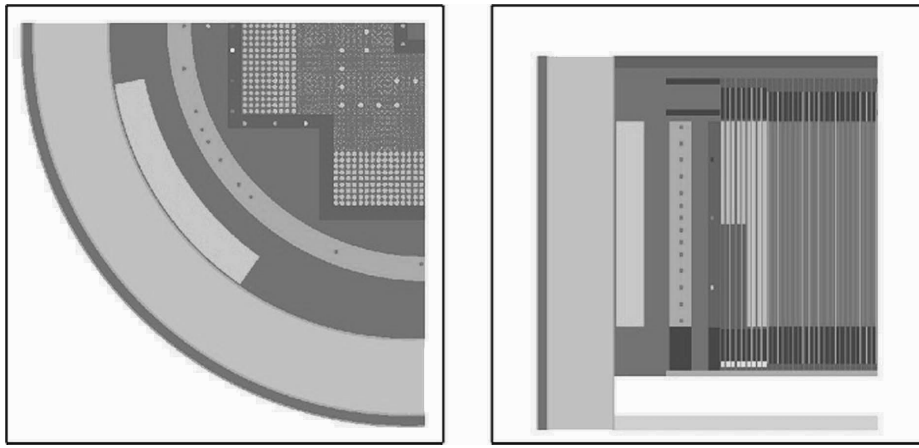

FIG. 2—*VENUS-3 core quadrant (left horizontal view and right vertical view with all measurement points located in inner baffle, outer baffle, water reflector, and core barrel) as simulated with TRIPOLI-4.3.*

than 160 tally volumes were modeled on the internal components with 14 axial levels and 10 azimuthal locations. Two figures in Fig. 2 show the horizontal view and the vertical view, respectively, of the VENUS-3 core quadrant as simulated with TRIPOLI-4.3.

Neutron Source Modeling

VENUS-3 core power map (12 600 values in 30×30×14 structure) taken from Ref. [9] was converted to the tabulated source type "F-UVW" in TRIPOLI-4.3. 30×30 horizontal meshes were prepared and 14 vertical meshes of neutron source were defined. The horizontal neutron source meshes cover the core quadrant with one mesh for each fuel pin. The fissile volumes defined in the six lattices of the core modeling intersect with the 30×30×14 neutron source meshes so as to assume that neutron emission is only from fissile zones. Vertical and horizontal variations of neutron source were considered in detail.

The neutron source intensity in the TRIPOLI-4 calculations was 1.375×10^{13} neutrons per second per core quadrant. It was obtained with 5.652×10^{12} fissions per second per core quadrant and an average number of neutrons per fission of 2.432. Two ^{235}U fission spectra, Watt spectrum and 581 group ENDF/B-VI.4 spectrum were separately applied. ^{235}U Watt fission spectrum was used with thermal neutron spectrum parameters $a=1.012$ and $b=2.249$ [6].

Automatic Variance Reduction

Variance reduction schemes available in TRIPOLI-4 code include exponential transform, splitting, Russian roulette, quota sampling, and collision biasing. In practice, an automatic importance graph generator called INIPOND is often used to reduce the user involvement [12].

In this study, a multigroup importance function defined on 3D meshes was generated with 30 000 neutron histories. The INIPOND module produced the importance graph according to the mesh structure, the material compositions, the neutron energy grid, and the detector locations. The collapsed cross sections are transport corrected to take into account deviations from diffusive flow.

For the pool critical assembly (PCA) benchmark study [4], only the axially maximum flux zones were calculated. The INIPOND scheme based on discrete point detectors was used in order to push the neutrons from the reactor core and the ex-core collision points to the detector points . In this study, to obtain the 14 axial and 10 azimuthal results in a single run with slightly scattered calculation errors, a new INIPOND biasing data set has been established using the cylindrical surface detector [3].

In fact, the 3D importance map of this biasing scheme was calculated with the new cylindrical biasing

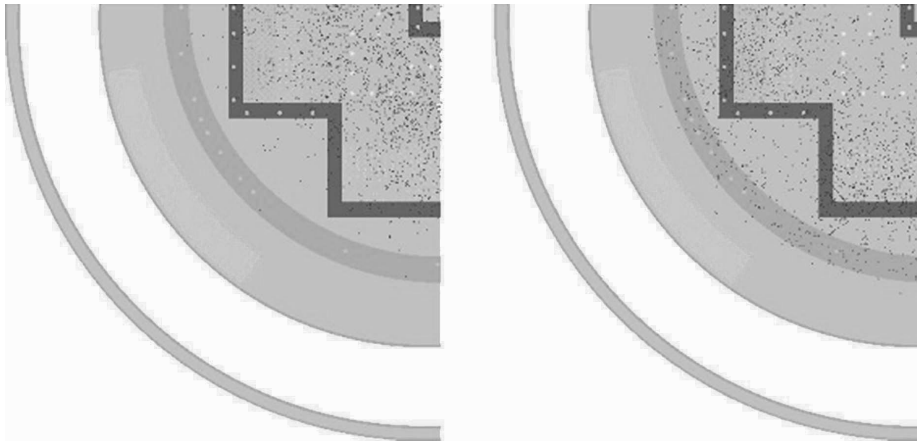

FIG. 3—*VENUS-3 core quadrant with projection of fast neutron (above 1 MeV) collision points of 1000 neutron histories in TRIPOLI-4 simulation (left analog simulation with few collision points arriving to core barrell, right one with variance reduction setting radius of cylindrical biasing surface on core barrel and collision points migrating from core area to core barrel).*

meshes after setting the cylinder axis of biasing on the center of the core. As the cylindrical surface detector of biasing was set on the core barrel with a radius of 51 cm, the neutrons from the core and the collision points were pushed to the tally points on the core barrel.

Two figures in Fig. 3 show the projection of fast neutron collision points (with 1000 neutron histories) in analog and biased simulations with a cylindrical surface detector in INIPOND biasing. It is clear that in the biased simulation of Fig. 3, the collision points migrate from the core area to the ex-core zone and different measurement locations on core barrel are uniformly showered by the collision points.

The mesh size used in INIPOND was 4.4 cm (r)×0.1429 rad (θ)×5.1 cm (h). As the importance map for cylindrical surface detector is generated in an analytical way, the required CPU time and memory size are strongly reduced when compared to discrete point detectors.

The threshold energies for the $^{27}Al(n,\alpha)$, $^{58}Ni(n,p)$, and $^{115}In(n,n')$ reactions are 5.0, 1.0, and 0.3 MeV, respectively. For the importance map, a five-group energy grid (20. -8. -5. -2. -1. -0.3 MeV) was prepared for Ni and In detectors to make a compromise with different detector responses and to generate converged results for each detector in the same run. A cutoff energy of 0.3 MeV was used in order to reduce the cost of the calculation. For $^{27}Al(n,\alpha)$ reaction, a higher cutoff energy of 5 MeV and a two-group energy grid (20. −8. −5. MeV) were set in a separate run in order to obtain a better convergence of the results. For each run, 50×10^6 neutron histories were simulated.

Tally and Simulation

Pointwise cross sections from ENDF/B-VI.4 were used in transport calculations. They were prepared by NJOY/94.105 processing system using RECONR and BROADR modules with a convergence criteria of 0.1 %. Using the IRDF-2002, IRDF-90.v2 files, and cross sections from ENDF/B-VI.4, the reaction rates of $^{27}Al(n,\alpha)$, $^{58}Ni(n,p)$, and $^{115}In(n,n')$ were calculated with TRIPOLI-4 fixed source simulation. Parallel calculations of TRIPOLI-4.3 were run with a cluster of PCs. For a calculation using above automatic biasing scheme and track-length estimators, six processors of 3 GHz had to run 14 h to produce an acceptable convergence of the results (standard deviation between 0.5 and 1 %) in the small tally volumes.

Comparison Calculation and Experiment Results

From Figs. 4–6, the calculation to experiment (C/E) ratios of detectors, Al, Ni, and In, are presented. For each measurement location, different C/E results, obtained with three nuclear data libraries corresponding

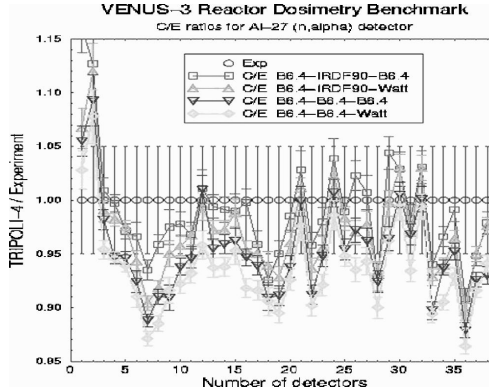

FIG. 4—*The C/E ratios and statistical error bars at 38 measurements locations for detector ^{27}Al (Red square: ENDF/B-VI.4 – transport calculation, IRDF90-detector cross sections and fission spectrum from ENDF/B-VI.4).*

to library of transport calculation, library of detector cross sections, and library of ^{235}U fission spectra, are given with distinct symbols and colors.

C/E Ratios of Detector $^{27}Al(n,\alpha)$

Figure 4 shows the C/E ratios of 38 measurement locations for the $^{27}Al(n,\alpha)$ detector. Detectors 1 and 2 were arranged in inner baffle; 3 to 5, in outer baffle; 6 to 8, in water reflector; and 9 to 38, in core barrel region (10 azimuthal locations from 0.7° to 89.3°, and three axial levels).

The results in Fig. 4 show that the high-energy tail of the ^{235}U fission spectrum from ENDF/B-VI.4 is helpful to improve the C/E ratios for the Al detector comparing with Watt fission spectrum. This conclusion confirms the previous TRIPOLI-4.3 calculation results on the ORNL PCA Pressure Vessel Facility Benchmark [4]. According to the calculated results with ^{235}U fission spectrum from ENDF/B-VI.4, 65 % contribution of the $^{27}Al(n,\alpha)$ reaction rates was found between 8 and 20 MeV and 35 % between 5 and 8 MeV.

The second interesting point obtained from Fig. 4 is that the detector cross sections from IRDF-90.v2 give higher and better C/E ratios than those from ENDF/B-VI.4. With a similar cross-section structure for

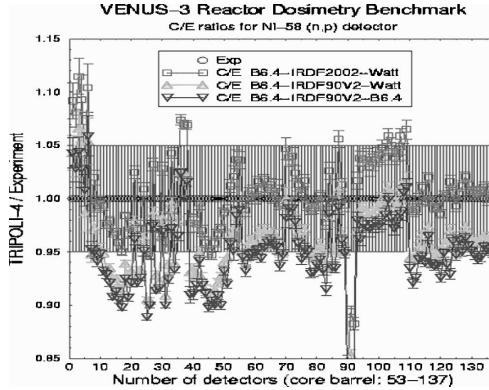

FIG. 5—*The C/E ratios and statistical error bars at 137 measurements locations for detector ^{58}Ni (Red square: ENDF/B-VI.4 – transport calculation, IRDF2002 - detector cross sections and Watt fission spectrum).*

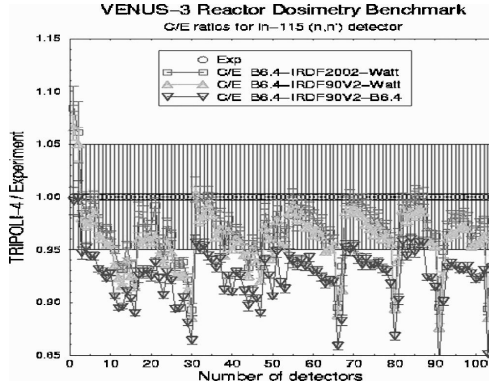

FIG. 6—*The C/E ratios and statistical error bars at 104 measurements locations for detector ^{115}In (Red square: ENDF/B-VI.4 – transport calculation, IRDF2002 - detector cross sections and Watt fission spectrum).*

these two detector responses, more energy groups were found in IRDF-90.v2 and different interpolation methods were applied. Thirdly, the calculated results for $^{27}Al(n,\alpha)$ detector from IRDF-2002 are identical to those from IRDF-90.v2.

C/E Ratios of Detector $^{58}Ni(n,p)$

Figure 5 shows the C/E ratios of 137 measurement locations for the $^{58}Ni(n,p)$ detector. Detectors 1 to 6 were arranged in inner baffle; 7 to 38, in outer baffle; 39 to 52, in water reflector (14 axial levels); and 53 to 137, in core barrel region (10 azimuthal locations from 0.7° to 89.3°, and 14 axial levels).

In general, $^{58}Ni(n,p)$ detector calculation results are found in good agreement with the experimental ones. The Ni response from IRDF-2002 gives 3 to 4 % higher and better C/E ratios compared to those from IRDF-90.v2 and ENDF/B-VI.4. These observations were also found in TRIPOLI-4.3 results on the recent mock-up of PV-CT50 steel dosimetry measurements [7].

As the structure of the $^{58}Ni(n,p)$ cross-section has a plateau between 5 to 12 MeV, the high-energy tail above 12 MeV of the ^{235}U fission spectrum from ENDF/B-VI.4 is useless compared to the Watt fission spectrum. For the calculated $^{58}Ni(n,p)$ reaction rates on the core barrel, more than 50 % contribution was found between 1 and 5 MeV and about 6 % between 1 and 2 MeV.

Detectors 90 to 92 correspond to measurements on the core barrel azimuthal angle 33.9°. These points have been considered as an experimental anomaly [13].

C/E Ratios of Detector $^{115}In(n,n')$

Figure 6 shows the C/E ratios of 104 measurement locations for the $^{115}In(n,n')$ detector. Detectors 1 and 2 were arranged in inner baffle; 3 to 16, in outer baffle (azimuthal angle 0.7°, and 14 axial levels); 17 to 30, in water reflector (azimuthal angle 0.7° and 14 axial levels); and 31 to 104, in core barrel region (10 azimuthal locations from 0.7° to 89.3°, and 14 axial levels).

Calculation results are within 5 % of experiment when using Watt fission spectrum. The regular lower C/E ratios, between 0.85 and 0.9, appear on axial end measurement locations and these were also observed in early MCNP4B simulations [13]. The $^{115}In(n,n')$ detector results from IRDF-2002 give higher, i.e., 1 to 1.5 %, and better C/E ratios comparing with IRDF-90.v2. This was also found in TRIPOLI-4.3 calculations on the PV-CT50 measurements [7].

About 50 % contribution of the calculated $^{115}In(n,n')$ reaction rates was found between 2 and 5 MeV and 35 % between 1 and 2 MeV. The ^{235}U Watt fission spectrum produced a higher C/E ratios about 5 % when compared to the 581 group fission spectrum from ENDF/B-VI.4.

Conclusions

VENUS-3 RPV dosimetry benchmark from the 2004 released SINBAD database has been investigated using TRIPOLI-4.3 Monte Carlo code and satisfactory C/E ratios have been obtained for 160 measurement locations. To compute the axial and azimuthal variation of measurements in a single simulation, new cylindrical biasing meshes and cylindrical surface detector in TRIPOLI-4.3/ INIPOND biasing module have been successfully validated.

For $^{58}Ni(n,p)$ and $^{115}In(n,n')$ detector responses, an improvement of C/E ratios has been observed when using the new IRDF-2002 file. The ^{235}U Watt fission spectrum has been validated to produce better C/E ratios than the 581 group fission spectrum from ENDF/B-VI.4. However, for $^{27}Al(n,\alpha)$ detector response, the high-energy tail of the 581 group fission spectrum from ENDF/B-VI.4 is needed in order to get better C/E ratios. Without taking into account the uncertainty of the nuclear data in transport calculation and the uncertainty of the 3D power map, a 10 % C/E tolerance margin should be accepted.

VENUS-3 RPV dosimetry benchmark is designed for a generic three-loop PWR reactor and only limited activation foil detectors are available. It would be interesting and useful to carry out the related RPV dosimetry mock-up experiments in the future with diverse dosimetry detectors covering different neutron energy ranges [14].

References

[1] "Computing Radiation Dose to Reactor Pressure Vessel and Internals: State-of-the-Art Report," NEA/NSC/DOC(96)5, 1997.

[2] Nimal, J. C., Bourdet, L., Zheng, S. H., Vergnaud, T., and Kodeli, I., "*French PWR 900 MWe Pressure Vessel Surveillance - TRIPOLI-3 Calculations and Experimental Determination*," *The 8th Int. Conf. on Radiation Shielding (8thICRS)*, Arlington, TX, April 24-28, 1994, pp. 699–705.

[3] Both, J. P., "*A Survey of TRIPOLI-4*," *Proc. of the 8th Int. Conf. on Radiation Shielding*, Arlington, TX, Apr. 24-28, 1994, Vol. I, p. 373; TRIPOLI-4 version 4.3 http://www.nea.fr/abs/html/nea-1716.html (2004).

[4] Lee, Y. K., "*Analysis of the NRC PCA Pressure Vessel Dosimetry Benchmark Using TRIPOLI-4.3 Monte Carlo Code and ENDF/B-VI.4, JEF2.2 and IRDF-90 Libraries*," *Nuclear Mathematical and Computational Sciences: A Century in Review*, *A Century Anew*, *M&C 2003*, Gatlinburg, Tennessee, April 6-10, 2003.

[5] "SINBAD—an International Database for Integral Shielding Experiments," http://www.nea.fr/html/science/shielding/sinbad/sinbadis.htm (Dec. 2004).

[6] Lee, Y. K., "*Investigation of ^{252}Cf Fission Spectra and SINBAD Water Shielding Benchmarks Using TRIPOLI-4.3 Monte Carlo Code*," *The ANS's 14th Biennial Topical Meeting of the Radiation Protection and Shielding Division*, *Carlsbad*, *NM. April* 2-6, 2006, *on CD-ROM*.

[7] Carcreff, H., Alberman, A., Barbot, L., Rozenblum, F., Beretz, D., and Lee, Y. K., "Dosimetry Requirements for Pressure Vessel Steels Toughness Curve in the Ductile to Brittle Range," *J. ASTM International (JAI)*, Vol. 3, No. 3, 2006.

[8] "Prediction of Neutron Embrittlement in the Reactor Pressure Vessel: VENUS-1 and VENUS-3 Benchmarks," OECD/NEA Report NEA/NSC/DOC(2000)5, 2000.

[9] VENUS-3 LWR-PVS Benchmark Experiment, http://www.nea.fr/html/science/shielding/sinbad/venus3/ven3-abs.htm (May, 2004).

[10] "IRDF – The International Reactor Dosimetry Files (IRDF-2002 and IRDF-90.v2)," http://www-nds.iaea.org/irdf2002/(2005).

[11] Lee, Y. K., "Analysis of the LEU-COM-THERM-049 MARACAS Critical Configurations Using TRIPOLI-4.3 3D Lattices Geometry and JEF3.0," *Proc. of the 7th Int. Conf. on Nuclear Criticality Safety, ICNC 2003*, Tokai, Japan, Oct. 20-24, 2003, pp. 289.

[12] Both, J. P., Nimal, J. C., and Vergnaud, T., "Automatic Importance Generation and Biasing Techniques in TRIPOLI-3," *Prog. Nucl. Energy*, Vol. 24, 1990, pp. 273–281.

[13] Perlado, J. M., Marian, J., and Sanz, J. G., "Neutron Fluence, Dosimetry and Damage Response Determination in In-core/Ex-core Components of the VENUS CEN/SCK LWR Using 3-D Monte Carlo Simulations: NEA's VENUS-3 Benchmark," *Nucl. Technol.*, Vol. 129, 2000, pp. 285–296.

[14] Blaise, P., Thiollay, N., Fougeras, P., Destouches, C., Beretz, D., Lee, Y. K., Chiron, M., and Janski, S., "*Neutron Fluence Vessel Assessment in the 1300 MWe NPP French Fleet*," *Int. Congress on Advances in Nuclear Power Plants, ICAPP'06*, Reno, NV., June 4-8, 2006, on CD-ROM.

Journal of ASTM International, Vol. 3, No. 10
Paper ID JAI100381
Available online at www.astm.org

Sergey I. Belousov,[1] *Desislava L. Kirilova,*[1] *Mladen R. Mitev,*[1] *and Krassimira D. Ilieva*[1]

Influence of the Multigroup Approximation on VVER-1000 RPV Neutron/Gamma Flux Calculation

ABSTRACT: One-dimensional calculations of neutron and gamma group fluxes and radiation damage in terms of DPA have been carried out for VVER-1000 mock-up realized at LR-0 critical assembly, Rez, Czech Republic in order to evaluate the influence of energy dependence multigroup approximation on VVER-1000 RPV Neutron/Gamma flux calculation. Two calculational methods have been applied: Monte Carlo method (MC) with continuous energy dependence description and discrete ordinates (DO) method with multigroup energy dependence approximation. Two different multigroup neutron/gamma cross section libraries have been used: BGL1000—created especially for VVER-1000 application and BUGLE96—created for PWR application. A good consistency between the results for both methods and different cross section libraries is obtained for neutrons with energy above 0.1 MeV. The worst consistency is obtained for the thermal neutrons. For gammas a better consistency between DO and MC results is obtained when BGL1000 library is applied.

KEYWORDS: neutron fluence, reactor pressure vessel, radiation damage, multigroup approximation

Introduction

Three-dimensional neutron/gamma transport calculations carried out under REDOS Project [1] demonstrated inconsistency between some neutron/gamma flux results obtained by the Monte Carlo (MC) method and by the discrete ordinate (DO) method. The calculations were carried out for VVER-1000 engineering benchmark created on the base of VVER-1000 mock-up realized at LR-0 critical assembly INR, Rez, Czech Republic. The MC calculations were carried out by the MCNP [2] code and cross section data from the DLC200/MCNPDATA library with continuous energy dependence description. The DO calculation were carried out in multigroup energy dependence approximation by the TORT [3] code. The neutron/gamma multigroup cross section library BGL1000 [4]—created especially for VVER-1000 application, was used in DO calculation.

To understand if the obtained inconsistency between the two methods results could be explained by multigroup cross section presentation used in DO calculation, one-dimensional calculation of neutron and gamma integral fluxes and irradiation damage in terms of DPA have been carried out for the cylindrical model of the same VVER-1000 mock-up. One-dimensional calculation allows the avoidance of all calculational models differences between MC and DO calculations except those related to the cross section presentation.

One-dimensional DO calculation has been carried out by the DORT [3] code with two broad group cross section libraries, BGL-1000 and SAILOR96t (BUGLE96) [5]—the most applicable worldwide nowadays. Both broad group libraries have been produced for light water reactor (LWR) shielding and reactor pressure vessel dosimetry application. Both problem oriented libraries have been produced at Oak Ridge National Laboratory by the same methodology (but by different teams) from fine group (problem independent) cross section library VITAMIN-B6. However, starting from the VITAMIN-B6 the next steps including production of self-shielded data and determination of the collapsing flux spectra have been performed for the different LWR models: VVER-1000 reactor model for BGL-1000, and PWR—for BUGLE96.

Manuscript received February 2, 2006; accepted for publication September 22, 2006; published online October 2006. Presented at ASTM Symposium on Reactor Dosimetry, 12th International Symposium on 8–13 May 2005 in Gatlinburg, TN; D. W. Vehar, D. M. Gilliam, and J. M. Adams, Guest Editors.

[1] Senior Research Scientist, Scientific Researcher, Ph.D. Student, and Senior Research Scientist, respectively, Institute for Nuclear Research and Nuclear Energy of Bulgarian Academy of Science, Tsarigradsko 72, Sofia 1784, Bulgaria.

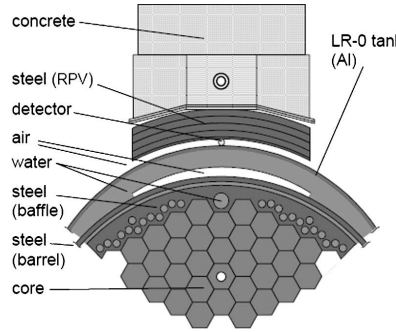

FIG. 1—*VVER-1000 LR-0 mock-up.*

It is known that BUGLE96 library is applied not only for PWR application but for VVER application as well. That is why the comparison of the results obtained with both multigroup cross section libraries is of definite interest itself.

The DO calculation has been carried out with the P3S8 direction scattering approximation [6] and with the convergence criteria parameter equal to 0.001. The MCNP results (surface fluxes) statistical uncertainty did not exceed 2 %.

Model Definition—Calculational Task

The VVER-1000 LR-0 mock-up geometry is presented in Fig. 1. The cylindrical one-dimensional geometry of VVER-1000 RPV mock-up includes VVER-1000 reactor core and baffle with corresponding effective radiuses, and subsequent shells for modeling of the out of baffle region of the mock-up. The shells' thicknesses have been taken equal to the mock-up geometry dimensions along the symmetry axis going through the registration positions.

The calculation results have been obtained in the registration positions (Table 1) corresponding to the points of measurement. Points' numbering are those applied in the VVER-1000 engineering benchmark.

The integral fluxes with the following energy limits: for neutrons, $E_n < 0.414$ eV; $E_n > 0.111$ MeV; $E_n > 0.498$ MeV; $E_n > 1$ MeV; $E_n > 3$ MeV; $E_n > 5$ MeV, $E_n > 0$ MeV, and for gammas, $E_\gamma > 1$ MeV; $E_\gamma > 3$ MeV; $E_\gamma > 5$ MeV, $E_\gamma > 0$ MeV, have been calculated and compared. Radiation damages in terms of DPA [7] have been calculated also.

There are some elements in the VVER-1000 mock-up steel constructions' content that are not presented in the SAILOR-96t library (Table 2). Although the content of these elements seems to be not significant, the impact of these missing elements has been estimated. The flux responses results have been compared for the cases when these elements are presented directly and when their content is substituted by iron. The obtained difference does not exceed 2 % for the responses of interest. Nevertheless, these elements have been taken out of consideration in the next calculations with BGL1000 library.

TABLE 1—*Registration positions.*

Point	Position	Radius, cm
2	Behind the barrel	184
3	In front of the RPV	209.2
4	$\frac{1}{4}$ thickness of the RPV	213.7
5	$\frac{1}{2}$ thickness of the RPV	218.7
6	$\frac{3}{4}$ thickness of the RPV	223.6
7	Behind the RPV	229.8

TABLE 2—*Elements missed in SAILOR-96t.*

	Contents, %		
Element	Baffle	Barrel	RPV
Si	0.48	1.0	0.2
P	0.008	0.045	0.04
S	0.005	0.03	0.04
Ti	0.5	0.15	
Cu	0.04		0.3
Total	1.033	1.225	0.58

DO versus MC Results Comparison

The comparison between the DO (with BGL1000 library) and MC results is demonstrated in Table 3 by the values of related difference [(DO/MC)−1], %.

Rather good agreement—within 7 %, is obtained for the integral neutron fluxes with low energy limit above 0.111 MeV. There is a significant discrepancy for the thermal neutrons, En < 0.414 eV, in points 2, 3, 4 (up to 72 %) and point 5. The consistency of the results for total neutron fluxes, En > 0 MeV, is within about 6 %, except in points 2, 3 where the difference is higher—up to 14 % (point 3).

The consistency of the results for the gamma integral fluxes is not worse than 13 % for the highest energy region, Eg > 1 MeV. The greater discrepancy, up to 22 %, (point 7) is obtained for the total gamma fluxes.

The comparison of the DO (with SAILOR96t library) results with those of MC is illustrated by the related differences in Table 4.

Again, as in the case of the BGL1000 library application, we have obtained a rather good agreement—within about 10 %, for integral neutron fluxes with low energy limit above 0.111 MeV. The discrepancy

TABLE 3—*Comparison between the DO (BGL1000) and MC results.*

Energy, MeV	Point 2	Point 3	Point 4	Point 5	Point 6	Point 7
neutron	%	%	%	%	%	%
E < 4.14E-07	34.2	64.0	71.9	38.2	10.3	0.35
E > 0.111	4.56	−0.19	4.85	6.65	5.46	−2.79
E > 0.498	5.56	−1.17	0.81	1.11	−0.11	−5.22
E > 1	5.36	−1.38	−1.01	−1.92	−3.35	−6.33
E > 3	3.19	−2.90	−3.67	−4.50	−4.78	−5.62
E > 5	5.04	1.25	0.74	−0.31	−1.15	−1.69
E > 0	9.46	13.8	6.17	6.11	4.91	−1.61
gamma						
E > 1	1.64	−6.04	−6.38	−8.33	−10.6	−12.2
E > 3	6.61	5.33	3.83	2.08	−0.32	−3.69
E > 5	7.60	8.59	6.88	4.77	1.94	−1.43
E > 0	−5.41	−27.3	−18.1	−18.9	−20.6	−21.8

TABLE 4—*Comparison between the DO (SAILOR-96t) and MC results.*

Energy, MeV	Point 2	Point 3	Point 4	Point 5	Point 6	Point 7
neutron	%	%	%	%	%	%
E < 4.14E-07	−42.42	−53.47	−37.85	−11.83	10.87	2.68
E > 0.111	3.58	−2.43	2.43	4.10	2.79	−6.39
E > 0.498	3.77	−3.98	−2.20	−2.25	−3.89	−10.03
E > 1	4.43	−3.86	−3.83	−5.05	−6.70	−10.05
E > 3	0.10	−5.63	−6.34	−7.51	−8.17	−9.67
E > 5	2.11	−2.32	−2.98	−4.35	−5.45	−6.54
E > 0	−5.60	−12.32	1.01	3.59	2.81	−4.35
gamma						
E > 1	−33.00	−32.53	−32.32	−32.35	−32.65	−28.96
E > 3	−24.29	−20.29	−21.72	−22.63	−23.85	−22.02
E > 5	−24.92	−20.36	−21.33	−22.16	−23.26	−20.62
E > 0	−23.56	−25.36	−37.61	−39.65	40.02	−35.66

TABLE 5—*Comparison between DO (BGL1000 and SAILOR-96t) and MC DPA results.*

	Point 2	Point 3	Point 4	Point 5	Point 6	Point 7
	%	%	%	%	%	%
BGL1000 library						
neutron	5.31	−0.40	2.05	3.40	2.98	−3.15
gamma	6.66	5.83	4.09	1.87	−0.97	−3.82
SAILOR-96t library						
neutron	3.89	−3.39	−0.74	0.44	−0.10	−6.96
gamma	−27.30	−23.51	−23.79	−24.34	−25.31	−22.34

for the thermal neutrons, En $<$ 0.414 eV, is significantly greater, in points 2, 3 (up to 54 %) and point 4. The consistency of the results for total neutron fluxes, En $>$ 0 MeV, is within 6 %, except point 3 where the difference is about 12 %.

However, for the gamma fluxes the situation is different in comparison with BGL1000 library usage case. The DO integral gamma fluxes are systematically (as minimum 20 %) lower than the MC ones. The related difference between DO (SAILOR-96t) and MC results reaches 40 % (total flux, point 6) that does not happen for the difference between DO (BGL1000) and MC results.

The greatest discrepancy between DO with BGL1000 and MC has been obtained for the thermal neutron fluxes, En $<$ 0.414 eV, for points 2, 3, 4, and 5. The same high discrepancy but with opposite sign has been obtained with SAILOR-96t application for points 2, 3, and 4. The DO (BGL1000) results overestimate the MC results, while the DO (SAILOR-96t) results underestimate them.

The relative difference between MC and DO results for DPA values that has been obtained for both multigroup cross section libraries is presented in Table 5.

As can be seen from the Table 5 data a rather good agreement, within 7 %, exists between all results for damage caused by neutron flux. The DO (BGL1000) results for damage caused by gamma flux are consistent with the MC results within the same limits. Such consistency, however, is not observed for DO (SAILOR-96t) results when the MC results significantly overcome (by more than 22 %) the DO ones.

The relative difference [(SAILOR96t/BGL1000)-1], %, between DO results obtained with the SAILOR-96t and with the BGL1000 cross section libraries is shown in Table 6.

For both libraries the consistency between the integral neutron fluxes with energy limits above 0.111 MeV and DPA values caused by neutrons is very good, within 1 %. This is in accordance with the above presented DO versus MC results comparison. The discrepancy between the results for the thermal neutrons fluxes is significant for points 2, 3 (up to 71 %), 4, and point 5. The discrepancy between the integral gamma fluxes and damages induced by the gammas is significant at all positions (up to about 30 % in point 2). The integral gamma flux and DPA results obtained with the BGL1000 library are higher than the corresponding ones obtained with SAILOR-96t.

TABLE 6—*Comparison of the DO results for SAILOR-96t and BGL1000 libraries.*

Energy, MeV	Point 2	Point 3	Point 4	Point 5	Point 6	Point 7
neutron	%	%	%	%	%	%
E $<$ 4.14E-07	−56.6	−70.9	−62.6	−33.8	4.31	5.59
E $>$ 0.111	0.63	0.07	0.06	0.08	0.10	0.22
E $>$ 0.498	0.05	−0.48	−0.46	−0.49	−0.54	−0.40
E $>$ 1	1.18	−0.15	−0.26	−0.28	−0.26	0.35
E $>$ 3	−0.43	−0.35	0.01	0.05	0.00	0.05
E $>$ 5	−0.26	−1.10	−0.96	−0.90	−0.81	−0.75
E $>$ 0	−12.6	−21.0	−2.72	−0.29	−0.04	0.30
DPA	0.42	−0.63	−0.24	−0.20	−0.19	0.03
gamma						
E $>$ 1	−33.2	−27.3	−26.5	−24.6	−22.6	−16.4
E $>$ 3	−28.1	−23.5	−23.4	−22.5	−21.5	−16.5
E $>$ 5	−29.4	−25.8	−25.2	−24.1	−22.7	−17.0
E $>$ 0	−18.1	4.08	−22.5	−23.9	−22.3	−15.0
DPA	−31.0	−26.9	−25.6	−24.1	−22.5	−16.7

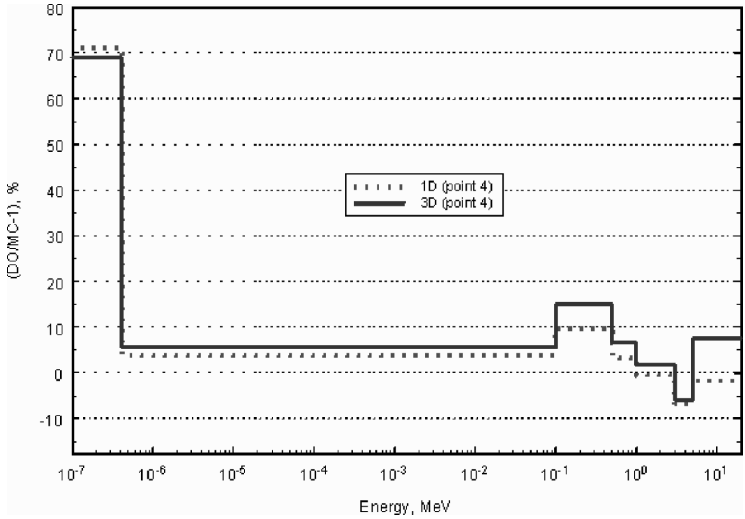

FIG. 2—*3-D versus 1-D consistency results.*

3-D versus 1-D Comparison

The consistency between DO (BGL1000) and MC for the integral neutron fluxes obtained for one-dimensional VVER-1000 mock-up calculation, and presented here, is very similar to the corresponding consistency obtained for three-dimensional VVER-1000 mock-up calculation [1]. The difference between $[(DO/MC)-1]$ values for one- and three-dimensional cases does not exceed 12 % for all registration positions. The comparison between one- and three-dimensional cases in corresponding energy regions is illustrated for point 4 in Fig. 2.

Conclusions

The influence of the multigroup approximation used in discrete ordinate calculation has been analyzed on the base of simplified one-dimensional cylindrical model of the VVER-1000 LR-0 mock-up.

One-dimensional calculation lets us estimate the differences due to the multigroup cross section presentation in discrete ordinates (DO) method in comparison with the MCNP method (MC, without multigroup energy dependence approximation), avoiding all geometry and calculational model differences between both methods.

A good consistency between the results obtained by MC and DO methods is obtained for neutrons with energy above 0.111 MeV. The application of the multigroup approximation leads to significant inconsistency of the results for thermal neutrons and gamma.

Comparison of the DO results obtained using two multigroup cross section libraries, BGL1000—created especially for VVER-1000 application, and SAILOR96-t (BUGLE96)—for PWR application, has been done. In general, the consistency of MC results to those of DO with BGL1000 is better, and especially for gamma. It could be expected taking into account that BGL1000 was created especially for VVER-1000. This has to be kept in mind when BUGLE96 cross section library is applied for VVER-1000 application.

Further analyses of the problem-oriented cross section libraries BGL1000 and BUGLE96 as well as problem-independent library VITAMIN-B6, are needed for explanation of significant inconsistency between DO and MC results obtained for thermal neutrons.

The consistency between DO (BGL1000) and MC for the integral neutron fluxes for one-dimensional VVER-1000 mock-up calculation is very similar to that obtained for three-dimensional calculation [1]. This led us to conclude that the multigroup approximation of the used cross section data is the main reason for the inconsistency between DO and MC three-dimensional calculations.

Acknowledgments

This work was carried out under the REDOS project of 5FP, Euratom, FIKS-CT-2001-00120.

References

[1] VVER-1000 Mock-up Experiment in LR-0 Reactor Mock-up Description and Experimental Data REDOS/R (01)/December 2002/Issue 01.

[2] Briesmeister, I. F., Ed., "MCNP—A General Monte Carlo N-Particle Transport Code, Version 4C," LA-13709-M (April 2000), RSICC ORNL, Code Package, CCC0700, 2000.

[3] DOORS3.2, RSICC ORNL, Code Package CCC-650, 1998.

[4] Bucholz, J., Antonov, S., and Belousov, S., "BGL440 and BGL1000 Broad Group Neutron/Photon Cross Section Libraries Derived from ENDF/B-VI Nuclear Data," IAEA, INDC(BUL)-15, April 1996.

[5] White, J. E. et al., "Production and Testing of the VITAMIN-B6 Fine-Group and the BUGLE-96 Broad Group Neutron/Photon Cross-Section Libraries Derived from ENDF/B-VI.3 Nuclear Data," ORNL-6795, R1, NUREG/CR-6214, Revision 1 (January 1995) (DRAFT), RSICC ORNL, Code Package DLC-185, 1996.

[6] Lewis, E. and Miller, W., Jr., *Computational Methods of Neutron Transport*, Wiley-Interscience Publications, 1984.

[7] Kwon, J. and Motta, A. T., "Gamma Displacement Cross-Sections in Various Materials," *Ann. Nucl. Energy*, 27, 2000, pp. 1627–1642.

Journal of ASTM International, Vol. 4, No. 5
Paper ID JAI100340
Available online at www.astm.org

Robert E. Keith[1]

A New Derivation of the Perturbation Operator Used in MCNP[2]

ABSTRACT: A new derivation of the perturbation operator used in the MCNP radiation transport code is presented, and equations are determined to evaluate the change in the response from a perturbation in macroscopic cross section due to the first, second, third, and fourth derivative terms, and the second-derivative cross term. The perturbation operator in MCNP currently can be used to determine the change in a response from the first and second order terms in Taylor expansion due to such a perturbation. The derivation presented here produces expressions that are equivalent to the expressions used in MCNP for the first and second derivative, but are simpler and are in a form that more readily reveals their physical significance. The perturbation operator is particularly useful for sensitivity and uncertainty analysis.

KEYWORDS: perturbation operator, MCNP, sensitivity analysis

Introduction

It is at times desirable to determine the effect that a small change in a cross section or in a geometric dimension might have on the response (the tallied result) of a radiation transport calculation. For example, the designer of a test object that will be used in a reactor experiment may want to have a knowledge of the change in response that would accompany an increased thickness of some component, or an experimentalist may want to determine how test results might vary if the fraction of an important isotope were greater than had been specified, or an analyst may need the sensitivity of the response to a series of cross sections for uncertainty analysis.

There are various methods for determining change in the response due to a change in a problem parameter (such as the cross section, isotope fraction, or thickness of an object). Several of the more popular methods are:

The Brute Force Method—The problem is executed to get the response at the nominal values, and then executed again for each parameter perturbation. This technique is quite straightforward, but care must be taken to ensure that the perturbation is large enough to overwhelm any numerical inaccuracy or sampling uncertainty. For deterministic calculations this caveat is relatively easy to handle for most cases, but it can be much harder to handle for Monte Carlo calculations where the statistical sampling uncertainty may be difficult to overcome with reasonable runtimes.

The Forward-Adjoint Coupling Method—For calculations where the forward and adjoint fluences can be determined and stored for the problem phase space, such as can be done with discrete ordinate transport calculations, the forward fluences and the adjoint fluences can be coupled with the cross sections to determine the sensitivity of the response to the specific cross sections. Details for this method can be found in various papers [1–3], and while this technique is extremely useful in that the sensitivity of all cross sections can be investigated after the transport calculations are completed, its use is limited in Monte Carlo calculations, since there is the need to have the forward and adjoint fluences available for the whole phase space of the problem.

Manuscript received June 20, 2005; accepted for publication April 26, 2007; published online May 2007. Presented at ASTM Symposium on Reactor Dosimetry, 12th International Symposium on 8–13 May 2005 in Gatlinburg, TN; D. W. Vehar, D. M. Gilliam, and J. M. Adams, Guest Editors.

[1] Principal Scientist, ITT Industries, AES, Colorado Springs, CO 80919.

[2]This work was supported by the United States Department of Energy under contract DE-AC04-94AL85000 with technical management by Sandia National Laboratories. Sandia is a multiprogram laboratory operated by Sandia Corporation, a Lockheed Martin Company, for the United States Department of Energy.

The Perturbation Operator Method—An operator is defined that determines the coefficients of a Taylor series expansion of the response to the problem parameters of interest. This perturbation operator allows the determination of the change in the response to perturbation in these parameters during the Monte Carlo transport calculation. This is the technique considered in this paper, and specifically this paper considers the implementation of this method that is used in the radiation transport code MCNP.

The perturbation operator formalism was originally described by Hall [4], and the MCNP manual [5] and the MCNP perturbation operator verification technical report [6] provide a derivation of the specific expressions as used in the MCNP code. As is described in the literature, the basis of method is to expand the response, R, to be calculated by a Monte Carlo run, with value a response of R_0 for the nominal value of the parameter, in terms of a parameter of interest, ν with nominal value ν_0, and the perturbation $\Delta\nu = \nu - \nu_0$. The Taylor expansion of R in ν is:

$$R = R_0 + \left.\frac{dR}{d\nu}\right|_{\nu=\nu_0} \cdot \Delta\nu + \frac{1}{2}\left.\frac{d^2R}{d\nu^2}\right|_{\nu=\nu_0} \cdot (\Delta\nu)^2 + \frac{1}{3!}\left.\frac{d^3R}{d\nu^3}\right|_{\nu=\nu_0} \cdot (\Delta\nu)^3 + \cdots \quad (1)$$

The goal of the perturbation operator method becomes then, to find expressions for the derivative terms ($dR/d\nu$, etc.) that can be calculated during a Monte Carlo calculation. The MCNP documentation [5,6] details a derivation that is based on determining these terms with the parameter of interest being the microscopic cross sections. Rather than deriving these expressions in the manner proposed in the MCNP documentation, this paper uses the macroscopic cross sections to simplify the derivation by the use of a surrogate density. This procedure results in expressions for the first and second derivatives that are equivalent to those found in the MCNP coding, but also allows for a clear physical interpretation for each term in the expressions. In addition, expressions for the third and fourth (and higher) derivative terms are readily obtained, as is an expression for the second derivative cross term that results when two perturbations are considered together.

The derived expressions for the third and fourth order correction terms were implemented in a test version of the MCNP code, and several of the test cases from the MCNP perturbation operator verification manual were executed. A comparison to the results of one of these calculations is discussed below.

General Derivation

As can be seen in the Boltzmann equation (Eq 2) that governs the radiation transport, the number density and the microscopic cross sections only appear through the macroscopic cross section.

$$\begin{aligned}\frac{1}{u}\frac{\partial\Phi(\vec{x},E,\vec{\Omega},t)}{\partial t} - \vec{\Omega}\cdot\nabla\Phi(\vec{x},E,\vec{\Omega},t) \\ = S(\vec{x},E,\vec{\Omega},t) + \int_{E_{min}}^{E_{max}} dE' \int_0^{4\pi} d\vec{\Omega}'\Sigma_s(\vec{x},E'\to E,\vec{\Omega}'\to\vec{\Omega})\cdot\Phi(\vec{x},E',\vec{\Omega}',t) \\ + \frac{1}{k_{eff}}\int_{E_{min}}^{E_{max}} dE' \int_0^{4\pi} d\vec{\Omega}'\chi_f(\vec{x},E'\to E)\cdot\Sigma_f(\vec{x},E')\cdot\nu_N\cdot\Phi(\vec{x},E',\vec{\Omega}',t) - \Sigma_t(\vec{x},E)\cdot\Phi(\vec{x},E,\vec{\Omega},t) \quad (2)\end{aligned}$$

where $\Phi(\vec{x},E,\vec{\Omega},t)$ is the fluence, u is the particle speed, $\vec{\Omega}$ is the direction of travel, $\vec{x}$ is the position, E is the particle energy, $S(\vec{x},E,\vec{\Omega},t)$ is the number of source neutrons at a location with energy E and direction $\vec{\Omega}$, $\Sigma_s(\vec{x},E'\to E,\vec{\Omega}'\to\vec{\Omega})$ is the scattering (macroscopic) cross section, $\chi_f(\vec{x},E'\to E)$ is the fraction of neutrons from a fission, $\Sigma_f(\vec{x},E)$ is the fission (macroscopic) cross section, $\Sigma_t(\vec{x},E)$ is the total (macroscopic) cross section, k_{eff} is the criticality coefficient, and ν_N is the number of neutron emitted by a fission.

The response is normally the integral of the number fluence multiplied by a response function, and this response function can involve the microscopic cross section or the number density individually, but this case can be handled separately if the response function is involved in the perturbation.

The macroscopic cross section for a single reaction for a single isotope is simply the number density of the isotope multiplied by the microscopic cross section for that reaction. The macroscopic cross section can also be defined as a sum over specific reactions and over all isotopes in a material. Although the

following derivation is presented in a form that is oriented to a single isotope, this basic method can be used quite generally. The specific orientation of the derivation towards one material is for compatibility with the input formulation used to specify a perturbation in MCNP [5].

If a single material is involved, the macroscopic cross sections can be expressed as the sum of unperturbed cross sections and cross sections to be perturbed. Further, if several perturbations are considered, the macroscopic cross section for an arbitrary reaction x, can be defined as the sum of the unperturbed microscopic cross section, σ_i, multiplied by the number density, ρ_0, of the isotopes and the sum microscopic cross section, σ_i^j (with the "j" in the superscript simply designating that the cross section is perturbed in the j^{th} perturbation group—each cross section channel can only be used once) to be perturbed multiplied by the isotope number density (Eq 3).

$$\Sigma_x(\vec{x},E,\vec{\Omega}) \equiv \sum_i^{N_0} \rho_0 \sigma_i(\vec{x},E,\vec{\Omega}) + \sum_j^n \rho_j \sum_i^{N_j} \sigma_i^j(\vec{x},E,\vec{\Omega}) \tag{3}$$

If a perturbation of some fraction, f_j, is made to the microscopic cross section, $\sigma_i^j(\vec{x},E,\vec{\Omega})$, clearly the macroscopic cross section will change by $\rho_0 f_j \sigma_i^j(\vec{x},E,\vec{\Omega})$. If the perturbation is grouped with the number density rather than the cross section, a perturbed density can be used to account for the perturbation, and ρ_j would take on the value $\rho_0 \times f_j$. In this manner, the perturbation of a group of cross sections by the same factor can be readily made, without dealing with the details of the dependency of one channel's cross section on another.

For ease of manipulation, the macroscopic cross section (Eq 3) can be rewritten as:

$$\Sigma_x(\vec{x},E,\vec{\Omega}) = \Sigma_x^0(\vec{x},E,\vec{\Omega}) + \sum_j^n \Sigma_x^j(\vec{x},E,\vec{\Omega}) \tag{4}$$

The surrogate density ρ_j, which is an implicit factor in the microscopic-to-macroscopic conversion of quantities, will take the place of the parameter ν in the Taylor expansion (Eq 1), and the first order term can then be expressed in terms of the macroscopic cross sections Σ_x^j, and the first order term in Eq 1 becomes:

$$\frac{\partial R}{\partial \rho_j} \cdot (\rho_j - \rho_0) = \frac{\partial R}{\partial \Sigma_x^j} \cdot \frac{\partial \Sigma_x^j}{\partial \rho_j} \cdot (\rho_j - \rho_0) = \frac{\partial R}{\partial \Sigma_x^j} \cdot \Delta\Sigma_x^j \tag{5}$$

The derivative of the response with respect to surrogate density requires an examination of the specific equations that are used in the Monte Carlo transport and scoring algorithms. In a Monte Carlo transport code, the number of particles at a location in the geometry is the sum of the possible paths that a particle can take to get to that region multiplied by the probability that a particle would take that path (and a normalization factor), and the response will be this number of particles multiplied by a suitable response function. The probability of the path is estimated by using a random walk procedure that divides a particle's path in small segments based in terms of probability of the particle interacting with the material in the geometry, and so the probability of a particle having a specific path through the geometry is the product of the individual probabilities of the segments that were sampled by the particle. So, the probability of particles taking path A is $p(A)=p(A\,|\,\vec{x}_{A;0},E_{A;0},\vec{\Omega}_{A;0},t_{A;0}) \cdot p(\vec{x}_{A;0},E_{A;0},\vec{\Omega}_{A;0},t_{A;0})$, where the variables $\vec{x}_{A;0},E_{A;0},\vec{\Omega}_{A;0},t_{A;0}$ define the phase space description of the path's starting location. The description of path A will include a definition of the starting point, and has a specific description of the particle motion and parameters from its start to the end of the path. If the path has N_A path segments, and the phase space variables at the end of each segment are given by $\vec{x}_{A;k},E_{A;k},\vec{\Omega}_{A;k},t_{A;k}$, then the probability of having particles take path A is:

$$p(A) = p(\vec{x}_{A;0},E_{A;0},\vec{\Omega}_{A;0},t_{A;0}) \cdot \prod_{k=1}^{N_A} p(\vec{x}_{A;k},E_{A;k},\vec{\Omega}_{A;k},t_{A;k}|\vec{x}_{A;k-1},E_{A;k-1},\vec{\Omega}_{A;k-1},t_{A;k-1}) \tag{6}$$

So then if there are N_P paths, if the response function is defined as $f_R(\vec{x},E,\vec{\Omega},t)$, and if the normalization factor is R_N, the response can be written as:

TABLE 1—*Four cases of the conditional probability.*

Case	Beginning Condition	Ending Condition	$p_{A;k}$
1	collision	collision	$\Sigma_a(E_{k-1})/\Sigma_T(E_{k-1})p_a(E_{k-1}\rightarrow E_k,\vec{\Omega}_{k-1}\rightarrow\vec{\Omega}_k)\cdot(e^{-\Sigma_T(E_k)\lambda_k})\cdot\Sigma_T(E_k)\lambda_k$
2	collision	boundary crossing	$\Sigma_a(E_{k-1})/\Sigma_T(E_{k-1})p_a(E_{k-1}\rightarrow E_k,\vec{\Omega}_{k-1}\rightarrow\vec{\Omega}_k)\cdot(e^{-\Sigma_T(E_k)\lambda_k})$
3	boundary crossing	collision	$(e^{-\Sigma_T(E_k)\lambda_k})\cdot\Sigma_T(E_k)\lambda_k$
4	boundary crossing	boundary crossing	$(e^{-\Sigma_T(E_k)\lambda_k})$

where $\Sigma_a(E_{k-1})$ is the cross section of the process that initiated the segment, $\Sigma_T(E_{k-1})$ is the total cross section at the beginning of the segment, $p_a(E_{k-1}\rightarrow E_k,\vec{\Omega}_{k-1}\rightarrow\vec{\Omega}_k)$ is the probability that the initiating reaction (a) would cause the energy to change from E_{k-1} to E_k, and the direction to go from $\vec{\Omega}_{k-1}$ to $\vec{\Omega}_k$. $\Sigma_T(E_k)$ is the total cross section at the end of the segment, and λ_k is the length of the segment.

$$R = R_N \sum_{A}^{N_P} f_R(\vec{x}_{A;N_A}, E_{A;N_A}, \vec{\Omega}_{A;N_A}, t_{A;N_A}) \cdot p(A) \tag{7}$$

If the response function and the initial path probabilities are not dependent on the perturbation parameters, the determination of the derivatives of the response with respect to the perturbation parameters becomes simply a summation of the derivatives of $p(A)$ for all paths, and this in turn is a combination of the derivatives of the path segment probabilities:[3]

$$\frac{\partial p(A)}{\partial \rho_j} = p(A) \sum_{k=1}^{N_A} \left(\frac{1}{p_{A;k}} \cdot \frac{\partial p_{A;k}}{\partial \rho_j} \right) \tag{8}$$

It is convenient at this point to define a term β as:

$$\beta \equiv \sum_{k=1}^{N_A} \left(\frac{1}{p_{A;k}} \cdot \frac{\partial p_{A;k}}{\partial \rho_j} \right) \tag{9}$$

The second derivative of $p(A)$ obtained is then:

$$\frac{\partial^2 p(A)}{\partial {\rho_j}^2} = p(A) \cdot \beta^2 + p(A) \cdot \frac{\partial \beta}{\partial \rho_j} \tag{10}$$

Similarly, the third derivative of $p(A)$ is simply:

$$\frac{\partial^3 p(A)}{\partial {\rho_j}^3} = p(A) \cdot \beta^3 + 3p(A) \cdot \beta \frac{\partial \beta}{\partial \rho_j} + p(A) \cdot \frac{\partial^2 \beta}{\partial {\rho_j}^2} \tag{11}$$

And the fourth derivative of $p(A)$ is:

$$\frac{\partial^4 p(A)}{\partial {\rho_j}^4} = p(A) \cdot \beta^4 + 6p(A) \cdot \beta^2 \frac{\partial \beta}{\partial \rho_j} + 3p(A) \cdot \left(\frac{\partial \beta}{\partial \rho_j} \right)^2 + 4p(A) \cdot \beta \frac{\partial^2 \beta}{\partial {\rho_j}^2} + p(A) \cdot \frac{\partial^3 \beta}{\partial {\rho_j}^3} \tag{12}$$

In the MCNP code [5,6], as well as many Monte Carlo transport codes, $p_{A;k}$ can take four forms dependent on the whether the path segment in question started at a collision, started at a geometrical boundary, ended at a collision, or ended at a boundary. Table 1 shows four forms with the condition that began and finished the specific segment, Table 2 shows the first and second derivatives for each case, and Table 3 shows the third and fourth derivatives of $p_{A;k}$.

If the response function is dependent on the perturbed cross section, the derivatives of the response (Eq 7) can readily be expressed in terms of derivatives of the response function, f_R, and the path probabilities, $p(A)$, although for the higher derivatives of the response function, the number of individual terms can become large.

[3]For convenience and clarity, the conditional probability $p(\vec{x}_{A;k}, E_{A;k}, \vec{\Omega}_{A;k}, t_{A;k} | \vec{x}_{A;k-1}, E_{A;k-1}, \vec{\Omega}_{A;k-1}, t_{A;k-1})$ will hereafter be referenced as $p_{A;k}$, and the explicit specification of the position and angular dependence of the cross sections will be dropped.

TABLE 2—*First and second derivatives of the conditional probabilities.*

Case	$\rho_j\left(\frac{1}{p_{A;k}}\cdot\frac{\partial p_{A;k}}{\partial \rho_j}\right)$	$\rho_j{}^2\frac{\partial}{\partial \rho_j}\left(\frac{1}{p_{a;k}}\cdot\frac{\partial p_{a;k}}{\partial \rho_j}\right)$
1	$\delta_{a\in j}\delta_{E_{k-1}\in j}-\delta_{E_{k-1}\in j}\Sigma_x^j(E_{k-1})/\Sigma_T(E_{k-1})$ $-\lambda_k\delta_{E_k\in j}\Sigma_x^j(E_k)+\delta_{E_k\in j}\Sigma_x^j(E_k)/\Sigma_T(E_k)$	$-\delta_{a\in j}\delta_{E_{k-1}\in j}+\delta_{E_{k-1}\in j}[\Sigma_x^j(E_{k-1})/\Sigma_T(E_{k-1})]^2$ $-\delta_{E_k\in j}[\Sigma_x^j(E_k)/\Sigma_T(E_k)]^2$
2	$\delta_{a\in j}\delta_{E_{k-1}\in j}-\delta_{E_{k-1}\in j}\Sigma_x^j(E_{k-1})/\Sigma_T(E_{k-1})-$ $\lambda_k\delta_{E_k\in j}\Sigma_x^j(E_k)$	$-\delta_{a\in j}\delta_{E_{k-1}\in j}+\delta_{E_{k-1}\in j}[\Sigma_x^j(E_{k-1})/\Sigma_T(E_{k-1})]^2$
3	$-\lambda_k\delta_{E_k\in j}\Sigma_x^j(E_k)+\delta_{E_k\in j}\Sigma_x^j(E_k)/\Sigma_T(E_k)$	$-\delta_{E_k\in j}[\Sigma_x^j(E_k)/\Sigma_T(E_k)]^2$
4	$-\lambda_k\delta_{E_k\in j}\Sigma_x^j(E_k)$	0

where $\delta_{a\in j}$ is one if the reaction, a, is in the set of the perturbed cross sections and zero otherwise, and $\delta_{E_{k-1}\in j}$ is one if the energy, $E_{k-1,}$ is in the range of energies of the perturbation and zero otherwise.

If two or more perturbations that involve different cross sections are considered together, a multivariable Taylor expansion can be performed and the second (and higher order) cross derivatives can be determined. For the second derivative term, the cross derivative probability, $p(A)$, with respect to density surrogates ρ_j and ρ_m can be written as:

$$\frac{\partial^2 p(A)}{\partial \rho_j\,\partial \rho_k}=\left[\sum_{k=1}^{N_A}\left(\frac{1}{p_{A;k}}\cdot\frac{\partial p_{A;k}}{\partial \rho_j}\right)\right]\cdot\left[\sum_{k=1}^{N_A}\left(\frac{1}{p_{A;k}}\cdot\frac{\partial p_{A;k}}{\partial \rho_k}\right)\right]+\sum_{k=1}^{N_A}\frac{\partial}{\partial \rho_k}\left(\frac{1}{p_{A;k}}\cdot\frac{\partial p_{A;k}}{\partial \rho_j}\right) \tag{13}$$

The conditional probability derivatives for each case can readily be determined from the expressions above in Table 2.

Comparison to Expressions in MCNP

The MCNP coding allows a user to specify the inclusion of the first and second derivative terms in determining the effect of a perturbation in the cross sections on the response. As mentioned above, the terms derived here are equivalent to the terms found in the MCNP coding. For the first derivative term, the expressions are identical, and for the second derivative term, the expression used in the MCNP code contains five terms for the second derivative of the conditional probability, but these terms can be shown to reduce to identically the expressions found here. For instance, using the terminology specified above, the expression for the second derivative term of the first conditional probability case in the MCNP code is:

$$\begin{aligned}\rho_j^2\frac{\partial}{\partial \rho_j}\left(\frac{1}{p_{a;k}}\cdot\frac{\partial p_{a;k}}{\partial \rho_j}\right)=2\delta_{E_{k-1}\in j}\left[-\delta_{a\in j}\frac{\Sigma_a^j(E_{k-1})}{\Sigma_T(E_{k-1})}+\frac{[\Sigma_a^j(E_{k-1})]^2}{[\Sigma_T(E_{k-1})]^2}\right]+\delta_{E_k\in j}[\lambda_k\Sigma_a^j(E_k)]^2-2\delta_{E_k\in j}\lambda_k\frac{[\Sigma_a^j(E_k)]^2}{\Sigma_T(E_k)}\\ -\left[\delta_{E_{k-1}\in j}\delta_{a\in j}-\delta_{E_{k-1}\in j}\frac{\Sigma_a^j(E_{k-1})}{\Sigma_T(E_{k-1})}\right]^2-\left[\delta_{E_k\in j}\lambda_k\Sigma_a^j(E_k)-\delta_{E_k\in j}\frac{\Sigma_a^j(E_k)}{\Sigma_T(E_k)}\right]^2\end{aligned} \tag{14}$$

and can be simplified by expanding the squares and canceling terms to yield exactly the Case 1 second

TABLE 3—*Third and fourth derivatives of the conditional probabilities.*

Case	$\rho_j{}^3\frac{\partial^2}{\partial \rho_j^2}\left(\frac{1}{p_{A;k}}\cdot\frac{\partial p_{A;k}}{\partial \rho_j}\right)$	$\rho_j{}^4\frac{\partial^3}{\partial \rho_j^3}\left(\frac{1}{p_{A;k}}\cdot\frac{\partial p_{A;k}}{\partial \rho_j}\right)$
1	$2\delta_{a\in j}\delta_{E_{k-1}\in j}-2\delta_{E_{k-1}\in j}[\Sigma_x^j(E_{k-1})/\Sigma_T(E_{k-1})]^3+$ $2\delta_{E_k\in j}[\Sigma_x^j(E_k)/\Sigma_T(E_k)]^3$	$-6\delta_{a\in j}\delta_{E_{k-1}\in j}+6\delta_{E_{k-1}\in j}[\Sigma_x^j(E_{k-1})/\Sigma_T(E_{k-1})]^4-$ $6\delta_{E_k\in j}[\Sigma_x^j(E_k)/\Sigma_T(E_k)]^4$
2	$2\delta_{a\in j}\delta_{E_{k-1}\in j}-2\delta_{E_{k-1}\in j}[\Sigma_x^j(E_{k-1})/\Sigma_T(E_{k-1})]^3$	$-6\delta_{a\in j}\delta_{E_{k-1}\in j}+6\delta_{E_{k-1}\in j}[\Sigma_x^j(E_{k-1})/\Sigma_T(E_{k-1})]^4$
3	$2\delta_{E_k\in j}[\Sigma_x^j(E_k)/\Sigma_T(E_k)]^3$	$-6\delta_{E_k\in j}[\Sigma_x^j(E_k)/\Sigma_T(E_k)]^4$
4	0	0

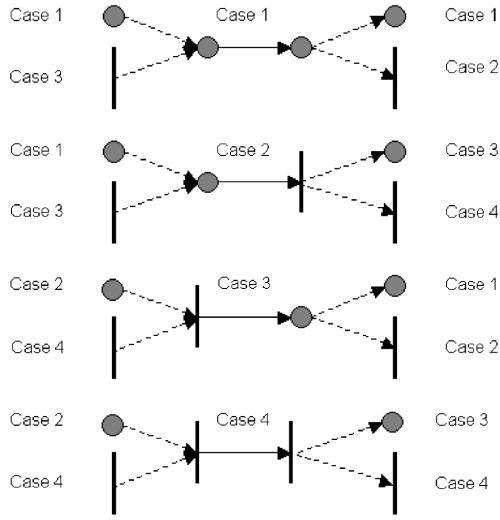

FIG. 1—*Schematic representation of the possible probability cases. A circle indicates a collision, while a vertical line represents a boundary crossing.*

order term in Table 2. Note that the expression in Table 2 makes it clear that the condition probability second derivative expression does not involve the path length (λ_k), but in the unsimplified form that is encoded in MCNP (Eq 14) it would appear that the expression is dependent on the path length.

Further Simplifications and Physical Interpretation

One important requirement of a model of a physical transport problem is that the solution be insensitive to the specific geometric constructs used unless they correspond to physical geometric aspects of a problem. For instance, it is quite acceptable to create ten geometric regions all with the same material properties to model a single slab of some material, but one would expect that the response estimations would be the same as if the slab was modeled by a single geometric region. The same requirement ought also to apply to the perturbation operator, and by examining the form of the expressions above, it is clear that this requirement is met. The only term that is contributed by the boundary crossings is the segment length term of the first derivative ($-\lambda_k \delta_{E_k \in j} \Sigma_x^j(E_k)$), and this will accumulate throughout all regions where the perturbation is valid. This term is simply the first derivative of the exponential attenuation factor, and is thus exactly what should be expected.

By looking at the equations, it is apparent that as a particle path is followed, certain terms in one step will be eliminated in the next. The possible conditional probability cases (whether the path segment begins at a collision or geometric boundary, and end at either a collision or a geometric boundary) that arise are schematically shown in Fig. 1.

If a path contains a segment corresponding to Case 1 (a collision initiated the segment, and a collision also terminates it), it is clear that the next segment must begin with a collision (either Case 1 or Case 2). The specific form of the formulae requires that the $\delta_{E_k \in j}[\Sigma_x^j(E_k)]/[\Sigma_T(E_k)]$ term be eliminated by the $\delta_{E_k \in j}[\Sigma_x^j(E_{k-1})]/[\Sigma_T(E_{k-1})]$ term of the next segment. This process simplifies Tables 2 and 3 somewhat, as is shown in Tables 4 and 5.

The sole remaining term from the collisions is the delta function term. This term indicates that the effect of the perturbation on the response is to increase the number of particles in the perturbed energy band and is related to the relative importance of the reaction (reflected in how often the reaction occurs). It is noteworthy that only the conditional probability first derivative contains an explicit use of the path length.

These simplified conditional probability terms must still be combined via Eqs 9–12 to determine the

TABLE 4—*First and second derivatives of conditional probabilities with redundant terms eliminated.*

Case	$\rho_j\left(\frac{1}{p_{A;k}}\cdot\frac{\partial p_{A;k}}{\partial \rho_j}\right)$	$\rho_j^2\frac{\partial}{\partial \rho_j}\left(\frac{1}{p_{a;k}}\cdot\frac{\partial p_{a;k}}{\partial \rho_j}\right)$
1	$\delta_{a\in j}\delta_{E_{k-1}\in j}-\lambda_k\delta_{E_k\in j}\Sigma_x^j(E_k)$	$-\delta_{a\in j}\delta_{E_{k-1}\in j}$
2	$\delta_{a\in j}\delta_{E_{k-1}\in j}-\lambda_k\delta_{E_k\in j}\Sigma_x^j(E_k)$	$-\delta_{a\in j}\delta_{E_{k-1}\in j}$
3	$-\lambda_k\delta_{E_k\in j}\Sigma_x^j(E_k)$	0
4	$-\lambda_k\delta_{E_k\in j}\Sigma_x^j(E_k)$	0

change in the probability of the path, $p(a)$. It is in the context of these equations that the simplified conditional probabilities reveal insights into the derivatives of the derivatives of the path probability. The first derivative of the path probability is simply the path probability multiplied by the term β, which is the sum of the relative partial derivatives of the conditional path segment probabilities. So from Table 4, it is clear that if a collision occurs that involves a perturbed cross section channel in the energy range of the perturbation, the first derivative of the path probability is incremented by the path probability over the surrogate perturbation density, and that the path probability will always be decremented by optical depth of the sum of the cross sections that are being perturbed for the particle energy of a path that travels in a region with a perturbed cross section over the surrogate perturbation density. The perturbation that this first order term will cause in the response can then be determined by the use of Eq 5.

The second order derivative of the path probability (Eq 10) includes two terms, the first is the square of the sum of relative first derivatives of the conditional path-segment probabilities, and this causes a correlation between the perturbations of different path segments in the same path. The second term is simply the number of collisions encountered in the path that involve the perturbed cross sections (in the applicable energy regime) divided by the surrogate density squared. Since the response contribution will be determined by multiplying by the square of the difference of the surrogate and actual densities, this later term is simply the number of collisions important to the perturbation moderated by the relative change in the cross sections. Similarly, the first terms in the third and fourth order terms (Eqs 11 and 12) provide further correlation between path segments, and the final term is the number of collisions important to the perturbation moderated by the relative perturbation of the cross section to the order of the derivative.

Utility of Third and Fourth Derivative Terms

The first derivative term is very useful. It is the principle term used in sizing studies and in sensitivity and uncertainty analysis. The second derivative term is currently used to determine if the first order term is sufficient to estimate the perturbed response. McKinney and Iverson [6] indicate that if the change in response from the second order term is over 20 % of that from the first order term, and higher order terms are required to calculate the change in the response, and they suggest that the magnitude of the perturbation be reduced. While a reduction in the magnitude of the perturbation will produce changes in the response that are better modeled with smaller perturbations, this often defeats the purpose of calculating the perturbation. For instance, if the perturbations are made to arrive at the Taylor series coefficients for a sizing study, it is useful to know where the approximation becomes invalid, but the recourse that is suggested requires more MCNP calculations to be performed. It would be more useful to understand how the higher order terms in the Taylor series are behaving, and to extend the domain in which reasonable results can be obtained.

As will be demonstrated for a sample calculation below, the third and fourth derivative terms provide additional insight into the behavior of the Taylor series expansion, and for cases where a perturbation is

TABLE 5—*Third and fourth derivatives of conditional probabilities with redundant terms eliminated.*

Case	$\rho_j^3\frac{\partial^2}{\partial \rho_j^2}\left(\frac{1}{p_{A;k}}\cdot\frac{\partial p_{A;k}}{\partial \rho_j}\right)$	$\rho_j^4\frac{\partial^3}{\partial \rho_j^3}\left(\frac{1}{p_{A;k}}\cdot\frac{\partial p_{A;k}}{\partial \rho_j}\right)$
1	$2\delta_{a\in j}\delta_{E_{k-1}\in j}$	$-6\delta_{a\in j}\delta_{E_{k-1}\in j}$
2	$2\delta_{a\in j}\delta_{E_{k-1}\in j}$	$-6\delta_{a\in j}\delta_{E_{k-1}\in j}$
3	0	0
4	0	0

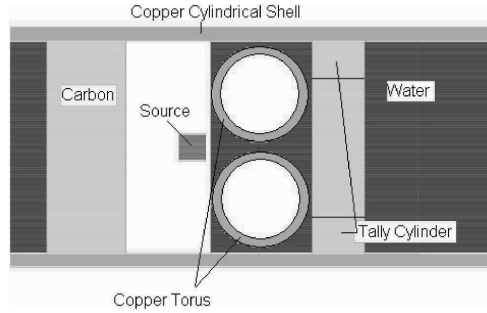

FIG. 2—*Sample problem geometry.*

made from optimal conditions, allow a useful approximation to be made where the first derivative is near zero, but higher order derivatives are not.

It should be remembered that for a Taylor series to converge, higher order terms must become vanishingly small, and that an approximation from a Taylor series should include all terms until the sum of contribution from the infinite number of ignored terms are less than the desired accuracy of the approximation. While it is useful to examine the second order term to determine whether the first term is sufficient, it is much more satisfying to have the third and fourth order terms available to indicate that the approximation is valid. The third order term is particularly useful for this additional check for series convergence. The second order term is symmetric for a perturbation about a cross section value of interest, and if the underlying response is asymmetric, the second order term will approach zero, while the third order term can be large, since it (like the first order term) is asymmetric to perturbations about a value.

The cost in computer runtime of determining the higher order terms to sufficient accuracy is quite variable. For one recent calculation of the activation of a nickel foil placed in the center of a polyethylene sphere with an 8.9-cm radius and expose to a reactor spectrum, the nickel activation had a sampling uncertainty of 0.6 %. For a perturbation of the total cross section, the sampling uncertainty was 0.6 % for the first order term, 0.8 % for the second order, 1.2 % for the third order term, and 2.0 % for the fourth order term. In the same calculation, for a response of scandium activation, the response calculation had a sampling uncertainty of 0.09 %, but the sampling uncertainty was 0.9 % for the first order term, 27 % for the second order term, 76 % for the third order term, and 100 % for the fourth order term.

To illustrate the utility of the calculating higher order terms, the following sample problem is presented that originated from the MCNP differential operator verification documentation [6]. The geometry of this sample problem is shown in Fig. 2, and consists of a copper pipe with a thickness of 5 cm and an inner radius of 40 cm. This pipe contains a cube of CuO with a Watt neutron fission source at its center. The CuO cube is surrounded by a vacated region, which is contained in the copper pipe. On one side of the vacated region there is a 30-cm thick carbon disk, and on the other is a torus with 3-cm thick walls inside a region of water. Beyond this water region, away from the source, there is another carbon disk, and the gamma fluence is tallied in the outer 15 cm of this disk. The density of the copper in the torus and the outer copper shell is varied as the perturbation in this problem.

The gamma fluence provides an interesting illustration of the use of perturbations in that the majority of the gamma rays created are produced in the copper torus and in the copper pipe, and a low density of copper in these regions (which would roughly correspond to using thinner copper walls in the outer shell and torus) will not generate many gamma rays, and the fluence at the tally location will be small. Conversely, copper at an ambient density ($8.94\ g/cm^3$) will attenuate many of the gamma rays, and a small fluence will be calculated in the tally region.

Figure 3 shows the results of this sample calculation over a large decrease in the copper density as calculated by direct calculations[4], and as calculated by using up to the fourth order terms in the Taylor series expansion. As is seen in this figure, the inclusion of four terms from the Taylor expansion fit the curve somewhat better than two terms, but this calculation took several days on a 2 GHz G5 computer to

[4]At many density values a direct calculation of the fluence was performed.

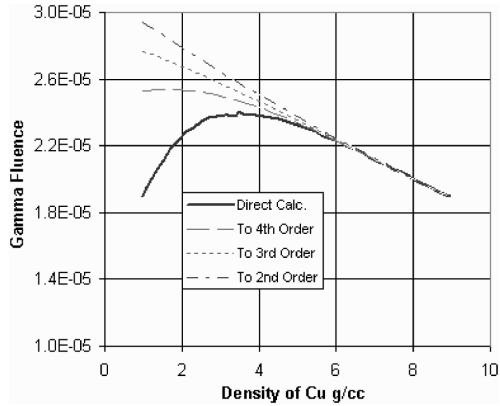

FIG. 3—*Comparison of the gamma fluence obtained by using direct calculations, and by using an increasing number of Taylor expansion terms as calculated from 8.94 gm/cm*^{3}.

reduce the uncertainty of the fourth order term to a 14 % sampling uncertainty. The approximation of the fluence using up to the fourth order term is clearly better than the estimation using just two terms of the expansion. However, none of these approximations adequately models the steep decline of the fluence as the density decreases to less than 2 g/cm^3. This result is not too surprising since this represents a rather large perturbation.

If the Taylor series coefficients are calculated about different points, approximations of different qualities are obtained. In Fig. 4, the results obtained when the Taylor series coefficients are calculated at starting densities of 8.94, 7.9, 6.9, 5, 3.5, and 1 g/cm^3. As this figure shows, the best approximations occur for starting densities near the optimal value for generating a gamma fluence in the tally region (about 5 and 3.5 g/cm^3), while the worst approximations are obtained from the tails of the distribution.

A particularly interesting result is obtained for a density very near the optimal density for causing a high gamma fluence in the tally region. At 3.5 g/cm^3 the first derivative term is very near zero, and the second and higher order terms dominate. At this location, the efficiency of obtaining a converged second and third order terms improved dramatically, although the fourth order term still required the same long runtime for similar sampling convergence as the 8.94 g/cm^3 case. Figure 5 presents a comparison of the direct calculation of the gamma fluence and the gamma fluence estimated from a Taylor series expansion

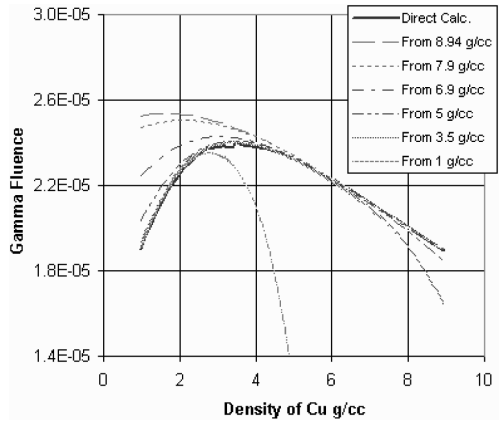

FIG. 4—*Comparison of fourth order Taylor series approximations started at different densities with the direct calculation results.*

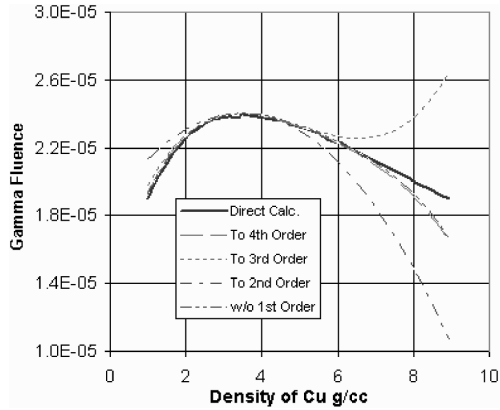

FIG. 5—*Comparison of the gamma fluence obtained by using direct calculations, and by using an increasing number of Taylor expansion terms as calculated from 3.5 gm/cm³.*

about a density of 3.5 g/cm^3 for a different number of Taylor series terms. As this figure shows, there is an appreciable underestimation of the fluence at a density of 8.94 g/cm^3 for the expansion including the fourth order term, but without this term the approximation deviates greatly from the value calculated directly. This sample problem illustrates the importance of being able to calculate these high order perturbation terms.

Conclusions

This new derivation for the MCNP perturbation operator leads to terms that are simpler in form than the expressions currently in MCNP, and allows the easy addition of higher order terms in the Taylor expansion. Also included is an expression for explicitly including second order cross terms for multiple perturbations. The simplified terms make it easier to see the physical significance of each term, and to see the increasing importance of the change of each path segment to the higher order terms, which explains the increased difficulty in obtaining convergence of the higher order terms when there are more scattering events.

The use of the higher order terms for situations where the first order term is adequate is primarily to assist in demonstrating that the Taylor series is converging, and that the first order term is indeed adequate. However, for other problems, and especially for those that are near optimal values, the higher order terms can be critical in obtaining an estimate that is useful over the desired perturbation domain.

References

Keith, R. E., "An Approach to Determining the Uncertainty in Reactor Test Objects Using Deterministic and Monte Carlo Methods," *J. ASTM Int.*, Vol. 3, Issue 10, 2006.

Kodeli, I., "Cross-Section Data Uncertainty and How Such Information is Used in Fusion Analysis," *International Conference Nuclear Energy in Central Europe*, Portoroz, Slovenia, September 6–9, 1999.

Childs, R. L., "SEN1: A One-Dimensional Cross-Section Sensitivity and Uncertainty Module for Criticality Safety Analysis," ORNL/TM-13738, Oak Ridge National Laboratory, July 1999.

Hall, M., "Cross-Section Adjustment with Monte Carlo Sensitivities: Application to the Winfrith Iron Benchmark," *Nucl. Sci. Eng.*, Vol. 81, No. 3, 1982, pp. 423–431.

MCNP: A General Monte Carlo N-Particle Transport Code, LA-13709-M, Los Alamos National Laboratories, April 2000.

McKinney, G. and Iverson, J. L., "Verification of the Monte Carlo Differential Operator Technique for MCNP," Study Results LA-13098, Los Alamos National Laboratory, February 1996.

Journal of ASTM International, Vol. 3, No. 6
Paper ID JAI100364
Available online at www.astm.org

D. A. Allen,[1] *C. Thiruarooran,*[1] *D. A. Thornton,*[1] *A. L. Fletcher,*[1] *A. J. Bird,*[2] *S. Rycroft,*[2] *and G. A. Wright*[2]

Calculation of Neutron Fluxes for Radioactive Inventory Assessment of Magnox Power Plant

ABSTRACT: This paper describes the methodology and results of Monte Carlo neutron transport calculations performed to determine the neutron fluxes required for assessments of radioactive inventories of Magnox power plant. Use has been made of existing validated Monte Carlo models of the plant, which have been extended to include details beyond the pressure vessels to the outer surface of the biological shield.

KEYWORDS: decommissioning, radioactive inventory, magnox power plant, monte carlo, MCBEND

Introduction

In 2000, BNFL Magnox Generation (now part of British Nuclear Group) announced closure dates for each of its operating Magnox power plants, and preparations for decommissioning are now well underway. Radionuclide inventory data are required by each of the plants as an input requirement of their safety cases for progression from "defuelling" to a state of "care and maintenance." They will also be used to aid the efficient management of wastes resulting from the decommissioning process. Assessments of life-time averaged neutron fluxes are necessary in order to calculate individual radionuclide components of the radioactive inventories.

This paper describes the radiation transport calculations performed to provide the neutron flux input data for the calculation of radioactive inventories for the UK's Magnox reactors. The methodology is based closely upon that developed for the dosimetry assessments of the reactor pressure vessels (RPV) of the Magnox plant [1–3] and uses detailed three-dimensional models created with the Monte Carlo code MCBEND [4].

Requirements

The current radioactive inventory analyses for Magnox power plant require neutron flux data in the form of two groups—thermal and epithermal. In subsequent analysis, these data are combined with the 2200 ms^{-1} cross sections and resonance integrals of specific activation reactions, along with their concentrations, to estimate the required reaction rates.

The neutron flux estimates are required for every component of the reactors. The larger components are split into subregions, since there may be marked differences in activation across them which may ultimately affect their disposal route. Since it is the long-lived isotopic species that are the principal interest for this work, the flux calculations have been based on mean-over-life reactor operating powers. For stations which are still generating, this mean-over-life power has been based on the anticipated end of generation core irradiation.

Monte Carlo Models

Detailed models of the Magnox reactors were originally developed for the assessment of neutron doses to the steel RPVs using the radiation transport code MCBEND [4]. These semi-explicit models were suc-

Manuscript received June 20, 2005; accepted for publication February 5, 2006; published online April 2006. Presented at ASTM Symposium on Reactor Dosimetry, 12th International Symposium on 8–13 May 2005 in Gatlinburg, TN; D. W. Vehar, D. M. Gilliam, and J. M. Adams, Guest Editors.

[1] British Nuclear Group, Berkeley Centre, Berkeley, Gloucestershire, GL13 9PB, UK.
[2] Serco Assurance, Winfrith Technology Centre, Dorchester, Dorset, DT2 8DH, UK.

cessfully validated against fast and thermal neutron activation measurements performed within and just outside the RPV [1–3]. Having given C/M (calculated/measured) ratios within 25 % of unity, there is a high degree of confidence in the predictions of these models. For simplicity, these models were defined using octant symmetry, bounded on the 0° and 45° boundaries by reflecting surfaces.

In order to use the models for the purpose of calculating fluxes for inventory analyses, it has been necessary to extend them in order to improve the representation of the plant out to the outer edges of their biological shields. Attention has been paid to key streaming pathways within components outside the RPV. In particular the standpipes, which penetrate the biological shield and RPV, provide neutron streaming paths from the core into the biological shield.

In each of the plants, the biological shields are the most massive components and these have been subdivided into layers. Figure 1 shows horizontal and vertical slices through the revised model for one of the power plants.

In addition to neutron fluxes, the models developed for this work have been able to provide accurate component volumes (and therefore masses) for some components which have been accurately represented within the models. This was achieved using the MCBEND SKETCH facility, which uses a track-length approach to calculate the volumes of components within the models. In some cases, this mass information was not readily available in the existing company literature.

Methodology

Multi-Stage Calculations

As with the RPV dosimetry program, neutrons emanating from the cores were considered in three distinct groups—those leaking from the top of the fuel channels, those from the bottom and those leaking through the side reflector. Thus three distinct sets of calculations were required, with the results for each component being the sum of all three calculations.

For the calculation of fluxes above and below the core, the calculations were performed in stages. Stage 1: Fuel channel leakage calculations were used to determine the distribution in energy and angle of neutrons emerging from the top and bottom of each channel. Stage 2: These distributions were then applied as sources above and below each of the fuel channels across the cores, with source particle weighting being used to account for radial power variation. Neutrons were then tracked to the inner surface of the biological shield and a leakage file used to record all their spatial, directional, and energy properties. Stage 3: Neutrons were tracked into the biological shield using multiple sampling of the leakage file created at Stage 2. Stage 4: Subsequent leakage surfaces were then used within the biological shield, with multiple sampling of tracks, to ensure an adequate population of Monte Carlo tracks right through to the outermost scoring regions of the biological shield.

The calculations for the fluxes at the side of the core followed a similar procedure. Neutrons from the outer four layers of fuel channels (accounting for ~90 % of the total side-core thermal neutron leakage flux) were tracked to the inner surface of the biological shield and recorded in a leakage file. A subsequent leakage surface was then used to complete the side-core calculations throughout the shield. Care was taken in all these multi-stage calculations to ensure that back-scattered contributions to components inside each leakage surface, from subsequent stages, were properly accounted for.

Analogue Monte Carlo

MCBEND has a robust and sophisticated automatic variance reduction capability and this was used extensively within the RPV dosimetry program. However, the calculations undertaken for this work were achieved largely without explicit variance reduction measures other than the staged, multi-sampling leakage surface approach outlined above. This analogue approach was made possible partly because of the availability of modern computing power, but also because of the requirements of the project. It was not necessary to determine a detailed neutron flux map throughout the biological shield, but instead it was only necessary to score within large scoring volumes. This meant that good statistical sampling of tracks within these volumes was relatively easy to achieve without resorting to splitting/Russian roulette methods. It was still possible to determine flux attenuation profiles within the shield to considerable depths using this analogue approach.

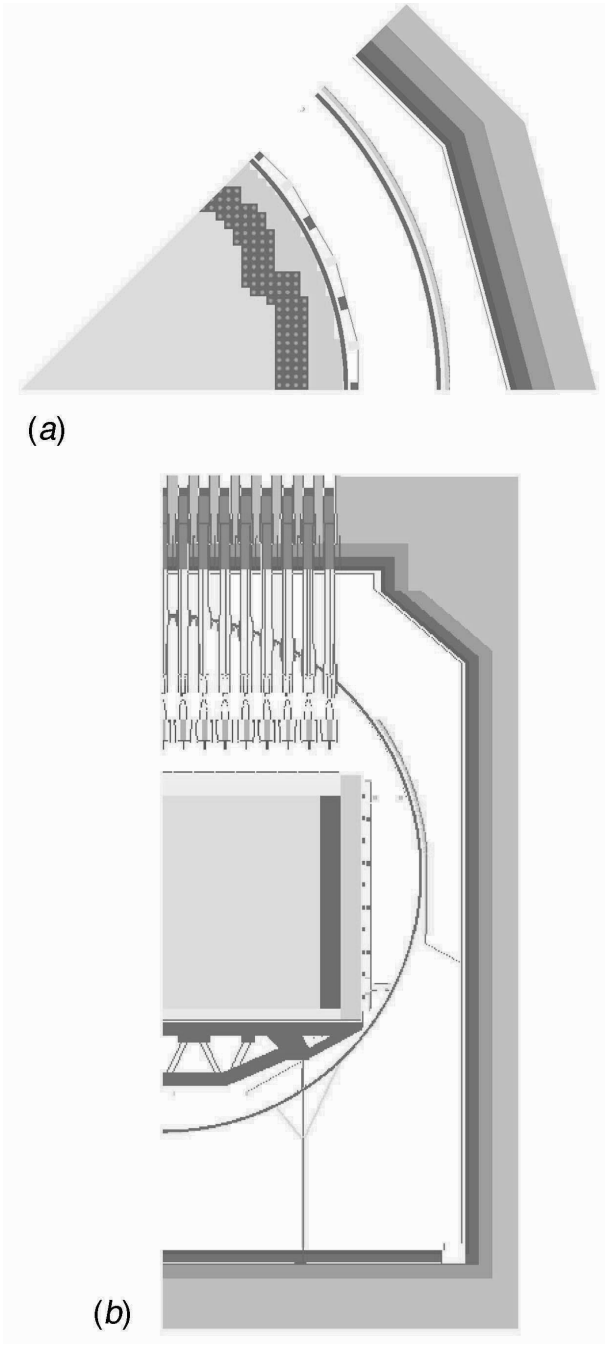

FIG. 1—*(a) Horizontal, and (b) vertical slices through the MCBEND model of a Magnox reactor.*

The use of the large-volume scoring method is justified because the method scored regionally averaged fluxes, thereby taking attenuation within components into account. For the massive outer regions of the biological shield, the fluxes calculated in this way are dominated by tracks within the high flux locations towards the inner parts of these regions. Provided the material within a region is uniform, the absence of scoring samples in the low flux parts of the region will not affect the suitability of the volume averaged flux for the prediction of total activation rates in that region.

Response Functions—Two-Group Approximation

While the calculations were performed using "continuous energy" nuclear data, the results of the calculations have been provided in two energy groups: thermal flux (ϕ_w—Westcott), and epithermal flux ($\phi_{E>0.5}$ eV). The activation rate of any particular species can be determined from these two fluxes using the following relationship:

$$R_{2g} \approx \phi_w \sigma_{2200} + \frac{\phi_{E>0.5eV} RI}{\ln(E_2/E_1)} \tag{1}$$

Where R_{2g} is the required activation rate determined using the two neutron energy group fluxes, σ_{2200} is the 2200 ms^{-1} cross section for the neutron reaction, and RI is its resonance integral. E_1 and E_2 are the upper and lower bounds for the resonance integral, which for this case were 14.6 MeV and 0.5 eV, respectively.

To assess the accuracy of this approximate approach, a study was undertaken in which activation rates were determined by two different methods—by the two-group method described above, and by direct Monte Carlo calculation using the IRDF-90 response functions supplied with MCBEND. The scoring region in this study was the external RPV insulation between the support skirt and RPV beneath the core at Trawsfynydd. This was chosen because the ratio of epithermal to thermal neutrons is high within this region and therefore the resonance integral contributions to the calculated reaction rates are also expected to be high. Because the lower bound of the resonance integral overlaps the 1/v response used to calculate ϕ_w, there is inevitably some "double accounting" of epithermal neutrons. This has its highest effect when the epithermal contribution to the calculated activation rates is most significant—i.e., when thermal neutron flux is low relative to epithermal flux.

Apart from this initial test, no attempt was made in these assessments to analyze responses for individual activation species. As well as increasing the cost of the work, such additional calculations would make the reported results highly dependent on material composition assumptions, which might later have to be revised.

The consistency of these calculations with the RPV dosimetry recommendations was confirmed by a successful comparison of the results from the modified models with those from the RPV dosimetry program. The displacement per atom (dpa) response function for iron was scored in the RPV and compared with previously reported values for each of the three regions of each Magnox station.

Results

For both fast neutron dpa (>1 keV) and thermal neutron dpa (<1 keV) good agreement was obtained between the predictions of the revised models and those reported previously. For example, the revised Sizewell A model gave agreement for RPV doses within 10 and 13 % for fast and thermal neutron dpa, respectively. Since the RPV dosimetry models were considered to be validated against plant measurements (where available), then the revised models are considered validated out as far as the RPV.

The Two-Group Flux Approximation

Table 1 presents the results of the comparison between activation rates calculated using the two-group approach outlined above and those calculated using direct Monte Carlo response function calculations. It can be seen that, as expected, the two-group approach generally over-predicts the calculated response, but in all cases, the two-group result is within 25 % of that calculated directly with MCBEND's response

TABLE 1—*The ratio of activation rates calculated using the two-group flux method to those calculated directly with MCBEND's response functions.*

Reaction	R_{2g}/R_{MC}
$^{6}Li(n,\alpha)$	1.24
$^{54}Fe(n,\gamma)$	1.21
$^{58}Ni(n,\gamma)$	1.23
$^{59}Co(n,\gamma)$	1.21
$^{62}Ni(n,\gamma)$	1.24
$^{93}Nb(n,\gamma)$	0.99
$^{107}Ag(n,\gamma)$	1.13
$^{133}Cs(n,\gamma)$	1.14
$^{150}Sm(n,\gamma)$	1.17
$^{151}Eu(n,\gamma)$	1.24
$^{153}Eu(n,\gamma)$	1.22
$^{165}Ho(n,\gamma)$	1.16

functions. This level of agreement is considered to be an adequate degree of accuracy for the purposes of the inventory assessments and direct Monte Carlo derivation of individual responses is not considered to be necessary.

Neutron Fluxes

Calculated neutron fluxes have now been obtained and reported for the following Magnox plants: Trawsfynydd, Hinkley Point A, Calder Hall/Chapelcross, Bradwell, and Sizewell A. These are not all reported here, since they are not of general interest. However, as an example, results for one of the power plants are provided in Fig. 2, which shows a vertical slice through the model with the local calculated thermal and epithermal neutron fluxes indicated. These fluxes are based on a nominal reactor power and can be scaled to an appropriate mean-over-life power if required.

Neutron Flux Attenuation Profiles in Bioshields

Figure 3 shows the attenuation of thermal and epithermal neutrons through the top, side, and bottom regions of the biological shield of a Magnox reactor. At very large distances into the shield, reliable data are not available and none are shown.

The attenuation profiles of epithermal neutrons within the concrete of the side and bottom biological shields show two distinct gradients. An initial region of rapid attenuation, up to ~0.5 m, and a less rapid exponential attenuation thereafter. This is indicative of some degree of spectral adjustment taking place up to ~0.5 m into the concrete. After ~0.2 m the thermal flux also follows an exponential attenuation. The ratio of thermal to epithermal neutrons remains approximately constant from about 0.5 m. Therefore, even though good statistical accuracy was not achieved throughout the whole thickness of the shield, it would be acceptable to extrapolate the available results to the outer edge of the shield provided there are no significant compositional or geometrical changes within the shield.

For the top region of the shield, however, because of the presence of steel structures (standpipes, control rods, and substantial reinforcement), there is a reduced and varying ratio of thermal to epithermal neutron fluxes. Indeed, the thermal neutron flux is considerably suppressed by the presence of the absorbing steelwork. Extrapolation to greater depths is not acceptable for this region.

Uncertainties

Within the Magnox RPV dosimetry program a rigorous uncertainty analysis has normally formed part of any particular dose assessment. For this work a fit-for-purpose approach has been adopted and an assessment based on judgment has been applied since, unlike the RPV dose assessments, the results are not of significant safety concern.

Within the envelope of the RPV, the models used have been validated against plant measurements and shown to give accurate RPV doses to within ~25 %. Therefore an uncertainty of this level has been adopted for all components within this envelope. For components between the RPVs and the inner surface

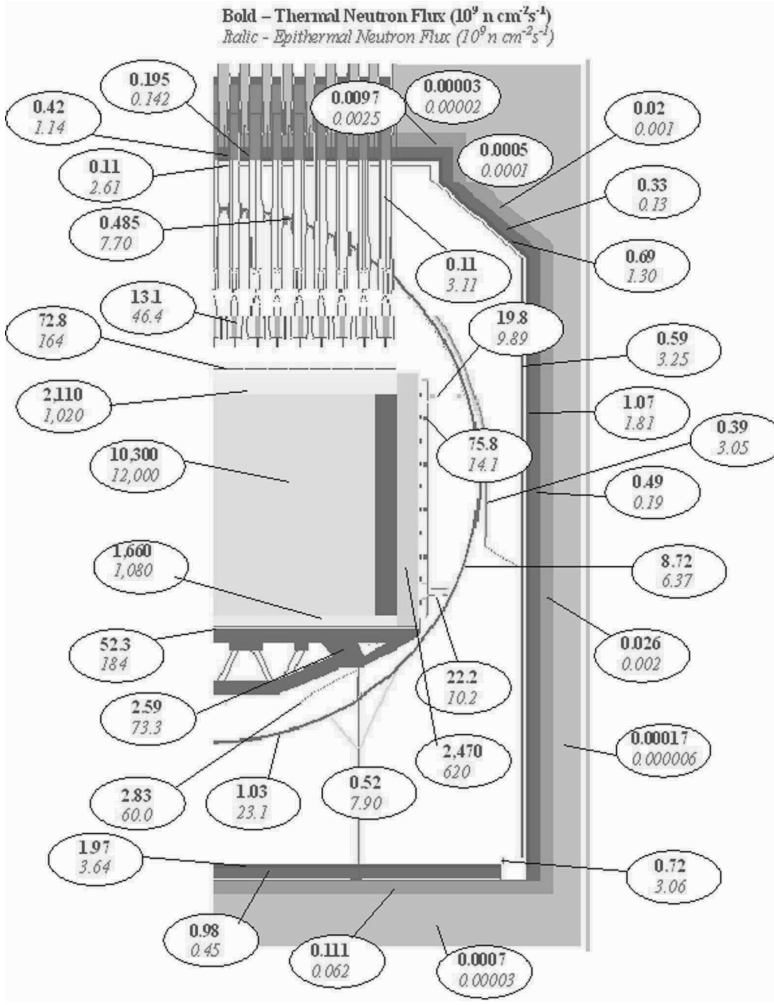

FIG. 2—*Vertical slice through MCBEND model of a Magnox reactor showing calculated thermal and epithermal neutron fluxes.*

of the biological shields, little further attenuation occurs and although this is beyond the validation envelope of the models, this simple extrapolation is not judged to introduce major calculational errors. An uncertainty of 50 % has been adopted for the fluxes in these components. Within the biological shield, the picture is less clear and the uncertainty on neutron flux attenuation rates is dominated by lack of precise knowledge of reinforcement, embedded steelwork and water content. Furthermore, the nuclear data on which the calculations are based have not been validated for concrete as they have for steel and graphite. For these reasons, an uncertainty of a factor of two has been adopted for the inner surface of the biological shield, rising to a factor of five towards the outside surface.

Conclusions

Assessments of the neutron fluxes within six of the eleven UK Magnox plants have been undertaken. Fluxes have been calculated throughout the reactor structures using the Monte Carlo code MCBEND and

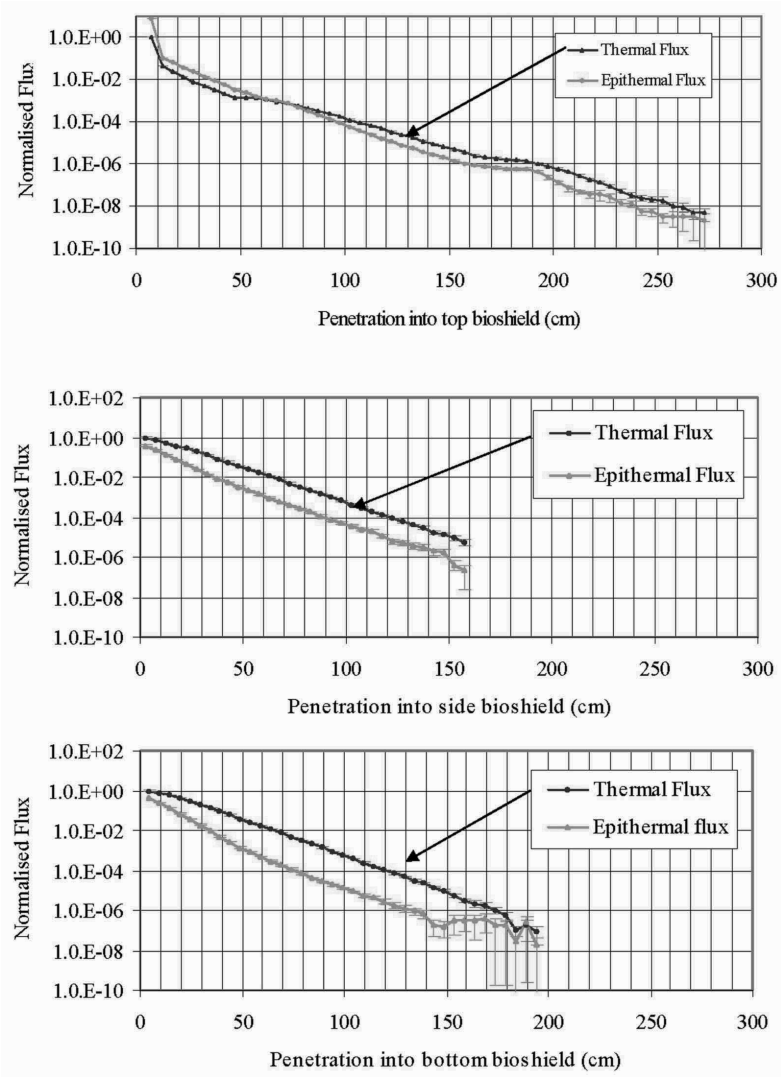

FIG. 3—*Neutron attenuation through the top, side and bottom biological shields of a Magnox reactor.*

reported in two energy groups, suitable for the calculation of the radioactive inventories of these power plants. This two-group approximation has been shown to be adequate for this purpose, with calculated activation rates within 25 % of those calculated using a direct Monte Carlo calculation of reaction responses. Good agreement has been obtained with previously-calculated RPV doses, so that the models can be considered to be validated up to the pressure vessel envelope. This has reduced calculational uncertainty and gives confidence in the results. Beyond the inner surface of the biological shields, the models cannot be considered as validated and larger uncertainties are applied.

Acknowledgment

Production of this paper was supported by the UK Health and Safety Executive. It is published with the permission of British Nuclear Group.

References

[1] Mossop, J. R., Thornton, D. A., and Lewis, T. A., "Validation of Neutron Transport Calculations on Magnox Power Plant," *Proceedings of the 8th International Symposium on Reactor Dosimetry*, ASTM Special Publication 1228, 1994, pp. 384–391.

[2] Lewis, T. A., Hopper, S. E., Mossop, J. R., and Thornton, D. A., "The Prediction of Fast and Thermal Neutron Dose Rates for the Pressure Vessels of Magnox Power Plant," *Proceedings of the 9th International Symposium on Reactor Dosimetry*, World Scientific, 1996, pp. 600–607.

[3] Lewis, T. A., and Thornton, D. A., "A Decade of Dosimetry for Magnox Reactor Plant," *Proceedings of the 11th International Symposium on Reactor Dosimetry*, World Scientific, 2003, pp. 269–277.

[4] Chucas, S. J., "MCBEND, A Monte Carlo Program for General Radiation Transport Solutions," ANSWERS Software Service, Serco Assurance, ANSWERS/MCBEND (94) 15.

Journal of ASTM International, Vol. 3, No. 3
Paper ID JAI13425
Available online at www.astm.org

Tom Serén[1] *and Frej Wasastjerna*[2]

Extensive Revision of the Kernel-Based PREVIEW Program and Its Input Data

ABSTRACT: The kernel-based PREVIEW program, which calculates fluences, fluence rates, reaction and damage rates, etc. at a few important out-of-core locations in the Loviisa VVER-440 reactors has been extensively revised. New location-specific dosimetry cross sections based on the newly released IRDF-2002 library have been developed. A few cross-section condensation codes are tried and compared. Generally the results are in good agreement. Small differences may be attributable to the use of single precision and to different representations of the weighting spectrum. Also, some codes use the basic ENDF-format data directly while others use processed data with reduced precision.

KEYWORDS: kernel methods, PWR surveillance dosimetry, VVER-440 reactors, cross sections

Introduction

The kernel-based PREVIEW (PREssure Vessel Irradiation Evaluation Working) program has been extensively and successfully used as a convenient tool in the surveillance dosimetry for the Loviisa VVER-440 reactors [1,2]. It calculates many quantities of interest, such as fluences, reaction rates, and activities, taking into account the detailed local irradiation history. An adjustment library based on a large number of activation measurements and spectrum adjustments at different locations has previously been developed [3]. A major revision of the code has been carried out and its database of dosimetry and damage cross sections is being updated. The tools for updating the cross sections have been developed and have been applied to the newly released IRDF-2002 library [4]. The old cross sections were common to all locations and mainly based on IRDF-90.

The dosimetry and damage cross sections have been separated from the main kernel library. This facilitates the use of dedicated location-specific cross sections.

The processing of the cross sections provided an opportunity to compare the results of different cross section processing codes as well as the influence of different weighting spectra.

Revision of the Code

The user input has been extensively revised and simplified. The output formats have also been revised and more complete information on the 47-group (BUGLE-80) neutron spectra is given. In addition to group fluxes, fluxes per unit energy and per unit lethargy are also printed in separate columns. To facilitate the editing and modification of the kernel file it is now read only in text form, since disk capacity and speed is no longer an issue. Some features of the Fortran 90 standard (such as date and time representation) have replaced previously system-dependent code so that it should now be completely portable between compilers and operating systems. Provisions have also been made to accommodate a larger number of fuel enrichment types, which have been taken into use during recent years.

The dosimetry and damage cross sections were previously part of the large kernel library, which made it tedious to make any changes to the cross sections. Thus common condensed cross sections in the 47-group BUGLE-80 structure were used for all radial locations (surveillance position, reactor pressure

Manuscript received June 20, 2005; accepted for publication September 29, 2005; published online December 2005. Presented at ASTM Symposium on Reactor Dosimetry, 12th International Symposium on 8–13 May 2005 in Gatlinburg, TN; D. W. Vehar, D. M. Gilliam, and J. M. Adams, Guest Editors.

[1] Senior Research Scientist, VTT Technical Research Centre of Finland, P.O.B. 1608, FI-02044 VTT, Finland.
[2] Senior Research Scientist, VTT Technical Research Centre of Finland, P.O.B. 1604, FI-02044 VTT, Finland.

vessel (RPV) inner surface, RPV quarter-thickness, and ex-vessel cavity). This is somewhat questionable if the best possible accuracy is desired. The dosimetry and damage cross sections are now read in from separate dedicated files, which are much easier to adapt to different locations and configurations (e.g., cadmium or gadolinium covers, different sets of reactions, etc.).

The adjustment library [3] has also been moved from the code itself into a separate file for easier modification. The new cross section data will be applied in a renewed adjustment for the ex-vessel cavity, based on extensive measurements in 1998–1999 [5]. A slightly less ambitious ex-vessel irradiation was carried out in Loviisa 2 in 2002–2003 and a detailed comparison will reveal whether there is a need to use different adjustment libraries for the two units. Some recent surveillance chain irradiations will also provide better data for height coordinates above the active core region, where PREVIEW yields bad results, probably because the nodewise axial division of the fuel region (ten nodes) is inaccurate in the presence of large and varying axial gradients.

Creating Location-Specific Cross-Section Files

Weighting Spectra

Weighting spectra for all the radial locations of interest have been constructed based on typical 47-group spectra calculated with PREVIEW and applying the adjustment library [3]. For the cavity location, the adjusted spectra from the 1998–1999 irradiation in Loviisa 1 [5] were used directly. A least-squares spline approximation on log-log scale [6] was applied to expand the 47-group spectra to a point representation at the 641 SAND-II group boundaries, with Maxwellian- and Watt-type extensions at the lower and upper end, respectively. To some extent this procedure smooths out sharp features in the spectrum, but it is still a better approximation than conventional Maxwell-1/E-Watt weighting spectra, which ignore any irregularities inevitably present in most real-world spectra. Furthermore, very sharp features in the calculated spectrum can be artifacts of narrow energy groups and introduce questionable irregularities in the condensed cross sections, especially if they occur close to group boundaries.

Special attention was paid to the choice of effective neutron temperatures in the thermal region. The effective neutron temperatures at the four radial locations were evaluated by P. Siltanen of Fortum Nuclear Services (private communication). As pointed out by Lamarsh [7], the Maxwellian representation with effective neutron temperature is only a rough approximation in the presence of absorbers, but it should be adequate for the present purpose, especially since thermal neutrons are not very important from the standpoint of neutron damage. The four weighting spectra are shown in Fig. 1 for the surveillance chain (SC), RPV inner surface (PVI), RPV quarter-thickness (PV T/4), and cavity. The respective neutron temperatures and joining energies (spline-Maxwellian) are given in Table 1. The presence of absorbers tends to raise the effective neutron temperature. Thus the temperature is much higher at the PV T/4 location than elsewhere.

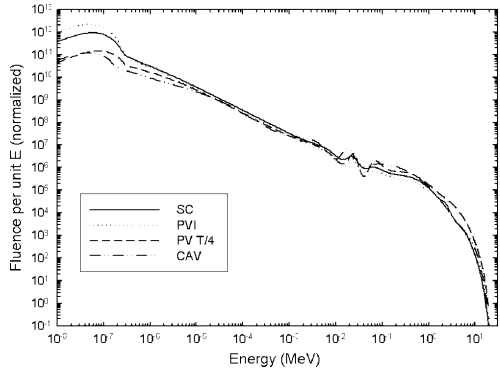

FIG. 1—*Normalized weighting spectra for four radial locations.*

TABLE 1—*Effective neutron temperatures and joining energies between Maxwellian and spline curve for the weighting spectra displayed in Fig. 1.*

Location	Temperature (K)	Joining point (eV)
SC	667	0.28
PVI	592	0.30
PV T/4	915	0.32
Cavity	560	0.19

Cross-Section Processing

These spectra have been applied to selected cross sections from the IRDF-2002 library to produce location-specific 47-group (BUGLE-80) cross-section files. As a first step, a "master library" based on IRDF-2002 was created for use with codes which do not use the ENDF-6 data format in IRDF-2002 (such as SAND-II and LSL-M2). The auxiliary programs CVXS and CVCT from the LSL-M2 package [8] were used for this purpose. The cross-section covariance processing code CVCT cannot handle the LB=8 format used for some reactions. Thus, some reactions were processed by P. Griffin at Sandia National Laboratories using the NJOY code.

The conversion of the covariance information in IRDF-2002 to the format used by LSL-M2 (a group-wise representation consisting of standard deviations followed by a correlation matrix) turned out to be problematic in some cases [notably some Ti reactions and the $^{55}Mn(n,\gamma)$ reaction, all with LB=8 uncertainty components]. These issues are being addressed by the IRDF-2002 team (P. Griffin, private communication). Because of these problems, the "master library" is not yet complete, but can well be utilized if uncertainty information is not needed or if the problematic reactions are not used. It also contains cross sections for a few reactions not included in IRDF-2002, however, without uncertainty information. The library is available from the authors on request.

Most of the reactions of interest in light water reactor (LWR) surveillance do not show very significant differences compared to IRDF-90. The most important reaction, $^{54}Fe(n,p)$, has in fact the same cross section (based on ENDF/B-VI) in both libraries. However, the $^{58}Ni(n,p)$ cross section (based on a new evaluation by K. Zolotarev, Obninsk) differs significantly in shape from the IRDF-90 cross section, especially near 5 MeV (see Fig. 2). This may be of importance for the Loviisa surveillance dosimetry since Fe-Ni plates have been used for individual specimen fluence determination for a number of years.

An important task for the near future is to establish correction factors for comparison between fluence values obtained with the old and new versions of the dosimetry cross-section libraries. This comparison will be carried out for the next surveillance chain under investigation. The results of the comparison will be utilized in a planned summary of all the dosimetry results for the Loviisa 1 post-annealing surveillance program comprising 12 surveillance chains with different irradiation-annealing sequences. Preliminary investigations indicate a slightly smaller response in a typical LWR spectrum for the new cross section (about 1 %).

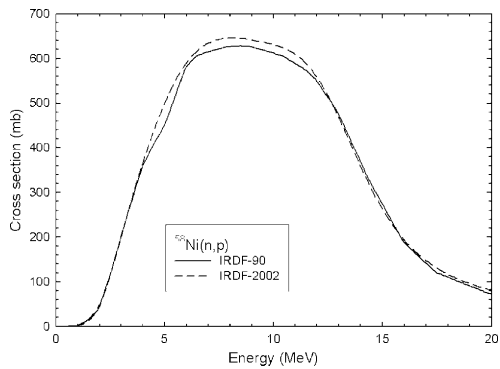

FIG. 2—*The $^{58}Ni(n,p)$ cross section from IRDF-90 and IRDF-2002.*

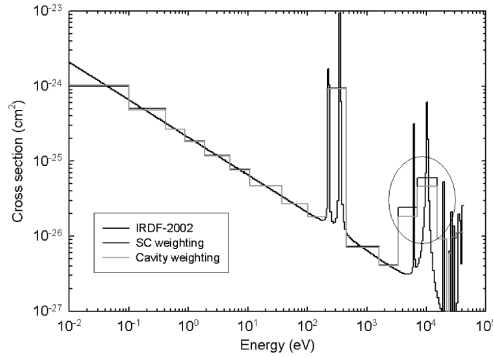

FIG. 3—*Comparison of $^{58}Fe(n,\gamma)$ BUGLE-80 group cross sections condensed with FLXPRO using surveillance chain (SC) and cavity weighting spectra. The most important differences are in the encircled region.*

The cross-section processing provided an opportunity to check the influence of different weighting spectra and to test and compare different codes for cross-section condensation, such as FLXPRO from the LSL-M2 package [8] and X333 from the NMF-90 package [9]. The JANIS software package [10] and the GROUPIE code from the PREPRO package [11] can perform similar tasks, but have not been used so far.

The Influence of Different Weighting Spectra

The effect of different weighting spectra on the condensed 47-group cross sections was tested for several reactions: $^{54}Fe(n,p)$, $^{58}Ni(n,p)$, $^{93}Nb(n,n')$, $^{58}Fe(n,\gamma)$, $^{59}Co(n,\gamma)$ and $^{93}Nb(n,\gamma)$. The effects on the total responses were generally negligible: about 0.1 % for the fast-neutron reactions and 1 % for the thermal-neutron reactions. For the fast-neutron reactions significant differences in the group cross sections were found only in the energy regions at or below the threshold where the cross sections are very small (several decades below the maximum values). For the (n,γ) reactions somewhat more significant differences were found in the vicinity of large resonances, as illustrated in Fig. 3, where the condensed $^{58}Fe(n,\gamma)$ cross sections in the resonance region with two different weighting spectra are shown. If all reactions with similar cross sections show the same differences it may have important consequences, e.g., for such applications as beam characterization for Boron Neutron Capture Therapy (BNCT) [12], where the epithermal region is of main interest. In those cases the correct choice of weighting spectrum is obviously important.

One problem in coarse-group neutron spectrum adjustment, not very often discussed to our knowledge, is whether the same group cross sections can be used for the adjusted spectrum as for the input spectrum. This, of course, is an argument for using a sufficiently large number of energy groups even in cases where a coarser group structure would otherwise be sufficient (such as damage fluence determinations). E.g., in the 20-group example adjustments in LSL-M2 [8] this might become an issue. In such cases one would have to resort to iterative procedures, which are both tedious and not very sound from the theoretical point of view. Fortunately it seems that minor changes in the weighting spectrum do not have a significant impact when using the 47-group BUGLE-80 structure.

Comparison between Different Processing Codes

In order to find out possible differences in the group cross sections produced with different codes and weighting spectrum representations two processing codes (FLXPRO and X333) and three reactions were investigated [$^{54}Fe(n,p)$, $^{58}Ni(n,p)$, and $^{58}Fe(n,\gamma)$]. Also, the effect of using different weighting spectrum representations in FLXPRO was investigated. In X333 the weighting spectrum is always given as a differential histogram representation in the 640-group SAND-II structure. In FLXPRO the weighting spectrum can be given in three formats: histogram with integral fluences (keyword *I, default), histogram with differential fluences (keyword *D), and point differential fluences at N + 1 group boundaries (keyword

*P). The group structure is in principle free, but it must be the same as for the cross sections, i.e., in this case, the SAND-II structure. X333 reads the cross-section data directly from IRDF-2002 in the ENDF-6 format, while FLXPRO uses the processed "master library." As an additional check the $^{58}Fe(n,\gamma)$ cross section was condensed using an Excel spreadsheet and extending the weighting spectrum and cross section down to 10^{-5} eV (the lowest BUGLE-80 group boundary). The results were in good agreement, also for the lowest group. Both FLXPRO and X333 ignore the energy region between 10^{-5} and 10^{-4} eV (the lowest SAND-II group boundary), but this does not seem to have any significant influence on the condensed cross section in the lowest BUGLE-80 group.

In principle, the *P option should give the best accuracy (trapezoid integration versus simple summing). However, no differences were observed between the three representations. Thus the SAND-II group structure seems to be fine enough for simple integration based on groupwise summing. On the other hand, omission of the correct keyword may lead to grossly incorrect results. This happened in the early stages of this exercise, when the *P keyword was omitted by mistake and FLXPRO assumed a *I representation. In that case the $^{58}Fe(n,\gamma)$ cross section in the lowest group was in error by +64%.

The results of X333 and FLXPRO were in good agreement for all reactions, but not identical. This may be due to the limited precision (three decimal places) in the processed "master library." Thus it would be advisable to increase the precision of the output from CVXS and to use double precision in the calculations.

Other Basic Data and Auxiliary Codes

IRDF-2002 also contains recommended values for basic nuclear data such as half lives and gamma emission probabilities. The dosimetry cross sections in PREVIEW are always accompanied by the decay constant of the reaction product. All these have been checked to conform to the recommended values in IRDF-2002.

The COVER code from the LSL-M2 package, which calculates attenuation factors for covers of different materials and thicknesses in the 640 SAND-II groups, has been extended to take into account various degrees of anisotropy (the original code assumed a parallel beam). Even this improved treatment of cover effects is not sufficient in all cases. In highly epithermal neutron fields one may obtain *higher* reaction rates with Cd cover than without for some reactions due to downscatter of neutrons into energy groups with strong resonances. The situations with and without Cd cover should therefore be modeled separately in the transport calculations.

A program has also been developed to calculate energy-dependent self-shielding corrections for both foil and wire geometries and for various degrees of anisotropy. Some formulas for these as well as cover corrections can be found in Appendix II of the IRDF-2002 documentation [4]. Obviously the simplified treatment of self- and cover shielding found, e.g., in ASTM standard E 262 is not applicable in this context. Both programs are available from the authors on request.

Self- and cover-shielded cross sections in PREVIEW are treated as separate reactions.

Conclusions

An extensive revision of the kernel-based PREVIEW code used for surveillance fluence evaluations in the Loviisa VVER-440 reactors has been carried out. New dosimetry cross sections from the IRDF-2002 library have been incorporated into separate location-specific files. Some minor problems with the covariances in IRDF-2002 were detected. The impact of the new cross sections on the fluence determinations for the Loviisa reactors will shortly be investigated. Two different cross-section processing codes were compared. No significant differences between group cross sections processed with different codes were detected. The effect of different weighting spectra was also investigated. Generally, the differences were small, with the exception of resonance regions in thermal-neutron reactions and are of main importance for other applications than LWR surveillance dosimetry (e.g., BNCT beam characterization).

Acknowledgments

The authors acknowledge the contribution of Pertti Siltanen of Fortum Nuclear Services for his evaluation of the effective neutron temperatures. Petri Kotiluoto assisted in the application of the X333 code. This work was performed within the INSEL project of the national SAFIR research programme.

References

[1] Wasastjerna, F., "PREVIEW—A Fast Kernel-based Program for Calculation of Pressure Vessel Irradiation," *ANS Topical Meeting on New Horizons in Radiation Protection and Shielding*, Pasco, Washington, April 26–May 1, 1992.

[2] Baers, L. B. and Serén, T. O., "Revision of Neutron Dosimetry for the Loviisa VVER-440 Reactors: Principles and Application," *8th ASTM-Euratom Symposium on Reactor Dosimetry*, Vail, Colorado, August 29-September 3, 1993, ASTM STP 1228, Philadelphia, 1994, pp. 45–54.

[3] Serén, T. O., "Development of an Adjustment Library for the Kernel-based PREVIEW Program," *9th International Symposium on Reactor Dosimetry*, Prague, Czech Republic, 2–6 September 1996, World Scientific, Singapore, 1998, pp. 278–285.

[4] International Reactor Dosimetry File - 2002 (IRDF-2002, IAEA Nuclear Data Section, Vienna 2005.

[5] Serén, T. O., Hógel, J. and Voorbraak, W. P., "Post-Annealing Ex-Vessel Dosimetry at Loviisa 1—An International Exercise," *11th International Symposium on Reactor Dosimetry*, Brussels, Belgium, 18–23 August 2002, World Scientific, Singapore, 2003, pp. 18–25.

[6] Thijsse, B. J., Hollanders, M. A. and Hendrikse, J., "A Practical Algorithm for Least-Squares Spline Approximation of Data Containing Noise," *Comput. Phys.* 12, 393–399 (1998).

[7] Lamarsh, J. R., *Nuclear Reactor Theory*, edited by H. Goldstein, Addison-Wesley, Reading, Massachusetts, 1966, pp. 247–249.

[8] Stallmann, F. W.," *LSL-M2: A Computer Program for Least-Squares Logarithmic Adjustment of Neutron Spectra," NUREG/CR-4349 (ORNL/TM-9933)*, Oak Ridge National Laboratory, March 1986.

[9] Szondi, E. J. and Nolthenius, H. J., *User's Guide to the Cross Section Processing Code X333, BME-NTI 222/95*, Technical University of Budapest, May 1995.

[10] Soppera, N. et al., *JANIS User's Guide*, OECD Nuclear Energy Agency, Paris, July 2004.

[11] Cullen, D. E., http://www-nds.iaea.org/ndspub/endf/prepro/DOCUMENT/PDF/Groupie.pdf

[12] Serén, T. O. et al., "Neutron Beam Characterization at the Finnish BNCT Facility-Measurements and Calculations" *10th International Symposium on Reactor Dosimetry*, Osaka, Japan, Sept. 12–17, 1999, ASTM STP 1398, West Conshohocken, Pennsylvania, 2001.

Journal of ASTM International, Vol. 4, No. 2
Paper ID JAI100915
Available online at www.astm.org

M. H. Sparks,[1] *W. W. Sallee,*[1] *and T. M. Flanders*[1]

Investigation of Radiation Transport Modeling Trends in the WSMR Fast Burst Reactor Environments

ABSTRACT: Radiation transport calculations provide the backbone for the spectrum characterization used to support experimenters at research reactors. The radiation transport calculations provide *a priori* neutron spectra used in least squares spectrum adjustment. In addition, calculations are often the sole source of baseline neutron spectra data when an experimental test object substantially perturbs the free-field spectrum. It is crucial that analysts provide high fidelity uncertainty quantification for the spectrum calculations. This is an investigation of systematic trends as the distance to the source is varied in calculated spectra at a fast burst facility. A comparison of ratios is designed to highlight trends in the C/E ratios that may shed light on deficiencies in the transport cross sections or sensitivities to the details of the facility modeling. Initial comparisons of the latest IRDF-2002 [1] dosimetry cross section library to the SNL RML [2] cross section library have been made and are discussed.

KEYWORDS: neutron spectra, monte carlo, cross section, spectrum adjustment, transport cross section

Introduction

There are several sources of uncertainty in a spectrum calculation including: (1) Monte Carlo statistical sampling and discrete ordinates numerical convergence, (2) modeling uncertainties, e.g., material densities and dimensions, and (3) underlying nuclear data, e.g., transport cross sections. The first uncertainty source, statistical sampling and numerical convergence, can be quantified by estimates routinely provided by the transport codes. The second source of uncertainty can be probed with sensitivity analysis tools. The status of the third source of uncertainty, the underlying nuclear data, is improving with respect to dosimetry reactions, where energy-dependent covariance matrices are available, but little progress has been made in getting quantified uncertainties for transport cross sections or in propagating the transport uncertainties through complex geometries.

This paper investigates the systematic trends that can be seen in calculated spectra at a fast burst reactor facility. At the White Sands Missile Range (WSMR) MoLLY-G fast burst reactor, experimenters can get a wide range of fast neutron spectra by varying the experimental location and without perturbing the environment. These locations are relative to the core center line from a close, newly measured, 15.24 cm (6 in.) position out to a distant 182.88 cm (72 in.) position. Fine-grouped, energy-dependent calculated neutron spectra have been produced using MCNP5 [3], a Monte Carlo code, and the ENDF-B-VI [4] cross sections. Integral metrics, spectrum-averaged cross sections for dosimetry-quality reactions, have been measured at five experimenter locations. A comparison of ratios is designed to highlight trends in the C/E ratios that may shed light on deficiencies in the transport cross sections or sensitivities to the details of the facility modeling. Initial comparisons of the latest IRDF-2002 dosimetry cross section library to the SNL RML cross section library have been made and are discussed.

Calculations

The WSMR MoLLY-G [5] is used for nuclear research, development, testing, and evaluation. It is an unmoderated, unreflected, bare critical assembly. The exposure cell is a 15.2 m by 15.2 m (50 ft by 50 ft)

Manuscript received June 20, 2005; accepted for publication January 19, 2007; published online March 2007. Presented at ASTM Symposium on Reacter Dosimetry, 12th International Symposium on 8–13 May 2005 in Gatlinburg, TN; D. W. Vehar, D. M. Gilliam, and J. M. Adams, Guest Editors.
[1] Reactor Physics Division, SVAD, White Sands Missile Range, White Sands, NM, 88002-5158, OPSEC 7-11-2006.

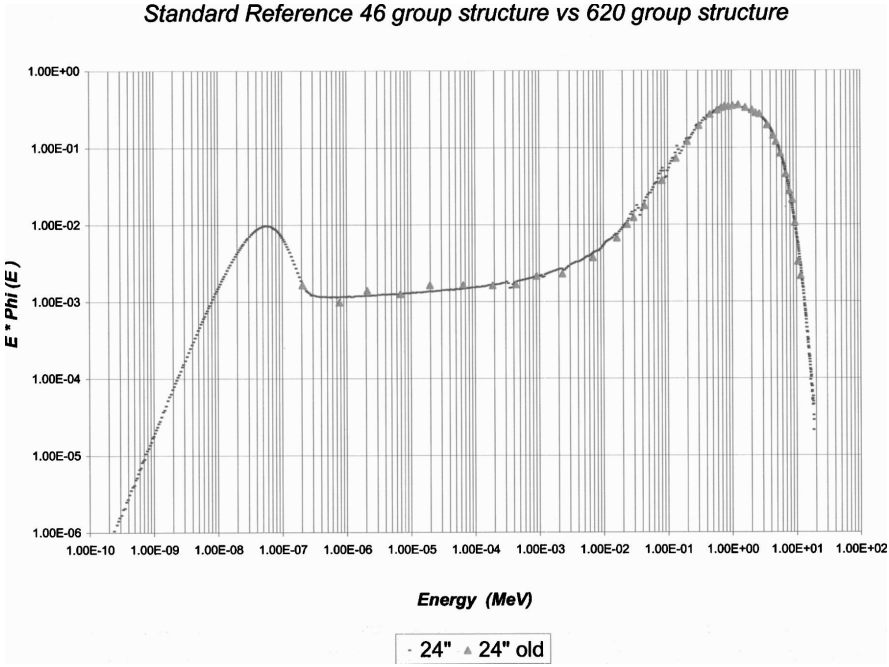

FIG. 1—*Standard reference 46 group structure versus 620 group structure.*

by 6.1 m (20 ft) concrete room lined with gypsum wall-board and borated gypsum wall-board. The source is a slightly degraded fission spectrum with wall return from the exposure cell.

Historically, calculations were performed using the DABL-69 [6] broad group structure. A new experimental position, 15.24 cm (6 in.) is being developed. This location provides a challenge to experimental measurements due to the proximity to the source. In order to obtain detailed spectral information, ring detectors were used in all calculations and run in the SAND-II [7] 640 group structure. The lower bound for this series of calculations has been set at 1E-10 MeV and the upper bound at 18 MeV, resulting in the older 620 group SAND structure. Over 2E9 source particles were used for each calculation.

In order to baseline the model, the spectral shape was first calculated at 60.96 cm (24 in.). The 60.96 cm (24 in.) position is the standard location and is very well known through extensive calculations and experimental measurement. Figure 1 is a comparison of known [8] 60.96 cm (24 in.) MoLLY-G spectra in 46 groups to the new 620 groups. Fractional standard deviations on individual group fluxes of the calculations, between 10 MeV and thermal energies, are $\sim$1 % and generally much less for well sampled regions.

An inspection of Fig. 1 shows some interesting structure from 10–100 keV. The structures were tentatively identified as correlating with resonance structures in the aluminum cross section. Aluminum is present in the shroud surrounding the reactor. The identification has been confirmed by artificially removing the aluminum cross sections and repeating the calculation.

As previously published, the environment is a two-component spectrum. The first component is the leakage spectrum produced by the core. The leakage spectrum is a slightly degraded fission spectrum and largely responsible for the general shape of the spectrum above about 1 keV. Below about 1 keV is the spectrum due to wall-return neutrons. This part of the spectrum is roughly constant throughout the exposure cell. The first component obeys the $1/R^2$ law of a point source for a source-to-detector distance which is large relative to the size of the core. The further the detector position is from the source the larger the fraction of wall return neutrons in the spectrum.

A re-evaluation of previously calculated/measured test locations has been initiated. Five different locations have been calculated using over 2E9 source particles for the 620 group study. Other positions

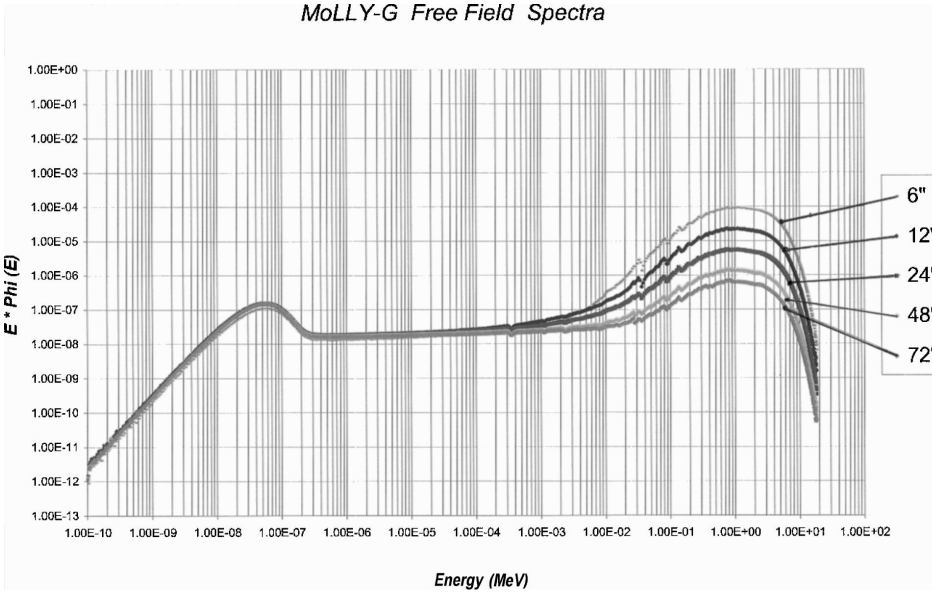

FIG. 2—*MoLLY-G free-field spectra.*

were selected based on a diversity of spectra readily available from previous calculations and measurements rigorously analyzed. The additional positions are 30.48 cm (12 in.), 121.92 cm (48 in.), and 182.88 cm (72 in.). These spectra are shown in Fig. 2.

Experiment/Measurements

Five measurements have been selected for this analysis. The measurements were selected based on the quality of the measurement and the regularity in the distance from the MoLLY-G. The chosen activities are a subset of collected data. The list of reactions represents data known to 6 % or better. Normalization is a critical issue in this study as the measurements were fielded over the last decade with different integrated power. Ni, present in every measurement (<4 % uncertainty), has been chosen to normalize all measurements and calculated activities. The data are presented as the ratio of Ni foil activity as measured or calculated from the MCNP5 runs.

TABLE 1—*Activities Derived from Transport Calculations. Reactions/nucleus/fission neutron in core.*

Reaction	Location (cm)				
	15.24	30.48	60.96	121.92	182.88
Sc45(n,g)	7.124E-30	7.669E-30	6.99E-30	6.749E-30	6.563E-30
Sc45(n,g)[a]	2.336E-30	2.375E-30	4.162E-31	2.85E-31	2.47E-31
Mn56(n,g)[a]	1.308E-30	1.339E-30	4.149E-30	3.150E-31	2.812E-31
Np237(n,f)[b]	2.605E-28	2.653E-28	1.526E-29	3.887E-30	1.797E-30
In115(n,n)[a]	3.084E-29	3.163E-29	1.788E-30	4.507E-31	2.055E-31
Ti47(n,p)	2.811E-30	2.903E-30	1.616E-31	4.029E-32	1.815E-32
Ni58(n,p)	1.639E-29	1.697E-29	9.412E-31	2.338E-31	1.049E-31
Fe56(n,p)	1.677E-31	1.751E-31	9.549E-33	2.340E-33	1.031E-33
Mg24(n,p)	2.560E-31	2.674E-31	1.456E-32	3.570E-33	1.570E-33
Fluence(n/cm^2)	2.519E-4	2.551E-4	1.586E-5	4.493E-6	2.377E-6

[a]Cd cover.

[b]Cd-B cover.

Note: Values in Table 1 are spectrum average cross section * total fluence.

TABLE 2—*Calculated Activities from MCNP5 Spectra. (Normalized to Ni).*

	Location (cm)				
Reaction	15.24	30.48	60.96	121.92	182.88
Sc45(n,g)	0.43	0.45	7.43	28.86	62.57
Sc45(n,g)[a]	0.14	0.14	0.44	1.22	2.35
Mn56(n,g)[a]	0.08	0.08	0.44	1.35	2.68
Np237(n,f)[b]	15.89	15.63	16.21	16.63	17.13
In115(n,n)[a]	1.88	1.86	1.90	1.93	1.96
Ti47(n,p)	0.17	0.17	0.17	0.17	0.17
Ni58(n,p)	1.00	1.00	1.00	1.00	1.00
Fe56(n,p)	0.01	0.01	0.01	0.01	0.01
Mg24(n,p)	0.02	0.02	0.02	0.02	0.02

[a]Cd cover.
[b]Cd-B cover.

To compare calculated to measured spectra, a metric must be chosen. For this work, activity is calculated from the transport calculations and compared to the measured activities. This removes ambiguity introduced by the adjustment technique used to produce a "measured" spectrum from the foil activities. Spectral activity is presented in Table 1 by folding the spectrum average cross section with total fluence (MCNP) for each foil per location. Cover adjustments were made where needed. The cross section data are from the SNL RML version 1 dosimetry library. The derived activities were then normalized to the Ni calculated activity and presented in Table 2. Table 3 is a list of ratio of activities, normalized calculated activity to normalized measured activity.

SNL RML/ISRD-2002 Ratios

The dosimetry cross sections from the SNL RML Compendium are compared to the recently released IRDF-2002 (Table 4). This is a preliminary table which demonstrates an indication of how the spectral adjustment will change with the progression to the new library and does not currently include the reactions with Cd or Cd-B covers. Most activities remain the same. In this list, only Fe56(n,p) and Ti46(n,p) change significantly.

Solid State Device Damage Parameters

Devices exposed for hardness assurance testing require damage equivalence multipliers which are derived from the spectral parameters and folded with the reported sulfur fluences. The Si and GaAs damage cross sections are published in ASTM Standard Practice for Characterizing Neutron Energy Fluence Spectra in Terms of an Equivalent Monoenergetic Neutron Fluence for Radiation-Hardness Testing of Electronics (E 722-02). The new calculations indicate good agreement with previously documented [10] calculations based on broad group evaluations. The broad group evaluations include calculations dating back to ENDF-B IV. Table 5 lists the damage parameters.

TABLE 3—*Ratio of Calculated/Measured Activities. (Normalized to Ni).*

	Location (cm)				
Reaction	15.24	30.48	60.96	121.92	182.88
Sc45(n,g)	1.56	…	2.52	3.00	2.98
Sc45(n,g)[a]	…	0.66	0.95	1.24	1.42
Mn56(n,g)[a]	0.64	0.42	0.76	1.19	1.22
Np237(n,f)[b]	…	1.10	1.08	1.12	1.12
In115(n,n)[a]	…	0.96	0.96	0.97	0.99
Ti47(n,p)	1.00	0.98	0.98	1.00	1.01
Fe56(n,p)	0.96	1.04	1.00	0.99	0.98
Mg24(n,p)	1.13	1.08	1.12	1.09	1.08

[a]Cd cover.
[b]Cd-B cover.

TABLE 4—*Spectrum Average Cross Section Comparison. IRDR-2002/SNLRML-1.*

	Location (cm)				
Reaction	15.24	30.48	60.96	121.92	182.88
Ni58(n,p)					
Sc45(n,g)	0.99	0.99	1.01	1.01	1.01
Au197(n,g)	1.00	1.00	1.00	1.00	1.00
Mn55(n,g)	1.00	1.00	1.00	1.00	1.00
U235(n,f)	1.00	1.00	1.00	1.00	1.00
Pu239(n,f)	1.00	1.00	1.00	1.00	1.00
Np237(n,f)	1.02	1.02	1.02	1.02	1.02
U238(n,f)	1.01	1.01	1.01	1.01	1.01
In115(n,n)	1.01	1.01	1.01	1.01	1.01
Ti47(n,p)	1.00	1.00	1.00	1.00	1.00
Fe54(n,p)	1.00	1.00	1.00	1.00	1.00
Fe56(n,p)	1.08	1.08	1.08	1.08	1.08
Ti46(n,p)	1.12	1.12	1.12	1.12	1.12
Mg24(n,p)	1.00	1.00	0.99	1.00	1.00
Al27(n,a)	1.01	1.01	1.01	1.01	1.01

TABLE 5—*Solid State Damage Parameters.*

	Location (cm)				
Parameter	15.24	30.48	60.96	121.92	182.88
Φ total[a]	2.52E-4	2.55E-4	1.59E-5	4.49E-6	2.38E-6
Φ>3 MeV[a]	3.29E-5	3.42E-5	1.89E-6	4.66E-7	2.08E-7
Shape Index	7.649	7.469	8.406	9.638	11.45
Shape Index (*46 group*)	7.864	7.763	8.208	9.153	10.44
HP-Si	0.8921	0.8963	0.8372	0.7564	0.6646
HP-Si (*46 group*)	0.913	0.903	0.873	0.812	0.754
HP-GaAs	0.6817	0.6841	0.6431	0.5835	0.5159
1 MeV-Si	6.824	6.694	7.038	7.290	7.610
1 MeV-GaAs	5.214	5.109	5.406	5.624	5.907

[a]Shape Index is ($\Phi_{tot}/\Phi_{>3\ MeV}$).

Observations

Comparisons of historical calculation in broad group structure, 46 group structure, to the current calculations demonstrate close agreement in both the fine group structure, 620 group, and the SNL RML compendium of cross section data to the newly released IRDF-2002 cross section data.

One of the important functions of the Monte Carlo calculations is to provide the *a priori* neutron spectra for least squares spectrum adjustment. These methods use covariance data as an important piece of input data. Calculating the total uncertainty in the calculated spectra can be a challenge at times. An important extension of the work is to obtain uncertainties to all the information provided from the calculation process, including the sensitivity of the calculation to various cross section sets, materials used in the calculation and geometric compromises.

A large base of foil activation data exists for many of the experimental locations of interest. Adjusting the neutron spectra using updated cross section sets can illustrate trends of spectrum adjustment techniques as the cross section data sets are updated.

Recommendations

To date, most of the calculations have focused on obtaining the neutron spectra at points of interest to the experimenter. Obtaining the estimated gamma spectra has received less attention. Obtaining a gamma spectrum is complicated by the fact that generally, only prompt gamma data are provided by the calculation. It is known there is some shift in the gamma spectrum due to the emission of delayed gammas as fission products build up during longer exposures from the test reactors. Including the delayed gamma

contribution to the prompt gamma emission can provide subtle changes to the gamma spectrum and ionizing dose received by the test device.

References

[1] Summary Report of the Final Technical Meeting on International Reactor Dosimetry File: IRDF-2002, International Atomic Energy Agency Nuclear Data Section, Vienna, Austria, report INDC(NDS)-448, October 2003.

[2] Griffin, P. J., Kelly, J. G., and Luera, T. F., "SNL RML Recommended Dosimetry Cross Section Compendium," SAND92-0094, Sandia National Laboratories, NM, 1993.

[3] X-5, Monte Carlo Team, "MCNP-A General Monte Carlo N-Particle Transport Code Version 5," report LA-CP-03-0245, Los Alamos National Laboratory, Los Alamos, NM, 2003

[4] V. McLane, Ed., ENDF/B-6 Summary Documentation, U.S. National Nuclear Data Center, Brookhaven National Laboratory, Upton NY, report BNL-NCS-17541ENDF-102, October 1991, Supplement 1, December1996.

[5] Flanders, T. M. and Sparks, M. H., "Calculated Neutron Spectra of Fast Pulsed Reactors," *Proceedings of the 7th ASTM-EURATOM Symposium on Reactor Dosimetry*, Strasbourg, France, 1990, pp. 575–582.

[6] Ingersall, D. T., Roussin, R. W., Fu, C. Y., and White, J. E., DABL-69: A Broad Group Neutron/Photon Cross Section Library for Defense Nuclear Applications, ORNL/TM-10568, Oak Ridge National Laboratory, Oak Ridge, TN, 1989.

[7] McElroy, W. N., Bert, S., Crockett, T., and Hawkins, R. G., "SAND-II, A Computer-Automated Iterative Method for Neutron Flux Determination by Foil Activation," AFWL-TR-41, Vol. I–IV, 1967.

[8] Flanders, T. M., Sparks, M. H., and Sallee, W. W., "Radiation Environment Produced by the White Sands Missile Range MoLLY-G Reactor," *Proceedings of the Physics, Safety, and Applications of Pulse Reactors International Embedded Topical Meeting*, ANS, 1994, pp. 137–144.

[9] ASTM, Standard E 720-02, "Standard Practice for Characterizing Neutron Energy Fluence Spectra in Terms of an Equivalent Monoenergetic Neutron Fluence for Radiation-Hardness Testing of Electronics," *Annual Book of ASTM Standards*, ASTM International, West Conshohocken, PA, 2002, pp. 264–275.

[10] Sparks, M. H. and Flanders, T. M., "Hardness Parameter Calculations at the White Sands Missile Range, Fast Burst Reactor," *Proceedings of Fast Burst Reactor Workshop* Vol. 1, 8–10 April, 1986, Albuquerque, NM, pp. 75–84.

Journal of ASTM International, Vol. 3, No. 9
Paper ID JAI13426
Available online at www.astm.org

Gabor Hordosy[1]

Coupled Neutron-Gamma Calculations for the LR-0 Experimental Benchmark

ABSTRACT: Benchmark calculations were performed for the mockup of a WWER-1000 reactor developed on the test reactor LR-0 in Nuclear Research Institute Rez (Czech Republic). The experimental arrangement is azimuthally and axially shortened, but the radial dimensions and material compositions are identical with the power reactors. The neutron and photon spectra, attenuation coefficients, and spectral indices were calculated and compared with measurements in all representative points of the mockups. The calculations were performed using the MCNP4C Monte Carlo code. A detailed geometrical model was developed. Most calculations were repeated using different nuclear data libraries. In some cases it was found that the difference of measured and calculated values is higher than could be explained by the experimental and calculational error.

KEYWORDS: reactor dosimetry, pressure vessel calculations, pressure vessel benchmark

Introduction

The lifetime of a nuclear power plant is greatly determined by the radiation load of the reactor pressure vessel, mainly due to the fast neutrons. Validation of the computer codes and nuclear data used for such calculations has vital importance. The LR-0 facility Rez offers unique possibilities for such benchmarking, because not only integral quantities but neutron and photon spectra can be measured, the measurements are performed on a facility with radial dimensions corresponding to a real power reactor, and the facility is (VVER) specific. In the framework of the (REDOS) project supported by the Fifth Framework Programme of the European Community, neutron and γ transport calculations were performed by seven institutes of five countries for LR-0, and they were compared with the measurements made by the Nuclear Research Institute Rez. In this paper the calculational results computed in the (KFKI) Atomic Energy Research Institute will be presented and compared with the measurements performed in Nuclear Research Institute Rez. A similar analysis was carried out previously and the results were published in Ref. [1]

Description of Measurements

The facility is an axially (1.25 m active height) and azimuthally (60 deg symmetry sector) shortened model of the reactor core. The radial dimensions and material compositions from the core boundary to the biological shielding correspond completely to the power reactors. The pressure vessel simulator is made up from separately movable layers with a thickness of 5 cm. This makes it possible to make measurements at different widths of the pressure vessel. Water density decrease due to the high temperature is simulated by using an air-filled displacer at the barrel. (The displacer is movable along the symmetry axis of the system.) Mockups for WWER-1000 and WWER-440 reactor cores were studied in the REDOS project, but in this paper only the VVER-1000 mockup will be considered. The horizontal view of the mockup is shown in Fig. 1. A detailed description of the mockup together with the experimental results is given in Ref. [2].

All calculations and comparisons with the measurements were done for the points at different radii in the central plane along the azimuthal symmetry axes of the mockup. The measurements of the azimuthal and axial fluence distributions were not considered, as preliminary investigations had shown that the

Manuscript received June 20, 2005; accepted for publication May 16, 2006; published online October 2006. Presented at ASTM Symposium on Reactor Dosimetry, 12th International Symposium on 8–13 May 2005 in Gatlinburg, TN; D. W. Vehar, D. M. Gilliam, and J. M. Adams, Guest Editors.
[1] Research Scientist, KFKI Atomic Energy Research Institute, H-1525 Budapest 114, P.O.B. 49, Hungary

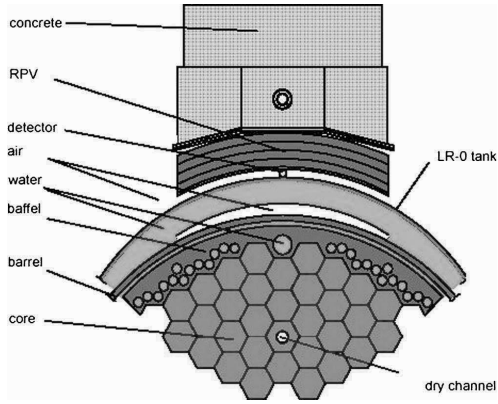

FIG. 1—*Horizontal cross section of VVER-1000 mockup on LR-0.*

changes expected and actually found, were in the range of the measurement errors. Measurements were made at different radii. The notation used for these locations throughout this paper is given in Table 1. The neutron flux was measured and evaluated at these points in 24 SAILOR group structure (for group boundaries, see Ref. [1]). Attenuation factors for the flux above threshold energies 0.111, 0.498, 1.0, 3.012, and 4.098 MeV and spectral indices were evaluated for neutrons. For photons, the fine group spectra from 0.2 MeV to 10 MeV was measured at these points with 0.1 MeV steps. Also, the ratio of photon flux above 1 MeV to neutron flux above 1 MeV was evaluated.

The power distribution in the fuel pins were given as part of the benchmark specification.

Description of the Calculations

All of the transport calculations were made by the MCNP4C2 Monte Carlo code. With the exception of the cross-sectional sensitivity study, ENDF/B-VI Rel. 1-2 data were used for all isotopes when these data were available. For variance reduction purposes, the Russian roulette/splitting method was used for neutrons and photons as well.

The geometrical models of the mockups were given in 60 deg. Inside the LR-0 tank, the 60 deg sector containing the core azimuthally was bounded by 20 cm water. Axially, the lower and upper passive parts of the fuel pins were taken into account. The hardware below and above the passive parts of the pins was approximated by water. All details were taken into account in radial direction, except that the "teeth" of the outer part of the baffle (see Fig. 8 in Ref. 1) were neglected and their influence was approximated by changing the steel density. The fuel assemblies were modeled in details. The lower/upper supporting plates and the spacer grids were neglected. The influences of the neutron and gamma detectors were not considered.

The neutron source was defined in the fuel pins according the pin power distributions given in the benchmark specifications. The axial dependence of the source intensity was defined as a cosine distribution with parameters given also in the benchmark specifications. The energy spectrum of the source neutron was given as a combination of the U-235 and U-238 fission spectra with 0.92 and 0.08 weights.

TABLE 1—*Places of measurements.*

Place of measurements	Notation
In the displacer, at the barrel (surveillance position)	P2
Before RPV	P3
5 cm thickness of RPV	P4
10 cm thickness of RPV	P5
15 cm thickness of RPV	P6
After RPV, before biological shielding	P7

TABLE 2—*Comparison of calculated and measured attenuation factors.*

	P2/P3		P3/P4		P4/P5		P5/P6		P6/P7		P3/P7	
E_{thr}	*R*	*Q*	*R*	*Q*	*R*	*Q*	*R*	*Q*	*R*	*Q*	*R*	*Q*
3.012 MeV	1.15	4.15	0.85	−4.6	0.94	−1.9	0.95	−1.4	1.05	1.29	0.80	−6.1
1.003 MeV	1.18	6.04	0.88	−4.2	0.97	−1.0	0.99	−0.4	1.03	0.88	0.87	−4.3
0.498 MeV	1.17	5.28	0.86	−4.3	0.96	−1.2	0.97	−0.8	1.01	0.31	0.80	−5.6
0.111 MeV	1.16	4.99	0.86	−4.2	0.95	−1.2	0.98	−0.6	1.00	0.13	0.81	−5.6

Only neutron induced photons were considered in the calculation, the photons from fissions—either prompt or delayed—were neglected. This approximation was justified by a criticality calculation made MCNP4C, where the prompt photons from fission were taken into account. This resulted changes of photon flux was less than the statistical uncertainties of the calculation at any investigated points. The energy emitted by the delayed photons from fission is roughly equal with the energy emitted by the prompt photons. This result shows that the dominant contribution to the photon flux comes from the neutron induced photons.

The neutron and photon fluxes in most cases were evaluated as averages on parts of the cylindrical surfaces at the places of the detectors. These parts of the tally surfaces were bounded by a cylinder having a common axis with the mockup and having a 15 cm radius. For the calculation of the flux inside the measuring channel and the displacer, the volume averaged fluxes were used with volumes having similar sizes. For comparison with measurements, the neutron and photon spectra, in SAILOR group structure, the integral fluxes, i.e., the neutron flux above 0.111, 0.5, 1, 2, 3, and 5 MeV, the photon flux above 1, 3, and 5 MeV were calculated at the measuring points. The photon spectra for the VVER-1000 mockup were calculated in fine group structure (0.1 MeV) for comparison with measurements.

The calculations were done according to the following strategy. At first, the neutron and gamma fluxes were evaluated in a course-group structure (for neutrons 0.414e-06, 0.111, 0.5, 1.0, 2.0, 3.0, and 5.0 MeV, for gammas 1.0, 3.0, and 5.0 MeV) using the source component flagging feature of MCNP. Using the results of this calculation, it was possible to identify by one calculation the part of the core, where the large majority of the neutrons contributing to the measured fluxes come from. It was found that 97–98.5 % of such neutrons come from a few assemblies close to the measuring points, and this percent practically does not depend on the energy. In the second step, the spectral calculations were performed considering the source in these assemblies only. The small contributions of the neglected assemblies were taken into account by a correction factor.

Comparison of Measurements and Calculations

The attenuation factors, i.e., the ratios of the fluxes at different points were evaluated for some threshold energies. The comparison of the measured and calculated values is given in Table 2. Here the following notation is used. If F_{meas} and F_{calc} are the measured and calculated values of a quantity, their ratio will be denoted by R, and their difference relative to the common statistical error will be denoted by Q. Formally, $R=F_{calc}/F_{meas}$ and $Q=(F_{calc}-F_{meas})/\sigma_t$, where $\sigma_t^2=\sigma_{meas}^2+\sigma_{calc}^2$. If the value of Q is greater than 2.5, the difference of the two quantities is significant statistically.

As can be seen from the above table, the attenuation is overestimated in water (P2/P3) and underestimated in the pressure vessel (P3/P7). The difference is statistically significant in the P2/P3, P3/P4, and P3/P7 cases.

The spectral indices defined as Φ_{E_1}/Φ_{E_2} for the investigated points. Here E_1 and E_2 are threshold energies, $E_1=0.5$ MeV or 1 MeV, while $E_2=3$ MeV. The calculated and measured values of these spectral indices are compared in Table 3 in a similar way to the attenuation factors.

The difference in some point is statistically significant; however, the agreement is acceptable.

TABLE 3—*Comparison of calculated and measured neutron spectral indices.*

	P2		P3		P4		P5		P6		P7	
E1/E2 (MeV)	*R*	*Q*	*R*	*Q*	*R*	*Q*	*R*	*Q*	*R*	*Q*	*R*	*Q*
0.5/3.0	1.12	4.62	1.10	3.98	1.10	3.81	1.08	3.18	1.06	3.18	1.09	−3.03
1.0/3.0	1.08	4.61	1.06	4.26	1.03	1.80	1.00	−0.17	0.96	−2.28	0.97	−1.48

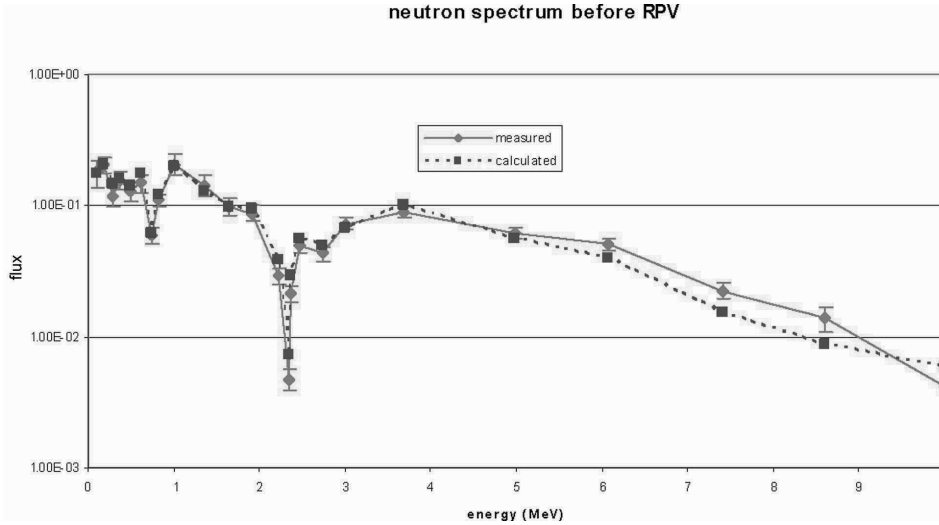

FIG. 2—*The calculated and measured neutron spectra before the pressure vessel.*

To see some more details about the neutron spectra, some examples are shown for selected points in Figs. 2 and 3. All the spectra are normalized in such a way that the flux integral above 1 MeV is equal with unity, i.e., only the shape of the spectra can be compared. As it can be seen in the figures, the agreement is fairly good; the difference is mostly within the statistical error.

The ratio $R=\Phi_{\mathrm{ph}}(E>1\ \mathrm{MeV})/\Phi_n(E>1\ \mathrm{MeV})$ of photon flux above 1 MeV to the neutron flux above 1 MeV was also evaluated and compared with the measured quantities. This is shown in Table 4. Here only the quantity $R_{\mathrm{calc}}/R_{\mathrm{meas}}$ is given, because in this case the error is rather small.

As can be seen, the deviation between the calculated and measured values is remarkably high, particularly at the barrel (Point 2), where the discrepancy is a factor of 2. This behavior has not yet been explained.

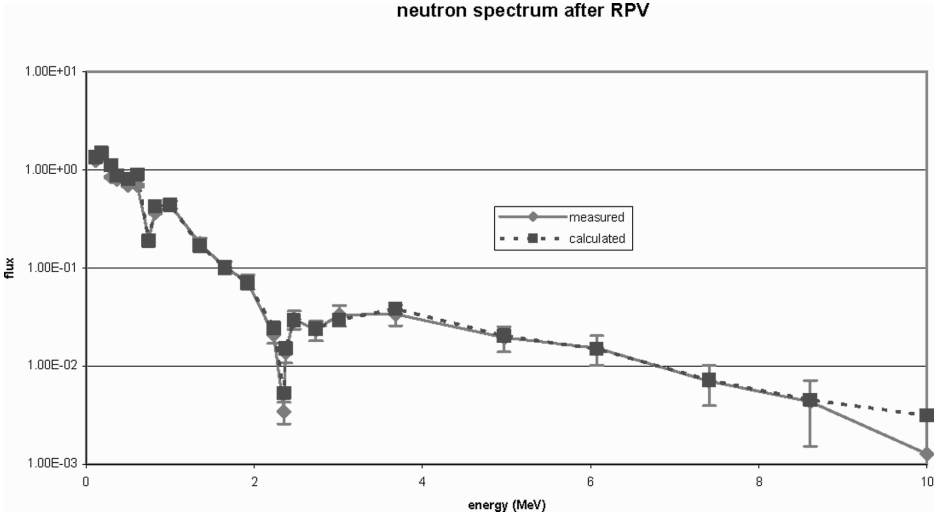

FIG. 3—*The calculated and measured neutron spectra after the pressure vessel.*

TABLE 4—*Comparison of calculated and measured photon flux/neutron flux ratio above 1 MeV.*

	P2	P3	P4	P5	P6	P7
R_{calc}/R_{meas}	0.44	0.81	0.85	0.82	0.80	0.90

The photon spectra also were measured and calculated at points 2–7. Because the measured results are given in 0.1 MeV steps, for comparison the calculated photon spectra were broadened by the detector resolution. These calculations were performed by two libraries, by the ENDF/B-VI.2 and FENDL 2.0. The comparison for some points is shown in Figs. 4 and 5. Here the spectra also have common normalization.

The photon spectra calculated using the ENDF/B-VI.2 library follow more or less the shape of the measured curves, the hydrogen peak and the major peaks from steel material coincide with the measurements. In the case of the FENDL 2.0 library, a remarkable shift and smoothing can be observed. It should be noted that above approximately 8 MeV, the accuracy of the measurements is strongly decreasing.

Influence of Changing the Nuclear Library

To have an impression about the influence of cross-sectional uncertainties, some of the calculations were repeated using the FENDL 2.0, JEF 2.2, and JENDL 3.3 libraries. In this section the ENDF/B-VI.2 library will be referred to as the basic library. The influence of the libraries on the ratio of photon flux above 1 MeV to neutron flux above 1 MeV was investigated for two libraries. The results are shown in Table 5.

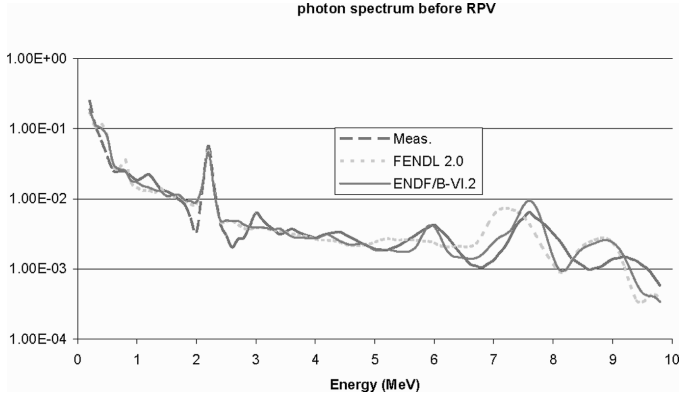

FIG. 4—*The calculated and measured photon spectra before the pressure vessel.*

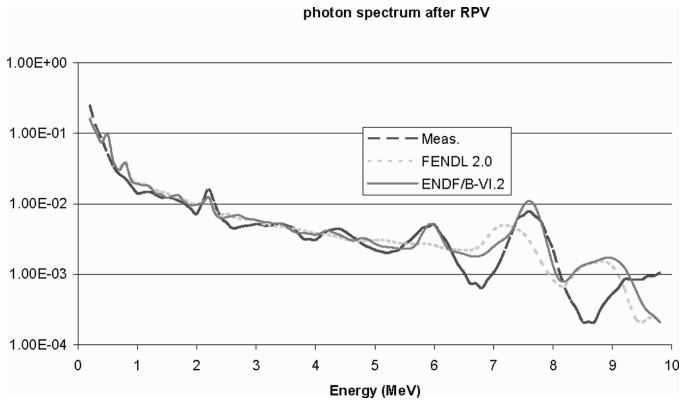

FIG. 5—*The calculated and measured photon spectra after the pressure vessel.*

TABLE 5—*Influence of the libraries on the ratio of photon flux to neutron flux above 1 MeV. The ratio calculated by a library was divided by the ratio calculated by the basic library.*

	Point 2	Point 3	Point 4	Point 5	Point 6	Point 7
FENDL 2.0	0.98	0.93	0.91	0.91	0.89	0.90
JENDL 3.3	0.96	0.93	0.94	0.94	0.95	0.96

The table shows that using these libraries, the agreement with the experimental measurements becomes weaker.

The influence of this change on the attenuation factor is summarized in Tables 6–8.

As can be seen from Tables 6–8, the maximum relative deviation in the attenuation factor caused by the replacement of library is 10 %, but mostly less than 5 %. The attenuation over the pressure vessel is a little less using FENDL 2.0 and somewhat larger using JENDL 3.3 and JEF 2.2. Recalling Table 2, it can be seen that the agreement with experiments improves a little bit.

TABLE 6—*Attenuation factors calculated by FENDL 2.0 divided by attenuation factors calculated by the basic library.*

	2/3	3/4	4/5	5/6	6/7	3/7
$E_n > 3.012$ MeV	0.96	0.98	0.98	1.00	0.98	0.95
$E_n > 1.003$ MeV	0.96	0.98	0.99	0.99	1.00	0.96
$E_n > 0.498$ MeV	0.96	0.98	0.99	0.99	1.00	0.96
$E_n > 0.111$ MeV	0.97	0.99	0.99	1.00	1.00	0.98

TABLE 7—*Attenuation factors calculated by JEF2.2 divided by attenuation factors calculated by the basic library.*

	2/3	3/4	4/5	5/6	6/7	3/7
$E_n > 3.012$ MeV	1.03	1.02	1.01	1.02	1.01	1.06
$E_n > 1.003$ MeV	0.94	1.02	1.02	1.01	1.01	1.07
$E_n > 0.498$ MeV	0.91	1.03	1.03	1.02	1.03	1.10
$E_n > 0.111$ MeV	0.91	1.00	1.00	1.00	1.02	1.03

TABLE 8—*Attenuation factors calculated by JENDL 3.3 divided by attenuation factors calculated by the basic library.*

	2/3	3/4	4/5	5/6	6/7	3/7
$E_n > 3.012$ MeV	0.94	1.03	1.02	1.03	1.02	1.09
$E_n > 1.003$ MeV	0.97	1.01	1.00	1.00	1.00	1.02
$E_n > 0.498$ MeV	0.93	1.01	1.01	1.01	1.01	1.05
$E_n > 0.111$ MeV	0.93	1.00	1.00	1.00	1.01	1.01

Conclusions

Coupled neutron-gamma Monte Carlo calculations were made for the LR-0 facility. Attenuation factors, spectral indices, neutron, and gamma spectra were calculated. The shape of the spectra is generally in a fairly good agreement with the measurements. The attenuation through the pressure vessel was calculated a little bit low. The ratio of the fast photon and neutron flux was calculated essentially lower than it was found in the experiment. The influence of using different nuclear data libraries was investigated. This change had only a minor impact on the measurable quantities.

References

[1] B. Osmear and S. Zaritsky, *9th International Symposium on Reactor Dosimetry, Prague, 2–6 September 1996*, pp. 778–784.

[2] B. Ošmera and S. Zaritsky, "WWER-1000 Mock-up Experiment in the LR-0 Reactor Mock-up Description and Experimental Data," REDOS/R(01)/December 2002/Issue 01, ÚJV-11815-R, RRC KI No. 36/27–2002.

Journal of ASTM International, Vol. 4, No. 4
Paper ID JAI100373
Available online at www.astm.org

F. Arzu Alpan, Ph.D.[1] *and Alireza Haghighat, Ph.D.*[2]

Use of CPXSD for Generation of Effective Fast Multigroup Libraries for Pressure Vessel Fluence Calculations

ABSTRACT: Multigroup (i.e., broad-group) libraries play a significant role in the accuracy of transport calculations. There are several broad-group libraries available for particular applications. For example the 47-neutron (26 fast groups), 20-gamma-group BUGLE libraries are commonly used for light water reactor shielding and pressure vessel dosimetry problems. However, there is no publicly available methodology to construct group structures for a problem and objective of interest. Therefore, we have developed the Contributon and Point-wise Cross-Section Driven (CPXSD) methodology, which constructs effective fine- and broad-group structures. In this paper, we use the CPXSD methodology to construct broad-group structures for fast neutron dosimetry problems. It is demonstrated that the broad-group libraries generated from CPXSD constructed group structures, while only 14 groups (rather than 26 groups) in the fast energy range are in good agreement (~1 %–2 %) with the fine-group library from which they were derived, in reaction rate calculations.

KEYWORDS: multigroup library, pressure vessel fluence, contributon, adjoint, cross section

Introduction

Multigroup (broad-group) libraries are required for deterministic transport calculations. However, one of the major uncertainties in deterministic transport calculations can be attributed to the multigroup cross sections. Therefore, it is important to analyze the procedure used to generate a standard multigroup cross-section library and to identify the processes that may be improved.

A standard broad-group cross-section library generation can be given as a three-step process, as listed below [1].

(i) Point-wise evaluated data are processed to obtain fine-group cross sections.
(ii) Self-shielding calculations are performed to correct cross sections in resonance regions.
(iii) Self-shielded fine-group cross sections are collapsed into broad-group cross sections using scalar fluxes as the weighting function.

Among the three steps listed above, three items are identified that may improve a broad-group library generation: multigroup structure, self-shielding method, and cross-section collapsing approach. In order to obtain an effective multigroup structure, the Contributon and Point-wise Cross-Section Driven (CPXSD) methodology was developed by Alpan and Haghighat [2,3]. For fine- to broad-group collapsing, the bi-linear adjoint weighting technique [4] was developed by Hanshaw and Haghighat as an alternative to scalar flux weighting [5]. Improvements to the self-shielding method are beyond the scope of this paper.

The CPXSD methodology is an iterative method that constructs effective fine- and broad-group structures for a problem and objective of interest. In this paper, the CPXSD is utilized to generate broad-group libraries for fast neutron dosimetry calculations at the cavity dosimeter for a light water reactor. Scalar flux and bilinear adjoint weighting techniques are used in generating broad-group libraries.

Manuscript received June 20, 2005; accepted for publication March 28, 2007; published online May 2007. Presented at ASTM Symposium on Reactor Dosimetry, 12th International Symposium on 8–13 May 2005 in Gatlinburg, TN; D. W. Vehar, D. M. Gilliam, and J. M. Adams, Guest Editors.
[1] Research and Development Associate, Oak Ridge National Laboratory, Oak Ridge, TN 37831-6171.
[2] Professor and Chair of Nuclear and Radiological Engineering, University of Florida, Gainesville, FL 32611.

Multigroup Transport Equations

The discrete ordinates (S_N) method is commonly used to solve the neutron transport equation. In order to solve the time-independent neutron transport equation by the S_N method, discretization is performed over space ($\vec{r}$), energy (E), and angle ($\hat{\Omega}$). Since our focus is on multigroup calculations, we present the formulations for energy discretization in this section.

The time-independent multigroup neutron transport equation is derived by integrating the linear Boltzmann equation over each energy interval g, as given below.

$$\hat{\Omega}\cdot\nabla\int_g dE\Psi(\vec{r},E,\hat{\Omega})+\int_g dE\sigma_t(\vec{r},E)\Psi(\vec{r},E,\hat{\Omega})$$
$$=\sum_{g'=1}^{G}\int_g dE\int_{g'} dE'\int_{4\pi} d\Omega'\sigma_s(\vec{r},E'\rightarrow E,\mu_o)\Psi(\vec{r},E',\Omega')+\int_g dEq_{\text{ex}}(\vec{r},E,\hat{\Omega}) \quad (1)$$

In Eq 1, Ψ is flux; σ_t and σ_s are total and scattering macroscopic cross sections, respectively; μ_o is the direction cosine between incident and emerging particle; and q_{ex} is the external source. Equation 1 is rewritten by preserving reaction rates as

$$\hat{\Omega}\cdot\nabla\Psi_g(\vec{r},\hat{\Omega})+\sigma_{t,g}(\vec{r},\hat{\Omega})\Psi_g(\vec{r},\hat{\Omega})$$
$$=\sum_{g'=1}^{G} d\Omega'\sigma_{s,g'\rightarrow g}(\vec{r},\mu_o,\hat{\Omega}')\Psi_{g'}(\vec{r},\hat{\Omega}')+q_{\text{ex},g}(\vec{r},\hat{\Omega}) \quad (2)$$

where the group flux is defined as

$$\Psi_g(\vec{r},\hat{\Omega})=\int_g dE\Psi(\vec{r},E,\hat{\Omega}) \quad (3)$$

The total and scattering group constants are defined by Eqs 4 and 5, respectively, as

$$\sigma_{t,g}(\vec{r},\hat{\Omega})=\frac{\int_g dE\sigma_t(\vec{r},E)\Psi(\vec{r},E,\hat{\Omega})}{\int_g dE\Psi(\vec{r},E,\hat{\Omega})} \quad (4)$$

and

$$\sigma_{s,g'\rightarrow g}(\vec{r},\mu_o,\hat{\Omega}')=\frac{\int_g dE\int_{g'} dE'\sigma_s(\vec{r},E'\rightarrow E,\mu_o)\Psi(\vec{r},E',\hat{\Omega}')}{\int_{g'} dE'\Psi(\vec{r},E',\Omega')} \quad (5)$$

Finally, the external group source is defined as

$$q_{\text{ex},g}(\vec{r},\hat{\Omega})=\int_g dEq_{\text{ex}}(\vec{r},E,\hat{\Omega}) \quad (6)$$

The total cross section formulated in Eq 4 has an additional angular dependency after energy discretization is introduced. Furthermore, if the scattering multigroup cross section is examined, it is seen that there is dependency on both the angle $\hat{\Omega}'$ and the scattering cosine μ_o. Note that the angular flux introduces additional angular dependency on the scattering cross section. The two techniques used to eliminate these additional dependencies in the multigroup cross sections are the scalar flux collapsing and bi-linear adjoint weighting approaches.

Scalar Flux Collapsing

The common procedure to collapse cross sections is to use scalar flux as the weighting function. The spatial domain integrated scalar flux is given as

$$\Phi(E) = \int_{D_s} dr \int_{4\pi} d\Omega \Psi(\vec{r}, E, \hat{\Omega}) \tag{7}$$

where D_s is the sub-domain. The total and scattering group constants weighted with the scalar flux are given as

$$\sigma_{t,g} = \frac{\int_g dE \sigma_t(E) \int_{D_s} dr \int_{4\pi} d\Omega \Psi(\vec{r}, E, \hat{\Omega})}{\int_g dE \int_{D_s} dr \int_{4\pi} d\Omega \Psi(\vec{r}, E, \hat{\Omega})} \tag{8}$$

and

$$\sigma_{s,g' \to g}(\mu_o) = \frac{\int_g dE \int_{g'} dE' \sigma_s(E' \to E, \mu_o) \int_{D_s} dr \int_{4\pi} d\Omega' \Psi(\vec{r}, E', \hat{\Omega}')}{\int_{g'} dE' \int_{D_s} dr \int_{4\pi} d\Omega' \Psi(\vec{r}, E', \Omega')} \tag{9}$$

Since the scattering group constant is dependent on angle, it is common to expand the differential scattering cross section in terms of Legendre polynomials.

$$\sigma_s(E' \to E, \mu_o) = \sum_{l=0}^{\infty} \frac{2l+1}{4\pi} \sigma_{s,l}(E' \to E) P_l(\mu_o) \tag{10}$$

where

$$\sigma_{s,l}(E' \to E) = 2\pi \int_{-1}^{1} d\mu_o \sigma_s(E' \to E, \mu_o) P_l(\mu_o) \tag{11}$$

Therefore, the multigroup scattering cross section becomes

$$\sigma_{s,g' \to g}(\mu_o) = \sum_{l=0}^{\infty} \frac{2l+1}{4\pi} P_l(\mu_o) \sigma_{s,l,g' \to g} \tag{12}$$

and

$$\sigma_{s,l,g' \to g} = \frac{\int_g dE \int_{g'} dE' \sigma_{s,l}(E' \to E) \Phi(E')}{\int_{g'} dE' \Phi(E')} \tag{13}$$

The scalar flux approximation is equal to the exact expressions given in Eqs 4 and 5 if the angular flux is isotropic. Although this method is commonly used, it has some limitations. Scalar flux weighting does not account for angular variations, and all scattering moments are weighted with the scalar flux. The bi-linear adjoint weighting technique overcomes this deficiency by using the adjoint function.

The Bi-linear Adjoint Weighting Technique

The bi-linear adjoint weighting technique was developed by Hanshaw and Haghighat. This method includes angular dependencies of a problem in multigroup constants by using the forward flux and adjoint function moments to weight cross sections. Weighting with angular dependencies is performed according to important particles that contribute to an objective. The bi-linear adjoint weighting formulation is derived by multiplying the numerator and denominator of Eqs 4 and 5 with the adjoint function and integrating over angle and space. The total collision term is given by

$$\sigma_{t,g} = \frac{\int_g dE\sigma_t(E)\int_{D_s} dr\int_{4\pi} d\Omega\Psi(\vec{r},E,\hat{\Omega})\Psi_g^+(\vec{r},\hat{\Omega})}{\int_g dE\int_{D_s} dr\int_{4\pi} d\Omega\Psi(\vec{r},E,\hat{\Omega})\Psi_g^+(\vec{r},\hat{\Omega})} \tag{14}$$

where

$$\Psi_g^+(\vec{r},\hat{\Omega}) = \int_g dE\Psi^+(\vec{r},E,\hat{\Omega}) \tag{15}$$

If flux expansions are inserted and the orthogonality property is used, Eq 14 reduces to

$$\sigma_{t,g} = \frac{\int_g dE\sigma_t(E)\int_{D_s} dr\left(\sum_{l=0}^{\infty}\frac{2l+1}{4\pi}\sum_{m=-l}^{l}\Psi_l^m(\vec{r},E)\Psi_{l,g}^{m,+}(\vec{r})\right)}{\int_g dE\int_{D_s} dr\left(\sum_{l=0}^{\infty}\frac{2l+1}{4\pi}\sum_{m=-l}^{l}\Psi_l^m(\vec{r},E)\Psi_{l,g}^{m,+}(r)\right)} \tag{16}$$

Accordingly, the scattering cross section is formulated by

$$\sigma_{s,l,g'\to g} = \frac{\int_g dE\int_{g'} dE'\sigma_{s,l}(E'\to E)\int_{D_s} dr\left(\sum_{m=-l}^{l}\Psi_l^m(\vec{r},E)\Psi_{l,g}^{m,+}(\vec{r})\right)}{\int_j dE'\int_{D_s} dr\left(\sum_{m=-l}^{l}\Psi_l^m(\vec{r},E)\Psi_{l,g}^{m,+}(\vec{r})\right)} \tag{17}$$

The bi-linear adjoint weighting technique is superior compared with the scalar flux weighting approach, especially for problems that have high angular dependencies (e.g., fast neutron dosimetry).

Energy Group Structure Construction Method of CPXSD

The CPXSD methodology constructs energy group structures by refining an arbitrary group structure. Refinement of the arbitrary group structure is performed according to the importance of groups in the group structure, and point-wise cross sections of an important isotope/material in the problem.

The importance of groups can be determined using the "response flux" (i.e., the contributon formulation) [6]:

$$C(E) = \int_V dr\int_{4\pi} d\Omega\Psi(\vec{r},E,\hat{\Omega})\Psi^+(\vec{r},E,\hat{\Omega}) \tag{18}$$

Considering spherical harmonics expansion of the flux and adjoint function, and using orthogonality, the group-dependent response flux is written as

$$C_g = \sum_{s\in D} V_s\sum_{l=0}^{L}\sum_{m=0}^{l}\frac{2l+1}{4\pi}\Psi_{l,g,s}^m\Psi_{l,g,s}^{m,+} \tag{19}$$

where g refers to energy group, s refers to a materially uniform sub-domain in domain D, and l and m refer to polar and azimuthal indices, respectively. The group-dependent response flux formulation given in Eq 19 represents the importance of particles in group g for an objective.

There is similarity between contributon and reaction rate formulations. The response at the cavity dosimeter can be written as

$$response = \langle\sigma_d\Psi\rangle = \langle q_{\rm ex}\Psi^+\rangle \tag{20}$$

where σ_d is the detector cross section. If the angular flux is substituted for the external source, q_{ex}, in Eq 20, it is possible to obtain an expression similar to that for the response flux.

The second item to determine in CPXSD is an important isotope in the problem of interest. For this study ^{56}Fe is chosen since this isotope plays an important role in the pressure vessel. The ^{56}Fe point-wise group structure is used to identify group boundaries in constructing new group structures.

TABLE 1—*Modules that are used in the generation of fine-group libraries.*

Module Name	Function
SMILER	Converts NJOY Group-wise Evaluated Nuclear Data Files (GENDF) to AMPX master library format
AJAX	Gathers AMPX master libraries
BONAMI	Performs self-shielding calculations
NITAWL	Converts AMPX master libraries to AMPX working library format (the code may also be utilized to use the Nordheim Integral method for resonance self-shielding)

The generation of a fine-group structure with CPXSD has been previously published [3,4], and this paper focuses on broad-group structure construction. Starting from a fine-group library, the construction of broad-group libraries for the purpose of calculating effective reaction rates at the cavity dosimeter of a reactor model is described as follows.

(i) An initial broad-group structure is selected. For fast neutron dosimetry calculations, the initial broad-group structure may be selected by considering energy thresholds of the dosimetry isotopes.

(ii) Fine-group cross sections are collapsed to the initial broad group, and a transport calculation is performed with the broad-group library to calculate the objectives.

(iii) The group that has the highest importance in the problem is identified, and the number of sub-groups to be added in this group is specified. Resonance and nonresonance parts of the point-wise cross sections of the important isotope are determined within this group, and their areas are calculated. The resonance that has the largest area is selected, and one sub-group is placed that encloses the resonance. Remaining resonance and non-resonance parts are combined such that they approach the size of the largest resonance area. Based on a user-input tolerance, the area of the largest resonance is modified until the number of sub-groups formed matches the number of sub-groups requested. If a resonance structure does not exist, the group is simply partitioned into even energy intervals.

(iv) The fine-group library is collapsed into the new broad-group library, and steps (ii) and (iii) are repeated until a user-specified convergence criterion is achieved on the calculated objectives.

Construction of Broad-Group Structures for Shielding Applications using the Three Mile Island-1 (TMI-1) Reactor

In this section, broad-group structures are constructed for pressure vessel dosimetry problems using the one-dimensional TMI-1 reactor model. The TMI-1 reactor consists of 27 nuclides, including ^{27}Al, ^{10}B, C, Ca, ^{50}Cr, ^{52}Cr, ^{53}Cr, ^{54}Cr, ^{54}Fe, ^{56}Fe, ^{57}Fe, ^{58}Fe, ^{1}H, K, Mg, ^{55}Mn, ^{23}Na, ^{58}Ni, ^{60}Ni, ^{61}Ni, ^{62}Ni, ^{64}Ni, ^{16}O, Si, Zr, ^{235}U, and ^{238}U.

In generating an effective fine-group library for the TMI-1 reactor, the NJOY code [7] was used for cross-section processing. NJOY version 94.15 was used for ^{27}Al and ^{235}U, and NJOY version 91.94m was used for the remaining isotopes. ENDF/B-VI release 3 was used for ^{235}U, and ENDF/B-VI release 2 was used for the remaining isotopes. The choice of the NJOY versions and ENDF data for the 27 isotopes was made considering the NJOY versions and ENDF data that were used in generating the 47-neutron-group BUGLE-96 library [5]. Note that the BUGLE-96 library uses ENDF/B-VI release 3 data for ^{27}Al; however, we used ENDF/B-VI release 2 for this isotope because of the difficulty we encountered in processing the release 3 data file.

The AMPX modules [8] were used for the post-processing of cross sections. The modules used from the AMPX code package and their functions in the cross-section library generation procedure for this study are listed in Table 1. Similar to the BUGLE-96 library generation procedure, water was not included in the self-shielding treatment of iron in the pressure vessel in the BONAMI calculations. The one-dimensional option of the two-dimensional DORT S_N code [9] was used for neutron transport calculations. For these calculations, a P_3 scattering order and a S_8 quadrature set were used.

For fast neutron dosimetry calculations, six reactions that are sensitive to energies above 0.1 MeV were selected. These are ^{63}Cu(n,α), ^{54}Fe(n,p), ^{58}Ni(n,p), ^{46}Ti(n,p), ^{237}Np(n,f), and ^{238}U(n,f). Group-

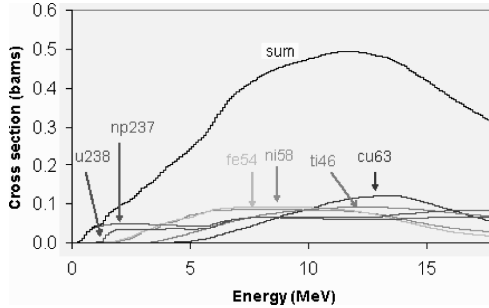

FIG. 1—*Normalized dosimetry cross sections and their sum.*

wise cross sections of these six reactions were normalized (l_1 norm) and summed to obtain one response function that represents the six reactions. The normalized cross sections of these dosimetry isotopes and their sum are shown in Fig. 1.

Broad-group structures were constructed from the 450-group LIB450 library [2,3]. LIB450 was generated from a fine-group structure constructed by CPXSD for fast neutron dosimetry problems. For broad-group structure construction, initial broad-group boundaries were selected based on the threshold energies of the six dosimeter isotopes. The initial broad-group structure boundaries were selected as follows: 18.032, 3.6815, 2.9737, 1.0196, 0.514 87, and 0.111 09 MeV. Except for the highest energy value, the remaining energies correspond to the threshold energies of the following interactions: ^{63}Cu(n,α), ^{46}Ti(n,p), ^{54}Fe(n,p), ^{58}Ni(n,p), and ^{238}U(n,f), and ^{237}Np(n,f), respectively.

A broad-group structure was generated for the isotope that has the highest threshold first [i.e., for ^{63}Cu(n,α)], which is sensitive to energies above 3.6815 MeV. After a group structure was obtained above 3.6815 MeV, the isotope with the next highest threshold energy [i.e., ^{46}Ti(n,p)] was considered. We proceeded with this procedure for the remaining dosimetry isotopes. When refining the initial broad-group structure, the number of groups was increased one at a time, until a relative difference of 1 % was achieved between fine- and broad-group reaction rates. By performing this procedure, 16- and 15-group libraries were generated considering the scalar flux and bi-linear adjoint weighting techniques, respectively. The 16-group LIB16 and the 15-group LIB15 libraries contain only one group below 0.1 MeV. Table 2 gives the group boundaries for the LIB16 and LIB15 libraries. Comparing the group structures of the two libraries, it is evident that for the bi-linear adjoint weighting technique, fewer groups are placed in very high energies where scattering is highly directional. For example, for the ^{63}Cu(n,α) reaction, placing

TABLE 2—*Group structures generated with the scalar flux and bi-linear adjoint technique.*

	Upper energy (MeV)	
Energy group number	Scalar flux weighting, LIB16	Bi-linear adjoint weighting, LIB15
1	18.032	18.032
2	14.832	8.132 0
3	11.632	3.681 5
4	8.632 0	2.973 7
5	7.132 0	2.651 5
6	5.955 3	2.332 0
7	4.832 0	2.000 0
8	3.681 5	1.701 6
9	2.973 7	1.405 3
10	2.472 6	1.019 6
11	1.973 4	0.827 06
12	1.532 0	0.702 18
13	1.019 6	0.514 87
14	0.772 60	0.321 68
15	0.514 87	0.111 09
	0.111 09	

TABLE 3—*Broad- (LIB16 and LIB15) to fine-group (LIB450) reaction rate ratios.*

Reaction	LIB16[a]/LIB450	LIB15[b]/LIB450
$^{63}Cu(n,\alpha)$	0.9882	1.006
$^{54}Fe(n,p)$	0.9884	0.9924
$^{58}Ni(n,p)$	0.9888	0.9946
$^{46}Ti(n,p)$	0.9896	1.005
$^{237}Np(n,f)$	0.9996	1.012
$^{238}U(n,f)$	0.9992	1.003

[a]Scalar flux weighting.
[b]Bi-linear adjoint weighting.

TABLE 4—*Broad-group to continuous-energy (CE) reaction rate ratios.*

Reaction	LIB16/CE	LIB15/CE	BUGLE-96/CE
$^{63}Cu(n,\alpha)$	0.9301	0.9056	0.9111
$^{54}Fe(n,p)$	0.9196	0.9152	0.9006
$^{58}Ni(n,p)$	0.9167	0.9168	0.9000
$^{46}Ti(n,p)$	0.9255	0.9059	0.9074
$^{237}Np(n,f)$	0.9052	0.9380	0.8984
$^{238}U(n,f)$	0.9063	0.9219	0.8990

seven groups using the scalar flux collapsing and two groups using the bi-linear adjoint weighting above 3.69 MeV results in comparable reaction rates. This means, as expected, the bi-linear weighting effectively includes the angular behavior of the differential scattering cross section.

Table 3 gives the broad- (LIB16 and LIB15) to fine-group (LIB450) reaction rate ratios. The reaction rate ratios of the broad- to fine-group library calculations are ~1 % different. The results indicate that the broad-group libraries compare closely with their respective fine-group libraries.

Broad-Group and Continuous-Energy Comparisons

In this section, LIB15, LIB16, and BUGLE-96 libraries are compared with continuous-energy calculations that are performed using Automated Adjoint Accelerated MCNP (A^3MCNP) [10,11]. The A^3MCNP code is a version of MCNP with automated variance-reduction capability. In the A^3MCNP calculations, fluxes were tallied within energy bins of the broad-group libraries. A^3MCNP flux tallies were calculated to have statistical errors below ~1 %.

Table 4 gives the reaction rate ratios calculated by DORT (broad group) to A^3MCNP (continuous energy). All broad-group calculations are 6 % to 10 % off the continuous energy calculations. The CPXSD libraries are about the same as, or in better agreement with, continuous-energy predictions as compared with BUGLE-96. The differences in LIB15 and LIB16 as compared with continuous energy are attributed to the 1 % convergence criteria used on reaction rates, when constructing group structures in CPXSD.

Summary and Conclusions

This paper presents the broad-group structure construction procedure used in CPXSD and compares the new broad-group libraries with their fine-group libraries as well as with continuous-energy cross sections. For fast neutron dosimetry calculations, broad- to fine-group reaction rate ratios are ~1 % for CPXSD libraries. Compared to BUGLE-96, calculated reaction rates by CPXSD libraries are about the same as or in better agreement with the continuous-energy predictions. Furthermore, CPXSD-constructed group structures have almost half the number of groups of the BUGLE group structure above 0.1 MeV that results in significant computational time.

References

[1] ANSI/ANS-6.1.2-1999, "Neutron and Gamma-Ray Cross Sections for Nuclear Radiation Protection Calculations for Nuclear Power Plants," 1999.

[2] Alpan, F. A., "An Advanced Methodology for Generating Multigroup Cross-Sections for Shielding Calculations," Ph.D. thesis, Nuclear Engineering, The Pennsylvania State University, May 2003.

[3] Alpan, F. A., and Haghighat, A., "Development of the CPXSD Methodology for Generation of Fine-Group Libraries for Shielding Applications," *Nucl. Sci. Eng.* 149, 2005, pp. 38–50.

[4] Hanshaw, H. L., "Multigroup Cross Section Generation with Spatial and Angular Adjoint Weighting," M.S. thesis, Nuclear Engineering, The Pennsylvania State University, August 1995.

[5] "BUGLE-96: Coupled 47 Neutron, 20 Gamma-Ray Group Cross Section Library Derived from ENDF/B-VI for LWR Shielding and Pressure Vessel Dosimetry Applications," DLC-76, Oak Ridge National Laboratory, Oak Ridge, Tennessee, March 1996.

[6] Williams, M. L., "Generalized Contributon Response Theory," *Nucl. Sci. Eng.* 108, 1991, pp. 355–383.

[7] "NJOY94.61: Code System for Producing Pointwise and Multigroup Neutron and Photon Cross Sections from ENDF/B Data," PSR-355, Los Alamos National Laboratory, Los Alamos, New Mexico, December 1996.

[8] "AMPX-77: Modular Code System for Generating Coupled Multigroup Neutron-Gamma Libraries from ENDF/B," PSR-315, Oak Ridge National Laboratory, Oak Ridge, Tennessee, October 1992.

[9] "TORT-DORT-PC, Two and Three Dimensional Discrete Ordinates Transport Version 2.7.3," CCC-543, Oak Ridge National Laboratory, Oak Ridge, Tennessee, June 1996.

[10] Wagner, J. C., "Acceleration of Monte Carlo Shielding Calculations with an Automated Variance Reduction Technique and Parallel Processing," Ph.D. thesis, Nuclear Engineering, The Pennsylvania State University, 1997.

[11] Wagner, J. C., and Haghighat, A., "Automatic Variance Reduction of Monte Carlo Shielding Calculations Using the Discrete Ordinates Adjoint Function," *Nucl. Sci. Eng.* 128, 1998, pp. 186–208.

Journal of ASTM International, Vol. 3, No. 7
Paper ID JAI13428
Available online at www.astm.org

Gianluca Longoni,[1] *Alireza Haghighat,*[2] *Ce Yi,*[3] *and Glenn E. Sjoden*[4]

Benchmarking of PENTRAN-SSN Parallel Transport Code and FAST Preconditioning Algorithm Using the VENUS-2 MOX-Fueled Benchmark Problem

ABSTRACT: The discrete ordinates method (Sn) is the most widely used technique to obtain numerical solutions of the linear Boltzmann equation, and therefore to evaluate radiation fields and dose rates in nuclear devices. However, it is well known that this method suffers from slow convergence for problems characterized by optically thick media and scattering ratio close to unity. To address this issue we have developed a new preconditioning algorithm based on the even-parity simplified Sn (EP-SSN) equations. The new method is based on the flux acceleration simplified transport (FAST) algorithm which is implemented into the PENTRAN-SSN code system. The code system is designed for parallel computing architectures; PENTRAN-SSN features spatial, angular, and energy domain decomposition algorithms. The FAST preconditioner is parallelized with a spatial domain decomposition algorithm. In this paper, our objective is to test the performance of the new preconditioning system for a three-dimensional shielding calculation based on the VENUS-2 MOX-fueled benchmark problem, issued by OECD/NEA (Organization for Economic Co-operation and Develpment/Nuclear Energy Agency.

KEYWORDS: VENUS benchmark, parallel computing, radiation transport

Introduction

The discrete ordinates method (Sn) is the most widely used technique to obtain numerical solutions of the linear Boltzmann equation [1], and therefore to evaluate radiation fields and dose rates in nuclear devices. However, it is well known that this method suffers from slow convergence for problems characterized by optically thick media and scattering ratio close to unity [2]. To address this issue, a number of acceleration techniques for the Sn method have been developed in the past, such as synthetic methods, and rebalance algorithms. However, the application of these acceleration methods to large three-dimensional (3D) problems characterized by material heterogeneities has been hindered by limited applicability mainly due to inherent instabilities of the methods [3]. In order to overcome these limitations, we have developed and analyzed a new preconditioning method based on the even-parity simplified Sn (EP-SSN) equations [4]. The new method is based on the flux acceleration simplified transport (FAST) algorithm which is implemented into the PENTRAN-SSN code system. The main philosophy behind the new algorithm is to use a simplified model like the EP-SSn equations to calculate an initial solution which is introduced as initial guess into a transport calculation. In our new methodology, the EP-SSn equations resolve the low-frequency part of the solution, while the Sn method is used to correct this initial solution with high-frequency components. It is worth noting that the EP-SSn equations are a higher-order approximation than the diffusion equation which is commonly used. Therefore, the new preconditioning algorithm is more suitable even for problems characterized by strong transport effects.

The FAST preconditioning algorithm is designed for parallel computing environments, with a spatial domain decomposition strategy. The code is parallelized using the message passing interface (MPI) par-

Manuscript received June 20, 2005; accepted for publication April 19, 2006; published online May 2006. Presented at ASTM Symposium on Reactor Dosimetry, 12th International Symposium on 8-13 May 2005 in Gatlinburg, TN; D. W. Vehar, D. M. Gilliam, and J. M. Adams, Guest Editors.

[1] Senior Engineer, Westinghouse Electric Co. LLC, P.O. Box 158 Interstate 70 Exit 57, Madison, PA 15663.

[2] Professor and Chair, Nuclear and Radiological Engineering, University of Florida, 202 Nuclear Science Building, Gainesville, FL 32611.

[3] Graduate Student, Nuclear and Radiological Engineering, University of Florida, 202 Nuclear Science Building, Gainesville, FL 32611.

[4] Professor, Nuclear and Radiological Engineering, University of Florida, 202 Nuclear Science Building, Gainesville, FL 32611.

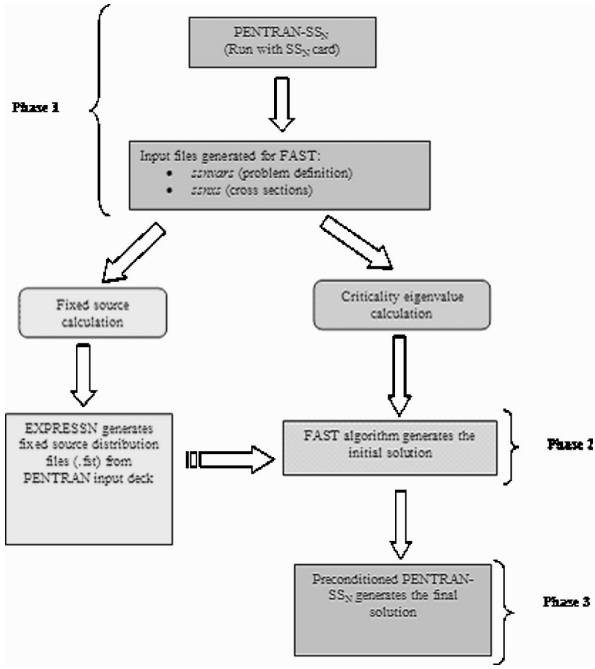

FIG. 1—*Flow-chart of the PENTRAN-SS$_N$ code system coupled with the FAST preconditioning algorithm.*

allel libraries [5]. The algorithm is fully integrated into the PENTRAN-SSN 3D parallel transport code [6], and from a user stand point, the new preconditioning system is totally transparent, requiring only a very limited number of parameters to be executed. In the past, we have tested PENTRAN-SSN with the C5G7 MOX Fuel Assembly benchmark, issued by OECD/NEA, without spatial homogenization, and we have obtained accurate results with a speedup ranging between ~3 and ~5 compared to a standard transport calculation [4].

In this paper, our objective is to test the accuracy and performance of the new preconditioning system for a 3D shielding calculation based on the VENUS-2 MOX-fueled benchmark problem, issued by OECD/NEA [7].

Description of the Flux Acceleration Simplified Transport (FAST) Algorithm

The flux acceleration simplified transport (FAST) algorithm is based on the even-parity simplified Sn (EP-SSN) equations, which, as compared with diffusion equations, represent a higher-order approximation to the discrete ordinates equations (Sn) [4]. The multigroup 3D EP-SSn equations with anisotropic scattering and source is written as

$$-\vec{\nabla}\left(\frac{\mu_m^2}{\sigma_{t,g}(\vec{r})}\vec{\nabla}\psi^E_{m,g}(\vec{r})\right)+\sigma_{t,g}(\vec{r})\psi^E_{m,g}(\vec{r})=\sum_{g'=1}^{G}\sum_{\substack{l=0,2..\\ even}}^{L-1}(2l+1)P_l(\mu_m)S_{sl,g'\to g}(\vec{r})\phi_{l,g'}(\vec{r})$$

$$-\vec{\nabla}\left(\frac{\mu_m}{\sigma_{t,g}(\vec{r})}\sum_{g'=1}^{G}\sum_{\substack{l=1,3..\\ \text{odd}}}^{L}(2l+1)P_l(\mu_m)\vec{S}_{sl,g'\to g}(\vec{r})\vec{\phi}_{l,g'}(\vec{r})\right)+\sum_{\substack{l=0,2..\\ even}}^{L-1}(2l+1)P_l(\mu_m)S_{l,g}(\vec{r})$$

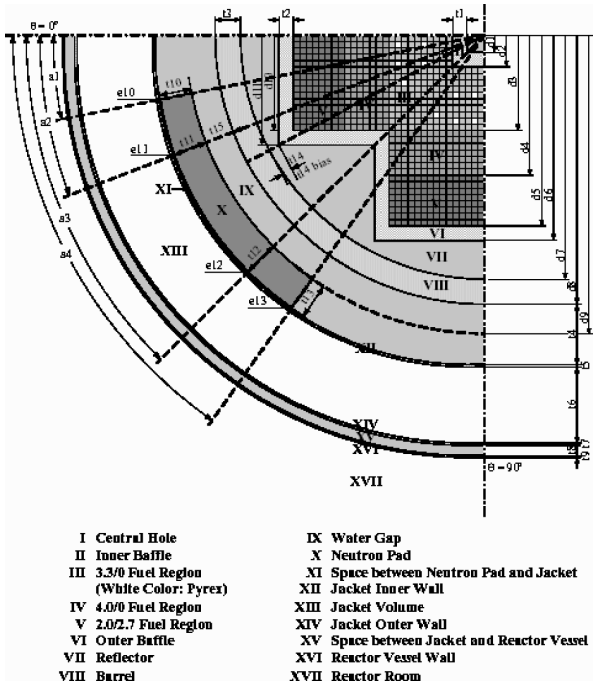

FIG. 2—*VENUS reactor horizontal core description.*

$$-\vec{\nabla}\cdot\left(\frac{\mu_m}{\sigma_{t,g}(\vec{r})}\sum_{g'=1}^{G}\sum_{\substack{l=1,3..\\ \text{odd}}}^{L}(2l+1)P_l(\mu_m)\vec{S}_{l,g'}(\vec{r})\right)+q_{f,g}(\vec{r}) \tag{1}$$

where,

$$\vec{\psi}^{O}_{m,g}(\vec{r})=-\frac{\mu_m}{\sigma_{t,g}(\vec{r})}\vec{\nabla}\psi^{E}_{m,g}(\vec{r})+\frac{1}{\sigma_{t,g}(\vec{r})}\sum_{g'=1}^{G}\sum_{\substack{l=1,3..\\ odd}}^{L}(2l+1)P_l(\mu_m)[\sigma_{sl,g'\to g}(\vec{r})\vec{\phi}_{l,g'}(\vec{r})+\vec{S}_{l,g'}(\vec{r})] \tag{2}$$

for $m=1,\ N/2$ and $g=1,\ G$.

$$\psi^{E}_{m,g}(\vec{r})=\frac{1}{2}[\psi(\vec{r},\mu_m)+\psi(\vec{r},-\mu_m)] \tag{2a}$$

Derivation of the above equations is given in Ref. [8]. Note that in Eqs 1 and 2, a Gauss-Legendre symmetric quadrature set (P_N) is considered, where $\mu_m\in(-1,1)$, $\Sigma_{m=1}^{M}w_m=2.0$, $M=N(N+2)$, and L is the order of the Legendre expansion for both the macroscopic scattering cross section and the inhomogeneous source ($L<N$). In Eqs 1 and 2, the terms $S_{l,g}(\vec{r})$ and $\vec{S}_{l,g}(\vec{r})$ represent the expansion in terms of Legendre polynomials of the inhomogeneous external source. The FAST algorithm solves Eqs 1 and 2 using a finite-volume approach for spatial discretization. The resulting linear system of equations is solved using

TABLE 1—*Computation time.*

Code	Wall clock time (h)
PENTRAN	4.4
PENTRAN-SSN[a]	3.5

[a]Includes FAST computing time.

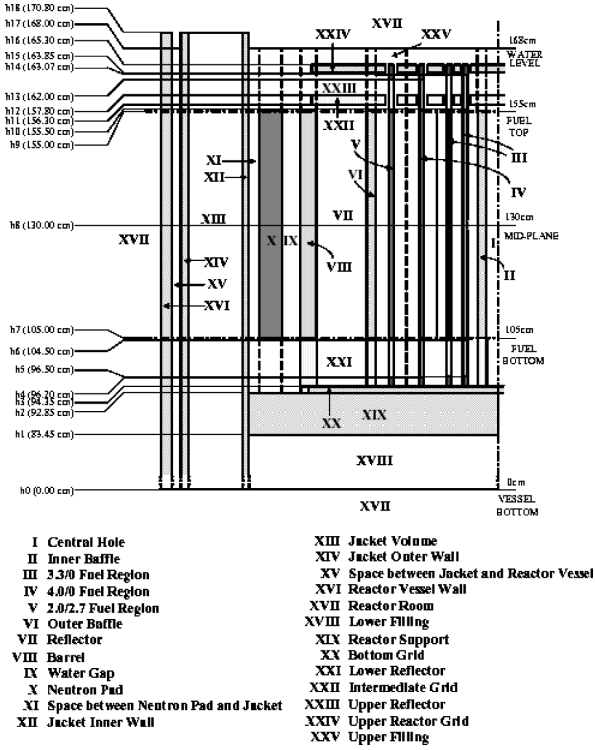

FIG. 3—*VENUS reactor vertical core description.*

the conjugate gradient method [9]. As mentioned above, the FAST algorithm is designed for parallel computing environments with a spatial domain decomposition strategy, where we partition the spatial domain into a number of coarse meshes and allocate them to different processors. The FAST algorithm prepares the initial solution for the Sn code and creates output files for scalar flux, currents, and criticality eigenvalue, if needed. These output files are prepared for each energy group and they are split into *file_a* for the first half of the spatial domain and *file_b* for the second half. This format is used to make sure that the file sizes are under the limits of the current operating systems. The files containing the initial solution are read successively by PENTRAN-SSN and used as initial guess for the SN PENTRAN calculations. Figure 1 shows a flow chart for the PENTRAN-SSN code system which uses the FAST preconditioning algorithm.

The main principle behind FAST preconditioning methodology is to use a simplified model such as the EP-SSN equations to quickly obtain an initial solution to the problem, and then use this solution as initial flux guess for the transport calculation. At this time, the FAST algorithm is capable of providing both scalar flux and first moment (current) as initial solutions.

TABLE 2—*Maximum and minimum relative differences of reaction rates calculated by PENTRAN-SSn and FAST code systems.*

Reaction	MAX rel. difference (%)	MIN rel. difference (%)
Ni-58	15.6	−1.3
In-115	22.4	−0.4
Rh-103	33.1	−11.7
Np-237	27.3	−4.5
Al-27	12.8	−4.8

TABLE 3—*(a)—PENTRAN-SSn reaction rates at 100 % power in stainless steel zones.*

Measurement position[a]	^{58}Ni(n,p)	^{115}In(n,n')	^{103}Rh(n,n')	^{64}Zn(n,p)	^{237}Np(n,f)	^{27}Al(n,α)
Inner baffle						
(−4.41,−0.63)	2.15E+08	4.47E+08	5.63E+08	2.15E+08	4.33E+09	1.46E+06
(−4.41,−4.41)	2.60E+08	5.43E+08	6.82E+08	2.60E+08	5.22E+09	1.72E+06
Outer baffle						
(−39.69,−0.69)	7.25E+07	1.51E+08	1.88E+08	7.25E+07	1.45E+09	4.86E+05
(−39.69,−5.67)	6.89E+07	1.43E+08	1.79E+08	6.89E+07	1.38E+09	4.62E+05
(−39.69,−11.97)	5.60E+07	1.17E+08	1.47E+08	5.60E+07	1.12E+09	3.78E+05
(−39.69,−18.27)	3.32E+07	7.04E+07	9.23E+07	3.32E+07	6.94E+08	2.28E+05
(−37.17,−20.79)	3.65E+07	7.78E+07	1.03E+08	3.65E+07	7.67E+08	2.48E+05
(−30.87,−20.79)	7.71E+07	1.62E+08	2.08E+08	7.71E+07	1.58E+09	5.12E+05
(−24.57,−20.79)	1.33E+08	2.82E+08	3.64E+08	1.33E+08	2.75E+09	8.64E+05
Barrel						
(−49.77,−0.63)	8.26E+06	1.35E+07	1.13E+07	8.26E+06	1.24E+08	7.93E+04
(−49.77,−9.45)	7.12E+06	1.16E+07	9.67E+06	7.12E+06	1.06E+08	6.91E+04
(−47.25,−18.27)	6.83E+06	1.15E+07	1.05E+07	6.83E+06	1.09E+08	6.38E+04
(−45.99,−22.05)	5.98E+06	1.02E+07	9.65E+06	5.98E+06	9.76E+07	5.61E+04
(−44.73,−24.57)	5.43E+06	9.42E+06	9.12E+06	5.43E+06	9.03E+07	5.05E+04
(−42.21,−28.35)	5.10E+06	8.71E+06	8.23E+06	5.10E+06	7.95E+07	4.97E+04
(−38.43,−33.39)	4.70E+06	8.92E+06	9.88E+06	4.70E+06	8.19E+07	4.37E+04
(−35.91,−35.91)	4.75E+06	8.97E+06	9.89E+06	4.75E+06	8.20E+07	4.45E+04
Neutron pad						
(−58.54,−22.47)	8.62E+05	1.18E+06	7.59E+05	8.62E+05	9.46E+06	1.17E+04
(−46.60,−41.95)	5.73E+05	9.86E+05	9.82E+05	5.73E+05	8.66E+06	6.83E+03
(b)						
Central hole						
(00.00, 00.00)	1.59E+08	2.96E+08	3.16E+08	1.59E+08	2.81E+09	1.22E+06
Water gap						
(−54.36,−9.59)	3.14E+06	4.73E+06	3.46E+06	3.14E+06	4.08E+07	3.51E+04
(−52.89,−15.80)	3.04E+06	4.67E+06	3.55E+06	3.04E+06	4.11E+07	3.27E+04
(−51.53,−19.78)	3.03E+06	4.66E+06	3.57E+06	3.03E+06	4.12E+07	3.32E+04
(−50.03,−23.33)	2.81E+06	4.41E+06	3.51E+06	2.81E+06	3.96E+07	3.01E+04
(−48.74,−25.91)	2.62E+06	4.13E+06	3.34E+06	2.62E+06	3.73E+07	2.80E+04
(−46.29,−30.06)	2.42E+06	3.77E+06	3.02E+06	2.42E+06	3.35E+07	2.69E+04
(−44.08,−33.22)	2.13E+06	3.42E+06	2.94E+06	2.13E+06	3.04E+07	2.36E+04
(−42.29,−35.48)	1.93E+06	3.25E+06	3.14E+06	1.93E+06	2.95E+07	2.10E+04
(−39.03,−39.03)	1.84E+06	3.15E+06	3.17E+06	1.84E+06	2.88E+07	2.01E+04
Reflector						
(−23.31,−23.31)	9.63E+07	1.97E+08	2.48E+08	9.63E+07	1.92E+09	6.64E+05
(−25.83,−25.83)	4.99E+07	9.32E+07	1.01E+08	4.99E+07	9.00E+08	3.87E+05
(−28.35,−28.35)	2.69E+07	4.73E+07	4.53E+07	2.69E+07	4.53E+08	2.30E+05
(−30.87,−30.87)	1.48E+07	2.48E+07	2.17E+07	1.48E+07	2.32E+08	1.38E+05
(−33.39,−33.39)	8.31E+06	1.39E+07	1.21E+07	8.31E+06	1.23E+08	8.11E+04

[a](x,y) in [cm,cm] coordinates with respect to core center.

Description of the VENUS-2 MOX-Fueled Reactor Dosimetry Benchmark

A new benchmark exercise has been issued by OECD/NEA based on the VENUS reactor owned and operated by (SCK·CEN) laboratory in Belgium. The VENUS reactor horizontal and vertical core descriptions are shown in Figs. 2 and 3, respectively.

The objective of this benchmark is to test the current state-of-the-art computation methods for calculating neutron flux in the VENUS-2 MOX-fueled critical experiments. The measured data for this benchmark are the equivalent fission fluxes and reaction rates obtained using ^{58}Ni(n,p), ^{115}In(n,n'), ^{103}Rh(n,n'), ^{64}Zn(n,p), ^{237}Np(n,f), and ^{27}Al(n,α) detectors at several locations on the core midplane of the reactor. The measurement positions in VENUS-2 are located along the core midplane at 34 locations in the outer core region, the core baffle, the water reflector, the core barrel, and the neutron pad. Note that we have used the same response functions for ^{64}Zn(n,p) as the ^{58}Ni(n,p), since the two elements present the same activation threshold of 2.8 MeV.

We have developed a 3D transport model of the VENUS reactor, which extends from the reactor center

TABLE 4—*(a)—FAST (EP-SS$_6$ P$_3$) Reaction rates at 100 % power in stainless steel zones.*

Measurement position[a]	^{58}Ni(n,p)	^{115}In(n,n')	^{103}Rh(n,n')	^{64}Zn(n,p)	^{237}Np(n,f)	^{27}Al(n,α)
Inner baffle						
(−4.41,−0.63)	2.13E+08	4.45E+08	5.92E+08	2.13E+08	4.39E+09	1.45E+06
(−4.41,−4.41)	2.63E+08	5.45E+08	6.97E+08	2.63E+08	5.26E+09	1.79E+06
Outer baffle						
(−39.69,−0.69)	6.96E+07	1.49E+08	2.03E+08	6.96E+07	1.49E+09	4.62E+05
(−39.69,−5.67)	6.62E+07	1.42E+08	1.93E+08	6.62E+07	1.41E+09	4.41E+05
(−39.69,−11.97)	5.41E+07	1.16E+08	1.59E+08	5.41E+07	1.16E+09	3.63E+05
(−39.69,−18.27)	3.20E+07	6.99E+07	1.03E+08	3.20E+07	7.25E+08	2.20E+05
(−37.17,−20.79)	3.58E+07	7.71E+07	1.11E+08	3.58E+07	7.90E+08	2.51E+05
(−30.87,−20.79)	7.64E+07	1.61E+08	2.18E+08	7.64E+07	1.60E+09	5.22E+05
(−24.57,−20.79)	1.31E+08	2.79E+08	3.75E+08	1.31E+08	2.76E+09	8.70E+05
Barrel						
(−49.77,−0.63)	7.59E+06	1.27E+07	1.11E+07	7.59E+06	1.16E+08	7.04E+04
(−49.77,−9.45)	6.56E+06	1.10E+07	9.58E+06	6.56E+06	9.96E+07	6.16E+04
(−47.25,−18.27)	6.30E+06	1.09E+07	1.04E+07	6.30E+06	1.04E+08	5.76E+04
(−45.99,−22.05)	5.52E+06	9.60E+06	9.49E+06	5.52E+06	9.27E+07	5.13E+04
(−44.73,−24.57)	5.15E+06	8.90E+06	8.79E+06	5.15E+06	8.58E+07	4.87E+04
(−42.21,−28.35)	4.76E+06	8.24E+06	8.15E+06	4.76E+06	7.66E+07	4.57E+04
(−38.43,−33.39)	4.70E+06	8.86E+06	1.03E+07	4.70E+06	8.24E+07	4.48E+04
(−35.91,−35.91)	4.80E+06	8.94E+06	1.03E+07	4.80E+06	8.26E+07	4.66E+04
Neutron pad						
(−58.54,−22.47)	7.91E+05	1.10E+06	7.30E+05	7.91E+05	8.63E+06	1.05E+04
(−46.60,−41.95)	4.84E+05	7.65E+05	6.57E+05	4.84E+05	6.29E+06	6.12E+03
(b)						
Central hole						
(00.00,00.00)	1.51E+08	2.86E+08	3.22E+08	1.51E+08	2.78E+09	1.14E+06
Water gap						
(−54.36,−9.59)	2.95E+06	4.54E+06	3.44E+06	2.95E+06	3.80E+07	3.20E+04
(−52.89,−15.80)	2.89E+06	4.51E+06	3.52E+06	2.89E+06	3.85E+07	3.10E+04
(−51.53,−19.78)	2.78E+06	4.37E+06	3.50E+06	2.78E+06	3.79E+07	2.97E+04
(−50.03,−23.33)	2.62E+06	4.14E+06	3.38E+06	2.62E+06	3.64E+07	2.81E+04
(−48.74,−25.91)	2.47E+06	3.90E+06	3.19E+06	2.47E+06	3.43E+07	2.68E+04
(−46.29,−30.06)	2.22E+06	3.50E+06	2.92E+06	2.22E+06	3.09E+07	2.43E+04
(−44.08,−33.22)	2.00E+06	3.24E+06	2.93E+06	2.00E+06	2.91E+07	2.18E+04
(−42.29,−35.48)	1.86E+06	3.15E+06	3.21E+06	1.86E+06	2.92E+07	2.00E+04
(−39.03,−39.03)	1.77E+06	3.08E+06	3.30E+06	1.77E+06	2.89E+07	1.88E+04
Reflector						
(−23.31,−23.31)	8.94E+07	1.89E+08	2.56E+08	8.94E+07	1.91E+09	5.86E+05
(−25.83,−25.83)	4.57E+07	8.85E+07	1.03E+08	4.57E+07	8.85E+08	3.38E+05
(−28.35,−28.35)	2.49E+07	4.51E+07	4.60E+07	2.49E+07	4.41E+08	2.04E+05
(−30.87,−30.87)	1.40E+07	2.39E+07	2.18E+07	1.40E+07	2.22E+08	1.28E+05
(−33.39,−33.39)	8.41E+06	1.37E+07	1.20E+07	8.41E+06	1.19E+08	8.50E+04

[a](x,y) in [cm,cm] coordinates with respect to core center.

hole out to the jacket outer wall, ranging from 0.0 cm to 70.0 cm on the x-y plane, and from 95.0 cm to 165.0 cm along the z axis. The model is divided in three z levels, which represent the reactor support, the reactor core, and a top layer of moderator (light water). The model is discretized with a total of 92 250 fine meshes. The multigroup cross sections used have been derived from the BUGLE-96 cross-sections library based on the ENDF-B/VI data set. The 47-group cross sections used for the benchmark are expanded up to P_3 order to account for anisotropic scattering. The fuel regions have been homogenized based on the relative volume fractions of water, cladding, and fuel. The reactor core is characterized by three regions: an inner region with UO_2 3.0 (w/o) enriched, an outer region composed of UO_2 4.0 w/o enriched, and a MOX region with 2.0 w/o UO_2 and 2.7 w/o Pu (Fig. 2).

The 3D fixed source distribution has been generated using the data provided in the benchmark specification. The data for the radial distribution was directly measured after an irradiation of 13.5 h at 90 % of the VENUS maximum power. In addition, the fission rate distribution of six fuel pins (two 3/0 UO_2, two 4/0 UO_2 and two 2/2.7 MOX pins) were measured by scanning the γ activity after an irradiation of 8 h at 90 % of the VENUS maximum power. The source distribution provided has been processed using the

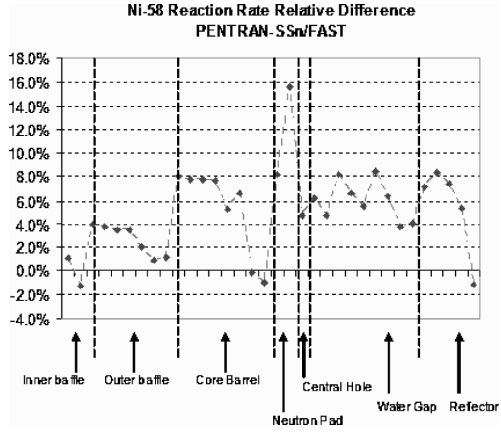

FIG. 4—*Dosimetry data relative difference for Ni-58.*

PENMSH code, which also prepares the mesh and material distribution for PENTRAN-SSN and FAST codes. Note that a normalization factor of 7.181E+9 was used for converting the arbitrary source distribution employed in the calculations to the source at 100 % power, which correspond to a power of 595 Watts.

Discussion of the Calculations and Results

The solution for the benchmark problem has been obtained with PENTRAN-SSN using the FAST preconditioning algorithm. All the calculations were run on the Einstein 64-Bit Beowulf cluster at the Nuclear and Radiological Engineering department located at the University of Florida. The results presented in this section were obtained using an S_8 level-symmetric quadrature set with a P_3 anisotropic scattering for the PENTRAN-SSN code; while, FAST used the EP-SS_6 equations with a P_3 Legendre expansion for accounting anisotropic scattering. The convergence criterion for the inner iteration was fixed to 1.0e-4 for both PENTRAN-SSN and FAST. The calculations were run on nine processors of Einstein cluster using the spatial domain decomposition strategy for both PENTRAN-SSN and FAST. The total computation time for the unaccelerated PENTRAN and PENTRAN-SSN runs is shown in Table 1.

As shown in Table 1, the preconditioning algorithm reduced the computation time by ~20 % compared to the unaccelerated PENTRAN calculation. FAST provided the initial solution in ~45 min, and scalar

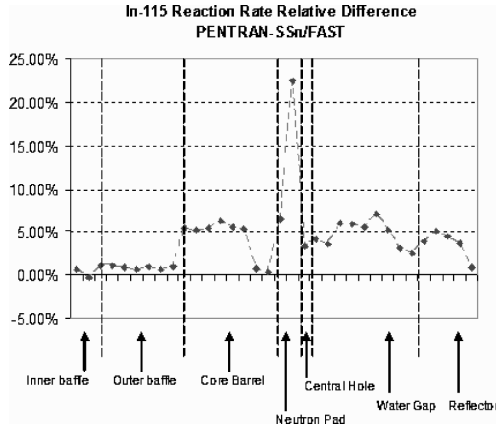

FIG. 5—*Dosimetry data relative difference for In-115.*

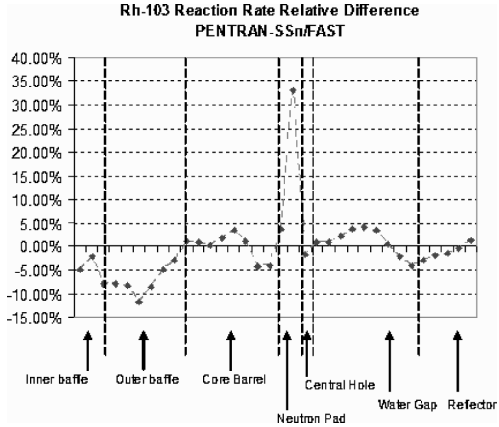

FIG. 6—*Dosimetry data relative difference for Rh-103.*

flux and first moment were used as the initial guess for the PENTRAN transport calculation. Note that this reduction is significantly smaller than was observed for the criticality problems. This can be attributed to the fact that criticality calculations generally require more iterations because of high c ratios as compared to the current fixed-source (shielding) problem.

Comparison of the dosimetry data obtained with PENTRAN-SSN and FAST shows good agreement for almost every detector. Table 2 shows the maximum and minimum relative difference between PENTRAN-SSN and FAST, for the dosimetry data obtained from different locations specified by the benchmark.

As shown in Table 2, the dosimetry data obtained with FAST present good agreement with the PENTRAN-SSN transport solution. For the Ni-58, In-115, Rh-103, and Np-237 reaction rates, the maximum relative difference is observed at the neutron pad detector location, specifically at $x=-46.60$ cm and $y=-41.95$ cm. The Al-27 reaction present the maximum relative difference in the reflector region at $x=-25.83$ cm and $y=-25.83$ cm. Tables 3 present the reaction rates obtained with PENTRAN-SSN in the stainless steel and water zones, respectively; while Tables 4(a) and (b) present the same reaction rates obtained with the FAST computer code. Figures 1–5, show the relative differences for the dosimetry data obtained with PENTRAN-SSN and FAST (Figs. 6–8).

Note that the dosimetry data obtained with FAST present good agreement ($\sim$10 % relative difference) in each region, except the neutron pad. The reason for large discrepancies observed in this region is due to

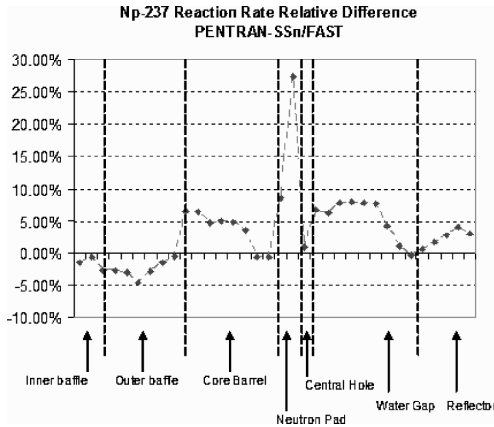

FIG. 7—*Dosimetry data relative difference for Np-237.*

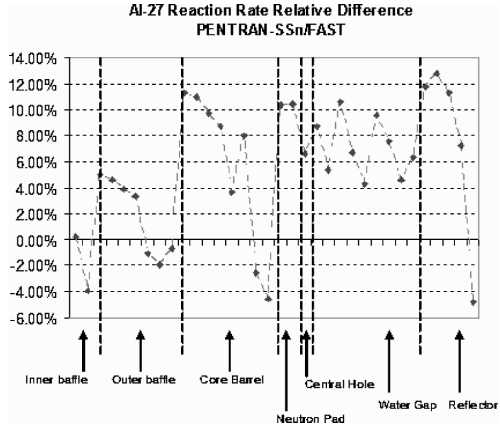

FIG. 8—*Dosimetry data relative difference for Al-27.*

the deep-penetration nature of the problem, where the EP-SSN equations are less effective in representing steep gradients of the neutron flux. However, the FAST algorithm produced accurate results for high energy level reactions such as $^{27}\mathrm{Al}(n,\alpha)$, with a maximum relative difference compared to PENTRAN-SSN of $\sim$13 %.

Conclusions

A new preconditioning algorithm, namely, flux acceleration simplified transport (FAST), has been developed based on the EP-SSN equations. We have coupled the algorithm to the PENTRAN-SSN code system in order to accelerate the solution process of the linear Boltzmann equation. The code systems are designed for parallel architectures, and they are suitable for determining radiation transport fields for large 3D models. The FAST preconditioning algorithm yielded a $\sim$20 % speed-up compared to an unaccelerated transport calculation. Note that this reduction is significantly smaller than was observed for the criticality problems. This can be attributed to the fact that criticality calculations generally require more iterations because of high c-ratios as compared to the current fixed-source (shielding) problem.

Nevertheless, the dosimetry data obtained with the FAST computer code yielded good agreement with the transport calculation performed using the PENTRAN-SSN code system.

References

[1] Lewis, E. E. and Miller, W. F. Jr., "*Neutron Transport*," American Nuclear Society, La Grange Park, IL, 1993.

[2] and Larsen, E. W., "Fast Iterative Methods for Discrete-Ordinates Particle Transport Calculations," *Prog. Nucl. Energy*, Vol. 40, No. 1, 2002.

[3] Warsa, J. S., Wareing, T. A., and Morel, J. E., "On the Degraded Effectiveness of Diffusion Synthetic Acceleration for Multidimensional S_N Calculations in the Presence of Material Discontinuities," *Proceedings of the ANS Topical Meeting on Nuclear Mathematical and Computational Sciences: A Century In Review - A Century Anew (M&C 2003)*, Gatlinburg, TN, April 6–11, 2003, on CD-ROM, American Nuclear Society, Inc., La Grange Park, IL, 2003.

[4] Longoni, G. and Haghighat, A., "The Even-Parity Simplified S_N Equations Applied to a MOX Fuel Assembly Benchmark Problem on Distributed Memory Environments," *PHYSOR 2004 - The Physics of Fuel Cycles and Advanced Nuclear Systems: Global Developments*, Chicago, IL, April 25–29, 2004, on CD-ROM, American Nuclear Society, Inc., Lagrange Park, IL, 2004.

[5] Gropp, W., Lusk, E., and Skjellum, A., *Using MPI Portable Parallel Programming with the Message Passing Interface*, The MIT Press, Cambridge, Massachussetts, 1999.

[6] Sjoden, G. E. and Haghighat, A., "PENTRAN – Parallel Environment Neutral-particle TRANsport in 3-D Cartesian Geometry," *Proceedings of the Joint International Conference on Mathematical Methods and Supercomputing for Nuclear Applications*, Vol. 1, pp. 232–234, Saratoga Springs, NY, October 6–10, 1997.

[7] Byung-Chan, Na et al., "VENUS-2 MOX-Fuelled Reactor Dosimetry Calculations – Benchmark Specification," NEA/NSC/DOC(2004)6, OECD/NEA.

[8] Longoni, G., Haghighat, A., and Sjoden, E. G., "A New Synthetic Acceleration Technique based on the Simplified Even-Parity S_N Equations," *Transp. Theory Stat. Phys.*, Vol. 33, 2004, pp. 347–360.

[9] Golub, G. and Ortega, J. M., *Scientific Computing An Introduction with Parallel Computing*, Academic Press, San Diego, CA, 1993.

Journal of ASTM International, Vol. 3, No. 4
Paper ID JAI13489
Available online at www.astm.org

Sergey I. Belousov,[1] *Krassimira D. Ilieva,*[2] *and Victor L. Matushko*[3]

Sensitivity Analysis and Neutron Fluence Adjustment for VVER-440 RPV

ABSTRACT: Adjustment of the neutron fluence on the VVER-440 reactor pressure vessel (RPV) inner wall has been carried out. For the purpose of this adjustment the neutron flux responses' sensitivity to the main parameters of calculation uncertainty has been calculated. The obtained sensitivities, the parameters uncertainty, and activity measurement data of iron, copper, and niobium detectors positioned behind the RPV of Kozloduy NPP Unit 1 have been used in this adjustment.

KEYWORDS: neutron fluence, adjustment, reactor pressure vessel

Introduction

The application of adjustment is a way for more precise evaluation of reactor pressure vessel (RPV) neutron fluence. The adjustment using the least-squares method [1] is performed on the base of the discrepancies between measured and calculated neutron flux response values. Correlation matrix of the responses and calculational parameters as well as sensitivity matrix of the neutron fluence on the RPV inner wall to the calculational parameters are needed for the adjustment. The calculational response correlation is determined through the parameters' correlation matrix and the matrix of the responses' sensitivity to these parameters.

The purpose of this paper is to extend to VVER-440 RPV the application of the neutron fluence adjustment approach that was developed and applied to VVER-1000. The adjustment relations for relative uncertainty analysis are the same as those derived in Ref. [2] for VVER-1000. These relations practically coincide with those derived by the approach of Perel et al. [3].

The main differences between the two types of reactors are related with the constructional geometry data and material content [4]. Additionally, the air gaps behind the RPV where the ex-vessel neutron detectors are positioned for measurement are with different size. The results of the calculations carried out and the following analysis give a quantitative representation on the applicability of the approach.

The adjustment was applied to the VVER-440 reactor with dummy cassettes core loading (36 dummy cassettes at the periphery of the reactor core instead of fuel assemblies). The responses taken into consideration were the induced activities of ex-vessel (behind the vessel) detectors and the integral neutron fluence (with energy above 0.5 MeV) on the RPV inner wall of Kozloduy NPP Unit 1.

Specification of Parameters and Model Definition

The applied parameter specification for VVER-440 has been those that usually are used for VVER and PWR neutron flux adjustment [2,5,6]. We have followed mainly the parametrization of the sources of uncertainties suitably well systematized in the review [5]. The uncertainty data for material densities and

Manuscript received June 20, 2005; accepted for publication January 25, 2006; published online March 2006. Presented at ASTM Symposium on Reactor Dosimetry, 12th International Symposium on 8–13 May 2005 in Gatlinburg, TN; D. W. Vehar, D. M. Gilliam, and J. M. Adams, Guest Editors.

[1] Senior Research Scientist, Institute for Nuclear Research and Nuclear Energy of Bulgarian Academy of Science, Tsarigradsko 72, Sofia 1784, Bulgaria.

[2] Senior Research Scientist, Institute for Nuclear Research and Nuclear Energy of Bulgarian Academy of Science, Tsarigradsko 72, Sofia 1784, Bulgaria.

[3] Senior Research Scientist, Institute for Nuclear Research of Russian Academy of Science, 60 October, 7a, Moscow 117312, Russia.

construction dimensions have been taken from [6]. The cross-section uncertainties data library (LUND) [7] created by Dr. G. Manturov has been used for evaluating the impact of cross-section uncertainties.

The following sources of uncertainties have been taken into account in our analysis:

- Inelastic, elastic, and absorption cross section of iron in the VVER-440 steel constructional materials.
- Chromium inelastic, elastic, and absorption cross section.
- Hydrogen and oxygen elastic cross section.
- Neutron source spectrum.
- Neutron source spatial distribution.
- Density of steel of the construction including baffle, basket, barrel, and RPV.
- Moderator density, i.e., density of the water between the baffle and basket, the basket and barrel, and in the downcomer.
- RPV inner radius.

These sources of uncertainties were previously considered in VVER-1000 adjustment analysis [2]. In addition, for the case of VVER-440 the activation cross-sectional uncertainties have been taken into consideration for evaluation of ex-vessel detectors' responses uncertainties.

The mentioned sources of uncertainties have been included into a simplified one-dimensional calculation model of the VVER-440 reactor with dummy cassettes' core loading. This model is represented by cylindrical shells whose surfaces are equal to the surfaces of the reactor core, baffle, and dummy cassettes correspondingly. The model has been prepared by space averaging along the axial and azimuthal direction of the real reactor geometry model. An axial averaging was applied for the region close to the reactor middleplane where the dependence of the neutron fluence rate properties on the axial direction was not very significant. An averaging over the azimuth has been applied for the reactor core, baffle, and dummy cassettes geometry description.

Independent of the simplification of the model applied takes into account the main parameters and lets us analyze the main properties of the adjustment procedure application.

In our model, for the parameters adjustment we have used the discrepancies between the calculated and measured values of detector responses from the reactions Fe54(n,p)Mn54, Cu63(n,α)Co60, and Nb93(n,n')Nb93m. The adjusted parameters have been used for estimation of the RPV neutron fluence with energy above 0.5 MeV.

Parameters and Sensitivity Values

The responses taken in consideration are the induced activity of ex-vessel (behind the vessel) detectors and the integral neutron fluence (with energy above 0.5 MeV) at the RPV inner wall.

The relative sensitivities of the RPV neutron fluence and the ex-vessel detector responses to the neutron cross sections have been calculated by the MCNP4C code [8]. The MCNP code gives an exceptional opportunity for calculation of the fluence rate response sensitivity to neutron cross-sectional perturbation. But it has to be kept in mind that the perturbation calculation, as a rule, needs significantly more time than the mean values' calculation so to obtain results satisfying all statistical tests requirements. The calculation of the sensitivity to the rest of the parameters has been carried out by the DOORS code system [9]. The sensitivity calculations have been performed for the same energy structure as of the applied cross-sectional uncertainty data LUND. The elastic and inelastic cross-sectional uncertainties have been considered uncorrelated because there are not data about it in the LUND. For illustration, the obtained sensitivities to the iron inelastic cross section which is the most important source of uncertainty for ex-vessel detector's responses are presented in Table 1.

The sensitivities to all other mentioned sources of uncertainties except the neutron cross sections have been calculated by the DORT code [9] with multigroup cross-sectional library BGL440 [10]. The Watt neutron source energy spectrum [5] was taken into consideration. The values of the sensitivity to the parameters a and b of the Watt neutron source energy spectrum are presented in Table 2.

The negative source gradient toward the core periphery, typical for the VVER-440 core [11] has been considered in the DORT sensitivity calculation. For description of the neutron source spatial uncertainty the reactor core spatial region has been divided into three areas:

- Area 1—within 5 cm from the core outer boundary;

TABLE 1—*Fluence and detector's responses sensitivity to the iron inelastic cross section in different energy ranges.*

Low energy, MeV	Responses			
	Fluence	Cu detector	Fe detector	Nb detector
14.0	−7.60e−04	−2.75e−02	−4.25e−03	−1.17e−03
10.5	−1.50e−02	−6.02e−01	−1.01e−01	−2.40e−02
6.5	−1.72e−01	−2.01e+00	−9.09e−01	−3.00e−01
4.0	−4.13e−01	−4.53e−01	−1.43e+00	−6.64e−01
2.5	−2.91e−01	−5.85e−03	−5.26e−01	−5.41e−01
1.4	−2.14e−01	−4.91e−05	−1.25e−01	−5.20e−01
0.8	−7.48e−02	0.00e+00	−2.24e−03	−1.62e−01
0.5	−2.44e−03	0.00e+00	−1.55e−07	−2.80e−03

- Area 2—within 5 to 10 cm from the core outer boundary;
- Area 3—the core up to 10 cm from the core outer boundary.

The standard deviation of neutron source in these areas has been assumed to be 10 %, 5 %, and 2 %, respectively. It has been considered that the uncertainties in different areas are correlated and the correlation coefficient values are equal to $\rho_{12}=-\rho_{23}=0.5$, and $\rho_{13}=-0.25$.

The calculated sensitivity for the RPV neutron fluence and ex-vessel detector responses to the neutron source in different spatial areas is presented in Table 3.

The standard deviation of the density of steel constructions—baffle, basket, barrel, and RPV has been considered to be 1 %, as it is usually given by design data. The standard deviation of the water density in the shell (WG1) between the baffle and the basket, in the shell (WG2) between the basket and the barrel, and in the downcomer has been considered to be 2 %. It has been assumed that the uncertainties of density in different regions are not correlated. The sensitivity to the density of the mentioned regions has been calculated. The results for the steel constructions are presented in Table 4, and in Table 5 for the moderator.

The uncertainty of the RPV inner radius has been considered as a consequence of the RPV thickness uncertainty. The standard deviation of RPV thickness uncertainty has been taken equal to 0.5 cm. This corresponds to relative value of 3.6 %. The results for sensitivity of the RPV fluence and the ex-vessel detector responses to the RPV inner radius are presented in Table 6.

The standard deviation of the contribution of the activation cross section to the ex-vessel detector' response uncertainty was taken equal to 5 %, one and the same for all considered types of detectors.

TABLE 2—*Fluence and detector's responses sensitivity to the neutron source spectrum parameters.*

Parameter	Responses			
	Fluence	Cu detector	Fe detector	Nb detector
a	3.02e+00	8.60e+00	5.15e+00	3.41e+00
b	5.63e−01	1.17e+00	8.37e−01	6.16e−01

TABLE 3—*Fluence and detector's responses sensitivity to the neutron source in different spatial areas.*

Area	Responses			
	Fluence	Cu detector	Fe detector	Nb detector
1	3.35e−01	2.80e−01	3.06e−01	3.29e−01
2	2.57e−01	2.42e−01	2.51e−01	2.56e−01
3	4.09e−01	4.78e−01	4.44e−01	4.16e−01

TABLE 4—*Fluence and detector's responses sensitivity to the steel construction densities.*

Region	Responses			
	Fluence	Cu detector	Fe detector	Nb detector
Baffle	−1.43e−01	−1.42e−01	−1.49e−01	−1.46e−01
Basket	−5.85e−01	−6.04e−01	−6.32e−01	−6.04e−01
Barrel	−9.65e−01	−1.01e+00	−1.06e+00	−1.00e+00
RPV	3.98e−02	−2.12e+00	−2.15e+00	−1.59e+00

TABLE 5—*Fluence and detector's responses sensitivity to the coolant densities.*

	Responses			
Region	Fluence	Cu detector	Fe detector	Nb detector
WG1	−6.53e−01	−4.56e−01	−5.34e−01	−6.22e−01
WG2	−1.98e−01	−1.28e−01	−1.52e−01	−1.85e−01
Downcomer	−2.04e+00	−1.32e+00	−1.56e+00	−1.89e+00

Adjustment Transformations

The MATLAB system [12] has been used for the creation of a software procedure package for interface operations and adjustment calculation in accordance with Eqs 5–8 from Ref. [2]. The application of this procedure package allows us to perform all needed operations and matrix transformation using the MATLAB high-performance language for technical computing. Associated database of the sensitivity and correlation matrix data has been prepared as a set of input files.

The adjustment has been performed on the base of the differences between calculated and experimental data for ex-vessel detector responses that have been obtained for cycle 20 of Unit 1, Kozloduy NPP. The values of the ratio of experimental to calculated responses—re/rc, the relative difference between experimental and calculated neutron fluence rate responses $-\delta\Delta r=(1-re/rc)$, and standard deviation (STD) of experimental data presented in Table 7, respectively, were the data used in the adjustment. The experimental responses' uncertainties of different detectors have been considered uncorrelated.

Before the adjustment, the consistency of the data applied has been tested by the weighted sum of squared residuals value Rmin. For the data applied we have obtained Rmin=4.34 when activation cross-sectional uncertainty has not been taken into account. Otherwise, Rmin=3.45. This result shows a satisfactorily good consistency of the adjusted data, especially when activation cross-sectional uncertainty is taken into account, according to the χ^2 distribution with 3 deg of freedom.

It has been assumed in the adjustment that the parameters' uncertainties and experimental responses' uncertainties have not been correlated, and that the contribution of activation cross-sectional uncertainty does not depend on the other sources of uncertainties.

Results and Analysis

The contribution of different uncertainty sources to the uncertainty of the calculated RPV neutron fluence and ex-vessel detector's responses before the adjustment is presented in Table 8.

The values of the uncertainty of the adjusted related responses $\delta\hat{r}$ of the ex-vessel detectors and RPV neutron fluence $\delta\hat{F}$ together with their standard deviations, when activation cross-sectional uncertainty is neglected, are presented in Table 9 and, otherwise, in Table 10. As it is seen the adjustment results do not change significantly when activation cross-sectional uncertainty is neglected.

A preliminary analysis of the obtained results shows that the adjusted detector response uncertainty values are comparable and even lower than the experimental ones. In this case the adjustment by the applied set of ex-vessel detector's data decreases the RPV fluence value by about 13 % and reduces about one and a half times the RPV fluence uncertainty. The uncertainty related to the RPV thickness is one of the main contributions to the neutron fluence uncertainty. The ex-vessel detectors with higher threshold are

TABLE 6—*Fluence and detector's responses sensitivity to the RPV inner radius.*

	Responses			
Parameter	Fluence	Cu detector	Fe detector	Nb detector
RPV inner radius	2.31e+00	−1.11e+00	−9.33e−01	9.71e−02

TABLE 7—*Data used in adjustment on neutron fluence for RPV of, Kozloduy NPP Unit, cycle 20.*

Detector	re/rc	$\delta\Delta r$, %	STD, %
Fe	0.877	14.0	5
Cu	0.909	10.0	5
Nb	0.781	28.0	10

TABLE 8—*Contribution of the sources of uncertainty to the RPV neutron fluence and ex-vessel detector responses before adjustment.*

Source of uncertainty	Fluence, %	Cu detector, %	Fe detector, %	Nb detector, %
Iron XS inelastic	6.1	28	24	10
Iron XS elastic	3.5	4.3	6.6	7.9
Iron XS absorption	0.80	5.3	2.7	1.3
Chromium XS inelastic	4.1	5.4	5.3	4.5
Chromium XS elastic	1.5	0.66	1.1	1.5
Chromium XS absorption	0.09	0.35	0.20	0.11
Hydrogen XS elastic	2.3	1.3	1.7	2.2
Oxygen XS elastic	2.5	1.6	2.2	2.5
Source Spectrum	4.3	11	7.1	4.9
Source Spatial Distribution	3.9	3.3	3.6	3.9
Steel Density	1.1	2.4	2.5	2.0
Moderator Density	4.3	2.8	3.3	4.0
RPV inner radius	8.3	4.0	3.4	0.35
Total[a]	14	32	27	16
Total	14	32	28	17

[a]Without contribution of activation cross-section uncertainty.

of greater importance for RPV thickness adjustment since these detectors have a higher sensitivity to the RPV thickness. The same results were obtained for the case of VVER-1000 [2]. It is necessary to note here that only the NPP ex-vessel detectors experimental data contain information appropriate for adjustment regarding the RPV thickness.

The adjustment presented here has been based on the discrepancies between the NPP measurement and calculation results only. The usefulness of the NPP data for adjustment of NPP specific parameters could become more significant if additional information from appropriate benchmarks for adjustment of parameters that are not specific for NPP is included into the model. The incorporation into adjustment of additional information for the parameters, such as neutron cross sections, neutron source spectrum, etc., would allow us to analyze the efficiency of corresponding associated database extension. This analysis should have the purpose to optimize associated database content for obtaining a higher effectiveness of neutron fluence adjustment by RPV ex-vessel dosimetry.

An extension of the NPP responses data (included into associated database) by data from more cycles of the same NPP unit would favor the RPV neutron fluence adjustment as well.

Conclusions

The neutron fluence adjustment approach that was developed for VVER-1000 RPV was extended and applied to the VVER-440 RPV. Additional analysis on the contribution of activity cross-sectional uncertainty was done. It was shown that their contribution to the adjustment results is insignificant.

The adjustment presented here has been based on the discrepancies between the NPP measurement and calculation results only. It has to be noted that only the NPP ex-vessel detectors experimental data contain

TABLE 9—*Adjusted uncertainty values and standard deviations of the ex-vessel detector responses and RPV neutron fluence without taking into account the contribution of activation cross-sectional uncertainty.*

Cu detector		Fe detector		Nb detector		Fluence	
$\delta\hat{r}$, %	STD, %	$\delta\hat{r}$, %	STD, %	$\delta\hat{r}$, %	STD, %	$\delta\hat{F}$, %	STD, %
−13	4.1	−13	4.0	−17	5.8	−14	10

TABLE 10—*Adjusted uncertainty values and standard deviations of the ex-vessel detector responses and RPV neutron fluence after adjustment with taking into account the contribution of activation cross-sectional uncertainty.*

Cu detector		Fe detector		Nb detector		Fluence	
$\delta\hat{r}$, %	STD, %	$\delta\hat{r}$, %	STD, %	$\delta\hat{r}$, %	STD, %	$\delta\hat{F}$, %	STD, %
−14	4.2	−10	4.2	−28	6.3	−13	10

information appropriate for adjustment regarding NPP specific parameters. One of the main contributions to the neutron fluence uncertainty gives uncertainty of the RPV thickness. For the RPV thickness adjustment the ex-vessel detectors with higher threshold are of greater importance since these detectors have a higher sensitivity to the RPV thickness.

Although simplified, the applied VVER-440 model imitates the real conditions of VVER-440 reactor and takes into account the main sources of uncertainties of calculation of RPV neutron fluence and responses of the RPV ex-vessel detectors. This model allows us to estimate the contribution of the main parameters, and to evaluate the importance of the responses included into the adjustment. The model provides an ability of clearer and easy analysis on the basis of a consistent and strict procedure for combined analysis of calculated and experimental NPP data. The obtained results have shown the effectiveness of the adjustment application. It allowed us to obtain the "best estimated" fluence.

The used VVER-440 RPV model could be extended and improved by including additional information of the uncertainty sources and by a more detailed geometry description.

The simplified model allows us the ability to analyze the importance of experimental data included into consideration to the neutron fluence adjustment. To increase the effectiveness of the adjustment approach a reduction of the cross-sectional uncertainties (having the greatest impact to the responses uncertainties) is necessary. This work has to be a separate task at specially designed facilities.

In conclusion, we want to emphasize that the neutron fluence adjustment based on the simplified geometry models of VVER-440 and NPP RPV ex-vessel detectors' data is a good enough approach for the fluence and uncertainty assessment.

Acknowledgments

The authors would like to express sincere thanks to Dr. G. Manturov for the kindly presented neutron cross-sectional uncertainty data. This work was carried out under the contract of the International Atomic Energy Agency, Vienna, RC10992 and the REDOS project of 5FP, Euratom.

References

[1] Hamilton, W., *Statistics in Physical Science*, Roland Press Company, New York, 1964.

[2] Belousov, S. I., Ilieva, K. D., and Kirilova, D., "Sensitivity Analysis and Neutron Fluence Adjustment for VVER-1000 RPV," *Reactor Dosimetry in the 21st Century*, World Scientific, Jan Wagemans et al., eds., New Jersey, London, Singapore, Hong Kong, 2003.

[3] Perel, R. L., Wagschal, J. J., and Yeivin, Y., "PV-Surveillance dosimetry and Adjustment: Review of Several Significant Oral Laws," *Reactor Dosimetry: Radiation Methodology and Assessment, ASTM STP 1398*, John G. Williams et al., eds., ASTM, W. Conshohocken, PA, 2001.

[4] Belousov, S. I., Ilieva, Kr. D., and Antonov, S. Y., "Three-Dimensional Neutron Flux Calculations for the VVER Pressure Vessel," *Nucl. Technol.*, 111, 270 (1995).

[5] Remec, I., "Uncertainty of the Calculated Neutron Flux," Report at Workshop on Processing of Nuclear Data for Use in Power Reactor Pressure Vessel Lifetime Assessment, IAEA Headquarters, Vienna, Austria 1998.

[6] Boehmer, B., Borodkin, G., and Manturov, G., "Improved Covariance Analysis and Spectrum Adjustment for VVER-1000 Pressure Vessel Fluence," *Reactor Dosimetry: Radiation Methodology and Assessment, ASTM STP 1398*, John G. Williams et al., eds., ASTM, W. Conshohocken, PA, 2001, pp. 508–515.

[7] Manturov, G., "Influence of Neutron Data Uncertainties on the Accuracy of Prediction of Advanced Reactor Characteristics," *Proceedings of the International Conference on Nuclear Data for Science and Technology*, Gatlinburg, TN, 1994, Vol. II, pp. 993–999.

[8] I. F. Briesmeister, ed., *MCNP-A General Monte Carlo N-Particle Transport Code, Version4C*, LA-13709-M (April 2000)., RSICC ORNL, Code Package, CCC0700, 2000.

[9] DOORS3.2, RSICC ORNL, Code Package CCC-650, 1998.

[10] Bucholz, J., Antonov, S., and Belousov, S., "BGL440 and BGL1000 Broad Group Neutron/Photon Cross Section Libraries Derived from ENDF/B-VI Nuclear Data," IAEA, INDC(BUL)-15, April 1996.

[11] Belousov, S., Kirilova, D., and Ilieva, K., "Development of the Processing Software Package for RPV Neutron Fluence Determination Methodology," *International Meeting "Nuclear Power in Eastern Europe: Safety, European Integration, Free Electricity Market,"* Bulgarian Nuclear Society, Varna, Bulgaria, 17–20 June 2001, CD-ROM, No 62.

[12] MATLAB is a copyright software product of The MathWorks, Inc., 24 Prime Park Way, Natick, MA 01760-1500.

Journal of ASTM International, Vol. 3, No. 7
Paper ID JAI13461
Available online at www.astm.org

B. L. Broadhead,[1] *M. L. Williams,*[1] *and J. J. Wagschal*[2]

Generalized Linear Least-Squares Adjustment, Revisited

ABSTRACT: TSURFER, a generalized linear least-squares (GLLS) code, is a new module of the SCALE system. After a short introduction outlining the history and applications of the GLLS methodology in reactor physics, a new application of the GLLS methodology in criticality safety is discussed. Some characteristic TSURFER input data are discussed in detail.

KEYWORDS: TSURFER, SCALE, GLLS, adjustment, uncertainties, LEPRICON, inconsistency, rejection, ENDF/B, ICSBEP

Introduction

Twenty-five years has passed since the Least-Square EPRI Consolidation (LEPRICON) methodology [1] was first proposed for the adjustment of pressure vessel fluence estimates by consolidating neutron transport calculations and surveillance dosimetry measurements. The generalized linear least-squares (GLLS) method has since been recognized as a comprehensive and technically correct approach to the analysis of reactor dosimetry data. The crux of the LEPRICON methodology is the simultaneous adjustment of (a) dosimetry measurements in benchmark fields, (b) surveillance dosimetry measurements in the reactor field under test, (c) dosimetry cross sections, and (d) transport-calculation parameters. This procedure results in the adjustment not only of the fluence *at the surveillance position* but also of the calculated fluence at any point *within the vessel steel*, in particular at the point of estimated maximum damage to the pressure vessel. The GLLS procedure also provides a rigorous estimate for the response uncertainties. This is of particular importance since the latest U.S. Nuclear Regulatory Commission (NRC) regulatory guide [2] emphasizes the need for uncertainty analysis in vessel fluence computations, although there is no well-defined rigorous approach specified for the analysis.

In order to perform the adjustment, each measured quantity must be accompanied by the corresponding calculated value, the experimental uncertainty, and possible correlations with other measured quantities. Uncertainty matrices associated with the dosimetry cross sections as well as with the transport-calculation parameters are also needed. Such a procedure also necessitates the calculation of the sensitivity profiles of the calculated fluences to the transport parameters at the surveillance position and at any other location of interest in the field under test. The inclusion of benchmarks in the adjustment requires the evaluation of the uncertainty matrix associated with the fluences in the benchmark experiments in addition to the evaluation of the uncertainty matrix associated with the field under test, and the cross-uncertainty matrices for the correlated quantities. Unfortunately, applications [3] of the methodology have been few and the original code package has not been maintained.

New GLLS Code

The GLLS methodology was introduced to reactor physics, in particular to fast reactor physics, approximately 40 years ago [4,5]. The sensitivity/uncertainty (S/U) techniques, based on the GLLS methodology, were further developed in the 1970s and 1980s for a variety of applications, including nuclear data evaluation [6], fast reactor design studies [7], and reactor pressure vessel damage predictions [3]. Recently

Manuscript received June 20, 2005; accepted for publication April 19, 2006; published online June 2006. Presented at ASTM Symposium on Reactor Dosimetry, 12th International Symposium on 8–13 May 2005 in Gatlinburg, TN; D. W. Vehar, D. M. Gilliam, and J. M. Adams, Guest Editors.

[1] Oak Ridge National Laboratory, P. O. Box 2008, Oak Ridge, TN 37830-6170.
[2] Racah Institute of Physics, Hebrew University of Jerusalem, Edmond Safra Campus, Givat Ram, 91904, Jerusalem, Israel.

a similar methodology has been applied to criticality safety analysis, and a GLLS code has been developed within the SCALE code system [8] to determine biases and uncertainties in neutron multiplication factors by consolidating differential data and benchmark integral experiments. The adjustment code uses the GLLS method to consolidate a prior set of integral responses measured in critical benchmark experiments and a corresponding set of calculated values obtained using the SCALE code system. The code improves the initial estimates for calculated and measured responses by varying the nuclear data used in the transport calculations as well as the values of the measurements, taking into account their correlated uncertainties, in the sense that the most self-consistent set of data is obtained. This approach forces the modified estimates of the calculated and measured responses to agree, while at the same time constraining the data variations to minimize a generalized chi-square. This ensures maximum overall consistency in the set of calculated and measured responses for a specified set of data and experimental uncertainties; thus, the posterior results represent the "best estimates" for the true response values. Consolidation of the original integral experiment data and calculated results reduces the prior uncertainty in the response estimates, since additional information has been incorporated, compared with either the measured or calculated results alone.

This paper describes the TSURFER code (tool for sensitivity/uncertainty analysis of response functionals using experimental results), which is a functional module in the SCALE S/U analysis methodology [8]. The main functions of the code are (a) to compute uncertainties in calculated integral responses, such as k_{eff}, due to uncertainties in the input nuclear data, and (b) to analyze measured responses from benchmark integral experiments in order to establish the bias and associated uncertainty in some application response that has been calculated. As a result, the observed discrepancies between the measured and calculated responses are reduced, as well as the uncertainties associated with the adjusted quantities.

The SCALE nuclear analysis system is comprised of (a) calculation modules (codes) and (b) control modules (sequences) that execute one or more codes to perform a particular function. Other modules in SCALE perform complementary S/U calculations and prepare input files for the TSURFER code. Some other routines involved with S/U are summarized below. Puff-III is described in Ref. [9], and descriptions of the other routines can be found in the SCALE 5 documentation [8]. The TSURFER code represents a component within the overall S/U capability of the SCALE system.

TSURFER provides an alternative approach to the traditional trending analysis used by the criticality safety community to determine "computational biases." Traditional trending analyses estimate the computational bias based on observed trends between calculated k_{eff} values versus system parameters such as hydrogen-to-fissile ratios (H/X) or energy of average lethargy causing fission (EALF). These physical parameters are widely accepted as reasonable measures of "similarity" between various systems, hence their use as bias predictors. Recent studies have shown that combinations of data sensitivity coefficients, either alone or in combination with cross-section uncertainty information, are also good indicators of system similarity [10]. S/U-based indices can be used in trending analyses similar to the widely used physical parameters. The inputs needed for S/U trending analysis (i.e., calculated and measured responses, sensitivity coefficients, cross-sectional and experimental uncertainties) are almost identical to those needed for GLLS analysis; therefore, it is not surprising that some by-products of TSURFER calculations (similarity coefficients, bias variation versus benchmark experiments) are similar to parameters applied for trending results. However, the TSURFER code can be used to address several other important validation issues.

Not only can the computational bias and the uncertainty be calculated by TSURFER for a given application, but the cumulative "combination" of experimental data from several critical benchmarks can also be used to determine the convergence of the procedure. Questions that can be addressed include the following: How many experiments are needed to verify an application? What degree of correlation between the experiment and the application is necessary to validate the application area? The GLLS methodology has been used to answer these questions [10]. Additionally, this tool is expected to be of value for criticality safety validation even when there are very few or no existing experiments considered to be similar to a particular application area. The GLLS technique is useful under these circumstances since individual experiments can be included that separately validate portions of the application area, even though none can be considered entirely similar [11].

Types of Responses

A "response" corresponds to a particular integral response *type* (e.g., k_{eff}, reaction rate ratio, material worth, radiation dose) in a particular *nuclear system* (e.g., a benchmark experiment, a power reactor, or a proposed storage arrangement of reactor fuel assemblies). In the TSURFER input, responses may be classified as "*experiments,*" "*applications,*" or "*omitted*."

An *experiment* response has both calculated and measured values input to TSURFER, and these play an active role in the GLLS procedure that attempts to minimize differences between the two results. A value for the uncertainty in the measured response, as well as any response correlations, is also input for experimental responses. Examples of experimental integral responses are the multiplication factor for the GODIVA critical benchmark experiment, the measured ρ^{28} (ratio of epithermal to thermal capture rate for ^{238}U) in the TRX-1 critical benchmark lattice, the coolant voiding reactivity in a pressurized-water reactor (PWR), or a surveillance dosimetry measurement in a PWR.

Applications are responses for which a calculated value is known but no measured value is available. Applications often correspond to hypothetical systems being considered within the context of a design study or a criticality safety analysis for which the computational bias and uncertainty values are desired. Examples of application responses are the multiplication factor (subcritical) for a proposed fuel assembly storage rack or for a shipping cask or the flux at any desired location in a PWR pressure vessel. An application response plays a passive role in the GLLS procedure. Since the application has no experimental values, it does not impact the values of the active responses included in the consolidation procedure. However, conversely, the GLLS procedure may modify the calculated value of the application if it is "similar" to some of the experimental responses. In this case, the application response shares similar data sensitivity characteristics with one or more of the active responses and hence will be indirectly affected by the same data variations that impact the similar experimental responses. This provides a systematic, well-defined method for utilizing experimental benchmark measurements to establish a bias and uncertainty in the calculation of application response or to estimate the fluence and its uncertainty at the quarter-thickness position of a PWR pressure vessel.

A response designated as *omitted* in the TSURFER input neither affects other responses nor is affected by them. These responses are completely isolated from the GLSS procedure. This capability is sometimes useful to easily "turn off" an active system to observe its impact on the application results or on the consistency (chi-square) of the set of remaining experimental responses.

Uncertainties

Experimental Uncertainty

Even "clean" critical benchmark experiments have uncertainties in the nominal system parameters, such as fuel enrichment, impurities, densities, critical dimensions, and numerous other components, that contribute to the observed discrepancy in the measured and calculated responses for the system. In TSURFER the impact of these uncertainties is designated as the "experimental uncertainty" in the response, since this uncertainty will be present even if no simplifications or approximations are made in the model used for the transport computation. The terminology is sometimes a source of confusion. For example, the measured k_{eff} in a critical experiment is usually known to be unity with a very small uncertainty associated with the long, but finite, stable period. While there is little doubt about the value of k_{eff} for a critical experiment, there may be considerable uncertainty in the system parameter values that describe the benchmark configuration. This contribution to the modeling uncertainty could be justifiably considered either "experimental" (because system parameters such as material compositions and dimensions are specified by the experimentalists) or "computational" (because uncertainties in the system parameters affect the calculation model). However, in TSURFER they are designated as experimental uncertainties. In any case, the uncertainty in each system parameter must be propagated to an uncertainty in the measured response. For a k_{eff} response, this may be done experimentally by physically varying the system parameter and measuring the reactivity effect or, more commonly, by performing auxiliary transport calculations to determine the k_{eff} eigenvalue sensitivity.

The response uncertainty components associated with the respective modeling uncertainties in system parameters determine the overall experimental uncertainty. Many benchmark experiment descriptions in

the *International Handbook of Evaluated Criticality Safety Benchmark Experiments* [12] include information about uncertainties in the system parameters and their estimated impact on the multiplication factor. The benchmark evaluators assign the standard deviations in k_{eff} due to uncertainties in various system parameters based on published or archived experiment descriptions, and sometimes on other considerations [13].

A complication in specifying the experimental uncertainty is how to treat correlations among the different experiments. Response correlations in two benchmark experiments may be caused by factors such as use of the same fuel pins or solutions, the same cladding material and container tank, and common instrumentation (same detectors, hydrometers, etc.). For example, if two different critical experiments use the same fuel material, then it is not justified in the GLLS analysis to conclude that the enrichment in one is too high while the other is too low, even if both differences fall within the specified standard deviation. Our experience and the experience of others [14] have shown that these correlations may not be negligible when applying the GLLS technique to a set of benchmark experiments. Unfortunately, only a limited amount of experiment correlation data has been published, although more is expected to be included in future revisions to the *International Handbook of Evaluated Criticality Safety Benchmark Experiments*. The TSURFER code allows experimental uncertainties caused by uncertainties in system modeling parameters to be input for individual components, and correlation coefficients can be specified for the shared system parameters of each response. This approach provides the capability for users to more easily describe the sources of benchmark experiment correlations, without having to know the overall correlation between two different experiments.

Parameter (Cross-Sectional) Uncertainties

In many instances, the major source of uncertainty in the calculated response is due to uncertainties in basic nuclear data such as microscopic cross sections, fission spectra, neutron yield (nu-bar), and scattering distributions. In dealing with multigroup cross-sectional libraries such as those utilized in typical SCALE calculations, uncertainties due to resonance self-shielding should also be included [15]. The nuclear data uncertainties are described by multigroup covariance matrices that contain variances in individual group cross sections for a given nuclide and reaction type, as well as covariances arising from the correlations between energy groups, and possibly between reactions and materials. Correlations, as well as uncertainties in nuclear data, can have a significant impact on the overall uncertainty in the calculated response; thus, it is important to include these in the TSURFER calculations.

Beginning with VERSION V formats, ENDF/B evaluations have had the capability to include covariance information describing uncertainties in the basic nuclear data [16]. ENDF/B-V included covariance data for several important materials needed in criticality safety and nuclear reactor calculations, but many materials had no covariance data in VERSION V. When ENDF/B-VI was released in 1989, it contained significant revisions to many of the cross-section evaluations in ENDF/B-V. For example, a more rigorous resonance treatment based on the Reich-Moore formalism was used to represent the cross sections of most nuclides. However, new covariance data were not evaluated in many cases, and, in fact, several evaluations that previously had covariance data in ENDF/B-V do not have corresponding data in VERSION VI. Notable among these are H, ^{10}B, N, O, and ^{239}Pu. Thus the ENDF/B covariance data are still incomplete at this time.

TSURFER calculations typically utilize the nuclear data covariance libraries distributed with the SCALE code package. Like the SCALE cross-sectional libraries, the covariance libraries currently available for S/U analyses were generated from ENDF/B-V evaluations. Because several important nuclides do not have uncertainty data in ENDF/B-V, approximate covariance evaluations produced by Argonne National Laboratory (ANL) for 30 additional materials [17] were obtained to supplement the ENDF data. Furthermore, fission spectrum uncertainties are not normally tabulated in the ENDF/B evaluations but can be important contributors to the overall uncertainty for some applications. Therefore, uncertainty information for the fission spectra of ^{235}U, ^{239}Pu, and ^{252}Cf was also added to the files. The generation of the fission spectrum uncertainties is described in Ref. [18].

Evaluated covariance files represent cross-sectional uncertainties using ENDF/B formats such as absolute or fractional variance components defined over fixed energy intervals, fractional variance components correlated over all energy intervals, and fractional variance components correlated over arbitrary energy intervals. The basic evaluated uncertainty files were processed by the PUFF-III computer code [9] into multigroup covariance data in the SCALE 44-neutron group structure. Two multigroup covariance libraries

TABLE 1—*Nuclides contained in 44GROUPV5COV library.*

Identifier	Isotope	Identifier	Isotope
13 027	Al-27	11 023	Na-23
95 241	Am-241	28 000	Ni
79 197	Au-197	92 237	Np-237
5010	B-10	8016	O-16
6012	C-12	82 000	Pb
27 059	Co-59	94 239	Pu-239
24 000	Cr	94 240	Pu-240
9019	F-19	94 241	Pu-241
26 000	Fe	94 242	Pu-242
1001	H-1	14 000	Si
49 115	In-115	90 232	Th-232
3006	Li-6	92 235	U-235
3007	Li-7	92 238	U-238
25 055	Mn-55	98 252	Cf-252
7014	N-14		

are currently available in the SCALE code package. The library named 44GROUPV5COV contains covariance matrices for all materials that have relative covariance information given in ENDF/B-V (Table 1). The other library, named 44GROUPANLCOV, contains the ENDF/B-V uncertainty information, plus relative covariance matrices for the additional nuclides processed from the ANL evaluations.

The covariance file should include standard deviations as well as correlations in the cross sections for different energy groups, reaction types, and materials used in the response calculations. Ideally, the covariance file should contain data for all materials, reactions, and energy groups that impact the set of responses considered in the GLLS analysis; however, covariance data are not currently available for some materials in the SCALE nuclear data libraries. For these data the user may input a default relative standard deviation and a default correlation coefficient that are used to define the uncertainty matrix of any nuclide-reaction combination that has no data in the covariance file. The default uncertainty value defines the variance in the group cross sections, which lies along the diagonal of the covariance matrix. TSURFER assumes that neighboring groups are correlated and assigns the input correlation coefficient to the matrix elements immediately to the left and right of the diagonal. All other elements in the multigroup covariance matrices are set to zero, indicating no "long-range" correlation among the groups. Values for the default relative standard deviation and neighboring correlation coefficient are set by TSURFER input parameters. These are used to define uncertainties for data that have no covariance information on the input file and that have sensitivities greater than a threshold value also specified as an input parameter. All these input parameters have standard default values.

Sensitivities

All active and passive responses considered in the GLLS analysis should have sensitivity data provided for each material and reaction type that significantly impact the response. The sensitivity coefficients are precalculated using other SCALE modules and are stored in individual files for each response included in the TSURFER analysis. The locations of the sensitivity files are specified in the TSURFER input data so that they can be read during the calculation. It is not required that all of the input sensitivity files have the same group structures; for example, the sensitivity coefficients for one response may have been computed using a 238-group cross-sectional library, while sensitivities for another response could have a 44-group structure. Whatever the group structure of the sensitivity data, it will be mapped into the same group structure as the covariance file. At present, the covariance files in SCALE use the standard 44-group structure.

Consistency

The value of *chi-square* χ^2 is a key to the proper interpretation of the TSURFER results. The χ^2 statistic is a measure of the overall consistency of the set of experimental values of the benchmark responses and the nuclear parameters used for their calculation. TSURFER edits the total χ^2 value, as well as individual values

TABLE 2—*HST systems properties.*

System no.	Name	c	Indep. χ^2	Diag. of χ^2
1	hst009-01	1.0033E+00	0.0646	1.1857
2	hst009-02	1.0038E+00	0.0972	2.6007
3	hst009-03	1.0029E+00	0.0681	2.4198
4	hst009-04	9.9681E−01	0.0937	1.7902
5	hst010-01	1.0030E+00	0.0965	17.3072
6	hst010-02	1.0038E+00	0.1527	**27.4728**
7	hst010-03	1.0004E+00	0.0013	0.2446
8	hst010-04	9.9859E−01	0.0205	3.7139
9	hst011-01	1.0067E+00	0.5041	**37.0796**
10	hst011-02	1.0025E+00	0.0699	5.0769
11	hst012-01	1.0019E+00	0.0567	1.6014
12	hst013-01	9.9980E−01	0.0265	0.399
13	hst043-01	9.9752E−01	0.0104	0.3155
14	hst043-02	1.0078E+00	0.8847	**20.6383**
15	hst043-03	1.0028E+00	0.1981	3.3844
16	hst042-05	1.0000E+00	0	0
17	hst042-06	1.0003E+00	0.0011	0.0105
18	hst042-07	1.0011E+00	0.016	0.1778
19	hst042-08	1.0014E+00	0.0265	0.3112

for each experiment. The individual χ^2 values may suggest which experiments contain inconsistencies (i.e., the magnitude of the measured-to-calculated k_{eff} discrepancy is larger than their combined uncertainties). However, the source of inconsistencies may well lie in the nuclear input parameters and, although all responses have small individual χ^2 values, the whole suite may not prove to be consistent. Values of chi-square per degree of freedom (χ^2/n) usually should be within about 20 % of unity for defensible results. Results in which this test is not met may still be valid. However, in general, these results should be viewed with skepticism unless the reasons for the test failure are understood.

Several established methods can be used to modify the value of χ^2/n. One includes a reevaluation of experimental uncertainties and their correlations. A high value of χ^2 indicates that the predicted data variations are well outside the bounds of the standard deviations. If the input experimental uncertainties are underestimated, the data movements can be too extreme and are reflected in high χ^2 values. Values of χ^2 that are too low often suggest that the input experimental uncertainty estimates might be too high, and again a reevaluation should be performed. Thus, it is quite important to utilize *realistic* (not "conservative") estimates for the uncertainties in nuclear data and experimental measurements. Yeivin et al. [19] presented a detailed discussion of inconsistencies and demonstrated a technique for rejecting the responses most responsible for the inconsistencies of the whole suite. An alternative rejection technique based on the value of the "diagonal contribution to χ^2," which is the product of the square of the deviation of the measured from the calculated response values and the respective diagonal value of the inverse of the deviation uncertainty matrix, is presented here.

Twenty-two International Criticality Safety Benchmark Evaluation Project (ICSBEP) [12] highly enriched thermal solution (HST) systems were used for this analysis. Throughout the calculations of proposed adjustments the last three responses (20, 21, and 22) were used only as "applications;" that is, they only passively participated in the adjustment. The chi-square per degree of freedom χ^2/n of this setup was 4.2598, an unacceptable result. The ICSBEP names, calculated k_{eff}, and the χ^2 properties for each of the remaining 19 systems are presented (Table 2). System 9 has the highest value of the "diagonal contribution to χ^2" and was thus excluded from the adjustment campaign, resulting in a χ^2/n of 3.4763, which is still too high. Next, system 6 was excluded and χ^2/n was reduced to 1.6267. Next, system 14 was deactivated. The adjustment campaign, without systems 9, 6, and 14, now yielded a χ^2/n value of 0.9976, which is quite acceptable. One could have guessed a priori that these three systems are candidates for rejection due to the deviation of their calculated k_{eff} values from the experimental value of 1. However, their individual χ^2 values do not deviate from unity and the criterion we chose takes into account the global effect of the information analyzed. The k_{eff} values of each of the systems are depicted in Fig. 1 for each of the adjustment campaigns. The curve labeled "c" shows the original calculated k_{eff} values; "a-4.3," the adjusted k_{eff} values using all 19 systems; "a-3.5," the adjusted k_{eff} values after system 9 was rejected; and

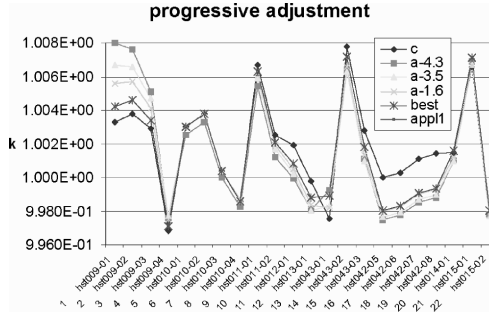

FIG. 1—*Inconsistent systems rejection. (appll is not visible since it is the same as best).*

"a-1.6," the adjusted values after the rejection of systems 9 and 6. The curve labeled "best" indicates the adjusted k_{eff} values after the rejection of the three systems 9, 6, and 14, resulting in a χ^2/n of $\sim$1.

It is interesting to note that although there are systems that seem insensitive to the consistency parameter, the adjusted k_{eff} values of systems 3, 2, and 1 are very sensitive to the inclusion of inconsistent systems. The effect is most profound in system 1, HST009-01. The curve labeled "appl1" is the result of an adjustment in which system 1 was also used as an application. There is no difference between the "best" and "appl1" curves, indicating the success of the method. Although system 1 did not actively participate in the adjustment, its adjusted value is the same as its value when actively participating in the adjustment. The adjusted values of system 1, without inactivating the inconsistent systems, differ by a few "mille-k" from the "best" value. The adjusted k_{eff} value of system 1 without the exclusion of any inconsistent system differs from both the experimental and calculated values by more than its experimental uncertainty (4 mille-k).

Summary and Conclusions

TSURFER, a GLLS module of SCALE, and its features were described followed by a numerical illustration showing the importance of rejecting inconsistent systems.

Acknowledgments

This work was sponsored by the U.S. Department of Energy under the Applicable Ranges of Bounding Curves and Data (AROBCAD) element of the Nuclear Criticality Safety Program (NCSP).

References

[1] Wagschal, J. J., Maerker, R. E., and Yeivin, Y., "Extrapolation of Surveillance Dosimetry Information to Predict Pressure Vessel Fluences," *Trans. Am. Nucl. Soc.*, Vol. 34, 1980, pp. 631–632. See also Maerker, R. E., Broadhead, B. L., and Wagschal, J. J., "Theory of a New Unfolding Procedure in Pressurized Water Reactor Pressure Vessel Dosimetry and Development of an Associated Benchmark Data Base," *Nucl. Sci. Eng.*, Vol. 91, 1985, pp. 369–392.

[2] Calculational and Dosimetry Methods for Determining Pressure Vessel Neutron Fluence, Regulatory Guide *1.190*, U.S. Nuclear Regulatory Commission, March 2001.

[3] Maerker, R. E., Broadhead, B. L., Worley, B. A., Williams, M. L., and Wagschal, J. J., "Application of the LEPRICON Unfolding Procedure to the Arkansas Nuclear One-Unit 1 Reactor," *Nucl. Sci. Eng.*, Vol. 93, 1986, p. 137–170.

[4] Cecchini, G., Farinelli, U., Gandini, A., and Salvatores, M., "Analysis of Integral Data for Few-group Parameter Evaluation of Fast Reactors," *Proceedings of the 3rd International Conference on Peaceful Uses of Atomic Energy*, Vol. 2, United Nations, New York, 1965, pp. 388–397.

[5] Humi, M., Wagschal, J. J., and Yeivin, Y., "Multi-Group Constants from Integral Data," *Proceedings*

of the 3rd International Conference on Peaceful Uses of Atomic Energy, Vol. 2, United Nations, New York, 1965, pp. 398–402.

[6] Pazy, A., Rakavy, G., Reiss, I., Wagschal, J. J., Ya'ari, A., and Yeivin, Y., "The Role of Integral Data in Neutron Cross Section Evaluation," *Nucl. Sci. Eng.*, Vol. 55, 1974, pp. 280–295.

[7] Weisbin, C. R., Marable, J. H., Lucius, J. L., Oblow, E. M., Mynatt, F. R., Peelle, R. W., and Perey, F. G., "Application of FORSS Sensitivity and Uncertainty Methodology to Fast Reactor Benchmark Analysis," *ORNL/TM-5563*, Union Carbide Corp., Oak Ridge National Laboratory, 1976.

[8] "SCALE: A Modular Code System for Performing Standardized Computer Analyses for Licensing Evaluations," *ORNL/TM-2005/39, Version 5*, Vols. I-III, 2005. Available from Radiation Safety Information Computational Center at Oak Ridge National Laboratory as CCC-725.

[9] Dunn, M. E., "PUFF-III: A Code for Processing ENDF Uncertainty Data into Multigroup Covariance Matrices," *ORNL/TM-1999/235 (NUREG/CR-6650)*, U.S Nuclear Regulatory Commission/Oak Ridge National Laboratory, June 2000.

[10] Broadhead, B. L., Rearden, B. T., Hopper, C. M., Wagschal, J. J., and Parks, C. V., "Sensitivity-and Uncertainty- Based Criticality Safety Validation," *Nucl. Sci. Eng.*, Vol. 146, 2004, pp. 340–366.

[11] Goluoglu, S., Elam, K. R., Rearden, B. T., Broadhead, B. L., and Hopper, C. M., "Sensitivity Analysis Applied to the Validation of the ^{10}B Capture Reaction in Nuclear Fuel Casks," *NUREG/CR-6845 (ORNL/TM-2004/48)*, U.S. Nuclear Regulatory Commission, Oak Ridge National Laboratory, 2004.

[12] *International Handbook of Evaluated Criticality Safety Benchmark Experiments*," NEA/NSC/DOC (95)03, Organization for Economic Cooperation and Development/Nuclear Energy Agency, 2004.

[13] "ICSBEP Guide to the Expression of Uncertainties," in *International Handbook of Evaluated Criticality Safety Benchmark Experiments*," NEA/NSC/DOC (95)03, Organization for Economic Cooperation and Development/Nuclear Energy Agency, 2004.

[14] Ivanova, T. T., Nikolaev, M. N., Raskach, K. F., Rozhikhin, E. V., and Tsiboulia, A. M., "Influence of the Correlations of Experimental Uncertainties on Criticality Predictions," *Nucl. Sci. Eng.*, Vol. 145, 2003, pp. 97–104.

[15] Williams, M. L., Broadhead, B. L., and Parks, C. V., "Eigenvalue Sensitivity Theory for Resonance-Shielded Cross Sections," *Nucl. Sci. Eng.*, Vol. 138, 2001, pp. 177–191.

[16] Perey, F. G., "The Data Covariance Files for ENDF/B-V," *ORNL/TM-5938* (ENDF-249), Oak Ridge National Laboratory, 1978.

[17] Naberejnev, D. G. and Smith, D. L., "A Method to Construct Covariance Files in ENDF/B Format for Criticality Safety Applications," *ANL/NDM-148*, Argonne National Laboratory, 1999.

[18] Broadhead, B. L. and Wagschal, J. J., "The Fission Spectrum Uncertainty," in "*PHYSOR 2004 –The Physics of Fuel Cycles and Advanced Nuclear Systems: Global Developments*," Chicago, Illinois, April 25–29, 2004, on CD-ROM, American Nuclear Society, La Grange Park, IL, 2004.

[19] Yeivin, Y., Wagschal, J. J., Marable, J. H., and Weisbin, C. R., "Relative Consistency of ENDF/B-IV and -V with Fast Reactor Benchmarks," *Proceedings of the International Conference on Nuclear Cross Sections for Technology*, J. L. Fowler, C. H. Johnson, and C. D. Bowman, eds., NBS SP 594, National Bureau of Standards, Washington, DC, 1980.

Journal of ASTM International, Vol. 3, No. 4
Paper ID JAI13451
Available online at www.astm.org

D. A. Thornton,[1] *C. Thiruarooran,*[1] *D. A. Allen,*[1] *A. M. Harris,*[1] *C. G. Holmes,*[2] *and C. R. Harvey*[2]

Retrospective Measurement of Neutron Activation within the Pressure Circuit Steelwork of a Magnox Reactor and Comparison with Prediction

ABSTRACT: This paper describes a retrospective measurement of neutron activation rates within steel standpipe penetrations of the pressure circuit of the Wylfa nuclear power plant. This was carried out in support of neutron dose calculations. Samples were taken from a length of irradiated thermocouple cable and counted for the fast neutron reactions $^{54}Fe(n,p)\,^{54}Mn$, and $^{58}Ni(n,p)\,^{58}Co$, and the thermal neutron reactions $^{59}Co(n,\gamma)\,^{60}Co$, $^{58}Fe(n,\gamma)\,^{59}Fe$, and $^{50}Cr(n,\gamma)\,^{50}Cr$. By isolating clean sheath material and performing elemental analysis, it was possible to obtain absolute neutron flux data from the measurements over a broad range of locations.The measured data were compared with results obtained from a Monte Carlo calculation performed with the code MCBEND. Structure observed within the measured and calculated thermal neutron flux distributions was used to confirm the position of the thermocouple samples relative to the reactor geometry. The measurements show that the calculations consistently over-predict fast and thermal neutron reactions. It is concluded that the model predicts spectra without significant bias, and consequently, that the standpipe dose recommendations are similarly over-predicted.

KEYWORDS: retrospective dosimetry, magnox power plant, Monte Carlo, MCBEND

Introduction

Unlike the earlier Magnox plant, the reactors of the last two Magnox power stations are contained within prestressed concrete pressure vessels (PCPVs). Although PCPVs are generally not susceptible to the deleterious effects of neutron irradiation, a number of welded steel penetrations form part of the pressure boundary of the reactors.

A recent safety review for the Wylfa reactors required a reassessment of the structural integrity of standpipe penetrations within the PCPVs, in order to demonstrate adequate temperature margins to embrittlement. Initially, these penetrations were not considered particularly susceptible to neutron irradiation and doses based entirely on calculations were recommended. These calculations used the Monte Carlo radiation transport code MCBEND [1].

Subsequently, it was decided that the dose recommendations for the structural integrity assessment of the Wylfa standpipes should be supported by neutron flux measurements performed on the plant. These measurements would be compared with predictions from MCBEND in order to confirm the suitability of the initial dose recommendations. This approach is broadly consistent with the methodology for recommending doses for the UK Magnox reactors with steel pressure vessels [2–4].

The need to minimize the time scale for this measurement required a retrospective technique using material that had already been irradiated and could be easily recovered. Thermocouple cables running from the pile cap into the active core were identified as the most suitable means of providing such a measurement.

Manuscript received June 20, 2005; accepted for publication October 25, 2005; published online January 2006. Presented at ASTM Symposium on Reactor Dosimetry, 12th International Symposium on 8–13 May 2005 in Gatlinburg, TN; D. W. Vehar, D. M. Gilliam, and J. M. Adams, Guest Editors.

[1] British Nuclear Group, Berkeley Centre, Berkeley, Gloucestershire, GL13 9PB, U.K.
[2] Nexia Solutions, Springfields, Salwick, Preston, Lancashire, PR4 0XJ, U.K.

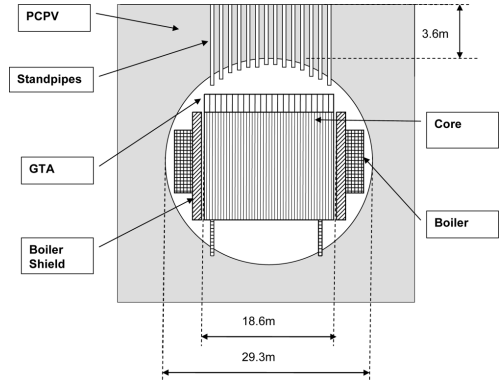

FIG. 1—*Layout of Wylfa reactors.*

Plant Description

Wylfa (Fig. 1) is the latest and largest of the UK's fleet of Magnox power plant. Commissioned in 1971, its two reactors each operate with a thermal power of 1600 MW. The reactors are graphite moderated, carbon dioxide (CO_2) cooled systems utilizing uranium metal fuel elements clad in a low oxidation magnesium alloy (i.e., "magnox").

The reactor coolant, at a pressure of 27 bar, is contained within the PCPV. Steel standpipes penetrate the PCPV from the pile cap at the top, down into the PCPV cavity (or above-core plenum). They provide access to the core for refueling and control rods. There are 397 standpipes per reactor, each accessing up to 16 fuel channels via an array of steel tubes, called a guide tube assembly (GTA), which sits immediately above the core.

The standpipes are vertical penetrations from the top of the PCPV, made from steel annuli joined by axial and circumferential welds (Fig. 2). The gap between the annuli contains PCPV cooling water designed to protect the surrounding concrete from the hot gas within the penetration. It is the combination of cool temperature and relatively high neutron dose rate that makes welds in this region potentially susceptible to embrittlement.

Approximately one quarter of the standpipes sit above channels containing "instrumented fuel elements." Thermocouples attached to these fuel elements run from the core, upward through the GTA and

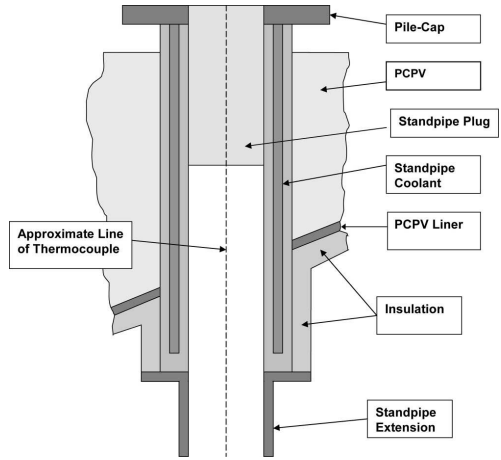

FIG. 2—*Schematic layout of Wylfa standpipe.*

associated standpipe assembly. These cables were identified as ideal for performing a measurement of neutron activation rates within the standpipes.

The thermocouple cables consist of an entwined "rope" of four nominally identical thermocouples. Each thermocouple comprises two fine nickel alloy conductors embedded in a compacted magnesium oxide (MgO) insulator and surrounded by a solid annular sheath of stainless steel. In the reactor, thermocouples are kept taut by two weighted and sprung pulleys.

Neutron Flux Measurements

The essential requirements of this measurement were accurate, absolute activity data, obtained from irradiation positions reliably located within the reactor geometry. The sections below describe how the measurements were obtained, and how these requirements were met.

Acquisition of Thermocouple Samples

When instrumented fuel elements are replaced, the attached thermocouples are normally discarded. For this measurement, a length of approximately 7 m was retained. It was cut into 50 contiguous sections following a predetermined cutting plan. No attempt was made to unwind the "rope" into individual thermocouples and each section consisted of four identical pieces of thermocouple.

Because the standpipes sit in locations with large neutron flux gradients, it was essential to reliably determine the position of the samples during their irradiation. Otherwise, misleading indications could be obtained when comparing predictions and measurements. It was recognized that it would not be possible to predict the precise route of the thermocouple cable through the standpipe from engineering drawings. Instead, the cutting plan was designed to provide fine detail at key locations and where fluxes were expected to vary rapidly. The aim was to use axial flux variations to confirm the irradiation locations of the samples in the reactor.

The sections varied in length, from ~5 cm near to the bottom of the standpipe to ~50 cm near to the top. Cutting distorted the sections at each end, so the weight of each section was used to determine its length. It is estimated that lengths obtained in this way were accurate to ±0.1 %.

Measurement Technique

Whole thermocouple samples are not suitable for absolute activation rate measurements because of uncertainties on the volumes of thermocouple components (and hence elemental content) arising from engineering tolerances on the composite construction. To address this, the approach taken was to determine axial profiles of relative activation rates along the length of the cable and to normalize these against accurate "spot" measurements. In this way, profiles of absolute measurements were obtained.

Initially, axial profiles of relative activation were determined from counting the "as cut" sections. Then, smaller pieces (~1 cm) were extracted from a selection of the original sections for the purpose of performing absolute flux measurements. To ensure greatest accuracy at the positions of greatest interest, these pieces were taken predominantly from sections located near to the bottom of the standpipe, with some check samples taken from other locations. Pieces were taken from each of the four thermocouples in the selected sections.

Stainless steel sheath was identified as the most suitable material for performing the absolute activation measurements; it is the most massive component and has a range of suitable elements. The need to count clean sheath material required isolation of this material from the rest of the thermocouple. This was achieved by bathing these pieces in 25 % nitric acid (HNO_3) to dissolve the MgO insulator and enabling the conductors to be discarded.

The samples of sheath material were weighed and counted. Once counted, the sheath samples were provided for elemental analysis by inductively coupled plasma-optical emission spectrometry (ICP-OES). Analyses of standard steels were used in both the calibration of the equipment and to provide quality control. Magnesium concentration was measured in order to provide confidence in the effectiveness of the MgO removal.

Having obtained the elemental composition, specific activities for the sheath components were calculated. Correcting these for radioactive decay during irradiation and reactor power variations gave reaction

TABLE 1—*Measured sheath compositions.*

Element	Mean proportion Set 1	Mean proportion Set 2
Fe	67.30±0.81 w/o	68.00±0.48 w/o
Cr	19.10±0.59 w/o	18.20±0.20 w/o
Ni	10.90±0.37 w/o	10.80±0.19 w/o
Co	0.020±0.001 w/o	0.0650±0.002 w/o
Other impurities (As, Cu, Mn, Mo, Nb, P, Si, Ti)	2.637±0.050 w/o	2.970±0.083 w/o

rates per unit reactor power. Reaction rates were then divided by cross sections to give fission equivalent and Westcott equivalent fluxes. Finally, the relative profiles of neutron activation were normalized by the sheath measurements giving absolute axial distributions of equivalent fluxes from the measured reactions.

All samples were counted by gamma spectrometry using high resolution germanium detectors calibrated against standard point sources of ^{54}Mn, ^{59}Fe, and ^{60}Co. Activation products of the following reactions were counted:

- Fast neutrons: $^{54}\mathrm{Fe}(n,p)^{54}\mathrm{Mn}$, $^{58}\mathrm{Ni}(n,p)^{58}\mathrm{Co}$
- Thermal/epi-thermal neutrons: $^{59}\mathrm{Co}(n,\gamma)^{60}\mathrm{Co}$, $^{58}\mathrm{Fe}(n,\gamma)^{59}\mathrm{Fe}$, $^{50}\mathrm{Cr}(n,\gamma)^{51}\mathrm{Cr}$

Table 1 shows the results of the elemental analysis. High degrees of consistency were obtained across the samples for all of the major constituents, except for cobalt which fell into two populations with significantly different concentrations. The most probable explanation for this was the use of sheath materials from different batches of stainless steel in the manufacture of the four individual thermocouples.

Results of Neutron Flux Measurements

Figures 3(*a*) and 3(*b*) show the equivalent fluxes for fast and thermal neutrons, respectively. On the horizontal axes, the positions of the samples relative to the bottom of the standpipe are based on the estimated location of the cable within the reactor. The $^{54}\mathrm{Fe}(n,p)$ and $^{58}\mathrm{Ni}(n,p)$ reactions have very similar energy dependencies, and consequently, their fission equivalent fluxes are very similar. The profiles exhibit some structure at approximately 50 cm below the bottom of the standpipe which may be associated with the looping of the cable over one of the tensioning pulleys. Thereafter, the reduction in flux going into the standpipe (0 cm) and then the concrete of the PCPV (50 cm) is relatively monotonic.

In contrast, the thermal neutron results show a significant range in values between the three reactions, and are far from monotonic. With almost pure 1/v neutron energy dependence, $^{50}\mathrm{Cr}(n,\gamma)\,^{51}\mathrm{Cr}$ is the most dependent upon low energy neutrons. This reaction shows a very clear rise due to thermalization of neutrons in the cooling water between the steel annuli of the standpipe. At its maximum, the flux peak is a factor of two higher than the relatively uniform value in the space below the standpipe. Iron and cobalt reactions both have significant resonances and the contributions made by higher energy, epithermal neutrons result in much larger fluxes than for chromium. These reactions too show thermalization peaks, but their relative magnitudes are much less due to dilution by epithermal neutrons. Each of the peaks is well

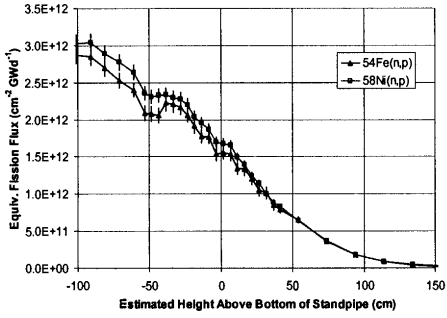

a) Fast neutrons

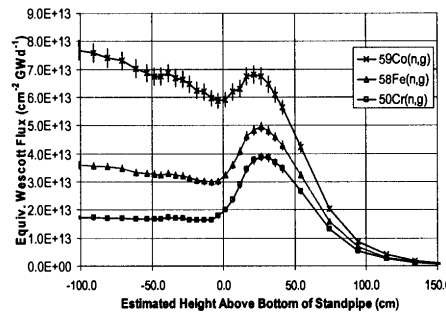

b) Thermal neutrons

FIG. 3—*Measured neutron fluxes in Wylfa standpipe.*

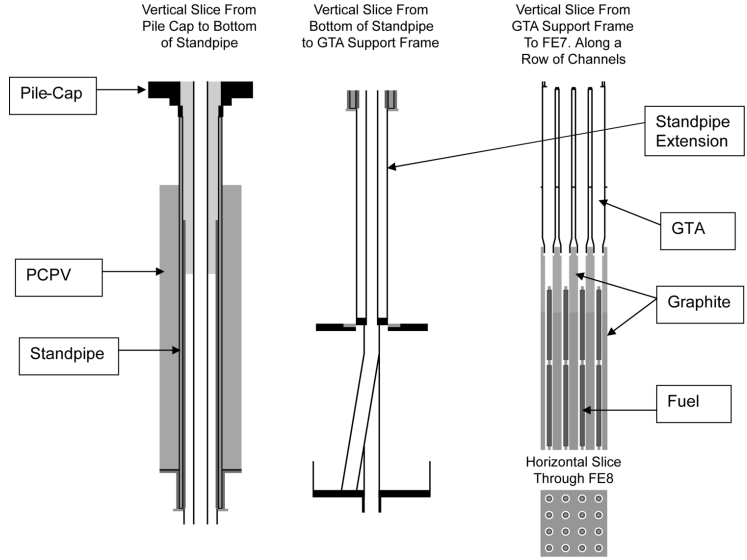

FIG. 4—*Images of MCBEND supercell model of Wylfa standpipe.*

aligned with the estimated position of the standpipe. It is also interesting to note the behavior of the iron and cobalt below the bottom of the standpipe (i.e., between −100 and 0 cm), where they show an attenuating flux more like that of the fast neutron reactions.

Monte Carlo Calculations

As in the dosimetry assessments for Magnox power plant with steel pressure vessels [2–4], calculations were performed with the general purpose Monte Carlo code MCBEND [1].

Due to the scale and complexity of the steel pipe-work constituting the GTA structures above the Wylfa core, a full three-dimensional model of the whole above-core plenum was not considered justified or practicable for the requirements of the original dosimetry assessment. Instead, recognizing the inherent repeatability of the structures, a model was created of a single standpipe and the reactor components beneath it. This represents the pilecap, PCPV, standpipe, above-core steelwork, and core, including the upper two layers of fuel elements (Fig. 4). Reflecting boundary conditions were applied to the vertical sides of this "supercell" implying that a laterally infinite reactor with a flat planar PCPV had effectively been modeled.

The calculations modeled the transport of neutrons from fuel elements, into the standpipe penetration, and beyond into the PCPV. Neutron source strengths were derived from three-dimensional reactor physics calculations performed with the PANTHER code [5].

The calculations were performed in two stages. In the first stage, neutrons were tracked from the fuel to an interface just above the reactor core. Neutrons reaching the interface were terminated and their trajectory details recorded to file. In the second stage, the recorded trajectory details were used as a leakage source, reinitiating each neutron several times in order to reduce stochastic uncertainties. Other than this, no other variance reduction techniques were employed.

The required reaction rates were scored in a radial mesh axially centred on the standpipe. Results obtained in the centre of the standpipe were attributed to the measurements. Calculated equivalent fast and thermal fluxes are shown in Figs. 5(a) and 5(b).

Comparison of Measured and Predicted Fluxes

It is evident that the two sets of calculated responses (Fig. 5) are very similar to their measured counterparts (Fig. 3) in virtually all respects, with the exception that they are both significantly greater at all points. C/M ratios of calculations (C) to measurements (M) for each of the five reactions are plotted in Fig.

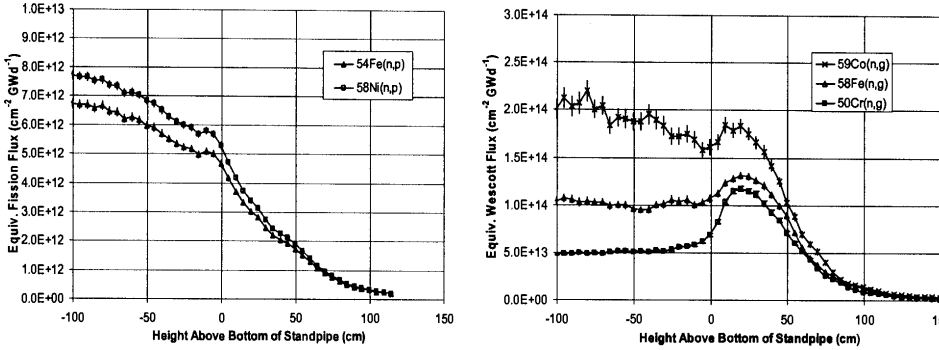

a) Fast neutrons *b) Thermal neutrons*

FIG. 5—*Calculated neutron fluxes in Wylfa standpipe.*

6(*a*), and mean C/M values averaged over the bottom 50 cm of the standpipe are given in Table 2. The results show that:

- Averaged over the lower standpipe, MCBEND overpredicts by factors between 2.5 and 3.2
- Over most of the axial range, the overprediction is reasonably consistent between the set of five different reactions
- Fast neutron and cobalt C/Ms are relatively uniform over the bottom 150 cm of the wire
- The lower energy C/Ms (^{58}Fe and ^{50}Cr) show a significant peak going upward into the standpipe, and falling rapidly thereafter.

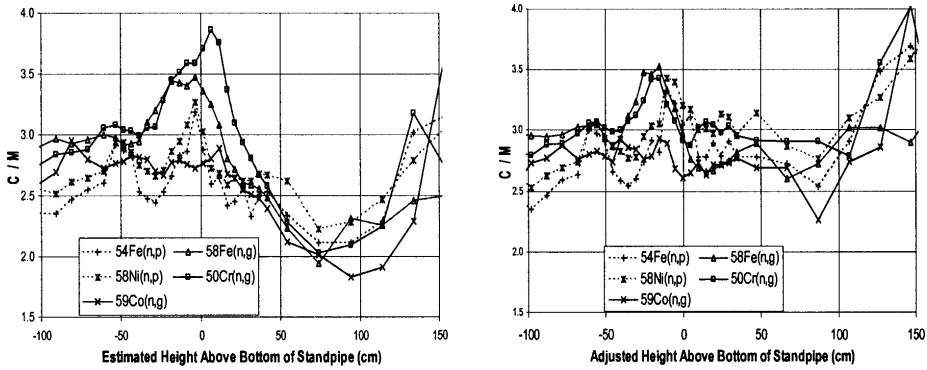

a) Estimated cable position *b) Adjusted cable position*

FIG. 6—*C/M ratios obtained from MCBEND predictions.*

TABLE 2—*Mean C/M ratios in lower 50 cm of standpipe.*

	Mean C/M	
Reaction	Estimated cable position	Adjusted cable position
^{54}Fe(n,p)^{54}Mn	2.55	2.85
^{58}Ni(n,p)^{58}Co	2.70	3.06
^{59}Co(n,γ)^{60}Co	2.63	2.70
^{58}Fe(n,γ)^{59}Fe	2.82	2.75
^{50}Cr(n,γ)^{51}Cr	3.20	2.99
Mean	2.78	2.87
1/2(Max-Min)/Mean	11.7 %	6.3 %

From these observations it was concluded that there may be a small systematic error in the estimated position of the samples relative to the standpipe. This was investigated by displacing the measured flux profiles relative to the calculated data and recalculating C/M ratios and discrepancies (this was equivalent to moving the cable up and down within the model). By minimizing least square residuals it was found that best agreements were obtained if the cable had been irradiated in a position 7 cm lower than estimated. Revised C/Ms corresponding to this displacement are shown in Fig. 6(*b*) and are also tabulated in Table 2. It can be seen from Table 2 that the net effect of the displacement on the overall agreement is not particularly significant. Most noticeable from this table, however, is the improvement in consistency between the five different reactions. The range of mean values is reduced to ±6 % (approximately halved), and provides compelling evidence that the model predicts neutron spectra without significant bias. Comparison of Figs. 6(*a*) and 6(*b*) shows that the peaking of C/Ms from the lower energy reactions within the standpipe is much reduced and is largely restricted to the region just below its bottom end. This probably corresponds to residual uncertainty in the region where the standpipe begins.

Discussion

The consistency between the measured and calculated flux distributions gives confidence that the model is a suitable representation of the plant. At only 7 cm, the adjustment required to the position of the measurements relative to the MCBEND model is small given the overall length of cable sampled, and its route within the reactor. It provides confidence that the original estimation of its position was good. The evidence for adjusting the position of cable is circumstantial based on a best fit to the measured data. However, the adjustment required can be easily reconciled against uncertainties in the MCBEND model and the estimated position of the cable within it. These include dimensional changes to the reactor components when hot and pressurized, the tension applied to the cable to keep it taut, and uncertainties and engineering tolerances in the data used to create the model. It is reasonable, therefore, to draw conclusions about the performance of the model based on the results obtained with the adjusted measurement position.

The consistency of C/M ratios obtained from the five reactions provides considerable confidence that the MCBEND model predicts neutron spectra without significant bias in the regions of interest. It follows that (dpa) rates in the standpipe will be similarly over-predicted by the calculations and, therefore, dose recommendations for the Wylfa standpipes have been shown to be conservative.

The extensive body of validation evidence for Magnox plant with steel pressure vessels shows that MCBEND predictions generally agree with plant measurements to within uncertainties of ±20 % [3]. Because the Wylfa modeling is more approximate, the estimated uncertainties are larger at ±40 %. However, the overprediction obtained is significantly greater than this by nearly a factor 5. It is probable that some source of modeling error is the cause of overprediction. Three possibilities have been identified:

- Fuel element power data (i.e., neutron source strengths)
- Height of fuel stack relative to the top of the core
- Super-cell approximation

Fuel element power data for this study were based on reactor physics calculations, rather than axial rating measurements, as used for assessments of other Magnox stations. A recent review has suggested that the power data used in the model could have been over-predicted by 20 %. If implemented, a change to power data would have no effect on the predicted spectra.

The separation between the fuel and the top of the graphite is a critical dimension in determining the intensity of neutron leakage from the core. Sensitivity studies [6] have shown that that above-core fluxes increase by ~5 % per 1 cm reduction in this separation, but that the effect is largely insensitive to neutron energy. The separation is known to reduce with operation due to dimensional changes in the core graphite. For previous Magnox assessments, best estimate values for the parameter were obtained from plant observations. However, for Wylfa, similar data were not available and a bounding value was used based upon the leading station. Because predicted spectra are not sensitive to this parameter, the resulting uncertainty does not affect the ability of the model to predict neutron spectra. The magnitude of any overprediction due to this uncertainty has not been quantified at this stage.

Finally, use of the "supercell" approximation was justified by the reactors' highly repetitive structures and very large size. However, the imposition of reflecting boundaries precludes any leakage of neutrons from the sides of the model resulting in some overprediction, which was recognized to be a conservative

assumption for dose predictions. Recent studies have shown that this approximation results in overprediction by ~20 %.

By revisiting the calculation of neutron source data and correcting for the effect of the supercell approximation, it would be possible to improve the C/Ms for the Wylfa model to approximately 2.0. This would bring the agreement to 2.5 standard deviations without addressing the issue of fuel to core separation. If that too were to be investigated, the improved agreement between measurement and prediction could approach that of previous Magnox assessments.

Conclusion

A discharged thermocouple cable has been used to provide material for neutron flux measurements in support of a dosimetry assessment for steel components within the pressure circuit above the core of the Wylfa reactors. Thermocouple samples were counted for a range of fast and thermal neutron reactions. Elemental analysis was required in order to obtain accurate and reliable absolute neutron fluxes from the measurements.

The measured flux data were compared with the results of a Monte Carlo supercell model produced with the code MCBEND. Both predicted and measured thermal neutron fluxes show a distinct thermalization peak corresponding to the cooling water contained within the standpipe. This was used to confirm the accuracy with which the irradiation locations of the measurement samples had been identified within the standpipe geometry.

The measurements have demonstrated that the model consistently overpredicts fast and thermal neutron reactions by a factor of approximately 3. The overprediction is spatially uniform and consistent between reactions, showing that the model predicts neutron spectra without significant bias. It is concluded that neutron doses calculated with this model are similarly overpredicted and, therefore, that dose recommendations for the Wylfa standpipes are conservative.

Potential causes of this overprediction are identified and discussed. If these were addressed, it is predicted that the agreement between measurement and prediction would improve, without significant impact on predicted spectra, and hence the conclusions of this work.

Acknowledgments

Production of this paper was supported by the U.K. Health and Safety Executive. It is published with the permission of British Nuclear Group.

References

[1] Wright, G. A., Shuttleworth, E., Cowan, P., Curl, I. J., and Mattsson, C. G., "MCBEND—A Fluence Modelling Tool," *Reactor Dosimetry: Radiation Metrology and Assessment*, ASTM STP 1398, pp. 540–548.

[2] Mossop, J. R., Thornton, D. A., and Lewis, T. A., "Validation of Neutron Transport Calculations on Magnox Power Plant," *Proceedings of the 8th International Symposium on Reactor Dosimetry*, ASTM Special Publication 1228, 1994, pp. 384–391.

[3] Lewis, T. A., Hopper, S. E., Mossop, J. R., and Thornton, D. A., "The Prediction of Fast and thermal Neutron Dose Rates for the Pressure Vessels of Magnox Power Plant," *Proceedings of the 9th International Symposium on Reactor Dosimetry*, World Scientific, 1996, pp. 600–607.

[4] Lewis, T. A., and Thornton, D. A., "A Decade of Dosimetry for Magnox Reactor Plants," *Proceedings of the 11th International Symposium on Reactor Dosimetry*, World Scientific, 2003, pp. 269–277.

[5] Bryce, P. and Fairbairn, S. A., eds., "PANTHER Software Release Note: Release 5.3.R1 for LWR, AGR and Magnox Reactors," British Energy Document E/REP/REAC/0022/GEN/01.

[6] Thornton, D. A., "Factors Affecting Predicted Neutron Dose Rates to Steel Pressure Vessels of Magnox Plant," *Reactor Dosimetry: Radiation Metrology and Assessment*, ASTM STP 1398, pp. 132–139.

Journal of ASTM International, Vol. 3, No. 3
Paper ID JAI13490
Available online at www.astm.org

Lawrence R. Greenwood[1] *and Brian M. Oliver*[1]

Comparison of Predicted and Measured Helium Production in U.S. BWR Reactors

ABSTRACT: Helium production in reactor steel is calculated as the summation of all neutron reactions that produce helium either with thermal or fast neutrons. Thermal helium production is due to elements or impurities that are known to have a thermal neutron cross section for helium production, including ^{10}B and ^{59}Ni. Fast neutrons produce helium in all materials due to the threshold (n,α) reactions as well as other reactions that include helium as one of the reaction products. A generalized equation is given for helium production in all reactor materials and comparisons are given for helium measurements in steel and inconel samples. The helium production calculated using the generalized equation is in good agreement with helium measurements in samples from BWR reactors. Simplified equations are given with numerical values and generic parameters to facilitate calculations. However, it is important to use the actual boron content when known to obtain reliable estimates of the helium production.

KEYWORDS: helium, BWR

Introduction

Helium production in reactor steels can lead to a variety of problems including swelling and difficulties in the weld repair of cracks. Helium production can be calculated by summing over thermal neutron reactions with boron, fast threshold reactions that produce helium, and second order reactions such as the production of helium from in-bred Ni-59. The generalized equation is, as follows:

$$He = B\{1 \bullet \exp[\bullet\ \sigma_B(\phi_0 t)]\} + (\phi_1 t)\sigma_{a1} + N(Ni)He(^{59}Ni) \quad (1)$$

where He=the atomic helium production, ϕ_0=the thermal neutron flux, t=the irradiation time, B=the atomic fraction of ^{10}B in the steel, σ_B=the thermal neutron cross section for the $^{10}B(n,\alpha)$ reaction, σ_{a1} =the spectral-averaged neutron cross section for helium production above 1 MeV weighted over the elemental distribution in the steel, ϕ_1 is the fast neutron flux above 1 MeV, N(Ni)=the atomic abundance of Ni in the steel, and He(^{59}Ni)=the two step helium production from the $^{58}Ni(n,\gamma)^{59}Ni(n,\alpha)$ reaction, as discussed below.

For the thermal neutron reactions, the boron and nickel cross sections are well known and the helium concentration can be calculated directly from the boron content and the thermal neutron fluence. However, if the neutron spectrum is known either from calculations or from retrospective neutron dosimetry measurements performed on the samples, then a correction can be included for the production of helium from epithermal neutrons using the resonance integrals and the epithermal neutron fluence. For the helium production from boron, the first term in Eq 1 is then:

$$B\{1 \bullet \exp[\bullet\ \sigma_B(\phi_0 t) \bullet I_B(\phi_E t)]\} \quad (2)$$

where I_B is the resonance integral for the $^{10}B(n,\alpha)$ reaction and ϕ_E is the epithermal neutron flux parameter. The boron-10 cross sections are listed in Table 1. As discussed below, this same methodology can also be used for the ^{59}Ni reaction equations by replacing the thermal reaction rate ($\sigma\phi$) with the sum of the thermal and epithermal reaction rates, for each of the relevant Ni reactions. The thermal neutron flux and cross section can also be adjusted for the temperature at the reactor location of interest. If this is done

Manuscript received June 20, 2005; accepted for publication September 29, 2005; published online December 2005. Presented at ASTM Symposium on Reactor Dosimetry, 12th International Sympoium on 8 13 May 2005 in Gatlinburg, TN; D. W. Vehar, D. M. Gilliam, and J. M. Adams, Guest Editors.
[1] Pacific Northwest National Laboratory, Richland, WA, 99354.

TABLE 1 *Thermal and epithermal neutron cross sections (barns) for helium production.*

Reaction	293 K	561 K	Res. Int., b	$r=I/\sigma_0$
$^{10}B(n,\alpha)^7Li$	3837	2458	1722	0.449
$^{59}Ni(n,\alpha)^{56}Fe$	12.3	7.88	21.8	1.77
$^{58}Ni(n,\gamma)^{59}Ni$	4.6	2.95	2.2	0.478
$^{59}Ni(n,abs)$	92	58.9	163	1.77

consistently, then the reaction rate is invariant for boron since the neutron cross section has classic 1/velocity dependence.

Helium production from boron and nickel depend very differently on the thermal neutron uence. Boron-10 only produces helium at relatively low thermal neutron uence since the boron will eventually burnout. At a thermal uence of 1×10^{21} n/cm^2, about 98 % of the boron will have been converted to helium such that additional irradiation will not produce much additional helium from the boron.

Helium production from nickel, on the other hand, is only important at higher neutron uences since there is no ^{59}Ni in the starting steel and it requires time to produce it from the $^{58}Ni(n,\gamma)^{59}Ni$ reaction. This source of helium can generally be neglected at thermal neutron uences below 1×10^{20} n/cm^2, unless there is no boron in the sample and the fast neutron ux is extremely low compared to the thermal neutron ux. At high thermal neutron uences above 1×10^{21} n/cm^2, helium production from nickel is more important than any other helium-producing reaction.

The fast neutron production of helium requires a calculation of the spectral-averaged helium production cross sections from each element in the steel, as follows:

$$\sigma_{a1} = \sum_i N_i \sigma_{i1} \tag{3}$$

where N_i is the atomic abundance of element i in the steel and σ_{i1} is the spectral-averaged cross section for helium production above 1 MeV for element i. Fast neutron helium production cross sections for the major elements in BWR reactor steel and Inconel are listed and averaged in Table 2, for the reactors we have measured. The helium production cross sections were taken from ENDF/B-V File 533 Gas Production File [1]. It is important to note that a special purpose le such as this one should be used since the authors included all known neutron reactions that produce helium, not just the (n,α) reaction channel. Newer les for some reactions are available in ENDF/B-VI [2] and other newer data compilations; however, the comprehensive special purpose gas production le in ENDF/B-V has not been generated with these newer data les.

The neutron spectral averaging obviously requires some knowledge of the fast neutron spectrum. For the jet pump locations, neutron spectra were available from EPRI (Electric Power Research Institute) and a new calculation was performed by Carew [3]. The two spectra gave spectral-averaged helium production cross sections that agreed within 1 %. However, the fast neutron spectra at other reactor locations vary signi cantly from the jet pump positions. Calculations of the neutron spectra using the RAMA [4] computer code were obtained for the shroud and top guide samples that we received. The spectral-averaged gas production cross sections are quite different at these locations, as shown in Table 3. It should be noted that these tables are meant to convey average values for the samples we have measured, rather than listing all the individual parameters for each speci c sample and neutron spectrum. Whereas it is always more accurate to perform detailed calculations tailored to each speci c sample and reactor location, as has been

TABLE 2 *Average fast (>1 MeV) helium cross sections for BWR jet pumps.*

Element	Jet Pumps	Atomic Abundance	
	σ_a, mb[a]	Steel	Inconel
Fe	3.34	0.678	0.071
Ni	23.42	0.112	0.690
Cr	2.70	0.182	0.146
Mn	2.03	0.014	0.070
Average σ_a, mb		5.41	16.92

[a]Helium cross sections are from the ENDF/B-V File 533 Gas Production File and the neutron spectrum was provided by Carew of BNL.

TABLE 3 *Average fast (>1 MeV) helium cross sections for BWR steel at shroud and top guide positions.*

Element	Steel Atomic Abn.	Shroud $\sigma_{a,mb}$[a]	Top Guide $\sigma_{a,mb}$[a]
Fe	0.678	0.621	0.366
Ni	0.112	7.70	5.40
Cr	0.182	0.352	0.205
Mn	0.014	0.311	0.172
Average $\sigma_{a,mb}$		1.35	0.893

[a]Average neutron spectra calculated with the RAMA code.

done in Table 4, one of the goals of this work is to provide typical parameters that can be used as a predictive tool rather than an exact fit to the data. Simplified equations with generic parameters are discussed later.

It is extremely important to note that the fast neutron helium calculations must be done consistently for a given neutron spectrum or reactor location. If retrospective dosimetry measurements are performed to determine the fast neutron fluence >1 MeV, then the same spectrum should be used to calculate the spectral-averaged dosimetry cross sections such as $^{54}Fe(n,p)^{54}Mn$ that are used for the helium production cross section spectral averaging. Otherwise large errors can be introduced into the helium calculation.

Helium production from fast neutrons is generally assumed to be constant as a function of the irradiation time. However, this is not correct at higher neutron fluences since thermal neutron transmutation of the various isotopes in each element of the steel will change the net helium production rate since each isotope has a different helium production cross section. Transmutation may also produce daughter isotopes that can have dramatically different fast or thermal helium production cross sections, as has been shown for Cu and Zn [5], Fe [6], as well as Ni. Such effects have not been included in this paper, but may need to be included at high neutron fluences or for materials other than reactor steel or Inconel.

Helium Production from ^{59}Ni

The isotope ^{59}Ni has relatively high thermal neutron cross sections for the production of helium and hydrogen, as shown in Table 1. As mentioned above, ^{59}Ni does not exist in natural nickel and must be generated from the thermal neutron capture reaction $^{58}Ni(n,\gamma)^{59}Ni(n,\alpha)$. The equation for helium production is:

$$He(^{59}Ni) = N(^{58}Ni)\{\sigma_{9a}[\sigma_{9T}(1 - \exp(\sigma_{8g}\phi_0 t)) - \sigma_{8g}(1 - \exp(-\sigma_{9T}\phi_0 t))] / [\sigma_{9T}(\sigma_{9T} - \sigma_{8g})] \quad (4)$$

where $He(^{59}Ni)$=the helium production from ^{59}Ni in Eq 1, $N(^{58}Ni)$=the atomic abundance of ^{58}Ni, σ_{9a} =the thermal neutron cross section for the $^{59}Ni(n,\alpha)$ reaction, σ_{9T}=the thermal neutron total absorption cross section for ^{59}Ni, σ_{8g}=the thermal neutron cross section for the $^{58}Ni(n,\gamma)$ reaction, $\varphi_0 t$=the thermal neutron fluence. As discussed above, if the epithermal neutron fluence is known, then all of the nickel isotopic reaction rates can be revised to include epithermal neutrons using the formalism of Eq 2. For simplicity, this substitution can be simplified if you define the cross sections as ratios to the thermal neutron cross sections, as follows:

$$\sigma\phi = \sigma_0\phi_0 + I\varphi_E = \phi_0(\sigma_0 + rg) \quad (5)$$

where $r = I/\sigma_0$ and $g = \phi_E/\phi_0$. All of the cross section (σ) terms in Eq 4 can thus be just replaced by (σ_0+rg) for each of the different reactions using the values listed in Table 1. The epithermal neutron flux can be determined either from neutron spectral calculations or from experimental dosimetry data. If reactions rates are measured for multiple thermal neutron reactions, then a least squares approach can be used to solve the family of Eq 5 for the common ϕ_0 and φ_E values. It is important to note that φ_E as defined in Eqs 2, 4, and 5 is not equal to the true epithermal neutron fluence but is formally defined as the epithermal fluence parameter. The reason for this difference is that the resonance integral is defined as the integral from 0.55 eV to 1 MeV of a given cross section divided by the neutron energy and as such is not equal to the spectral-averaged cross section, which would require division of the resonance integral by the integral of the neutron flux. The true epithermal neutron fluence is thus related to the epithermal neutron parameter by a factor of 14.4, which is the integral of the neutron flux for a 1/E neutron spectrum from 0.55 eV to 1 MeV.

Correction to Thermal Cross Sections and Fluences for Reactor Temperature

In any calculation of thermal neutron effects, it is critically important to specify how thermal neutrons are de ned. There are three possible ways to specify the thermal neutron cross sections or uences. Standard references such as the Chart of the Nuclides list the thermal neutron cross sections at the velocity corresponding to room temperature which is 2200 m/s. However, calculations of the thermal neutron uence are always de ned as the total number of neutrons in an energy group less than 0.5 eV (Cd cutoff energy). These two conventions are not the same and care must be taken to specify which convention is being used for any given application. The relationship between these two conventions can be calculated from the energy spectrum of the thermal neutrons, which is described by a Maxwellian distribution centered on the operating temperature of the reactor. Since reactors operate at temperatures considerably above room temperature, the third way to specify thermal neutrons is at the temperature of the reactor rather than room temperature. Consequently, when quoting a thermal neutron uence or average cross section, it is necessary to specify whether the values are given at 2200 m/s, the group ux below 0.5 eV, or whether corrections have been applied for the reactor temperature.

The integral of a Maxwellian thermal energy distribution is related to the 2200 m/s value by the factor of $(4\ T/\pi To)^{1/2}$ where T is the reactor temperature in Kelvin and To is 293.2 K or room temperature. At room temperature, the group thermal neutron uence below 0.5 eV is thus equal to a factor of $(4/\pi)^{1/2} = 1.128$ times the 2200 m/s thermal neutron uence. The thermal neutron cross sections have the inverse relationship such that the product of the thermal cross section times the thermal uence does not change, regardless of how the thermal uences and cross sections are de ned as long as the cross section exhibits the classical 1/v energy dependence. (If there are low-lying resonances below 0.5 eV, then a correction factor known as the Wescott g factor [7] is required to take the resonance effects into account.)

For the speci cation of a generalized equation to be used for the calculation of the helium production in BWR reactors, the thermal neutron uence will be de ned as the group uence below 0.5 eV at a reactor operating temperature of 550 F, which is equal to 288 C or 561 K. The thermal neutron uences will thus be a factor of 1.56 higher than the 2200 m/s values and the thermal cross sections will be a factor of 0.641 lower than the 2200 m/s value. Table 1 also lists the corrected thermal cross section values for ^{10}B and ^{59}Ni at a typical BWR operating temperature of 550 F. The resonance integrals also have some dependence on the reactor temperature due to Doppler broadening of the resonances. However, the effects for the ^{10}B and ^{59}Ni reactions are relatively small and can be neglected for the helium calculations.

Relative Contribution of Helium Source Terms

Equations 1, 4, and 5 can be used to accurately calculate helium in all reactor steels or Inconel for any reactor location. In order to perform the calculation it is necessary to know the neutron ux spectrum in order to calculate the fast neutron gas production cross sections and to correct the thermal reactions for epithermal neutrons. It is also necessary to know the boron content as well as the exact composition of the steel. Unfortunately, the neutron spectrum, boron content, and steel composition are not always well known. As will be discussed later, the boron content is critical to the calculation and may lead to signi cant errors if an average boron value is used. Some guidance on the relative importance of the various terms in Eq 1 can be obtained by looking at the plot of helium production as a function of the thermal neutron uence. Figure 1 shows the dependence of each helium production source term for calculations that were performed for BWR samples taken from jet pump, shroud, and top guide locations. (Figure 1 uses the same calculations that were used for the comparison of calculations and measurements shown in Fig. 2.) Figure 1 shows that at all neutron uences and reactor locations, the contribution of helium from fast neutron reactions is about 20 30 % of the total and cannot be neglected. At uences above 1×10^{20} n/cm^2, the ^{10}B starts to be burned out and becomes less important relative to the fast neutron and ^{59}Ni source terms.

Figure 1 also shows that for neutron uences below 1×10^{20} n/cm^2 (jet pump and shroud locations) the ^{59}Ni contribution to the total helium production is small and can be neglected. However, at higher uences (top guide samples), the helium production from ^{59}Ni becomes more important and is the dominant source of helium above 1×10^{21} n/cm^2. The relative dependence of the various sources of helium shown in Fig. 1 will of course change with the boron content of the samples as well as the shape of the

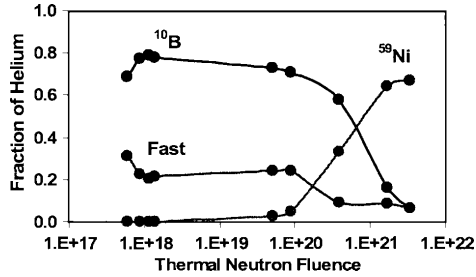

FIG. 1 *Relative fraction of helium produced by B-10, fast neutrons, and Ni-59 in BWR stainless steel specimens that have been analyzed.*

neutron ux spectrum. However, Fig. 1 can be used as an indicator of the relative importance of the various terms and offers some guidance on whether the ^{59}Ni effects need to be included.

Comparison of He Calculations and Measurements

Retrospective neutron dosimetry, helium, and boron measurements have been performed on samples from a number of different BWR reactors. Samples were provided by EPRI during reactor outages by using a small drill and water pump system to collect the drill lings on a lter. The lters were then sent to Battelle Northwest where the drill lings were removed, inspected, and prepared for analysis. Only samples that were representative of the complete sample batch were used in the subsequent analyses. The samples were gamma counted to determine the activation products. Chemical separations and liquid scintillation or X-ray counting was also performed to determine additional activation products such as ^{63}Ni, ^{55}Fe, and/or ^{93m}Nb. Energy dispersive X-ray uorescence measurements were performed to accurately determine the elemental composition of each sample. The as-received helium content of each sample was determined by isotopic dilution gas mass spectrometry. The samples were then irradiated in a well-characterized higher thermal neutron uence environment at the McMaster University Reactor designed to burn out additional boron and again measured for the helium content to determine the original boron content of each sample. This second irradiation was not performed for the top guide samples since the boron was already depleted by the original irradiation. In all cases, the helium produced from the second irradiation was substantially higher than from the original BWR neutron exposure. Helium measurements were accomplished by vaporizing each sample in a small resistance-heated crucible in a high-temperature furnace attached to a gas mass spectrometer [8]. The absolute amount of ^{4}He released (in atoms) was measured relative to a known quantity of added ^{3}He spike; the spike was obtained by expanding and partitioning a known quantity of gas through a succession of calibrated volumes [9]. Conversion from total atoms to atom concentration

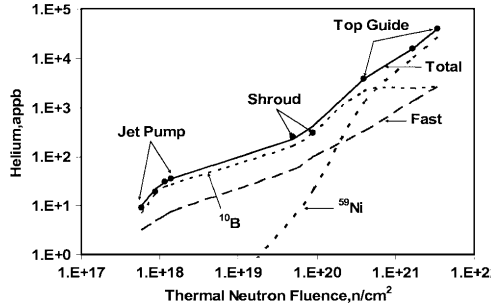

FIG. 2 *Selected helium measurements (dots) in BWR stainless steel samples are compared with calculated values for each of the three helium production source terms (shown as dotted and dashed lines). The sum of the three helium contributions is shown by the solid line.*

TABLE 4 *Comparison of helium calculations with measurements for BWR samples.*

	Fluence, n/cm[b]		Boron[b]	Helium, appb					
Sample[a]	Thermal[c]	>1 MeV	wppm	B-10	Fast	Ni-59	Calc.	Exp.	C/E
SS1	1.86E+18	1.02E+18	1.63	11.8	5.46	6.84E• 3	17.3	18.3	0.94
SS3	8.69E+17	8.07E+17	1.87	6.33	4.32	1.49E• 3	10.7	8.0	1.33
SS4	1.71E+18	1.02E+18	3.22	21.4	5.46	5.78E• 3	26.8	25.5	1.05
SS5	7.68E+17	5.87E+17	2.30	6.89	3.14	1.17E• 3	10.0	8.90	1.13
In3	9.96E+17	8.20E+17	7.54	30.8	13.9	1.24E• 2	44.7	40.6	1.10
In5	4.94E+17	4.73E+17	6.87	13.9	8.00	3.05E• 3	21.9	19.4	1.13
In13	7.62E+17	7.32E+17	9.44	29.5	12.4	7.26E• 3	41.9	41.3	1.02
In15	4.40E+17	4.37E+17	7.57	13.7	7.39	2.42E• 3	21.1	19.90	1.06
JP3	1.06E+18	9.19E+17	3.98	17.5	5.01	2.99E• 3	22.5	24.7	0.91
JP5	1.80E+18	1.40E+18	3.70	27.6	7.63	8.62E• 3	35.3	35.2	1.00
JP11	1.02E+18	8.90E+17	3.97	16.8	4.85	2.77E• 3	21.7	18.8	1.15
JP13	1.47E+18	1.17E+18	4.01	24.5	6.37	5.75E• 3	30.9	30.9	1.00
S1	5.21E+19	5.04E+19	0.86	166	54.5	5.87	226	257	0.88
S2	5.10e+19	6.00E+19	1.80	284	76.1	7.78	468	264	1.77
S3	9.84E+19	8.98E+19	0.90	300	100.9	20.9	422	310	1.36
TG1	7.54E+20	3.92E+20	2.23	2159	332.5	1233	3724	3730	1.00
TG2	2.19E+21	1.65E+21	2.23	2270	1316	9876	15029	15300	0.98
TG3	3.70E+21	3.41E+21	2.23	2270	2650	26670	35789	39800	0.90

[a]The rst twelve samples are at jet pumps locations. The S samples are shroud and TG are top guide. The jet pump samples starting with In are Inconel rather than stainless steel.

[b]Measured boron values except for the top guide locations which were estimated.

[c]Thermal uences are quoted at 2200 m/s. The thermal group uence at a reactor temperature of 550 F (561 K) is a factor of 1.56 higher.

was based on the measured elemental compositions and the sample mass. Replicate helium measurements were performed for all samples and the measured values have an estimated absolute accuracy of 1 %.

Table 4 summarizes all of our measurements and calculations for the stainless steel and Inconel samples using the best available data for the material composition, fast and thermal neutron uences, and calculated neutron spectra at each location. Figure 2 shows the contribution from each of the three helium production source terms for stainless steel samples with similar boron content, as was shown on a relative basis in Fig. 1. The Inconel measurements were not included since they have a different dependence on the neutron uence. The thermal and fast neutron uences were determined from the analysis of the activation products in each sample. Whenever possible, RAMA neutron spectral calculations were used to determine the fast neutron spectral averaged activation and gas production cross sections. Table 4 shows that the ratios of the calculated to measured helium values for all of the BWR samples (stainless steel and Inconel) have an average value of 1.10 ± 0.21 at one standard deviation.

Conclusions

Ideally, calculations of helium in reactor materials should be performed including all known sources of helium, the exact material composition, the measured boron content, fast helium production cross sections that are averaged over a calculated neutron spectrum, and corrections to the thermal cross sections for epithermal neutrons. Table 4 and Fig. 2 demonstrate that if the exact calculations are performed, then very good agreement is obtained between measured and calculated helium values. Uncertainties in the fast neutron cross sections based on the RAMA calculations of the neutron spectra are not known. However, for all of the samples, retrospective neutron dosimetry measurements were used to adjust the calculations for the fast and thermal neutron uences.

In many cases, all of the information mentioned above is not available for every reactor location where an estimate of the helium content of samples is required. Consequently, it is worthwhile to ask how well we can t the data if various approximations are made. At lower neutron uences, ^{10}B is the major source of helium in BWR samples. Consequently, it is very important to know the boron content of the material. For the stainless steel samples, the average boron content was 2.6 wppm with a standard deviation of 1.3 wppm. For the Inconel samples, the average boron content was 7.8 ± 1.1 wppm. If average or typical boron values are used, then the helium calculations can easily be in error by a factor of two or more.

As shown in Fig. 1, it is always necessary to include the fast neutron helium production. The material

TABLE 5 *Summary of BWR fast helium spectral-averaged cross sections, mb.*

		σ_{a1}(mb) > 1 MeV		
Material	Ni Content	Jet Pumps	Shroud	Top Guide
Stainless Steel	0.11	5.41	1.35	0.893
Inconel	0.69	16.92	5.43	3.79

composition strongly affects the average helium cross section for stainless steel or Inconel; however, using generic values doesn t have much impact on the accuracy of the helium calculations since the fast neutron contribution only comprises 20 30 % of the total helium that is generated. The neutron spectral effects, however, are quite large and need to be considered. The spectral averaged fast neutron helium production cross section above 1 MeV for stainless steel is 5.4 mb at the jet pump location, but decreases to 1.4 mb at the shroud and 0.89 mb at the top guide locations. For Inconel jet pump samples, the average fast helium cross section was calculated to be 16.9 mb. Of course, the fast neutron calculations rely on accurate calculations or measurements of the fast neutron uence above 1 MeV.

At lower uence locations, the ^{59}Ni contribution can be neglected for stainless steel samples with little impact on the results, although it is more important for Inconel samples due to the higher nickel content. At the top guide locations (uence above 1×10^{20} n/cm^2) the ^{59}Ni term becomes the major source of the helium and cannot be ignored. The epithermal correction to the thermal neutron uences is not very important for the ^{10}B reaction since it has classic 1/v energy dependence. However, the epithermal correction is more important for the ^{59}Ni reactions due to a large resonance in the cross sections.

Simplified Helium Equations

Helium calculations should always be performed using Eqs 1 and 4, repeated below with numerical values. In these equations, the thermal uence is de ned as the group uence below 0.5 eV at a reactor temperature of 550 F or 288 C. At neutron uences below about $1 \times 10^{+20}$ n/cm^2, the Ni-59 term can be neglected. However, the fast neutron term must always be included and may be the dominant source of helium if the boron content of the steel is very low. In order to simplify the use of the equations, Table 5 summarizes typical parameters that have been determined for all BWR samples that we have analyzed for helium, boron, and retrospective dosimetry. In order to use the equation at any reactor location, it is necessary to use appropriate values for the boron content and type of steel using the typical values in Table 5 or more exact values, when available.

$$\mathrm{He(appm)} = \mathrm{B}\{1 - \exp[-\sigma_{\mathrm{B}}(\phi_0 t)]\} + (\phi_1 t)\sigma_{a1} + \mathrm{N(Ni)He}(^{59}\mathrm{Ni}) \tag{1'}$$

where the individual terms can be written as follows:

$$\mathrm{He(B)} = \mathrm{B(wppm)}\{1 - \exp(-2.46 \times 10^{-21}\phi_0 t)\}, \text{ where B is the natural boron content} \tag{6}$$

$$\mathrm{He(fast} > 1) = \sigma_{a1} \times 10^{-21}\phi_1 t \tag{7}$$

$$\mathrm{N(Ni)He}(^{59}\mathrm{Ni}) = \mathrm{N(Ni)}(6.81 \times 10^5)\{0.14084(1 - \exp(-2.95 \times 10^{-24}\phi_0 t)) - 0.0070540(1 - \exp(-5.89 \times 10^{-23}\phi_0 t))\} \tag{8}$$

All of the numerical equations are designed to give results in appm (atomic parts per million) in the steel or Inconel. It is important to note that at lower neutron uences, Eq 8 must be calculated using all the signi cant gures provided to avoid numerical accuracy problems. Such problems can be avoided by simply neglecting this term below a thermal uence of 1×10^{20} n/cm^2 or using an approximation formula:

$$\mathrm{N(Ni)He}(^{59}\mathrm{Ni}) = \mathrm{N(Ni)}(7.91 \times 10^{-42})(\phi_0 t)^2 \tag{9}$$

The N(Ni) in Eqs 8 and 9 is the atomic fraction of nickel in the steel or Inconel and is the product of the weight fraction times a conversion factor for appm rather than wppm (about 0.94 for typical BWR stainless steel or about 0.99 for Inconel).

The natural boron content has been measured to be in the range of 1 to 10 wppm in stainless steel and from 5 to 40 wppm in Inconel samples. Hence, it is always necessary to know the boron content to get a reliable estimate of the helium production. If the exact composition of the material is not known, then an

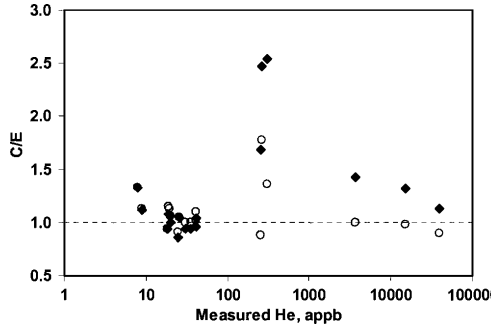

FIG. 3 *Ratio of calculated (C) to experimental (E) helium values for various BWR samples. The open circles are calculated using the exact parameters shown in Table 4, and the solid diamonds are calculated using the generic nickel and jet pump fast helium cross sections in Table 5.*

average Ni content may be used, as given in Table 5. Average spectral-averaged fast helium cross sections are also listed for the samples studied in this report; however, these values may not represent a comprehensive range for BWR samples due to the large variations in the neutron spectra that are possible. A more comprehensive study is needed to determine recommended cross sections for use at any BWR sampling location.

A recalculation of the data in Table 4 using the above methodology including the average Ni and fast helium cross sections for the jet pump neutron spectra in Table 5 gives helium values that show considerably worse (up to a factor of three) agreement with the measurements, as illustrated in Fig. 3. The most important parameter is the boron content and reliable helium estimates cannot be obtained without some knowledge of the boron in the samples. The nickel content can be taken from Table 5 or from generic tables of the type of reactor material as appropriate. Since we have not conducted a comprehensive study of the fast neutron helium cross sections at all possible locations in a BWR, we recalculated the helium production using the jet pump fast neutron cross sections at the shroud and top guide locations. Using the fast helium cross sections from the jet pump locations clearly overestimates the fast helium production at the shroud and top guide locations. However, without a more comprehensive study of the neutron spectra at other locations in a BWR, it is unknown if the shroud and top guide fast helium cross sections in Table 5 are appropriate at other locations that we have not studied. Clearly, a more comprehensive study is needed in order to con dently predict helium production at all sample locations of interest in a BWR. Using the jet pump fast helium cross sections in Table 5 are expected to overestimate the helium production at other BWR locations.

Acknowledgments

This work was supported by the EPRI BWR Vessel and Internals Project and by the U.S. Nuclear Regulatory Commission.

References

[1] Evaluated Nuclear Data File, Version V, Gas Production File 533, Brookhaven National Laboratory (http://www.nndc.bnl.gov/).
[2] Evaluated Nuclear Data File, Version VI, Brookhaven National Laboratory.
[3] Carew, J., Brookhaven National Laboratory, private communication 2002.
[4] BWRVIP-126: BWR Vessel and Internals Project, RAMA Fluence Methodology Software Version 1.0, *EPRI CD 1007823*, 2003.
[5] Kneff, D. W., Greenwood, L. R., Oliver, B. M., Skowronski, R. P., and Callis, E. L., Helium Production in Copper by a Thermal Three-Stage Reaction, *Radiat. Eff.*, Vol. 92 96, 1983, pp. 553 556.

[6] Greenwood, L. R., Graczyk, D. G., and Kneff, D. W., A New Technique for Enhancing Helium Production in Ferritic Materials, *J. Nucl. Mater.*, Vol. 155 157, 1988, pp. 1335 1339.

[7] Westcott, C. H., Walker, W. H., and Alexander, T. K., Effective Cross Sections and Cadmium Ratios for the Neutron Spectra of Thermal Reactors, *Proceedings of the International Conference on Peaceful Uses of Atomic Energy*, PIPAA, United Nations, Vol. 16, 1958, 70 pp.

[8] Farrar, H. and Oliver, B. M., A Mass Spectrometer System to Determine Very Low Levels of Helium in Small Solid and Liquid Samples, *J. Vac. Sci. Technol. A*, Vol. A4, 1986, p. 1740.

[9] Oliver, B. M., Bradley, J. G., and Farrar, H., Helium Concentration in the Earth s Lower Atmosphere, *Geochim. Cosmochim. Acta*, Vol. 48, 1984, p. 1759.

Journal of ASTM International, Vol. 3, No. 6
Paper ID JAI13462
Available online at www.astm.org

C. O. Slater,[1] *D. L. Selby,*[2] *J. A. Bucholz,*[3] *J. L. Robertson,*[4] *and M. L. Crow*[5]

Shielding Calculations for the Upgrade of the HFIR HB 2 Beam Line

ABSTRACT: Experimental facilities at the Oak Ridge National Laboratory's High Flux Isotope Reactor are being upgraded through the redesign of beam tubes supplying neutrons to those facilities. In support of the shield design for one of the beam lines HB-2, calculations were performed to determine dose rates outside the shielding as well as background radiation levels at various locations around the instrumentation. Low-power (10 % power) as well as full-power measurements were made at key locations, and calculated results were compared with corresponding measured results. This paper describes the calculations and compares the measured and calculated results. Most of the measured results, when normalized to the full-operating-power level, compared favorably with the calculated results. One differed by a factor of 2.5, and another differed by a factor of 6. Based on this agreement, one can infer that reasonable calculations for some three-dimensional shield designs can be performed using two-dimensional methods and two-dimensional approximations to the three-dimensional geometry. The results confirmed the adequacy of the design.

KEYWORDS: shielding calculations, HFIR, dose rates, dose measurements, beam line, discrete ordinates, Monte Carlo

Introduction

The High Flux Isotope Reactor (HFIR) at the Oak Ridge National Laboratory (ORNL) began operation in 1966. It has one of the highest neutron ux levels in the world, and this ux has been used to produce various radioisotopes for medical and industrial applications in addition to supplying neutron beams that are used for various scienti c applications. Its normal operating power is 85 MW, and its design power is 100 MW. In recent years, the HFIR has undergone upgrades to its experimental facilities, including the enlargement of beam tubes to provide more neutrons at the experimental stations. Figure 1 shows the layout of HFIR s four beam tubes. As part of the upgrade for the radial beam tube HB-2, a shield tunnel was designed and constructed, allowing the beam to extend approximately 4.5 m into the beam room. This modi cation allowed the inclusion of three additional experimental facilities on the HB-2 beam line [a powder diffractometer, a residual stress diffractometer, and a wide-angle neutron diffractometer (WAND)]. In addition, a triple-axis spectrometer will be tied to the monochromator drum, which serves as the beam stop for the primary beam. A single 15.24-cm-tall $\times$ 5.08-cm-wide guide supplies neutrons to the HB-2D triple-axis spectrometer at the end position of the tunnel. The guide is angled at •0.64 with respect to the beam tube centerline. A layout of the instruments and shielding around the HB-2 beam is shown in Fig. 2, and a picture of the guide installed inside the shielding is shown in Fig. 3. The shield tunnel consists of bulk top, bottom, side, and end shields that protect the instruments and experimenters from the dose generated by the neutron and photon ux emanating from the HB-2 beam tube. Shielding calculations were performed to determine dose rates outside the bulk shielding as well as at heterogeneous regions of the shielding, such as beam shutters within the shields, access ports for the monochromator crystals, and gaps at the junctions of shield sections. The calculations were designed to determine the adequacy of

Manuscript received June 20, 2005; accepted for publication April 19, 2006; published online May 2006. Presented at ASTM Symposium on Reactor Dosimetry, 12th International Symposium on 8 13 May 2005 in Gatlinburg, TN ; D. W. Vehar, D. M. Gilliam, and J. M. Adams, Guest Editors.

[1] Senior Research Staff, Oak Ridge National Laboratory, Oak Ridge, TN 37831-6172.
[2] Senior Research Staff, Oak Ridge National Laboratory, Oak Ridge, TN 37831-6430.
[3] Senior Research Staff, Oak Ridge National Laboratory, Oak Ridge, TN 37831-6172.
[4] Senior Research Staff, Oak Ridge National Laboratory, Oak Ridge, TN 37831-6393.
[5] Senior Research Staff, Oak Ridge National Laboratory, Oak Ridge, TN 37831-6474.

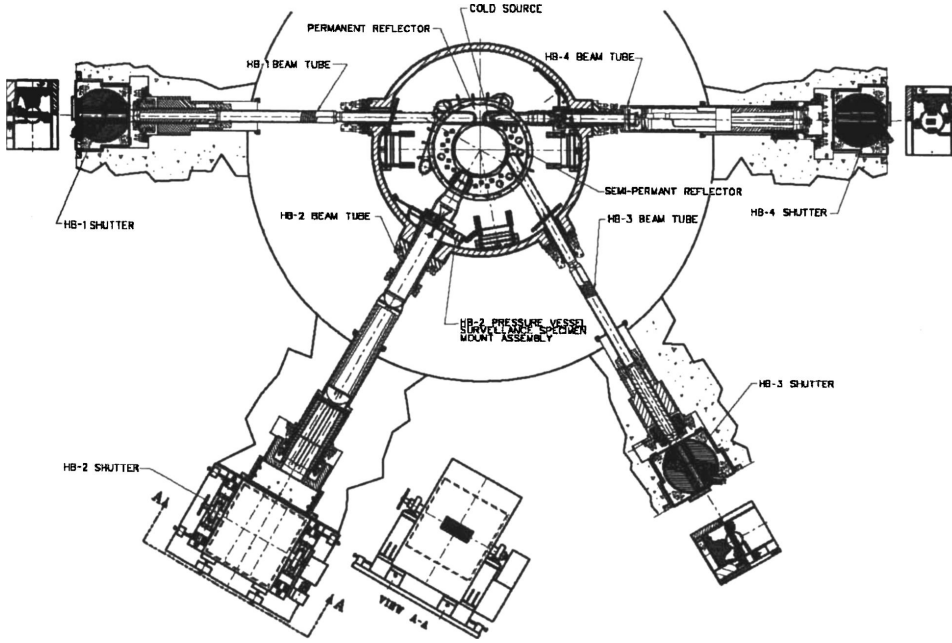

FIG. 1 *Layout of the HFIR's four beam tubes.*

proposed shielding designs and to determine if changes to the shield design were needed (i.e., if more or less shielding is required). In general, the shielding should limit the dose rate 30 cm from the shield surface to a level less than 5 mrem/h. This paper describes the shielding calculations for HB-2 and gives a comparison of calculated and measured results.

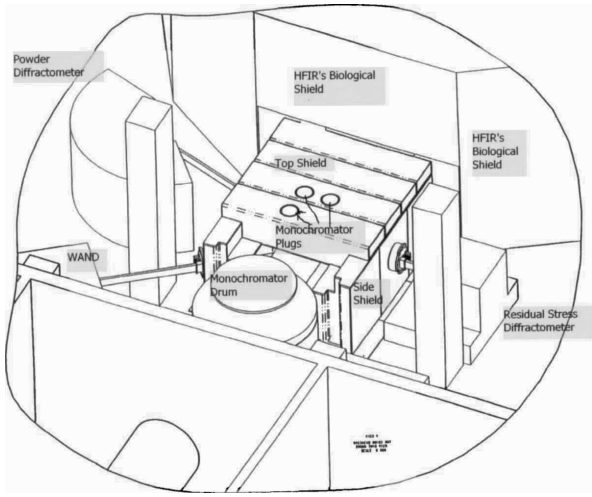

FIG. 2 *Layout of the instruments and shielding for HB-2.*

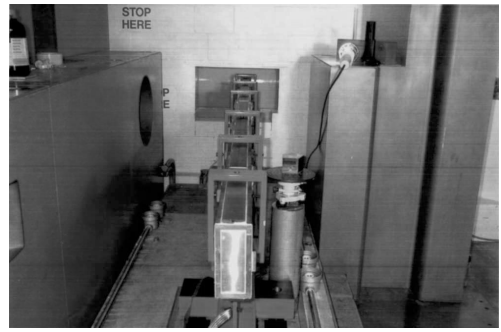

FIG. 3 *The installed guide in the partially shielded tunnel.*

Source for the Calculations

Neutrons and photons leaking from the core into the beryllium re ector provided the source for the beam tube calculations. Monte Carlo N-Particle (MCNP) [1] calculations were performed on a three-dimensional (3D) model of the HFIR and its beam tubes, and equivalent point sources that could be used to perform shielding calculations for each of the beam tubes were determined [2]. These point sources, normalized to the reactor s operating power, were located along the centerline of the beam tubes, and the distances of the point sources from reference planes (along a diameter of the reactor and perpendicular to the selected beam tube) varied by energy group, varying from 34.5 cm to 93.7 cm for HB-2. Using these point sources, one would calculate essentially the same spectrum at reference locations along the axes of the beam tubes as would be calculated using MCNP and the full HFIR model. The normalized HB-2 point source spectrum served as the basis for the subject shielding calculations. Sources for the localized calculations for the guide shield penetrations were spectra calculated at the insides of the bulk shield walls. The sources due to thermal neutrons scattered from the main beam and directed to the instrument ports by the instrument monochromator crystals were estimated by the HFIR Center for Neutron Scattering (CNS) physicists.

Calculations

The beam tube, portions of the HFIR vessel and biological shielding, the monochromator drum, and the beam-line bulk shielding were modeled with the combinatorial geometry package of the MORSE[6] Monte

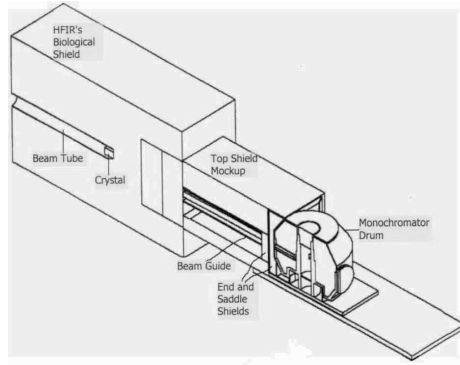

FIG. 4 *Cutaway elevation view of the MORSE HB-2 geometry mockup with an interim shutter design.*

[6]A multigroup Monte Carlo code whose acronym was derived from Multigroup Oak Ridge Stochastic Experiment.

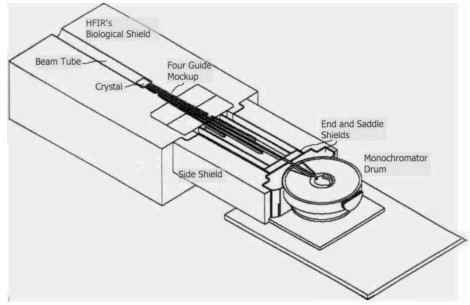

FIG. 5 *Cutaway plan view of the MORSE HB-2 geometry mockup with a silicon crystal fast-neutron filter.*

Carlo computer code [3]. Cutaway elevation and plan views of the geometry mockup with an interim shutter design and with a silicon crystal fast-neutron lter inside the biological shielding are shown in Figs. 4 and 5 respectively. Initial bulk shield calculations consisted of a MORSE calculation coupled with DORT [4][7] calculations (either *R-Z* or *X-Y*) at the inner walls of the bulk shields. However, nal calculations for the side and monochromator shields were performed entirely with the DORT code because a full energy spectrum could be calculated using that procedure. In the latter method, rst-collision sources were calculated within the 3D geometry at predetermined DORT *R-Z* coordinates (with the *Z* axis along the beam tube) and at a speci ed number of azimuthal angles, giving an *R*-Θ-*Z* spatial distribution of the source. The material used to calculate the rst-collision source was that within which the mesh point lay. The source was averaged over the azimuthal angle Θ to arrive at the two-dimensional *R-Z* rst-collision source for the DORT calculation. Averaging over the third quadrature direction is implicit, since for a given *R* and *Z*, the same μ value (the direction cosine for the radial variable *R*) will be calculated for any Θ. In a similar manner, a second rst-collision source and a second DORT calculation were performed for the monochromator drum. The monochromator drum was modeled with stepped cylindrical regions, the axes being oriented along the axis of the guide supplying the drum. A saddle shield upstream of the drum, but none of the other upstream shielding, was included in the mockup. In addition, DORT calculations were performed for the shield gaps and access ports for the monochromator crystals, and TORT [5][8] calculations were performed for the beam-line shutters. These calculations used isotropic uxes from the rst DORT calculation as boundary sources. All of the calculations were performed using cross sections from the VELM61 61-neutron-group/23-photon-group coupled library [6].

Results

Top and Sides of the Tunnel

The top and sides of the shield tunnel are sectioned in Fig. 2. The side shields consist essentially of a 73.66-cm-thick region of a steel shot and borated paraf n mixture sandwiched between two 1.905-cm-thick carbon steel walls. A thin layer of borated rubber lines the outer wall. The top shields are 2.54-cm thinner than the side shields. The regions representing the side, top, and bottom shields in the two-dimensional model were formed by cylindrical bodies that have volumes equal to those of the parallelepipeds that bound the shield regions. The DORT calculation yielded a maximum dose rate of 3.0 mrem/h outside the shield wall (Fig. 6). As shown in Table 1, the average dose rate measured by Research Reactor Division s radiological control technicians was about 3.5 mrem/h,[9] which is 1.17 times the calculated value. At the interface of the side shield with the biological shield, a 60.0-mrem/h dose rate

[7]A multigroup, two-dimensional discrete ordinates radiation transport code.
[8]A Multigroup, three-dimensional discrete ordinates radiation transport code.
[9]Measurements were made using two detectors. The photon detector was an Eberline RO-20, an air- lled ionization chamber used to detect photon, x-ray, and beta radiation. The neutron detector was a NRC model NP-2A instrument which uses a BF3 detector shielded by polyethylene. It gives true rem-per-hour (rem/h) measurement capability independent of neutron energies in the range of 0.025 eV to 15 MeV.

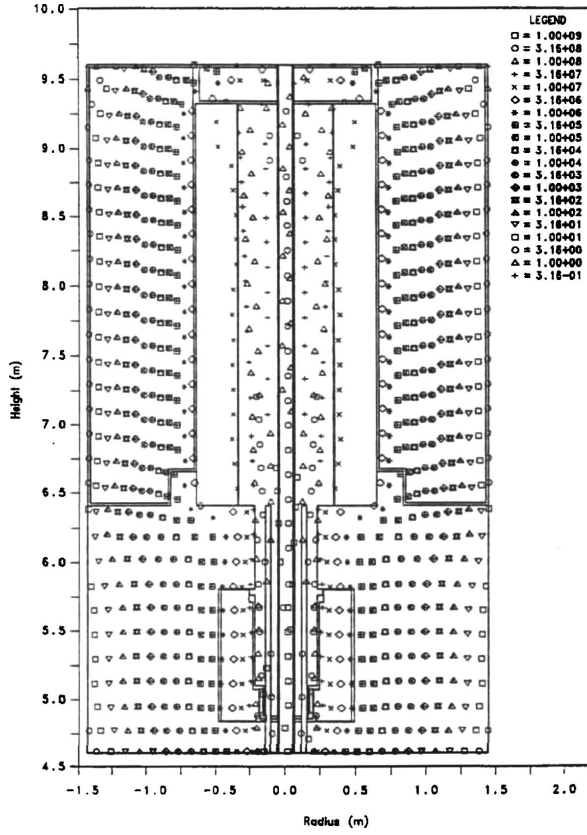

FIG. 6 *DORT-calculated total dose rate (mrem/h) for the HB-2 guide shield assembly.*

was measured. This measurement was 6.0 times the calculated value. The high measurement value is unexplained, but added shield wedges at the interface decreased the measured dose rates considerably.

The MORSE-calculated leakage into the top shield region was somewhat lower than that into the side shield region. Therefore, a separate calculation was performed for the top shield, one for which a lower incident source was used. DORT *R-Z* calculations were performed for a re ected cell mockup of the solid

TABLE 1 *Comparison of calculated and measured dose rates for the HFIR HB-2 beam line.*

Measurement location	Total dose rate, mrem/h[a]		Ratio, meas./calc.
	Calculated	Measured	
Basic shield tunnel	3	3.5	1.17
Interface with biological shield wall	10	60.0	6.0
Shield tunnel roof	0.73	0.6	0.82
Roof plug over monochromator crystal	4.66	4.5	0.97
HB-2B shutter hole with shutter closed[b]	10	9.0	0.9
HB-2B shutter hole with shutter open[b]	32 000	36 400	1.14
HB-2C shutter interface with shield wall[c]	30	12	0.4
HB-2C shutter hole with shutter closed[c]	2.0	2.0	1.0
Back of HB-2D monochromator drum[d]	32	33	1.03

[a]The total dose rate is the sum of the neutron and photon dose rates.

[b]HB-2B is the residual stress diffractometer.

[c]HB-2C is the wide-angle neutron diffractometer.

[d]HB-2D is the triple-axis spectrometer.

TABLE 2 *Maximum dose-rate ratios for gapped versus solid shields.*

Shield description	Neutron	Photon	Total
Keyed side shield (30.48-cm × 30.48-cm key with a 0.635-cm gap)	3.82	0.97	1.42
Keyed side shield (30.48-cm × 40.64-cm key with a 1.27-cm gap)	8.64	1.26	3.16
Stepped side shield (30.48-cm overlap, 0.635-cm gap)	3.22	0.98	1.31
Stepped side shield (15.24-cm overlap, 1.27-cm gap)	11.6	1.02	3.72
Stepped side shield (15.24-cm overlap, 1.27-cm × 0.318-cm × 1.27-cm gap)	10.2	1.01	3.31
Stepped side shield (15.24-cm overlap, 0.318-cm gap)	2.42	1.00	1.05
Stepped top shield (10.16-cm overlap, 1.27-cm × 0.318-cm × 1.27-cm gap)	12.7	1.03	4.70
Stepped top shield (10.16-cm overlap, 0.635-cm × 0.318-cm × 0.635-cm gap, cross gap at 1/3 shield depth)	3.08	0.996	1.41
Stepped top shield (10.16-cm overlap, 0.635-cm × 0.318-cm × 0.635-cm gap, cross gap at 2/3 shield depth)	2.97	1.01	1.38

shield and for a mockup containing a monochromator plug shield, the *Z* axis pointing upward through the top shield. The maximum dose rates were 0.73 mrem/h for the solid shield and 4.66 mrem/h for the monochromator plug. The measured value (Table 1) for the solid shield was 0.6 mrem/h, about 0.82 times the calculated value, and the measured value for the monochromator plug was 4.5 mrem/h, about 0.97 times the calculated value.

Dose-rate perturbations due to shield penetrations were studied also. Possible penetrations introduced by the fabrication tolerances of the shield sections were examined using DORT *X-Y* calculations, the *Y* axis pointing outward through the side shield. Shield designs mated with overlapping sections produce a three-legged gap, two offset radial segments and one cross gap joining the two radial segments. Keyed shield designs had gaps consisting of two aligned radial segments joined by two U-shaped paths around the key. Dose rates for the various designs were compared with dose rates calculated for the solid shield. The results in Table 2 show that dose rates can be signi cantly higher near gaps in the shields. As expected, the neutron dose rate is much more sensitive to the gap size than is the photon dose rate. The dose-rate increase appears to be tolerable for shields with gaps smaller than 0.635 cm. No spikes in the dose rate were measured outside the shield, so gap streaming is not a problem for the as-built design.

Other penetrations introduced by the beam shutters for the instruments were studied using the TORT three-dimensional radiation transport code. Geometries for the shutters were modeled using the MORSE combinatorial geometry package. The shutters were modeled with the beam channels both open and closed. The TORT spatial mesh was superimposed over each model through translation and rotation, and a material zone was assigned to each mesh based on the material region in which the mesh center resided. A VARMAP le [5], which contains all the information needed to describe the TORT geometry, was created for each shutter. An isotropic ux spectrum averaged over a portion of the wall where the shutter was located served as the source for the TORT calculation for a speci c shutter. In addition, an angle-dependent, thermal-neutron spectrum supplied by CNS staff was included in some calculations. Results in Table 1 for the HB-2B and HB-2C shutters show good agreement of calculated and measured dose rates for both open and closed shutters. The HB-2B measurement with the shutter open includes thermal neutrons scattered from the monochromator crystal. The number of neutrons and their angular distribution were supplied by CNS staff. The calculation involved streaming through a beam channel with a tapered borated sleeve inserted near the end of the channel. The calculated dose rate for this case was about 18 000 mrem/h. The dose rate without the sleeve was estimated at 32 000 mrem/h because the dose rate was constant at that level along the channel until the sleeve was encountered in the model.

The Monochromator Shield

The monochromator drum is located at the end of the HB-2 shield tunnel and has a direct view of a guide lying 0.64 to the left of the beam tube centerline. It is shielded by a borated paraf n and steel shot mixture, various supportive steel struts, and lifts that allow the drum to be rotated about 110 . As seen in

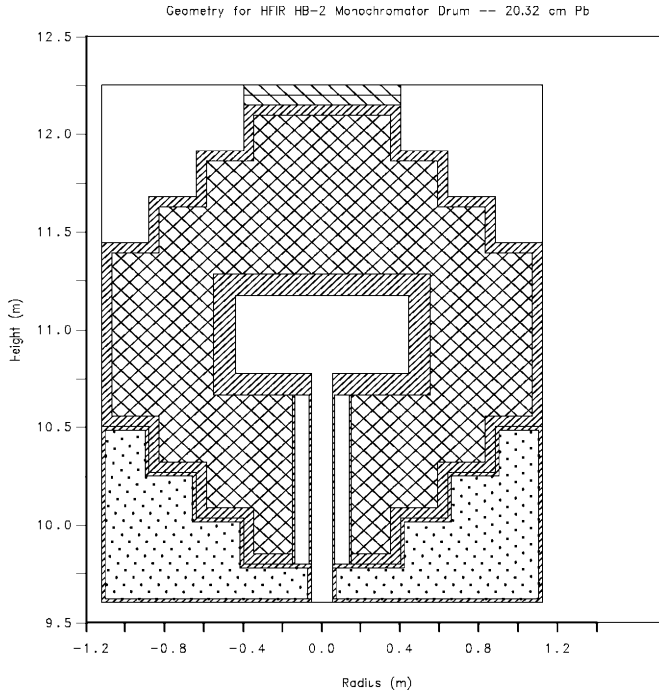

FIG. 7 *DORT geometry model for the HB-2 monochromator drum shielding calculation.*

Fig. 4, the drum consists of a cylinder sandwiched between two frustums of cones. The shielding calculation for the drum was also performed with the DORT two-dimensional discrete ordinates radiation transport code. The drum and the saddle shield upstream of it were modeled as stepped cylinders with axes aligned with that of the guide supplying neutrons to the drum (Fig. 7). An effort was made to conserve the volumes of the different regions. A rst-collision source averaged over the azimuthal angle served as the source for the calculation. In the model in Fig. 7, lead shielding was included on the back side of the drum (top of the cylinder in the two-dimensional geometry) to limit the dose rate there. However, calculations were performed with no lead, 10.16 cm lead, and 20.32 cm lead. As shown in Table 1, the calculated dose rate at the back of the drum without lead was about 32 mrem/h, while the measured value was 33 mrem/h. This agreement is very good.

Conclusions

Calculations were performed in support of the shield design for the upgraded HFIR HB-2 beam line. Calculated results were compared with measured results and were in generally good agreement. The adequacy of the design was con rmed. Areas where dose rates exceeded the limit have been or will be dealt with, either by the use of additional shielding or by restricting access.

References

[1] Briemeister, J. F., editor, *MCNP—A General Monte Carlo N-Particle Transport Code, Version 4B*, Los Alamos National Laboratory Report No. LA-12625-M, 1997.

[2] Bucholz, J. A., *Source Terms for HFIR Beam Tube Shielding Analyses, and a Complete Shielding Analysis of the HB-3 Tube*, Oak Ridge National Laboratory Report No. ORNL/TM-13720, 2000.

[3] Straker, E. A., Scott, W. H., and Byrn, N. R., *The MORSE Code with Combinatorial Geometry*,

DNA-2860-T, 1972.

[4] Rhoades, W. A., and Childs, R. L., The DORT Two-Dimensional Discrete Ordinates Transport Code, *Nucl. Sci. Eng.*, Vol. 99, No. 1, 1988, pp. 88 89.

[5] Rhoades, W. A., and Childs, R. L., *The TORT Three-Dimensional Discrete Ordinates Neutron/Photon Transport Code*, Oak Ridge National Laboratory Report No. ORNL-6268, 1987.

[6] Fu, C. Y., and Ingersoll, D. T., *VELM61 and VELM22: Multigroup Cross-Section Libraries for Sodium-Cooled Reactor Shield Analysis*, Oak Ridge National Laboratory Report No. ORNL/TM-10302, 1987.

Journal of ASTM International, Vol. 3, No. 10
Paper ID JAI100345
Available online at www.astm.org

Robert E. Keith[1]

An Approach to Determining the Uncertainty in Reactor Test Objects Using Deterministic and Monte Carlo Methods*

ABSTRACT: A procedure for determining an estimate of the uncertainty in test objects components using discrete ordinates and Monte Carlo methods has been developed. The procedure is described, and a review of the advantages and disadvantages of these methods is presented with the emphasis on the advantage of employing both transport methods in analysis. The discrete ordinates-based techniques use the DOORS and DANTSYS radiation transport codes (with the SUSD3D code for the determination of sensitivity of the response parameter to cross sections), and the Monte Carlo-based techniques primarily employ the MCNP code (using the general MCNP perturbation operator in a manner that determines the sensitivities to transport cross sections). The focus of the analysis presented is on experiments that are preformed at the Annular Core Research Reactor (ACRR) at Sandia National Laboratories (SNL), and includes uncertainty contributed by the uncertainties in the source spectrum, in response functions, and in transport cross sections.

KEYWORDS: uncertainty analysis, sensitivity analysis, Monte Carlo, discrete ordinates

Introduction

Whenever experiments are conducted, one of the major parameters that needs to be presented is an estimate of the uncertainty associated with the test results or calculations, and for experimentalists this has been a task that has accompanied research efforts for some time. This uncertainty information, if done well, aids analysts and reviewers in understanding the test results and aids in comparing the results of one test with the results of another and in the design of future tests. Similarly, when numerical calculations are made to model experiments, a good estimate of the uncertainties associated with the prediction is also of great importance for the calculations to be useful. However, the estimation of uncertainty (with the exception of reporting the statistical deviation for Monte Carlo calculations), has typically received less care than it should. Frequently, the better uncertainty reports are composed of the estimates of the uncertainty of the various aspects of the problem summed in quadrature, and often the estimates of some of the uncertainty aspects are subjective and are based primarily on past experience of the analyst with similar models.

A study effort has been undertaken to quantify reasonable uncertainty bounds for the response of sensitive portions of a test object exposed to a reactor neutron environment. The goal of the study was not simply to perform a series of calculations for a single series of tests, but rather to establish procedures that can be used for general, and perhaps complicated test objects. The emphasis is on using techniques that rely on accepted uncertainty values (covariance matrices) as the underlying data uncertainty information—rather than considerations involving only the historical perceived accuracy of calculations. Computer codes like SUSD3D [1] and SEN1 [2], which are useful for determining the uncertainty from the cross section uncertainty, were used when applicable, but additional software was written to handle situations when current tools were not available.

Manuscript received June 20, 2005; accepted for publication August 24, 2006; published online October 2006. Presented at ASTM Symposium on Reactor Dosimetry, 12th International Symposium on 8-13 May 2005 in Gatlinburg, TN; D. W. Vehar, D. M. Gilliam, and J. M. Adams, Guest Editors.
[1] Principal Scientist, ITT Industries, AES, Colorado Springs, CO 80919.
*This work was supported by the United States Department of Energy under contract DE-AC04-94AL85000 with technical management by Sandia National Laboratories. Sandia is a multiprogram labortory operated by Sandia Corporation, a Lockheed Martin Company, for the United States Department of Energy.

Background

For the purposes of this paper, a "contributor" will be defined as anything in the experiment being modeled that can add to the response parameter uncertainty (an example would be the thickness of a cadmium cover on an activation foil—or the aluminum elastic cross section at 1 MeV). The possible contributors to the uncertainty of an estimate of the response parameter of a portion of a test object can be grouped into the following contributor classes: (1) source uncertainties, (2) transport cross sections uncertainties[2], (3) response-function uncertainties, (4) geometrical inaccuracies (including geometric modeling simplifications and gaps caused by material size variations), (5) thickness (aspect of material size variations that has the affect of increasing or decreasing optical depth with possible gaps treated as geometric inaccuracy) and density uncertainties, and (6) numerical inaccuracies. For each of these classes, an estimate of the uncertainty in the response parameter due to the uncertainties of the specific contributors is determined using techniques that are applicable to that class. Under these broad contributor classes, many specific contributors contribute to the overall uncertainty, and these are combined to get a relative variance of the response parameter using the familiar expression given in Eq 1.

$$\frac{\mathrm{var}(R)}{R^2} = \sum_i \sum_j P_i \cdot r\mathrm{cov}(i,j) \cdot P_j \tag{1}$$

where var(R) is the variance of the response parameter, P_i is the sensitivity of the response parameter to some parameter referenced by i, and $r\mathrm{cov}(i,j)$ is the relative covariance of the parameter referenced by i with the parameter referenced by j.

If R is the response parameter, and x_i is a parameter referenced by i, the sensitivity can be expressed as in Eq 2.

$$P_i = \frac{\partial R}{\partial x_i} \cdot \frac{x_i}{R} \tag{2}$$

The quest to find the variance in the response parameter becomes a quest to identify the relative covariances and to determine the sensitivities P_i, and a quest to determine covariances for the underlying parameters. The latter issue, while critically important, will not be considered further here, but it will be assumed that the covariance data are available or can be estimated.

Depending on whether a discrete ordinates or a Monte Carlo approach is being used, the form of the sensitivity calculation differs. Traditionally, radiation-transport problems have been approached by selecting a transport method (discrete ordinates or Monte Carlo) based on the details of the geometry and the expertise of the analyst. Then whatever uncertainty analysis tools are readily available for that method may be employed to help establish a defensible estimate of the uncertainty. However, the determination of the sensitivities of the response parameter (transport result) to the basic source or transport cross section data can be much more complicated than the actual calculation, and this sensitivity information is critical to determining a mathematically justifiable estimate of the response parameter uncertainty. Hence, the choice of the transport method used should include consideration of the uncertainty analysis that is also to be done. The approach that is recommended in this paper is to employ both methods when possible to provide a point of comparison and to better exploit the advantages of each technique. Some primary advantages of each transport technique are listed in the following subsections.

Discrete Ordinates Transport Advantages

Full Energy and Angle Dependent Forward and Adjoint Fluence Data Available for Post Processing—This allows the use of techniques such as the forward-adjoint folding techniques used in SUSD3D. It is possible then to determine the uncertainty from quantities such as material minor constituents and impurities that weren't considered in the original calculations (as long as their effect is "small"). For instance, for the example described later in this paper, the forward and adjoint fluences for the aluminum 6061 sphere could have been calculated using a material of pure aluminum, and then the forward-adjoint folding technique could be used with the magnesium cross sections to determine whether the response parameter

[2]Hereafter "transport cross sections" will be referred to as "cross sections." The response functions used in this paper are also cross section, but for clarity are always referred to simply as "response functions."

is sufficiently sensitive to require inclusion of the magnesium in the calculation of the forward and adjoint fluences. Similarly, the sensitivity of the response parameter to the total cross section of a possible impurity material can be made, and by multiplying by an assumed density of the impurity, an estimate of the uncertainty of the response parameter due to the possible presence of the impurity can be made. In Monte Carlo transport a similar minor constituent or impurity uncertainty contribution calculation requires that the sensitivity calculation must be made during the transport, and this can become very expensive computationally.

Effect of Problem Input Variation Apparent in the Response Parameter—If an input parameter, such as a thickness of a cover, is changed by a small amount, the effect can be clearly quantified in the response parameter. This allows reliable brute force calculations of sensitivity if needed, and the interplay of the elements of a problem can be studied better. In Monte Carlo, the ever-present statistical sampling uncertainty requires that any such comparisons be made with enough particles to reduce the statistical standard deviation to far below change in response parameter due to the variation in the problem input.

Monte Carlo Advantages

Complex Geometries Relatively Easy to Model—The input for modern Monte Carlo codes like MCNP [3] or Geant4 [4] make it relatively easy to model very complicated geometries without the difficulties associated with a discrete-ordinates spatial grid.

Ray Effects Can Be Avoided—Discrete ordinate codes divide the angular component of transport into discrete angular bins, and for problems with small source regions and small scoring regions the response parameter can be artificially increased or decreased by the chosen resolution in angular quadrature.

Minimal Grid Effects in the Response Parameter—Point cross section energy-dependent based transport codes produce response parameters that are mostly free of errors caused by poorly defined grids and poorly resolved spectra. Care needs to be exercised in defining the resolution used in each approximation in a discrete-ordinates calculation, and even then it is possible to be surprised. As is mentioned below, the source uncertainty contribution in a calculation with cadmium-covered gold foil changed over an order-of-magnitude when a fine grid (640 energy bins) was used as compared to less resolved grid (89 bins) in a discrete-ordinates calculation, but the important cross sections were transparently handled in a similar Monte Carlo calculation.

The desire for a procedure that is somewhat general made it important to be able to use both discrete-ordinates and Monte Carlo transport techniques, and the methods needed to determine uncertainty from each differ. For some contributor classes, the difference in procedure might simply be making sure that the Monte Carlo results have a low enough statistical standard deviation; for others, such as for the cross section contributor class, very different techniques are used.

Below, the general procedure that was developed is outlined, then a specific example is described, and the methods used in this study for discrete ordinates and Monte Carlo techniques are described, and some results of the study problem are presented. Although the procedure below describes the uncertainty for all contributors, only the contribution from the three major contributor classes will be presented.

General Procedure

The procedure for determining the uncertainty in the response parameter from the uncertainty contributors is straightforward and will involve using a coarse calculation for identifying the most important contributors, and a detailed calculation to determine the uncertainty contribution from the major contributors. It is recommended that a discrete ordinates approach be used for the coarse initial calculations, and that the detailed uncertainty estimates be done using a Monte Carlo approach. The general procedure is:

- Determine the methods and tools that are to be used, and make an initial (coarse) calculation of the response parameter(s). The method determination chiefly consists of deciding whether to use discrete ordinates, Monte Carlo, or combined methods, and choosing the basic tools (e.g., DANTSYS [5] versus DOORS [6], SUSD3D versus SEN1 for discrete ordinates, and MCNP versus Geant4 for Monte Carlo). Ideally, the initial calculation should be good enough to get close to the actual

response parameter, but coarse enough to be solved quickly. For the study problem the DOORS code system was used for the coarse transport model, although the DANTSYS code system could have been used just as well. Both the SUSD3D code and SEN1 codes could have been used for the sensitivity and uncertainty analysis, but since SUSD3D can be used for three-dimensional problems it has been used even though the particular study problem did not require this capability.

- Determine all discernable contributors to the response parameter uncertainty, and obtain uncertainty data for the contributors. These data will include the energy-dependent covariance matrices for the source, response functions, and cross sections, and will include standard deviations for the other contributors—such as geometric dimensions.
- Perform an initial (coarse) calculation of the uncertainty from the major three contributor classes (source contributor class, response function contributor class, cross section contributor class). This calculation is performed using the techniques described in the following sections. For the cross section uncertainty calculation, sensitivity and uncertainty calculations (e.g., using SUSD3D) should be performed using cross sections and covariances for the major material constituents of the geometry. As with other transport problems the energy grid should be chosen so that the true energy dependent fluence profile inside each bin should not change greatly throughout the geometry. The spatial grid should be chosen so that the fluence is smoothly varying through the grid. Practically, the grids are generally checked by performing calculations at a higher grid resolution, and checking for significant variations in the response parameter and response parameter uncertainty calculated. For the study problem a one-dimensional geometric model was sufficient, but for more involved geometries a two- or three-dimensional model might be required.
- Estimate possible uncertainty contributions from minor contributors. If the contribution from the minor contributor classes (geometrical inaccuracies, thickness and density uncertainties, and numerical inaccuracies) is much less than that from the major classes, that fact is recorded but no further calculation is warranted for these classes.
- Refine the calculation procedures and make detailed response parameter estimates. Before the response parameter was calculated using simple models, and in this step the calculation is refined to include potentially important details. The Monte Carlo code MCNP was used for the study problem, since Geant4 usage for the cross section sensitivity calculation would require significant programming.
- Make detailed calculations of the uncertainty from the major contributor classes using the initial uncertainty calculations as a guide to the important contributors. The use of the initial uncertainty calculations is especially useful for Monte Carlo methods. The perturbation operator in MCNP increases the runtime of the calculation by about 10 % for each perturbation [3]. For the example calculation of the uncertainty given in this paper addressing the effect of the elastic aluminum scattering uncertainties, 152 individual perturbations were used.
- Perform any needed detailed calculations for the minor contributors.
- Combine the uncertainty contributions from the various classes to determine the total uncertainty of the response parameter (Eq 1).

Problem Geometry

Generally this study addresses the contributors to the uncertainty of the calculation of the response parameter of some component (a critical element of a device or a sensor or an activation foil) of a test object that is subject to a neutron environment in a reactor core. In the example discussed here, the work performed considers the simple geometry of tests that were being performed in the Sandia National Laboratories (SNL) Annular Core Research Reactor (ACRR) using several test spheres with activation foils. Figures 1 and 2 show the basic geometry of the problem. A sphere containing foils placed at various locations along in the horizontal plane just below the sphere's center (Fig. 2) is placed in the core of the ACRR (Fig. 1) and exposed to a neutron environment. The sphere is later removed from the reactor, and the γs coming from the decay of the activated isotopes in the foils are measured.

In this series of experiments at SNL, several spheres were used—two seven-in. (0.1778 m) diameter spheres—one made of aluminum and one of polyethylene, four four-in. (0.1016 m) diameter spheres—one of aluminum, one of polyethylene, one of iron, and one of lead. There were six kinds of activation foils

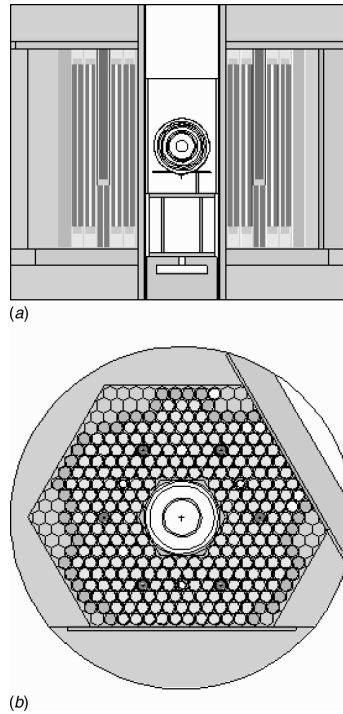

FIG. 1—*ACRR reactor (from MCNP model) (a) vertical slice, (b) horizontal slice.*

used—nickel (for $^{58}Ni(n,p)^{58}Co$ activation), cadmium covered gold (for $^{197}Au(n,\gamma)^{198}Au$), cadmium covered cobalt (for $^{59}Co(n,\gamma)^{60}Co$), scandium (for $^{45}Sc(n,\gamma)^{46}Sc$), sulfur (for $^{32}S(n,p)^{32}P$), and titanium (for $^{nat}Ti(n,X)^{46}Sc$, $^{nat}Ti(n,X)^{47}Sc$, and $^{nat}Ti(n,X)^{48}Sc$ activation). For brevity, analysis and results for only one sphere will be considered (the 7-in. (0.1778 m) aluminum sphere) and two activation foil types (nickel and cadmium covered Au).

For the initial coarse model, the sphere was modeled as a one-dimensional single-material sphere, and the activation foils were modeled as spherical shells in the geometry. For this model the one dimension discrete-ordinate code from the DOORS codes system (ANISN) was used. This approach was ideal to investigate the sensitivity of the various uncertainty contributors for this example—in general the coarse model would have to be somewhat more complicated. For the fine detail model, a full three-dimensional MCNP model was created. For both models, ENDFB-VI [7] cross sections were used. To provide a connection between the fine detail model and the simple one-dimensional mode, a spherical-shell model was also developed in MCNP that corresponded directly to the ANISN geometric model. The source for most of these calculations was the ACRR spectrum obtained from SNL [8]. Figure 3 shows the calculation versus experiment (C/E) ratio curves for both of the transport models for both of the response functions.

The data in these figures are normalized to the experimentally measured activity of cobalt-58 (from the $^{58}Ni(n,p)^{58}Co$ reaction) from a nickel monitor foil placed on the surface of the sphere to eliminate the uncertainty associated with the magnitude of the source.

Source Uncertainty Contribution Calculation

The source for this study is defined as the fluence at the surface of the sphere, and the SNL provided ACRR spectrum [8] was used. This spectrum had been calculated from a least-squares fit to activation data, and has an associated covariance file that was produced as part of the least-square fitting process. An

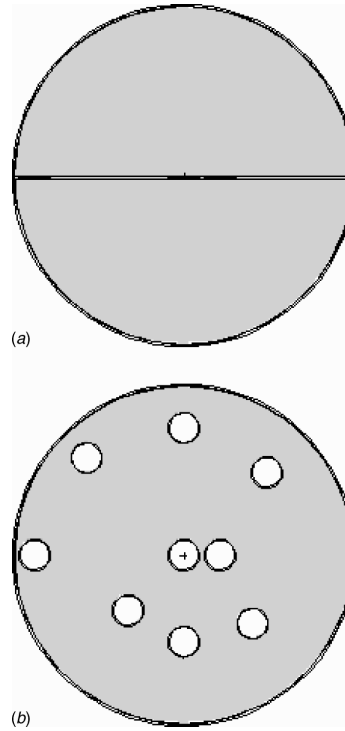

FIG. 2—*Test sphere with activation foil placements shown (a) vertical slice, (b) horizontal slice.*

alternative approach would be to model the entire reactor, and attempt to estimate the uncertainty in the spectrum from the fission distribution in the fuel and the transport through the reactor, and this was deemed beyond the scope of this study and it seemed unlikely that the uncertainty estimate would be more reliable than using the experimentally determined free-field spectrum. However, the use of this experimental spectrum introduces several issues: (1) the neutron environment in the reactor core is assumed to be approximately isotropic, and (2) the spectrum energy dependence really corresponds to the reactor configuration that was used to measure the spectrum, and may need to be modified to account for the presence of the test object.

To assess the impact of assuming that the neutron environment is isotropic, a full reactor model was used to calculate an anticipated neutron environment at the sphere. For this calculation, a sphere of aluminum was modeled in the core with nickel activation foils placed at various angles on the surface of the sphere, and the fluence and ^{58}Ni(n,p) response functions were used. An approximately 20 % reduction in the activation of nickel-58 to cobalt-58 for a foil on the top of the sphere compared with those on the midline highlighted the asymmetry of the higher energy (>1 MeV) portion of the source. However, for this series of calculations on the centerline of the sphere it is not anticipated that this will be a major effect, or significantly increase the uncertainty of the calculations. The statistical uncertainty of these calculations was approximately 1 % for the fluences, and 4 % for the activation response functions.

The second source issue is that the test object will cause a slight change in the energy spectrum of neutron. An estimate of this change of the source spectrum can be made by modeling the reactor in a criticality code (MCNP can be used in its criticality mode) both with and without the test object and tallying the inward fluence around the test object. The energy-dependent source can then be modified by the difference in the fluence with the test object and without the test object for each source energy bin. This can be important when the test object acts as a moderator (e.g., a polyethylene sphere). The study problem did not require such a modification, and the reference source spectrum was used without modification.

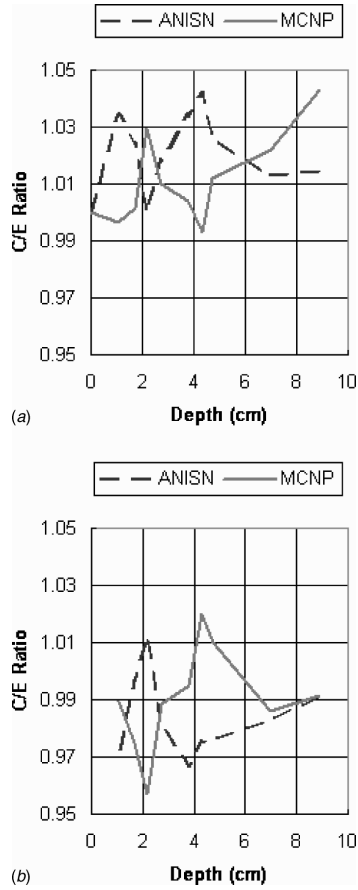

FIG. 3—*Calculation versus experiment for the (a) $^{58}Ni(n,p)^{58}Co$ and (b) Cd covered $^{197}Au(n,\gamma)^{198}Au$ response function in the aluminum sphere.*

A more significant issue is making sure that the magnitude of the source is what was expected. To assist in comparisons a nickel foil was placed on the exterior surface of the sphere in each test for normalization, and the response parameters were calibrated to the activation ($^{58}Ni(n,p)^{58}Co$) of this foil. In calculating the source and response function uncertainty, it is important to take this normalization into account.

The contribution of the source uncertainty to the response parameter is best obtained through the adjoint fluence for the response function of interest. The modified response parameter (response parameter at a component divided by the activity from the exterior nickel foil activation) is given by:

$$R' = \frac{\int_{\substack{source \\ region}} d\vec{r}' \int d\vec{\Omega}' \int dE' S(\vec{r}',E',\vec{\Omega}') \cdot \Phi^*(\vec{r}',E',\vec{\Omega}')}{\int_{\substack{source \\ region}} d\vec{r}' \int d\vec{\Omega}' \int dE' S(\vec{r}',E',\vec{\Omega}') \cdot \Phi^*_{^{58}Ni^*}(\vec{r}',E',\vec{\Omega}')} \tag{3}$$

where, R' is the modified response parameter, $S(\vec{r}',E',\vec{\Omega}')$ is the source function, $\Phi^*(\vec{r}',E',\vec{\Omega}')$ is the adjoint fluence for the original response function from the component of interest, and $\Phi^*_{^{58}Ni^*}(\vec{r}',E',\vec{\Omega}')$ is

TABLE 1—*Source uncertainty contributions (in percent standard deviations) for aluminum sphere using ANISN and MCNP versus depth of foil.*

Depth of Foil Center (cm)	^{58}Ni(n,p)^{58}Co		Cd-covered ^{197}Au(n,γ)^{198}Au	
	ANISN	MCNP	ANISN	MCNP
0 (exterior)	0	0	9.5	…[a]
1.04	0.021	0.39	13	12
1.70	0.030	0.72	15	15
2.18	0.036	0.81	16	16
2.72	0.042	0.74	17	16
3.78	0.051	0.84	18	17
4.32	0.055	0.97	19	18
4.75	0.058	0.92	19	19
6.99	0.068	1.1	21	20
8.89 (center)	0.070	1.1	21	21

[a]The experiment did not include an external cadmium-covered gold foil so none was included in the MCNP model.

the adjoint fluence for the ^{58}Ni(n,p) reaction in the exterior foil. The source is normally input as a fluence binned in energy, and the contribution of the source uncertainty to the total uncertainty is given by:

$$\mathrm{var}(R')_S = \sum_i^{N_E} \sum_j^{N_E} \frac{\partial R'}{\partial S_i} \cdot \mathrm{cov}(S_i, S_j) \cdot \frac{\partial R'}{\partial S_j} \tag{4}$$

where, N_E is the number of energy bins, S_i is the source fluence in an energy bin for E_i to E_{i+1}, and $\mathrm{cov}(S_i, S_j)$ is the covariance of the source. The derivative of the response parameter with respect to the source in a bin is of course:

$$\frac{\partial R'}{\partial S_i} = \frac{1}{R_{^{58}\mathrm{Ni}}} \cdot \left\{ \int_{\substack{source \\ region}} d\vec{r}' \int d\vec{\Omega}' \int_{E_i}^{E_{i+1}} dE' \Phi^*(\vec{r}', E', \vec{\Omega}') \cdot \omega(\vec{\Omega}') \right.$$
$$\left. - R' \cdot \int_{\substack{source \\ region}} d\vec{r}' \int d\vec{\Omega}' \int_{E_i}^{E_{i+1}} dE' \Phi^*_{^{58}\mathrm{Ni}}(\vec{r}', E', \vec{\Omega}') \cdot \omega(\vec{\Omega}') \right\} \tag{5}$$

where, $R_{^{58}\mathrm{Ni}}$ is the activation from ^{58}Ni(n,p) reaction in the exterior foil and $\omega(\vec{\Omega}')$ is a factor that takes the input source fluence at a source into an angle dependent density function.

Using the adjoint fluence presents no problem for the discrete ordinates method. However, for the Monte Carlo method, there are still few codes that can properly handle calculating a true adjoint without using group-averaged cross sections (MCBEND might be an exception to this [9]). The usefulness of the adjoint fluence makes it useful to create a pseudo-adjoint solution. By recording the response parameter binned according to original source bins and dividing by the original source strength in each bin, an adjoint-like function can be developed for the source location. This was done for this study using the MCNP and Geant4 codes (the results of the MCNP code runs are those reported here).

The form of the derivative of the response parameter to the source (Eq 5) properly captures the reduction in the uncertainty that occurs when the results are calibrated in the fashion described. Note that if the response function of the exterior foil does not match well in energy with the calibration foil, this can increase the source uncertainty. The source uncertainties calculated for the response functions for the aluminum 7-in. (0.1778 m) sphere are given in Table 1. The modified response parameter derivatives (Eq 5) and the folding with the covariance (Eq 4) was performed for both the ANISN and MCNP calculations using a code created for this purpose named COVFOLD. Also in COVFOLD, if the transport energy grid does not match the covariance energy grid, the transport results are effectively rebinned to match the energy grid of the covariance matrix. The MCNP calculations were run until the sampling standard deviations were less than 2 % for the most important bins.

If the results were not normalized to the exterior foil, the ^{58}Ni(n,p)^{58}Co response parameter would be rather flat versus depth due to the fact that the portion of the energy spectra important for that response parameter changes little through the material (however, this is not always the case for all response functions). In this case the difference in the fluence versus depth is highlighted, and the results are exceedingly

small due to fact that the normalization foil uses the same response function. Without normalizing to the exterior foil (i.e., assuming that the source integrated fluence is known exactly), the standard deviation of the source error is about 2 %.

The very high uncertainty in the source for the cadmium-covered gold foil is due primarily to the details the neutron interactions in two source bins: a lower bin, 3.059 eV to 5.0484 eV, and an upper bin, 5.0484 eV to 7.8 eV. The lower bin has an associated uncertainty of about 14 %, and the upper bin has an associated uncertainty of about 60 %. The cadmium cover cross section of interest for this source uncertainty calculation is cadmium-113 absorption, and in the lower bin the $^{113}\mathrm{Cd}(\mathrm{n},\gamma)$ cross section drops several orders of magnitude, effectively eliminating the contribution of neutron in the lower energy portion of the lower bin. The gold absorption cross section is high (over 10^4 barns) near the 5.0484 eV bin edge, and then drops dramatically, so that the neutrons just under the 5.0484 eV bin edge (within about an eV) dominate in the calculation of the response parameter. For an estimate of the source uncertainty contribution for a cadmium-covered gold foil, the lower bin dominates, and an uncertainty contribution of about 3 % is calculated. However, in the aluminum sphere, the neutrons can lose energy due to elastic scattering prior to reaching the cadmium cover, and the neutrons that started in the upper bin can contribute as much or more than the neutrons that started in the lower bin to the response parameter. The very high uncertainty of the upper bin causes the high estimate of the uncertainty contribution to the response parameter uncertainty.

Unfortunately, the details involved can be lost if a too coarse energy grid is used without great care. For the 89 group energy structure the initial ANISN calculations, the bin width at these energies was too large to capture the details of the uncertainty calculation, and the uncertainty contributions from the source were much less (around 6 to 9 %), while the response parameters calculated were very similar (about 1 to 2 % difference). This particular phenomenon was limited to the aluminum sphere, the polyethylene sphere calculation did not exhibit the effect, and it appears that the aluminum scatters a somewhat larger number of neutrons from these bins to lower energies that still penetrate the cadmium foil than occurs with the polyethylene sphere. In the 640-bin structure runs, the resolution was sufficient to reflect the uncertainty contributed by these values. The MCNP calculation, not using an energy grid internally, addresses this circumstance properly.

Response Function Uncertainty Contribution Calculation

The response function uncertainty contribution is very similar to the source calculation, except that the forward fluence is used to define the response parameter. The modified response parameter is written in the forward transport form:

$$R' = \frac{\int_{component} d\vec{r}' \int d\vec{\Omega}' \int dE' f_R(\vec{r}',E',\vec{\Omega}') \cdot \Phi(\vec{r}',E',\vec{\Omega}')}{\int_{\substack{exterior \\ foil}} d\vec{r}' \int d\vec{\Omega}' \int dE' f_{^{58}\mathrm{Ni}(n,p)}(\vec{r}',E',\vec{\Omega}') \cdot \Phi(\vec{r}',E',\vec{\Omega}')} \tag{6}$$

where R' is the modified response parameter, $f_R(\vec{r}',E',\vec{\Omega}')$ is the original response function, $f_{^{58}\mathrm{Ni}(n,p)} \times(\vec{r}',E',\vec{\Omega}')$ is the $^{58}\mathrm{Ni}(\mathrm{n},\mathrm{p})$ activation response function, and $\Phi(\vec{r}',E',\vec{\Omega}')$ is the forward fluence as a function of position $(\vec{r})$, energy (E'), and direction $(\vec{\Omega})$. Similar to the source uncertainty contribution, the uncertainty contributed to the response parameter uncertainty can be captured as a variance of the form:

$$\mathrm{var}(R')_R = \sum_i^{N_E}\sum_j^{N_E} \frac{\partial R'}{\partial f^i_R} \cdot \mathrm{cov}(f^i_R, f^j_R) \cdot \frac{\partial R'}{\partial f^j_R} + (1-\delta_{R,^{58}\mathrm{Ni}}) \cdot \sum_i^{N_E}\sum_j^{N_E} \frac{\partial R'}{\partial f^i_{^{58}\mathrm{N}}} \cdot \mathrm{cov}(f^i_{^{58}\mathrm{N}}, f^j_{^{58}\mathrm{N}}) \cdot \frac{\partial R'}{\partial f^j_{^{58}\mathrm{N}}} \tag{7}$$

where f^i_R is the response function in an energy bin for E_i to E_{i+1}, $\mathrm{cov}(f^i_R, f^j_R)$ is the covariance of the response function, and $\delta_{R,^{58}\mathrm{Ni}}$ is one if the response function is the nickel activation response function, and zero otherwise. This last variable indicates the need to add the uncertainty of the normalization response function into the calculation if the normalization response function is different that the response function (in this case it is assumed that the response function, f^i_R, has no correlation with nickel monitor foil

TABLE 2—*Response function uncertainty contributions (in percent standard deviations) for aluminum sphere using ANISN and MCNP.*

Depth of Foil Center (cm)	^{58}Ni(n,p)^{58}Co		^{197}Au(n,γ)^{198}Au	
	ANISN	MCNP	ANISN	MCNP
0 (exterior)	0	0	2.5	2.5
1.04	0.034	0.030	2.5	2.5
1.70	0.048	0.052	2.5	2.5
2.18	0.058	0.059	2.5	2.5
2.72	0.066	0.068	2.5	2.5
3.78	0.080	0.081	2.5	2.5
4.32	0.086	0.086	2.5	2.5
4.75	0.090	0.087	2.5	2.5
6.99	0.10	0.11	2.5	2.5
8.89 (center)	0.11	0.17	2.5	2.5

response function, $f_{^{58}\mathrm{Ni}(n,p)}$). The derivative of the response parameter with respect to the response function in a bin is of course:

$$\frac{\partial R'}{\partial f_R^i} = \frac{1}{R_{^{58}\mathrm{Ni}}} \cdot \left\{ \int_{\substack{source \\ region}} d\vec{r}' \int d\vec{\Omega}' \int_{E_i}^{E_{i+1}} dE' \Phi(\vec{r}', E', \vec{\Omega}') - \delta_{R,^{58}\mathrm{Ni}} R' \cdot \int_{\substack{source \\ region}} d\vec{r}' \int d\vec{\Omega}' \int_{E_i}^{E_{i+1}} dE' \Phi_{^{58}\mathrm{Ni}}(\vec{r}', E', \vec{\Omega}') \right\} \tag{8}$$

For the response function uncertainty, the differences between the discrete-ordinates approach, and the Monte Carlo approach are minimal, and the main additional concern when using Monte Carlo is simply to ensure that the statistical uncertainties of the Monte Carlo runs are low enough for meaningful results. As was done for the source uncertainty contribution, the modified response parameter derivatives (Eq 8) and the folding with the response function covariance (Eq 7) was performed for both the ANISN and MCNP calculations using the COVFOLD code. The MCNP calculations were run until the standard deviations were less than 2 % for the most important bins. The response function uncertainties that were calculated for the response functions for the aluminum 7-in. (0.1778 m) sphere are given in Table 2.

For the ANISN calculations with the cadmium-covered gold foils, the basic calculations were performed using a response function that was generated by an adjoint run through the cadmium cover, and for the response parameter uncertainty calculation, the forward fluence was used at the location of the foils as a source for transport through the cover to obtain a forward fluence at the gold foil, and then the gold covariance matrix could be used to determine the uncertainty.

Cross Section Uncertainty Contribution

The uncertainty to the response parameter contributed by the cross section uncertainty is the focus of many sensitivity and uncertainty studies using a forward fluence—adjoint fluence folding technique (Eq 9) and several computer codes have been written to accomplish this task [1,2].

$$P_x(E) = \frac{1}{R} \cdot \int d\vec{r} \int d\vec{\Omega} \left\{ -\Sigma_T^x(\vec{r}, E) \cdot \Phi(\vec{r}, E, \vec{\Omega}) \cdot \Phi^*(\vec{r}, E, \vec{\Omega}) + \int d\vec{\Omega}' \int dE' \Sigma_s^x(\vec{r}, E' \rightarrow E, \vec{\Omega}' \rightarrow \Omega) \cdot \Phi(\vec{r}, E, \vec{\Omega}) \cdot \Phi^*(\vec{r}, E', \vec{\Omega}') \right\} \tag{9}$$

where $P_x(E)$ is the sensitivity of the cross section being evaluated, $\Sigma_T^x(\vec{r}, E)$ is the total component of the reaction of interest, $\Sigma_s^x(\vec{r}, E' \rightarrow E, \vec{\Omega}' \rightarrow \Omega)$ is the scattering cross section being evaluated. If the forward and adjoint fluences are known throughout the problem, the sensitivity of the response parameter to the cross sections can be determined. For the investigation of the effects of impurities this is especially useful, since the impurities need not be modeled in the basic transport. The SUSD3D code was used to perform the calculation of cross section sensitivities and uncertainty contribution (via Eq 1) for the discrete ordinates calculations.

TABLE 3—*Cross section uncertainty contributions (in percent standard deviations) for the aluminum sphere using ANISN and MCNP.*

Depth of Foil Center (cm)	$^{58}Ni(n,p)^{58}Co$		$^{197}Au(n,\gamma)^{198}Au$	
	ANISN	MCNP	ANISN	MCNP
0 (exterior)	1.2	0.99	0.034	…
1.04	1.8	1.6	0.049	0.042
1.70	2.1	1.9	0.054	0.028
2.18	2.2	2.1	0.058	0.042
2.72	2.4	2.2	0.062	0.067
3.78	2.6	2.5	0.066	0.057
4.32	2.7	2.6	0.068	0.046
4.75	2.8	2.7	0.069	0.053
6.99	2.8	3.0	0.068	0.041
8.89 (center)	2.4	3.1	0.057	0.067

For Monte Carlo applications, the sensitivity is more difficult to obtain. The adjoint and forward fluence are generally difficult to know over the geometry of interest. For this study, the MCNP perturbation operator method was used to get the amount of change that the response parameter would have if the cross sections were perturbed some amount, and dividing that by the change cross section perturbation. This method can be called in a manner that allows one to get the actual calculated first derivative, and this is converted to a sensitivity via Eq 2. The problem that occurs is that it can take many perturbation calculations to properly calculate the uncertainty (one recent calculation used over 150 perturbations to model the uncertainty to aluminum cross sections), and this is very time consuming. Computer codes were written to set up and use the perturbation results (SENSMCNP2) to properly fold the sensitivities with covariance matrices. It proved very useful to use the simpler discrete ordinates calculations to reduce the number of calculations to focus on those with greatest impact.

One issue faced with both methods is obtaining covariance matrices for the materials of interest. While the situation improves constantly, the major evaluated cross section sets still lack covariance data for many isotopes of interest.

Table 3 shows the results of calculating the transport cross section uncertainty contribution for both activation foils for ANISN and MCNP calculations. The aluminum covariance information was obtained from the COVFIL2 [10] data, and has low uncertainties that are reported, especially in the region that influences the cadmium-covered gold foil, the cross section uncertainties were about 0.3 %, and that is reflected in the ANISN values in Table 3—also reflected is the difficulty that can be encountered in the MCNP calculations if the uncertainty in response parameter is not low enough. The cadmium covers increase the statistical variation in the results, and the high variation in cadmium-covered gold uncertainty contributions may reflect that.

Combined Results from Major Contributors

The uncertainties addressed above for the three major contributor classes can be combined to obtain a total estimate of the uncertainty. For specific studies, these uncertainties would be combined in quadrature with the uncertainty estimates from the minor classes to obtain the final uncertainty estimate. The total uncertainties are plotted for the aluminum sphere in Fig. 4.

Conclusions

A procedure was defined to assist in determining the uncertainty in the response parameter of test object components in reactor experiments. This procedure can be employed with either Monte Carlo or discrete ordinates techniques, but it is recommended that a combined approach be used. The procedure was applied to calculate the uncertainty contribution of three major contributors (source, response function, and cross section uncertainty) to the response parameter in an example study problem of activation foils placed inside an aluminum sphere that was placed in a nuclear reactor.

The procedure described consisted of deciding on the modeling approach to be used, enumerating all the possible contributors, determining which uncertainty contributors should be studied in detail by the use

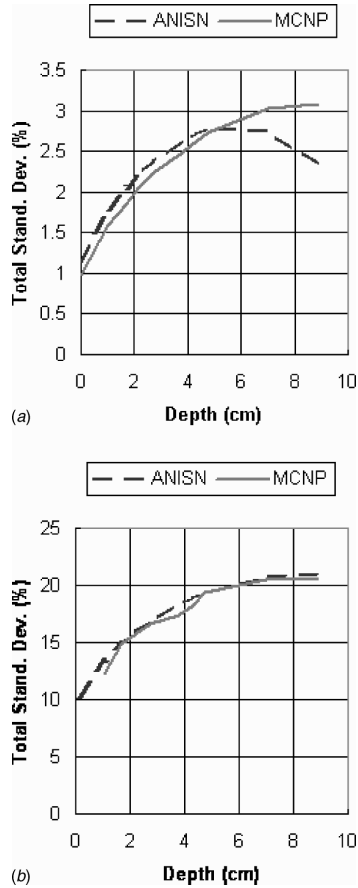

FIG. 4—*Estimated standard deviation for the (a)* $^{58}Ni(n,p)^{58}Co$ *and (b) Cd covered* $^{197}Au(n,\gamma)^{198}Au$ *response function in the aluminum sphere.*

of a simple (or coarse) model, making an estimate of minor contributor uncertainty contributions, using a refined model for detailed calculation, and combining the uncertainty contributions to arrive at an estimate of the response parameter uncertainty.

In the study problem, a particularly interesting result was obtained for cadmium-covered gold activation foils in the aluminum sphere. The details of elastic scattering in the aluminum combined with the specifics of the cadmium and gold absorption cross sections and the peculiarities of the source covariance matrix caused a rather high uncertainty to be calculated. However, this phenomenon only appeared with the use of cross sections that were adequately finely binned or with point cross sections. This result underscores the importance of ensuring that the energy grid structure is fine enough for the problem being analyzed.

References

[1] Kodeli, I., "SUSD3D: A Multi-Dimensional, Discrete-Ordinates Based Cross Section Sensitivity and Uncertainty Analysis Code System," CCC-695, Oak Ridge National Laboratory, 2000.

[2] Childs, R. L., "SEN1: A One-Dimensional Cross Section Sensitivity and Uncertainty Module for Criticality Safety Analysis," ORNL/TM-13738, Oak Ridge National Laboratory, July 1999.

[3] *MCNP: A General Monte Carlo N-Particle Transport Code*, LA-13709-M, Los Alamos National Laboratories, April 2000.
[4] *Geant4 User's Guide*, Centre Europen de Recherche Nuclaire (CERN), 2002.
[5] Alcouffe, R. E., Baker, R. S., Brinkley, F. W., May, D. R., O'Dell, R. D., and Walters, W. F., "DANTSYS A Diffusion Accelerated Neutral Particle Transport Code System," LA-12969-M, Los Alamos National Laboratory, June 1995.
[6] *DOORS3.2 Discrete Ordinates Transport Code System*, CCC-650, Oak Ridge National Laboratory, 2002.
[7] Rose, P. F., Ed., *ENDF/B-VI Summary Documentation*, Report BNL-NCS-17541 (ENDF-201), National Nuclear Data Center, Brookhaven National Laboratory, New York, 1991.
[8] Griffin, P. J., "Consistency Test of the Cross Section Data in Reference Neutron Fields," *International Reactor Dosimetry File-2002 (IRDF-2002)*, International Atomic Energy Agency, Vienna, 2006, pp. 51–66.
[9] Hoogenboom, J. E., "Methodology of Continuous-Energy Adjoint Monte Carlo for Neutron, Photon, and Coupled Neutron-Photon Transport," *Nucl. Sci. Eng.*, Vol. 143, Feb. 2005.
[10] Muir, D. W., "COVFILS-2, Neutron Data and Covariances for Sensitivity and Uncertainty Analysis," *Fusion Technol.*, Vol. 10, 1986.

Journal of ASTM International, Vol. 3, No. 10
Paper ID JAI100380
Available online at www.astm.org

S. Michael Luker,[1] *Patrick J. Griffin,*[1] *K. Russell DePriest,*[1] *Donald B. King,*[1] *Gerald E. Naranjo,*[2] *Ahti J. Suo-Anttila,*[3] *and Ned Keltner*[4]

Development of a Silicon Calorimeter for Dosimetry Applications in a Water-Moderated Reactor*

ABSTRACT: High fidelity active dosimetry in the mixed neutron/gamma field of a research reactor is a very complex issue. For passive dosimetry applications, the use of activation foils addresses the neutron environment while the use of low neutron response CaF_2:Mn thermoluminescent dosimeters (TLDs) addresses the gamma environment. While radiation-hardened diamond photoconducting detectors (PCD) have been developed that provide a very precise fast response (picosecond) dosimeter and can provide a time-dependent profile for the radiation environment, the mixed field response of the PCD is still uncertain and this interferes with the calibration of the PCD response. In order to address the research reactor experimenter's need for a dosimeter that reports silicon dose and dose rate at a test location during a pulsed reactor operation, a silicon calorimeter has been developed. This dosimeter can be used by itself to provide a dose in rad(Si) up to a point in a reactor pulsed operation, or, in conjunction with the diamond PCD, to provide a dose rate. This paper reports on the development, testing, and validation of this silicon calorimeter for applications in water-moderated research reactors.

KEYWORDS: thermal neutron, silicon calorimeter, PCD

Introduction

In this calorimeter design, a Type E 1-mil diameter thermocouple is sandwiched between two silicon disks. The thermocouple is used to measure the temperature rise in the silicon disks. The measurement is a change in silicon temperature that can be converted into a rad(Si) metric using the specific heat for silicon. The temperature-dependent specific heat of the (undoped) Ultrasil® silicon used in the calorimeter has been measured with an accuracy of $\sim 1\%$. The exact mass of the silicon disks is not important since this term cancels out when converting deposited energy to rad(Si). The silicon disks are supported on thin thermally isolating alumina (Al_2O_3) pegs so that the heat is not lost due to conduction. Thermal radiation loss is still a consideration and is addressed in the uncertainty quantification of the dosimeter response. The thermal inertia of the thermocouple is designed to be small so that it does not significantly affect/delay the temperature measurement. A 1-mil thermocouple is used in order to minimize the delay due to heat transfer to the thermocouple. The gamma heating of the thermocouple material itself is a potential interference, but, since the thermocouple has a very small mass, its temperature quickly equilibrates to the silicon wafer temperature. The calorimeter can be considered to be a primary dosimeter and its temperature rise does not require a calibration. The thermocouple used to measure the temperature is calibrated in a NIST-traceable manner and the calorimeter does require a detailed analysis and uncertainty quantification of all thermal loss mechanisms. The uncertainty in the calorimeter response is dominated by the knowledge of the specific heat for the actual silicon form used in the wafer and by the thermal diffusion issues.

Manuscript received June 20, 2006; accepted for publication June 30, 2006; published online October 2006. Presented at ASTM Symposium on Reactor Dosimetry, 12th International Symposium on 8–13 May 2005 in Gatlinburg, TN; D. W. Vehar, D. M. Gilliam, and J. M. Adams, Guest Editors.

[1] Senior Member of the Technical Staff, Distinguished Member of the Technical Staff, Principal Members of the Technical Staff, respectively, Sandia National Laboratories, Applied Nuclear Technologies, Sandia National Laboratories, P.O. Box 5800, MS1146, Albuquerque, NM 87185-1146.

[2] Distinguished Technologist, Advanced Nuclear Concepts, Sandia National Laboratories, P.O. Box 5800, MS1143, Albuquerque, NM 87185-1143.

[3] Research Engineer, Alion Science and Technology, Albuquerque, NM 87110.

[4] Research Engineer, Ktech Corporation, 1300 Eubank Blvd. S.E., Albuquerque, NM 87123-3336.

*This work was supported by the United States Department of Energy under contract DE-AC04-94AL85000. Sandia is a multi-program laboratory operated by Sandia Corporation, a Lockheed Martin Company, for the United States Department of Energy.

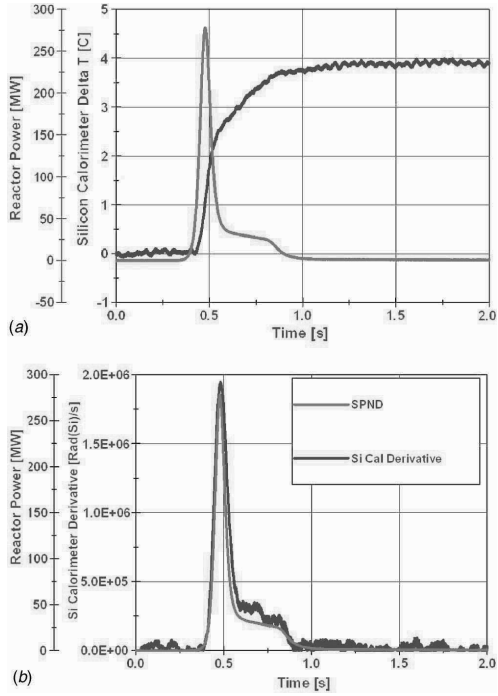

FIG. 1—*(a) Silicon calorimeter response with reactor power signal; (b) derivative of calorimeter with reactor power.*

Confidence in the fidelity of the early-time calorimeter response and the validation of the uncertainty analysis has been accomplished by fielding the calorimeter in the Hermes-III bremsstrahlung X-ray field during a pulsed operation with a full width at half-maximum (FWHM) pulse width of ~20 ns. When the calorimeter is used to determine the gamma dose in a mixed neutron/gamma radiation field, corrections need to be applied to account for heating due to neutrons in the mixed reactor environment. The neutron correction is ~10 % for a pulse in the free-field central cavity of the water-moderated Annular Core Research Reactor (ACRR) at Sandia National Laboratories (SNL). The temperature rise in the silicon of the calorimeter when fielded in this environment is about 0.111 K/MJ from gammas and 0.0126 K/MJ from neutrons.

This silicon calorimeter is designed to report the total dose at a time during or soon after a reactor pulse. Figure 1(*a*) shows an example of the time-dependent silicon calorimeter response and the ACRR power profile (as determined by a Cd-based self-powered neutron detector located next to the reactor fuel rods) for a 32-MJ reactor pulse with a FWHM of ~65 ms. The dosimeter response can be differentiated to produce a time-dependent silicon dose rate that can be directly compared to the reactor power, as shown in Fig. 1(*b*), but the signal noise makes the direct use of this dose rate of marginal value. The main application for this silicon calorimeter is as a very accurate silicon integral dose measurement just after the reactor pulse that can be used to normalize the time dependent transient profile from the PCD or other reactor power metric. If one waits too long after a pulse to do this normalization, thermal diffusion and loss terms within the calorimeter become important and the PCD is measuring a background signal. Experience and calculations show that the optimal point to use to normalize the PCD integral to the calorimeter in ACRR pulses is at the reactor pulse peak plus 3 FWHM.

Development to Current Design

The design goal for the new silicon calorimeter was to build a real time calorimeter suitable for use in gamma and neutron environments in the Sandia-National Laboratories (SNL) reactors. Numerous integral

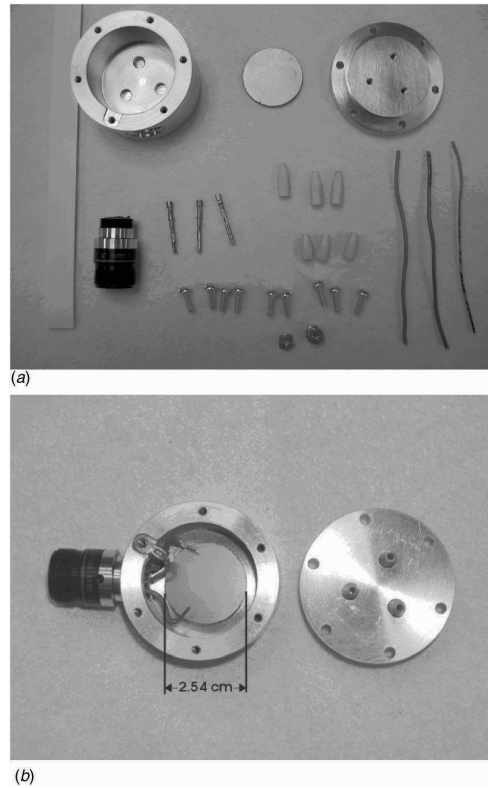

FIG. 2—*Calorimeter with shielded connector, (a) components, (b) partially assembled.*

calorimeters exist that will measure-total energy deposited at late times after a pulse. The competition between the presence of the late-time delayed gamma dose and the calorimeter thermal loss mechanisms do not make these dosimeters attractive for use on a reactor environment. Very few devices exist which will measure a properly calibrated neutron (or gamma) dose in real time [5,6]. Early SNL versions of the design used 5 mil (0.0127 cm) type K thermocouples that were insulated from the aluminum housing using a foam material. The cabling was standard type-K, parallel wire extension cable that was unshielded and used subminiature thermocouple connectors. The early calorimeters exhibited rapid cooling and had very high noise levels. Only small pulses were tried because the calorimeters were easily damaged. The next design utilized alumina (Al_2O_3) standoffs to replace the foam insulation that was so easily damage. The thermopile was now isolated by three alumina supports which were known to be very resistant to radiation damage, have a very high electrical resistance, and have a low thermal conductivity. The two silicon wafers in this next design were 2.54-cm diameter and were 1.016-mm in thickness. The thermocouple (TC) wire diameter was reduced to 0.0025 cm to shorten the thermal equilibration time between the TC wires and the silicon wafers. In Fig. 2(*b*) this large style of calorimeter is shown with the shielded connector which was added when the cabling was modified to an "all shielded" design using twisted-shielded pair cable. The type K extension cable was replaced by a type E thermocouple to reduce signal interference from the radiation response of the thermocouple itself. The latest change in the design was prompted by the need to make the calorimeter small so that it could integrate easily into experiments that were already crowded with circuit boards and cabling and did not allow room for the larger calorimeter housing or the large cables. The new small design, shown in Fig. 3, uses two 0.9525-cm diameter silicon wafers in a 1.905-cm diameter cylinder that is 2.301-cm in length. The small calorimeter design has performed better than the earlier large configuration and does not have any evidence of the photocurrent

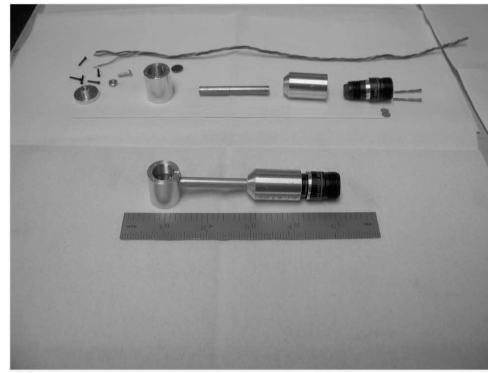

(*a*)

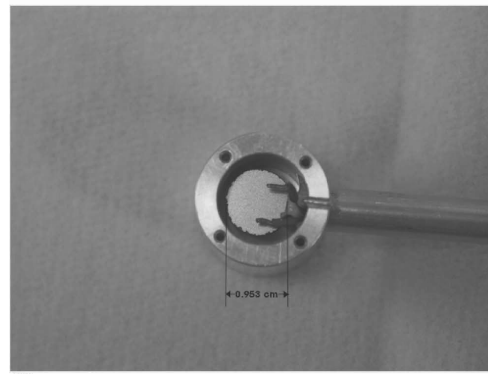

(*b*)

FIG. 3—*Silicon calorimeter: (a) components, (b) partially assembled calorimeter.*

anomaly that distorts the signal and interferes with a clean interpretation of the derivative of the calorimeter signal.

Prior to the latest small calorimeter design, all calorimeter signals were processed like a standard thermocouple measurement. Our design goal of a real-time calorimeter required that we reduce the noise level as much as possible to be able to resolve the derivative of the calorimeter signal. For a standard thermocouple, noise is normally not a problem since temperature usually is a slowly varying parameter and can be measured very accurately at slow sample rates. For our requirements, the original calorimeter signal needs to be as noise free as possible so that only minimal smoothing is necessary before interpreting the response. The derivative of the signal is routinely computed and compared to the reactor power in order to confirm the fidelity with which we have captured the real time dose. Any small changes in voltage in the original signal will result in a large noise voltage appearing in the signal derivative. To achieve the highest level of noise reduction it was necessary to remove all breaks in shielding, so we added transitions in the diameter of the thermocouple wire and focused on making our measurements based on the change in voltage from the room ambient temperature rather than the absolute temperature at the junction location [1,2].

MCNP Calculations of Thermal Source Term

Calculations were performed with the MCNP model of the SNL silicon calorimeter to determine total heating (neutron and γ) per mega-joule (MJ) in the ACRR central cavity. The following assumptions were made to perform the calculations:

TABLE 1—*Material heating in ACRR central cavity.*

Material Found in Calorimeter	Neutron Heating (J/g per MJ)	γ Heating (J/g per MJ)	Total Heating (J/g per MJ)
Ultrasil (silicon)	8.16635E−3	7.66441E−2	8.48104E−2
Alumina	1.45492E−2	7.29800E−2	8.75291E−2
Chromel	5.78699E−3	9.05320E−2	9.63190E−2
Constantan	4.45612E−3	9.05624E−2	9.51085E−2
Al6061	8.29765E−3	7.35654E−2	8.18631E−2

1. The incident radiations (neutron and γ) were assumed to impinge isotropically on the silicon calorimeter body. The neutron source used was the ACRR ACF9 neutron spectrum in 640 energy groups [3] obtained by a spectrum unfolding using activation foils. The γ source used was a calculated spectrum in 48 energy groups.
2. The radiation source (neutron and γ) was normalized to give one particle/cm^2 everywhere inside the source sphere. This procedure reflects a free-field spectrum normalization is valid only when there is no "test" object within the sphere that would perturb the spectrum assumptions.
3. The source strength used to normalize the energy deposited per reactor MJ originates from a calculation using the full reactor model.
4. The requirements for proper use of an F6 type tally for heating in MCNP/MCNPX are assumed to be met (e.g., charged particle equilibrium is assumed).
5. All the radiation heating numbers assume adiabatic heating of the materials.

Table 1 shows the results of calculations performed using the MCNPX code, version 2.5.c. This table gives the adiabatic heating in the silicon calorimeter properly normalized to the modeled reactor power. While the MCNP calculations shown in Table 1 used a general three-dimensional neutron/gamma radiation transport geometry, they did assume charged particle equilibrium (assumption 4 above). One-dimensional electron/photon calculations were also performed with the ADEPT code to examine the importance of the assumption of charged particle equilibrium from the photon spectra. For the gamma spectrum in the ACRR central cavity, this assumption has negligible effect on the bulk heating of silicon and, subsequently, on the thermocouple response, but, obviously, did affect the heating gradient within a material, e.g., dose enhancement at material boundaries. Thermal conduction was fast enough in the materials of interest and the calorimeter components small enough that the thermal gradient over relevant calorimeter components rapidly reached equilibrium. This is consistent with assumption 5 above regarding adiabatic heating. An exception to the fast thermal conduction was, obviously the alumina offsets that were selected specifically to provide thermal insulation. The conclusion of the ADEPT analysis was that for this calorimeter design in the ACRR gamma spectrum, as assumption of charged particle equilibrium did not affect the neutron/gamma heating estimates. This conclusion needs to be confirmed if the calorimeter is used in other, softer, gamma spectra or if the calorimeter housing were to be changed to permit softer photons to directly impact the silicon rather than be attenuated by the aluminum housing.

Thermal Analysis

A thermal analysis of the Sandia silicon calorimeter has been performed. These calculations were compared to measured data from ACRR operation 7801 (198 MJ pulse). The uncertainty in the temperature-dependent specific heat for silicon was found to drive the uncertainty quantification in early thermal analysis. As a consequence, the thermal properties of the exact silicon wafers used in the calorimeter design were experimentally determined. Thermophysical Properties Research Laboratory Inc. (TPRL) provided a laboratory measurement of the silicon specific heat, which they quote as accurate to 1 %. In this thermal model there are no free parameters to vary when comparing prediction with experimental measurement. Nevertheless there remain several sources of uncertainty that can affect the comparison between experiment and model prediction.

The result of the calculated-to-measured comparison indicates that for times less than two seconds after the peak of the ACRR pulse, good agreement (within 5 %) can be obtained when using measured silicon specific heat and MCNP generated heating profiles. Beyond two seconds the heat generation curve, which is based upon a radiation source term obtained from scaled self-powered neutron detector (SPND)

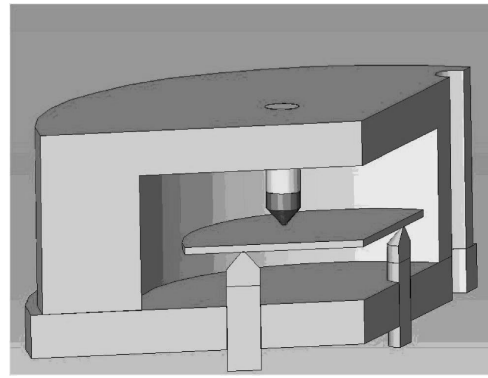

FIG. 4—*The SNL Si calorimeter showing 1/3 cut view.*

data for the reactor power, becomes too noisy to be reliable. The 5 % discrepancy between measured and predicted values can be due to several possible sources.

1. Use of the facility-supplied conversion factor to convert the SPND voltage to reactor power. This conversion was derived from pool heating experiments and is part of the operational definition of the reactor MJ. The MCNP modeling used fission energy release to independently calibrate the modeled reactor MJ.
2. Uncertainty in the material cross sections that affect the MCNP model prediction of heat production in Si, Al, Al_2O_3.
3. Uncertainty in the calibration curve used to convert the TC voltage and associated instrumentation to temperature.

The SNL silicon calorimeter consists of two silicon wafers pinched by two sets of three alumina cones inside an aluminum housing. A 1 mil (0.0254 mm) type E thermocouple (with a 2 mil (0.0508 mm) bead) is placed between the 1.016 mm wafers. The calorimeter is depicted in Fig. 4.

Rather than including all of the calorimeter parts in the numerical model, a symmetry plane through the middle of the silicon wafers was chosen and a circumferential symmetry of a single alumina support. This type of symmetry assumes that the support cones are aligned. From a thermal heat transport modeling perspective, the cone alignment has no effect upon the thermocouple bead response due to the large distance between the bead location (at wafer center) and the cone supports. The contact area of the cone support with the silicon wafer is unknown, but small, since the alumina supports are ground to a point.

The temperature dependent specific heat of silicon measured by TPRL, is shown in Table 2. These values were used in the model calculations. The heat generation in the respective materials is obtained by multiplying the numbers in the table by 8880 MJ/volt, the voltage trace from the reactor SPND, and the material density. The result is the volumetric heating rate [W/cm^3], which is required by the thermal analysis code. Although the material density is included in this conversion, it cancels itself out in the heat-up terms of the energy equation. However, density does play a role in the heat transfer between the

TABLE 2—*Specific heat of silicon wafer from TRPL.*

Temperature [C]	Specific Heat [J/kg K]
10	692.4
20	705.2
30	718.0
40	729.9
50	741.5
60	752.0
70	760.8
80	767.9
90	774.2

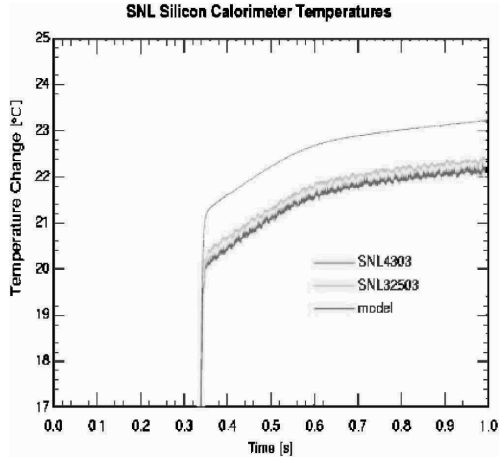

FIG. 5—*The predicted and measure temperature response.*

various components of the calorimeter which is a long-term effect (i.e., >2 s). Thus, the uncertainty introduced by using a material density in the conversion is negligible at short times.

Model Results

The thermal analysis model used calculated, published, and measured data only, that is, it used no adjustable parameters. The only adjustments that could be made were unmeasurable quantities such as the TC bead contact area and the alumina support cone contact area. Previous analysis indicated best agreement was obtained by assuming good contact between the TC bead and the silicon wafers. The calorimeter design and the attachment of the aluminum housing were, in fact, designed to provide the best possible contact. Therefore this tight contact geometry was selected, a priori, as the baseline for the model and was, in fact, not an adjustable parameter. Since there are no adjustable parameters, this calculation can be used to establish an error bound for the computational methodology and accuracy for the comparison of the measurement to the thermal modeling of the MCNP-calculated source term. The thermal model of the calorimeter was validated by comparing measurements from ACRR 7801 (198 MJ pulse) with model calculations produced with no adjustable parameters. Figure 5 shows the excellent agreement of the model results with the measured responses from two of the SNL silicon calorimeters.

The short 10 ms ACRR pulse started at 0 seconds. The *y*-axis in the figure is offset to highlight the agreement of the temperature changes, in magnitude and shape, near the end of the pulse. The model included source terms for the heating profiles for all materials as derived from the MCNP model calculations normalized to the calculated reactor MJ. Standard values were used for the thermal and physical properties of all materials, except for the silicon wafer specific heat where the temperature-dependent measured values from TPRL were used. Good thermal contact between the TC bead and the silicon wafers was assumed, so the TC measurement tracked with that for the silicon wafer. The figure shows that the model overpredicts the temperature by approximately 0.8–1.0°C for a total silicon heating of about 22°C. This corresponds to an approximate error of 4.5—5 % and can easily be attributed to the modeling of the source term. The time profile for the calorimeter heating is shown to have the same shape as that in the model, indicating that the model has captured the relevant thermal processes.

Measurement Circuit

The circuit used for connecting the calorimeter to the data acquisition system utilizes twisted-shielded pair cable from the thermocouple inside the calorimeter through to the digitizer. Referring to Fig. 6, a thermocouple connector that maintains the good electromagnetic shielding is used to connect the calorimeter to

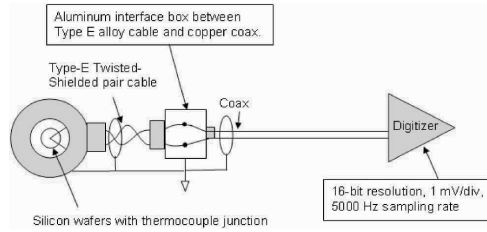

FIG. 6—*Calorimeter measurement circuit at thermal reactor (ACRR).*

the cable system. The cable system converts to a coaxial cable within an aluminum "insertion box" that is located within a short distance from the digitizer. In addition to functioning as a shield, the insertion box also functions as an isothermal zone for the two junctions that are formed between the Type-E alloy wire and copper wire. During the pulse, the isothermal zone maintains the two junctions at nominally the same temperature so the additional junction voltage offset before and after the pulse can be subtracted with minimal error. At ACRR the gamma dose is large enough so that an amplifier is not required so that a coaxial cable can route the signal directly from the insertion box to a Yokogawa 16-bit digitizer where the signal is digitized at 1 mV/div.

Dose-rate Normalization Procedure

The silicon calorimeter must be fielded with a PCD to be able to recover dose rate information from a pulse. This is necessary since a direct differentiation of the calorimeter signal magnifies noise in the calorimeter signal, particularly in the later part of the pulse and tail. The PCD is a two-port device that requires a positive bias of +750 VDC on one port. The photocurrent from the other port must be terminated into a resistance either in the form of a 50Ω terminator at the digitizer or at the input of a current amplifier with at least 1 MHz bandwidth. Coaxial cable is used to route the PCD signal from near the reactor to the data acquisition system normally 26 m away in a shielded data acquisition area. To process the PCD signal, the baselining procedure described in Eq. 1 is used. This procedure involves taking an average of a few data points in the pre-trigger area and subtracting the baseline offset value from the whole set of PCD data points in order to remove some of the leakage current in the PCD and other radiated noise signals. A more effective baseline of the PCD is obtained by integrating the signal and fitting the integrated signal to a linear offset value. Normally there will be a small positive slope in the integrated PCD signal leading up to the onset of the actual pulse. Performing a linear regression on a sample of these pre-trigger data will yield a slope which can be subtracted from the previously baselined data.

The calorimeter signal, which is already an integral metric, must similarly be processed by first baselining the calorimeter signal by averaging a few points in the pre-trigger region and then subtracting this average from the data for the detector as in Eq. 1. After baselining, the calorimeter data should be divided by the gain and then converted to temperature using a set of inverse polynomial coefficients available from the NIST website for Type-E thermocouples, as depicted in Eq. 2. The data should be smoothed due to unavoidable noise in the calorimeter measurement. A symmetric moving average has been effective but often it helps to perform a fast Fourier transform (FFT) on a sample of the data to ensure that the moving average spans at least a cycle of all of the major harmonic noise components. The data should now be converted to dose by using Eq. 3 with a silicon specific heat, C_p, applicable to the silicon sample used in the calorimeter [4].

$$V_{50\Omega\_baselined\_data(t)} = V_{50\Omega}(t) - \left[\frac{\sum_{1}^{n} V_{50\Omega}(t)}{n} \right] \tag{1}$$

$$\Delta t_{90}[K](t) = c_0 + c_1 V^1_{50\Omega\_baselined} + \cdots + c_9 V^9_{50\Omega\_baselined} \tag{2}$$

$$[\mathrm{rad(Si)}](t) = \Delta t_{90}[\mathrm{K}](t) \times \left[C_p \times \frac{\mathrm{J}}{\mathrm{kg \cdot K}} \right] \times \left[100.019 \times \left[\frac{\mathrm{kg \cdot rad}}{\mathrm{J}} \right] \right] \quad (3)$$

Summary and Conclusions

A silicon calorimeter has been developed for use at the water moderated research reactors. This calorimeter is suitable for performing active measurements of the silicon dose during a reactor pulsed operation. When used in conjunction with a PCD, the calorimeter can provide the normalization for a dose rate measurement during a pulse. Inspection of the derivative of the calorimeter signal and comparison with other active dosimeters confirms that it captures the transient behavior of the reactor pulse. A thermal model of the calorimeter has been constructed and, when used in conjunction with an MCNP calculation of the heating source term, can be used to validate the interpretation of the silicon calorimeter signal during and after the pulse. A comparison of the calculation, with no adjustable parameters, and measurements for a 198-MJ reactor pulse demonstrates that the calorimeter provides a good measurement (C/E of less than 5 %) of the cumulative dose during a pulse for times out to two seconds after the peak of the pulse. The rapid response and thermal isolation of the calorimeter has also been demonstrated at Hermes (bremsstrahlung) irradiations with pulse widths of 20 ns. This calorimeter is now available for routine use to experimenters at the ACRR reactor facility.

References

[1] Zielenkiewicz, W. and Margas, E., *Theory of Calorimetry*, Kluwer Academic Publishers, Dordrecht/Boston/London, pp. 87–88.

[2] Hemminger, W. and Hohne, G., *Calorimetry: Fundamentals and Practice*, Verlag Chemie, Weinheim, Deerfield Beach, FL.

[3] Griffin, P. J., Kelly, J. G., and Vehar, D. W., "Updated Neutron Spectrum Characterization of SNL Reactor Environments, Vol. 1: Characterization," Sandia National Laboratories, Albuquerque, NM, SAND93–2554, 1994.

[4] Luker, S. M. et al., "Application of a Silicon Calorimeter in Fast Burst Reactors," Sandia National Laboratories, Albuquerque, NM, submitted to ISRD12.

[5] Curl, I. J., Mason, J. A., Packwood, A., and Miller, P. C., "Adiabatic Microcalorimetry in Shielding Benchmark Experiments," *Proceedings, 6th International Conference on Radiation Shielding*, Tokyo, 1983.

[6] Mason, J. A., "Development of Sensitive Micro-calorimeters for Absorbed Dose Measurements in Benchmark Radiation Fields," *4th ASTM-EURATOM Symposium on Reactor Dosimetry*, Gaithersburg, MD, 22–26 March 1982.

Journal of ASTM International, Vol. 3, No. 10
Paper ID JAI100365
Available online at www.astm.org

S. M. Zaritsky,[1] *V. I. Vikhrov,*[1] *D. Yu. Erak,*[1] *V. N. Kochkin,*[1] *E. B. Brodkin,*[1] *and A. L. Egorov*[1]

Measurement and Calculation of WWER-440 Pressure Vessel Templates Activity for Support of Vessel Dosimetry

ABSTRACT: Activity of templates (specimens), which were cut out from the inner surface of Kola-1 and Kola-2 WWER-440 reactor pressure vessels (RPVs), were measured, and the results were used to support the RPV dosimetry. Twelve weld and two base metal templates of Kola-1 RPV were cut out after 25 fuel cycles. Thirteen weld and two base metal templates of Kola-2 RPV were cut out after 24 fuel cycles. Probes were taken from four corners of each template for dosimetry measurements. Activity of ^{54}Mn in each probe was measured and the average activity of template material was determined. Calculations were carried out in P_3S_8 approximation of discrete ordinates method using the DOORS 3.2 code package and BUGLE-96 nuclear data library. Calculated activities were compared with experimental ones. Neutron fluence (for neutrons with $E>0.5$ MeV) was calculated and calculation uncertainty evaluated based on the comparison of calculated and measured RPV templates activities and on some results of WWER-440 mock-up experiments carried out earlier on the reactor LR-0.

KEYWORDS: reactor pressure vessel, dosimetry, activity measurement, template, ^{54}Mn, neutron fluence, WWER-440

Introduction

The first and second units of the Kola nuclear power plant (NPP) with WWER-440 (series 230) reactors were set in operation in 1973 and 1974, respectively.

The standard core loading was used in the first ten fuel cycles of Kola-1; high-burn-up fuel assemblies were located in the core periphery in the 11th cycle and in 19th–25th cycles; besides 36 steel shielding assemblies were located in the core periphery instead of fuel assemblies after 11 fuel cycles. A reactor pressure vessel (RPV) weld No. 4 of Kola-1 (located opposite to the lower region of the core) was annealed after 15 fuel cycles in 1989.

The standard core loading was used in the first eight fuel cycles of Kola-2; high-burn-up fuel assemblies were located in the core periphery in the 9th–10th and in 16th–24th cycles; 36 steel shielding assemblies were located in the core periphery instead of fuel assemblies after ten fuel cycles. Kola-2 RPV weld No. 4 was also annealed after 14 fuel cycles in 1989.

It is urgently necessary now to justify the possibility of these NPPs for further safe operation. Thereupon, the RPV metal embrittlement must be carefully investigated and RPV dosimetry must be improved. The reactors WWER-440/230 have no cladding on RPV and templates (specimens) of RPV materials could be cut out for mechanical testing and dosimetry measurements.

^{54}Mn Activity Measurements

Twelve weld and two base metal templates of Kola-1 RPV were cut out by electro-erosion method after 25 fuel cycles in 2001; 13 weld and 2 base metal templates of Kola-2 RPV were cut out after 24 fuel cycles in 1999 (Figs. 1 and 2). The dimensions of each template were equal to ≈60 by 100 mm. Mini-Charpy specimens were made from template material for mechanical testing (dimensions of weld specimens are ≈5 by 5 by 28 mm, base metal specimens ≈4 by 5 by 28 mm)—see Fig. 3.

Manuscript received June 20, 2006; accepted for publication July 27, 2006; published online September 2006. Presented at ASTM Symposium on Reactor Dosimetry, 12th International Symposium on 8–13 May 2005 in Gatlinburg, TN; D. W. Vehar, D. M. Gilliam, and J. M. Adams, Guest Editors.

[1] Head of Department, Head of Laboratory, Head of Laboratory, Staff Scientist, Senior Staff Scientist, Senior Staff Scientist, respectively, Russian Research Center "Kurchatov Institute," 123182Moscow, Russia.

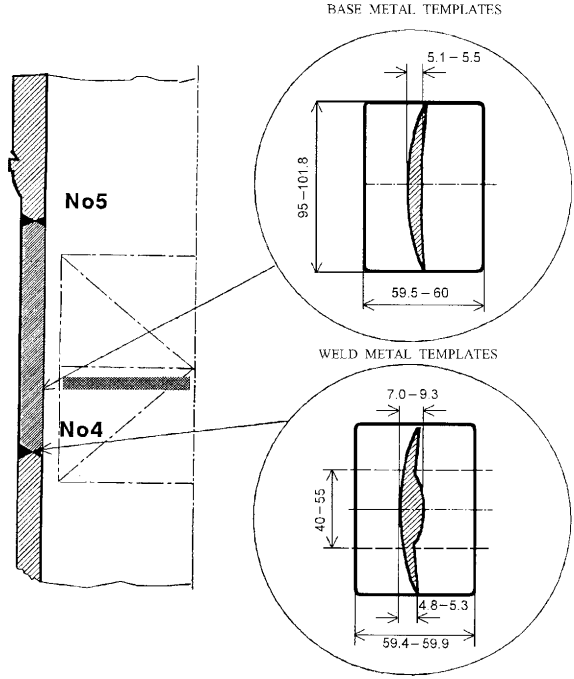

FIG. 1—*Templates cutting out scheme (dimensions in millimeters).*

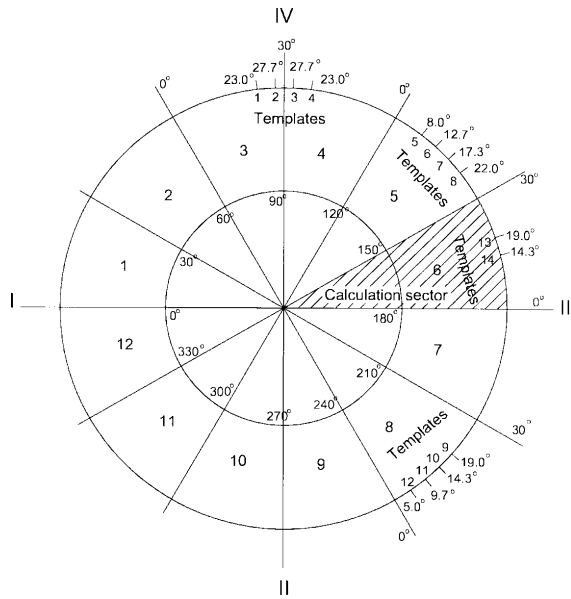

FIG. 2—*Azimuth coordinates of RPV Kola-1 templates. The azimuth coordinates of RPV Kola-2 templates were approximately the same size as coordinates of RPV Kola-1 templates.*

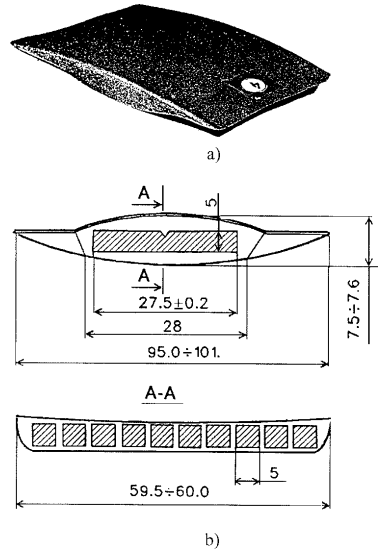

FIG. 3—*Weld No. 4 template (a) and scheme (b) of mini-Charpy specimens cut out (dimensions in millimeters).*

Probes for activity measurements (mass 10–12 mg) were taken from four corners of each template (Fig. 4). The activity of ^{54}Mn in each probe was measured and average activity of template material was determined.

^{54}Mn gamma activity (E_γ=842 keV) in probes material was measured using pure germanium crystal and gamma-spectrometer ORTEC.

Absolute specific activity of ^{54}Mn in probes was measured in the following order:

(1) measurement of relative ^{54}Mn activity: counting rate from each probe for all templates
(2) spectrometer calibration using standard source
(3) determination of absolute ^{54}Mn activity in each probe
(4) determination of specific ^{54}Mn activity per 1 g of steel in each probe
(5) recalculation of specific activity to the moment of template irradiation ending.

After that the average value of ^{54}Mn activity was determined for each template and this average value attributed to the geometrical center of inner template surface:

$$\bar{A} = \frac{1}{4}(A_a + A_b + A_c + A_d), \tag{1}$$

where a, b, c, d are the probes notations (Fig. 4).

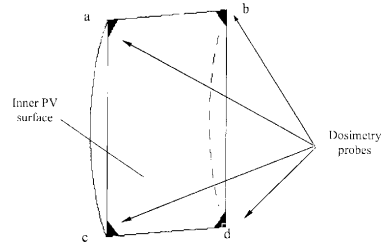

FIG. 4—*Cutting of dosimetry probes a, b, c, and d out of template.*

Russian standard calibration gamma-source ^{54}Mn (initial activity 93.5 kBq) was used for gamma-spectrometer calibration. According to certificate the uncertainty of this source activity is equal to ~1.7 % in the confidence interval 0.95.

Uncertainty of ^{54}Mn activity measurements were determined as:

$$\sigma_A = \sqrt{\sigma_s^2 + \sigma_\varepsilon^2 + \sigma_t^2 + \sigma_m^2 + \sigma_\lambda^2}, \quad (2)$$

where in confidence interval 0.95:

$\sigma_s \approx 1$ % – error of photo-peak area determination

$\sigma_\varepsilon \approx 4$ % – error of spectrometer efficiency determination (it includes the uncertainties of standard source activity and geometry correction considering differences between standard source and probe geometry)

$\sigma_t \approx 0.01$ % – error of time measurement

$\sigma_m \approx 0.1$ % – error of probe mass measurement

$\sigma_\lambda \approx 0.1$ % – uncertainty of decay constant.

Errors σ_t, σ_m, and σ_λ are much less than σ_s and σ_ε, so the uncertainty of measurement of relative ^{54}Mn activity distribution is approximately equal to ±1 % (0.95), and σ_A value is approximately equal to ±4 % (0.95). Uncertainty of averaged activity A also depends mainly on σ_ε and amount to approximately ±4 % (0.95).

^{54}Mn Activity Calculations and Comparison with Experimental Data

Calculations were carried out by the methodology, which is routinely used in Russia for RPV dosimetry. Three-dimension neutron field was synthesized from two-dimension ($R\theta$ and RZ) and one-dimension (R) components [1], which are calculated in P_3S_8 approximation of discrete ordinates method using DOORS 3.2 [2] code package and BUGLE-96 [3] nuclear data library.

The horizontal cross section of WWER-440/230 reactor is shown in Fig. 5. The analysis of all fuel cycles in consideration showed that in all cases fuel patterns of the core and power distribution inside it had symmetry closed to 30° symmetry. It allowed "to move" all templates into the single 30° sector of calculation model (shaded sector in Fig. 2), although really they were cut out from different sectors of RPV.

For solving such kind of problems it is very important to describe precisely the complicated reactor geometry and the neutron source (fuel burn-up and power) distribution in the core.

Detail $R\theta$-grid was used for describing the complicated reactor geometry, especially the polygonal border between core and out-of-core constructions. The grid is uniform for θ (total 150 intervals inside the 30° sector) and nonuniform for r (according to the regions geometry the grid step changes from 4 to 10 mm).

Pin-by-pin neutron source distribution was specified in the peripherical fuel assemblies, and assembly-by-assembly distribution was specified in the inner fuel assemblies. These distributions (fuel burn-up increment in all fuel cycles) were calculated with standard codes, which are used for fuel cycle designing during NPP operation. These codes are certified by GOSATOMNADZOR (Russian Regulatory Authority).

^{54}Mn activity in 1 g of RPV material at the irradiation ending is calculated as

$$A = RRN_{54}K_t \ [\text{Bq/1 g steel}], \quad (3)$$

where $N_{54} = N_{Av}X_{Fe}\varepsilon_{54}/A_{Fe}$, $N_{Av} = 6.0221 \times 10^{23}$ is the Avogadro number, $X_{Fe} = 0.954$ is the contents of iron in steel, $\varepsilon_{54} = 0.0585$ is the contents of ^{54}Fe in Iron, $A_{Fe} = 55.845$ is the iron atomic weight.

^{54}Fe(n,p)^{54}Mn reaction rate (per 1 nucleus of ^{54}Fe) is calculated as:

$$RR = \sum_{g=1}^{22} \varphi_g \sigma_g \ [1/\text{s}], \quad (4)$$

where

φ_g – group neutron fluxes at nominal reactor power

σ_g – group cross sections of ^{54}Fe(n,p)^{54}Mn reaction from IRDF-90.v2 library

g – energy group number (lower boundary of group 22 in the BUGLE96 format is equal to 0.498 MeV).

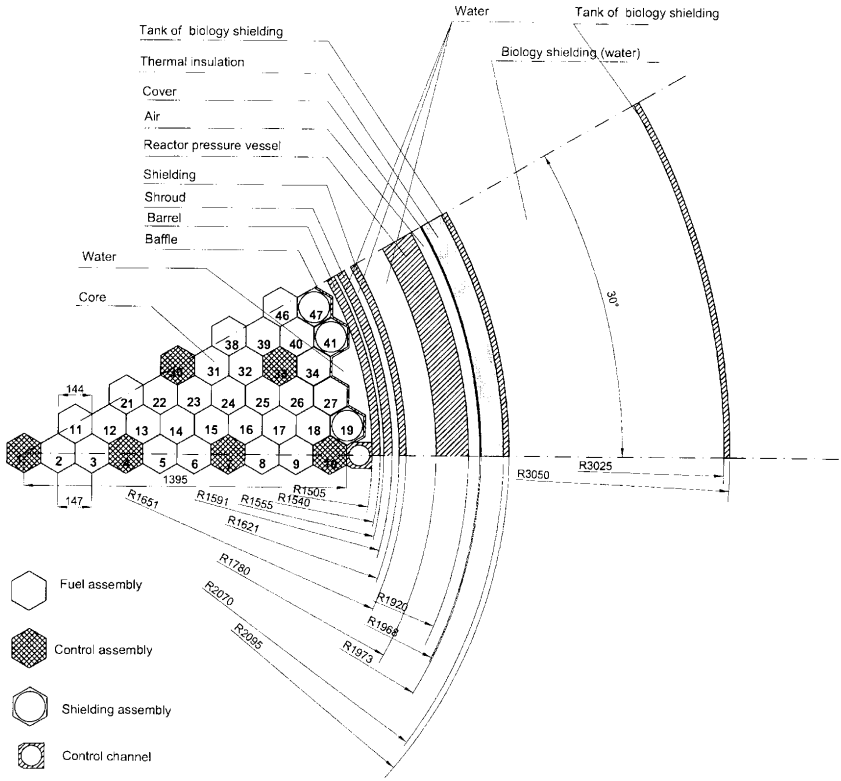

FIG. 5—*Horizontal cross section of WWER-440/230 reactor (dimensions in millimeters).*

Coefficient K_t in 3 takes into account the reactor power history:

$$K_t = \sum_j \frac{T_{eff,j}}{T_j}(1 - e^{-\lambda T_j})e^{-\lambda \tau_j}, \tag{5}$$

where

j – number of time interval

$T_{eff,j}$ – effective duration of time interval j

T_j – real duration of time interval j (T_j=1 day in our calculations)

τ_j – time between end of time interval j and irradiation ending

λ – decay constant of ^{54}Mn.

Azimuth distributions of ^{54}Mn activity were calculated for axial coordinates of the geometry centers of templates. Average experimental activities were attributed to these points.

Since the half-life of ^{54}Mn is equal to 312.12 days, only several last fuel cycles before template cut out give a contribution to measured activity.

The contribution of individual fuel cycle depends on cycle duration and power history. Data in Table 1 show that last 3–4 fuel cycles gave the main contribution.

Calculation and experimental data are compared in Fig. 6.

The average ratio of calculated to measured activities (C/E) for unit 1 weld No. 4 is equal to 1.036 (minimal and maximal ratios are 0.96 and 1.10). For unit 2 it is equal to 0.984 (minimal and maximal ratios are 0.91 and 1.06). The common value for welds of units 1 and 2 is 1.009 (minimal and maximal ratios are 0.91 and 1.10).

Thus, the local and average agreement of calculated and measured ^{54}Mn activities on the RPV welds of Kola-1 and Kola-2 can be considered as a good one: average discrepancies are inside experimental error

TABLE 1—*Accumulation of ^{54}Mn activity after RPV annealing.*

Kola-1		Kola-2	
Fuel cycle number	Relative A_{Mn} %	Fuelcycle number	Relative A_{Mn} %
25	70.4	24	21.6
24–25	91.5	23–24	78.2
23–25	93.5	22–24	93.4
22–25	97.5	21–24	98.0
21–25	98.9	20–24	98.5
20–25	99.3	19–24	99.4
19–25	99.5	15–24	100
16–25	100	…	…

limits (±4 % at 0.95 confidence interval), discrepancies in the individual templates are also inside experimental error limits in most cases, maximal discrepancies are ±10 %, there are no systematic trends in both units.

Neutron Fluence Calculations

Thus, we can conclude that uncertainty of calculated neutron fluence with $E > 3.0$ MeV is closed to the ^{54}Mn activity uncertainty (effective threshold of ^{54}Fe(n,p)^{54}Mn reaction is close to 3 MeV).

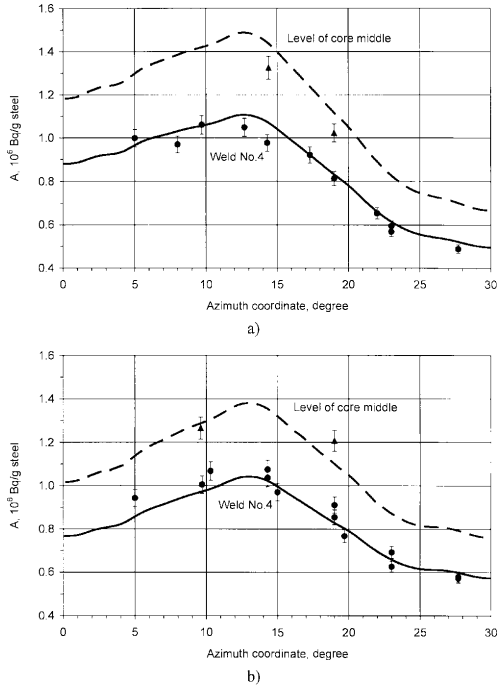

FIG. 6—*Calculated and measured distribution of ^{54}Mn activity on the weld No.4 and base metal of Kola RPV. (a) Kola-1. (b) Kola-2. - - - calculated ^{54}Mn activity in the RPV base metal on the level of core middle. —- calculated ^{54}Mn activity in the weld No. 4 material. Azimuth distributions of ^{54}Mn activity were calculated for axial coordinates of the geometry centers of templates. measured ^{54}Mn activity in the centers of templates from the RPV base metal on the level of core middle. measured ^{54}Mn activity in the centers of templates from the weld No. 4. Activity measurements error is equal to ±4 % (0.95 confidence level).*

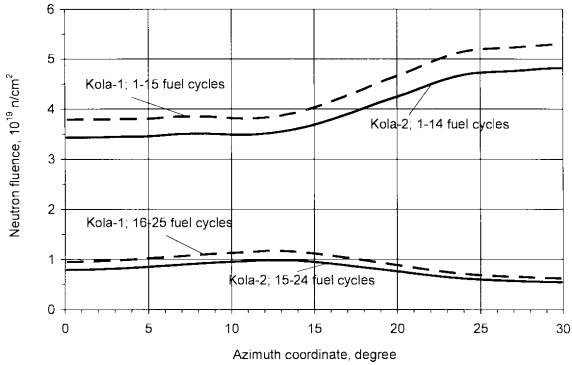

FIG. 7—*Calculated azimuth distributions of neutron fluence (E > 0.5 MeV) accumulated on the weld No. 4 before and after annealing.*

The distributions of calculated neutron fluence with $E > 0.5$ MeV $\Phi_{calc}(>0.5)$ on the inner surfaces of RPVs are shown in Fig. 7. The shape of the distributions is different before and after shielding assemblies' insertion.

The experimental data obtained on the WWER-440 mock-up in reactor LR-0 [4,5] can be used for evaluation of uncertainty of calculated neutron fluence with $E > 0.5$ MeV.

The neutron spectrum was measured on the inner surface of RPV in mock-up No. 2 (Fig. 8)—model of WWER-440 with shielding assemblies—and spectral index:

$$SI(0.5/3.0) = \int_{0.5}^{\infty} \varphi(E)dE \Big/ \int_{3.0}^{\infty} \varphi(E)dE \tag{6}$$

was determined. Comparison of measured and calculated *SI* (0.5/3.0) is shown in Table 2 (as well as other data, which will be discussed below), where data are given for RPV inner surface at azimuth coordinate $\theta = 30°$ of reactor model, i.e. behind shielding assemblies (see Figs. 5 and 8).

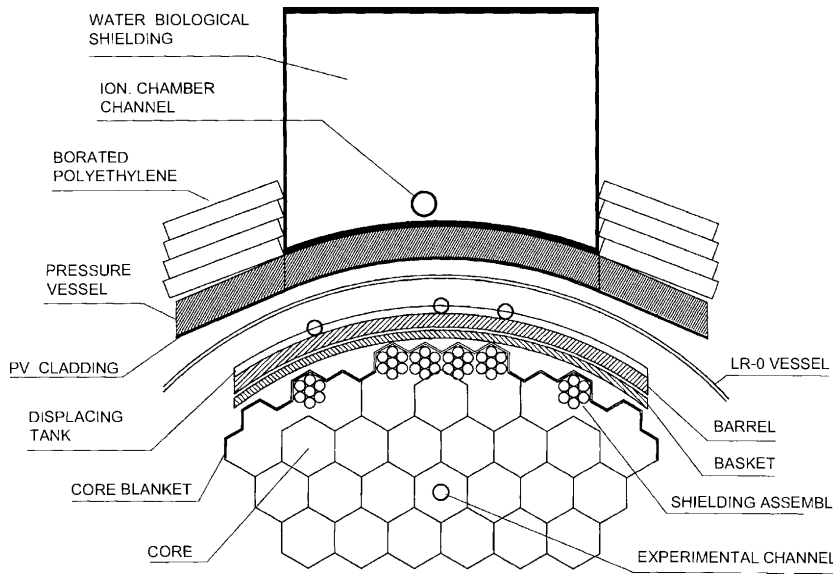

FIG. 8—*Mock-up No. 2 in the reactor LR-0.*

TABLE 2—*Comparison of integral parameters.*

		SI (0.5/3.0)		$\sigma_{eff}(>0.5)$, mbarn		$\sigma_{eff}(>3.0)$, mbarn	
	θ,°	Exp.	Calc.	Exp.	Calc.	Exp.	Calc.
Mock-up No. 2	30	6.52 ±8 %	6.36	64.3 ±8 %	66.8	420 ±8 %	425
Kola-1 fuel cycle 25	30	···	6.42	···	67.6	···	426

Calculated and measured *SI* (0.5/3.0) agree within experimental error ±8 %. Thus, taking into account agreement between calculated and measured ^{54}Mn activity in average within experimental error ±4 % it can be concluded that average uncertainty of calculated neutron fluence with $E>0.5$ MeV is closed to ±10 % on the inner surface of RPV weld No. 4.

The routine experimental-calculation procedure of fluence determination is based on the following formula using the measured ^{54}Mn activity:

$$\Phi_{exp}(>0.5) = A_{exp} T_{eff} / N_{54} \sigma^{54}_{eff}(>0.5) K_t, \tag{7}$$

where

A_{exp} – measured ^{54}Mn activity

T_{eff} – effective time of fluence accumulation, N_{54} and K_t – see 3 and 5

$$\sigma^{54}_{eff}(>0.5) = \int_0^\infty \sigma^{54}(E)\varphi(E)dE \Big/ \int_{0.5}^\infty \varphi(E)dE \tag{8}$$

is the effective cross section of ^{54}Fe(n,p)^{54}Mn reaction for threshold 0.5 MeV. The effective cross section for threshold 3.0 MeV is determined similarly.

If σ_{eff} is calculated in each point of RPV inner surface using the same neutron flux as for Φ_{calc} (>0.5) calculation, then

$$\Phi_{exp}(>0.5)/\Phi_{calc}(>0.5) = A_{exp}/A_{calc} \tag{9}$$

i.e., discrepancies between "experimental" and calculated fluence distributions are shown for this case in Fig. 6.

In practice sometime a constant value of $\sigma^{54}_{eff}(>0.5)$ (from preliminary calculations or experiments like mock-ups) is used in formula 7. Effective cross sections, which were determined using measured (mock-up No. 2) and calculated spectra, are shown in Table 2.

However, it is necessary to take into account that neutron spectrum changes significantly on the inner surface of RPV, especially in case shielding assemblies are located on the core periphery. Azimuth distributions of spectral index on the inner surface of unit 1 weld No. 4 are shown in Fig. 9 for fuel cycles 10 and 25, before and after insertion of shielding assemblies. One can see that neutron spectrum is significantly different on different templates, especially after shielding assemblies' insertion. The azimuth de-

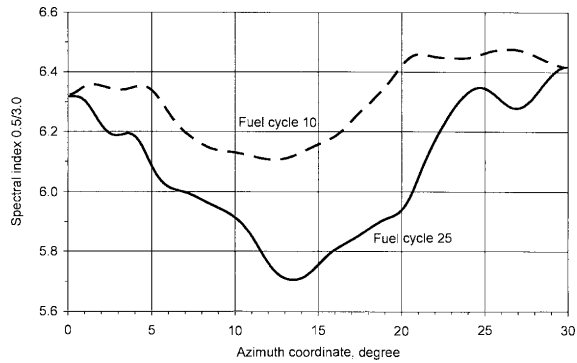

FIG. 9—*Azimuth dependence of spectral index on the inner surface of weld No. 4 (Kola-1).*

pendence of effective cross section $\sigma_{eff}(>0.5)$ on the inner surface of weld No. 4 is shown in Fig. 10. It is necessary to take these facts into account using templates activities for fluence evaluation. Different *SI* and σ_{eff} must be used for different templates. Table 2 and Fig. 10 show that the use of common $\sigma_{eff}(>0.5)$ for all templates leads to significant errors in determining $\Phi_{exp}(>0.5)$.

Summary

Measurements of ^{54}Mn activity in the templates cut out from RPV inner surface give the valuable information for RPV dosimetry validation.

Measured and calculated ^{54}Mn activities in the templates of Kola-1 and Kola-2 RPV weld No. 4 agree on average within experimental error limits ±4 % (0.95 confidence interval). Discrepancies for individual templates are in ±10 % interval and there are no trends in azimuth distribution of discrepancies.

Basing on these data and taking into account spectral indices measured and calculated on WWER-440 Mock-up in the reactor LR-0, it can be accepted that the uncertainty of calculated fluence of neutrons with $E>0.5$ MeV on the weld No. 4 is close on average to ±10 %.

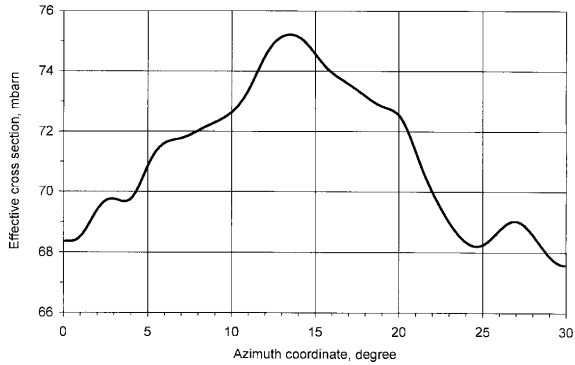

FIG. 10—*Azimuth dependence of reaction $^{54}Fe(n,p)^{54}Mn$ effective cross section for threshold $E=0.5$ MeV on the inner surface of weld No. 4 (Kola-1, 25th fuel cycle).*

Spectral index and effective cross section of ^{54}Fe(n,p)^{54}Mn reaction for threshold 0.5 MeV on the weld No. 4 depend significantly on the azimuth coordinate, and this dependence must be taken into account at the evaluation of neutron fluence based on ^{54}Mn activity measured in templates.

The serious problem of extrapolation of neutron fluence beyond several ^{54}Mn half-lives is out of the scope of this report.

Acknowledgments

Authors are heartily thankful to Dr. Tamara S. Zaritskaya for valuable support and help during report preparation.

References

[1] Brodkin, E. B., Kozhevnikov, A. N., and Khrustalev, A. N., "Determination of Characteristics of Neutron Field Affecting on the WWER Reactor Vessel," *6th International Conference on Radiation Shielding*, Tokyo, Japan, 1983, Conf-850538.

[2] DOORS 3.2: One-, Two- and Three-Dimensional Discrete Ordinates Neutron/Photon Transport Code System, *RSIC CODE PACKAGE CCC-650*, Oak Ridge National Laboratory, USA.

[3] White, J., et al., BUGLE-96: Coupled 47 Neutron, 20 Gamma-Ray Group Cross Section Library

Derived from ENDF/B-VI for LWR Shielding and Pressure Vessel Dosimetry Applications. *RSIC DATA LIBRARY DLC-185*, March 1996, Oak Ridge National Laboratory, USA.

[4] Ošmera, B. and Zaritsky, S. M., "WWER-440 Mock-up Experiments in the LR-0 Reactor. Mock-up No. 2 Description," NRI Řez UJV-11812-R, RRC KI 36/24-2002, *Fifth Framework Programme of European Community 1998-2002*, *Project REDOS*, Report REDOS/R(05)/ ISSUE 0, Dec. 2002.

[5] Ošmera, B., Zaritsky, S. M., and Holman, M., "WWER-440 Mock-up Experiments in the LR-0 Reactor. Experimental Data," NRI Řez UJV-11813-R, RRC KI 36/25-2002, *Fifth Framework Programme of European Community 1998-2002, Project REDOS*, Report REDOS/R(03)/ ISSUE 0, Dec. 2002.

Journal of ASTM International, Vol. 3, No. 3
Paper ID JAI13452
Available online at www.astm.org

Frank H. Ruddy,[1] *John G. Seidel,*[1] *and Abdul R. Dulloo*[1]

Fast Neutron Dosimetry and Spectrometry Using Silicon Carbide Semiconductor Detectors

ABSTRACT: Silicon carbide semiconductor neutron detectors have been irradiated with ^{252}Cf fission neutrons, thermal-neutron induced fission neutrons from ^{235}U, and 14-MeV neutrons from a deuterium-tritium neutron generator. In the latter case, reaction peaks corresponding to $^{12}C(n,\alpha)^{9}Be$ and $^{28}Si(n,\alpha)^{25}Mg$ reactions have been observed. Multiple reaction branches to the ^{25}Mg ground state and several excited states are observed for the $^{28}Si(n,\alpha)^{25}Mg$ reaction, and the detector energy calibration for these reactions can be derived from the peak positions. Although only the ground state branch is observed for the $^{12}C(n,\alpha)^{9}Be$ reaction, the shift of the reaction energy with angle relative to the 14-MeV source can be used to derive an energy scale based on this reaction. These energy response measurements will form the basis for neutron spectrum unfolding methods for inferring incident neutron energy spectra from the resulting recoil-ion energy spectra in silicon carbide detectors.

KEYWORDS: silicon carbide, semiconductor, neutrons, detector, spectrometry, dosimetry

Introduction

Silicon carbide (SiC) semiconductor radiation detectors [1] are being developed for a variety of neutron monitoring and dosimetry applications [2,3]. As a consequence of the wide SiC band gap, SiC detectors are able to operate at elevated temperatures greater than 300 °C [4]. Furthermore, SiC detectors have been shown to be highly resistant to radiation effects due to prolonged exposures to gamma rays, fast neutrons, and charged particles [5,6].

Initial fast-neutron response measurements were reported at the previous meeting in this series [4]. Neutron detectors based on a Schottky diode design were exposed to fast neutrons from ^{252}Cf, ^{241}Am-Be, cosmic-ray, and deuterium-tritium (D-T) sources. It was shown that the pulse-height spectrum response was dependent on the incident neutron energy spectrum and spectral features due to specific neutron reactions could be identified.

A limitation of that work was that the thickness of the active volume of the SiC neutron detector was only 10 μm, which represented the state-of-the-art at the time the detectors were manufactured. The neutron response of these detectors was consequently perturbed by finite-volume effects, because the ranges in SiC of some of the neutron-induced charged particle reaction products are not small compared to 10 μm. More recently, SiC devices with thicker epitaxial layers up to 100 μm have become available, enabling the production of SiC neutron detectors with thicker active layers, larger active volumes, and higher intrinsic efficiencies. These larger-volume detectors are much less susceptible to finite-volume effects.

Detector Design

Both SiC Schottky diodes and p-i-n diodes were used in the present measurements.

SiC p-i-n diodes with 4.4-mm × 4.4-mm dimensions were fabricated by chemical vapor-phase deposition epitaxy onto 350-μm 4H-SiC n-type substrate wafers with 20 milliohm-cm resistivity. A SiC n^- layer with a nitrogen dopant concentration of $(1.5-2.5)\times10^{14}$ cm^{-3} and 90-μm thickness was grown on

Manuscript received June 20, 2005; accepted for publication October 3, 2005; published online December 2005. Presented at ASTM Symposium on Reactor Dosimetry, 12th International Symposium on 8–13 May 2005 in Gatlinburg, TN; D. W. Vehar, D. M. Gilliam, and J. M. Adams, Guest Editors.
[1] Westinghouse Electric Company, 1332 Beulah Road, Pittsburgh, PA 15235-5081.

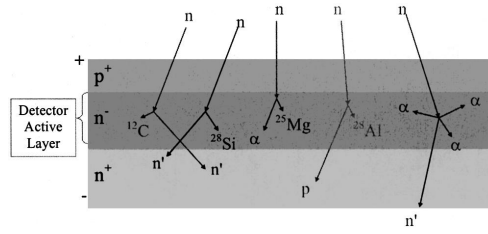

FIG. 1—*Fast neutron reactions in a SiC p-i-n diode.*

the Si face of the substrate. Next, a 2-μm SiC p^+ layer with an aluminum concentration of (5–8) $\times 10^{18}$ cm^{-3} was grown over the n^- layer followed by a 0.5-μm p^{++} layer containing an aluminum concentration of 5×10^{19} cm^{-3}. The p^{++} contact layer was covered with an 8-μm layer of gold and the back ohmic contact consisted of 4 μm of gold. Reverse biases in the 0–1000 V range are applied to create the depleted regions, which act as the active region in the diode for detection of the ionization produced by charged particles. Reverse biases up to −900 V were applied in most measurements to create depletion depths up to 90 μm while avoiding excessive diode leakage currents.

In the case of Schottky diodes, lightly doped n-type epitaxial layers, with a target nitrogen doping concentration of 1×10^{14} cm^{-3}, were grown onto 7.62-cm diameter ×300 μm n^+ 4H-SiC substrates. A 100-μm n^- epitaxial layer thickness was applied to the substrate. Multiple floating guard ring termination structures were used to suppress diode leakage current and to optimize the blocking characteristics. The n^- layer was covered with a contact consisting of titanium (800 Å), platinum (1000 Å), and gold (9000 Å) layers, which served as bonding pads. The doping of the epitaxial layer was verified after the completion of device fabrication by reverse bias capacitance versus voltage measurements. A doping concentration of 1.2×10^{14} cm^{-3} was measured. For this doping concentration, a reverse bias of 1085 V is required to fully deplete the epitaxial layer. 19.4-mm^2 Schottky diodes were used for the present measurements.

Neutron Detection

As is the case with all neutron detectors, SiC detectors rely on the production of neutron-induced charged particles. The ionization produced by these charged particles forms the basis for the detector signal. Thermal [2,7,8] and epithermal [9,10] neutron detection with SiC detectors has been accomplished by juxtaposing a layer of ^{6}LiF next to a detector diode. Tritons and alpha particles from the $^6Li(n,\alpha)^3H$ reaction produce the neutron-response signal in the detector. As noted previously [4], fast neutrons interact directly with the detector and its surroundings to form energetic reaction products that are capable of producing ionization in the detector. A schematic representation of some of the fast-neutron reactions that will occur in a SiC detector based on a p-i-n diode is shown in Fig. 1. At all neutron energies greater than a few hundred keV, the predominant reactions will be neutron elastic and inelastic scattering with silicon and carbon nuclei in the SiC detector. For the $^{28}Si(n,n')^{28}Si$ and $^{12}C(n,n')^{12}C$ scattering reactions, the scattered silicon and carbon reaction-product ions will lose some of their reaction energy through ionization in the detector. In the case of a p-i-n diode as shown in Fig. 1, the n^--layer will be depleted by an applied voltage. This depleted region becomes the detector active volume. When charge is produced in this layer, it will be collected under the influence of the applied voltage, comprising the detector signal. Because both the reaction angle and scattered neutron energy are not fixed, the scattering reactions will be observed as continua with the carbon ions having a higher energy distribution than the silicon ions as was observed in reference [4]. Potentially, these scattering continua can yield useful information on the energy characteristics of the neutron spectrum impinging on the detector by using spectral unfolding techniques similar to those used in proton and helium recoil spectrometers or in plastic scintillator detectors.

At higher neutron energies, threshold neutron reactions become possible as is shown in Table 1. With the exception of neutron-scattering reactions, most of the neutrons in a fission neutron-spectrum will lie at energies below the listed thresholds. However, irradiating the detector with mono-energetic neutrons with an energy greater than the reaction threshold will produce a reaction peak for those cases where the

TABLE 1—*Fast neutron-induced reactions in silicon carbide.*

Reaction	Q Value (MeV)	Energy Threshold (MeV)
$^{12}C(n,n')^{12}C$ ground state	0	0
$^{12}C(n,n')^{12}C2+$	−4.4389	4.8088
$^{12}C(n,\alpha)^{9}Be$	−5.7012	6.4196
$^{12}C(n,n')3\alpha$	−7.3666	8.4286
$^{12}C(n,p)^{12}B$	−12.5865	13.7401
$^{28}Si(n,n')^{28}Si$ ground state	0	0
$^{28}Si(n,n')^{28}Si2+$	−1.7790	1.8425
$^{28}Si(n,\alpha)^{25}Mg$	−2.6537	2.7653
$^{28}Si(n,p)^{28}Al$	−3.8599	4.0042

energies of the product ions are fixed by reaction kinematics. For example, the $^{12}C(n,\alpha)^{9}Be$ reaction peak was observed in 14-MeV neutron irradiations of a SiC detector [4].

Observations of SiC detector response to high-energy threshold reactions can be used to gather insight on the nature of the detector energy response, which can be used to aid in the unfolding of the SiC detector response to neutron energy spectra derived from fission neutron sources.

Results and Discussion

The SiC detectors were exposed to 14-MeV neutrons, ^{252}Cf fission neutrons, and neutron-induced ^{235}U fission neutrons.

Initial 14-MeV measurements were carried out by exposing a SiC p-i-n diode to a deuterium-tritium (D-T) neutron generator. The detector was placed at an angle 90° to the generator beam line and at a distance of 5.08 cm with the plane of the detector perpendicular to a line drawn to the source. The D-T neutron generator intensity was 10^7 $cm^{-2}-s^{-1}$ and at the 100 kV acceleration potential, the neutron energy impinging on the detector is 14.09±0.04 MeV. The quoted energy spread results from the range of angles subtended by the SiC detector surface relative to the D-T target.

A multi-channel pulse-height spectrum collected over 180 min is shown in Fig. 2. Shown for comparison is a spectrum reported for a 28 $mm^2 \times 10$-μm Schottky diode [4]. It can be seen that much more detail is present in the spectrum taken with the larger detector used in the present measurements. The various spectral features can be related to specific neutron-induced reactions with silicon and carbon atoms in SiC as shown in Fig. 3. Whereas only the $^{12}C(n,\alpha)^{9}Be$ reaction peak was present in the spectrum reported for the smaller diode, this peak plus multiple $^{28}Si(n,\alpha)^{25}Mg$ peaks can be seen for the larger diode. The multiple $^{28}Si(n,\alpha)^{25}Mg$ peaks correspond to reaction branches to the ground state and excited states in the ^{25}Mg product nucleus. The reaction energy for each branch can be calculated, and are tabulated for the ^{25}Mg ground state and first seven excited states in Table 2. Six ^{28}Si reaction peaks are clearly resolved in the p-i-n neutron-response spectrum as indicated in Fig. 4. The ground-state and first

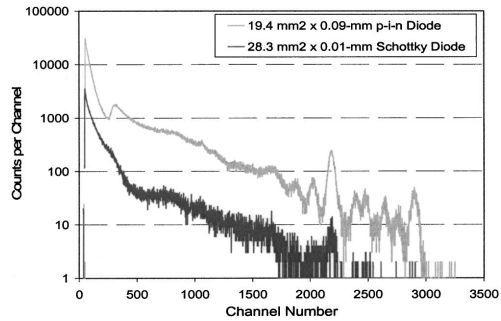

FIG. 2—*Comparison of the 14-MeV neutron pulse height response spectrum in a 19.4 $mm^2 \times 90$ μm SiC p-i-n diode with a 28.3 $mm^2 \times 10$ μm SiC Schottky diode.*

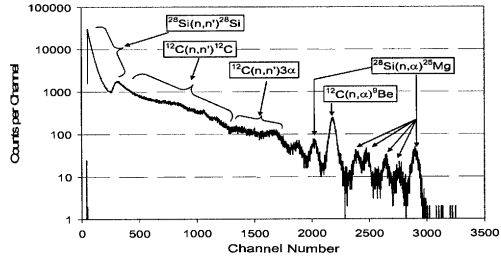

FIG. 3—*Pulse height response in a 19.4 mm^2 × 90 μm SiC p-i-n diode for 14-MeV neutrons.*

four excited state reactions form individual peaks. The branch to the fifth excited state is obscured by the $^{12}C(n,\alpha)^{9}Be$ reaction peak, and the sixth and seventh excited states form a single peak as their 8.77-keV energy difference cannot be resolved by the SiC detector. A plot of calculated energy for each of these reaction peaks as a function of channel number is shown in Fig. 5. It can be seen that the SiC pulse-height response is linear for the $^{28}Si(n,\alpha)^{25}Mg$ reactions. Note that the $^{12}C(n,\alpha)^{9}Be$ point does not fall on the straight line defined by the $^{28}Si(n,\alpha)^{25}Mg$ reaction data, because of differences in the detector pulse height defect for the two types of reactions as was discussed in detail elsewhere [11]. The pulse height defect, which is defined as the difference between the true energy of a heavy ion and its apparent energy which is observed as a result of ionization produced in the detector, will be different for the $^{12}C(n,\alpha)^{9}Be$ and $^{28}Si(n,\alpha)^{25}Mg$ reactions, because of differences in the details of the energy loss processes in SiC for the different heavy ion reaction products. The energy calibration derived from the linear

TABLE 2—*$^{28}Si(n,\alpha)^{25}Mg$ reaction ground state and excited state energy thresholds.*

Reaction Branch	Notation	Energy (keV)
Ground state	α_0	11346.30
First Excited State	α_1	10761.26
Second Excited State	α_2	10371.56
Third Excited State	α_3	9734.53
Fourth Excited State	α_4	9381.69
Fifth Excited State	α_5	8544.83
Sixth Excited State	α_6	7941.10
Seventh Excited State	α_7	7932.33

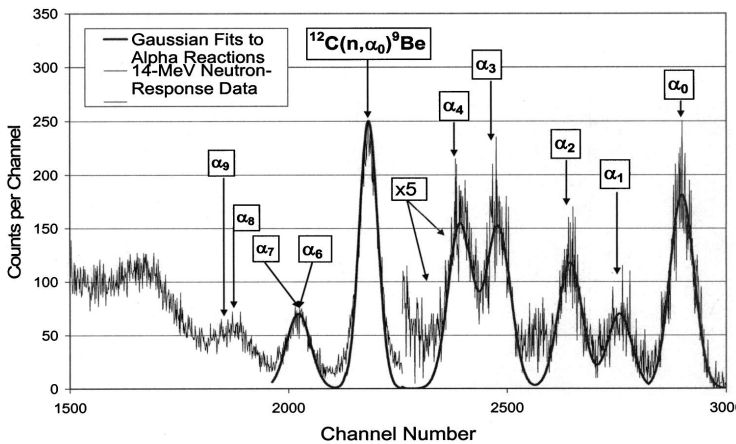

FIG. 4—*$^{28}Si(n,\alpha)^{25}Mg$ and $^{12}C(n,\alpha)^{9}Be$ reaction peaks from 14-MeV neutron interactions with a 19.4 mm^2 × 90 μm SiC p-i-n diode.*

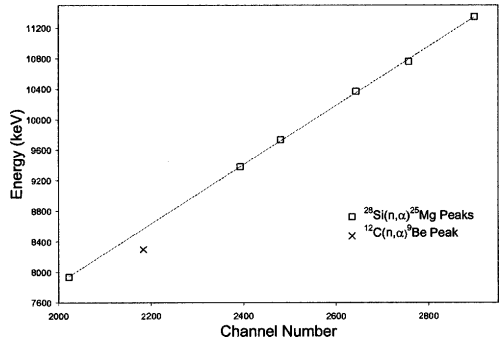

FIG. 5—*Pulse height energy calibration for $^{28}Si(n,\alpha)^{25}Mg$ reaction peaks in a 19.4 mm^2 × 90 μm SiC p-i-n diode.*

fit in Fig. 5 can be used to predict the positions of other $^{28}Si(n,\alpha)^{25}Mg$ reaction peaks as shown in Fig. 6. Note that clearly resolved peaks for none of the reaction branches corresponding to higher than the seventh excited state of ^{25}Mg can be identified due to a combination of closer energy spacing with increased excited state energy and interference from the $^{12}C(n,n')3\alpha$, $^{12}C(n,n')^{12}C$, and $^{28}Si(n,n')^{28}Si$ continua. Approximate positions for excited state branches of the $^{12}C(n,\alpha)^{9}Be$ reaction are also indicated, based on the preliminary assumption that the slope of the energy calibration derived from these reactions is the same as that of the $^{12}C(n,\alpha)^{9}Be$ reactions with a displacement defined by the position of the $^{12}C(n,\alpha)^{9}Be$ ground state branch peak. Note that excited state branches for the $^{12}C(n,\alpha)^{9}Be$ reaction cannot be separated from the continua, thereby preventing the derivation of a $^{12}C(n,\alpha)^{9}Be$ reaction energy scale from these data. Similarly, $^{12}C(n,p)$ reaction peaks lie in the energy range of data presented in Fig. 6, but these peaks also cannot be separated from the continua in order to enable an energy scale to be derived for these reactions. In the case of the $^{28}Si(n,p)^{28}Al$ reactions, peak energies lie in the 8–10 MeV range as discussed in Ref. [11]. However, the ranges in SiC of the protons produced in these reactions are larger than the dimensions of the SiC detector active volume, resulting in loss of reaction energy. Therefore, these peaks are not clearly defined in the spectrum. Calculated ranges in SiC based on the SRIM code [12] for protons and alpha particles for the ground state branches of the ^{12}C and $^{28}C(n,p)$ and (n,α) reactions are contained in Table 3.

An alternative method exists for determining the detector energy calibration for $^{12}C(n,\alpha)^{9}Be$ reactions. A Schottky diode was exposed to a D-T generator at a distance of 5.72 cm and at sequential angles (lab coordinates) of 45, 90, and 135° resulting in the data shown in Fig. 7. The $^{12}C(n,\alpha)^{9}Be$ reaction peak shift corresponds to the kinematic energy shift for the D-T neutrons, which results from the neutron generator acceleration potential as indicated in Fig. 8. At an acceleration potential of 100 kV and angles of

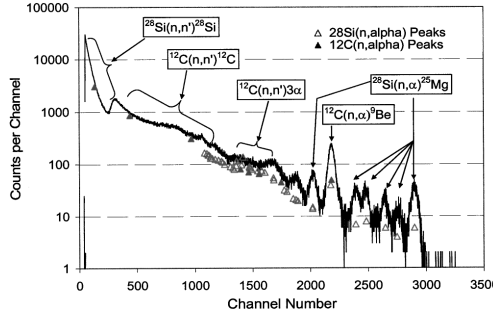

FIG. 6—*Projected locations for $^{28}Si(n,\alpha)^{25}Mg$ and $^{12}C(n,\alpha)^{9}Be$ reaction peaks from 14-MeV neutron interactions with a 19.4 mm^2 × 90 μm SiC p-i-n diode.*

TABLE 3—*Calculated proton and alpha particle ranges in SiC.*

Reaction	Mean α Energy (MeV)	Mean Range in SiC (μm)
$^{12}C(n,\alpha_0)^{9}Be$	5.745	19.5
$^{28}Si(n,\alpha_0)^{25}Mg$	9.781	44.6
Reaction	**Mean Proton Energy (MeV)**	**Mean Range in SiC (μm)**
$^{12}C(n,p_0)^{12}B$	1.305	16.2
$^{28}Si(n,p_0)^{28}Al$	9.790	467

45, 90, and 135°, the corresponding neutron energies are 14.57, 14.09, 13.62 MeV, respectively. A plot of the peak-centroid channel numbers (initially Gaussian shapes have been used) as a function of calculated $^{12}C(n,\alpha)^{9}Be$ reaction energies is shown in Fig. 9. As was the case for the $^{28}Si(n,\alpha)^{25}Mg$ energy calibration scale derived from multiple peaks in the same spectrum, the $^{12}C(n,\alpha)^{9}Be$ energy calibration scale derived from the angular energy shift is also linear.

The pulse height versus energy calibrations derived from the $^{28}Si(n,\alpha)^{25}Mg$ and $^{12}C(n,\alpha)^{9}Be$ high-energy neutron reaction data provide some initial insights on the nature of the SiC detector response to lower energy neutrons, such as those derived from scattered fission neutrons. Response spectra for ^{252}Cf fission neutrons and thermal neutron-induced ^{235}U fission neutrons are shown in Fig. 10. No reaction peak structure is present in either spectrum as expected, because most of the fission spectrum neutrons have energies lower than the reaction thresholds of (n,p) and (n,α) reactions, and the small fraction of neutrons above the threshold are not mono-energetic and therefore cannot form a reaction peak. The SiC detector

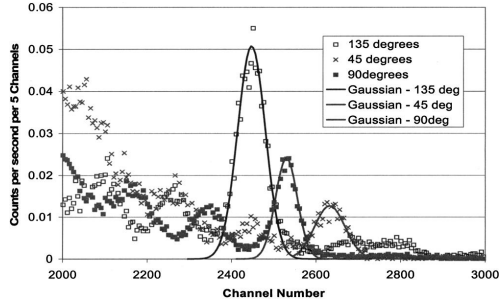

FIG. 7—*$^{12}C(n,\alpha)^{9}Be$ reaction peak locations as a function of angle relative to a 14-MeV D-T neutron source.*

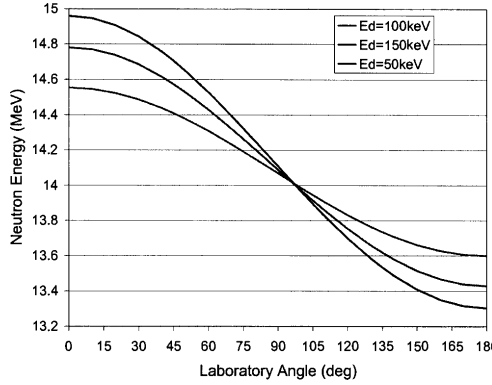

FIG. 8—*Neutron energy from a D-T generator as a function of angle and acceleration potential.*

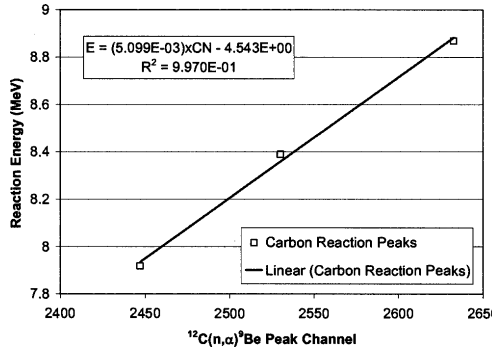

FIG. 9—*Calculated neutron energy vs. pulse height for $^{12}C(n,\alpha)^{9}Be$ reaction peaks measured at 45, 90, and 135°.*

response is predominantly from $^{12}C(n,n')^{12}C$, and $^{28}Si(n,n')^{28}Si$ reactions. Because of pulse-height defect effects, the neutron-response pulses in SiC will have different energy calibrations for the $^{12}C(n,n')^{12}C$ and $^{28}Si(n,n')^{28}Si$ reactions. Generally, the energetic carbon ions produced in carbon neutron scattering reactions lose less energy to nonionizing processes in the detector than the higher atomic number silicon ions.

Conclusions

Fast-neutron interactions with SiC neutron detectors provide the basis for neutron energy spectrometry measurements. However, in order to perform recoil-ion energy spectrometry with SiC neutron detectors, detailed information is needed on the energy response characteristics for the various reaction-product ions. In the case of neutron spectrometry in spectra derived from fission-neutron sources, ^{28}Si and ^{12}C neutron scattering reactions will account for most of the recoil-ion spectrum. As a result of pulse height defects caused by the nonelectronic component of the ion stopping process [11], different energy response scales must be derived for the ^{28}Si and ^{12}C scattered ions. The observation of reaction peaks resulting from mono-energetic 14-MeV neutrons provides useful data for interpreting the SiC detector response function.

In follow-up work, SiC detectors will be exposed to mono-energetic neutrons from deuterium-deuterium sources to calibrate the detector response to neutrons of 2.5 MeV and higher. Modeling of the SiC detector response will be carried out with the goal of accomplishing recoil-ion neutron energy spectrometry.

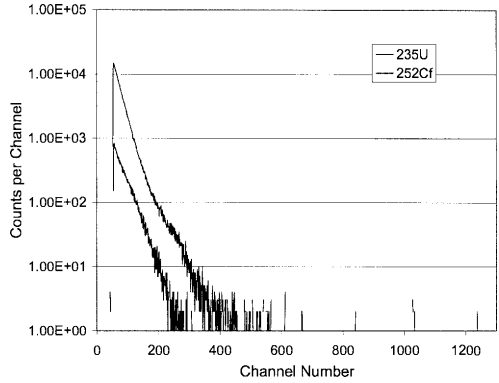

FIG. 10—*Fission-neutron response spectra in a 19.4 $mm^2 \times 90$ μm SiC p-i-n diode for ^{252}Cf and $^{235}U(n,f)$ induced by thermal neutrons.*

Acknowledgments

This work was supported by the Office of Science (BER), United States Department of Energy, Grant No. DE-FG02-04ER63734. We are grateful to Ms. Haoqian Chen for her assistance with data analysis. We are grateful to Drs. Sei-Hyung Ryu and Mrinal Das of Cree, Inc., for helpful discussions on SiC detector manufacture and characteristics.

References

[1] Ruddy, F. H., Dulloo, A. R., Seidel, J. G., Seshadri, S., and Rowland, L. B., "Development of a Silicon Carbide Radiation Detector," *IEEE Trans. Nucl. Sci.*, Vol. NS-45, 1998, pp. 536–541.

[2] Ruddy, F. H., Dulloo, A. R., Seidel, J. G., Hantz, F. W., and Grobmyer, L. R., "Nuclear Reactor Power Monitoring Using Silicon Carbide Semiconductor Radiation Detectors," *Nucl. Technol.*, Vol. 140, 2002, pp. 198–208.

[3] Natsume, T., Doi, H., Ruddy, F. H., Seidel, J. G., and Dulloo, A. R., "Spent Fuel Monitoring with Silicon Carbide Semiconductor Neutron/Gamma Detectors," (this conference).

[4] Ruddy, F. H., Dulloo, A. R., Petrovi, B., and Seidel, J. G., "Fast Neutron Spectrometry Using Silicon Carbide Detectors," in *Reactor Dosimetry in the 21st Century*, J. Wagemans, H. A. Abderrahim, P. D'hondt, and C. De Raedt, Eds., World Scientific, London, 2003, p. 347–355.

[5] Seshadri, S., Dulloo, A. R., Ruddy, F. H., Seidel, J. G., and Rowland, L. B., "Demonstration of a SiC Neutron Detector for High Radiation Environments," *IEEE Trans. Electron Devices*, Vol. 46, 1999, p. 567.

[6] Ruddy, F. H., Dulloo, A. R., and Seidel, J. G., "Study of the Radiation Resistance of Silicon Carbide Radiation Detectors," *Trans. Am. Nucl. Soc.*, Vol. 90, 2004, pp. 348–349.

[7] Dulloo, A. R., Ruddy, F. H., Seidel, J. G., Adams, J. M., Nico, J. S., and Gilliam, D. M., "The Neutron Response of Miniature Silicon Carbide Semiconductor Detectors," *Nucl. Instrum. Methods Phys. Res. A*, Vol. 422, 1999, pp. 47–48.

[8] Dulloo, A. R., Ruddy, F. H., Seidel, J. G., Adams, J. M., Nico, J. S., and Gilliam, D. M., "The Thermal Neutron Response of Miniature Silicon Carbide Semiconductor Detectors," *Nucl. Instrum. Methods Phys. Res. A*, Vol. 498, 2003, pp. 415–423.

[9] Dulloo, A. R., Ruddy, F. H., Seidel, J. G., Davison, C., Flinchbaugh, T., and Daubenspeck, T., "Simultaneous Measurement of Neutron and Gamma-Ray Radiation Levels from a TRIGA Reactor Core Using Silicon Carbide Semiconductor Detectors," *IEEE Trans. Nucl. Sci.*, Vol. 46, 1999, pp. 276–279.

[10] Dulloo, A. R., Ruddy, F. H., Seidel, J. G., Flinchbaugh, T., Davison, C., and Daubenspeck, T., "Neutron and Gamma Ray Dosimetry in Spent-Fuel Radiation Environments Using Silicon Carbide Semiconductor Radiation Detectors," in *Reactor Dosimetry: Radiation Metrology and Assessment*, *ASTM STP 1398*, J. G. Williams, D. W. Vehar, F. H. Ruddy, and D. M. Gilliam, Eds., ASTM International, West Conshohocken, PA, 2001, pp. 683–690.

[11] Ruddy, F. H., Dulloo, A. R., Seidel, J. G., Das, M. R., Ryu, S.-H., and Agarwal, A. K., "The Fast Neutron Response of Silicon Carbide Semiconductor Radiation Detectors," *IEEE Trans. Nucl. Sci.*, (to be published).

[12] Ziegler, J. F. and Biersack, J. P., "SRIM-2003.26: The Stopping and Range of Ions in Matter," SRIM.com, Annapolis, MD, 2003.

Journal of ASTM International, Vol. 4, No. 4
Paper ID JAI101142
Available online at www.astm.org

W. P. Voorbraak,[1] *T. Kekki,*[2] *T. Serén,*[2] *M. Van Bockxstaele,*[3] *J. Wagemans,*[4] *and J. R.W. Woittiez*[5]

Retrospective Dosimetry of Fast Neutrons Focused on the Reactions ^{93}Nb(n,n')^{93}Nb^{m} and ^{54}Fe(n,p)^{54}Mn

ABSTRACT: An overview is given of practices for "retrospective" dosimetry based on extraction and counting of niobium and manganese present in typical pressure vessel materials. The main problem of counting structural materials is the overwhelming presence of the nuclide ^{60}Co in the gamma-ray spectra of irradiated materials. Chemical separation of niobium and manganese is needed to determine the induced ^{93}Nb^{m} and ^{54}Mn activities. Procedures have been developed for retrospective dosimetry applicable at normally equipped radiochemical laboratories. Chemical separation procedures have been applied followed by determination of the amount of niobium in dissolution after separation. Special attention has been given to the accurate counting of the very weak X rays of ^{93}Nb^{m}. Different techniques have been applied. Advantages, disadvantages, and the accuracy that can be achieved are discussed. Special attention has been given to the maximum accuracy that can be reached and the minimum amount of niobium that has to be collected to reach this accuracy.

KEYWORDS: retrospective dosimetry, neutron fluence, neutron damage, niobium, manganese, column anion exchange, liquid scintillation counting, neutron activation analysis

Introduction

Retrospective dosimetry (RetroD) refers to the use of structural materials in reactors not originally intended for dosimetric purposes. The neutron fluence can be derived from the activity induced in small amounts of material that has been obtained by collecting a few milligrams of reactor material at the location of interest. Particularly material from the reactor pressure vessel, as one of the most critical reactor components, can be analyzed in this way. RetroD can be applied to both operating ("biopsy") and shut-down facilities ("autopsy"). This has been reported at earlier International Symposiums on Reactor Dosimetry, but none of the proceedings gives detailed information about the technique that has been applied or the accuracy that can be achieved. This article gives an overview of the various steps needed to get reliable results for RetroD with the reactions ^{93}Nb(n,n')^{93}Nb^{m} and ^{54}Fe(n,p)^{54}Mn. Due to the page limit of this paper, it is not possible to present the salient details of this work. Detailed information is presented in the institute reports [1–5].

From the viewpoint of material damage, the fast-neutron fluence is of main interest. Several elements with reactions sensitive to fast neutrons are present in structural materials, iron, and the reaction ^{54}Fe(n,p)^{54}Mn being the most obvious. However, this reaction is not ideal for long-term irradiations because of the fairly short half-life (312 days) [6] and limited response region above 2.5 MeV. If niobium is present in a structural material, the best reaction for RetroD is ^{93}Nb(n,n')^{93}Nb^{m} with a half-life of 16.13 years [6] and a threshold energy of 100 keV being comparable with the threshold energy in the damage cross section of iron. The ratio of reaction rates of ^{93}Nb(n,n')^{93}Nb^{m} and ^{54}Fe(n,p)^{54}Mn gives useful additional information about the neutron spectrum above 100 keV, being responsible for neutron damage. Therefore reaction rates for the reaction ^{54}Fe(n,p)^{54}Mn have been measured with some extra

Manuscript received June 20, 2005; accepted for publication March 28, 2007; published online May 2007. Presented at ASTM Symposium on Reactor Dosimetry, 12th International Symposium on 8–13 May 2005 in Gatlinburg, TN; D. W. Vehar, D. M. Gilliam, and J. M. Adams, Guest Editors.

[1] MMI-Monitoring, Netherlands Research and Consultancy Group NRG, P.O. Box 25, 1755ZG Petten, The Netherlands.
[2] VTT Technical Research Centre of Finland, P.O.B. 1608, FI-02044 VTT.
[3] SCK-CEN, Boeretang 200, 2400 Mol, Belgium.
[4] SCK-CEN, Reactor Physics & Myrrha Department, Boeretang 200, B2400 Mol, Belgium.
[5] Medical Applications, Netherlands Research and Consultancy Group NRG, P.O. Box 25, 1755ZG Petten, The Netherlands.

effort also. As a by-product the easy measurable ^{94}Nb activity induced by the reaction, ^{93}Nb(n,γ) will give information on the fluence of thermal neutrons.

The problem of counting structural materials is the overwhelming presence of the nuclide ^{60}Co in the gamma-ray spectra of irradiated steels. This effect is even worse if the cooling time of the scraped structural material is longer. Chemical separation of niobium and manganese is needed to determine the induced ^{93}Nb^{m} and ^{54}Mn activities.

Different procedures for the determination of the amount of niobium in dissolution as inductively coupled plasma-mass spectrometry (ICP-MS) and instrumental neutron activation analysis (INAA) have been applied.

The accurate counting of the very weak X rays of ^{93}Nb^{m} was also tackled. Various methods as the counting of a few drops of a niobium solution deposited on filter paper, counting of niobium in solution, and liquid scintillation counting (LSC) were tested and reviewed

This work is a joint project of NRG, Petten, The Netherlands, SCK·CEN, Mol, Belgium, and VTT, Espoo, Finland. The know-how on chemistry and reactor dosimetry in the institutes was combined. The aim was to develop a procedure for RetroD that can be widely applied in chemical laboratories of an average standard. The method should depend neither on the type of steel nor on the length of the cooling time of the steel. The only condition should be the presence of sufficient niobium in the materials pieces that serve as monitor. The three institutes have investigated the various techniques in parallel. The same starting materials have been used; final results obtained after the different processes in parallel have been compared and analyzed. The project was organized within the EU 5th framework program, sponsored by the European Commission under contract number FIKS-CT-2000-91.

The procedures have been tested on four different irradiated materials, three typical VVER 440 cladding steels, the Nb content of which varied from about 0.8 % to 35 ppm and one base material (15Kh2MFA) containing substantial less niobium, about 5 ppm. These materials were selected because of the variation in niobium content and cooling time. The chosen materials originate from surveillance irradiations in the Dukovany NPP Unit 4 in the Czech Republic and in the Loviisa NPP, units 1 and 2 in Finland. The base material 15kH2MFA originates from a material test irradiation in the HFR Petten in the Netherlands. Composition and cooling time of the used materials are given in [1]. This reference shows also a substantial difference in composition between cladding materials and the base material which is mainly iron. The yield of niobium in the departure materials scatters as well. This made a determination of the amount of niobium after isolation necessary.

The irradiation of the starting materials is described in detail in [5]. The original samples were cut in smaller pieces. The activity of the pieces was measured separately with HPGe gamma spectrometers in advance of the chemical processing to get information about deviations due to in homogeneity or local fluence rate gradients. If present, these effects may also influence the results of the applied RetroD. Processing of series of smaller pieces also gives information on the reproducibility of this type of dosimetry.

The Reaction ^{93}Nb$(n,n')^{93}$Nb^{m}

Guidelines for niobium processing and counting are given in ASTM Standard Test for Measuring Fast-Neutron Reaction Rates by Radio activation of Niobium (E 1297-96), however, only for pure niobium material. The advantage of using the reaction ^{93}Nb$(n,n')^{93}$Nb^{m} is the attractive long half-life of the reaction product, 16.13 years [6]. Therefore, the conversion from measured reaction rate to neutron fluence is less dependent on the reactor irradiation history. The reaction has some disadvantages also:

- The X-ray radiation ($K_{\alpha 2}$, $K_{\alpha 1}$, $K_{\beta 1}$, and $K_{\beta 2}$ with energies of, 16.521, 16.615, 18.623, and 18.952 keV, respectively [6]) of ^{93}Nb^{m} cannot be measured directly, due to the presence of cobalt in most of the steels that leads to a major contribution in the gamma-ray spectrum of the nuclide ^{60}Co. This is due to the relatively large cross section for thermal neutrons of the reaction ^{59}Co(n,γ) ^{60}Co. But also after separation of the niobium, its weak gamma rays require special counting techniques to limit the correction for self-absorption.
- Niobium is only present in East European reactor steels. The amount of niobium in these steels varies from a few ppm for base material up to 1 % for cladding material. These amounts are sometimes specified, but mostly not.

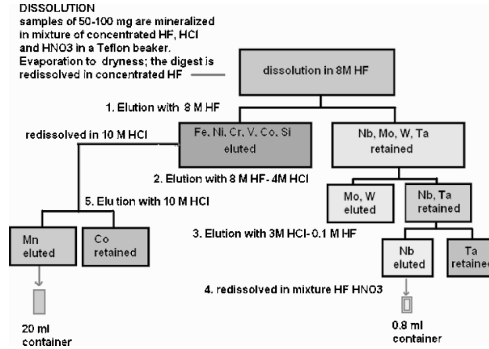

FIG. 1—*Separation scheme of niobium developed by VTT and NRG.*

- Homogeneous distribution of the niobium is not self-evident, especially if the material of interest is welded to another steel. For instance, the surface layer of the cladding of the VVERs contains over a thickness of 8 mm 2 different layers containing 0.861 (surface) and 0.008 % niobium [1]. Both layers, indicated as "red" and "blue," have been analyzed (Table 5).

Procedures for Separating Niobium and Manganese

Dissolution

The samples have been dissolved in a mixture of concentrated HCl, HNO_3, and HF according to the practice of the participating institutes. The temperature varied from a process of 16 h at room temperature up to 20 min, in a microwave at 200 °C.

Separation of Niobium and Manganese

Column chromatographic anion exchange has been applied as technique to eliminate the spectral interference of ^{60}Co. Two approaches have been used:

- Karnani [7] developed a procedure to separate niobium (right branch of the flow chart in Fig. 1). This procedure has been extended with an extra step for separation of manganese. The fractions from step 2, containing Fe, Ni, Cr, Mn, V, Co, and Si were collected and processed with a second column chromatographic anion exchange procedure for the separation of Mn and Co (left branch).
- SCK-CEN used a two-step approach. A rough separation in which most of the ^{60}Co and ^{54}Mn is removed, followed by a second step in which also nuclides with a short half-life were removed. Detailed results, reported in [4], show that the removal of ^{60}Co and ^{54}Mn is already very high after the first step. In general the second step is only necessary for reactor vessel samples that had a short cooling period less than 1 year. This approach is focused on the isolation of niobium only; manganese will not be isolated.

Determination of the Amount of Niobium After Isolation

The yield of the separation has been studied in the development of the separation process. Reference [2] reports that for niobium a yield of 96±8 % (n=13 samples) can be realized. The yield of the Mn-Co separation pointed out to 99.0±4.4 % (n=30 samples). As long as the actual determination of the amount of niobium will be done on the collected samples after separation, a 100 % yield of the separation of niobium is not required. Two procedures have been applied for the determination of the amount of niobium: ICP-MS and INAA.

TABLE 1—*Overall accuracy liquid scintillation counting.*

Contribution	1σ uncertainty
Counting statistics unknown samples	1 %
^{93m}Nb decay constant	0.1 %
Calibration LSC	2.5 %

ICP-MS

Measurement of the ^{93}Nb content was performed at SCK·CEN, using a VG Plasmaquad PQ3N. Here the sample introduction part of the instrument was fitted within a glove box, permitting the measurement of radioactive samples.

VTT Processes also measured the stable Nb concentration in the purified solutions with highly sensitive ICP-MS equipment. Here the samples were diluted 1/1000 first.

Results and details about the calibration are given in [4,5]. The overall estimated uncertainty of the ICP-MS results is 5 % (1σ) for samples with niobium content of the order of 1 %. This accuracy may increase up to to 10 % (1σ) if the amount of niobium is less than 50 μg/g.

Neutron Activation Analysis of Niobium

This method was applied at NRG. A central position inside the Low Flux Reactor was used via a pneumatic shuttle system, which ends in the counting laboratory. The thermal neutron fluence rate in this position is 3.24×10^{15} m^{-2} s^{-1} and the epithermal neutron fluence rate is 1.09×10^{14} m^{-2} s^{-1}. Samples were placed in a polyethylene (PE) shuttle, which was transferred to the irradiation position (and vice versa) within 3 s. Each sample was irradiated during 20 minutes. After a decay period of 2.5 min, so as to allow ^{19}F activity to vanish, samples were counted in a fixed position 50 mm from the low energy Ge detector. The counting time was 20 min. Use was made of the reaction ^{93}Nb$(n,\gamma)^{94}$Nb^{m}. The half-life of ^{94}Nb^{m} is 6.26 min [6], the principle gamma ray is 871.097 keV. Also measured were the combined 16.521+16.615 keV X rays. A correction has been applied for the extra radiation originating from ^{94}Nb^{m} and ^{93}Nb^{m} (16.5 keV) as well as ^{94}Nb (871 keV) being identical to the gamma-ray energies of ^{94}Nb^{m} [3]. INAA is done in the relative mode, i.e., all elemental contents are determined by comparing the count-rate of an element in a sample to that in a traceable standard. The Nb standard is a dilution of NIST SRM 3137, with a certified Nb content of 10.04±0.04 mg/ml.

In general, the uncertainty (1σ) varies from 1.5 % up to 5 % for the samples with 0.8 % niobium and up to 20 % for the samples with only 35 μg/g in a sample of 100 mg. Counting statistics attribute more than 50 % to this uncertainty. Increase of the number of registered counts, e.g., by repeating the irradiation and to increase the activity will reduce the uncertainty substantially. There are possibilities to do so.

^{93}Nb^{m} Activity Measurements

Liquid Scintillation Counting

The liquid scintillation counting (LSC) samples for ^{93}Nb^{m} activity measurements contained 1-ml samples from the 1/10 dilution of the purified base solutions and 10-ml HiSafe3 scintillation liquid together in 20-ml glass bottles. The calibration and fine-tuning of the equipment is described in [5]. The accuracy of the LSC-based ^{93}Nb^{m} activity measurements is estimated to 2.5 % (1σ), arising mainly from calibration uncertainties. Table 1 shows the items that have been taken into account. This results in an overall accuracy of the specific activity, including accuracy and precision of ICP-MS of 6.2 %.

Counting ^{93}Nb^{m} Solution in a Well Known Geometry

The dissolving of niobium in a 1:1 mixture of concentrated HF and HNO_3 is practiced at NRG since 1988 [8,9]. The relatively low density of the dissolved material reduces the correction for the absorption of the Nb X rays. Also the correction for the extra generation of characteristic Nb X rays due to photo fluores-

TABLE 2—*Overall accuracy counting activity $^{93}Nb^{m}$ solution.*

Contribution	1σ uncertainty
Activity of secondary standard	1.5 %
Counting statistics in secondary standard	0.2 %
Counting statistics unknown samples	0.2 % to 1.4 %
^{93m}Nb decay constant	0.1 %
Ratio in counting rate between distances 4 cm and 1 cm	0.5 %

cence of gamma rays emitted by other niobium nuclides (^{94}Nb, ^{95}Nb) and impurities like tantalum is reduced to a negligible contribution in comparison with corrections that have to be applied in case of counting of fractions of solid material like wire or foil.

Absolute activities have been obtained by comparing the number of counts in the region around the double photon peak of both K_α X rays for the sample of interest and a $^{93}Nb^{m}$ secondary standard distributed by CBNM (now IRMM) in Geel, Belgium in April 1984, with the same geometry. Table 2 presents the single items that have been taken into account to determine the overall accuracy of the activity. Details are given in [2].

This results in accuracy for the specific activities varying from 2.1 % to 5.4 % for the samples with about 0.8 % niobium and an accuracy of 20 % for the samples with only 35 ppm Nb. This includes the uncertainty in neutron activation analysis.

Counting of Niobium Deposit

The experimental procedure applied for the niobium target preparation and the $^{93}Nb^{m}$ activity measurements is based mainly on techniques formerly developed at SCK·CEN (see, e.g., [10,11] and references therein) and elsewhere (see, e.g., [12]). In this way, the efficiency calibration and the actual measurements can be performed in exactly the same detection geometry. Five ^{93m}Nb secondary standard samples are available at SCK·CEN. These are deposits containing a few drops from the same solution that was standardized at IRMM (see above) using liquid scintillation. The use of thin deposits for $^{93}Nb^{m}$ activity measurements has the advantage that X-ray self-absorption and interfering effects like X-ray fluorescence are reduced to negligible effects. The target preparation procedure is similar to the technique applied for the calibration samples. A detailed description and overview of the obtained results, including uncertainties for all materials is presented in [4]. Table 3 shows the different items that contribute to the uncertainty.

This results in an overall 1σ uncertainty on the specific activities of about 6 % for the "1 % samples." This includes the ^{93}Nb mass determination in solution with ICP, estimated as 5 % for the "1 % samples."

Counting of ^{54}Mn

Originally, the spectrometer used for the measurements of the ^{54}Mn solutions is calibrated for point sources using typical standards that cover a wide energy range. The use of the 20 ml PE container with manganese solution required an extra conversion. To reduce counting time, also a distance between sample and detector was introduced of 1 cm. The following single items have been taken into account to determine the overall accuracy. This results in an overall accuracy varying from 1.6 % to 2.3 % (Table 4).

Comparison of Results Between Partners

The project was organized in a way that comparisons could be made at many occasions. The selection of the materials was made in such a way that results of activation monitor sets, including niobium wires, calculations, or both, were available to check the results for the locations of the samples. Activities have

TABLE 3—*Uncertainty counting of niobium deposit.*

Contribution	1σ uncertainty
Efficiency calibration	2 %
Mass determination on deposit	1 %
^{93m}Nb decay constant	0.1 %
K_α peak area	3 %

TABLE 4—*Accuracy activity measurements ^{54}Mn.*

Contribution	1σ uncertainty
Activity of secondary standards	1.3 %
Counting statistics in secondary standard	0.4 %
Counting statistics unknown samples	0.4 % to 1.7 %
Ratio in counting rate between distances 10 cm and 1 cm	0.8 %
Nuclear data	0.2 %

been measured as much as possible in advance of the chemical separation and thereafter. Between the different steps of the chemical separation, gamma-ray spectrometry was performed to check whether elements were still present or not. Results are presented in [2–5]. Results obtained by the partners from the same material irradiated at nearly the same place are presented in [1]. An example is presented in Table 5 for the different LOVIISA materials.

For the LOVIISA old material two different compositions can be identified; the "red material" with about 0.75 % Nb and the "blue material" with only 35 ppm niobium. It appeared that the amount of niobium in the "blue material" is too low for proper counting using the drop deposition technique on filter paper.

No results are reported for the base material 15kH2MFA. The material was dissolved properly at SCK·CEN and NRG only. The ICP-MS technique performed at SCK·CEN showed a niobium concentration of 3 ppm [4]. This is a factor of 10 lower than the "blue LOVIISA material" and could not be measured either. VTT was not able to dissolve the material.

Conclusions and Recommendations

Conclusions

The project has demonstrated that RetroD is a useful tool to determine the number of fast neutrons for locations inside a NPP, for instance the RPV. The reaction $^{93}Nb(n,n')^{93}Nb^{m}$ will give information about the fluence of neutrons with an energy above 100 keV. Information about the neutron spectrum above 100 keV can be obtained in combination with results obtained with the reaction $^{54}Fe(n,p)^{54}Mn$. Procedures are available to remove the large amount of ^{60}Co which facilitates direct counting of $^{93}Nb^{m}$ and also ^{54}Mn.

In conclusion, it may be said that the success of RetroD applied for the reaction $^{93}Nb(n,n')^{93}Nb^{m}$ is directly related to the amount of niobium present in the material. Cladding materials of VVER type reactors contain sufficient niobium for a successful application of the technique for a laboratory of an average standard. The lower limit of the amount of niobium that can be handled depends on the presence of a reactor with easy access or ICP-MS equipment.

For cladding materials, typical for VVERs, containing 0.8 % Nb (8 mg Nb/g), accuracies better than 5 % can be achieved. At least 50 μg Nb/g in a sample of 100 mg is required to achieve an accuracy of 10 %. The niobium detection limit of the INAA procedure under optimal conditions is 2 μg.

RetroD on base material with only a few ppm Nb is near or even beyond the limit of application. A well-equipped radiochemical laboratory is needed, including a reactor for INAA and also a counting chain with high efficiency. But even if these conditions are all fulfilled, an uncertainty of at least 25 % should be accepted.

The results in the previous section show good agreement between the different partners, even better than may be expected from the reported uncertainties.

Recommendations

There is no preference for one of both separation procedures. The Belgian approach is rather simple and can be reduced to one step for older samples. An advantage of the Karnani approach is the extension with a separation of manganese. Dissolving of steel cladding will give no problems. Base material like 15kH2MFA, used in our project, requires extra equipment (microwave), but this is not a large investment.

TABLE 5—*Comparison of $^{93}Nb^{m}$ specific activities of Loviisa samples between partners SCK-CEN measures a niobium deposit, NRG measures niobium in solution; VTT used a liquid scintillator.*

Comparison of $^{93}Nb^{m}$ specific activities of Loviisa new samples			
Sample/partner	C/SCK·CEN	A/NRG	B/VTT
Spec. Activity, Bq/g	1.87×10^{7}	1.66×10^{7}	1.76×10^{7}
Number of samples	1	6	3
Uncertainty % (1σ)	6.2	3.9	6,2
Comarison of $^{93}Nb^{m}$ specific activities of Loviisa old samples, "red material," 0.75 % Nb			
Sample/partner	3/SCK·CEN	1/NRG	2/VTT
Spec. activity, Bq/g	3.42×10^{7}	3.25×10^{7}	3.28×10^{7}
Number of samples	1	6	3
Uncertainty % (1σ)	6.2	3.9	6,2
$^{93}Nb^{m}$ activities obtained from the Loviisa old samples, "blue material," 35 ppm Nb			
Sample/partner	3/SCK	1/NRG	2/VTT
Spec. activity, Bq/g	No result	3.39×10^{7}	3.42×10^{7}
Number of samples	0	3	1
Uncertainty % (1σ)	···	20	6,2

The determination of the amount of niobium in solution used for the actual counting of $^{93}Nb^{m}$ is the limiting factor for the application of RetroD. A reactor with easy access, resulting in the possibility of counting nuclides with short half-life or an ICP-MS system that facilitates the measurements with radioactive samples, is required. The minimum estimated uncertainty of the measurements with ICP-MS as applied for niobium will be 5 % (samples in the range 100 ppm to 1 %). The uncertainty for samples with less Nb will increase to 10 %. Straight on application of Instrumental Activation Analysis gives uncertainties of the same order of magnitude. But in principle, lower values can be realized. The accuracy is directly related to the number of counts that can be collected in a period of three half-lives of the nuclide $^{94}Nb^{m}$.

A review of the X-ray counting of $^{93}Nb^{m}$ shows preference for the counting of niobium as encapsulated solution or as drop deposition above liquid scintillation counting. A disadvantage of the drop deposition method is the small amount of niobium present in the deposit. If then the niobium solution itself contains little niobium, for instance, less than 100 ppm, enormous counting times are needed for one sample. The advantage of LSC is the high efficiency. On the other hand, LSC requires besides special equipment and also technicians skilled in this technique.

Application Boundaries

The results presented in this report are based on samples from specimens from surveillance capsules. Thus, sampling was an easy job. In practice taking samples from a reactor vessel will be more complex. Škoda, Pilzen has developed equipment for this aim [13].

This project has been focused in particular on the reaction $^{93}Nb(n,n')^{93}Nb^{m}$, which is of great interest for the determination of the fluence of neutrons that impinge on reactor vessels. Unfortunately, the reactor vessels built in the US and the European Union do not contain any niobium. Greenwood et al. [14] mention some other reactions as candidates, but cross-section information for these reactions is poor and the counting technique not standard. They also propose to use Inconel® as a structural material (e.g., applied in bolts).

Acknowledgments

We thank Jozef Hógel from Škoda, Pilzen, Czech Republic, who initiated the work on RetroD in the Reactor Dosimetry community, at the 10th International Symposium on Reactor Dosimetry in Osaka, Japan in September 1999. At that time, he distributed a batch of cladding material irradiated in the Dukovany NPP to a large group of partners. This report is an outcome of his initiative. We also thank the Joint Research Centre Petten for supplying VVER base material and the European Commission for their

financial support. This work is a joint exercise of NRG, Petten, The Netherlands, SCK·CEN, Mol, Belgium, and VTT Processes, Espoo, Finland, sponsored by the European commission, Contract No. FIKS-CT-2000-91.

References

[1] Voorbraak, W. P., Kekki, T., Serén, T., Van Bockxstaele, M., Wagemans, J., and Woittiez, J. R. W., "Retrospective Dosimetry of Fast Neutrons Focussed on the Reaction ^{93}Nb(n,n')^{93}Nb^{m}," NRG report 20576/03.53641/C, NRG Petten, May, 2003.

[2] Voorbraak, W. P., Aaldijk, J. K., and Woittiez, J. R. W., "Retrospective Dosimetry of Fast Neutrons Focussed on the Reactions ^{93}Nb(n,n')^{93}Nb^{m} and ^{54}Fe(n,p)^{54}Mn," Contribution of NRG, NRG Report 20576/03.53535/C, NRG, Petten May, 2003.

[3] Woittiez, J. R. W., Beemsterboer, B., and Zwaagstra, O., "RETROSPEC; Contribution of NAMS; Radioactive Vessel Steel: Separation of Nb and Mn from Co and Determination of the Nb," NRG Report K5160/03.53122/I, NRG, April, 2003.

[4] Wagemans, J., Van Bockxstaele, M., Gysemans, M., and Van der Meer, K., "Retrospective Dosimetry Based on the ^{93}Nb(n,n')^{93}Nb^{m} reaction," Techniques applied at SCK-CEN, SCK-CEN Scientific Report SCK·CEN-BLG-948, SCK·CEN, May, 2003.

[5] Serén, T., and Kekki, T., "Retrospective Dosimetry Based on Niobium Extraction and Counting," VTT's Contribution to the RETROSPEC Project, VTT Research Notes 2203, Espoo, 2003.

[6] Chu, S. Y. F., Ekström, L. P., and Firestone, R. B., WWW Table of Radioactive Isotopes, Version 2.1, LUNDS University website, http://ie.lbl.gov/toi/, January, 2004.

[7] Karnani, H., "Chemical Methods for the Use of Niobium Vessel Cladding as a Fast Neutron Dosimeter," Research Notes 605, VTT Technical Research Centre of Finland, 1986.

[8] Polle, A. N., and Nolthenius, H. J., "Activity Determination of a ^{93}Nb^{m} Solution," ECN Report ECN-84-131, ECN Petten, 1984.

[9] Appelman, K. H., "Counting of Niobium Foils (Reaction ^{93}Nb(n,n')^{93}Nb^{m})," ECN Report FYS/RASA-88/06, ECN, 1988.

[10] Tourwé, H., and Maene, N.., "Fast Neutron Fluence Measurements with the Nb-93(n,n')Nb-93m Reaction and the Application to Long-Term Irradiations," Proc. 3rd ASTM-Euratom Symposium on Reactor Dosimetry, Ispra, 1979.

[11] Tourwé, H., et al., "Niobium Dosimetry Intercomparison in EBRII and BR2," Proc. 4th ASTM-Euratom Symposium on Reactor Dosimetry, Gaiterburg, 1982.

[12] Hegedüs, F., "Fast Neutron Dosimetry by the Reaction ^{93}Nb(n,n'). Counting Technique for ^{93}Nb activity," Proc. 2nd ASTM-Euratom Symposium on Reactor Dosimetry, Palo Alto, 1977.

[13] Ruchař, M., and Hógel, J., "Sampling of Reactor Pressure Vessel Inner Cladding for Retrospective Dosimetry Analysis," presented at the 18th Intern. Conf. on Structural Mechanics in Reactor Technology (SMiRT 18), Beijing, China, August 7–12, 2005.

[14] Greenwood, L. R., and Oliver, B. M., "Retrospective Reactor Dosimetry for Neutron Fluence, Helium and Boron Measurements," *Proceedings of the 11th International Symposium on Reactor Dosimetry: Reactor dosimetry in 21st Century*, J. Wagemans, H. Ait Abderrahim, P. J. d'Hondt, and Ch. De Raedt, Eds., World Scientific, Singapore.

Journal of ASTM International, Vol. 3, No. 3
Paper ID JAI13430
Available online at www.astm.org

T. Natsume,[1] *H. Doi,*[2] *F. H. Ruddy,*[3] *J. G. Seidel,*[3] *and A. R. Dulloo*[3]

Spent Fuel Monitoring with Silicon Carbide Semiconductor Neutron/Gamma Detectors

ABSTRACT: Silicon carbide semiconductor radiation detectors have been demonstrated for neutron and gamma-ray monitoring of spent nuclear fuel. Neutrons and gamma rays were monitored simultaneously over a 2050-h period, resulting in a gamma dose of over 6000 Gy to the SiC detector. No changes in the neutron and gamma-ray sensitivity were observed as a result of the gamma-ray exposure. After the spent-fuel measurements, the absolute neutron sensitivity was determined in a standard neutron field, and the degree of gamma-ray and neutron spectrum overlap were determined through exposures in intense gamma ray fields. No overlap was observed for gamma-ray dose rates up to 100 G/h.

KEYWORDS: silicon carbide, detectors, semiconductor, spent fuel, neutrons, gamma rays, burnup

Introduction

Previously, neutron and gamma-ray response measurements in simulated spent fuel environments using silicon carbide (SiC) semiconductor detectors were reported [1]. In the present paper, measurements carried out in an actual PWR spent nuclear fuel pit using a SiC detector are presented and discussed. The purposes of the measurements were to confirm that the neutron and gamma-ray response pulses can be separated in an actual spent nuclear fuel environment, which has a large gamma-ray background, and to demonstrate the stability of the neutron and gamma-ray responses during long-term exposure to the spent-fuel radiation field. Neutron and gamma-ray dosimetry measurements on spent fuel assemblies are useful for characterization of parameters such as fuel burnup.

Background

During burnup of enriched ^{235}U nuclear fuel, higher actinides are produced through a build-up chain that originates with ^{238}U. Neutrons can be produced by these higher actinides either through spontaneous fission or through (α, n) reactions on the ^{17}O and ^{18}O isotopes in oxide fuel. It has been demonstrated by many workers that there is a relationship between the neutron specific activity of spent fuel and burnup [2–10]. During the first operating cycle in a reactor, neutrons will result initially from the decay of plutonium isotopes [3,6]. Eventually, the dominant isotopes will be ^{242}Cm (163-day half life) and ^{244}Cm (17.9-year half life). Chickering and Goldstein [7] derived a two-term empirical relationship where burnup is proportional to neutron emission rate to the 1.75 power and 4.098 power for the ^{242}Cm and ^{244}Cm contributions, respectively. Generally, the relationship will hold for all fuel assemblies of a particular design with different exponents for a particular design type. An additional proportionality factor based on initial enrichment is also required. The same functional form has been reported by several workers [2,4,10].

A relationship also exists between the measured gamma-ray output of a spent fuel assembly and burnup. If the gamma activity can be attributed to individual isotopes [11] or if the gross gamma activity can be attributed to a single isotope [10], as is the case when the time since discharge is greater than ten

Manuscript received June 20, 2005; accepted for publication September 29, 2005; published online December 2005. Presented at ASTM Symposium on Reactor Dosimetry, 12th International Symposium on 8–13 May 2005 in Gatlinburg, TN; D. W. Vehar, D. M. Gilliam, and J. M. Adams, Guest Editors.

[1] Mitsubishi Heavy Industries, LTD. Wadasaki-cho 1-1-1, Hyogo-ku, Hyogo-ken, 652-8585, Japan.
[2] Nuclear Development Corporation 622-12, Funaishikawa, Tokaimura Ibaraki, 319-1111, Japan.
[3] Westinghouse Electric Company, 1332 Beulah Road, Pittsburgh, PA 15235-5081.

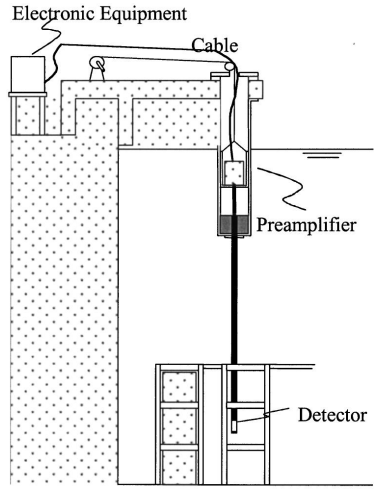

FIG. 1—*Measurement configuration.*

years and 30.1-year half-life ^{137}Cs is the dominant activity, burnup is directly proportional to observed gamma-ray activity.

Silicon Carbide Semiconductor Radiation Detectors

SiC radiation detectors have been shown to provide a linear response to gamma rays [12] as well as to thermal [13,14] and epithermal [12] neutrons. The thermal and epithermal neutron response is produced by placing a thin ^{6}LiF layer adjacent to the SiC detector surface. Neutron-induced tritons and alpha particles from the $^{6}\mathrm{Li}(\mathrm{n},\alpha)^{3}\mathrm{H}$ reaction produce the signal pulses in the detector. Because the 10-μm thickness of the active volume of the detectors used for the present measurements is small compared to the distances traveled by the electrons produced by gamma interactions, only a small fraction of incident gamma ray energies can be deposited in the detector. As a result, the gamma-ray response is a low pulse-height amplitude continuum that may be completely separated from the neutron response on the basis of pulse height. In addition, the gamma-ray detection efficiency is very low as a result of the small detector active volume, enabling the detection of relatively low neutron fluence rates in the presence of extremely high gamma-ray dose rates. Therefore, the gamma-ray and neutron responses can be tracked simultaneously in a spent fuel radiation environment, which is characterized by gamma-ray intensities of 10^{2}-10^{3} Gy/h and neutron intensities of 10^{2}-10^{4} $\mathrm{cm}^{-2}-\mathrm{s}^{-1}$.

It was demonstrated through previous measurements [1] that SiC detectors perform well in a simulated spent fuel environment produced at a TRIGA research reactor where the gamma-ray and epithermal neutron intensities were 350–450 Gy/h and 600 $\mathrm{cm}^{-2}-\mathrm{s}^{-1}$, respectively. It has been shown previously that both the SiC detector gamma-ray [12] and neutron [13,14] responses are linear and have a precision of ±6 %.

Furthermore, SiC detectors have high radiation resistance [15,16] and operate stably in elevated and changing temperatures [17], both of which make SiC detectors an attractive candidate for spent fuel monitoring measurements.

Measurements

The measurements were carried out at the spent fuel pool of the Nuclear Development Corporation (NDC). Fuel assemblies contained in this pool produce gamma-ray intensities up to about 10 Gy/h and have neutron fluence rates up to about 2×10^{2} $\mathrm{cm}^{-2}-\mathrm{s}^{-1}$ at selected measurement locations. The measurement geometry is shown in Fig. 1. The detector was contained within a tungsten case and placed in a water-

proof tube adjacent to a fuel assembly. The SiC detector has a 28 mm^2 active area and was placed adjacent to a 25-μm thick ^{6}LiF foil to enable thermal and epithermal neutron detection [1,12]. The detector assembly was movable in the axial direction. Periodic measurements in a constant position as well as axial distribution measurement were carried out over the period from October 2003 to February 2004.

Following the spent-fuel measurements, neutron and gamma-ray sensitivity measurements were carried out in established radiation fields in a graphite pile and in a Co-60 facility. Measurements to determine the degree of separation of the neutron and gamma-ray pulse-height responses were also performed.

Results and Discussion

The measured neutron and gamma-ray response spectrum from a spent fuel assembly producing a gamma dose of 1.9 Gy/h is shown in Figs. 2 and 3. The neutron response is clearly separated from the gamma-ray response, enabling simultaneous neutron and gamma-ray intensity measurements. The gamma counts were taken to be the sum of the spectrum counts up to channel 350, and the neutron counts were the sum from channels 351 to 4095.

Measurements of the gamma count rate as a function of axial location were carried out, resulting in the data shown in Fig. 4. For comparison, gamma-response measurements were also carried out using a fiber-optic detector [18] as shown in Fig. 5. Both devices show decreases in the gamma count rate at locations shielded by the rack support plates.

The gamma-ray response was found to have good linearity in a comparison with a fiber-optic gamma-ray detector as shown by the data of Fig. 6. The SiC gamma count rates are plotted as a function of each of two fiber-optic count rates at the corresponding locations. The SiC count rate is proportional to the fiber-optic count rate for both sets of fiber-optic data, and the fits to both sets of data are nearly identical.

Long-term SiC gamma-ray and neutron monitoring data are shown in Fig. 7. Both the gamma-ray and neutron response data are constant over periods where the detector position or electronics setting are unchanged. Expanded views of the neutron count rates during intervals where measurement geometry and electronics settings were unchanged are shown in Figs. 8–11. The error bars for the points correspond to the standard deviation predicted by Poisson statistics. The first counts during Interval 1, which were

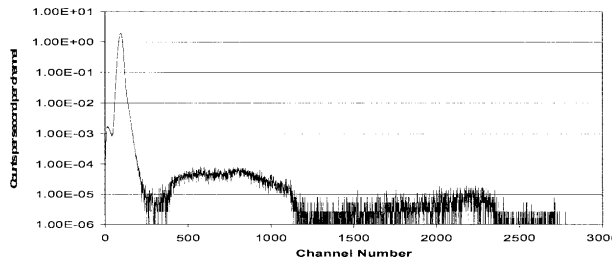

FIG. 2—*Neutron and gamma-ray response spectrum for a SiC detector adjacent to a spent fuel assembly (logarithmic display).*

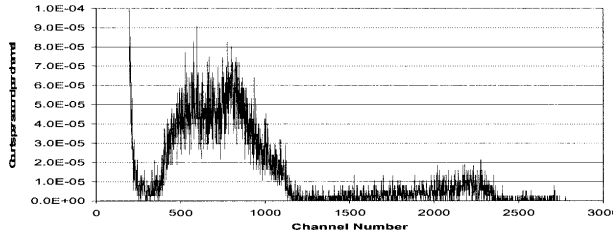

FIG. 3—*Neutron and gamma-ray response spectrum for a SiC detector adjacent to a spent fuel assembly (linear display).*

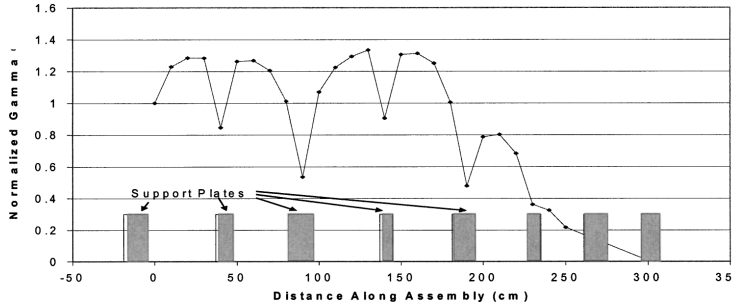

FIG. 4—*SiC gamma-ray response as a function of axial location along a spent fuel assembly. All response data are normalized to the value at 0 cm.*

affected by early detector instability, have been omitted in Fig. 8. The remaining count count rate data for Interval 1 are constant with a standard deviation of ±2.7 % compared to the ±3.1 % standard deviation predicted by Poisson statistics. The average count rate, calculated standard deviation, and Poisson standard deviation for each of the counting intervals are contained in Table 1.

Whereas the neutron counts during the first two intervals have standard deviations that are consistent with Poisson statistics, the second two intervals have standard deviations that exceed Poisson predictions. Omitting the final point in Interval 3 reduces the standard deviation to 2.7 %, indicating that the apparent

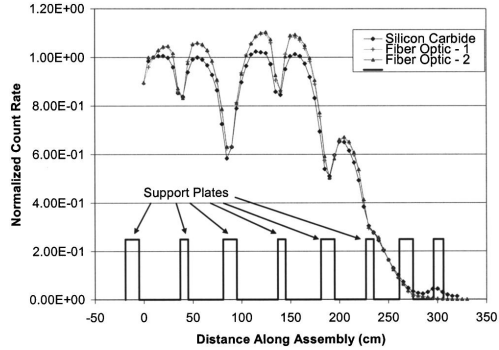

FIG. 5—*Comparison of the gamma ray responses for SiC and a fiber-optic detectors.*

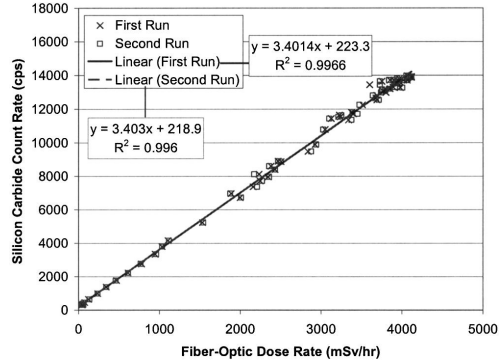

FIG. 6—*Comparison of the gamma ray responses for SiC and a fiber-optic detectors.*

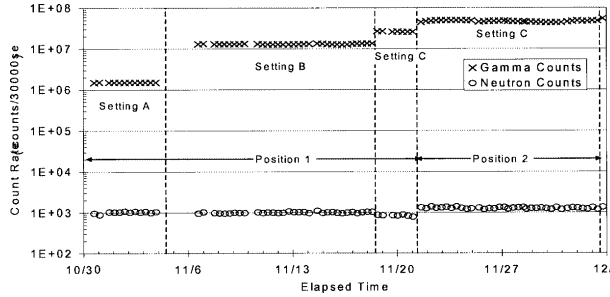

FIG. 7—*SiC gamma and neutron count rates as a function of time.*

departure from Poisson statistics may be due to the small number of data points. However, the data of Interval 4 indicate that a noise component may be present in the counting data.

Although the data of Fig. 7 indicate that the gamma response of SiC detectors are constant with time, a closer look at the data reveal counting instabilities. For example, an expanded view of the gamma counting data during Interval 2 is shown in Fig. 12. Although the Poisson standard deviation on the average of the gamma counts during the interval is ±0.03 %, the observed standard deviation is ±1.9 %. Also, the data of Fig. 12 indicate that the magnitudes of the gamma counts drift with time. Low-amplitude noise pulses were observed in the region of the spectrum corresponding to gamma counts, and a likely explanation for the variations in the gamma counts is the presence of electronic noise, which is varying with time. In order to obtain gamma counts with better than ±2 % uncertainties, improved noise discrimination is needed.

Following the measurements in the spent fuel pool, the SiC detector was taken to the Takasaki Laboratory at the Japan Atomic Energy Research Institute (JAERI) for neutron and gamma response

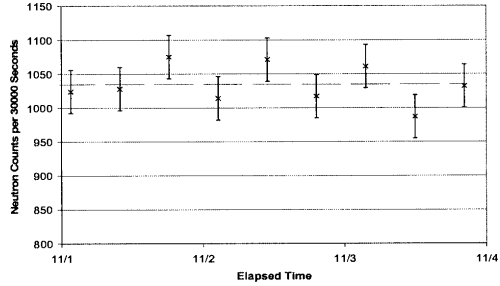

FIG. 8—*SiC neutron count rate during Interval 1 (Position 1, Setting A).*

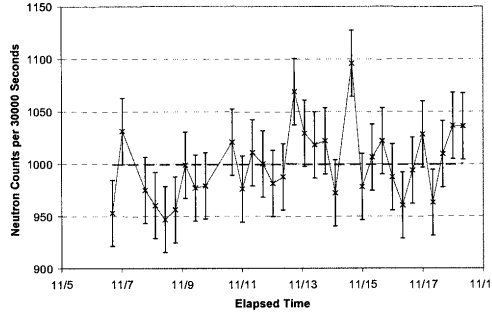

FIG. 9—*SiC neutron count rate during Interval 2 (Position 1, Setting B).*

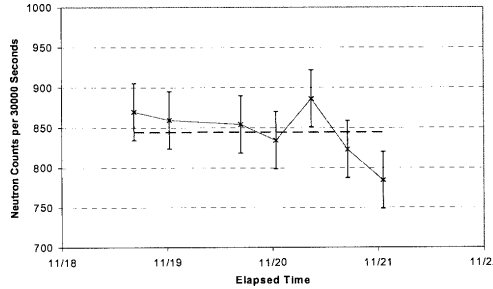

FIG. 10—*SiC neutron count rate during Interval 3 (Position 1, Setting C).*

measurements. Based on neutron measurements in an established radiation field in a graphite pile, the neutron sensitivity for the single 28-mm^2 SiC detector is 0.0015cps/nv. Higher sensitivities are obtained by using arrays containing multiple SiC detectors.

A series of gamma-response measurements were performed in intense ^{60}Co gamma-ray fields at Takasaki Laboratory and in ^{137}Cs fields in the Westinghouse Gamma Hot Cell. Generally, the high pulse-height portion of the gamma-ray continuum becomes more apparent as the strength of the gamma-ray field

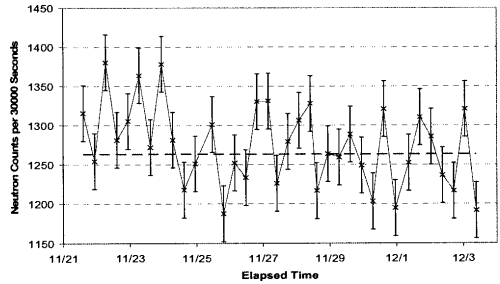

FIG. 11—*SiC neutron count rate during Interval 4 (Position 2, Setting C).*

TABLE 1—*Measured and predicted uncertainties for neutron count rates.*

Interval	Average Number of Counts	Standard Deviation, %	
		Measured	Poisson
1	1034.5	2.7	3.1
2	999.4	3.4	3.2
3	844.5	4.0	3.4
4	1263.4	4.1	2.8

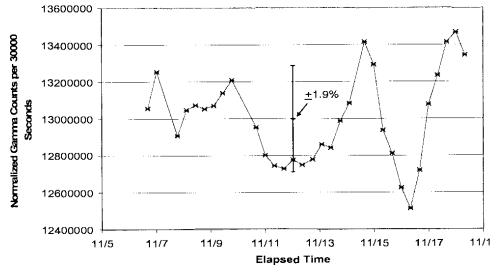

FIG. 12—*SiC gamma-ray count rate during Interval 2 (Position 1, Setting B).*

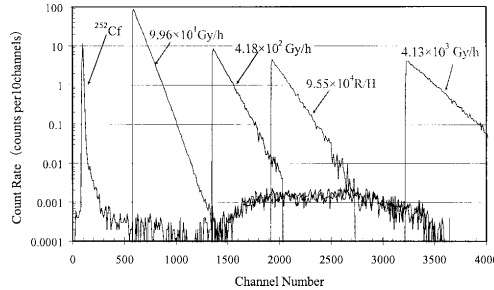

FIG. 13—*Comparison of SiC neutron response (thermalized 252Cf neutrons) with the responses to ^{60}Co fields of various intensities.*

is increased, leading to more overlap with the neutron response spectrum (see Fig. 13). In the Takasaki measurements, it was demonstrated that the SiC neutron response is completely separable from the gamma-ray response up to a gamma-ray dose of 100 Gy/h (see Fig. 3). Using improved pulse processing techniques in the Westinghouse Hot Cell measurements, the neutron and gamma signals were separable up to 400 Gy/h, and at a dose of approximately 2000 Gy/h the gamma-ray response overlapped 50 % of the SiC neutron response. For comparison, in a boron-lined proportional counter with a sensitivity of 4 cps/nv, approximately 50 % of the neutron response spectrum is obscured by the gamma-ray response at a dose of about 10 Gy/h.

Conclusions

The measurements confirmed that the SiC detector can simultaneously measure both neutron and gamma-ray intensities in the radiation field surrounding a spent nuclear fuel assembly. Furthermore, both the neutron and gamma-ray sensitivities were found to be stable during prolonged exposure to the spent fuel radiation field over a period of almost four months.

The neutron sensitivity of SiC detectors will limit their usefulness for cases where low geometry and/or short counting intervals are required while maintaining low statistical uncertainties on the number of counts. On the other hand, higher SiC detector sensitivity can be achieved by using large-area arrays of SiC diode detectors.

The gamma-counting capabilities of SiC detectors for spent-fuel monitoring should be explored further. It has been shown previously that SiC gamma count rates are proportional to gamma intensity in fields up to 2700 Gy/h [12], and the range can be extended to higher doses by using smaller diode sizes.

Recently SiC p-n diode radiation detectors were shown [19] to still have 100 % charge collection efficiencies following ^{60}Co doses up to 2.5 MGy, confirming the stable detector performance observed in cumulative spent fuel gamma-ray exposures of more than 6000 Gy in the present work. Measurements in progress indicate that only a negligible change in charged-particle response characteristics are observed for SiC detectors exposed to ^{137}Cs gamma-ray doses of greater than 5 MGy [20]. The high radiation resistance of SiC detectors, their stability in elevated and changing temperatures, and their small size and versatility make them ideal for spent-fuel monitoring applications.

References

[1] Dulloo, A. R., Ruddy, F. H., Seidel, J. G., Flinchbaugh, T., Davison, C., and Daubenspeck, T., "Neutron and Gamma Ray Dosimetry in Spent-Fuel Radiation Environments Using Silicon Carbide Semiconductor Radiation Detectors," in *Reactor Dosimetry: Radiation Metrology and Assessment, ASTM STP 1398*, J. G. Williams, D. W. Vehar, F. H. Ruddy, and D. M. Gilliam, Eds., ASTM International, West Conshohocken, PA, 2001, pp. 683–690.

[2] Smith, R. C., Bartko, J., and Fero, A. H., "Rapidly Evaluating Burnup in Spent Nuclear Fuel by Measuring its Neutron Emission," R&D Report 79-1C65-BUNRA-R1, Westinghouse Electric Co.,

Pittsburgh, PA, September 28, 1979.

[3] Gold, R., Ruddy, F. H., Lippincott, E. P., McElroy, W. N., and Roberts, J. H., "Spent Thermal Reactor Fuel Assembly Characterization with Solid State Track Recorders," *Dosimetry Methods for Fuels Cladding and Structural Materials—Proceedings of the Third ASTM-Euratom Symposium on Reactor Dosimetry*, Ispra, Italy, Oct. 1–5, 1979, EUR-6813, 1980, pp. 858–867.

[4] Phillips, J. R., Halbig, J. K., and Bosler, G. E., "Passive Neutron Measurements and Calculations of Irradiated PWR Fuel Assemblies," *Proceedings, Third Annual Symposium on Safeguards and Nuclear Material Management*, Karlsruhe, Germany, ESARDA 13, 1981, pp. 169–176.

[5] Levine, S. H., Schultz, M. A., and Chang, D., "A Method of Performing Shutdown Reactivity Measurements in Spent Nuclear Fuel Storage Pools," *Nucl. Technol.*, Vol. 52, 1981, pp. 347–353.

[6] Ruddy, F. H., Roberts, J. H., Gold, R., Preston, C. C., and Ulseth, J. A., "Solid State Track Recorder Neutron Dosimetry Measurements for Fuel Debris Assessment of TMI-2 Makeup and Purification Demineralizer-A," *Nucl. Tracks Radiat. Meas.*, Vol. 8, 1984, pp. 473–479.

[7] Chickering, R. W. and Goldstein, N. P., "Development of a Burnup Meter for Irradiated Nuclear Fuel," Nuclear Energy Systems Report WCAP-10536, Westinghouse Electric Co., Pittsburgh, PA, February, 1984.

[8] Debrue, J., De Raedt, Ch., and Minsart, G., "Analysis of Neutron Emission on PWR Spent Fuel Assemblies for Burn-up Assessment," *Reactor Dosimetry Methods, Applications, and Standardization, ASTM STP 1001*, H. Farrar and E. P. Lippincott, Eds., West Conshohocken, PA, 1989, pp. 710–719.

[9] Goldstein, N. P., "Measurements to Establish Burnup Credit for Spent Fuel Assemblies," *Proceedings of a Workshop on the Use of Burnup Credit in Spent Fuel Transport Casks, SAND89-0018*, 1989.

[10] Ewing, R. I., Bosler, G. E., Siebelist, R., and Walden, G., "Burnup Verification Measurements on Spent Fuel Assemblies in Oconee Nuclear Station," EPRI Report TR-103591, Electric Power Research Institute, Palo Alto, CA, January 1994.

[11] Chesterman, A. S. and Clark, P. A., "Radiometric Instrumentation for Burnup Credit, Safeguards and Waste Characterization of Spent Fuel," *INMM 37th Annual Meeting Proceedings*, Palm Desert, CA, July 28–31, 1996.

[12] Dulloo, A. R., Ruddy, F. H., Seidel, J. G., Davison, C., Flinchbaugh, T., and Daubenspeck, T., "Simultaneous Measurement of Neutron and Gamma-Ray Radiation Levels from a TRIGA Reactor Core Using Silicon Carbide Semiconductor Detectors," *IEEE Trans. Nucl. Sci.*, Vol. 46, 1999, pp. 276–279.

[13] Dulloo, A. R., Ruddy, F. H., Seidel, J. G., Adams, J. M., Nico, J. S., and Gilliam, D. M., "The Neutron Response of Miniature Silicon Carbide Semiconductor Detectors," *Nucl. Instrum. Methods Phys. Res. A*, Vol. 422, 1999, pp. 47–48.

[14] Dulloo, A. R., Ruddy, F. H., Seidel, J. G., Adams, J. M., Nico, J. S., and Gilliam, D. M., "The Thermal Neutron Response of Miniature Silicon Carbide Semiconductor Detectors," *Nucl. Instrum. Methods Phys. Res. A*, Vol. 498, 2003, pp. 415–423.

[15] Seshadri, S., Dulloo, A. R., Ruddy, F. H., Seidel, J. G., and Rowland, L. B., "Demonstration of a SiC Neutron Detector for High Radiation Environments," *IEEE Trans. Electron Devices*, Vol. 46, 1999, pp. 567–571.

[16] Ruddy, F. H., Dulloo, A. R., and Seidel, J. G., "Study of the Radiation Resistance of Silicon Carbide Radiation Detectors," *Trans. Am. Nucl. Soc.*, Vol. 90, 2004, pp. 348–349.

[17] Ruddy, F. H., Dulloo, A. R., Seidel, J. G., Seshadri, S., and Rowland, L. B., "Development of a Silicon Carbide Radiation Detector," *IEEE Trans. Nucl. Sci.*, Vol. 45, 1998, pp. 536–541.

[18] Terada, H., Urayama, K., Atsumi, Y., and Takebe, M., "Development of a Simplified Detector Using Wavelength Shifting and a Light Transmission Technique and a Test for Identifying Assemblies in the Spent Fuel Pond," *Proceedings, IAEA Symposium on International Safeguards*, IAEA-SM-333, 1994 p. 151.

[19] Kinoshita, A., Iwami, M., Kobayashi, K., Nakano, I., Tanaka, R., Kamiya, T., Ohi, A., Oshima, T., and Fukushima, Y., "Radiation Effect on pn-SiC Diode as Detector," *Nucl. Instrum. Methods Phys. Res. A*, Vol. 541, 2005, pp. 213–220.

[20] Ruddy, F., work in progress under research supported by the Office of Science (BER), United States Department of Energy, Grant No. DE-FG02-04ER63734.

Journal of ASTM International, Vol. 4, No. 4
Paper ID JAI100375
Available online at www.astm.org

Z. Bureš,[1] *F. Cvachovec*,[2] *P. Čeleda*,[1] *J. Kroupa*,[1] *B. Ošmera*,[3] *and S. Pošta*[3]

Digital Multiparameter System for Characterizing the Neutron-Gamma Field in the LR-O Experimental Reactor

ABSTRACT: The present paper points toward the possibility of reducing the proportion of analog processing in an apparatus employed to measure the neutron and photon energy spectra. The digitization of the detector output pulses makes it possible to process the information contained in the pulses either instantaneously or subsequently. The present paper deals with the method of digitizing the leading edge of the pulses generated by a stilbene organic scintillator or an NE-213 scintillator. The neutron versus gamma discrimination can be carried out on the basis of the pulse leading edge duration. Coping with this task requires a digitizer featuring quite a high sampling frequency, which must exceed 1 GHz. The requirements for the amplitude digitization frequency are less severe, however, the amplitude resolution must be better than 8 bits. Both of the above requirements can be met with present-day components. The digitization is expected to result in reducing the apparatus size and improving its functionality.

KEYWORDS: neutron and gamma spectrometry, digitizer, pulse shape discrimination, stilbene

Introduction

Within the framework of the REDOS (Fifth Framework Programme of the European Community) project, the space-energy distribution of the neutron and gamma radiation in energetic interval E-$\varepsilon(0.5, 10)$ MeV near the reactor pressure vessel walls and over the pressure vessel thickness has been studied in a WWER-1000 model, placed in the LR-0 experimental reactor (NRI Řež). A scintillation detector using a stilbene-type organic scintillator is employed, among others, to carry out the required measurements. This spectrometric detector is capable of measuring the spectrum of both components of the mixed field simultaneously. It is able to discriminate between neutrons and photons by virtue of a difference in the time response of the luminescence process in a scintillator during the neutron or gamma photon interaction. In the detector output voltage pulses, the response of the neutron pulse rise time is longer than that of the photon one. The actual output pulse of the rise time from 10 % to 90 % of the pulse amplitude amount is about 13 ns for photons and 16 ns for neutrons. Estimated uncertainty is approximately 1 ns up to 2 ns (small energy) for sampling frequency 2 GHz (see Fig. 1). Until now, analog circuits called pulse shape discriminators (PSDs) have been used exclusively to discriminate between the different rise-time pulses. The system, which has been employed by the authors of the present paper until now, is described in [1].

Digital Processing of Experimental Data

Recent progress in digital technology has resulted in a successful solution to the pulse waveform discrimination problem by means of the pulse digitization. The world-wide digital processing trend has motivated us to reduce the amount of analog components in our apparatus, replacing them by a digital system.

The two basic parameters to be retrieved from the digitized form of the output pulse are the pulse amplitude and the rise time. The problem of the amplitude numerical processing was resolved a long time ago. Analog-to-digital converters with sufficient resolution can be used [2]. To process the output of

Manuscript received June 20, 2005; accepted for publication March 28, 2007; published online May 2007. Presented at ASTM Symposium on Reactor Dosimetry, 12th International Symposium on 8–13 May 2005 in Gatlinburg, TN; D. W. Vehar, D. M. Gilliam, and J. M. Adams, Guest Editors.
[1] Professor assistant, University of Defense, 612 00 Brno, Czech Republic.
[2] Professor, University of Defense, 612 00 Brno, Czech Republic.
[3] Chief Scientist, Senior researcher respectively, Nuclear Research Institute, 250 68 Řež, Czech Republic.

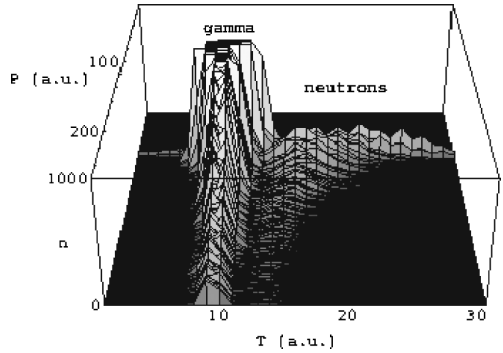

FIG. 1—*Plot of T, P, and n (number of pulses). Sampling frequency 2 GHz, P_{min}–P_{max} 20 %–80 % [5].*

stilbene-type scintillators (NE-213), showing relatively poor amplitude resolution, a 10-bit converter (corresponding to 1024 memory channels) is sufficient. However, to determine from the digitized data the rise time or any other quantity carrying the information of the detected particle type is a problem that is considerably more difficult to solve. The reason is obvious. As mentioned above, the estimated neutron and photon pulse rise times are extremely short, their measurement is at the very margin of technical feasibility for the current instrumentation available. An ACQIRIS DP 210 8-bit digitizer with a sampling frequency up to 2 GHz has been chosen from several options available. The maximum input voltage is 5 V at the 50 Ω input impedance [3].

To evaluate the sampled pulses from the data acquired, the evaluation program [4] finds out the pulse amplitude and subsequently the time interval $\Delta\tau$ between the samples is chosen in the range $P_{\min}$ % to $P_{\max}$ % of 5 % to 95 %, 10 % to 90%, 15% to 85% and 20 % to 80 % of the pulse amplitude. The quantity $\Delta\tau$ is estimated as the averaged value of the digital derivation of the time-dependent pulse between $P_{\min}$ and $P_{\max}$ and it is used as a parameter characterizing the pulse rise time, i.e., type of particle. The other parameter to evaluate is P the pulse amplitude, which is expressed as the median of the six highest sample values. Once the two parameters $\Delta\tau$ and P are evaluated, they are plotted in a three-dimensional diagram along, x- and y-axes respectively, and the number of events occurring within a narrow interval of both parameter values (1/256 of the interval measured) is plotted on the z-axis. The examples are shown in Figs. 1 and 2. The data measured with sampling frequency of 2 GHz are represented here. The $\Delta\tau$ (rise time) parameter has been evaluated for the following amplitude windows: 20 % to 80 % (Fig. 1), 5 % to 95 % (Fig. 2). As it is seen from the figures, $\Delta\tau$ is best defined for the interval from 20 % to 80 %. Further $P_{\min}$ %, $P_{\max}$ % narrowing results in worse separation of the neutron and photon pulses.

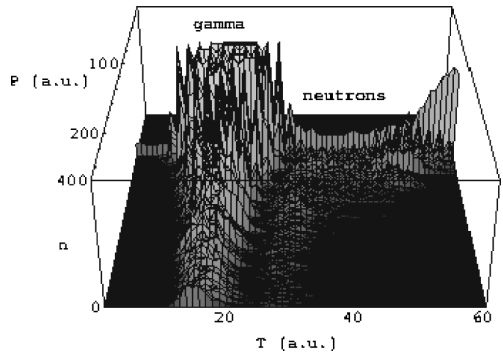

FIG. 2—*Plot of T, P, and n (number of pulses). Sampling frequency 2 GHz, P_{min}–P_{max} 5 %–95 % [5].*

Neutron-Photon Discrimination

To identify unambiguously the parameter distributions corresponding to the neutron and photon pulses, a Cf neutron source and a Cs gamma source were used in the measurements.

The photon and neutron distributions were determined as a function of:

- the set-point values of the rise time lower and upper limits P_{min} and P_{max},
- the sampling frequency,
- the pulse amplitude (detected particle energy),
- the detector output pulse counting rates.

As compared with the analog PSDs, the P_{min} and P_{max} settings can also be optimized with respect to the data measured even in different ways if various amplitude intervals are required. In general, the values lying in the interval of 20 % to 80 % seems to be most acceptable. It is evident that higher sampling frequencies result in better rise time resolution and consequently more reliable determination of the particle type. The 2 GHz sampling frequency provides the best results. However, even a substantially lower frequency of 500 MHz provides quite acceptable photon-neutron discrimination, which is still substantially better than that obtained by a single-parameter processing. As could be expected, lower amplitudes (lower photon and neutron energies) provide lower resolution, similar to the analog processing. This is apparently a matter of principle. Lower-amplitude pulses are more likely to be distorted by noise. In this part of the spectrum, the ratio of the photon and neutron pulses is about 10:1. In the high energy area this ratio is lower and the pulse shape distinguishing between neutrons and photons is better (see Figs. 1 and 2).

In the present analog processing mode, the maximum pulse counting rate the apparatus is capable to process is restricted, namely, by the PSD circuits (in our case, 2000 imp/s approximately). In case of digital processing chain, the particle type discrimination characteristics at higher counting rates are better than those achieved in the analog processing; we have reached acceptable discrimination for count rate 6000–8000 imp/s. Note that the possibility to increase the pulse counting rate is not exhausted by the present measuring setup design. For example, the pulse decay time can be shortened prior to the digitization. It is important to note that the pulse decay does not contain any necessary information. Another interesting option consists in discriminating between the superimposed pulses corresponding to the particles being recorded so close to each other that their waveforms are overlapping. Digital processing can "rescue" these pulses, i.e., segregate them from each other and determine their parameters, which cannot be performed by analog PSDs. These possibilities are now studied experimentally.

The low dynamic range of the digitizer can limit the energy range of the measured spectra In that case, the input pulse compression can be applied.

Amplitude Distribution Measurement

For this purpose, the resolution and the dynamic range of the DP 210 measuring card are too low, namely in the case of measurements of spectrum with fine (peak) structure, which is typical for the photon spectra. It can be solved, for example, in feeding the signal into the above digitizer and, in parallel, into a measuring system showing a better, at least 10-bit, resolution. In the case of the DP 210 digitizer, the complete impulse waveform, or its representative part, is saved in the memory. Thus, saved data are used for the detected particle type identification. The parallel system is formed by the amplitude section of the original Bubulak system [1]. The drawback of this design is a certain cumbersomeness of the off-line processing.

The simplest solution is the use of a 10-bit or better resolution digitizer operating at a sampling frequency of 2 GHz at least. If a detector with better amplitude resolution, e.g., the hydrogen-filled proportional detector, is used, the circuit parameters would be upgraded again.

Conclusion

The properties of the above-mentioned digitized system and achieved results make evidence for the changeover from analog to digital methods of processing the organic scintillator detector output pulses very promising. It is to be said that the current solution level shows certain restrictions, for example, the need for off-line processing. In the cases where routine experiments are concerned, the previous solution

employing analog components still appears to be more convenient and, to a certain extent, also better quality. Nevertheless, the advantages and benefits of the numerical system as well as the rapid development of its circuit components are self-evident. They include, among others, a substantial reduction in the setup volume and weight and possibility to control the experiments via a computer network.

Acknowledgments

The work was done in the frame of Grant No. MSM 26722 44501 of the Czech Ministry of Education, Youth and Sports and grant of the Czech Ministry of Industry and Trade No. 1H-PK/20.

References

[1] Bureš, Z., Cvachovec, J., Cvachovec, F., Čeleda, P., and Ošmera, B., "Multiparameter Multichannel Analyser System for Characterisation of Mixed Neutron-Gamma Field in the Experimental Reactor LR-0," in *Reactor Dosimetry in the 21st Century*, Brussels, 2003, World Scientific Publishing Co. Pte. Ltd., Singapore, p. 194.

[2] Knoll, G., *Radiation Detection and Measurement*, John Wiley & Sons, Inc., New York, 2000.

[3] *User Manual, Family of 8-bit Digitizers, ACQIRIS*, Agilent Technologies, Honroe, NY; for more information, see: http://www.acqiris.com/products/digitizers/8-bit-pci-digitizer-cards/dp210/datasheet/DP210.pdf

[4] Evaluation software made by Z. Bures, written in Perl language.

[5] Visualization software GNUPLOT 4.0, http://www.gnuplot.info/

Journal of ASTM International, Vol. 3, No. 7
Paper ID JAI13432
Available online at www.astm.org

Y. Sakurai[1] *and A. Maruhashi*[2]

A Beam-Monitor System for Neutrons and Gamma Rays in the Medical Irradiation Facility of the Kyoto University Research Reactor

ABSTRACT: The first clinical trial of neutron capture therapy (NCT) using the epithermal neutron beam at the medical irradiation facility of the Kyoto University Reactor was carried out for oral cancer in December 2001. A beam monitor system is required for accurate dose estimation in our present NCT. As the components of thermal, epithermal and fast neutrons and gamma rays must be separately measured, the multi-chamber method was adopted using a combination of four kinds of ionization chambers. Each chamber has a two-layer wall; the outer wall has a thickness of about 5 m, and the inner wall has a thickness of 10–100 λm. The response can be adjusted by regulating the chamber-gas components. A trial beam-monitor system was made using IC-17M type chambers of Far West Technology, Inc., and its characteristics were experimentally determined.

KEYWORDS: neutron capture therapy, mixed field of neutrons and gamma rays, beam monitor system, ionization chamber, chamber wall, chamber gas

Introduction

The Heavy Water Neutron Irradiation Facility of the Kyoto University Reactor (KUR) was updated in March 1996 [1], as a medical irradiation facility with several neutron energy spectra, mainly for an improved application in neutron capture therapy (NCT). In this facility, a total of 188 clinical trials of NCT were carried out until February 2005. As 104 trials were performed after December 2001, nearly 55 % of all trials were done during the last three years. Especially, 50 % of the epithermal neutron irradiations were applied to refractory tumors in head and neck. It is recognized that the wider application of NCT to other kinds of tumors is highly desirable in the future.

Simultaneously with the beginning of epithermal neutron irradiation, the dose estimations for preirradiation and postirradiation using a dose planning system were initiated. The several topics to be improved have been identified in our present NCT. Namely, the preparation and installation of beam monitors are urgently necessary, because the neutron-beam intensity and quality are easily affected by the fuel arrangement, etc., in the KUR medical irradiation field. The beam monitor system is one part of the "dose estimation joint system under NCT clinical irradiation," which is planned to be installed at the KUR [2].

In the "dose estimation joint system under NCT clinical irradiation," the data from the on-line measurement systems such as beam monitors, gamma-ray telescopes, etc., are fed back to the preirradiation and postirradiation results by a treatment planning system, and then the information concerning the irradiation field and the patient are gathered to estimate the dose received during the treatment. This system consists of the following five parts: (1) a treatment planning system; (2) a beam-monitor system for neutrons and gamma rays; (3) gamma-ray telescope systems including the position-fixing equipments; and (4) a patient-position checking system.

In this paper, our concept and study results are reported concerning the beam-monitor system for neutrons and gamma rays in the NCT medical irradiation field.

Manuscript received June 20, 2005; accepted for publication April 19, 2006; published online June 2006. Presented at ASTM Symposium on Reactor Dosimetry, 12th International Symposium on 8–13 May 2005 in Gatlinburg, TN ; D. W. Vehar, D. M. Gilliam, and J. M. Adams, Guest Editors.

[1] Lecturer, Kyoto University Research Reactor Institute, Asashiro-nishi 2-1010, Kumatori-cho, Sennan-gun, Osaka 590-0494, Japan.
[2] Professor, Kyoto University Research Reactor Institute, Asashiro-nishi 2-1010, Kumatori-cho, Sennan-gun, Osaka 590-0494, Japan.

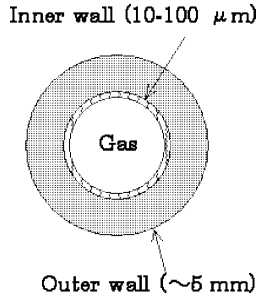

FIG. 1—*Schematic cross section of the ionization-chamber head.*

Concept

Three kinds of neutron beam, which are thermal-neutron beam, epithermal-neutron beam, and mixed-neutron beam of thermal and epithermal, are applied for NCT in the medical irradiation facility of KUR. So, the dose estimation consistent among those beams is required, and the thermal, epithermal, fast, and gamma-ray components must be separately measured using the beam-monitor system. The multichamber method is adopted using a combination of four kinds of ionization chambers.

Figure 1 shows the schematic cross section of the ionization-chamber head. Each chamber has a two-layer wall. The outer wall has a thickness of about 5 mm, and it is employed as a neutron filter, namely, a local spectrum shifter. The inner wall has a thickness of 10–100 λm, and it is employed as an absorber for the heavy charged particle generated in the inner side of the outer wall due to neutron reactions. The response for each component can be adjusted also by regulating the chamber-gas components.

Some chamber walls were made for trial in our laboratory, for the IC-17M type chamber of Far West Technology, Inc. Nonfoamed polyurethane ($-H_2NCONH_2-$) with LiF was selected as the outer-wall material for the four chambers. Molds for the IC-17M-chamber wall were made from silicone rubber, the mixture of LiF powder and polyurethane resin were run into the mold, and then the hand-made chamber walls were obtained. The chamber volumes were 1 cc and the wall thicknesses were 5.3 mm.

The weight percent of LiF to polyurethane was 35. For the neutron chambers, the neutron-filtering characteristics were controlled by changing the ^{6}Li ratio in LiF. The ^{6}Li ratio was adjusted by mixing enriched ^{6}LiF and natural LiF. Chamber walls with ^{6}Li enrichment of 7.5 % (natural), 20 %, 40 %, 60 %, 80 %, and 96 %, were prepared.

For the inner wall, carbon paste was coated about 100-λm thickness on the inner surface of the outer wall. This inner wall plays a role not only as an absorber for the heavy charged particle from the outer

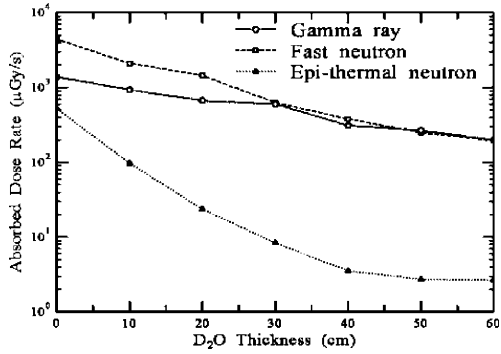

FIG. 2—*Relations of the beam parameters to the heavy water thickness in the fast neutron irradiation mode group.*

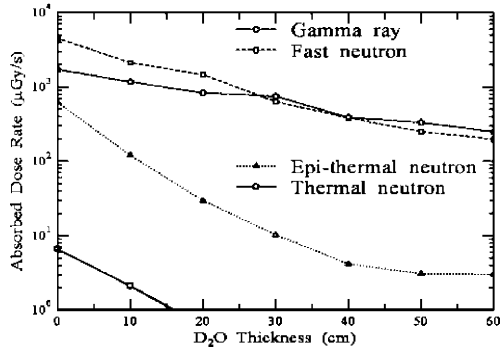

FIG. 3—*Relations of the beam parameters to the heavy water thickness in the epithermal neutron irradiation mode group.*

wall, but also as an electric conductor, because the outer wall of nonfoamed polyurethane is practically insulating. From the measured result for the polyurethane chamber with ^{6}Li-enrichment of 7.5 %, it was confirmed that the response to neutrons decreased to be approximately 90 % by this inner wall.

Testing Conditions

The characteristic experiment for the trial-made multichamber was performed using the several irradiation modes at the KUR-HWNIF [1].

In this facility, the heavy-water spectrum shifter is installed for varying the neutron energy spectrum. The spectrum shifter consists of three small tanks of 10 cm, 20 cm, and 30 cm in thickness. The heavy water in the small tanks can be independently filled and drained. By combining these small tanks, the total heavy-water thickness can be changed from 0 cm to 60 cm in 10-cm increment. Thermal-neutron filters of 0.1-cm-thick cadmium and 0.64-cm-thick boral are installed after the heavy water spectrum shifter, for the regulating the thermal neutron component. Thus, neutron beams with various energy spectra, from almost pure thermal to fast, are available using this facility.

In this study, three irradiation mode groups were selected. One is the fast neutron irradiation mode group, in which both thermal-neutron filters are perfectly closed. Figure 2 shows the relations of the beam parameters, such as absorbed dose rates for gamma rays and thermal, epithermal and fast neutrons, to the heavy water thickness. The gamma-ray dose rates are the measured values by thermoluminescent dosimeter (TLD) of beryllium oxide (BeO) enclosed in quartz glass capsule. The neutron dose rates are the

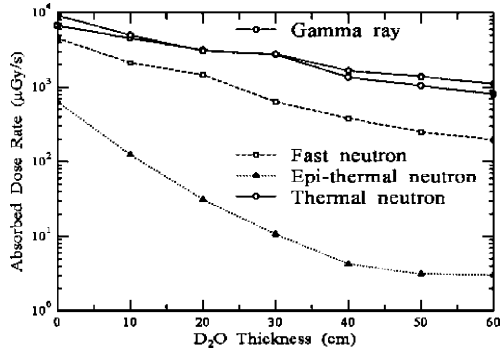

FIG. 4—*Relations of the beam parameters to the heavy water thickness in the thermal neutron irradiation mode group.*

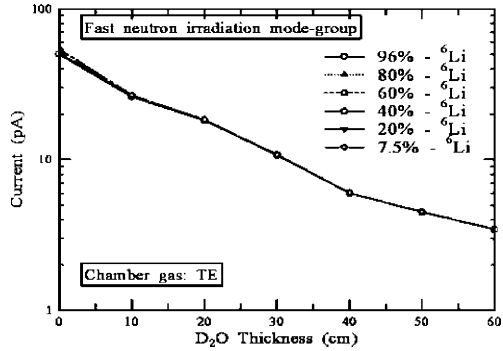

FIG. 5—*Measured results for TE gas in the fast neutron irradiation mode group.*

calculated values using the neutron energy spectra in Ref. [3] and the kerma factors in Ref. [4]. As the heavy-water thickness is larger, the neutron spectrum is softer, and the beam intensity is smaller. From the results obtained in this mode group, the response factors can be fixed for fast-neutron and gamma-ray components.

Figure 3 shows the relations of the beam parameters to the heavy water thickness for the epithermal neutron irradiation mode group. In this mode group, only the cadmium thermal-neutron filter is perfectly closed. The neutron beams contain higher epithermal neutron components, compared to those in the fast neutron irradiation mode group. Then, the response factors can be fixed for epithermal neutron component.

Figure 4 shows the relations for the thermal neutron irradiation mode group. In this mode group, both thermal-neutron filters are fully opened. The thermal neutrons are the most significant component in this mode group, so the response factors for thermal neutron component can be fixed.

In the irradiation room of this facility, temperature and pressure is almost stable. The temperature is 30 deg±2 deg centigrade and the pressure is almost 99.5 % of atmospheric pressure, 101 kPa±2 kPa at the chamber positions. These influence about 1 % on the temperature correction and about 2 % on the pressure correction for the chambers. Those are within the measurement uncertainty of this chamber system, as described below.

Results

Figures 5 and 6 show the measured results for the ionization chambers in the fast neutron irradiation mode group, respectively, with tissue equivalent (TE; CH_4 64.4 %, CO_2 32.5 %, and N_2 3.1 %) gas and CO_2 gas. The horizontal and vertical axes represent the heavy water thickness and the chamber response as electric current (pA), respectively. The uncertainties of the determined current are almost 3 %.

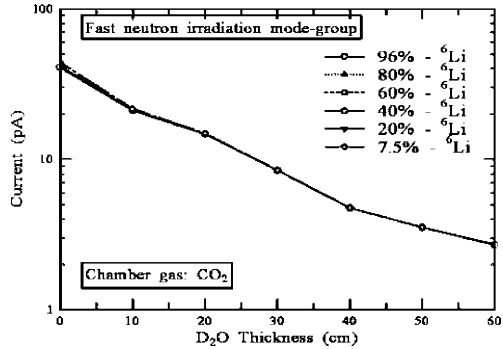

FIG. 6—*Measured results for CO_2 gas in the fast neutron irradiation mode group.*

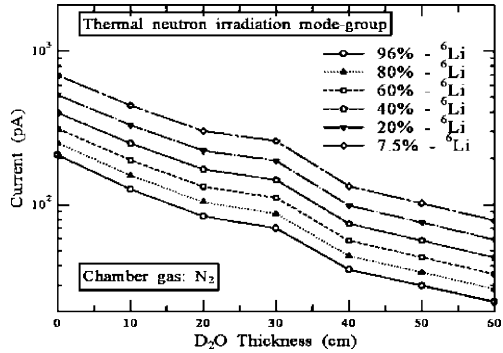

FIG. 7—*Measured results for N_2 gas in the thermal neutron irradiation mode group.*

It is shown that the curves are almost the same for the various ^{6}Li enrichments. The responses for TE gas are about 20 % larger than those for CO_2 gas. This difference originated from the different neutron interactions with the chamber gas. It is thought that the interaction with hydrogen has a larger influence.

Figure 7 shows the measured results for nitrogen gas in the thermal neutron irradiation mode-group. The shapes of the curves are almost the same, but the absolute values are larger as the ^{6}Li enrichment is smaller. It is apparent that these differences are mainly from the thermal-neutron absorbing characteristics for the various ^{6}Li enrichments.

Figure 8 shows the measured results for nitrogen gas in the epithermal neutron irradiation mode group. The differences among the respective curves are not so large. The currents are larger for smaller ^{6}Li enrichments, especially for the smaller heavy-water thickness.

For the dose estimation of the epithermal neutron component, the lower ^{6}Li enrichment is more adequate. For the discrimination between the thermal and epithermal neutron components, the higher ^{6}Li enrichment is more adequate. As the ^{6}Li enrichment is over 60 %, the ratio of the response for epithermal neutrons to that for thermal neutrons is below 3 %, which is the measurement uncertainty. In this study, the combination of a 40 % ^{6}Li enrichment and a 7.5 % ^{6}Li enrichment was selected for the separation of thermal and epithermal neutron components.

Conclusion

For the outer wall, the ^{6}Li enrichment was fixed to be 96 % for fast neutrons and gamma rays. For the separation of thermal and epithermal neutrons, a combination of 40 % and 7.5 % ^{6}Li enrichments was selected. For the chamber gas, TE gas was selected for fast neutrons, N_2 gas for thermal and epithermal

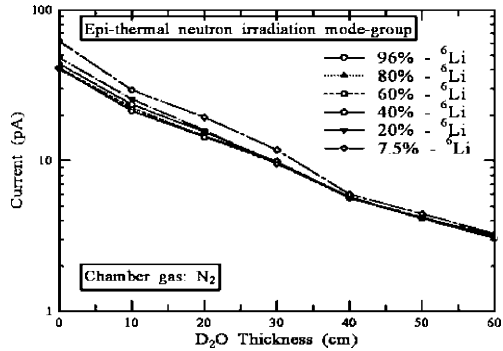

FIG. 8—*Measured results for N_2 gas in the epithermal neutron irradiation mode group.*

TABLE 1—*The responses for the respective chambers.*

Chamber	^{6}Li enrichment (%)	Gas	Thermal (pA/λGy s^{-1})	Epithermal (pA/λGy s^{-1})	Fast (pA/λGy s^{-1})	Gamma (pA/λGy s^{-1})
Fast	96	TE	3.60E−03[a]	1.70E−05	8.46E−03	8.93E−03
Thermal and Epi 1	40	N_2	4.28E−02	2.83E−03	6.29E−03	8.55E−03
Thermal and Epi 2	7.5	N_2	8.46E−02	3.25E−02	6.31E−03	8.58E−03
Gamma	96	CO_2	2.11E−03	1.39E−05	7.13E−03	6.55E−03

[a]3.60E−03 means 3.60×10^{-3}.

neutrons, and CO_2 gas for gamma rays. The responses for the respective chambers are listed in Table 1. At present, this beam monitor system is being tested at the KUR medical irradiation facility.

Acknowledgments

This study was partially supported by the Japan Society for the Promotion of Science, Grant-in-Aid for Young Scientists (A) 15680016.

References

[1] Sakurai, Y., and Kobayashi, T., "Characteristics of the KUR Heavy Water Neutron Irradiation Facility as a Neutron Irradiation Field with Variable Energy Spectra." *Nucl. Instrum. Methods Phys. Res. A*, Vol. 453, 2000, pp. 569–596.

[2] Sakurai, Y., Maruhashi, A., and Ono, K., "The Irradiation System and Dose Estimation Joint-system for NCT Wider Application in Kyoto University." *Appl. Radiat. Isot.*, Vol. 61, 2004, pp. 829–533.

[3] Sakurai, Y., and Kobayashi, T., "Spectrum Evaluation at the Filter Modified Neutron Irradiation Field for Neutron Capture Therapy in Kyoto University Research Reactor." *Nucl. Instrum. Methods Phys. Res. A*, Vol. 531, 2004, pp. 585–595.

[4] Caswell, R. S., Coyne, J. J., and Randolph, M. L., "Kerma Factors for Neutron Energies below 30 MeV," *Radiat. Res.*, Vol. 83, 1980, pp. 217–254.

Journal of ASTM International, Vol. 4, No. 5
Paper ID JAI100376
Available online at www.astm.org

S. Michael Luker,[1] *Patrick J. Griffin,*[1] *K. Russell DePriest,*[1] *Donald B. King,*[1] *Gerald E. Naranjo,*[1] *and Ahti J. Suo-Anttila*[2]

Application of a Silicon Calorimeter in Fast Burst Reactor Environments

ABSTRACT: Frequently in experiments at fast burst reactors (FBRs), it is necessary to know the dose and peak dose rate absorbed by a material in terms of dose to silicon. The dose to silicon at a given point in an irradiation cannot be reliably measured by a passive dosimeter retrieved at late times from a mixed field environment, so we rely on the silicon calorimeter as the true standard. A silicon calorimeter has been developed for applications in a water-moderated pulsed reactor. In this paper, the authors investigate the application of this silicon calorimeter in an FBR environment. Tests have been conducted at the White Sands Missile Range (WSMR) FBR, also known as MoLLY-G, to develop techniques to use this silicon calorimeter for a measure of rad(Si) during and soon after a pulsed operation. This calorimeter can be coupled with the response of a diamond photoconductive detector (PCD) in order to derive a dose rate monitor suitable for application during an FBR operation [1].

KEYWORDS: calorimeter, silicon, fast burst reactor, PCD, dose, FBR, active dosimeter

Introduction

In principle, the measurement of the silicon dose in a reactor using the silicon calorimeter should be a very accurate dosimetry method since neutron and gamma absorbed energy will contribute to the integral dose for the material of interest. This is a much higher fidelity approach than relying on calibrations of detectors in inadequately characterized neutron and gamma fields. However, several measurement issues make the use of the calorimeter difficult to use in the very short pulsed radiation fields at fast burst reactors (FBRs). Whereas the peak signal level from the silicon calorimeter in a large water-moderated reactor pulse provides a temperature rise of 5–20°C (~1.5 mV in voltage measurement), in an FBR environment the signal is much smaller (temperature rises of 0.2°C) and the presence of electromagnetic and radiation-induced cable noise sources can swamp the signal unless proper cabling, amplifier common-mode rejection and cable shielding techniques are chosen [1,2].

The silicon calorimeter was developed for applications in a water-moderated reactor, such as the Annular Core Research Reactor (ACRR), with pulse widths from 10–100 ms. In an FBR environment, the pulse width can be as short as 50 μs and the heat transfer between the thermocouple wire and the silicon wafers can be significantly slower than the reactor pulse width. The slow thermal equilibration of the thermocouple wire heating with the much more massive silicon wafers can interfere with efforts to infer the radiation pulse shape. The actual temporal response of an active dosimeter, such as a PCD (or the reactor power transient behavior as measured with a self-powered neutron detector (SPND) or fission chamber), occurs on a much shorter time scale than the apparent rise in the early calorimeter response. Indeed, even the thermal equilibration of a thin thermocouple (TC) with the silicon wafers of the calorimeter occurs at longer times than the radiation pulse. This difference in the temporal profiles is aggravated by noise filtering in the data acquisition system that essentially time-averages the calorimeter response over intervals larger than the actual reactor pulse (~50 μs). In Fig. 1(*a*), the full bandwidth

Manuscript received June 20, 2005; accepted for publication March 4, 2007; published online June 2007. Presented at ASTM Symposium on Reactor Dosimetry, 12th International Symposium on 8–13 May 2005 in Gatlinburg, TN; D. W. Vehar, D. M. Gilliam, and J. M. Adams, Guest Editors.

[1] Senior Member of Technical Staff, Distinguished Member of Technical Staff, Senior Member of Technical Staff, Principal Member of Technical Staff, and Distinguished Technologist, respectively, Sandia National Laboratories, MS 1146, Albuquerque, NM 87185.

[2] Research Engineer, Alion Science and Technology, Albuquerque, NM 87110.

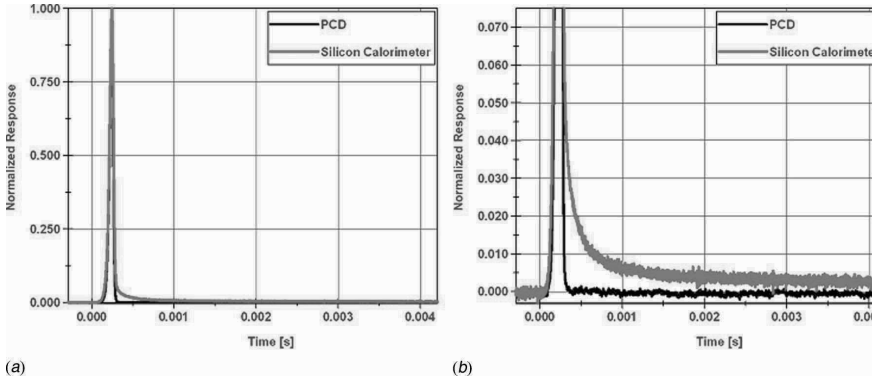

FIG. 1—*(a) Full bandwidth signals from silicon calorimeter and PCD, (b) zoomed view.*

response of the calorimeter is compared to a PCD response to show the large noise signal present on the calorimeter signal and the settling time. Figure 1(*b*) is a zoomed view to better highlight the settling time due to thermal equilibration of the larger gamma heating in the TC with that for the silicon wafers. The calorimeter signal requires amplification and the noise component can be very large (~3.5 Volts) compared to the signal of interest (~3 mV, with gain of 500). Use of silicon calorimeter at the WSMR FBR does not allow us to achieve a real-time dose rate measurement during a reactor pulse since the derivative of the calorimeter signal is distorted by the noise pulse. Since the noise level is very high, we use a 400 Hz low-pass filter, 16-bit digitizers, twisted-shielded pair cabling and lower sampling rates to improve the noise rejection. The use of a filter requires taking the calorimeter dose at a later time than desired, but our investigations into the thermal response of the calorimeter show that the signal is a reliable metric for the cumulative dose in the silicon and has an error of less than 5 %, after an interval of ~100 ms after the pulse. Once the calorimeter dose has been measured, this dose can be used to normalize a PCD time profile and to infer the time history for the dose rate [3,4].

When using a silicon calorimeter at ACRR, the reference dose is taken at a point during the reactor pulse where the calorimeter (TC and silicon wafers) has achieved thermal equilibrium and before the PCD response is reduced to background levels. The difference in the efficiency of the PCD in responding to dose from neutrons and from gammas makes the use of the temporal profile provided by the PCD to infer the shape of the radiation pulse suspect late in the tail of a pulse. During the development of this calorimeter, the normalization for the calorimeter dose to the integral of the PCD response at water-moderated reactors was taken at time-to-peak plus three full width half maximum pulse widths in order to avoid these problems. To apply this ACRR criterion at an FBR would require reading the normalization dose at 285 μs, which occurs before a stable calorimeter value can be read. The filtered pulse distorts the early time response but gives stable readings from as early as 25 ms to several seconds after the pulse. The optimal point to normalize the PCD integral response to the calorimeter was found to be ~100 ms after the pulse peak.

Typical Fast Burst Reactor Characteristics

The experimental work described in this paper was performed at the WSMR FBR but the techniques are general enough to apply to any FBR and, of particular interest to the authors is the Sandia Pulse Reactor (SPR-III). SPR-III is shown in Fig. 2(*a*). SPR differs from the WSMR FBR in that it has a large central cavity 17.8 cm in diameter and 48.3 cm in depth. The central cavity is desirable for very uniform radiation environments with the highest available fluence and dose rates available from the reactor. At the WSMR FBR, our experiments are positioned radially away from the reactor at a position that will give the experiment the desired fluence per pulse within the limits of Table 1. Figure 2(*b*) shows the WSMR FBR experiment table and hardware used for an ongoing SNL testing of the calorimeter. Typical pulse characteristics of an FBR are entered in Table 1.

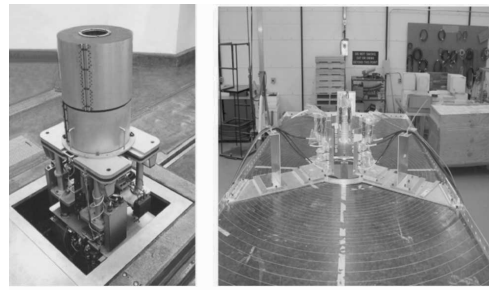

(*a*) (*b*)

FIG. 2—*(a) Sandia pulsed reactor (SPR), (b) WSMR FBR experiment table.*

Calorimeter Construction

In early silicon calorimeter designs, several problems were encountered at the Annular Core Research Reactor (ACRR). These issues included thermal conduction between the silicon wafers and the calorimeter housing resulting in rapid cooling and a noise term generated in the silicon or due to wire heating that distorts the derivative. The issue of thermal conduction to the housing was addressed by using alumina (Al_2O_3) standoffs instead of foam insulation. The alumina standoff also extended the life of the calorimeter since the foam material was very sensitive to radiation damage. An early-time transient signal anomaly, thought to be due to conductivity of the silicon during an Annular Core Research Reactor (ACRR) pulse, was eliminated by reducing the wafer diameter from 2.54 to 0.95 cm. While these design modifications eliminated the problems at the ACRR, the same types of problems were found to re-occur for the faster pulse typical of an FBR. Noise sources being investigated include radiation-induced conductivity in the silicon, gamma heating of the thermocouple wire, and cable system generated EMP (SGEMP) in the signal cables. Work is continuing to address the origin of the new noise sources seen in testing at the FBRs.

The SNL calorimeter is normally fabricated with a 5.08-cm extension tube but has also been fabricated in a 15.24 and 45.7-cm extension length for experimenters. The aluminum housing is an extension of the twisted-shielded pair cable shield and must be isolated from ground at the reactor test location to prevent ground loops. In Fig. 3(*a*) the components used to construct the calorimeter are shown. Figure 3(*b*) is an illustration showing the bottom silicon wafer with the 0.03-mm diameter Type E thermocouple.

TABLE 1—*Fast burst reactor pulse characteristics.*

Description	Value	Units
Maximum Fuel Temp.	450	[°C]
Full Width at Half Max Power	45 to 76	[μs]
Max Neutron Fluence	6.5E13 to 5.4E14	[n/cm^2 1-MeV(Si)-Eqv.]
Gamma Dose	1.4E4 to 1.2E5	[rad(Si)]
Peak Neutron Flux	1.6E18 to 8.6E18	[n/cm^2-s]
Peak Gamma Dose Rate	3.0E8 to 1.6E9	[rad(Si)/s]

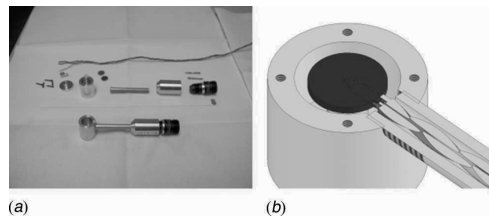

(*a*) (*b*)

FIG. 3—*(a) Silicon calorimeter components, (b) depiction of silicon wafer with thermocouple.*

MCNP Calculations

Based on MCNP calculations, the dose to silicon at the WSMR FBR is 2.89 rad(Si)/[Bq/g] of $^{58}Ni(n,p)^{58}Co$ activity [5]. Neutrons account for 31.6 % and gammas for the remaining 68.4 % of the dose measured by the calorimeter. Comparisons of the calculated-to-experimental (C/E) ratio of neutron nickel activation with the silicon dose show excellent agreement. One representative calorimeter co-located with the nickel dosimeter reported 13 992 [rad(Si)] for a difference from calculation of 9 % from the calculated dosimetry ratio. Another calorimeter, also very near the nickel dosimeter, reported 14 530 [rad(Si)] for a difference of 5 % from the calculated value.

Thermal Modeling

The pulse reactor at WSMR can potentially heat the silicon calorimeter in three ways, first by direct neutron and gamma energy deposition during the pulse, second by direct thermal radiation from the reactor core, and third by heat conduction between the components of the calorimeter (housing and alumina stand-offs) with the silicon wafer. The first heating mode is related to the direct metric being measured by the calorimeter. The second heating mode is a result of the 300° reactor core that radiates thermal energy directly to the exposed side of the silicon calorimeter. The calorimeter is positioned 1.905 cm (0.75 in.) away from the reactor core boundary in order to maximize the neutron fluence. The third mode of heat transfer within the calorimeter, conduction heat transfer between the components of the calorimeter, is a problem at late times. The calorimeter is constructed of four different types of material: silicon wafers, thermocouple wires, alumina supports, and aluminum housing. Each of these materials will heat at different rates during the reactor pulse, and will subsequently come to some equilibrium temperature over a longer time period. Since the aluminum housing is heating over time, all of the calorimeter components will show a transient heating profile [6].

Lumped Parameter Thermal Radiation Model

A simplified thermal radiation model was built to analyze the second heating mode, radiative heating from the reactor core. The assumptions in this model and analysis are:

1. Each component of the calorimeter is treated as a lumped mass, at a single uniform temperature. Thermal gradients within the calorimeter are not included.
2. The calorimeter was modeled as composed of three materials: a hot reactor with a temperature as the boundary condition, aluminum calorimeter housing, and silicon wafer.
3. Each component uses its actual surface area for calculating the radiation heat transfer and all heat transfer was by thermal radiation.
4. Surface emissivities of the materials are modeled as aluminum=0.1, silicon=0.9, and reactor core=1.0.
5. The view factor between silicon wafer and (aluminum) calorimeter housing is 1.0
6. The surface area for heat transfer from the reactor to the calorimeter is equal to the bottom surface area plus 10 % of the side area. The view factor between this area and the reactor is 1.0.
7. The entire surface area of the calorimeter housing is cooled by convection ($h=10\ W/m^2K$) to an air temperature of 25°C.
8. This reactor operation is a 300°C operation resulting in an initial, post-pulse, reactor temperature of 325°C.
9. The initial temperature of the calorimeter is 25°C (after the pulse).

The calculated results are shown in Fig. 4.

As shown in Fig. 4, the temperature of the aluminum calorimeter housing increases a large amount, approximately 1°C in two seconds, due to thermal radiation from the pulse reactor. In contrast, the silicon wafers inside the aluminum housing do not even register a temperature change—i.e., they increase a very small fraction of a degree.

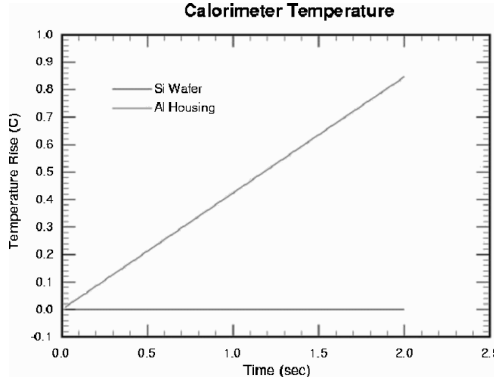

FIG. 4—*Predicted calorimeter housing and wafer temperatures.*

Thermal Conduction Model

The initial lumped radiation model only addresses heat transfer to the silicon calorimeter by thermal radiation from the reactor core. It did not show any significant heating, but it also did not address thermal conduction between the various components of the calorimeter. During the pulse each component heats up a slightly different amount due to the different elements in each component. After the pulse, these various components transfer heat to each other by thermal conduction, thus changing temperature with time. Conduction heat transfer within the calorimeter to other components such as the alumina cone support was addressed by a three-dimensional heat transfer code. This is the same model as was used in previous lumped radiative heating analyses, except that an idealized Gaussian-shaped pulse is used to heat the components. In addition, continuous heating of the aluminum housing has been added as a boundary condition such that the housing heats at the same rate as in the thermal radiation model described above. The inclusion of a Gaussian pulse plus aluminum housing heating simulates the actual radiation pulse plus the thermal radiation from the heated reactor core. One feature that is not included in the idealized Gaussian approach is the heating effect of delayed neutrons and gammas. Heating by the delayed radiation can be included in the model but radiation transport calculations using the time-varying radiation have not yet been performed.

There is one parameter in the calorimeter conduction model that is poorly defined; that is the contact area between the alumina support and the silicon wafer. The alumina support is filed down to a point so that the contact area is minimized. However, depending upon construction and handling, the point could be worn down so that a larger contact area exists. In order to include both possibilities, two calculations were made with a low and a moderate contact area. For both calculations a 200 microsecond Gaussian pulse heated the materials. During a pulse, the direct energy deposition results in the silicon getting the hottest, followed by aluminum, and finally alumina. After the initial direct material heating, the calculation is followed through two additional seconds allowing the materials to conduct heat to one another. In these calculations the aluminum housing heats approximately one degree in two seconds due to thermal radiation heating from the nearby reactor core.

For the low contact case, the heating profile of the materials in the silicon calorimeter is shown in Fig. 5. As seen in the radiative heating case in Fig. 4, the silicon wafer remains isolated from the other components and sustains very little cooling/heating during the two second transient.

For the case of high contact area between the silicon wafer and the alumina support, significant ($\sim$10 %) variations in the silicon wafer temperature are observed as shown in Fig. 6. The silicon wafer first cools due to contact with the cooler alumina support. The aluminum housing is continuously heated due to thermal radiation from the WSMR reactor core. This heating profile is conducted to the alumina support and subsequently to the silicon wafer, resulting in the turnaround of the silicon heating profile. The change in silicon wafer temperature is approximately 10 % cooling in the first second followed by 10 % heating in the next second.

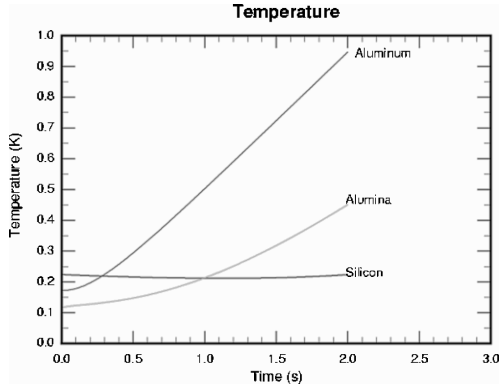

FIG. 5—*Material heating in calorimeter—low contact area.*

Measurement Circuits

The circuit used for connecting the calorimeter to the data acquisition system utilizes twisted-shielded pair cable from the thermocouple inside the calorimeter to digitizer. Referring to Fig. 7, a thermocouple connector that maintains the shield is used to connect the calorimeter to the cable system.

The cable system converts to coaxial cable within an aluminum "insertion box" located within a short distance from the digitizer. In addition to functioning as a shield, the insertion box also is an isothermal zone for the two junctions that are formed between the Type-E alloy wire and copper. During the pulse, the

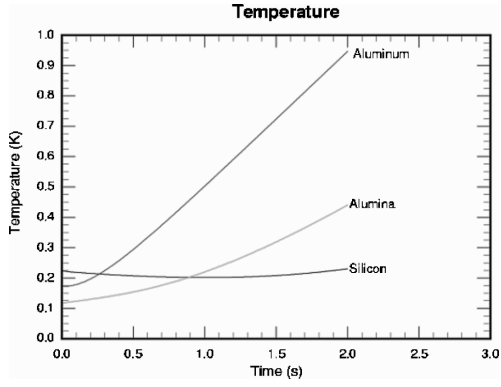

FIG. 6—*Material heating in calorimeter—high contact area.*

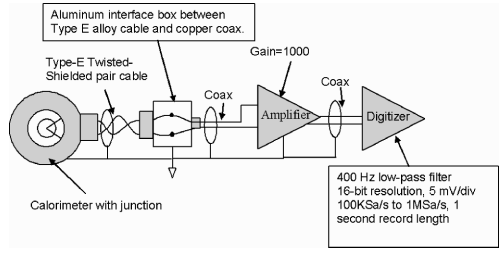

FIG. 7—*Calorimeter measurement circuit at fast burst reactor.*

isothermal zone maintains the two junctions at nominally the same temperature so the offset before and after the pulse can be subtracted with minimal error due to the additional junctions. A coaxial cable routes the signal from the insertion box to an amplifier with a gain of either 500 or 1000 depending upon the noise environment at the facility. Coax cable is used to route the signal from the amplifier to the Yokogawa 16-bit digitizer where the signal is filtered with a 400 Hz low-pass filter and then digitized at 1 mV/div.

Normalization Procedure

The silicon calorimeter must be fielded with a PCD to be able to recover dose rate information from a pulse. This is necessary since the calorimeter has noise terms from the reactor pulse that distort the result when its signal is differentiated. The PCD is a two-port device that requires a positive bias of +750 VDC on one port and the photocurrent from the other port must be terminated into a resistance either in the form of a 50 Ω terminator at the digitizer or at the input of a current amplifier with at least 1-MHz bandwidth. Coaxial cable is used to route the signal from near the reactor to the data acquisition system normally 26 m away from the reactor. To process the PCD signal, a base-lining procedure is used as described in Eq 1. In this procedure, an average of a few data points in the pre-trigger area is subtracted from the whole set of data to remove some of the leakage current in the PCD and other radiated noise signals. To more effectively baseline the PCD, it is necessary to integrate the baselined data and then examine the pre-trigger region. Normally there will be a positive slope leading up to the onset of the pulse. Performing a linear regression on a sample of this pre-trigger data will yield a slope which can then be subtracted from the previously baselined data. The baselined data should then be integrated and checked again for a nonzero slope [1].

The calorimeter signal must also be baselined by averaging a few points in the pre-trigger region and then subtracting this average from the data for the detector as in Eq 1. After baselining, the calorimeter data should be divided by the gain and then converted to temperature using a set of inverse polynomial coefficients available from the NIST website [7] for Type E thermocouples, as in Eq 2. The data should be smoothed due to unavoidable noise in the calorimeter measurement. A symmetric moving average of about 160 points has been effective but often it helps to perform an FFT on a sample of the data to ensure that the moving average spans at least a cycle of all of the major harmonic noise components. The data should then be converted to dose by using Eq 3 after selecting the most applicable silicon specific heat, c_p, for the application.

$$V_{50\ \Omega\_baselined\_data(t)=}V_{50\ \Omega}(t) - \left[\frac{\sum_{1}^{n} V_{50\ \Omega}(t)}{n}\right] \tag{1}$$

$$\Delta t_{90}[K](t) = c_0 + c_1 V^{1}_{50\ \Omega\_baselined} + \cdots + c_9 V^{9}_{50\ \Omega\_baselined} \tag{2}$$

$$[rad(Si)](t) = \Delta t_{90}[K](t) \times \left[Cp \times \frac{J}{kg \cdot K}\right] \times \left[100.019 \times \left[\frac{kg}{g}\right]\left[\frac{cal(g)}{J}\right]\left[\frac{erg}{cal(g)}\right]\left[\frac{rad}{\frac{erg}{g}}\right]\right] \tag{3}$$

Summary and Conclusions

This paper reports on the application of a silicon calorimeter, which had been developed for use in water-moderated reactors, for use at the WSMR FBR. There are limitations in the applicability of the calorimeter at the FBR due to large noise terms, so the recommended application is restricted to use after the pulsed reactor operation. Work is continuing to investigate the source of the persistent early-time noise terms with the eventual goal of being able to use the calorimeter as a real-time dosimeter for times as early as 1 ms after the peak FBR pulse.

Acknowledgments

This work was supported by the United States Department of Energy under contract DE-AC04-94AL85000. Sandia is a multiprogram laboratory operated by Sandia Corporation, a Lockheed Martin Company, for the United States Department of Energy.

References

[1] Luker, S. M., Griffin, P. J., DePriest, K. R., King, D. B., Naranjo, G. E., Suo-Anttila, A. J., and Keltner, N., "Development of a Silicon Calorimeter for Dosimetry Applications in a Water-Moderated Reactor," Sandia National Laboratories, Albuquerque, NM, submitted to ISRD12.

[2] Griffin, P. J., Kelly, J. G., and Vehar, D. W., "Updated Neutron Spectrum Characterization of SNL Reactor Environments, Vol. 1: Characterization," Sandia National Laboratories, Albuquerque, NM, SAND93-2554, April 1994.

[3] Zielenkiewicz, W. and Margas, E., *Theory of Calorimetry* Kluwer Academic Publishers, Dordrecht/Boston/London, pp. 87–88.

[4] Hemminger, W. and Hohne, G., *Calorimetry: Fundamentals and Practice* Verlag Chemie, Weinheim, Deerfield Beach, Fl, Basel.

[5] Brown, F. B. (Team Leader) and X-5 Monte Carlo Team, "MCNP—A General Monte Carlo N-Particle Transport Code, Version 5," Los Alamos National Laboratory, Los Alamos, NM, April 2003.

[6] Suo-Anttila, A., Wagner, K. C., and Greiner, M., "Analysis of Enclosure Fires Using the Isis-3D™ CFD Engineering Analysis Code," *Proceedings of ICONE12, 12th International Conference on Nuclear Engineering*, Arlington, VA, 25–29 April 2004.

[7] NIST ITS-90 coefficients for inverse polynomials are located at the following web address: http://srdata.nist.gov/its90/main/

Journal of ASTM International, Vol. 3, No. 9
Paper ID JAI100363
Available online at www.astm.org

D. A. Allen,[1] *D. A. Thornton,*[1] *A. M. Harris,*[2] *and J. W. Sterbentz*[3]

The Validity of the Use of Equivalent DIDO Nickel Dose for Graphite Dosimetry

ABSTRACT: Fast neutron dose recommendations for the graphite moderators of Magnox power plant are expressed in terms of Equivalent DIDO Nickel Dose (EDND). EDND is a calculated property that relates the damage rate in graphite at a given location to the fast neutron fluence experienced by graphite test samples irradiated in the DIDO reactor.This paper describes a study undertaken to determine the sensitivity of EDND recommendations to assumptions made in the modeling of neutron damage in graphite. These include different scattering cross sections and damage weighting functions. It is concluded that, although apparently significant differences exist between the available graphite damage response functions, their net effect is not significant in determining EDND. Therefore, confidence in past calculations has been improved and continued use of existing methods is supported.

KEYWORDS: graphite, neutron dosimetry, Monte Carlo, MCBEND, MCNP, Magnox reactors

Introduction

Equivalent DIDO Nickel Dose (EDND) is the U.K. standard unit for representing fast neutron dose to graphite. EDND is used as a correlation parameter to relate the physical properties of reactor core graphite to the measured properties of graphite samples irradiated in materials test reactors and surveillance specimen locations. EDND is a calculated property which has the units of uence (i.e., n $cm^{\bullet 2}$), but represents a damage rate calculated in units of displacements per atom (dpa).

This paper describes a study undertaken to determine the sensitivity of EDND recommendations to assumptions made in the modeling of neutron damage in graphite specimens. By recalculating EDND values using a variety of alternative neutron damage response functions, it has been possible to determine the sensitivity of EDND recommendations to the use of different scattering cross sections and graphite damage weighting functions. Three reactor locations have been chosen for these calculations, representing the broad range of irradiation environments pertinent to the Magnox graphite program:

graphite samples within the central fuel element in the DIDO reactor
graphite moderator in a Magnox reactor
graphite irradiation experiment in the Idaho National Laboratory (INL) Advanced Test Reactor (ATR)

The calculations have been performed using the Monte Carlo radiation transport codes MCBEND [1] and MCNP [2].

Equivalent DIDO Nickel Dose

The standard U.K. unit for the representation of neutron dose to reactor graphite is the Equivalent DIDO Nickel Dose (EDND). For a given location in any speci c reactor, this is de ned as the ssion equivalent uence in DIDO, which would give rise to the same amount of graphite damage in DIDO as occurs at the given location in the reactor of interest. The ssion equivalent uence is de ned relative to the $^{58}Ni(n,p)^{58}Co$ reaction. Similarly, the Equivalent DIDO Nickel Flux (EDNF) is related to the ssion

Manuscript received June 20, 2005; accepted for publication May 25, 2006; published online July 2006. Presented at ASTM Symposium on Reactor Dosimetry, 12th International Symposium on 8 13 May 2005 in Gatlinburg, TN; D. W. Vehar, D. M. Gilliam, and J. M. Adams, Guest Editors.

[1] Serco Assurance, Berkeley Centre, Berkeley, Gloucestershire, GL13 9PB, U.K.
[2] British Nuclear Group, Project Services, Olympus Business Park, Quedgeley, Gloucestershire GL2 4NG, U.K.
[3] Idaho National Laboratory, Idaho Falls, ID 83415-3885.

equivalent ux in DIDO, which produces the same rate of graphite damage in the reactor of interest. In this work, EDNF is de ned mathematically as follows:

$$\mathrm{EDNF} = \frac{\int_0^\infty \Sigma_d(E)\phi(E)dE}{\int_0^\infty \Sigma_d(E)\phi_s(E)dE \Big/ \left(\frac{1}{\langle\sigma_{\mathrm{Ni}}\rangle}\int_0^\infty \sigma_{\mathrm{Ni}}(E)\phi_s(E)dE\right)}$$

The terms in this expression are as follows:

$\phi(E)$ is the ux density spectrum in the reactor of interest

$\phi_s(E)$ is the ux density spectrum in the center of a fuel element in the center of DIDO (the standard DIDO position)

$\sigma_{\mathrm{Ni}}(E)$ is the cross section for the reaction $^{58}\mathrm{Ni(n,p)}^{58}\mathrm{Co}$

$\langle\sigma_{\mathrm{Ni}}\rangle$ is the mean cross section for the above reaction weighted by the ^{235}U ssion spectrum, and $\Sigma_d(E)$=the graphite damage function=$\Sigma_s(E)P(E)$ (where $\Sigma_s(E)$ is the carbon scattering cross section and $P(E)$ is a graphite damage weighting function)

The integral that forms the numerator of this expression is the graphite damage rate displacements per atom (dpa) per second in the reactor of interest. The rst part of the denominator is the equivalent dpa rate in the standard DIDO position, and the second part of the denominator, within the brackets, is the nickel ux at the standard DIDO position. The denominator in this expression forms the commonly used conversion factor between graphite damage in the reactor of interest and EDND. It is denoted here by D_{DIDO}. It has historically been given the standard value of 1.313×10^{-21} dpa/n cm^{-2}, based on a published spectrum from 1962 that would have used early nuclear data and methods in its evaluation.

Response Functions

This section describes the neutron response functions that have been used to recalculate D_{DIDO} and EDND data.

Graphite Damage

There are a range of graphite responses available, using a variety of scattering cross-sectional data and damage weighting functions. The following were used in this study:

(1) DAMSIG-84 [3]: based on the Thomson and Wright damage weighting function [4], and the U.K. nuclear data library (UKNDL)

(2) Genthon/JEF: a damage weighting function from [5] multiplied by the carbon scattering cross-section from the JEF2.2 library

(3) Genthon/ENDF/B-V: graphite damage weighting function as for Genthon/JEF, but multiplied by the carbon scattering cross section from the ENDF/B-V library

(4) Genthon Group Values: the graphite damage function as for Genthon/JEF and Genthon/ENDF/B-V, but using a scattering cross section of unknown origin

(5) SPECTER: a damage function proposed by Greenwood and Smither [6], using the ENDF/B-V carbon scattering cross section

By using all of these different graphite damage responses, it is possible to ascertain the sensitivity of EDND calculations to the choice of the particular damage weighting functions and scattering cross sections. The ve response functions are compared in Fig. 1. It can be seen that there are considerable differences between them at high neutron energies. However, the ssion spectrum is low in this region and these differences are not expected to be signi cant. Another observed difference is that the higher resolution functions follow the cross section resonances (Nos. 1, 2, 3), while the low resolution functions do not (Nos. 4, 5).

The most signi cant difference between these functions occurs over the energy range of greatest interest (~0.5 3 MeV). It is in this region that different values for the carbon displacement energy (E_d) used in the damage weighting functions also become signi cant. This energy is sometimes referred to as

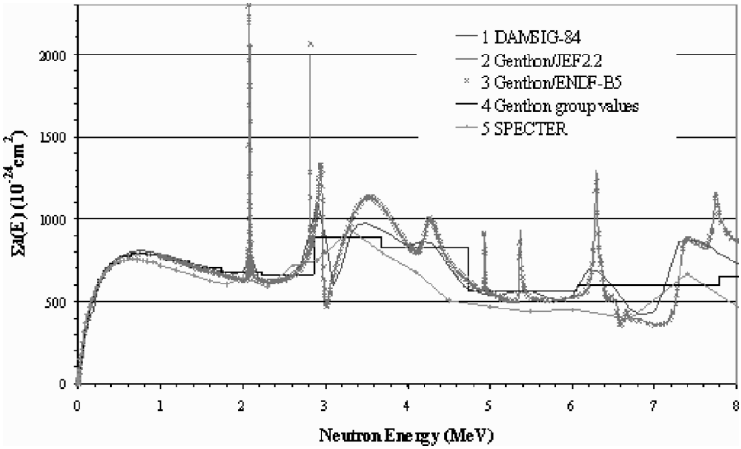

FIG. 1 *Graphite damage response functions.*

the Lindhard cutoff. Both the Thompson-Wright [4] and Genthon [5] damage weighting functions were calculated assuming E_d for carbon of 60 eV. However, the damage function proposed by Greenwood and Smither [6] assumed E_d to be 31 eV.

Nickel Activation

The value of $\langle\sigma_{Ni}\rangle$ is variously quoted in the literature as having a value between 102.8 mb, the value used in the Magnox reactor pressure vessel dosimetry program [7], and 111 mb [8]. Clearly, this value has a direct bearing on the calculated conversion factor D_{DIDO} for the evaluation of EDND. However, it is most important that the value used should be consistent with the response function $\sigma_{Ni}(E)$ used to calculate the $^{58}Ni(n,p)^{58}Co$ reaction. In this work, the cross-sectional evaluation was taken from the IRDF-90 library, as supplied with MCBEND [1], and the ssion spectrum averaged value was calculated to be 103.4 mb.

DIDO Reactor

The standard position for the de nition of EDND is de ned as within a hollow fuel element in the center of the DIDO reactor (Fig. 2: Zone 15). DIDO was a heavy water moderated materials test reactor operating at low temperature (~65°C) using enriched uranium hollow fuel elements. The fuel was uranium of variable enrichment, typically 75 % ^{235}U.

The fuel element consisted of four concentric tubes of aluminum-encased enriched uranium. These tubes were separated by heavy water coolant owing axially upwards. A core quadrant is shown schematically in Fig. 2. The fuel elements were arranged in a square array of 25 elements, but with the central row of ve elements offset by half a pitch, such that the central element was actually surrounded by six others in a slightly irregular hexagonal arrangement. Two of the nearest neighbors were centered at a distance of 15.24 cm from the central element, and the other four located at a distance of 17.04 cm away.

DIDO Model

A MCBEND model of the central fuel element was constructed representing the hollow fuel element surrounded laterally by a re ecting hexagonal boundary (Fig. 3). In effect this treats DIDO as an in nite hexagonal array of fuel elements. Since contributions to the fast neutron ux from any fuel elements beyond nearest neighbors are of much less signi cance, this modeling approximation is justi ed. Heavy water moderator was included above and below the element before absorbing boundaries de ned the edges of the model. The model of the graphite testing rig includes an aluminum thimble and pressure vessel, a

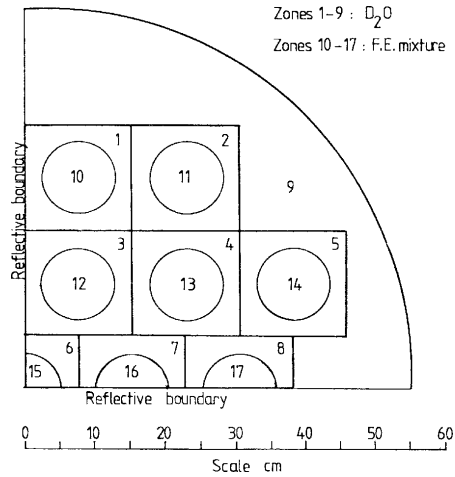

FIG. 2 *Schematic of DIDO core layout.*

stainless steel ow divider and the graphite samples, located in the center. The sample thimble was divided axially into three equal lengths. For this study, Monte Carlo scoring was within the central region.

The neutron source spectrum used in the simulation was the MCBEND default for thermal ssion in ^{235}U. Relative source strengths in the fuel tubes were taken from contemporary records.

DIDO Results

Table 1 presents the values of the ratio of *DIDO graphite damage/nickel fission equivalent flux*, or D_{DIDO}, calculated using this model with the alternative response functions and compares them with the standard value of 1.313×10^{-21} dpa/n cm^2. Uncertainties given in Table 1 are expressed at the level of one standard deviation and are due solely to Monte Carlo stochastic contributions. It is appropriate to consider only stochastic uncertainties for the comparison of these data because all aspects of the simulation are the same for each calculated response.

When compared with the standard historical value these results range from only 2.7 % less than this standard value (GENTHON/JEF2.2) to only 2.4 % greater than this standard value (DAMSIG-84). Of particular interest is the result for the SPECTER response function, which is based on a carbon displace-

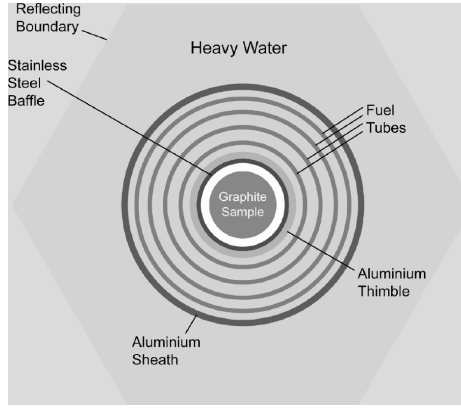

FIG. 3 *MCBEND model of DIDO central fuel element (distance across parallel faces: 17.04 cm).*

TABLE 1 *Calculated values of D_{DIDO} using different response functions.*

	Response Function	D_{DIDO} [$10^{\bullet 21}$ dpa/(n cm$^{\bullet 2}$)]	Percent Change from Standard
	Standard historical value	1.313	···
1	DAMSIG-84	1.344±0.006	+2.4±0.5
2	Genthon/JEF2.2	1.278±0.006	• 2.7±0.4
3	Genthon/ENDF/B-V	1.298±0.006	• 1.1±0.4
4	Genthon (group)	1.344±0.006	+2.4±0.5
5	SPECTER	1.308±0.006	• 0.4±0.4

ment energy (E_d) of 31 eV. This choice of a lower cutoff makes little difference to the calculation of graphite damage in DIDO, with the result being only 0.4 % less than the standard historical value, and only 0.8 % greater than the GENTHON/ENDF/B-V cross section, both based on E_d of 60 eV. Inspection of the response functions reveals that although the SPECTER data are less than the DAMSIG-84 data for much of the energy range of interest, this is compensated for at energies below ~0.3 MeV, where SPECTER data are greater.

By comparing results for GENTHON responses evaluated with JEF2.2 and ENDF/B-V carbon scattering data, it is seen that the choice of scattering cross section makes a difference of only 1.6 %.

Considering the apparently signi cant differences between the graphite damage response functions, the level of agreement observed between these results is reassuring and gives con dence that the uncertainty assigned to D_{DIDO}, due to the choice of graphite damage response function, should be no more than 3 %.

Magnox Reactor Graphite

The Magnox reactors were the rst generation of power reactors in the U.K. They are graphite moderated, carbon dioxide (CO_2) cooled systems utilizing natural uranium fuel elements clad in a magnesium alloy (magnox). The reactors contain typically between 3000 and 6000 vertical fuel channels on a square lattice of pitch of 19.685 cm (20.32 cm for the earliest plant). These usually contain seven or eight fuel elements (approximately 1 m long). In addition to fuel channels, there are interstitial channels for the insertion of control rods and absorbers used for reactor control and trimming.

Historically, EDND recommendations for the Magnox reactors have been calculated with MCBEND using the DAMSIG-84 damage response function and the standard scaling factor D_{DIDO} of 1.313 $\times 10^{\bullet 21}$ dpa/n cm$^{\bullet 2}$.

Magnox Lattice Model

The model used in this study is shown in Fig. 4 and is typical of the models used to produce EDND recommendations. The model is a two-dimensional super-cell representing the core repeat unit of 2 by 2 channels, interstitial channels, and associated moderator graphite. The two interstitial channels are located

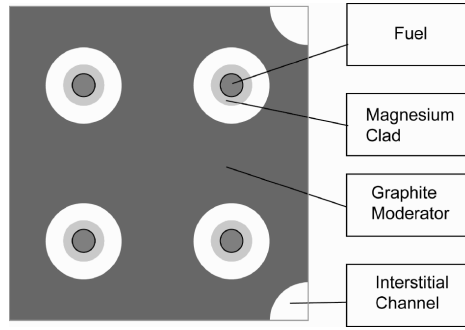

FIG. 4 *MCBEND model for Magnox reactor graphite calculations (width of cell is 19.685 cm).*

TABLE 2 *Calculated values of EDND in Magnox graphite using different response functions.*

	Response Function	D_{DIDO} [$\times 10^{-21}$ dpa/(n cm^{-2})]	EDNF ($\times 10^{12}$ n cm^{-2} s^{-1} GW^{-1})	Percent Change from Standard
	Standard value	1.313	1.75±0.02	···
1	DAMSIG-84	1.344	1.71±0.02	•2.3±1.1
2	Genthon/JEF2.2	1.278	1.66±0.02	•5.0±1.1
3	Genthon/ENDF/B-V	1.298	1.68±0.02	•3.8±1.1
4	Genthon (group)	1.344	1.71±0.02	•2.2±1.1
5	SPECTER	1.308	1.74±0.02	•0.3±1.1
	MEAN (1–5)	···	1.70±0.01	•2.9±0.7

at corners of the super-cell. The use of re ecting boundary conditions on all external surfaces implies a lattice that is effectively in nite. This is an appropriate approximation for central channels at core mid-height, which is where the highest doses occur. Graphite is at a density of 1.51 g cm^{-3}, typical of moderator conditions at mid-life.

Neutron damage rates were scored in a 9 by 9 interval scoring mesh, superimposed upon the model. The results reported are from the central mesh, located in graphite.

Magnox Results

The results for Magnox graphite are presented in Table 2, where the calculated graphite damage rates using each response function have been converted to EDNF by dividing by the conversion factor D_{DIDO}. For each damage response function in Table 2, the Magnox EDNF value was calculated using the value of D_{DIDO} (Table 1) determined using the same response function. Thus, the EDNF values given in Table 2 are derived from the consistent use of the same response functions in Magnox and DIDO. As for the DIDO results, uncertainties represent one standard deviation and are solely due to Monte Carlo stochastic contributions, which in all cases are within approximately ±1 %.

All of the alternative values are within 2.7 % of their mean value. EDNF values calculated using the SPECTER and GENTHON/ENDF/B-V differ by 3.6 %, showing there to be little sensitivity to the differences between damage weighting functions. Similarly, comparing the results for the GENTHON responses evaluated with JEF2.2 and ENDF/B-V carbon scattering data, it can be seen that the choice of scattering cross section makes a difference of only 1.2 %. Therefore, Magnox EDNF recommendations are insensitive to the choice of damage response function, and are not sensitive to changes in damage weighting function and carbon scattering cross section.

The standard value for D_{DIDO} is based on the Thompson-Wright damage weighting function and has been used, in conjunction with the DAMSIG-84 graphite damage response function, for all of the recent Magnox core dose evaluations. The continued use of this standard conversion factor and the DAMSIG-84 response function is supported by these results, which show that EDNF recommendations are insensitive to the choice of data.

The standard value shown in the table corresponds to the use of the value that would be obtained using the currently recommended data, i.e., DAMSIG-84 damage response functions in conjunction with the historical standard value for D_{DIDO} (1.313×10^{-21} dpa/n cm^{-2}). In all of the cases, the alternative EDNF is less than the standard result, but only by a maximum of 5 %. This is comparable to an uncertainty contribution of ±5 %, currently assigned to the graphite response functions. The standard result and the alternative value calculated with DAMSIG-84 differ by •2.3 % because of the small difference between the standard D_{DIDO} value and that calculated with DAMSIG-84, which is attributed to uncertainties in the original calculation of D_{DIDO}.

In calculating EDND, it is accepted that the same response function should be used for the calculation of graphite damage in both DIDO (i.e., D_{DIDO}) and the Magnox reactors. However, it is accepted that this may not always have been achieved. The results show that the discrepancies resulting from such inconsistencies are small, and would result in systematic error within the range •9.7 % to +2.9 % compared with the standard result. These gures were arrived at by recalculating the EDNF for each response function using the maximum and minimum D_{DIDO} values.

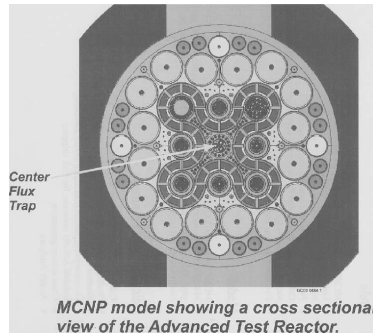

FIG. 5 *Horizontal slice through the MCNP model of ATR (center flux trap diameter is 7.47 cm).*

INL ATR Accelerated Graphite Irradiation

In 2003 BNFL (now British Nuclear Group) commissioned an experiment to irradiate samples of graphite in the Advanced Test Reactor (ATR) of the Idaho National Laboratory (INL) in the U.S.A. The ATR is a water moderated system, consisting of a serpentine fuel con guration, enclosing four peripheral lobes and one central lobe. The enclosed lobes contain facilities for irradiation of samples. Outside these lobes, hafnium control drums rotate about vertical axes in order to regulate core reactivity without perturbing the axial power distribution.

The Magnox graphite irradiation took place inside the central lobe, or center ux trap and within one of its mini in-pile tubes. Besides the graphite samples, the graphite irradiation capsules contained ux monitor wires, including iron (Fe) and niobium (Nb).

ATR Model

A detailed MCNP model of the ATR, containing a representation of the graphite irradiation capsules, was created and run by INL staff on behalf of British Nuclear Group. Figure 5 shows an image of a horizontal slice through the model. Key features such as the serpentine fuel assembly and the enclosed lobes are easily visible.

ATR Results

The model was run to calculate reaction rates of $^{54}\mathrm{Fe}(n,p)$ and $^{93}\mathrm{Nb}(n,n')$ as well as neutron damage rates (IRDF-90 data used for ^{54}Fe and ^{93}Nb reactions). The predicted reaction rates were compared with measurements performed on the ux monitors to give C/M ratios of calculation (C) to measurement (M). Axially consistent C/M values were obtained, and with mean values as follows:

$^{54}\mathrm{Fe}(n,p)$ 1.029 ± 0.045
$^{93}\mathrm{Nb}(n,n')$ 1.027 ± 0.034

Being both close to unity and mutually consistent, these C/M from energetically different reactions demonstrate that the MCNP model of the experiment predicts neutron uxes accurately and consistently across a range of energies. In particular, the niobium reaction provides a good match for the graphite damage function.

Neutron damage rates were calculated using the DAMSIG-84, Genthon-JEF, and SPECTER damage response functions. Table 3 shows the mean neutron damage rates calculated with these response functions converted to EDND using the respective D_{DIDO} values from Table 1. These are compared with the standard EDND value calculated using DAMSIG-84 in conjunction with the historical value for D_{DIDO} ($1.313 \times 10^{\bullet 21}$ dpa/n cm$^{\bullet 2}$).

As a water moderated reactor, the ATR has relatively hard neutron spectra that are very different from those of either the DIDO or Magnox reactors. Despite this, the data in Table 3 once again show that there is very little sensitivity to the use of alternative graphite damage response functions. The range of EDND values obtained is just under 7 %, comparable with the spread obtained for the Magnox reactor calcula-

TABLE 3 *Calculated values of EDND in INL ATR using different response functions.*

	Response Function	D_{DIDO} [$\times 10^{-21}$ dpa/(n cm^{-2})]	EDND ($\times 10^{12}$ n cm^{-2})	Percent Change from Standard
	Standard value	1.313	2.47±0.01	···
1	DAMSIG-84	1.344	2.41±0.01	• 2.3±0.4
2	Genthon/JEF2.2	1.278	2.57±0.01	3.9±0.4
5	SPECTER	1.308	2.55±0.01	3.1±0.4
	MEAN (1, 2, 5)	···	2.51±0.03	1.6±1.6

tion, and consistent with the uncertainty contribution of ±5 % currently assigned to damage response functions. The use of the existing standard produces results that are well placed in the center of the distribution. Hence, these results justify continued use of current practice for the calculation of EDND for this experiment.

Conclusion

An investigation has been carried out to determine the sensitivity of graphite damage predictions to the choice of damage response function. Monte Carlo radiation transport models have been used to calculate neutron dose rates in terms of Equivalent DIDO Nickel Dose (EDND) using a range of alternative graphite damage response functions. The calculations were carried out in three graphite irradiation environments of key signi cance to the Magnox graphite program. These are the original DIDO reactor, the graphite moderator of a Magnox reactor, and the accelerated irradiation carried out in the INL Advanced Test Reactor.

From the results, it has been shown that, within computational uncertainties, the alternative EDND calculations are consistent with predictions made using the established data and methods for Magnox plant. Although signi cant differences between the available graphite damage response functions are apparent, their net effect is not signi cant in determining EDND. There is very little sensitivity of EDND predictions to the choices of either graphite damage weighting function, or carbon scattering cross section.

Therefore, con dence in past calculations has been improved and continued use of existing data and methods is supported for graphite irradiation in Magnox reactors and the INL Advanced Test Reactor.

Acknowledgments

Production of this paper was supported by the U.K. Health and Safety Executive and is published with the permission of British Nuclear Group.

References

[1] Chucas, S. J., MCBEND, a Monte Carlo Program for General Radiation Transport Solutions, ANSWERS Software Service, AEA Technology, ANSWERS/MCBEND(94)15.

[2] MCNP A General Purpose Monte Carlo N-Particle Transport Code, version 4C, J. F. Briesmeister, Ed., Los Alamos Document, LA-13709-M.

[3] Zijp, W. L., Nolthenius, H. J., and Verhaag, G. C. H. M., Damage Cross-Section Library DAMSIG84, ECN Report ECN-159, NEA Data Bank NEA 0791/04, October 1984.

[4] Thompson, M. W., and Wright, S. B., A New Damage Function Predicting the Effect of Reactor Irradiation on Graphite in Different Neutron Spectra, *J. Nucl. Mater.*, Vol. 16, 1965, pp. 146 154.

[5] Genthon, J. P., Hasenclever, B. W., Mas, P., Schneider, W., Wright, S. B., and Zijp, W. L., Recommendations on the Measurement of Irradiation Received by the Structural Materials of Reactors, European Commission Report EUR 5274, 1975.

[6] Greenwood, L. R., and Smither, R. K., SPECTER: Neutron Damage Calculations for Materials Irradiations, ANL Report ANL/FPP/TM-197, January 1985.

[7] Lewis, T. A., and Thornton, D. A. A Decade of Dosimetry for Magnox Reactor Plants, *Proceedings*

of the 9th International Symposium on Reactor Dosimetry, World Scienti c, Singapore, 2003, pp. 269 277.

[8] Grundl, J. A., and Eisenhauer, C. M., Compendium of Benchmark Neutron Fields for Reactor Dosimetry, Report NBSIR 85-3151, NBS Gaithersburg, 1986.

Journal of ASTM International, Vol. 3, No. 8
Paper ID JAI13434
Available online at www.astm.org

T. E. Blue,[1] *B. Lohan,*[2] *B. Khorsandi,*[3] *and D. W. Miller*[1]

Neutron Damage in SiC Semiconductor Radiation Detectors in the GT-MHR

ABSTRACT: As a part of a U.S. Department of Energy Nuclear Engineering Research Initiative (NERI) project, we are evaluating the potential for using silicon carbide (SiC) semiconductor radiation detectors, operating in the pulse mode, as power monitors for gas turbine modular helium reactor (GT-MHR) [1]. Locations for the power monitors will be selected considering acceptable detector count rates and lifetimes. We have characterized the radiation environment at various locations in the GT-MHR, where detectors may be placed, in terms of the 1 MeV equivalent neutron flux in SiC ($\phi_{eq,1\ MeV,\ SiC}^{Total}$). Also, we have characterized the radiation field in beam part 1 (BP1) of the Ohio State University Research Reactor (OSURR) in these same terms, with the intent of correlating observed degradation of the SiC detectors in the OSURR to the degradation that can be expected for various detector locations in the GT-MHR. Comparing $\phi_{eq,1\ MeV,\ SiC}^{Total}$ for the GT-MHR and for the OSURR, we conclude that SiC devices cannot be adequately tested in the characterization vessel in OSURR BP1 for the radiation damage that would be incurred over a refueling cycle for detectors placed in-core. Also, we note that the radiation environment in the OSURR BP1 is harder than the radiation environment in the GT-MHR.

KEYWORDS: GT-MHR, displacement damage kerma factor, 1 MeV equivalent neutron fulx, MCNP

Nomenclature

Indices

mat = material
eq = equivalent

Abbreviations

GT-MHR = gas turbine modular helium reactor
OSURR = Ohio State University Research Reactor
BP1 = beam port 1
RC = reactor cavity
RCCS = reactor cavity cooling system

Greek symbols

ϕ = flux
ν = number of neutrons produced per fission

Latin symbols

H = hardness factor
E = energy
F = damage function
R = radius
$\dot{S}_n$ = neutron production rate
$\dot{d}$ = damage rate

Manuscript received June 20, 2005; accepted for publication May 17, 2006; published online June 2006. Presented at ASTM Symposium on Reactor Dosimetry, 12th International Symposium on 8–13 May 2005 in Gatlinburg, TN; D. W. Vehar, D M. Gilliam, and J. M. Admas, Guest Editors.

[1] Professor, The Ohio State University, Nuclear Engineering Program, Columbus, OH 43202.
[2] Engineer, Westinghouse Electric Company, Monroeville, PA, 15146.
[3] Graduate Student, The Ohio State University, Nuclear Engineering Program, Columbus, OH 43202.

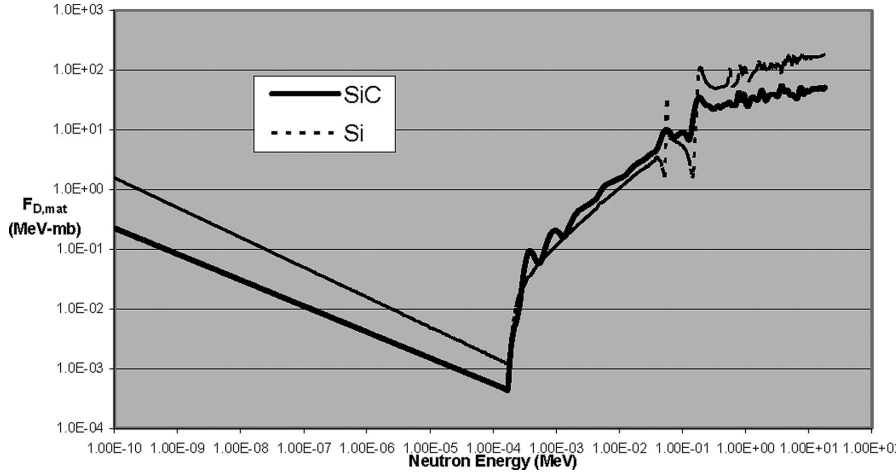

FIG. 1—*The damage functions (the displacement damage kerma factors) for Si[$F_{D,Si}(E)$] and SiC[$F_{D,SiC}(E)$]: Logarithmic scales are used for the ordinate and for the abscissa.*

Introduction

This paper describes the results of our efforts to characterize the radiation environment at various locations in the gas turbine modular helium Reactor (GT-MHR) where detectors may be placed, and in beam part 1 (BP1) of the Ohio State University Research Reactor (OSURR) in terms of $\phi^{\text{Total}}_{\text{eq,1 MeV,mat}}$ (ASTM E 722-94) [2]. Displacement damage arising from gamma-ray interactions is insignificant and is not included in our analysis. Displacement damage arising from Si and C atoms recoiling in radiative capture events is included in the displacement damage kerma factor which is discussed below.

For the purpose of predicting detector lifetime, one is interested in knowing the displacement damage rate $\dot{d}$. It can be calculated with knowledge of the energy integrated neutron flux (ϕ^{Total}) (also called the total neutron flux) and the hardness factor (H_{mat}), where

$$H_{\text{mat}} = \phi^{\text{Total}}_{\text{eq,1 meV,mat}}/\phi^{\text{Total}} \tag{1}$$

$$\phi^{\text{Total}} = \int_0^{\infty} \phi(E)dE \tag{2}$$

and the total 1 MeV equivalent neutron flux $\phi^{\text{Total}}_{\text{eq,1 MeV,mat}}$ is defined as:

$$\phi^{\text{Total}}_{\text{eq,1 meV,mat}} = \int_0^{\infty} \frac{F_{D,\text{mat}}(E)}{F_{D,1\text{ MeV,mat}}}\phi(E)dE \tag{3}$$

where $F_{D,\text{mat}}(E)$ is the damage function (the displacement damage kerma factor), which is given below in Fig. 1 for Si and SiC. In this figure, $F_{D,\text{Si}}(E)$ is from ASTM Standard 722-94. Data given by Heinisch et al. [3] was used to estimate $F_{D,\text{SiC}}(E)$, assuming the average E_d for SiC is 22 eV [4].

With a knowledge of $F_{D,1\text{ MeV,mat}}$ and $\phi^{\text{Total}}_{\text{eq,1 MeV,mat}}$, or with a knowledge of $F_{D,1\text{ MeV,mat}}$, H_{mat}, and ϕ^{Total}, one can calculate $\dot{d}$ as

$$\dot{d} = F_{D,1\text{ MeV,mat}}\phi^{\text{Total}}_{\text{eq,1 meV,mat}} = F_{D,1\text{ MeV,mat}}H_{\text{mat}}\phi^{\text{Total}} \tag{4}$$

In this paper, we present and compare values of $\phi^{\text{Total}}_{\text{eq,1 MeV,mat}}$ and H_{mat} calculated for SiC in the GT-MHR and in the OSURR BP1.

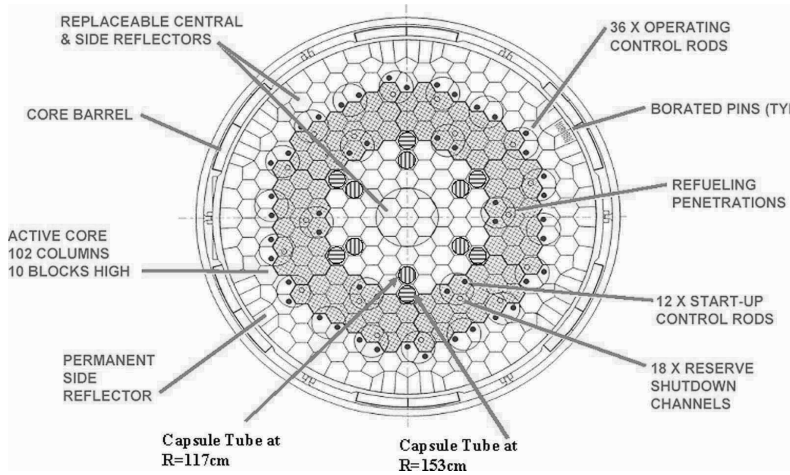

FIG. 2—*Core arrangement and the capsule tube positions. It should be noted that the capsule tubes are not in the original design of GT-MHR.*

Background

GT-MHR

This section provides background information about the GT-MHR conceptual design based on the General Atomics report submitted to U.S. Nuclear Regulatory Commission [1]. The primary components for each module are reactor vessel and power conversion vessel, connected by a cross vessel. The vessel systems are located inside an underground silo 23.9 m in diameter × 42.7 m deep, which serves as the containment structure. The reactor vessel is made of high strength alloy steel and is approximately 7.58 m in diameter and about 31.2 m high. It contains the reactor core, core supports, internal structure, reactivity control assemblies, and hot duct.

The reactor core consists of hexagonal fuel and reflector elements, plenum elements, and reactivity control material, all located inside a reactor pressure vessel. The core is designed to provide 600 MW thermal (MWth) at a power density of 6.6 MW/m^3. The active core consists of an assembly of hexagonal graphite fuel elements (blocks) containing blind holes for fuel compacts and full-length channels for helium coolant flow. Figure 2 presents a cross section of the reactor vessel. The active fuel region of the core consists of 102 fuel columns that are ten blocks high, arranged in three annular rings. Above and below the active core there are upper and lower replaceable reflectors. The reflector above the active core is composed of one and one-half layers of H-451 graphite, for a total reflector height of 1.2 m. The reflector below the core has a total height of 1.6 m. It consists of two layers: one layer of two half-height reflector elements above a layer of two half-height flow distribution and supports elements.

The active core has columns of hexagonal graphite reflector elements in the inner and outer regions. The outer side reflector is split into two rows of replaceable reflector and one row of permanent side reflector. The permanent side reflector blocks are solid except for the inclusion of boronated steel pins, which act as neutron absorber poisons. A metallic core support, the core barrel, is provided around the outside of the core assembly for lateral support. The core is cooled by helium, which flows through the outer annulus within the cross vessel, up the core inlet riser channels located between the core barrel and reactor vessel, and finally down through the core. The helium that is flowing into the reactor vessel is the working fluid in the power conversion system as well. GT-MHR operates at an elevated temperature with helium inlet temperatures of 491°C and outlet temperatures of 850°C.

The reactor vessel is surrounded by a reactor cavity cooling system (RCCS). The RCCS removes heat from the reactor vessel by radiation and natural convection from the uninsulated vessel. It also protects the

TABLE 1—*Geometrical data for MCNP GT-MHR model for in-core detector positions.*

Region number	Region	Hexagonal flat-to-flat (cm)	Inner diameter (cm)	Outer diameter (cm)	Height (cm)
1	Core	467.65	…	…	800
2	Central replaceable reflector	…	…	…	1080
	Ring 1	93.52	…	…	1080
	Ring 2	155.88	…	…	1080
	Ring 3	218.23	…	…	1080
	Ring 4	280.59	…	…	1080
3	Side reflector	…	…	617.6	1080
4	Upper replaceable reflector	…	…	484.0	120
5	Lower replaceable reflector	…	…	484.0	160
6	Permanent side reflector	…	617.6	671.0	1080
7	Permanent side reflector with boron carbide pins	…	671.0	682.0	1080
8	Core barrel	…	682.0	693.0	1080
9	He	…	693.0	720.0	1080
10	Gas duct shell	…	704.5	708.5	1080
11	Reactor vessel	…	720.0	758.0	1080
11	Reactor vessel flange	…	720.0	854.0	100
12	Reactor cavity	…	758.0	1180.0	1080
13	RCCS wall	…	1180.0	1212	1080
15	Cavity liner	…	1280.0	1281.2	1080
16	Concrete	…	1281.2	1341.2	1080
17	Capsule—inner tube	…	3.89	4.22	1080
18	Capsule—outer tube	…	6.66	8.89	1080
20	Porous carbon	…	9.70	14.90	1080

concrete wall of the reactor cavity from exceeding design temperature limits for all modes of operation. The RCCS includes a cooling panel placed around the reactor vessel. Heat is removed from the reactor cavity by natural circulation of outside air through the RCCS cooling panels.

Methods

MCNP Computer Model

A model for the GT-MHR in-core detectors within capsule tubes (henceforth called simply "capsules") in the central reflector was designed using MCNP [4] version 4C. The computer model consists of a geometric representation of the GT-MHR core, reactor vessel, capsule, cavity, and RCCS. The model includes a particle specific source term, neutron and photon tallies, and variance reduction techniques to allow for accurate as well as timely results. The model was run on UNIX based computer systems.

The GT-MHR reactor geometry is defined in MCNP using a series of vertical surfaces and horizontal planes. Consequently, all the regions of the reactor have finite length. Table 1 presents the geometrical data for the all regions of the in-core detector model.

The central reflector (2) consists of graphite hexagonal elements, with a distance between flats of 46.76 cm (the distance between two opposite sides of the hexagon), that occupy the central region of the reactor. The central reflector's hexagonal shape allows six locations for the placement of the capsules. We have considered placing the capsules within the central reflector at 0, 60, 120, 180, 240, and 300 deg, as shown in Fig. 2. Moreover, we have considered placing the capsules at two different radii, first at $R = 153$ cm and second at $R = 117$ cm.

Figure 3 presents transverse and lateral cross sections of the MCNP GT-MHR in-core model. The model is described below outwardly from the center of the core.

The fueled region of the GT-MHR core (1) was defined as existing between the boundaries of two hexagons. The inner hexagon has a distance between flats of 280.592 cm and the outer hexagon has a distance between flats of 467.724 cm. Moreover, six prismatic elements of the outer side reflector (3) are inserted into the active core in order to match as closely as possible the real geometry. The active core

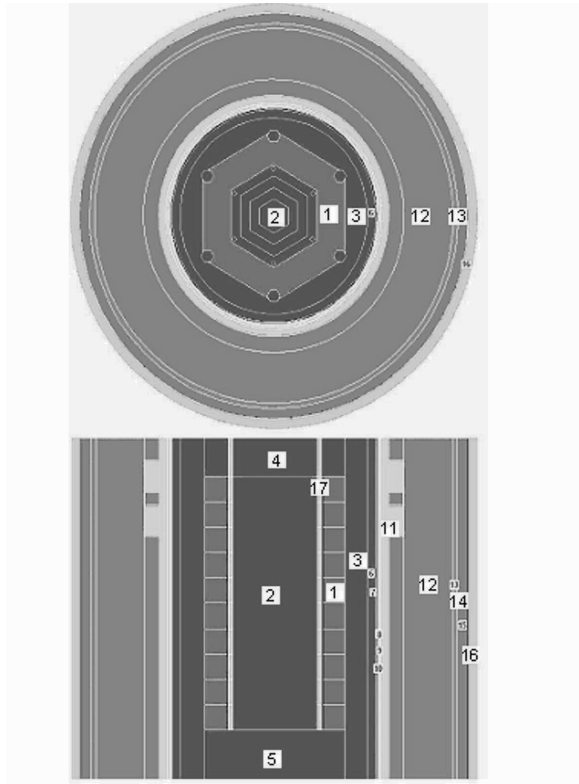

Legend

1. Core	5. Lower Ref.	10. Gas Duct Shell	14. Air RCCS
2. Central Ref.	6. Permanent Ref.	11. Reactor Vessel	15. Cavity Liner
3. Side Ref.	7. Boron Pins	12. Reactor Cavity	16. Concrete
4. Upper Ref.	8. Core Barrel	13. RCCS	17. Capsule Tube

FIG. 3—*Cross section of the MCNP GT-MHR model for in-core detector positions.*

volume was divided into ten axial layers according to height of the hexagonal graphite fuel elements of which the core is composed. As can be seen in Fig. 3, above and below the core, there are, respectively, an upper replaceable reflector (4) and a lower replaceable reflector (5). The height of the upper reflector is one and one-half blocks (120 cm), and the height of the lower reflector is two blocks (160 cm). The active core volume is surrounded radially by the outer side replaceable reflector (3). The outer side replaceable reflector is surrounded by an annular region, which defines the permanent side reflector (6). The permanent side reflector is surrounded by a region which contains the boron carbide pins (7). The region of boron carbide pins is surrounded by the core barrel (8). Outboard of the core barrel, between the outer surface of the core barrel and the inner surface of the reactor vessel, there are two annular regions with helium (9), divided by a gas duct shell (10). An annular region defines the reactor vessel wall (11). Outboard of this annular region, two ring regions define the reactor vessel flanges. Between the reactor vessel and the RCCS there are cells filled with air (12). The RCCS panel (13), cavity liner (15), and concrete wall (16) were modeled in detail as a part of an ex-core detector model. The detailed description of those elements of the model is not relevant for calculations for detector locations within the core, so, for this reason, we

will not discuss them further. A sphere with a radius of 900 cm surrounds the MCNP GT-MHR in-core model. This sphere defines the "universe" for the Monte Carlo calculation. Particles transported outside of this sphere are ignored.

Material Cards and Cross-Section Libraries for GT-MHR

The material composition for each the structural elements that are listed in the legend was defined in the MCNP model as a homogenous mixture for a core completely loaded with fresh fuel. The homogenization of the fuel and binder in the core was judged to be adequate for our calculations, since, as described below, the source was defined with an axial power profile that was generated using a more detailed model geometry. The cross-section libraries used to perform the computations are based on the Evaluated Nuclear Data Files ENDF/B-VI. For carbon, the neutron scattering $S(\alpha,\beta)$ thermal treatment was taken into account. Furthermore, for each cell in the model, the temperature was indicated in order to take into account the Doppler effect. For the MCNP GT-MHR model, the neutron multiplication by fission was turned off by setting a "nonu" card to zero for all cells in the model.

Characteristics of the Neutron Source for GT-MHR

In the GT-MHR model, the source was defined in active core cells. The source was assigned an axial probability distribution function, based upon the power in ten core vertical cells. The relative probability of a source neutron being emitted from a cell was proportional to the cells contribution to the axial power profile. Each source within a cell was modeled as an isotropic neutron source uniformly distributed within the cell. The energy distribution of source neutrons was sampled using the watt neutron spectrum for U-235.

The neutron production rate ($\dot{S}_n$) was used to calculate the absolute neutron flux based on the flux per source particle that MCNP yields. The neutron production rate was calculated based on the thermal power of the core, which was assumed to be 600 MWth, the average fission neutron energy that is converted into thermal energy (E_f), which was assumed to be 190 MeV, and the number of neutrons produced per fission (ν), which was assumed to be 2.43.

Particle Tallies for GT-MHR Models

Tally number four yields the flux averaged over a volume and normalized on a per source particle basis. For the in-core detector model, tally number four was chosen to provide neutron flux values in ten cells in the capsule. The heights of the tally volumes correspond to the lengths of the corresponding fuel blocks. The neutron flux tally output was split into 101 energy bin groups plus one bin for the total flux. Thus, for an individual cell it is possible to determine the neutron flux energy spectrum.

Tally number two yields the flux, averaged over a surface and normalized to the number of source particles

The variance reduction techniques that were applied are geometrical splitting and energy splitting. For the detector tallies, the MCNP cases were run until the errors in the total fluence were smaller than 5 %.

Results

As an example of the results that were obtained, Fig. 4 shows the neutron energy spectra (neutron flux per MeV) for both in-core positions $R=153$ cm and $R=117$ cm, at $Z=320$ cm. For $R=153$ cm the neutron flux energy spectra is shown within the capsule and in the absence of the capsule. As can be seen, the presence of the capsule causes the thermal neutron flux to be smaller within the capsule than it is without the capsule, due to the absorption of thermal neutrons in the capsule wall.

Results similar to those shown in Fig. 4 were obtained at other in-core locations. The spectra that were obtained were processed using Eqs 1–3 to obtain $\phi^{\text{Total}}_{\text{eq,1 MeV,SiC}}$ and H_{SiC}.

Figure 5 presents a graph of $\phi^{\text{Total}}_{\text{eq,1 MeV,SiC}}$ for two in-core radii (117 cm and 153 cm) and three axial positions for the GT-MHR reactor core. Figure 6 presents H_{SiC} versus axial layer, with radius as a parameter, for the same detector positions as for Fig. 5. For purposes of comparison, $\phi^{\text{Total}}_{\text{eq,1 MeV,SiC}}$ and H_{SiC}

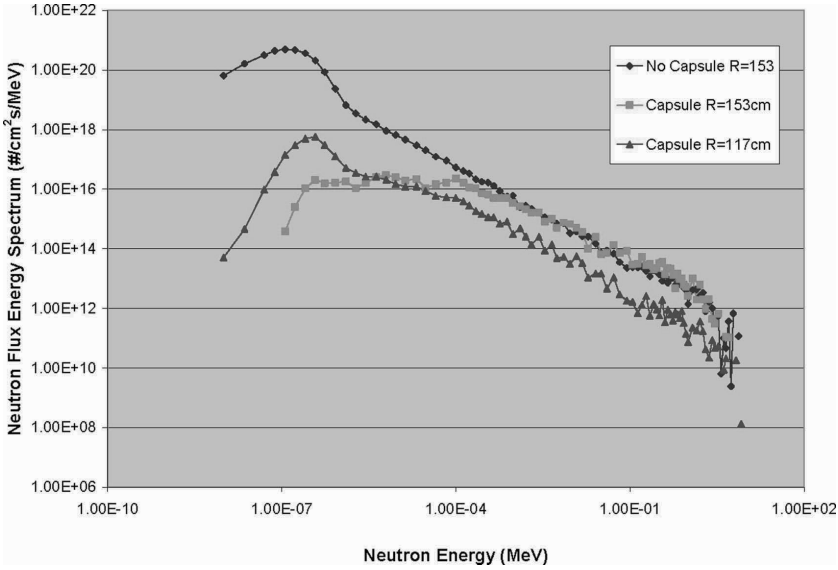

FIG. 4—*Neutron flux energy spectra for in-core positions at R = 153 cm and Z = 320 cm (with and without the capsule), R = 117 cm and Z = 320 cm, for full power operation (P = 600 MWth).*

are presented in these figures for ex-core locations at the indicated radii in the RC (Region 12 in Fig. 3) and in the RCCS air (Region 14 in Fig. 3).

For purposes of comparison, $\phi^{\text{Total}}_{\text{eq,1 MeV,SiC}}$ were calculated in the manner described above for Position 4 in the semiconductor device characterization vessel in Beam Port 1 (BP1) of the OSURR. The values of $\phi(E)$ that were used in the calculations were determined using foil activation data and the SAND-II neutron energy spectrum deconvolution code. The results of the calculations are $\phi^{\text{Total}}_{\text{eq,1 MeV,SiC}} = 7.20 \times 10^{11}$ neutrons cm^{-2} s^{-1} for operation at 500 kW (nominal full power). Also, $H_{\text{SiC}} = 0.66$

In conclusion, it can be seen by comparing the values of $\phi^{\text{Total}}_{\text{eq,1 MeV,SiC}}$ and H_{SiC} for the GT-MHR with the value of $\phi^{\text{Total}}_{\text{eq,1MeV,SiC}}$ and H_{SiC} for the OSURR, that SiC devices cannot be adequately tested in the

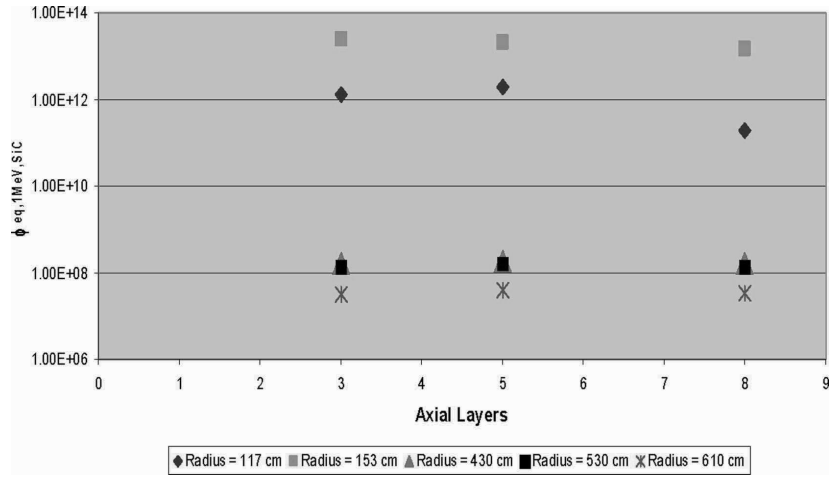

FIG. 5—$\phi^{Total}_{eq,1\ MeV,SiC}$ *versus reactor layer, with radii as a parameter, for five in-core radii.*

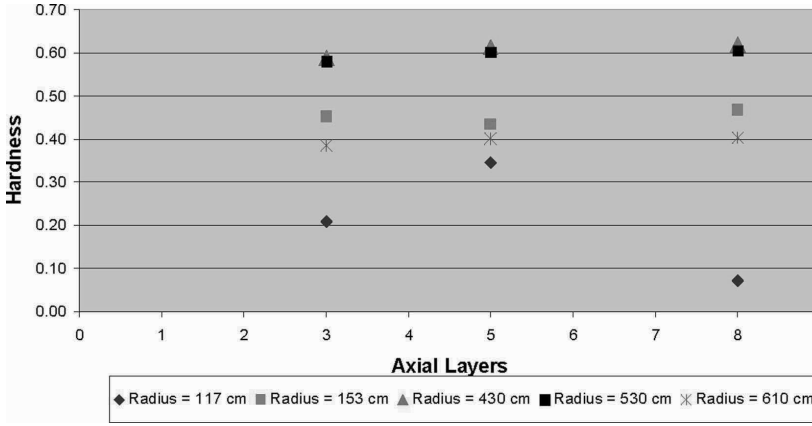

FIG. 6—*Hardness plot for five in-core radii as a function of reactor axial layer.*

characterization vessel in BP1 of the OSURR, for the radiation damage that would be incurred over a refueling cycle, for detectors located in core in the GT-MHR. Although the differences in the radiation hardness, between the characterization vessel in BP1 of the OSURR and the GT-MHR for in-core locations, can be compensated for by simply irradiating the devices to equal 1 MeV equivalent neutron fluence ($\Phi^{\text{Total}}_{\text{eq.,1 MeV,SiC}}$); equal ($\Phi^{\text{Total}}_{\text{eq.,1 MeV,SiC}}$) cannot be practically attained in a reasonable time, since the OSURR is run only upon demand (which is on average a small fraction of a working day) and not often at full power. An analysis of ex-core locations is underway.

Acknowledgments

This material is based upon work supported by the U.S. Department of Energy under the NERI program Award No. DE-FG-07-02SF22620 and NERI Project Number 02-207. Any opinions, findings, and conclusions or recommendations expressed in this material are those of the authors and do not necessarily reflect the views of the Department of Energy.

References

[1] General Atomics, "Gas Turbine-Modular Helium Reactor (GT-MHR) Conceptual Design Description Report," Project No. 7658 1996.

[2] ASTM, Standard E 722-94, "Standard Practice for Characterization Neutron Energy Fluence Spectra in Terms of an Equivalent Monoenergetic Neutron Fluence for Radiation-Hardness Testing of Electronics," *Annual Book of ASTM Standards*, Vol. 12.02, ASTM International, West Conshohocken, PA, pp. 318–333.

[3] Heinisch, H. L., Greenwood, L. R., Weber, W. J., and Williford, R. E., "Displacement Damage in Silicon Carbide Irradiated in Fission Reactors," *J. Nucl. Mater.*, Vol. 327, 2004, pp. 175–181.

[4] Devanathan, R., Weber, W. J., and Gao, F., "Atomic Scale Simulation of Defect Production in Irradiated 3C-SiC," *J. Appl. Phys.*, Vol. 90, No. 5, 2001, pp. 2303–2309.

[5] Briesmeister, J. F. ed., "MCNP-A General Monte Carlo N-Particle Transport Code, Version 4C," Los Alamos National Laboratory Report No. LA-13709, 2000.

Journal of ASTM International, Vol. 3, No. 6
Paper ID JAI13437
Available online at www.astm.org

V. A. Nikolaenko,[1] *S. M. Zaritsky,*[1] *and I. V. Bachuchin*[1]

Evaluation of Diamond Detectors for Fast Neutron Fluence Measurements in WWER-1000 Surveillance Assemblies

ABSTRACT: The commonly used method of WWER-1000 surveillance dosimetry is based on the measurement of ^{54}Mn absolute activity in the material of surveillance specimens. Special procedures are necessary for the determination of the spectral index for each specimen, which depends on surveillance assembly orientation in the reactor during the irradiation period, and for fluence extrapolation beyond several ^{54}Mn half-life periods taking into account the detailed local power history in the core periphery. The application of the diamond detectors technique is proposed as an alternative method of fast neutron fluence determination. These detectors are located in the surveillance containers as irradiation temperature monitors. The diamond lattice extends under the influence of neutron irradiation, and it allows the fluence measurements after corresponding calibration. The calibration of diamond detectors was carried out using fluence data for 123 surveillance containers irradiated in different WWER-1000 reactors for different fluences. Some results of fluence measurements carried out by two methods are compared.

KEYWORDS: WWER-1000, surveillance specimens, fast neutron dosimetry, manganese-54, activity, diamond detectors, diamond lattice extension

Introduction

Surveillance assemblies are located in the reactors WWER-1000 on the baffle, over the upper boundary of the core (Fig. 1). There are six sets of surveillance assemblies and every set contains five two-level assemblies (Fig. 2), six cylindrical containers with Charpy specimens on each level (Fig. 3), and two Charpy specimens in each container (Fig. 4).

Some features of the WWER-1000 surveillance program (the location of specimens in the region of high neutron field gradient, sufficient distinctions of neutron spectra on different specimens and pressure vessel etc.) and concerned dosimetry problems and difficulties were discussed in [1]. In particular, it was shown, that more accurate fluence determination of WWER-1000 surveillance specimens can lead to significant changes in an evaluation of radiation embrittlement of reactor pressure vessel materials.

That is why the problem of WWER-1000 reliable and accurate surveillance program dosimetry is very important and alternative methods of surveillance dosimetry are very desirable.

"Manganese" Method of Surveillance Dosimetry

Fast neutron fluence ($E>0.5$ MeV) received by each WWER-1000 surveillance specimen is usually determined by means of direct measurement of ^{54}Mn absolute activity in the material of specimen (in the region of surveillance specimen notch) before mechanical tests.

The effective threshold energy of the $^{54}\mathrm{Fe}(n,p)^{54}\mathrm{Mn}$ reaction is approximately 3 MeV. To obtain fluence of neutrons with $E>0.5$ MeV a spectral index (ratio of integral neutron flux densities for $E>0.5$ and $E>3.0$ MeV) should be calculated with necessary precision for every specimen position.

Due to high neutron field gradients at surveillance assemblies locations the spectral index for a given specimen depends on a surveillance assembly position and orientation. The core-referenced orientation of a surveillance assembly should be evaluated considering the measured specimens activities and local

Manuscript received June 20, 2005; accepted for publication April 19, 2006; published online May 2006. Presented at ASTM Symposium on Reactor Dosimetry, 12th International Symposium on 8–23 May 2005 in Gatlinburg, TN; D. W. Vehar, D. M. Gilliam, and J. M. Adams, Guest Editors.

[1] Head of Group, Head of Department, and Staff Scientist, respectively, Russian Research Center Kurchatov Institute, 123182 Moscow, Russia.

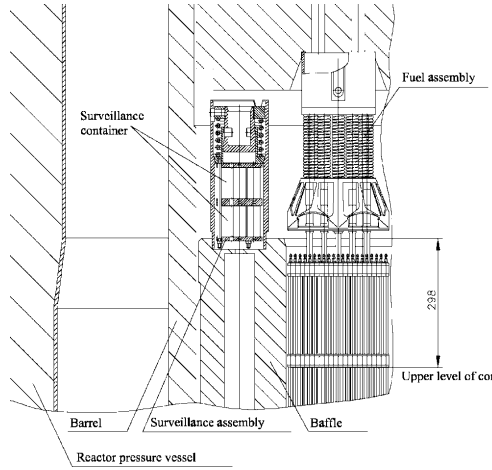

FIG. 1—*Location of surveillance assembly in the reactor WWER-1000.*

power distribution in the nearest fuel assemblies, e.g., comparing the experimental and calculated ^{54}Mn activities accumulated in specimen material during the last years of irradiation.

The half-life of ^{54}Mn is equal to 312 days, and this method determines the specimen fluence only for about the last three years of specimen irradiation. After a few years of irradiation, the activity of ^{54}Mn in a specimen material reaches saturation and does not depend on fluence thereafter. Some extrapolation is necessary to evaluate fluence beyond this period. The analysis showed that it is highly required in this case to take into account the detailed (pin-by-pin) local power distribution and its history in the upper parts of the fuel assemblies nearest to the surveillance assembly under consideration [2].

This local power history can be rather complicated due to cycle-by-cycle changes of core periphery pattern and control rods movement. Figure 5 demonstrates the core patterns in the tenth and eleventh fuel cycles of the Balakovo-1 WWER-1000. One can see that environment and irradiation conditions of surveillance assemblies (power of adjacent fuel assemblies and neutron flux distribution) can be significantly different in different fuel cycles during the irradiation period.

Thus, the routine method of fluence determination is rather complicated and it would be desirable to consider any alternative in order to check the routine method and guarantee the necessary reliability of WWER-1000 surveillance dosimetry. It would be very desirable to utilize some integrating-type detector

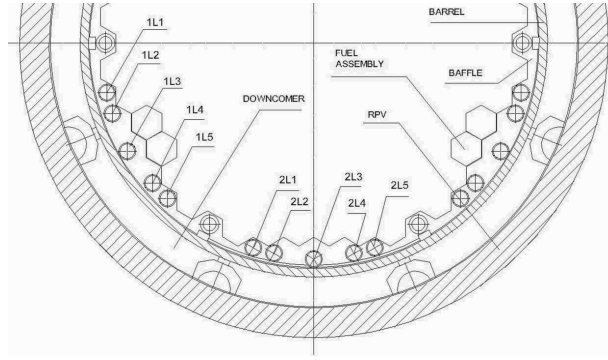

FIG. 2—*Location of surveillance assemblies sets on the baffle of WWER-1000. First two sets of surveillance assemblies are enumerated. Total number of sets is equal to 6.*

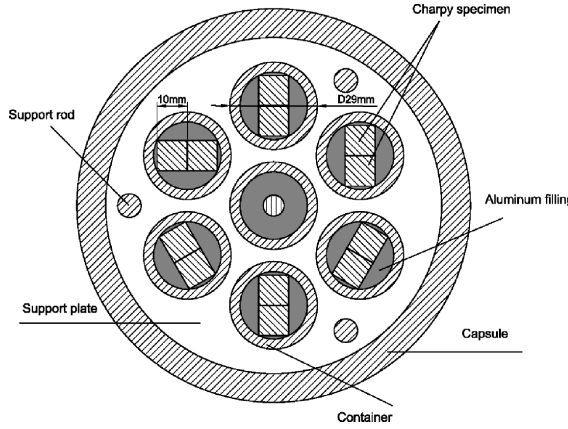

FIG. 3—*Distribution of surveillance containers in surveillance assembly.*

saturated at very high fluence values and — as a result — to develop an extrapolation-free method of fluence determination.

Using the Diamond Detectors

The diamond detectors, which are located inside surveillance containers (see Fig. 4) as irradiation temperature monitors [3], can give another opportunity for neutron fluence measurements [4–6].

Our goal is to evaluate the possible use of these standard diamond temperature monitors, which are inserted in each WWER-1000 surveillance assembly, for fluence measurements also. Therefore, do not consider in this paper any other options, such as SiC or $\alpha - Al_2O_3$ detectors [7].

The standard diamond temperature monitor is an aluminum capsule of 3 mm diameter and 10 mm length filled by a few milligrams of natural diamond powder with a fraction size of 14–20 μm. Neutron irradiation causes an extension of a diamond crystal lattice, and this extension ($\Delta V/V$) can be measured easily by x-ray diffractometry. The uncertainty of this method of $\Delta V/V$ measurements is defined by expression $\Delta\theta \operatorname{ctg}\theta$, where θ is the angle of x-ray reflection. Therefore, we do not consider there is no problem to achieve the absolute $\Delta V/V$ uncertainty value ±0.01 % at 0.99 confidence level using high ($\sim 80°$) angles of x-ray detection.

Thus, diamond detectors could be used for neutron fluence measurement after corresponding calibration. Diamond integrates fluence over a long period of irradiation, and there is no need for information concerning local power history and for any extrapolation.

Diamond lattice extension depends also on an irradiation temperature; hence detector temperature constancy in all specimens for the whole irradiation period is important for diamond technique. Recent

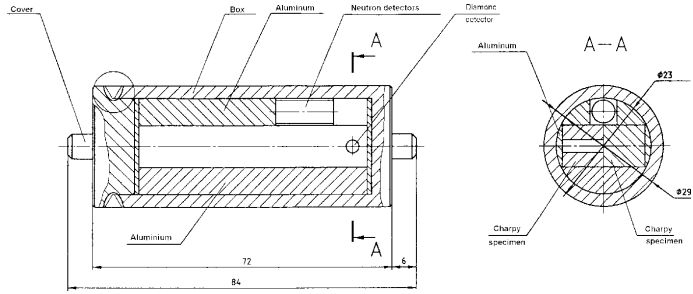

FIG. 4—*WWER-1000 surveillance container.*

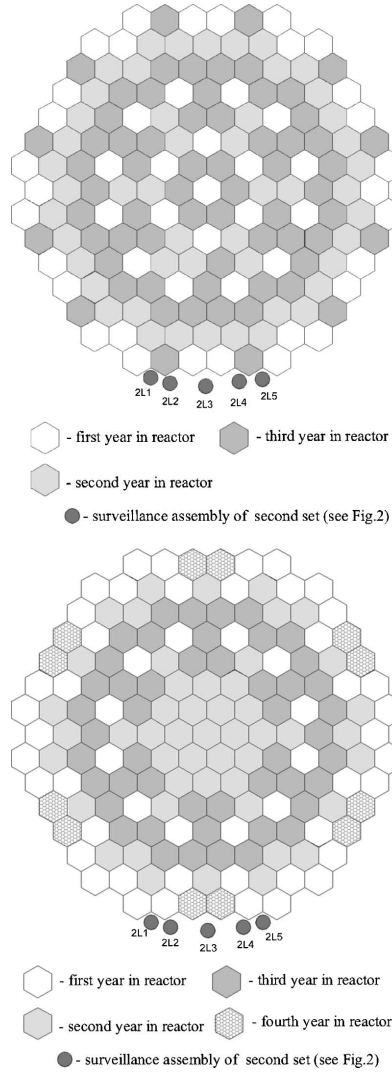

FIG. 5—*Core patterns of Balakovo-1 WWER-1000 reactor. (a) in the tenth fuel cycle, (b) in the eleventh fuel cycle.*

experiments [2] showed that WWER-1000 surveillance specimens temperature is practically stable at approximately 300°C in all surveillance containers. The tight fit of the detector capsule in the inlet (see Fig. 4) ensures good thermal contact between detector capsule and specimen and temperature equality of the both.

Another issue is a diamond amorphization. Having been irradiated up to certain fluence, diamond structure becomes amorphous and the Bragg's reflection peaks are no longer revealed on the difractogram. The value of fluence, which is necessary to provoke a diamond amorphization, increases with diamond irradiation temperature increasing. It follows from [8–10] that for irradiation temperature and neutron flux, typical for WWER-1000 surveillance specimens, the irradiation time, needed for diamond amorphization to start, is much more than the reactor pressure vessel operation time.

Diamond detectors were calibrated using the most reliable fluence (above 0.5 MeV) values obtained by "manganese" method for surveillance specimens of several WWER-1000 units. The surveillance assemblies irradiated up to 8.8 years in different WWER-1000 units were considered for primary analysis (the more irradiation time the less reliable is fluence determination by the "manganese" method). Certain assemblies were excluded from consideration for following reasons: some assemblies had only upper level of surveillance containers, some diamond monitors missed during surveillance specimens unloading and tests, some containers were not equipped with diamond monitors. Only assemblies with full set of diamond monitors were considered (i.e., with diamond monitor in each surveillance container on both levels). Experimental data ("manganese" fluence) for those assemblies were statistically treated and after rejection of unreliable data the set of fluence values for 123 surveillance containers was selected for calibration of diamond detectors irradiated in the same containers.

The whole selected set can be used to determine the unified calibration curve because the diamond lattice extension depends on the "manganese" fluence in the same way for different surveillance assemblies. This fact follows from the experiment in the Balakovo-1 WWER-1000 [2], where two experimental surveillance assemblies L1 and L3 [see Figs. 2 and 5(*a*)] with diamond and different activation detectors were irradiated during one fuel cycle. It was shown in this experiment that a dependence of diamond lattice extension on fluence has the same character for different assemblies and different levels inside them. The azimuthal (container-by-container) distribution of neutron flux inside assembly was shown to be proportional to $\sin\alpha$, where α is the azimuthal coordinate of the container on the upper or lower level in the assembly (see Fig. 3).

The form of calibration curve was chosen starting from the physical model of diamond radiation damaging:

$$(\Delta V/V) = A \cdot [1 - \exp(-B\Phi)] \tag{1}$$

where $\Delta V/V$ is the diamond lattice extension, Φ is the neutron fluence, A and B are coefficients to be determined in calibration.

This form of calibration curve was chosen taking into account the saturation of diamond lattice extension at fluence increasing (the relative volume change of diamond lattice decreases due to radiation annealing). The saturation depends on irradiation temperature and decreases with temperature increasing: the saturation $\Delta V/V$ value is equal to 4.1 % at the irradiation temperature 100°C and 2.5 % at 270°C [11]. There are no experimental data on $\Delta V/V$ saturation value at 300°C, so we use at this temperature the value 2.4 % obtained by extrapolation of the above-mentioned data.

The coefficients A and B in formula (1) were determined using the mentioned set of 123 fluence values and corresponding $\Delta V/V$ in the region below 1.25 % and the saturation value of the lattice extension at the irradiation temperature 300°C. Finally, fluence versus $\Delta V/V$ dependence was derived from the formula (1):

$$\Phi = -57 \ln[1 - 0.417(\Delta V/V)] \times 10^{18}\ \mathrm{cm}^{-2}. \tag{2}$$

Analysis of the inaccuracies distribution shows that the relative uncertainty of the fluence determination with calibrated diamond detectors is close to 6 % (0.95 confidence level) with the exception of "small" and "large" $\Delta V/V$ regions. At $\Delta V/V < 0.2$ % the absolute uncertainty of $\Delta V/V$ determination is comparable with absolute $\Delta V/V$ values and the relative uncertainty of the fluence increases. The relative uncertainty increases also at $\Delta V/V$ close to the saturation value 2.4 %, where the derivative $\mathrm{d}\Phi/\mathrm{d}(\Delta V/V)$ significantly increases.

The curve (2) is shown in Fig. 6 (the solid line), and the distribution of the fluence relative uncertainty is also included (the dotted line). The limits of reasonable application of the diamond technique (region of the diamond lattice extension between 0.2 % and 2.3 %) are also shown.

Thus, formula (2) allows to determine neutron fluence above 0.5 MeV at diamond lattice extension $\Delta V/V$ interval ~(0.2–2.3) % with relative uncertainty ~6 % at confidence level 0.95. This extension interval is sufficiently enough for fluence measurements for the whole surveillance specimens irradiation time, which corresponds to the designed reactor pressure vessel lifetime.

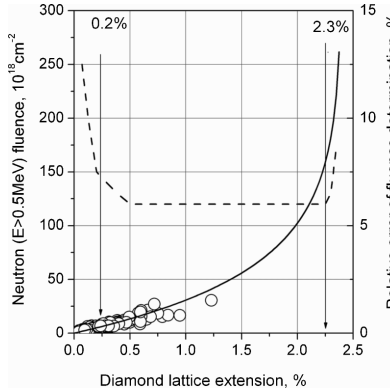

FIG. 6—*Calibration curve for diamond detectors.*

Comparison of Two Methods of Fluence Determination

The examples of comparison of the described neutron fluence determination methods — by measurement of ^{54}Mn activity and diamond lattice extension – are shown in Fig. 7. The data in Fig. 7 were chosen in order to illustrate different possible relationships between "manganese" and "diamond" fluences, and these data should not be considered as demonstration of any systematic dependencies. As one should expect, maximum disagreement takes place for long irradiation time, when the influence of irregular surveillance irradiation history increases.

Data for assembly 1L1 of the first set of surveillance assemblies taken out after 3.3 effective years of Zaporozhie-1 WWER-1000 operation, are shown in Fig. 7(*a*), data for assembly 2L1 of Kalinin-1 second set (8.1 effective years of operation) are in Fig. 7(*b*), and data for assembly 1L1 of South Ukraina-1 first set (8.8 effective years) are in Fig. 7(*c*). Each assembly contains 12 surveillance containers: six containers on each level. Two Charpy specimens are located notch-to-notch in each container, and fluence was determined in the notch region of each specimen by measuring the ^{54}Mn activity; i.e., 24 measurements in each assembly were done. Only one diamond detector is located in each surveillance container, and the fluence is measured by diamond detector using calibration curve (2) in the notch region of the specimen equipped with diamond. "Diamond" fluence in the other specimen was determined taking into account the symmetry of fluences in the adjacent specimens relating to the above-mentioned curve $\sin\alpha$, which was established experimentally [2,5].

One can see that for short irradiation, results of both methods are in satisfactory agreement: the average discrepancy is less than 6 %. In this case the "manganese" method works well, because manganese activity has not reached saturation and no fluence extrapolation is needed.

Other situation takes place for longer irradiation (8–9 effective years). In case of Kalinin-1 WWER-1000 "manganese" fluences are significantly less (42 % in average) than "diamond" ones. In case of South Ukraina-1 WWER-1000 the "manganese" fluences are 65 % higher (in average) than the "diamond" ones. For both levels of the assemblies the "diamond" fluence data shift towards the same direction (upward for Kalinin-1 and downward for South Ukraina-1).

Perhaps it is a consequence of local power changes (in core region nearest to surveillance assemblies) at early period of reactor operation that cannot be taken into consideration by "manganese" method.

Conclusions

Our experience shows that diamond detectors can be applied as useful alternative tool for improvement of WWER-1000 surveillance specimens dosimetry.

Information concerning global and local irradiation (fuel cycle) histories is not necessary when diamond detectors are applied. These detectors can be used as the "integrating-type" devices for neutron

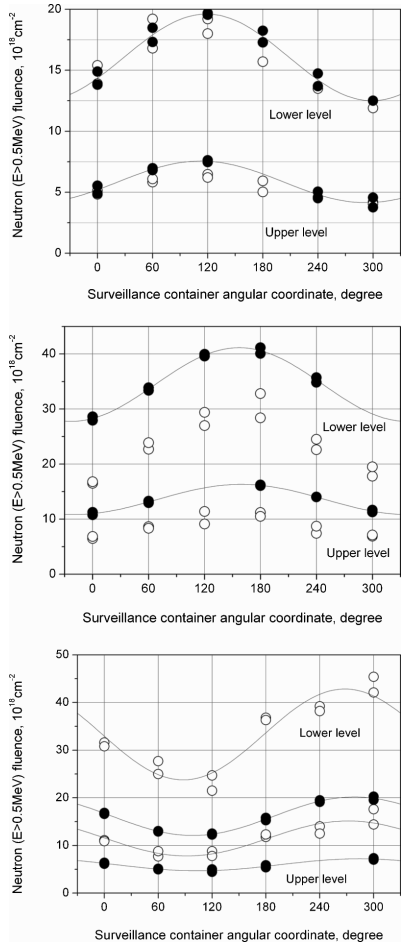

FIG. 7—*Neutron ($E > 0.5$ MeV) fluence on the notch region of Charpy specimens volume. (a) Surveillance assembly 1L1 of Zaporozhie-1 (3.3 effective years of operation). (b) Surveillance assembly 2L1 of Kalinin-1 (8.1 effective years of operation). (c) Surveillance assembly 1L1 of South Ukraina-1 (8.8 effective years of operation).* ∘ *– Manganese,* • *– Diamond.*

fluence determination for long periods of surveillance specimens irradiation corresponding to pressure vessel lifetime.

Thus, diamond detectors are promising, but further investigation is required, e.g., comparison of diamond and activation detectors for a long irradiation with a well-known irradiation history and temperature control (or for relatively short irradiation at high level of neutron flux).

Acknowledgments

Authors express their sincere gratitude to Dr. Yu. A. Nikolaev for discussions and support and Dr. T. S. Zaritskaya for valuable help in the report preparation.

References

[1] Zaritsky, S. M., Platonov, P. A., Nikolaev, Yu. A., Ošmera, B., and Valenta, V., "Review of Problems and Requirements in VVER Reactor-Type Pressure Vessel Dosimetry," *Reactor Dosimetry, ASTM STP 1398*, J. G. Williams, D. W. Vehar, F. H. Ruddy, and D. M. Gilliam, Eds., ASTM International, West Conshohocken, PA, 2001, pp. 53–60.

[2] Gérard, R., Karzov, G., Margolin, B., Shtrombakh, J., Zaritsky, S., Vasiliev, V., Langer, R., and Van Walle, E., "Main Achievements of the TACIS R2.06/96 Project: Surveillance Program for VVER 1000 Reactor Pressure Vessels," *Fontevraud 5 Symposium "Contribution of Materials Investigation to the Resolution of Problems Encountered in Pressurized Water Reactors*," 23–27 Sept., 2002.

[3] Pravdjuk, N. F., Nikolaenko, V. A., Karpukhin, V. I., and Kuznetsov, V. N., "Investigation of Diamond and Silicon Carbide as Indicator of Irradiation Conditions," *Proc. of the Intern. Conf. "Properties of Reactor Materials and the Effects of Radiation Damage*," Barkeley Castle, Gloustershire, England, 30 May–2 June 1961, p. 57–62.

[4] Primak, W., Fuchs, L. H., and Day, P. P., *Phys. Rev.*, Vol. 103, No. 5, 1956, p. 1184.

[5] Nikolaenko, V. A., Zaritsky, S. M., and Bachuchin, I. V., "Fast Neutron Fluence Determination Using Diamond Detectors," *At. Energy*, Vol. 98, No. 2, 2005, pp. 118–123 (in Russian).

[6] Zaritsky, S. M., Baryshnikov, M. V., Bachuchin, I. V., Koroliov, Yu. N., Erak, D. Yu., Kuznetsov, V. N., Nikolaenko, V. A., and Platonov, P. A., "Method of Determination of Fast Neutron Fluence in WWER-1000 Type Reactors," Russian Federation Patent No. 2243604 (in Russian).

[7] Pells, G. P., "Colour Centres in α-Al_2O_3 and Their Application to Fast Neutron Dosimetry," *Radiat. Phys. Chem.*, Vol. 22, No. 6, 1983, pp. 1053–1056.

[8] Levy, P. W. and Kammerer, O. F., "Radiation-Induced Amorfism of Diamond," *Phys. Rev.*, Vol. 100, 1956, pp. 1787–1788.

[9] Vance, E. R., "X-Ray Study of Neutron Irradiated Diamonds," *J. Phys. C*, Vol. 4, 1971, pp. 257–262.

[10] Nikolaenko, V. A. and Gordeev, V. G., "Diamond Amorphization in Neutron Irradiation," *Radiat. Eff. Defects Solids*, Vol. 139, 1996, pp. 183–188.

[11] Nikolaenko, V. A. and Karpukhin, V. I., "Temperature Measurements Using Irradiated Materials," Energoatomizdat, Moscow, 1986, p. 121 (in Russian).

Journal of ASTM International, Vol. 3, No. 9
Paper ID JAI100377
Available online at www.astm.org

Michael T. Wenner,[1] *Alireza Haghighat,*[1] *Steven S. Grimes,*[2] *Thomas N. Massey,*[2] *Allan D. Carlson,*[3] *and James M. Adams*[3]

A New Methodology for Adjustment of Iron Scattering Cross Sections Using Time-of-Flight Spectroscopy

ABSTRACT: Monte Carlo analysis of a time-of-flight experiment was performed to investigate the iron scattering cross section. Experimental data were utilized to build a Monte Carlo source for simulation of a time-of-flight (ToF) experiment with a spherical iron shell, different source spectra, and different angular beam source alignments. For this study, two pointwise cross section libraries, ENDF/B-VI and JEFF 3.0 are examined. Comparison of calculation and experimental results indicates differences that are larger than experimental and calculation errors. To reduce the observed discrepancy, pointwise data in the ENDF/B-VI iron scattering cross section file were adjusted at a few energy intervals using a utility code developed for this purpose. Adjusted cross sections resulted in closer agreement of calculated results with the experimental Time-of-Flight data. Multigroup cross sections were generated with the adjusted cross sections and results indicate pressure vessel fluence may be underestimated.

KEYWORDS: iron, scattering cross section, fluence, pressure vessel

Introduction

Traditionally, fast-neutron fluence in the reactor pressure vessel has been obtained by performing multi-dimensional transport calculations. Clearly, safe design and operation of nuclear systems are largely dependent on the nuclear data used. An important cross section for pressure vessel fluence estimation is the iron scattering cross section for which it is suspected improved measurements (and evaluations) are needed, especially for neutron energies between 1 and 8 MeV.

In this study, time-of-flight (TOF) spectroscopy was applied to a neutron spherical shell transmission experiment. The spectroscopy data were then utilized to provide a detailed Monte Carlo neutron source distribution. Sources were generated for 3, 5, and 7 MeV incident deuterons with the $D(d,n)$ source reaction.

For each incident particle energy and neutron source reaction, measurements were made at several different angles to provide data about the neutron angular source spectrum. Each of these measurements provides a spectrum that covers a range of neutron energies. For the work presented here, a spherical shell iron target of 8-cm thickness was used for all the sources. In addition, measurements were made with a shell of ~3-cm thickness with the $^{15}N(p,n)$ source reaction [1]. These thicknesses were chosen to optimize the effect of neutron inelastic scattering [2]. Analysis of the data exhibited discrepancies between experiment and calculation. This work investigates these discrepancies that may lead to an underestimation of neutron fluence in the reactor pressure vessel.

Experimental Background

Experimental data were obtained using the time-of-flight spectroscopy technique, and the spherical-shell transmission method. Iron shells were employed with different thicknesses, and neutron TOF spectra were

Manuscript received June 20, 2005; accepted for publication June 11, 2006; published online October 2006. Presented at ASTM Symposium on Reactor Dosimetry, 12th International Symposium on 8–13 May 2005 in Gatlinburg, TN; D. W. Vehar, D. M. Gilliam, and J. M. Adams, Guest Editors.

[1] Graduate Student and Chair, respectively, University of Florida, Gainesville, FL 32608

[2] Professor and Research Professor, respectively, Institute of Nuclear and Particle Physics, Department of Physics and Astronomy, Ohio University, Athens, OH 45701

[3] Researchers, National Institute of Standards and Technology, Gaithersburg, MD 20899

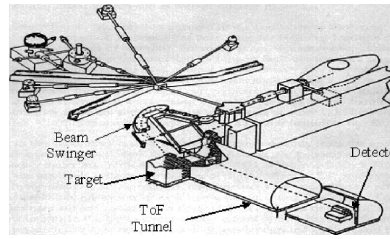

FIG. 1—*Experimental facilities schematic.*

obtained. All experimental work was performed at the Ohio University accelerator laboratory. A unique feature of this facility is the beam swinger that allows angular distributions of the outgoing neutrons to be measured without moving the neutron detector [3]. A schematic of the facility is shown in Fig. 1.

Similar work was done in the past with a nearly monoenergetic 14 MeV neutron source, and a solid iron sphere, at Lawrence Livermore National Laboratory (LLNL) [4]. The present work, however, was done with a number of different source reactions, with a range of neutron energies in which a monoenergetic source was not obtained, and utilized iron shells instead of solid spheres.

Monte Carlo Modeling

Monte Carlo Model

A sectional view of the MCNP [5] model utilized is shown in Fig. 2. This effectively shows the whole system comprised of the source/iron sphere region, a void region up to the concrete wall, the concrete wall/collimator region, another void region, and a detector located at ~5.06 m (detector midplane), from the source position. Impurities in the spherical shell were determined to be less than 0.5 % and were included into the MCNP model. The detector material itself is not modeled and a surface tally estimator is utilized for particle tallying.

Monte Carlo Source Generation

Performing the detailed particle transport simulations necessary for accurate modeling of the experimental system hinges primarily on the acquisition of an accurate neutron source distribution inside of the source gas cylinder.

In the Monte Carlo simulations, the azimuthal angles are always sampled uniformly from 0 to 360 deg; however, for the μ (cosine of the polar angle between the source reference vector and particle direction (Ω)) dependence, the probability density distributions were obtained from experimental data [6].

Briefly, in order to obtain source data from the experiment, it was assumed that the detected neutrons from the experimental runs when the spherical shell was not in place represent the neutron source at that beam angle. Considering the distance to the detector a known quantity, the TOF spectra obtained for the sphere-off cases can be converted directly to energy spectra using relativistic kinematics.

This procedure was repeated for each experimental angular beam alignment and each charged particle source in an attempt to characterize each source reaction in both angle and energy. Table 1 lists the experiments performed for this study. For the range of energy discussed in this work, only the $D(d,n)$ data were utilized.

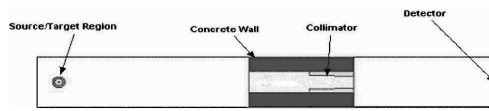

FIG. 2—*Sectional view of the MCNP model of the TOF tunnel.*

TABLE 1—*Experimental source reactions and beam angles (deg).*

5.1 MeV $^{15}N(p,n)$			3.0 MeV $D(d,n)$		5.0 MeV $D(d,n)$		7.0 MeV $D(d,n)$	
Sphere Off	Small Sphere	Large Sphere	Sphere Off	Large Sphere	Sphere Off	Large Sphere	Sphere Off	Large Sphere
0	0	0	0	0	0	0	0	0
15	45	45	15	45	15	45	15	45
45	90	90	45	90	45	90	45	90
60	120	120	60	120	60	120	60	120
90	135	135	90	135	90	135	90	135
100			100		100		100	
120			120		120		120	
135			135		135		135	

To obtain a more reliable estimate of the actual angular and energy dependent source distribution, several options were considered, and a computer code was developed (NERISRC) to automate the source generation using a bilinear interpolation technique preserving peak behavior on energy and angle. A representative example of one set of experimental data for the 5 MeV $D(d,n)$ experiments is shown in Fig. 3.

The eight experimental datasets are interpolated over the complete angular range. A total of three source distributions are generated: The source distributions for the $D(d,n)$ reaction with incident deuteron energies of 3, 5, and 7 MeV. Subsequent calculations are performed for these sources with and without the iron shells. The source distribution resulting from the interpolation procedure utilized is shown in Fig. 4, while a summary of the source distribution analysis (cases without the sphere) is provided in Table 2.

The above results indicate that the peak behavior (peak area) is well represented; however outside of the peak regions, larger differences exist as shown in Table 2 for maximum relative difference. Since

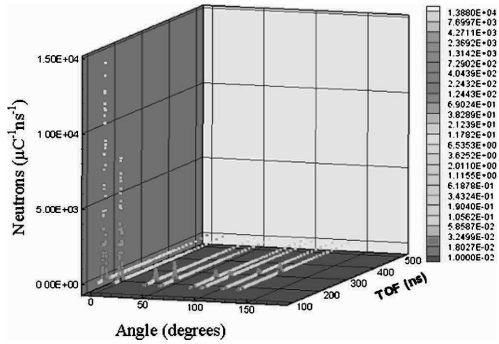

FIG. 3—*Experimental source distributions.*

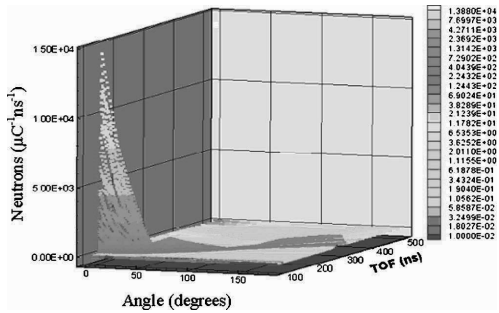

FIG. 4—*Interpolated source distribution.*

TABLE 2—*Experiment and calculation differences for selected beam sources (peak statistical error for both experiment and calculation <1 %).*

Beam Energy	Angle (deg)	Difference at the Peak (%)	Max Relative Difference (%)
3 MeV $D(d,n)$	0	1.5	48
	45	16	52
	90	4.6	85
5 MeV $D(d,n)$	0	0.22	41
7 MeV $D(d,n)$	0	1.0	30
	45	14	45
	90	2.6	54

sources were generated based on a limited amount of angular dependent spectra, we have concluded [6] that mainly the 0 deg cases in the peak regions are reliable. Contributing error sources may be due to poor experimental time resolution in a portion of the spectrum and the source interpolation procedure. Given the source is adequate in the peak areas, scoping calculations were performed for the the 3, 5, and 7 MeV $D(d,n)$ "sphere-on" cases for the 0 deg angle only. Accurate determination of the complete source uncertainty is beyond the scope of this work.

Results with Iron Shells

Experiments were performed at beam source angles of 0, 45, 90, 120, and 135 deg with iron shells surrounding the target. The measured spectra were then compared to Monte Carlo simulations for several cases. A representative example shown in Fig. 5 compares the experimental and Monte Carlo results for the 0 deg case with the $D(d,n)$ source for an incident deuteron energy of 3 MeV. Reasonable agreement is achieved between experiment and calculation distributions; however, a difference of approximately 8 % is observed in the peak region.

For the 3, 5, and 7 MeV cases at 0 deg, differences between the calculated spectra and experimental values of ~8, ~13, and ~18 % were obtained. These results were all for peak regions only. Outside of the main peak region, larger differences were observed because of the limited experimental data available for determination of the source.

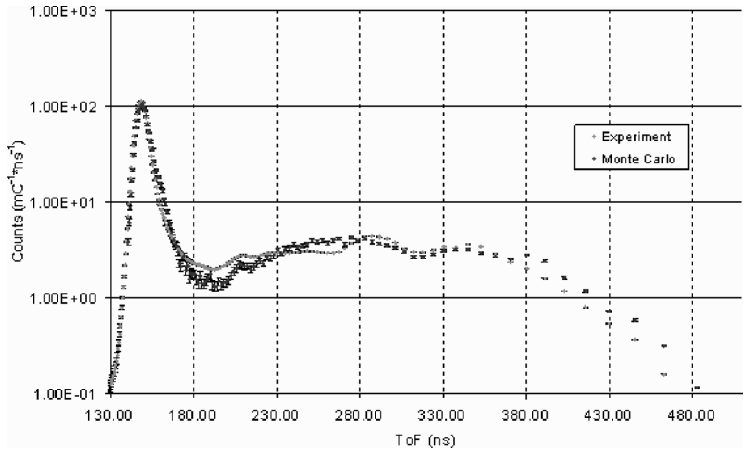

FIG. 5—*Comparison of the D(d,n) Monte Carlo calculations for 3 MeV incident deuterons and experimental data for the 0 deg angle (sphere-on).*

TABLE 3—*Cross section adjustments and their associated energy bin.*

Interaction	Energy Bin (MeV)	% Change in Inelastic Cross Section
3 MeV incident $d,D(d,n)$	6.153–6.203	−21
5 MeV incident $d,D(d,n)$	8.155–8.205	−29
7 MeV incident $d,D(d,n)$	10.756–10.806	−35

Cross Section Modification

A menu driven utility code (XSMOD) [7] was developed in FORTRAN-90 for modifying neutron cross sections in ENDF-6 format which depend on energy. Input for XSMOD is in the form of an extracted material (MAT) from the ENDF data tape. Cross sections may be modified by a constant change or a percent change over user defined energy intervals and output is in the form of two files. One file contains all the rebuilt and decomposed cross sections, along with the input cross section data, and their corresponding pointwise energy in tabular form. This file is useful for plotting. The second file contains an updated version of the input cross section file for the cross section processed. This file is in the ENDF-6 format.

The XSMOD code was utilized to modify cross sections in energy corresponding to the energy bins in Table 3. A larger difference between experiment and calculation was observed with increasing source energy as given in Table 3. With the increasing differences observed, the Fe-56 inelastic cross section was decreased by greater percentages corresponding to the energy regions shown for the peak regions as seen in Table 3. During cross section modification, the total cross section is kept constant and changes in the inelastic cross section are compensated for by changing (increasing) the elastic cross section.

To examine the effect of the adjusted cross sections, both continuous energy and multigroup cross sections were generated. NJOY [8] was utilized to generate continuous energy cross sections for the MCNP code in ACE format, while a multigroup library was generated utilizing the standard collapsing methods described in Ref [9].

Results

The calculated spectra based on the adjusted cross sections are closer to the experimental predictions in the peak regions. Relative differences were reduced to ~3.5, ~8, and ~11 % for 3, 5, and 7 MeV incident deuterons, respectively with the 0 deg spectra. These results indicate a reduction of differences by ~40 %. To test the multigroup cross sections, a typical 1-D reactor pressure vessel (PV) model was simulated corresponding to Fig. 6 using a one-dimensional discrete ordinates transport code.

Flux was obtained from transport calculation utilizing multigroup cross sections collapsed from the original ENDF/B-VI data and the adjusted cross sections. Reaction rates for the ^{63}Cu(n,α), ^{54}Fe(n,p), ^{58}Ni(n,p), ^{46}Ti(n,p), ^{237}Np(n,f), and ^{238}U(n,f) interactions were determined at the cavity dosimeter and compared to the test results obtained from the library derived from the original ENDF/B-VI library. Table 4 gives the reaction rate ratios (ENDF/B-VI/adjusted cross section) for the six interactions. Given that the adjusted cross sections were in better agreement with experiment, we can see from the data in Table 4 that the model predicts the calculated neutron fluence will increase with these changes.

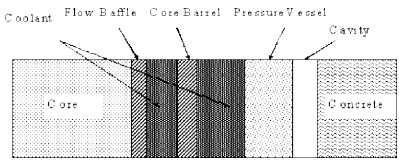

FIG. 6—*One-dimensional reactor pressure vessel model.*

TABLE 4—*Reaction rate ratios (ENDF/B-VI/adjusted cross section) at the cavity dosimeter.*

Interaction	Threshhold Energy (MeV)	ENDF/B-VI / Adjusted
63Cu(n,α)	1.71	0.9410
54Fe(n,p)	2.8	0.9862
58Ni(n,p)	0.5	0.9877
46Ti(n,p)	2.97	0.9627
237Np(n,f)	0.1	0.9986
238U(n,f)	0.5	0.9958

Other Cross Section Libraries

Besides the ENDF/B-VI cross section library, we examined another cross section library, namely the JEFF 3.0 cross section library. Plotting of the pointwise data for this library reveals significantly more detail for higher energies. In order to compare the average cross section values in ENDF and JEFF, the XSMOD code was modified in order to collapse the pointwise data to a user defined equal spaced group structure (flat weight). Our analysis showed that differences exist between the two libraries.

In order to see the impact of these differences, continuous energy cross sections derived from the JEFF 3.0 library were utilized in the MCNP code and calculations performed for the 3 MeV $D(d,n)$ case. Figure 7 compares the JEFF calculation results to the experimental data in the peak region.

Figure 7 indicates that for this particular case, there is no statistical difference between the JEFF and ENDF cases. However, for this particular case, the energy corresponding to the peak of the 3 MeV 0 deg $D(d,n)$ spectrum is ~6.15 to 6.20 MeV. At this energy, there is only an ~1 % difference between the pointwise JEFF 3.0 and ENDF/B-VI inelastic cross section data. At other energies, this difference is greater due to different energy structure of the JEFF 3.0 library which can cause differences of several percent. Further studies are needed.

Summary and Conclusion

We have developed a methodology that can be utilized to model a TOF experiment utilizing the MCNP code. An automated source distribution generation methodology was developed to utilize experimental data to provide a detailed angular and energy dependent source distribution to provide the source in MCNP. Utilizing this methodology, we have shown deficiencies may exist in the Fe-56 cross section data.

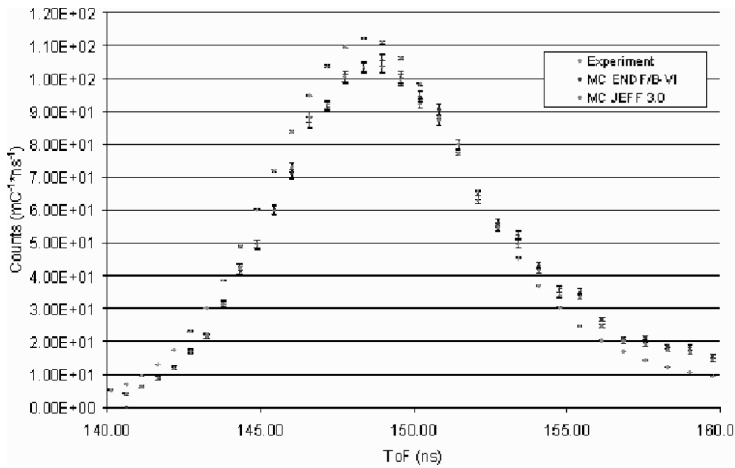

FIG. 7—*Comparison of the 3 MeV D(d,n) calculation with JEFF 3.0 and ENDF/B-VI library.*

A computer code was developed for modifying cross sections in ENDF-6 format. We have shown that the differences between experiment and calculation can be effectively utilized to provide a means for adjustment of the pointwise cross section values. Our findings indicate that pressure vessel fluences might be underestimated based on the currently available libraries. This would be a very important issue for reactor material integrity and lifetime. Future studies are needed.

Future Effort

The limiting factor in our determination of the accuracy of our simulation is the source generation procedure for use in MCNP. With a limited amount of angular information from experiment, more experimental work, obtaining data at smaller angular intervals, must be completed in order to greatly increase the confidence in the generated source distributions.

We are currently studying the impact of combining the experimental bins in order to decrease the impact of the detector resolution, which is poor at higher energies. Using this new source generation procedure, we have generated new source distributions, and analysis is pending. Future work is needed to further assess the accuracy of the generated sources.

Lastly, we have shown that differences exist in the pointwise data between the JEFF 3.0 and ENDF/B-VI libraries; however, the effects of these differences when applied to the time of flight experiment must be more thoroughly evaluated.

References

[1] Gardner, S., Haghighat, A., and Patchimpattapong, A., "Monte Carlo Analysis of a Spherical Shell Transmission Experiment with New Tallying Methodology," *Proceedings of American Nuclear Society Mathematics and Computation Topical Meeting*, Salt Lake City, UT, 2001 (ANS, 2002), pp. 154–156.

[2] Gardner, S., Haghighat, A., Patchimpattapong, A., Adams, J., Carlson, A., Grimes, S., and Massey, T., "A New Monte Carlo Methodology for Optimizing the NERI Spherical-shell Transmission Experiment," *Trans. Am. Nucl. Soc.*, Vol. 84, 154–156 (2001).

[3] Finlay, R. W., Brient, C. E., Carter, D. E., et al., "The Ohio University Beam Swinger Facility," *Nucl. Inst & Meth.*, Vol. 198, 197 (1982).

[4] Hansel, L., Anderson, J., Brown, P., et al., "Measurements and Calculations of the Neutron Spectra from Iron Bombarded with 14-MeV Neutrons," *Nucl. Sci. Eng.* Vol. 51, pp. 278–295.

[5] Breismeister, J. F., MCNP—"A General Monte Carlo N-Particle Transport Code, Version 4C," LA 13709-M, Los Alamos National Laboratory, 2000.

[6] Wenner, M., Haghighat, A., Adams, J., Carlson, A., Grimes, S., and Massey, T., "Monte Carlo Modeling of a Time-of-Flight (TOF) Experiment for Determination of Fe Scattering Cross Sections," *Proceedings of American Nuclear Society PHYSOR 2004 Topical Meeting*, Chicago, IL, 25–29 April 2004.

[7] Wenner, M., Haghighat, A., Adams, J., Carlson, A., Grimes, S., and Massey, T., "Development of a Methodology for Analysis of the Impact of Modifying Neutron Cross Sections," *Proceedings of American Nuclear Society PHYSOR 2004 Topical Meeting*, Chicago, IL, 25–29 April 2004.

[8] MacFarlane, R. and Boicourt, R., "NJOY: A NEUTRON and PHOTON PROCESSING SYSTEM," *Trans. Am. Nucl. Soc.*, Vol. 22, 720 (1975).

[9] Alpan, A. and Haghighat, A., "Advanced Methodology for Selecting Group Structures for Multigroup Cross Section Generation," *Proceedings of American Nuclear Society PHYSOR 2004 Topical Meeting*, Pittsburgh, PA, 7–12 May 2000.

Journal of ASTM International, Vol. 3, No. 2
Paper ID JAI13439
Available online at www.astm.org

Jan Wagemans,[1] *Luc Borms,*[1] *Marcel Willekens,*[1] *Jos Oeyen,*[1] *Andre Moens,*[2] *and Vyacheslav Kochkin*[3]

Reactor Dosimetry with Niobium

ABSTRACT: The main advantages of using niobium in reactor dosimetry are briefly summarized. Some experimental aspects and complications of niobium dosimetry are discussed. Special techniques can be applied to overcome most of these problems. Particular concern has to be given to the detector calibration for the X-ray measurements. The main problem however, embrittlement of pure niobium under intense neutron irradiation, is still not solved. For this purpose a new type of material (Al-10%Nb alloy) was prepared. Although testing of this material is still ongoing, preliminary results are promising. This material moreover does not necessarily require applying special techniques for the X-ray measurements. Finally it is explained that niobium is a suitable material for the determination of thermal and epithermal fluences in high flux environments.

KEYWORDS: neutron dosimetry, niobium, neutron activation, neutron fluence

Introduction

For several decades, niobium has been recognized as a very favorable neutron activation material for reactor dosimetry purposes. The main advantages of this material are the long half life of its fast neutron activation product ^{93m}Nb, which allows neutron fluence determinations for long irradiations, and the low threshold energy of the ^{93}Nb(n,n′)^{93m}Nb reaction, which makes it very suited for the determination of neutron induced damage fluences.

The disadvantages of using niobium as activation dosimeter are twofold: (i) pure niobium can become brittle under neutron irradiation; and (ii) special techniques are required for an accurate detection of the low-energy X-rays that are emitted during the decay of ^{93m}Nb. A straightforward solution to the first difficulty would be the usage of low-purity niobium. This material however contains impurities of tantalum, and the decay gamma rays from its activation product ^{182}Ta induce X-ray fluorescence in niobium, which hampers a correct activity determination and thus neutron fluence determination.

The problems of X-ray self-absorption and fluorescence can be overcome applying special experimental techniques [1]. These techniques have been proven to be successful but they are less straightforward than measuring activation dosimeters as such. Moreover material embrittlement remains a problem. It was therefore decided to look for an alternative way of using niobium for reactor dosimetry. Wires of high-purity niobium alloyed with aluminium (Al-10%Nb) were prepared at IRMM (Geel, Belgium) and irradiated in the BR2 material testing reactor at SCK•CEN (Mol, Belgium).

A third complication with using niobium for reactor dosimetry is the availability of a reliable reference source. From a recent intercomparison on retrospective dosimetry using niobium (see [2,3] and references therein), it appeared that the three participating laboratories all use niobium calibration sources that are prepared from the same standard solution. Thus although the results from the intercomparison are in good agreement, the absolute value of the specific ^{93m}Nb activities could be questioned. It was therefore decided to prepare new ^{93m}Nb calibration sources from a ^{93m}Nb solution with a radioactivity certificate independent from the existing one. In addition, a small scale interlaboratory exercise on ^{93m}Nb activity measurements with Kurchatov Institute (Russia) was initiated.

Manuscript received June 20, 2005; accepted for publication August 29, 2005; published online December 2005. Presented at ASTM Symposium on Reactor Dosimetry, 12th International Symposium on 8–13 May 2005 in Gatlinburg, TN; D. W. Vehar, D. M. Gilliam, and J. M. Adams, Guest Editors.

[1] SCK•CEN, 2400 Mol, Belgium.
[2] EC-IRMM, 2440 Geel, Belgium.
[3] Kurchatov Institute, 123182 Moscow, Russia.

TABLE 1—*Measured and nominal activities of the new ^{93m}Nb standard deposits.*

Sample	Measured activity [Bq]	Nominal activity [Bq]	Ratio (nominal/measured) activity
Nb1	6408	6443	1.005
Nb2	4479	4542	1.014
Nb3	6883	6960	1.011
Nb4	7433	7500	1.009
Nb5	8905	9069	1.018

Finally, niobium dosimeters cannot only be used for fast neutron flux determination but are also suited for thermal and epithermal neutron flux determination, in particular, in high flux environments. The advantages of using niobium for this purpose are presented.

This paper first gives a discussion on ^{93m}Nb calibration deposits. The results obtained from the interlaboratory intercomparison with Kurchatov institute are presented. The dosimetry set that was irradiated in the BR2 reactor for the purpose of this intercomparison includes the newly developed Al-10%Nb dosimeters. A description of the material preparation procedure of the Al-10%Nb alloy and the first tests of these dosimeters is given. Finally it is discussed that niobium is a very suited material for thermal and epithermal neutron flux monitoring in high flux environments.

Calibration Sources for ^{93m}Nb X-ray Measurements

The technique applied for the deposit preparation was intensively studied at SCK•CEN in the 1970s–1980s for the measurement of niobium dosimeters (see, e.g., [4] and references therein). Niobium dosimeters are dissolved in a mixture of HF and HNO_3 and from this solution thin deposits are prepared. Detailed investigations were performed demonstrating that effects like X-ray self-absorption and X-ray fluorescence are very small for such samples, and the ability of accurately determining ^{93m}Nb activities using this technique was shown.

The efficiency calibration of detectors for γ-spectrometry measurements is usually performed by detecting γ rays with accurately known energies over the entire energy region of interest. Interpolation of these data results in an efficiency curve for this energy region. For low-energy X-rays however the efficiency curve is very steep and therefore it is desirable to perform relative measurements. An example is ^{93m}Nb, which emits X-rays in the energy intervals 16.5–16.6 keV and 18.6–19.0 keV.

For the purpose of an intercomparison of ^{93m}Nb X-ray emission probabilities in 1985 [5], a ^{93m}Nb solution was standardized at IRMM using liquid scintillation in 1984. From this solution five thin niobium deposits were prepared at SCK•CEN for the intercomparison, which were through this intercomparison proven to be suitable calibration samples for absolute ^{93m}Nb activity measurements. Since then at SCK•CEN all ^{93m}Nb activity determinations were done relative to the above-mentioned calibration deposits.

From a recent intercomparison on retrospective dosimetry using niobium (see [2,3] and references therein) it appeared that the ^{93m}Nb calibration sources used in the participating laboratories (SCK•CEN, Belgium, VTT, Finland and NRG, The Netherlands) have the same origin. All calibration sources were prepared from the ^{93m}Nb solution that was purchased at AERE Harwell and standardized at IRMM in 1984. As a consequence, although the agreement between the results obtained at NRG, VTT, and SCK•CEN is good, the absolute activities could be questioned. Therefore it was decided to prepare new ^{93m}Nb calibration sources from a solution with an independent certified ^{93m}Nb activity.

A standardized niobium solution with a ^{93m}Nb activity concentration of (372 ± 3)kBq/g was purchased at Physikalisch-Technische Bundesanstalt (PTB). In March 2004 five new deposits were prepared from this solution applying the routinely used technique (see e.g., [1,4]). The nominal ^{93m}Nb activities of these deposits range from 4.5 to 9 kBq, with a 1σ uncertainty ranging from 1.4 to 1.0 %.

The ^{93m}Nb activity of the new deposits was measured on a low energy germanium detector that was calibrated with the existing ^{93m}Nb standard deposits. Measurements at different sample-to-detector distances have been carried out. For each deposit an average measured activity was determined and compared with its nominal activity (nominal activity = mass of niobium deposited $\times$ certified activity concentration). These values and the ratio (nominal activity / measured) are presented in (Table 1). All activities are reported at reference date 01/01/2004.

TABLE 2—*Intercomparison of ^{93m}Nb specific activities between KI and SCK•CEN.*

		^{93m}Nb[Bq/g] SCK•CEN	^{93m}Nb[Bq/g] KI	Ratio SCK•CEN/KI
Set 1	Al-10%NbAa		3.44E+08	1.04E+00
	Al-10%NbAb	3.57E+08		
	Al-10%NbBa		3.63E+08	1.01E+00
	Al-10%NbBb	3.65E+08		
	Nba		3.68E+08	1.04E+00
	Nbb	3.83E+08		
Set 2	Al-10%NbAa		5.58E+08	1.05E+00
	Al-10%NbAb	5.87E+08		
	Al-10%NbBa		5.54E+08	-
	Al-10%NbBb	-		
	Nba		5.51E+08	1.06E+00
	Nbb	5.82E+08		
Set 3	Al-10%NbAa		8.99E+08	9.93E−01
	Al-10%NbAb	8.93E+08		
	Al-10%NbBa		9.12E+08	9.84E−01
	Al-10%NbBb	8.97E+08		
	Nba		9.26E+08	1.03E+00
	Nbb	9.54E+08		

For each deposit the nominal and measured activity agree within 2 %, which confirms the correctness of the absolute ^{93m}Nb activity of all deposits.

Niobium Dosimetry Intercomparison with Kurchatov Institute

An additional verification of the applied technique and efficiency calibration was made by setting up a collaboration with Kurchatov Institute (KI, Russia). Three sets of niobium dosimeters were irradiated in the BR2 reactor at SCK•CEN. The dosimeters were then cut in two pieces (labeled "a" and "b") and one piece of each dosimeter ("a") was sent to KI for intercomparison of ^{93m}Nb specific activities. Both laboratories use independent calibration sources and apply a slightly different technique. Whereas at SCK•CEN the measurements are performed with a low energy germanium detector that is calibrated with the previously mentioned ^{93m}Nb reference deposits, at Kurchatov Institute the measurements are carried out with a Si(Li) X-ray detector that is calibrated with four secondary ^{93m}Nb reference sources.

The results of the intercomparison are summarized in (Table 2). These results have been obtained after dissolution of the niobium wires and deposit preparation both at KI and at SCK•CEN. The specific activities of the Al-10%Nb dosimeters have been multiplied by ten to allow direct comparison with the pure niobium dosimeters. The agreement between the results obtained by the two institutes is good and no systematic bias is observed. Details on the Al-10%Nb dosimeters mentioned in (Table 2) are given further in this paper.

Preparation and Investigation of Al-10%Nb Material

Pure niobium tends to embrittle under high neutron fluence irradiation. In order to overcome this problem, an Al-10%Nb alloy was prepared at IRMM and from this 1 mm diameter wire dosimeters were made. These dosimeters have been irradiated in the BR2 reactor at SCK•CEN and the material and nuclear properties have been investigated.

Advantages of Al-10%Nb

The main advantage of the Al-10%Nb material would of course be that thanks to its different lattice structure it is more radiation resistent than pure Nb. But in addition to possibly solving the embrittlement problem, this material also has other advantages.

When Nb dosimeters have been irradiated in high thermal neutron flux environments, the thermal

TABLE 3—*Comparison of X-ray transparancies (T) in Al-10%Nb and pure Nb.*

Material	Thickness [mm]	Diameter [mm]	*T* for 16.6 keV	T for 18.6 keV
Nb foil	0.1		0.48	0.58
Al-10%Nb foil	0.1		0.90	0.93
Nb wire		0.5	0.15	0.20
Al-10%Nb wire		0.5	0.66	0.74
Nb wire		1	0.07	0.10
Al-10%Nb wire		1	0.47	0.57

neutron induced activation product ^{95}Nb forces the experimenter to wait approximately half a year before activity measurements can be carried out (high radiation doses during manipulation, detector dead time, etc.). The ^{95}Nb activity is ten times lower when using Al-10%Nb instead of pure Nb.

The mass density and photon interaction cross sections of Al-10%Nb are much lower than for pure Nb. Therefore the X-ray transparency corrections to be applied are much smaller. In (Table 3) the calculated transparencies for different dosimeter dimensions for Al-10%Nb and for pure Nb are summarized. The photon interaction cross sections were taken from [6]. As can be seen, the X-ray self-absorption for a 0.1 mm Al-10%Nb foil is of the order of 10 %, thus the possible error on the specific activity due to this correction is small. For pure Nb the transparency correction for a 0.1 mm foil is of the order of 200 %. When using Al-10%Nb dosimeters, special experimental procedures to prepare thin samples may therefore not be needed. This would be of particular interest for the monitoring of low neutron fluxes, where niobium deposits would require very long measuring times.

Material Preparation Procedure

The Al-10%Nb alloy was prepared using the levitation melting technique in an inert-gas (He) atmosphere. This method produces highly homogeneous compositions and the crucibleless nature of the method minimizes contamination of the melt. For the first irradiation experiments 1.0 mm diameter wires were produced.

Because of the high melting-point difference between Al (660°C) and Nb (2468°C) a step-wise method was applied:

1. A 16 g sample of pure Al (99.995 %) is levitated and melted in an open-bottom coil. When the coil current is switched off, the molten and levitating Al drops into a cold copper mold directly below the coil. The copper mold contains 2 % of pure Nb metal (99.994 %) and produces an inhomogeneous Al-2%Nb composition.
2. The inhomogeneous cast is melted while levitated and as soon as all the Nb specimens are dissolved in the molten state the homogeneous composition is cast into an empty cold copper mold.
3. The produced Al-2%Nb alloy is remelted and cast into the cold copper mold containing again 2 % of pure Nb metal to produce an inhomogeneous Al-4%Nb composition.

   Steps two and three are carried out five times, each time adding 2 % of Nb metal to the copper mold.
4. Finally, the homogeneous Al-10%Nb cast is transformed into a 1.0 mm diameter wire by using an automatic wire drawing machine. The wire is reduced stepwise into the required diameter by taking smaller diamond dies after each pass.

Irradiations

In order to study the material behavior and the activation properties of this alloy, a dedicated irradiation in the BR2 reactor at SCK•CEN was set up. Al-10%Nb dosimeters were irradiated together with pure Nb to compare possible material embrittlement, and with Al-1%Co, Al-1%Ag, and Fe to investigate its application as thermal (and epithermal) neutron dosimeter. All dosimeters were wires of 15 mm length and 0.5 mm diameter, except the Al-10%Nb wires that had a 1 mm diameter. Each set contained two Al-10%Nb dosimeters. After this investigation these dosimeters were used for the previously mentioned intercomparison with Kurchatov Institute.

TABLE 4—*Verification of the homogeneity of the Al-10%Nb material.*

		^{94}Nb[Bq/g]	^{94}Nb a/b	^{95}Nb[Bq/g]	^{95}Nb a/b	^{93m}Nb[Bq/g]	^{93m}Nb a/b
Set 1	Al-10%NbAa	5.46E+06	1.02E+00	5.06E+09	1.02E+00	3.77E+08	1.02E+00
	Al-10%NbAb	5.34E+06		4.94E+09		3.68E+08	
	Al-10%NbBa	5.58E+06	1.02E+00	5.19E+09	1.02E+00	3.81E+08	9.82E−01
	Al-10%NbBb	5.48E+06		5.09E+09		3.88E+08	
	Nba	5.22E+06	1.00E+00	4.76E+09	1.01E+00	3.93E+08	9.90E−01
	Nbb	5.22E+06		4.74E+09		3.98E+08	
Set 2	Al-10%NbAa	8.36E+06	9.85E−01	8.47E+09	9.90E−01	5.75E+08	9.40E−01
	Al-10%NbAb	8.48E+06		8.56E+09		6.11E+08	
	Al-10%NbBa	8.17E+06	1.00E+00	8.24E+09	1.00E+00	5.84E+08	9.86E−01
	Al-10%NbBb	8.13E+06		8.24E+09		5.92E+08	
	Nba	8.00E+06	9.98E−01	8.14E+09	9.94E−01	6.29E+08	9.85E−01
	Nbb	8.02E+06		8.19E+09		6.38E+08	
Set 3	Al-10%NbAa	1.28E+07	9.86E−01	1.58E+10	9.79E−01	8.91E+08	9.79E−01
	Al-10%NbAb	1.29E+07		1.62E+10		9.10E+08	
	Al-10%NbBa	1.28E+07	9.92E−01	1.59E+10	9.83E−01	9.25E+08	1.01E+00
	Al-10%NbBb	1.29E+07		1.61E+10		9.18E+08	
	Nba	1.32E+07	9.89E−01	1.63E+10	9.87E−01	9.83E+08	1.01E+00
	Nbb	1.34E+07		1.65E+10		9.69E+08	

The dosimeters were irradiated in In Pile Section 2 of the BR2 reactor at SCK•CEN. Two sets were irradiated during cycle 03/2003 at a temperature of 265°C; one set was then replaced by a new set. The irradiations in cycles 04-05/2003 were conducted at a temperature of 300°C.

In this way the three sets of dosimeters were exposed to different neutron fluences:

- Set 1: ~2.0E20 cm^{-2} fast neutron fluence and 2.5E20 cm^{-2} thermal neutron fluence;
- Set 2: ~3.0E20 cm^{-2} fast neutron fluence and 3.5E20 cm^{-2} thermal neutron fluence;
- Set 3: ~5.5E20 cm^{-2} fast neutron fluence and 6.0E20 cm^{-2} thermal neutron fluence.

Measurements and Results

For the purpose of the earlier mentioned intercomparison with Kurchatov Insitute, all niobium dosimeters were cut in two pieces (labeled "a" and "b"). In order to verify the homogeneity of the Al-10%Nb material, the thermal (and epithermal) neutron induced ^{94}Nb, ^{95}Nb specific activities and the fast neutron induced ^{93m}Nb specific activities have been determined for each piece. All γ and X-ray measurements were performed on the wires prior to the destructive analyses (dissolution and deposit preparation) for the measurements of the intercomparison with Kurchatov Institute. For each dosimeter the ratio (piece a/piece b) is presented in (Table 4). The specific activities of the Al-10%Nb dosimeters have been multiplied by ten to allow direct comparison with the pure niobium dosimeters. One can clearly observe that the niobium is homogeneously distributed in the Al-10%Nb material.

Each set of niobium dosimeters (one pure and two alloy) was irradiated in the same capsule. Therefore the differences in specific activity of the three dosimeters in each set are expected to be small. Comparison of specific activities of the pure and alloy dosimeters thus allows us to verify the nominal niobium enrichment of 10 % in the alloy dosimeters. It is easily calculated from the results in (Table 4) that the average ^{94}Nb and ^{95}Nb specific activities of the pure and alloy dosimeters agree within 5 %, which confirms the nominal niobium enrichment of the alloy material.

The ^{93m}Nb specific activities of all niobium dosimeters given in (Table 3) were obtained from X-ray counting of thin deposits. It takes about six hours to obtain a complete dissolution of the Al-10%Nb wires in a HF-HNO_3 mixture that is routinely used to dissolve pure niobium. This process can be accelerated by heating the solution. Comparison of the ^{93m}Nb specific activities from (Table 3) (X-ray counting of deposits) and from (Table 4) (X-ray counting of wires, prior to dissolution) shows that the transparancy corrections for the pure and alloy wires were correctly applied. This good agreement is also thanks to the purity of the samples (no interference from ^{182}Ta) and, to a lesser extent, to the sufficiently long cooling time (no interference from ^{95}Nb). Small deviations are observed for some dosimeters but these are due to uncorrected geometry effects.

TABLE 5—*Relevant reaction cross sections.*

Reaction	IRDF-2002 [8]		Mughabghab [9]		JENDL3.3		JEFF3.0	
	σ_0 [b]	I_{res} [b]	σ_0 [b]	I_{res} [b]	σ_0 [b]	I_{res} [b]	σ_0 [b]	I_{res} [b]
$^{109}Ag(n,\gamma)^{110m}Ag$	4.21	68.6	3.95(5)	65.1(29)				
$^{109}Ag(n,\gamma)^{110}Ag$			91(1)	1470(48)	90.6	1471	90.7	1473
$^{110m}Ag(n,\gamma)^{111}Ag$					82	90	165	2473
$^{93}Nb(n,\gamma)^{94}Nb$	1.16	9.91	1.15(5)	8.3(4)	1.15	9.25	1.16	9.75
$^{94}Nb(n,\gamma)^{95}Nb$			14.9(10)	125(8)	15.8	125	13.6	117

Neither of the niobium dosimeters (pure nor alloy) has become brittle during the irradiation. Therefore no conclusive evidence exists that the Al-10%Nb material is more resistant against embrittlement than pure niobium. In order to further test the material behavior of the Al-10%Nb alloy, 0.1 mm thin foils of this material have been prepared. Thin foils are presumably more susceptible to embrittllement than a 1 mm diameter wire. Irradiations of these dosimeters (simultaneously with pure niobium foils) in high flux environments in the BR2 reactor are scheduled.

Niobium for Thermal and Epithermal Neutron Flux Determination

An additional advantage of using Nb for fast neutron flux determination is that at the same time this dosimeter can be used for the determination of thermal and epithermal neutrons. It is indeed known that Nb is a suited material for monitoring thermal and epithermal neutrons applying the so-called multiple foil method. It will be shown in this chapter that for long term irradiations in high flux environments Nb is better suited than Ag for the determination of thermal and epithermal neutron fluxes.

The two-foil method is based on the simultaneous irradiation of a "1/v" dosimeter and a "resonance" dosimeter. Co and Ag are examples of a "1/v" and a "resonance" dosimeter and mainly thanks to the suitably long half life of their activation products these materials are widely used for the determination of thermal and epithermal neutron fluxes for long term irradiations [7]. Instead of using Ag, Nb could also be used in combination with Co. The thermal neutron induced cross section (at 25.3 meV) and resonance integral of the $^{109}Ag(n,\gamma)^{110m}Ag$ and $^{93}Nb(n,\gamma)^{94}Nb$ reactions from different sources are summarized in (Table 5). These cross sections are rather well-known, although more accurate data for the thermal cross section of the first and the resonance integral of the second reaction is desirable.

When dealing with high thermal and epithermal neutron flux environments and long irradiations, dosimeter burnup effects have to be accounted for. The cross sections of the most import burnup reactions for Ag and Nb are given in italics in (Table 5). It is not the purpose of this paper to make a quantitative analyses of the influence of burnup effects, instead some qualitative considerations will be presented.

It can be seen in (Table 5) that the $^{109}Ag(n,\gamma)^{110}Ag$ reaction has a huge resonance integral. Due to this, Ag target burnup is very important in high neutron fluences. Also product burnup can be considerable through the $^{110m}Ag(n,\gamma)^{111}Ag$ reaction. Note that the information on the $^{110m}Ag(n,\gamma)^{111}Ag$ cross section is scarce and very discrepant hence the product burnup is difficult to quantify.

The application of niobium for dosimetry in high fluence irradiations is more favorable. Dosimeter target burnup is very small. Product burnup exists mainly through the $^{94}Nb(n,\gamma)^{95}Nb$ reaction with resonance neutrons but this effect is much smaller than is the case for Ag.

The magnitude of the influence of dosimeter burnup and the burnup reaction cross sections is presented in (Fig. 1). Here the ratio of burnup corrected to uncorrected reaction rates is plotted for irradiations of 20, 40, 60, 80, and 100 days in a typical thermal flux of 2E14 $cm^{-2}\,s^{-1}$ and epithermal flux of 2E13 $cm^{-2}\,s^{-1}$. For niobium the correction remains small, even for the highest thermal neutron fluence. For Ag three different cross sections for product burnup were used in the calculations: no product burnup (black squares), JENDL3.3 (red circles) and JEFF3.0 (green triangles). It is clear from this figure that burnup of Ag dosimeters is high and that accurate cross section data are required in order to correct for burnup.

Finally, an obvious advantage of using niobium is that one dosimeter can be used to monitor fast and thermal-epithermal neutrons at the same time, requiring less material and space in the experimental setup.

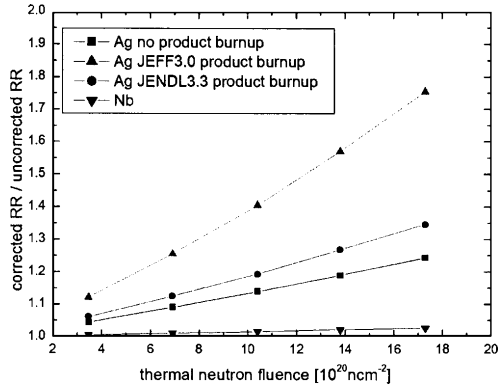

FIG. 1—*Influence of dosimeter burnup on the reaction rate.*

Conclusion

In this work different aspects of niobium dosimetry have been investigated:

- The correctness of absolute ^{93m}Nb activity determinations has been verified by comparing independent calibration sources and by an intercomparison between two independent laboratories.
- A homogeneous Al-10%Nb alloy has been prepared and investigated. This material has several advantages compared to pure niobium. Further investigation to test possible embrittlement under intense neutron irradiation is ongoing.
- The need for accurate cross section data to correct for dosimeter burnup for thermal and epithermal neutron flux determination in high flux environments is shown. Niobium is not very sensitive to burnup and therefore this material is suited for both fast and thermal-epithermal neutron flux determinations.

Acknowledgments

The authors gratefully acknowledge the Belgian Ministry of Economic Affairs for its financial support of part of this work.

References

[1] ASTM Standard E 1297, "Standard Test Method for Measuring Fast-neutron Reaction Rates by Radioactivation of Niobium," *Annual Book of ASTM Standards*, Vol. 12.02, ASTM International, West Conshohocken, PA

[2] Voorbraak, W., Woittiez, J., Wagemans, J., Van Bockxstaele, M., Kekki, T., and Serén, T., "Retrospective Dosimetry of Fast Neutrons Focussed on the Reactions ^{93}Nb(n,n′)^{93m}Nb and ^{54}Fe(n,p)^{54}Mn", *these proceedings*.

[3] Voorbraak, W. P., Kekki, T., Serén, T., Van Bockxstaele, M., Wagemans, J., and Woittiez, J. R. W., "Retrospective Dosimetry of Fast Neutrons Focussed on the Reaction 93Nb(n,n′)93mNb, 20576/03.53641/C," NRG (Petten, The Netherlands) May, 2003.

[4] H. Tourwé and N. Maene, 'Fast Neutron Fluence Measurements with the Nb-93(n,n′)Nb-93m Reaction and the Application to Long-Term Irradiations," *Proc. 3rd ASTM-Euratom Symposium on Reactor Dosimetry*, Ispra, 1979.

[5] P. D'hondt, "Nb-93(n,n′)Nb-93m Measuring Method, Revised on Basis of the DAVIS-BESSE intercomparison exercise," *SCK•CEN report* R-3152, 1997.

[6] Cullen, D. E. et al., "Tables and Graphs of Photon Interaction Cross Sections from 10 eV to 100 GeV Derived from the LLNL Evaluated Nuclear Data Library (ENDL)", UCRL-50400, Vol. 6, Rev. 4, Lawrence Livermore National Laboratory, 1989.

[7] ASTM Standard E 481, "Standard Test Method for Measuring Neutron Fluence Rates by Radioactivation of Cobalt and Silver", *Annual Book of ASTM Standards*, Vol. 12.02, ASTM International, West Conshohocken, PA.

[8] http://www-NDS.iaea.org/irdf2002

[9] Mughabghab, S. F., *Atlas of Neutron Resonances*, Elsevier, to be published.

Participants

Adams, Dr. James M
National Inst. of Standards and Technology
100 Bureau Drive Stop 2000
Gaithersburg MD 20899-2000
USA
james.adams@nist.gov

Alberman, Dr. Alain
CEA/ Saclay
Bât 526 - DRSN
Gif-sur-Yvette cedex 91191
FRANCE
alain.alberman@cea.fr

Alpan, Dr. F. Arzu
Oak Ridge National Laboratory
Nuclear Science and Technology Division
P. O. Box 2008, Mail Stop 6171
Oak Ridge TN 37831-6171
USA
alpanfa@ornl.gov

Anderson, Mr. Stan
Westinghouse Electric Company
P.O. Box 158
Interstate 70, Exit 54
Madison PA 15663-0158
USA
anderssl@westinghouse.com

Anness, Michael
Westinghouse Nuclear Services
Bay 145D
P. O. Box 158
Madison PA 15663
USA
annessm@westinghouse.com

Bikah, Myriam
University of Nebraska
Lincoln Dept of Industrial Engineering
175 Nebraska Hall
Lincoln NE 68588
USA
sandrinebikah@yahoo.com

Blue, Dr. Thomas E
The Ohio State University
Suite 255
650 Ackerman Rd
Columbus OH 43202
USA
blue.1@osu.edu

Borodkin, Mr. Gennady
Scientific and Engineering Centre for Nuclear and Radiation Safety of Rostechnadzor
Malaya Krasnoselskaya ul., 2/8, bld. 5
Moscow 107140
RUSSIA
borodkin@secnrs.ru

Broadhead, Dr. Bryan L
Oak Ridge National Laboratory
P.O. Box 2008
Oak Ridge TN 37831-6170
USA
zbynek.bures@unob.cz

Bures, Zbynek
University of Defence K-269
Kounicova 65
612 00 BRNO
CZECH REPUBLIC
broadheadbl@ornl.gov

Carcreff, Mr. Hubert HC
Commissariat A L'Energie Atomique
CEA Saclay DEN/DRSN/SIREN/LASPI
Bât 635
Gif-sur-Yvette F-91191
FRANCE
hubert.carcreff@cea.fr

Carlson, Dr. Allan D
National Inst. of Standards and Technology
100 Bureau Drive STOP 8463
Gaithersburg MD 20899-8463
USA
carlson@nist.gov

Conwell , Maj. William Dale
New Mexico Tech
4245 John Oblinger Dr.
El Paso TX 79934
USA
william.conwell@us.army.mil

DePriest, Dr. Russell K
Sandia National Laboratories
P.O. Box 5800
MS 1146
Albuquerque NM 87185-1146
USA
krdepri@sandia.gov

D'hondt, Dr. Pierre
SCK•CEN
Boeretang 200
Mol 2400
BELGIUM
pdhondt@sckcen.be

Ferguson, Dr. Phillip D
Oak Ridge National Laboratory
Spallation Neutron Source
Building 8600, MS 6474
Oak Ridge TN 37830-6474
USA
fergusonpd@ornl.gov

Fero, Mr. Arnold H
Westinghouse Electric Company
P. O. Box 158
Interstate 70, Exit 54
Madison PA 15663-0158
USA
feroah@westinghouse.com

Forsberg, Dr. Charles W
Oak Ridge National Laboratory
P.O. Box 2008
Oak Ridge TN 37831-6165
USA
forsbergcw@ornl.gov

Gallmeier, Mr. Franz X
Oak Ridge National Laboratory
P.O. Box 2008, MS6474
Oak Ridge 37830
USA
gallmeierfz@ornl.gov

Delauder, Nathan
Department of Nuclear Engineering
208 Pasqua Engineering Building
The University of Tennessee
Knoxville TN 37996-2300
USA

Destouches, Mr. Christophe
CEA/Cadarache
DEN/DER/SPEX/LPE
batiment 242 - MASURCA
saint paul lez durance 13108
FRANCE
christophe.destouches@cea.fr

Draper-Donaldson, Susan
UNL
Dept. Industrial Engineering
175 Nebraska Hall
Lincoln NE 68588
USA
susandonaldson@direcway.com

Fernandes, Dr. Ana
Nuclear and Technological Institute
Estrada Nacional 10
Sacavem 2686-953
PORTUGAL
anafer@itn.pt

Flanders, Dr. T Michael
Reactor Physics Division
CSTE-DTC-WS-SV-R
White Sands Missile Range NM 88002-5158
USA
t.michael.flanders@us.army.mil

Gabriel, Tony A
Oak Ridge National Laboratory
P.O. Box 2008
Oak Ridge TN 37831
USA
forsbergcw@ornl.gov

Gilliam, Dr. David M
National Inst. of Standards and Technology
Reactor Bldg / B187
Gaithersburg MD 20899-8461
USA
David.Gilliam@nist.gov

Greenwood, Dr. Larry R
Pacific Northwest National Laboratory
P. O. Box 999, MS P7-22
Richland WA 99354
USA
larry.greenwood@pnl.gov

Griffin, Dr. Patrick J
Sandia National Laboratories
PO Box 5800
MS 1146
Albuquerque NM 87185-1146
USA
pjgriff@sandia.gov

Gritzay, Dr. Olena Oleksandrivna
Institute for Nuclear Research
pr. Nauky, 47
03680 Kyiv
UKRAINE
ogritzay@kinr.kiev.ua

Haghighat, Dr. Alireza
University of Florida
Nucl & Radiological Eng.
202 Nuclear Sci Bldg
Gainesville FL 32611
USA
haghighat@ufl.edu

Hawari, Prof. Ayman I
North Carolina State University
Department of Nuclear Engineering
P.O. Box 7909
Raleigh NC 27695-7909
USA
ayman.hawari@ncsu.edu

Hayashi, Dr. Katsumi
Hitachi, Ltd.
Saiwai-cho
Hitachi Ibaraki 317-8511
JAPAN
katsumi-a_hayashi@pis.hitachi.co.jp

Heimbach, Dr. Craig R
National Inst. of Standards and Technology
100 Bureau Drive
Mail Stop 8461
Gaithersburg MD 20899
USA
Craig.Heimbach@nist.gov

Hinrichsen, Paul
NNR-South Africa
P.O. Box 7106
Centurion 0046
SOUTH AFRICA
phinrich@nnr.co.za

Hógel, Mr. Josef
koda JS, a.s.
Orlik 266
31606 Plzen
CZECH REPUBLIC
Josef.Hogel@skoda-js.cz

Holden, Dr. Norman E
Brookhaven National Laboratory
National Nuclear Data Center
Building 197D
Upton NY 11973-5000
USA
holden@bnl.gov

Hordósy, Dr. Gábor
KFKI Atomic Energy Research Institute
1121 Budapest, Konkoly Thege út 29-33.
H-1525 Budapest 114, P.O.B. 49
Budapest
HUNGARY
hordosy@sunserv.kfki.hu

Houssay, Laurent P
Westinghouse Nuclear Services
PO Box 158
Madison PA 15663-0158
USA
houssal@westinghouse.com

Kalchenko, Oleksandr
Institute for Nuclear Research
pr. Nauky, 47
03680 Kyiv
UKRAINE
kaltchenko@kinr.kiev.ua

Kasraie, Mohammad
Department of Nuclear Engineering
208 Pasqua Engineering Building
The University of Tennessee
Knoxville TN 37996-2300
USA
mkasraie@ut.edu

Keith, Mr. Robert E
ITT Industries
5009 Centennial Blvd
Colorado Springs CO 80919
USA
robert.keith@itt.com

Khorsandi, Mr. Behrooz
The Ohio State University
650 Ackerman Rd
Columbus OH 43202
USA
khorsandi.1@osu.edu

Kim, Dr. Do Heon
Korea Atomic Energy Research Institute
P.O.Box 105
Yuseong
Daejeon 305-600
KOREA
kimdh@kaeri.re.kr

Kim, Byoung C
Korea Atomic Energy Research Institute
P.O.Box 105
Yuseong
Daejeon 305-600
KOREA
bckim@kaeri.re.kr

King, Dr. Donald B
Sandia National Laboratories
PO Box 5800
MS1136
Albuquerque NM 87185
USA
dbking@sandia.gov

Kirilova, Desislava
INRNE-BAS
72 Tsarigradsko shossee Blvd
1784 Sofia
BULGARIA
dkirilova@inrne.bas.bg

Konheiser, Jörg
FZ-Rossendorf
P.O. Box 510119
Dresden 01314
GERMANY
J.Konheiser@fz-rossendorf.de

Kotiluoto, Mr. Petri M
VTT Technical Research Centre of Finland
Otakaari 3 A, Espoo
P.O. Box 1608
FI-02044 VTT
FINLAND
petri.kotiluoto@vtt.fi

Lee, Dr. Yi-Kang
CEA/Saclay
DEN/DM2S/SERMA/LEPP
Gif sur Yvette Cedex 91191
FRANCE
yklee@cea.fr

Lippincott, Dr. Ezra Parvin
1776 McClure Road
Monroeville PA 15146
USA
eplippincott@adelphia.net

Longoni, Dr. Gianluca
Westinghouse Nuclear
P.O. Box 355
Pittsburgh PA 15235
USA
longong@westinghouse.com

Luker, Mr. Spencer Michael
Sandia National Laboratories
PO Box 5800
MS1146
Albuquerque NM 87185
USA
smluker@sandia.gov

Maeda, Mr. Shigetaka
Japan Nuclear Cycle Development Institute
4002, Narita
O-arai Ibaraki 311-1393
JAPAN
maeda-s@oec.jnc.go.jp

Mansur, Dr. Louis K
Oak Ridge National Laboratory
Oak Ridge TN 37831-6138
USA
mansurlk@ornl.gov

Marek, Dr. Milan
Nuclear Research Institute
Rez, plc
25068 Rez
CZECH REPUBLIC
mam@ujv.cz

Marshall, Frances
Irradiation Test Programs
Idaho National Laboratory
PO Box 1625
Idaho Falls ID 83415-7101
USA
Frances.Marshall@inl.gov

Miller, Dr. Laurence F
Department of Nuclear Engineering
208 Pasqua Engineering Building
The University of Tennessee
Knoxville TN 37996-2300
USA
lfmiller@utk.edu

Miller, Matthew
Department of Nuclear Engineering
208 Pasqua Engineering Building
The University of Tennessee
Knoxville TN 37996-2300
USA
mmiller5@utk.edu

Natsume, Toshihiro
Misubishi
1-1-1 Wadamisaki-cho
Hyogo-ku Kobe City
652-8585
JAPAN
toshihiro_natsume@mhi.co.jp

Noack, Dr. Karl Klaus
Forschungszentrum Rossendorf
Institute of Safety Research
Postfach 51 01 19
Dresden 01314
GERMANY
K.Noack@fz-rossendorf.de

Nolthenius, Mr. Henk J
Consultant, Institute of Nuclear Technology
Budapest Univ. of Technology & Economics
Muegyetem rkp. 3-9
Budapest H-1111
HUNGARY
henk@freestart.hu;
H.Nolthenius@worldonline.nl

Ošmera, Dr. Bohumil
Nuclear Research Institute
Husinec-Rez 130
Rez 25068
CZECH REPUBLIC
osm@ujv.cz

Perlov, Mary
Westinghouse
2010 Columbia Ave
Pittsburgh PA
USA
mvp46@pitt.edu

Plaschy, Michael
Paul Scherrer Institute (PSI)
NES/LRS
5232 Villigen PSI
SWITZERLAND
michael.plaschy@psi.ch

Polacek, Alexander
koda JS, a.s.
Orlik 266
31606 Plzen
CZECH REPUBLIC
alexandr.polaceak@skoda-js.cz

Remec, Dr. Igor
Oak Ridge National Laboratory
P.O. Box 2008
Oak Ridge TN 37831-6172
USA
remeci@ornl.gov

Rosseel, Dr. Thomas M
Oak Ridge National Laboratory
P.O. Box 2008
Oak Ridge TN 37831-6161
USA
rosseeltm@ornl.gov

Ruddy, Dr. Frank H
Westinghouse Electric Co.
Science & Technology Department
1332 Beulah Rd.
Pittsburgh PA 15235-5081
USA
ruddyfh@westinghouse.com

Sakurai, Dr. Yoshinori
Kyoto University Research Reactor Institute
Asashironishi 2-1010
Osaka 590-0494
JAPAN
ysakurai@rri.kyoto-u.ac.jp

Sallee, Dr. Wesley W
Reactor Physics Division
CSTE-DTC-WS-SV-R
White Sands Missile Range NM 88002-5158
USA
Wesley.Sallee@us.army.mil

Selby, Douglas L
Oak Ridge National Laboratory
1 Bethel Valley Rd
Building 7964-I
Oak Ridge TN 37831-6087
USA
selbydl@ornl.gov

Serén, Mr. Tom O
VTT Technical Research Centre of Finland
P.O.B. 1608
Otakaari 3 A, Espoo
FI-02044 VTT
FINLAND
tom.seren@vtt.fi

Slater, Dr. Charles O
Oak Ridge National Laboratory
Building 5700, MS-6172
P. O. Box 2008
Oak Ridge TN 37831-6172
USA
slaterco@ornl.gov

Smutny, Vladimir
Škoda JS, a.s
Orlik 266
31606 Plzen
CZECH REPUBLIC
vladimir.smutny@skoda-js.cz

Sparks, Mary H
Reactor Physics Division
CSTE-DTC-WS-SV-R
White Sands Missile Range NM 88002-5158
USA
mary.helen.sparks@us.army.mil

Stoller, Roger E
Oak Ridge National Laboratory
Bldg 45005, MS-6138
PO Box 2008
Oak Ridge TN 37831-6138
USA
rkn@ornl.gov

Thornton, Dr. Dean A
British Nuclear Group
Berkeley Centre
Berkeley Gloucestershire GL13 9PB
UNITED KINGDOM
dean.a.thornton@magnox.co.uk

Vehar, Dr. David W
Sandia National Laboratories
P.O. Box 5800
MS1136
Albuquerque NM 87185
USA
dwvehar@sandia.gov

Voorbraak, Mr. Willem P
Netherlands Research and Consultancy Group
P.O.Box 25
Petten 1755 ZG
THE NETHERLANDS
voorbraak@nrg-nl.com

Wagemans, Dr. Jan
SCK•CEN
Boeretang 200
Mol 2400
BELGIUM
jwageman@sckcen.be

Wagschal, Dr. Jehudah J
Hebrew University of Jerusalem
Racah Institute of Phys.
Safra Campus, Givat Ram
Jerusalem 91904
ISRAEL
wagschal@vms.huji.ac.il

Wenner, Mr. Mike T
University of Florida Transport Theory Group
104 Nuclear Science Center
Gainsville FL 32611-6550
USA
mtw125@ufl.edu

Williams, Prof. John G
University of Arizona
PO Box 210119
Dept. of Aerospace and Mech. Engineering
Tucson AZ 85721-0119
USA
jgw@engr.arizona.edu

Williams, Dr. Mark L
Oak Ridge National Laboratory
PO Box 2008
Oak Ridge TN 37831-6170
USA
williamsml@ornl.gov

Yoo, Choon Sung
Korea Atomic Energy Research Institute
P.O.Box 105
Yuseong
Daejeon 305-600
KOREA
csyoo@kaeri.re.kr

Zaritsky, Dr. Sergei M
RRC "Kurchatov Institute"
Kurchatov Sq. 1
Moscow 123 182
RUSSIA
zaritsky@adis.vver.kiae.ru

Zsolnay, Dr. Eva Maria
Institute of Nuclear Technology
Budapest Univ. of Technology & Economics
Muegyetem rkp. 3-9
Budapest H-1111
HUNGARY
Zsolnay@reak.bme.hu

Author Index

Subject Index

www.astm.org

ISBN: 978-08031-3412-6

ASTM Stock# STP1490